# ENGINEERING APPLICATIONS OF NEUROCOMPUTING

EDITED BY: Long Wang, Zhe Song, Zijun Zhang and Chao Huang

PUBLISHED IN: Frontiers in Neurorobotics, Frontiers in Energy Research, Frontiers in Genetics, Frontiers in Oncology and Frontiers in Environmental Science

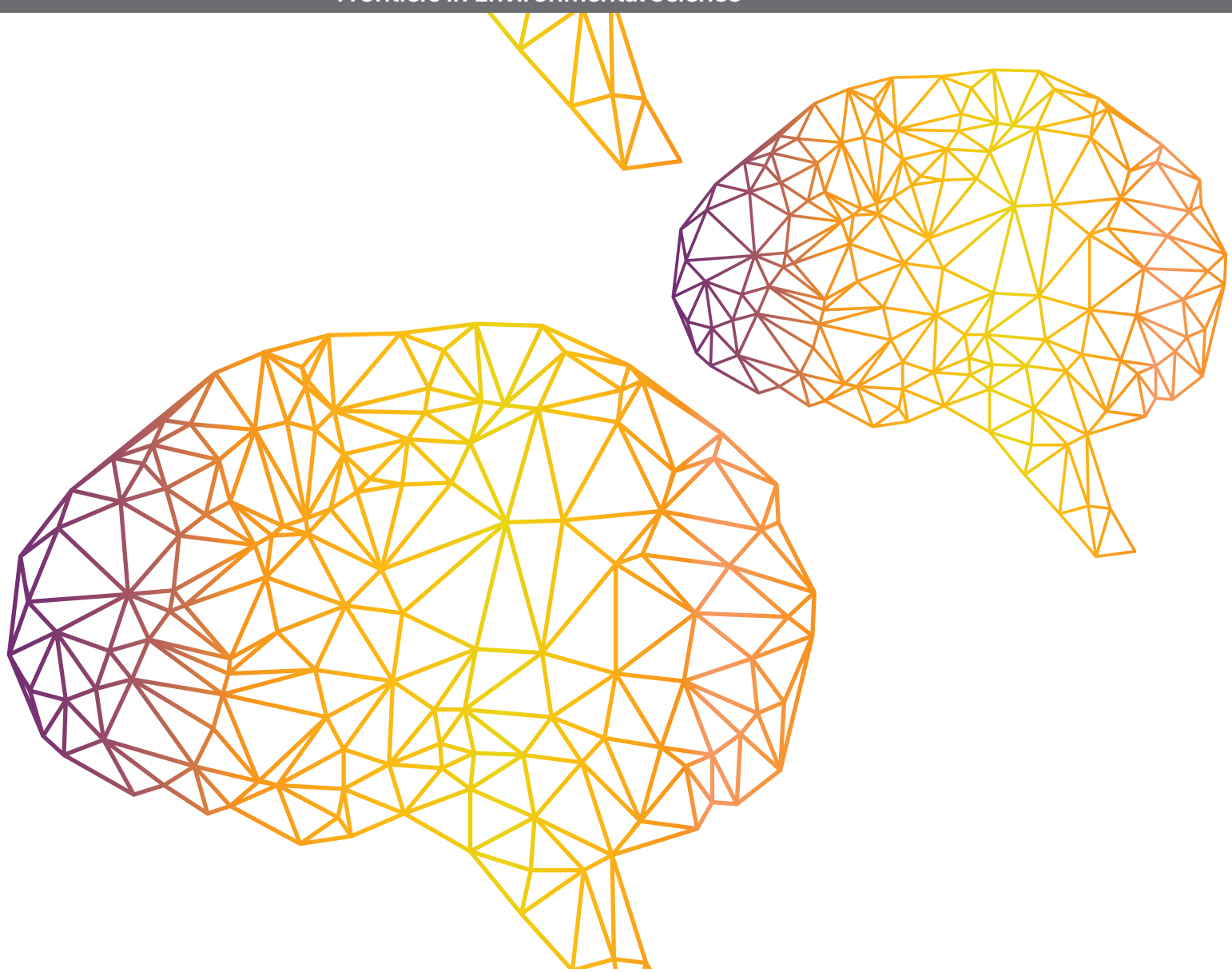

frontiers Research Topics

# frontiers



ISSN 1664-8714
ISBN 978-2-88974-540-1
DOI 10.3389/978-2-88974-540-1

## About Frontiers

Frontiers is more than just an open-access publisher of scholarly articles: it is a pioneering approach to the world of academia, radically improving the way scholarly research is managed. The grand vision of Frontiers is a world where all people have an equal opportunity to seek, share and generate knowledge. Frontiers provides immediate and permanent online open access to all its publications, but this alone is not enough to realize our grand goals.

## Frontiers Journal Series

The Frontiers Journal Series is a multi-tier and interdisciplinary set of open-access, online journals, promising a paradigm shift from the current review, selection and dissemination processes in academic publishing. All Frontiers journals are driven by researchers for researchers; therefore, they constitute a service to the scholarly community. At the same time, the Frontiers Journal Series operates on a revolutionary invention, the tiered publishing system, initially addressing specific communities of scholars, and gradually climbing up to broader public understanding, thus serving the interests of the lay society, too.

## Dedication to Quality

Each Frontiers article is a landmark of the highest quality, thanks to genuinely collaborative interactions between authors and review editors, who include some of the world's best academicians. Research must be certified by peers before entering a stream of knowledge that may eventually reach the public - and shape society; therefore, Frontiers only applies the most rigorous and unbiased reviews.
Frontiers revolutionizes research publishing by freely delivering the most outstanding research, evaluated with no bias from both the academic and social point of view. By applying the most advanced information technologies, Frontiers is catapulting scholarly publishing into a new generation.

## What are Frontiers Research Topics?

Frontiers Research Topics are very popular trademarks of the Frontiers Journals Series: they are collections of at least ten articles, all centered on a particular subject. With their unique mix of varied contributions from Original Research to Review Articles, Frontiers Research Topics unify the most influential researchers, the latest key findings and historical advances in a hot research area! Find out more on how to host your own Frontiers Research Topic or contribute to one as an author by contacting the Frontiers Editorial Office: frontiersin.org/about/contact

# ENGINEERING APPLICATIONS OF NEUROCOMPUTING

Topic Editors:
**Long Wang,** University of Science and Technology Beijing, China
**Zhe Song,** Nanjing University, China
**Zijun Zhang,** City University of Hong Kong Kowloon, SAR China
**Chao Huang,** University of Macau, China

**Citation:** Wang, L., Song, Z., Zhang, Z., Huang, C., eds. (2022). Engineering Applications of Neurocomputing. Lausanne: Frontiers Media SA.
doi: 10.3389/978-2-88974-540-1

# Table of Contents

frontiers in Neurorobotics

EDITORIAL
published: 28 January 2022
doi: 10.3389/fnbot.2022.839505

# Editorial: Engineering Applications of Neurocomputing

*Long Wang*[1], *Zhe Song*[2], *Zijun Zhang*[3] *and Chao Huang*[1,4]*

[1] School of Computer and Communication Engineering, University of Science and Technology Beijing, Beijing, China, [2] School of Business, Nanjing University, Nanjing, China, [3] School of Data Science, City University of Hong Kong, Kowloon, Hong Kong SAR, China, [4] State Key Laboratory of Internet of Things for Smart City, University of Macau, Macau, China

**Keywords: neurocomputing, engineering systems, neural networks, manufacturing, healthcare**

## Editorial on the Research Topic

## Engineering Applications of Neurocomputing

Inspired by how the human brain works, neurocomputing algorithms, including deep learning, reinforcement learning, and neurodynamic optimization, have achieved tremendous success in various applications across many domains, e.g., visual object tracking, speech recognition, human-level control, text understanding, and real-time optimization.

Various types of intelligent equipment and hardware devices have been developed to implement neurocomputing models for engineering systems. Deep learning has been employed for industrial robotic applications, including stereo reconstruction, object pose recognition, and product quality check. With the advent of the Internet of Things and edge computing devices, deep reinforcement learning has become popular in the predictive maintenance of engineering equipment. Embedded convolutional neural networks are widely utilized for autonomous vehicle control. The success of applying neurocomputing approaches and related hardware implementations in different engineering domains, such as intelligent manufacturing, energy internet, and smart healthcare, has proven the potential of employing neurocomputing for solving real problems in various engineering fields.

In recent years advances in sensor and data storage technologies have enabled the accumulation of a large amount of data from engineering systems. Driven by big data generated from engineering systems, neurocomputing, and its hardware implementation will continually transform engineering systems into more intelligent forms.

This Research Topic aims to provide a forum for researchers to present the latest research on applications of neurocomputing algorithms and neurocomputing-based hardware in engineering systems. It brings together 14 high quality papers reporting on the latest applications of neurocomputing in transportation, manufacturing, biomedical engineering, electrical engineering, and knowledge management.

In the paper entitled "*Self-Triggered Consensus of Vehicle Platoon System With Time-Varying Topology*," Wang et al. designed a secure event-triggered controller considering the safe distance for the vehicle platoon system. Based on the new event-triggered function, a more energy efficient self-triggered control strategy was developed by using the Taylor formula. The new self-triggered control strategy could avoid continuous calculation and measurement of vehicles.

The paper on "*Industrial Control Malicious Traffic Anomaly Detection System Based on Deep Autoencoder*" by Wang et al. proposes a method of detecting abnormal traffic in industrial control networks based on autoencoder technology. The Kullback–Leibler divergence was added to the loss function of the proposed model to improve the ability of feature extraction and the ability to recover raw data. The gas pipeline dataset was used to verify the performance of the proposed method.

OPEN ACCESS

***Edited and reviewed by:***
*Florian Röhrbein,*
*Technische Universität Chemnitz, Germany*

***Correspondence:**
*Chao Huang*
*chao.huang@my.cityu.edu.hk*

***Received:*** *20 December 2021*
***Accepted:*** *03 January 2022*
***Published:*** *28 January 2022*

***Citation:***
*Wang L, Song Z, Zhang Z and Huang C (2022) Editorial: Engineering Applications of Neurocomputing. Front. Neurorobot. 16:839505. doi: 10.3389/fnbot.2022.839505*

In a contribution on "*Data-Driven Hybrid Equivalent Dynamic Modeling of Multiple Photovoltaic Power Stations Based on Ensemble Gated Recurrent Unit*" Long et al. report on a data-driven hybrid equivalent model for the dynamic response process of the multiple PV power stations. The data-driven hybrid equivalent model contained the simple equivalent model and data-driven error correction model. The simulation results validated the super-performance of the proposed model both in response speed and accuracy.

Sun et al. contribute a paper on "*AutoPath: Image-Specific Inference for 3D Segmentation*," which introduces *AutoPath*, an image-specific inference approach for more efficient 3D segmentations. The proposed AutoPath dynamically selected enabled residual blocks regarding different input images during inference, thus effectively reducing total computation without degrading segmentation performance. Experimental results on a liver CT dataset showed that the proposed approach not only provided an efficient inference procedure but also attained satisfactory segmentation performance.

A paper on "*Boosting Knowledge Base Automatically via Few-Shot Relation Classification*" by Pang et al. investigated a fully automatic method to train a relation classification model which facilitates to boost the knowledge base. In the proposed method, various multiple instance learning methods were incorporated into the classic prototypical networks, reducing sentence-level noises.

Gu et al.'s article "*Investigating the Impact of the Missing Significant Objects in Scene Recognition Using Multivariate Pattern Analysis*" adopted multivariate pattern analysis to explore the object-scene association in scene recognition when different amounts of significant objects were masked. The analysis results suggested that the lateral occipital complex was sensitive to the loss of significant objects and mainly involved in scene recognition by the object-scene semantic association.

In the paper "*Machine Learning Models to Predict Primary Sites of Metastatic Cervical Carcinoma From Unknown Primary*," Lu et al. conducted a series of bioinformatics analyses based on a dataset from The Cancer Genome Atlas (TCGA) RNA-Seq data of squamous cancer and TCGA Pan-Cancer data. Three machine learning models, random forest, neural networks, and support vector machine, were developed to explore potentially effective tools to distinguish these squamous cancers.

In their contribution examining "*A Manufacturing-Oriented Intelligent Vision System Based on Deep Neural Network for Object Recognition and 6D Pose Estimation*" Liang et al. present a new two-stage intelligent vision system based on a deep neural network with RGB-D image inputs for object recognition and 6D pose estimation. A dense-connected network fusing multi-scale features was first built to segment the objects from the background. The 2D pixels and 3D points in cropped object regions were then fed into a pose estimation network to make object pose predictions based on the fusion of color and geometry features.

The paper titled "*Artificial Intelligence-Based Application to Explore Inhibitors of Neurodegenerative Diseases*" by Deng et al. explores an integrated new approach for finding lead compounds that inhibit galectin-3, by combining universal artificial intelligence algorithms with traditional drug screening methods. Manifold artificial intelligence algorithms were performed to validate the docking results and further screen compounds.

In their "*Energy Investment Risk Assessment for Nations Via Seq2seq Model*" Liang et al. propose a sequence to sequence model to evaluate the energy investment risk of 50 countries. Bi-long-short term memory was used as an encoder to process the historical statistics in the proposed method.

The paper on "*A Relational Adaptive Neural Model for Joint Entity and Relation Extraction*" by Duan et al. describes a relational-adaptive entity relation joint extraction model based on multi-head self-attention and densely connected graph convolution network. In the model, the multi-head attention mechanism was specifically used to assign weights to multiple relation types among entities to ensure that the probability space of multiple relations was not mutually exclusive.

An article on the "*Classification of Metastatic and Non-Metastatic Thoracic Lymph Nodes in Lung Cancer Patients Based on Dielectric Properties Using Adaptive Probabilistic Neural Networks*" by Lu et al. proposes a classifier to identify metastatic and non-metastatic thoracic lymph nodes in lung cancer patients based on dielectric properties. Compared with the other methods, the proposed classifier achieved a higher classification accuracy based on dielectric property data collected from lung cancer patients.

Xiang et al.'s contribution on the "*Prediction of Dangerous Driving Behavior Based on Vehicle Motion State and Passenger Feeling Using Cloud Model and Elman Neural Network*" presentes a new method for dangerous driving behavior prediction using a hybrid model consisting of cloud model and Elman neural network based on vehicle motion state estimation and passenger's subjective feeling scores.

The paper titled "*A New Way of Airline Traffic Prediction Based on GCN-LSTM*" by Yu employed graph convolutional neural network and long short memory network to construct an airline traffic prediction system with short-term prediction ability.

These successful applications of neurocomputing in various domains demonstrate the significant potential of applying neurocomputing approaches to solving complex engineering problems. With the help of big data and increasing computing power, neurocomputing will play a vital role in future engineering systems.

## AUTHOR CONTRIBUTIONS

LW wrote the manuscript. ZZ, ZS, and CH edited the manuscript. All authors contributed to the article and approved the submitted version.

## FUNDING

This work was supported in part by the National Natural Science Foundation of China under Grant 62002016, in part by the Guangdong Basic and Applied Basic Research Foundation under Grants 2020A1515110431 and 2019A1515111165, and in part by

the Fundamental Research Funds for the Central Universities and the Youth Teacher International Exchange & Growth Program under Grant QNXM20210037.

**Conflict of Interest:** The authors declare that the research was conducted in the absence of any commercial or financial relationships that could be construed as a potential conflict of interest.

**Publisher's Note:** All claims expressed in this article are solely those of the authors and do not necessarily represent those of their affiliated organizations, or those of the publisher, the editors and the reviewers. Any product that may be evaluated in this article, or claim that may be made by its manufacturer, is not guaranteed or endorsed by the publisher.

frontiers in Neurorobotics

ORIGINAL RESEARCH
published: 24 July 2020
doi: 10.3389/fnbot.2020.00049

# *AutoPath*: Image-Specific Inference for 3D Segmentation

*Dong Sun, Yi Wang*, Dong Ni and Tianfu Wang**

*National-Regional Key Technology Engineering Laboratory for Medical Ultrasound, Guangdong Provincial Key Laboratory of Biomedical Measurements and Ultrasound Imaging, School of Biomedical Engineering, Health Science Center, Shenzhen University, Shenzhen, China*

In recent years, deep convolutional neural networks (CNNs) has made great achievements in the field of medical image segmentation, among which residual structure plays a significant role in the rapid development of CNN-based segmentation. However, the 3D residual networks inevitably bring a huge computational burden to machines for network inference, thus limiting their usages for many real clinical applications. To tackle this issue, we propose *AutoPath*, an image-specific inference approach for more efficient 3D segmentations. The proposed *AutoPath* dynamically selects enabled residual blocks regarding different input images during inference, thus effectively reducing total computation without degrading segmentation performance. To achieve this, a policy network is trained using reinforcement learning, by employing the rewards of using a minimal set of residual blocks and meanwhile maintaining accurate segmentation. Experimental results on liver CT dataset show that our approach not only provides efficient inference procedure but also attains satisfactory segmentation performance.

**Keywords: segmentation, 3D residual networks, reinforcement learning, policy network, image-specific inference**

OPEN ACCESS

***Edited by:***
*Long Wang,*
*University of Science and Technology Beijing, China*

***Reviewed by:***
*Ziyue Xu,*
*Nvidia, United States*
*Wellington Pinheiro dos Santos,*
*Federal University of Pernambuco, Brazil*

****Correspondence:***
*Yi Wang*
*onewang@szu.edu.cn*
*Tianfu Wang*
*tfwang@szu.edu.cn*

***Received:*** *02 June 2020*
***Accepted:*** *19 June 2020*
***Published:*** *24 July 2020*

***Citation:***
*Sun D, Wang Y, Ni D and Wang T (2020) AutoPath: Image-Specific Inference for 3D Segmentation. Front. Neurorobot. 14:49. doi: 10.3389/fnbot.2020.00049*

## 1. INTRODUCTION

Automated segmentation is useful to assist doctors in disease diagnosis and surgical/treatment planning. Since deep learning (LeCun et al., 2015) has utilized widely, medical image segmentation has made great progresses. Various architectures of deep convolutional neural networks (CNNs) have been proposed and successfully introduced to many segmentation applications. Among various architectures, the residual structures in ResNet (He et al., 2016) play an important role in the rapid development of CNN-based segmentation. The backbone which contains the residual blocks has become essential support for many segmentation models, such as DeepLab V3 (Chen et al., 2017), HD-Net (Jia et al., 2019), Res-UNet (Xiao et al., 2018), and so on. Despite the superior performance of residual blocks, these structures inevitably bring a huge computational burden for network inference. This leads to the difficulty of introducing deep models (such as 3D ResNet-50/101) in clinical practice.

Recently, some strategies for model compression have been devoted to tackling the problem of large computation, among which the network pruning approaches have been extensively investigated (Li et al., 2016; He et al., 2017, 2018; Liu et al., 2017; Luo et al., 2017). In addition, other researches are focusing on lightweight network architectures (Howard et al., 2017; Ma et al., 2018; Mehta et al., 2018). However, all aforementioned methods including pruning, knowledge distillation, and lightweight structures all require network retraining and hyper-parameters retuning, which may consume plenty of extra time.

This paper explores the problem of dynamically distributing computation across all residual blocks in a trained ResNet for image-specific segmentation inference (see **Figure 1**). Relevant studies have been investigated in classification tasks. Teerapittayanon et al. (2016) developed BranchyNet to conduct fast inference via early exiting from deep neural networks. Graves (2016) devised an adaptive computation time (ACT) approach for recurrent neural network (RNN), by designing a halting unit whose activation indicates the termination probability of computations. Huang et al. (2016) proposed stochastic depth for deep networks, a training strategy that enables the seemingly contradictory setup to train short networks and use deep networks at test time. Veit et al. (2016) proposed a description of residual networks in classification showing that residual blocks can be seen as a collection of many paths and they do not strongly depend on each other thus can be selectively dropped. However, there are two obvious differences between segmentation and classification tasks: (1) The neural networks for classification often take a short approach, such as identifying a car by its shadow. Segmentation is classifying each pixel, thus the neural networks cannot be lazy; (2) Classification can work with local features, but segmentation needs to take global information (such as shape priors) into consideration.

In this study, we propose *AutoPath*, an image-specific strategy to design the inference path that uses minimal residual blocks but still preserves satisfactory segmentation accuracy. Specifically, a policy network is trained using reinforcement learning, by using the rewards of involving a minimal set of residual blocks and meanwhile maintaining accurate segmentation. To the best of our knowledge, this is the first investigation of the dynamic inference path for 3D segmentation using residual networks. Experimental results demonstrate that our strategy not only provides efficient inference procedure but also attains satisfactory segmentation accuracy.

## 2. METHODS

**Figure 2** illustrates the proposed framework. Given a new 3D volume, the policy network outputs "keep" or "drop" decisions for each residual block in the pretrained 3D DeepLab V3 network. Such image-specific inference path is then used for the segmentation prediction. The policy network is trained using reinforcement learning by rewarding accurate segmentation with minimal involved blocks.

### 2.1. 3D Residual Backbone

We implement a 3D DeepLab V3 based on the original DeepLab V3 (Chen et al., 2017), and further set its backbone to 3D ResNet according to ResNet (He et al., 2016) (the classification head is removed). We then specifically modify the 3D residual blocks to achieve better baseline results. Optimized 3D residual blocks assign the stride of each convolutional layer along $z$ axis to 1 to constrain downsampling along the slice direction. In addition, we replace the straightforward upsampling operations after atrous spatial pyramid pooling (ASPP) with a decoder consisting of a series of convolutions according to Chen et al. (2019).

### 2.2. *AutoPath* Strategy

Backbone, as an indispensable part of segmentation networks, occupies most of the memory and calculation. Generally, the popular residual backbone consists of multiple repeated residual blocks. We regard each block as an independent decision unit by assuming that different blocks do not share strong dependencies in segmentation. Then as shown in **Figure 2**, we introduce

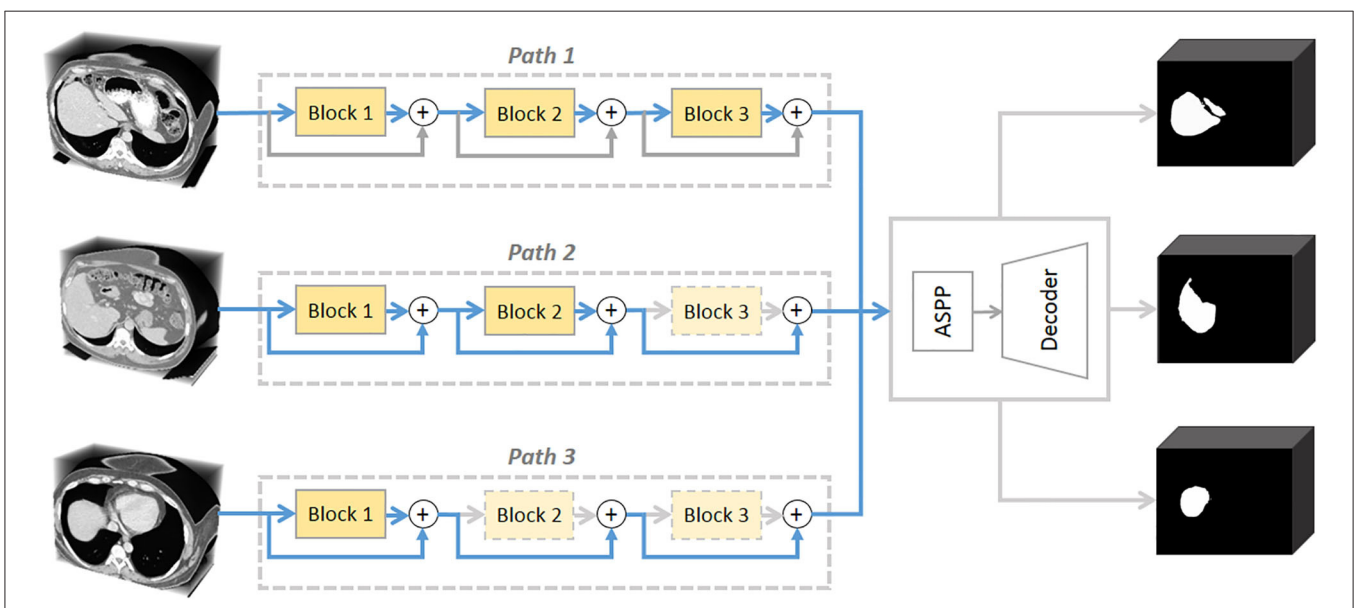


**FIGURE 1 |** A conceptual illustration of the proposed *AutoPath*. The motivation is to dynamically distributing computation across a ResNet. *AutoPath* selectively drops unnecessary residual blocks for image-specific inference. Such inference simultaneously achieves efficiency and accuracy.

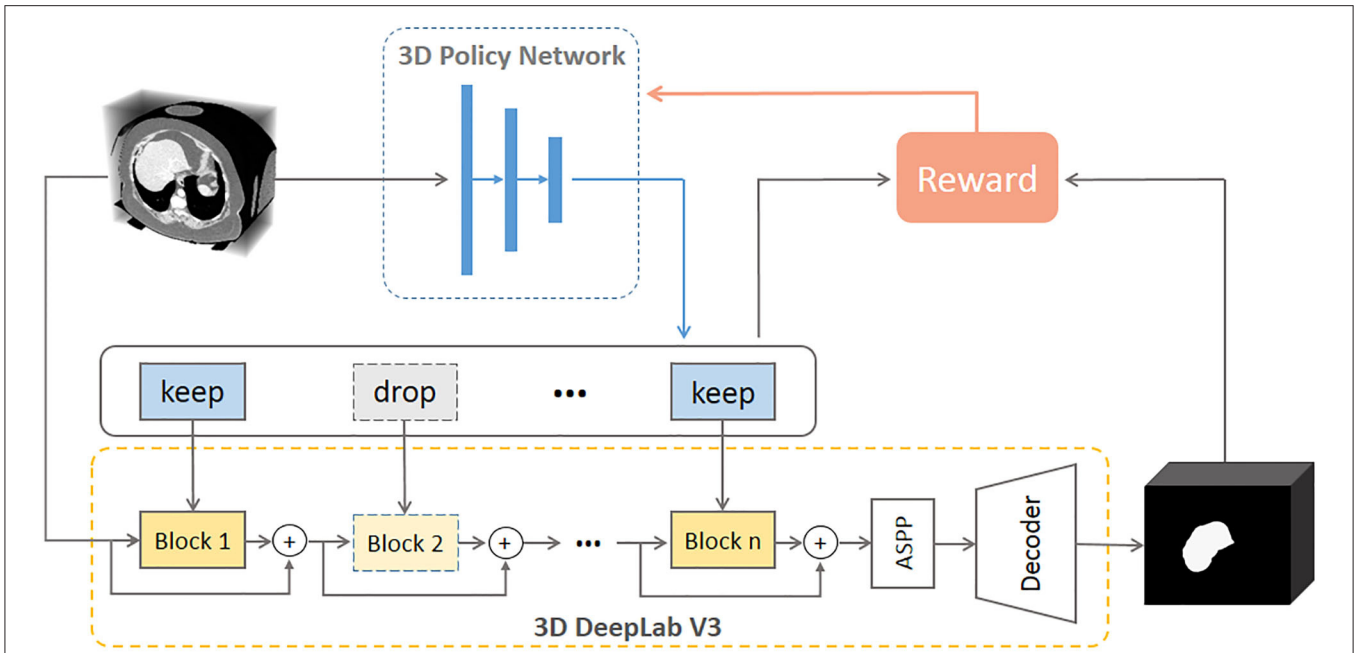


**FIGURE 2 |** Illustration of the proposed network. The 3D policy network is trained using reinforcement learning with the reward as both segmentation performance and residual block usage. The 3D DeepLab V3 leverages the decisions made by the policy network to keep or drop corresponding residual blocks then outputs the segmentation prediction for a given 3D volume. ASPP: atrous spatial pyramid pooling.

reinforcement learning to train a policy network to intelligently conduct block dropping and explore the inference path that generates accurate segmentation with fewer blocks.

### 2.2.1. 3D Policy Network

Considering the actions for residual blocks can only be "keep" or "drop," we define the policy for block dropping as a Bernoulli distribution (Wu et al., 2018):

$$\pi_{\mathbf{W}}(\mathbf{a}|\mathbf{x}) = \prod_{n=1}^{N} \mathbf{p}_n^{\mathbf{a}_n}(1-\mathbf{p}_n)^{1-\mathbf{a}_n}, \tag{1}$$

where $\mathbf{x}$ denotes the input 3D image and $N$ is the total number of residual blocks in the pretrained 3D DeepLab V3 network. $\mathbf{W}$ denotes the weights of the policy network. $\mathbf{p}$ represents the "drop" likelihood ($\mathbf{p}_n \in [0, 1]$), and is the policy network's output after sigmoid activation. The action vector $\mathbf{a}$ is determined by $\mathbf{p}$, where $\mathbf{a}_n = 0$ refers to drop the $n$-th block, otherwise keeping the corresponding block.

### 2.2.2. Reward Function

3D Segmentation is generally considered to be voxel-level classification, thus every voxel has to receive evaluation feedback for the corresponding action. Thus, we design the following voxel-level reward function:

$$R(\mathbf{a}) = \begin{cases} 1 - (\frac{|\mathbf{a}|_0}{N})^2 & if\ VDC(i) = \frac{1}{2} \\ -\tau & if\ VDC(i) = 1, \end{cases} \tag{2}$$

where $(\frac{|\mathbf{a}|_0}{N})^2$ calculates the block usage. When the prediction of a voxel $i$ is the same as the label, we encourage dropping more blocks by giving a larger reward to the policy. On the other hand, we penalize using $\tau$, which balances block usage and segmentation accuracy. When $\tau$ is a large value, the policy is prone to have a more solid segmentation result; otherwise, it is more likely to drop blocks. We designed Voxel Dice Coefficient (VDC) to identify which pixel should be penalized:

$$VDC(i) = \frac{2 * (y_i' \bigcap y_i) + 1}{y_i' + y_i + 1}, \tag{3}$$

where $y_i \in \{0, 1\}$ and $y_i' \in \{0, 1\}$ denotes the ground truth and prediction for voxel $i$, respectively.

### 2.2.3. Learning Strategy

Finally, we maximize the expected reward $\mathbb{E}_{\mathbf{a}\sim\pi_{\mathbf{W}}}[R(\mathbf{a})]$ to train the policy network. We employ policy gradient to calculate the gradient of the expected reward:

$$\nabla_{\mathbf{W}}\mathbb{E}_{\mathbf{a}\sim\pi_{\mathbf{W}}}[R(\mathbf{a})] = \mathbb{E}[R(\mathbf{a})\nabla_{\mathbf{W}}\log\pi_{\mathbf{W}}(\mathbf{a}|\mathbf{x})] \tag{4}$$

$$= \mathbb{E}[R(\mathbf{a})\nabla_{\mathbf{W}}\log\prod_{n=1}^{N}\mathbf{p}_n^{\mathbf{a}_n}(1-\mathbf{p}_n)^{1-\mathbf{a}_n}] \tag{5}$$

$$= \mathbb{E}[R(\mathbf{a})\nabla_{\mathbf{W}}\sum_{n=1}^{N}\log[\mathbf{p}_n\mathbf{a}_n + (1-\mathbf{p}_n)(1-\mathbf{a}_n)]]. \tag{6}$$

The Equation (6) can be approximated by Monte-Carlo sampling strategy.

To achieve efficient training, we further employ curriculum learning (Bengio et al., 2009) to train the policy network. Specifically, for epoch $c$ ($c < N$), the first $N - c$ blocks are kept, while the learning is conduct on the last $c$ blocks. As $c$ increases, more and more blocks join the optimization until all blocks are involved. Algorithm 1 shows the training procedure of the proposed network.

# 3. EXPERIMENTS AND RESULTS

## 3.1. Materials and Implementation Details

### 3.1.1. Materials

Experiments were carried on liver CT images from LiTS challenge (Bilic et al., 2019). LiTS dataset contains 131 contrast-enhanced CT images acquired from six clinical centers around the world. 3DIRCADb is a subset from the LiTS dataset with 22 cases. Our network was trained using 109 cases from LiTS without data from 3DIRCADb, and then evaluated on the 3DIRCADb subset using Dice metric.

**Algorithm 1 |** Training of the policy network

**Input** : An input 3D image $\mathbf{x}$ and corresponding label $\mathbf{y}$

Initialize policy network $\mathbf{W}$ randomly
Set epochs for curriculum training to $C$
**for** $c \leftarrow 1$ *to* $C$ **do**
  $\mathbf{p} \leftarrow$ output of policy network
  **if** $c < N$ **then**
    set $\mathbf{p}[1 : N - c] = 1$ ▷ curriculum training
  **end**
  $\mathbf{a} \sim Bernoulli(\mathbf{p})$
  Run the 3D DeepLab V3 based on $\mathbf{a}$
  Calculate $R(\mathbf{a})$ using Eq (2)
  Gradients back-propagation using Eq (6)
**end**

### 3.1.2. Implementation Details

The experiments were conducted using 3D DeepLab V3 network with 18-layers and 50-layers, respectively. We adopted Adam (Kingma and Ba, 2014) with learning rate of 0.01 and batch size of 4 and 11 for ResNet-18 and ResNet-50, respectively. In addition, we utilized learning rate scheduler that decreases by 0.1 for every 100 epochs. The maximum epoch was set to 400.

For the policy network, we set learning rate to 0.001, $\tau$ to 50 and used the batch size of 1 and 5 for ResNet-18 and ResNet-50, respectively.

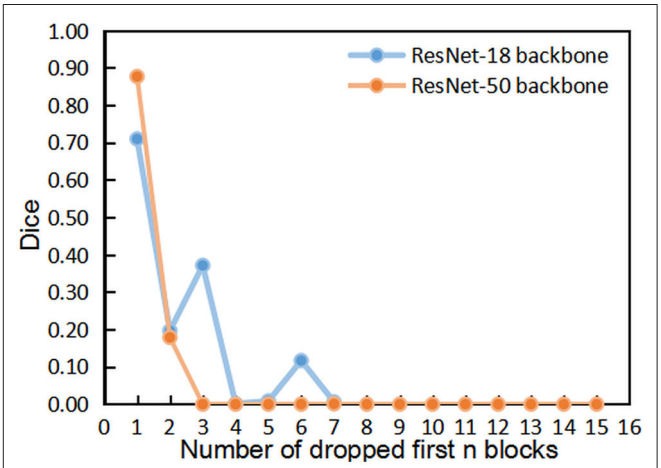


**FIGURE 4 |** The comparisons of segmentation performance from dropping the first $n$ blocks of residual backbones.

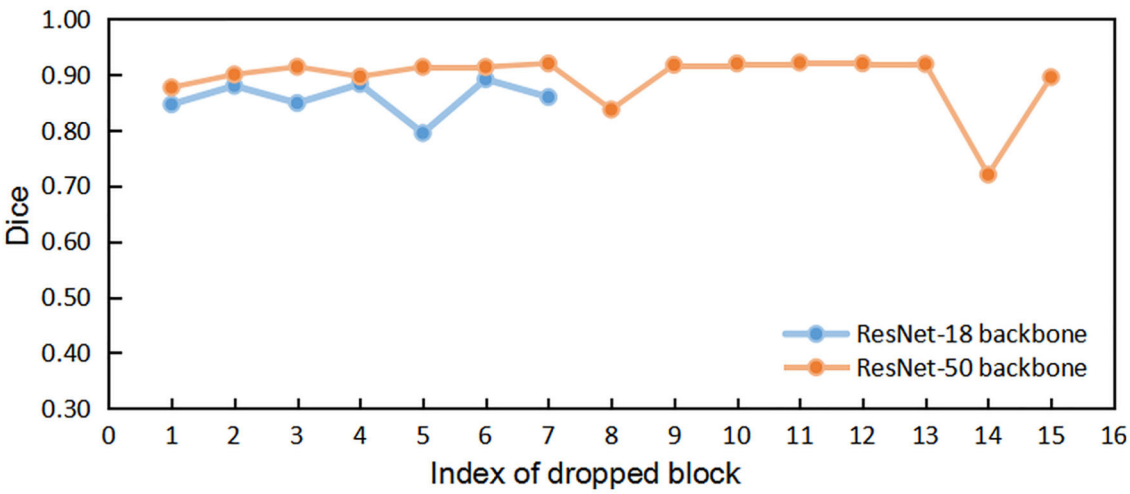


**FIGURE 3 |** The comparisons of segmentation performance from dropping different individual block of residual backbones.

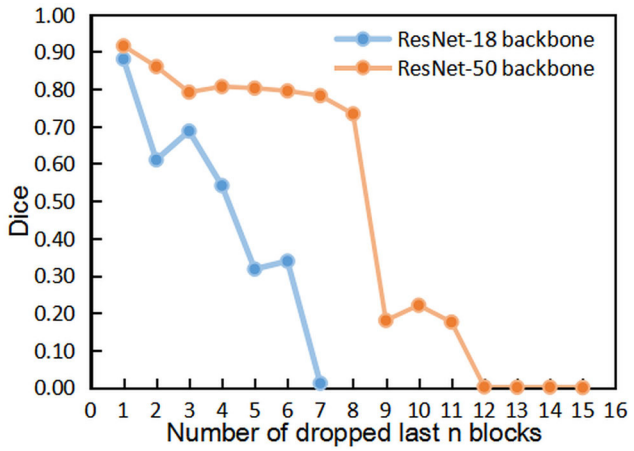


**FIGURE 5 |** The comparisons of segmentation performance from dropping the last *n* blocks of residual backbones.

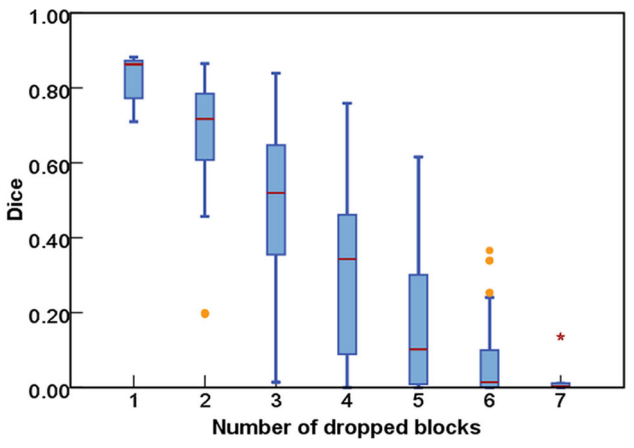


**FIGURE 6 |** The comparisons of segmentation performance from randomly dropping *n* blocks of ResNet-18.

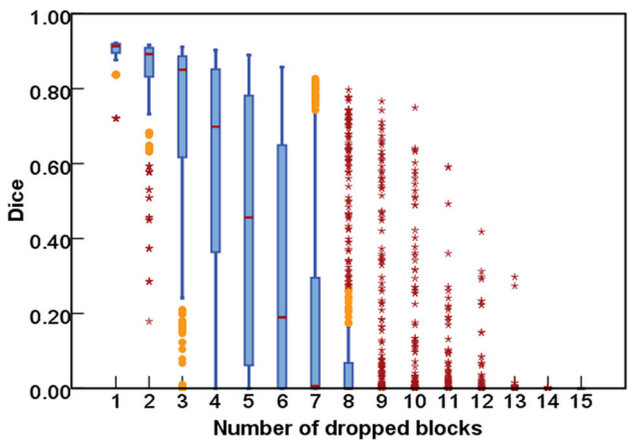


**FIGURE 7 |** The comparisons of segmentation performance from randomly dropping *n* blocks of ResNet-50.

## 3.2. Performance Evaluation

### 3.2.1. Investigation of Blocks' Dependencies

We first implemented the DropN strategy, which means dropping a single *n*-th block in residual backbone, to observe the dependencies of different blocks. We executed this strategy to ResNet-18 and ResNet-50 backbone which has 8 and 16 residual blocks, respectively. **Figure 3** shows that dropping individual block from residual backbone has a minimal impact on Dice evaluation except for few blocks. This suggests that different blocks in ResNet backbone do not share strong dependencies and most blocks are not indispensable for the accurate segmentation. Thus, dropping blocks in inference is feasible for segmentation.

### 3.2.2. Heuristic Dropping Strategies

We then evaluated three manual dropping strategies as follows:

1) DropFirstN, which means to drop all blocks before the *n*-th block;
2) DropLastN, which means to drop all blocks after the *n*-th block;
3) DropRandomN, which means to drop *n* blocks randomly.

Note that DropRandomN is a random strategy, thus for each *n* we performed 100 and 500 repeated experiments for ResNet-18 and ResNet-50, respectively.

**Figures 4**, **5** show the results of DropFirstN and DropLastN, respectively. It can be observed from **Figure 4** that first several blocks were relatively important for ResNet backbone. The Dice value dropped to almost 0 when the first three blocks were dropped. As shown in **Figure 5**, for ResNet-50, dropping the last 8 blocks didn't affect segmentation performance sharply.

As for the DropRandomN, with the increase of dropped blocks in the shallow backbone, the segmentation performance gradually decreased, as seen in **Figure 6**. In contrast, for the ResNet-50, the average Dice was almost 0 when 8 blocks were randomly dropped, as shown in **Figure 7**.

**TABLE 1 |** The comparisons of segmentation performance from heuristic strategies and *AutoPath* at the same dropping level.

| | ResNet-18 backbone | | ResNet-50 backbone | |
|---|---|---|---|---|
| | Dice | Dropped blocks | Dice | Dropped blocks |
| DropFirstN | 19.67% | 2 | 0.00% | 4 |
| DropLastN | 61.03% | 2 | 80.66% | 4 |
| DropRandomN | 67.80% | 2 | 59.11% | 4 |
| Ours | 87.11% | 2.4 | 89.14% | 4.5 |
| Full backbone | 89.54% | 8 used | 93.16% | 16 used |

### 3.2.3. *AutoPath*

We compared the segmentation performance of heuristic strategies (i.e., DropFirstN, DropLastN, DropRandomN) and the proposed *AutoPath* at the same dropping level. **Table 1** reports that by considering image-specific input, our *AutoPath* can achieve an average block dropping ratio of more than

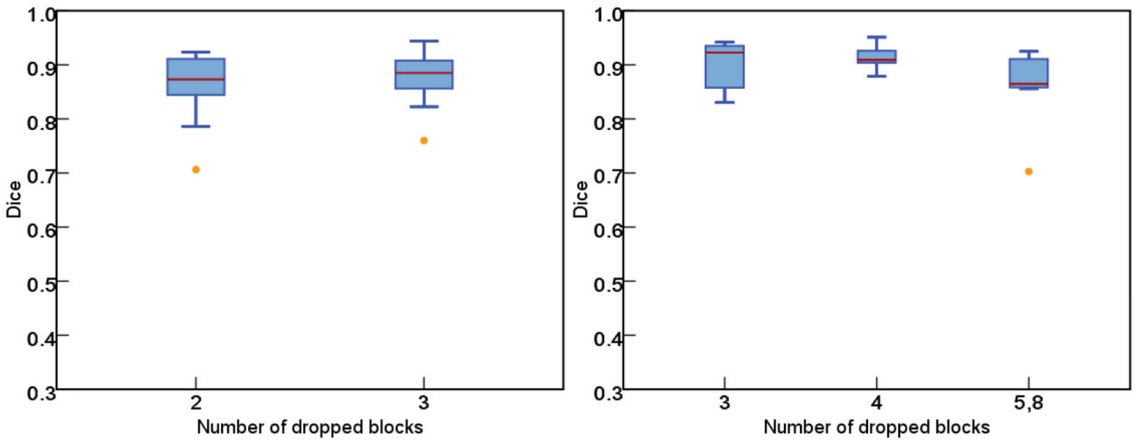


**FIGURE 8 |** The statistics of the *AutoPath* for all testing data. For most cases, *AutoPath* can provide high quality segmentation with fewer block usage. Left: ResNet-18; Right: ResNet-50.

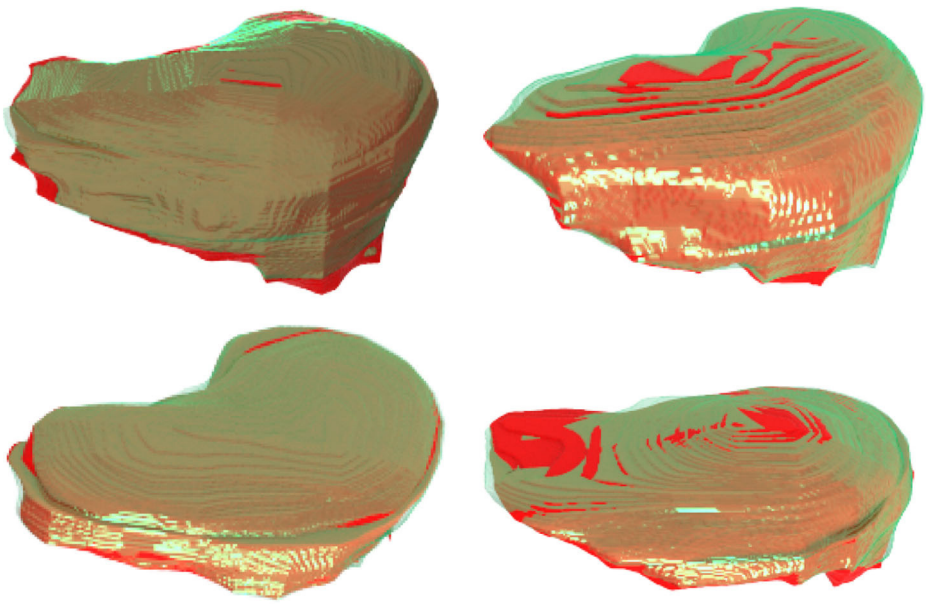

**FIGURE 9 |** 3D visualizations of some segmentation results obtained using *AutoPath* (green) and full backbone (red), respectively. It can be observed that the segmentation performance from the proposed *AutoPath* was comparable to that of the full backbone architecture.

25%, meanwhile with only 2 and 4% decrease of Dice values for ResNet-18 and ResNet-50, respectively. Also can be seen from **Table 1** that by dropping the same number of residual blocks, our *AutoPath* outperformed other heuristic strategies by a large margin.

**Figure 8** further plots the statistics of the *AutoPath* for all testing data. For the image-specific inference, the *AutoPath* selectively dropped 2 or 3 blocks for ResNet-18, and 3, 4, 5, or 8 blocks for ResNet-50. For most cases, *AutoPath* can maintain a high quality segmentation with fewer block usage, which demonstrates its promising application for real clinical circumstance. **Figures 9**, **10** visualizes some 3D and 2D segmentation results obtained using *AutoPath* and full backbone, respectively. It can be observed that the segmentation performance from the proposed *AutoPath* was comparable to that of the full backbone architecture.

## 4. DISCUSSION AND CONCLUSION

This paper develops a reinforcement learning method to select image-specific and efficient inference paths for 3D segmentation, which addresses the problem of huge computational burden for 3D segmentation networks. To our best knowledge, this is the first study of the dynamic inference path for 3D segmentation. We refer to it as *AutoPath*, which can leverage an image-specific path including fewer residual blocks to attain accurate prediction.

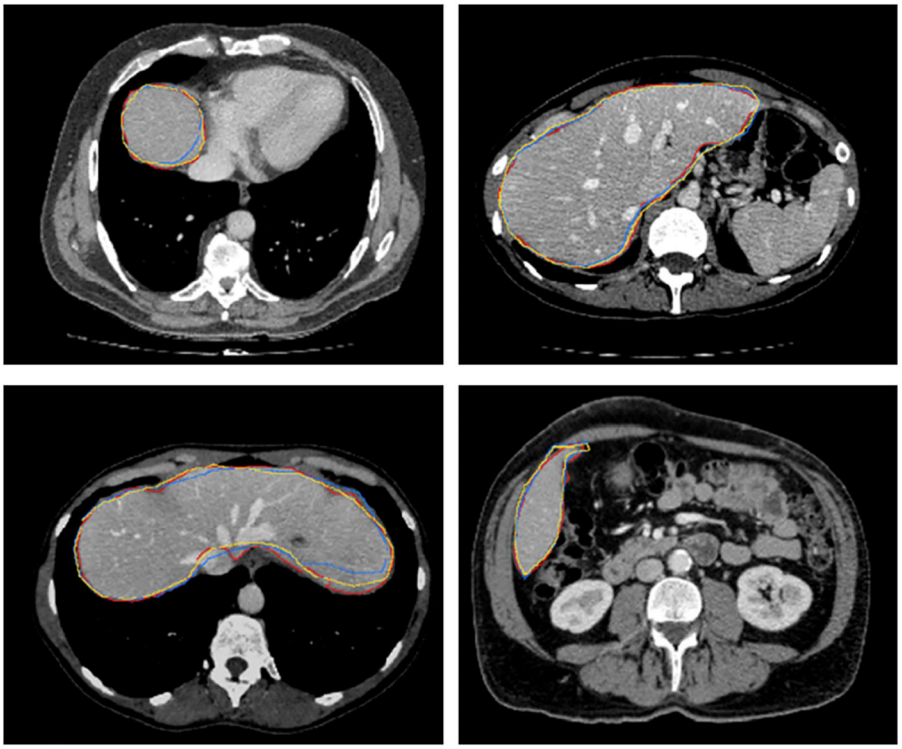

**FIGURE 10 |** 2D slices of some segmentation results obtained using *AutoPath* (yellow), full backbone (blue), and the ground truth (red), respectively.

To achieve this, we train a network to determine the policy of block dropping and the pretrained segmentation network executes inference according to this policy. We conducted extensive experiments on the liver CT dataset using 3D DeepLab V3 network with 18-layers and 50-layers, respectively. Experimental results demonstrate that *AutoPath* is a reliable method for the dynamic inference in 3D segmentation.

Deep neural networks offer excellent segmentation performance, yet their computational expense restrict their clinical usage, especially for the 3D segmentation. To tackle this issue, various compressed models have been proposed (Li et al., 2016; He et al., 2017, 2018; Liu et al., 2017; Luo et al., 2017). While the network efficiency has been improved somehow, the solution is a one-size-fit-all network that omits different inputs' complexity. In contrast, we investigate adaptively allocating computation across a CNN model according to specific input. Furthermore, our image-specific inference is conducted on the trained network, thus do not have to spend extra time for the network retuning.

In this study, although the DeepLabV3 network was employed as backbone to equip with residual structures, it could be replaced using other backbone architectures. With regard to our image-specific inference method, the residual structures are the most crucial components but not the design of backbones. In medical segmentation tasks, various CNN-based approaches have employed residual structures. For example, the encoder of HD-Net (Jia et al., 2019) is based on 3D ResNet-101 and BOWDA-Net (Zhu et al., 2019) utilizes dense connection multiple times. In addition, Xiao et al. (2018) propose a weighted Res-UNet which replaces the convolution block with residual block to achieve remarkable results in retina vessel segmentation. Furthermore, there are some improved structures based on ResNet, such as ResNext (Xie et al., 2017), SE-Net (Hu et al., 2018), and SK-Net (Li et al., 2019). Our proposed method can be utilized to dynamically distribute computation across their residual blocks for image-specific segmentation inference.

Our current scheme mainly focuses on the usage reduction of the residual blocks due to their independent design. It may not be directly adopted to other network configurations without residual structures. Future work may further investigate the dynamic inference for other network configurations. In addition, although our method attained satisfactory performance on liver CT volumes, further validations on large amount of various medical images will be conducted to investigate the robustness and generalization ability of the proposed scheme.

## DATA AVAILABILITY STATEMENT

Publicly available datasets were analyzed in this study. This data can be found here: https://chaos.grand-challenge.org/Combined_Healthy_Abdominal_Organ_Segmentation.

## AUTHOR CONTRIBUTIONS

DS, YW, DN, and TW response for study design. DS implemented the research. DS and YW conceived the

experiments. DS conducted the experiments. DS, YW, and TW analyzed the results. DS and YW wrote the main manuscript text and prepared the figures. All authors reviewed the manuscript.

## FUNDING

This work was supported in part by the National Natural Science Foundation of China under Grant 61701312, in part by the Guangdong Basic and Applied Basic Research Foundation (2019A1515010847), in part by the Medical Science and Technology Foundation of Guangdong Province (B2019046), in part by the Shenzhen Key Basic Research Project (No. JCYJ20170818094109846), in part by the Natural Science Foundation of SZU (Nos. 2018010 and 860-000002110129), in part by the SZU Medical Young Scientists Program (No. 71201-000001), and in part by the Shenzhen Peacock Plan (KQTD2016053112051497).

## REFERENCES

Bengio, Y., Louradour, J., Collobert, R., and Weston, J. (2009). "Curriculum learning.," in *Proceedings of the 26th Annual International Conference on Machine Learning, ICML '09* (New York, NY: Association for Computing Machinery), 41–48.

Bilic, P., Christ, P. F., Vorontsov, E., Chlebus, G., Chen, H., Dou, Q., et al. (2019). The liver tumor segmentation benchmark (lits). *arXiv preprint* arXiv:1901.04056.

Chen, L.-C., Papandreou, G., Schroff, F., and Adam, H. (2017). Rethinking atrous convolution for semantic image segmentation. *arXiv preprint* arXiv:1706.05587.

Chen, S., Ma, K., and Zheng, Y. (2019). Med3d: transfer learning for 3d medical image analysis. *arXiv preprint* arXiv:1904.00625.

Graves, A. (2016). Adaptive computation time for recurrent neural networks. *arXiv preprint* arXiv:1603.08983.

He, K., Zhang, X., Ren, S., and Sun, J. (2016). "Deep residual learning for image recognition," in *Proceedings of the IEEE Conference on Computer Vision and Pattern Recognition* (Las Vegas, NV), 770–778.

He, Y., Kang, G., Dong, X., Fu, Y., and Yang, Y. (2018). Soft filter pruning for accelerating deep convolutional neural networks. *arXiv preprint* arXiv:1808.06866.

He, Y., Zhang, X., and Sun, J. (2017). "Channel pruning for accelerating very deep neural networks," in *Proceedings of the IEEE International Conference on Computer Vision* (Venice), 1389–1397.

Howard, A. G., Zhu, M., Chen, B., Kalenichenko, D., Wang, W., Weyand, T., et al. (2017). Mobilenets: efficient convolutional neural networks for mobile vision applications. *arXiv preprint* arXiv:1704.04861.

Hu, J., Shen, L., and Sun, G. (2018). "Squeeze-and-excitation networks," in *Proceedings of the IEEE Conference on Computer Vision and Pattern Recognition* (Salt Lake City, UT), 7132–7141.

Huang, G., Sun, Y., Liu, Z., Sedra, D., and Weinberger, K. Q. (2016). "Deep networks with stochastic depth," in *European Conference on Computer Vision* (Amsterdam: Springer), 646–661.

Jia, H., Song, Y., Huang, H., Cai, W., and Xia, Y. (2019). "Hd-net: hybrid discriminative network for prostate segmentation in mr images," in *International Conference on Medical Image Computing and Computer-Assisted Intervention* (Shenzhen: Springer), 110–118.

Kingma, D. P., and Ba, J. (2014). Adam: a method for stochastic optimization. *corr abs*/1412.6980.

LeCun, Y., Bengio, Y., and Hinton, G. (2015). Deep learning. *Nature* 521, 436–444. doi: 10.1038/nature14539

Li, H., Kadav, A., Durdanovic, I., Samet, H., and Graf, H. P. (2016). Pruning filters for efficient convnets. *arXiv preprint* arXiv:1608.08710.

Li, X., Wang, W., Hu, X., and Yang, J. (2019). "Selective kernel networks," in *Proceedings of the IEEE Conference on Computer Vision and Pattern Recognition* (Long Beach, CA), 510–519.

Liu, Z., Li, J., Shen, Z., Huang, G., Yan, S., and Zhang, C. (2017). "Learning efficient convolutional networks through network slimming," in *Proceedings of the IEEE International Conference on Computer Vision* (Venice), 2736–2744.

Luo, J.-H., Wu, J., and Lin, W. (2017). Thinet: a filter level pruning method for deep neural network compression. in *Proceedings of the IEEE International Conference on Computer Vision* (Venice), 5058–5066.

Ma, N., Zhang, X., Zheng, H.-T., and Sun, J. (2018). "Shufflenet v2: practical guidelines for efficient cnn architecture design," in *Proceedings of the European Conference on Computer Vision (ECCV)* (Munich), 116–131.

Mehta, S., Rastegari, M., Caspi, A., Shapiro, L., and Hajishirzi, H. (2018). "Espnet: Efficient spatial pyramid of dilated convolutions for semantic segmentation," in *Proceedings of the European Conference on Computer Vision (ECCV)* (Munich), 552–568.

Teerapittayanon, S., McDanel, B., and Kung, H.-T. (2016). "Branchynet: fast inference via early exiting from deep neural networks," in *2016 23rd International Conference on Pattern Recognition (ICPR)* (Amsterdam: IEEE), 2464–2469.

Veit, A., Wilber, M. J., and Belongie, S. (2016). "Residual networks behave like ensembles of relatively shallow networks," in *Advances in Neural Information Processing Systems* (Barcelona), 550–558.

Wu, Z., Nagarajan, T., Kumar, A., Rennie, S., Davis, L. S., Grauman, K., et al. (2018). "Blockdrop: dynamic inference paths in residual networks," in *Proceedings of the IEEE Conference on Computer Vision and Pattern Recognition* (Salt Lake City, UT), 8817–8826.

Xiao, X., Lian, S., Luo, Z., and Li, S. (2018). "Weighted res-unet for high-quality retina vessel segmentation," in *2018 9th International Conference on Information Technology in Medicine and Education (ITME)* (Hangzhou: IEEE), 327–331.

Xie, S., Girshick, R., Dollár, P., Tu, Z., and He, K. (2017). "Aggregated residual transformations for deep neural networks," in *Proceedings of the IEEE Conference on Computer Vision and Pattern Recognition* (Honolulu, HI), 1492–1500.

Zhu, Q., Du, B., and Yan, P. (2019). Boundary-weighted domain adaptive neural network for prostate mr image segmentation. *IEEE Trans. Med. Imaging* 39, 753–763. doi: 10.1109/TMI.2019.2935018

**Conflict of Interest:** The authors declare that the research was conducted in the absence of any commercial or financial relationships that could be construed as a potential conflict of interest.

frontiers in Energy Research

ORIGINAL RESEARCH
published: 31 July 2020
doi: 10.3389/fenrg.2020.00185

# Data-Driven Hybrid Equivalent Dynamic Modeling of Multiple Photovoltaic Power Stations Based on Ensemble Gated Recurrent Unit

*Huan Long[1,2]*, Shaohui Xu[1], Xiao Lu[3], Zijun Yang[3], Chen Li[4], Jiangping Jing[3] and Zhi Wu[1]*

*[1] School of Electric Engineering, Southeast University, Nanjing, China, [2] Jiangsu Key Laboratory of Smart Grid Technology and Equipment, Nanjing, China, [3] State Grid Jiangsu Electric Power Company Limited, Nanjing, China, [4] National Electric Power Dispatching and Communication Center, Nanjing, China*

With the increasing penetration of the photovoltaic (PV) in the distributed grid network, the dynamic response analysis of the system becomes more and more complex and costs lots of computational time in the simulation. To cut down the computational resources while guaranteeing the accuracy, this paper proposes a data-driven hybrid equivalent model for the dynamic response process of the multiple PV power stations. The data-driven hybrid equivalent model contains the simple equivalent model and data-driven error correction model. In the equivalent model, the distributed PV power stations in the same branch are equivalent to one power station model based on the parameter equivalence and feeder equivalence. The data-driven error correction model tracks and corrects the difference of dynamic response between the equivalent model and precise model. The ensemble Gated Recurrent Unit (GRU) model based on the bagging ensemble structure utilizes the simple equivalent dynamic response as input to learn the dynamic response errors. The simulation results validate the super-performance of the proposed model both in the response speed and accuracy.

**Keywords: central PV power station, distributed PV power station, data-driven dynamic modeling, equivalent model, gated recurrent unit**

OPEN ACCESS

***Edited by:***
*Long Wang,*
*University of Science and Technology Beijing, China*

***Reviewed by:***
*Shancheng Jiang,*
*Sun Yat-sen University, China*
*Wei Liu,*
*Nanjing University of Science and Technology, China*

****Correspondence:***
*Huan Long*
*hlong@seu.edu.cn*

***Specialty section:***
*This article was submitted to Smart Grids, a section of the journal Frontiers in Energy Research*

***Received:*** *27 May 2020*
***Accepted:*** *14 July 2020*
***Published:*** *31 July 2020*

***Citation:***
*Long H, Xu S, Lu X, Yang Z, Li C, Jing J and Wu Z (2020) Data-Driven Hybrid Equivalent Dynamic Modeling of Multiple Photovoltaic Power Stations Based on Ensemble Gated Recurrent Unit. Front. Energy Res. 8:185. doi: 10.3389/fenrg.2020.00185*

## INTRODUCTION

With the aggravation of energy crisis, the advantages of PV power generation become increasingly apparent. In recent years, due to the government policy support (Ferreira et al., 2018), a large number of PV stations, including central and distributed PV stations, are constructed. It brings in the increase of PV penetration and affects the power quality and stability. While the central and distributed PV stations are different in physical and control parameters, their dynamic characteristics of active and reactive power response are quite different. The disturbances of solar irradiance and load could change the power flow and node voltage fluctuation. In addition, if the solar irradiance changes rapidly, grid stability would face a great challenge. In order to research the system dynamic characteristics containing the central and distributed PV stations, it is necessary to establish a model to describe it.

The equivalent physical model and precise physical model are the common models to represent the system dynamic characteristics (Batzelis, 2017; Abido and Sheraz Khalid, 2018). However, the PV station is a high-order non-linear system including many internal states (Xiang et al., 2016). Describing each PV stations precisely in the system makes the mathematical model extremely complex and contains dozens of orders, which enlarges computation cost. With the aim of reducing the complexity of the system and the cost of simulation, the equivalent model is introduced. However, if the equivalent model ignores too many internal states, it cannot reflect the dynamic characteristics accurately. Since the data of the dynamic process reflects the system dynamic characteristics, the data-driven model can be utilized to track and correct the difference between the precise and equivalent models.

At present, several researches based on PV physical model have been developed. The current literatures mainly focus on establishing the static model (Piazza et al., 2017), daily average power generation of PV station (Muhammad Qamar et al., 2016),main components of the PV station, such as PV array (Hariharan et al., 2016; Shao et al., 2018), DC-DC (Direct Current/Direct Current) converter (Chandra Mouli et al., 2017; Siouane et al., 2019; Zapata et al., 2019) and DC-AC (Direct Current/Alternating Current) inverter (Kim et al., 2018). In addition, PV-grid connected devices, such as filters (Dehedkar and Vitthalrao Murkute, 2018) and transformers (Yamaguchi and Fujita, 2018), are also widely studied.

The equivalence modeling of the system dynamic process containing PV stations have been widely researched. A two-staged PV station model was proposed which simplified the boost converter but established the precise filter (Piazza et al., 2017). But this model was considered as an independent system which ignored its grid-connected dynamic characteristics. In Remon et al. (2016), the large-scale distributed PV stations were equivalent to a single PV station. However, this method only considered the equivalence of the physical parameters but disregarded the difference of control parameters, which impacted the model accuracy. Literatures (Zou et al., 2015; Li W. et al., 2018) proposed a dynamic modeling which was similar as the wind farm. Based on proportional and integral parameters, this method clustered PV station through K-means algorithm and built a multi-turbine equivalent model. Literatures (Li P. et al., 2018; Li et al., 2019) clustered the distributed PV stations based on the dynamic affinity propagation. It considered the dissimilar physical and control parameters of different PV stations and introduced the long short-term memory neural network to improve the model accuracy. Many studies have been conducted in building the equivalent model of the PV clusters. However, the equivalent model combined with the data-driven model is still in its infancy.

Clustering algorithm building the equivalent distributed PV stations are based on certain indicators, such as the number of clusters, which are set artificially. The selection of clustering indicators usually needs lots of engineering experience and mathematical knowledge. Considering the assistance of the error correction model, the accuracy requirement of the equivalent model is reduced. Therefore, the equivalent process in this paper is simplified and all the distributed PV stations are divided based on the feeder. The feeder equivalent and parameter equivalent are used to establish the simple equivalent model. Following the above researches, we propose a hybrid equivalent model combining the data-driven correction model with physical equivalent model to describe the dynamic characteristics of multiple PV stations. The main contributions of this paper are concluded as follows:

(1) The framework of data-driven hybrid equivalent model for the dynamic process of the multiple PV stations is proposed.
(2) The error correction model is built based on the ensemble GRU model. Several GRU based models are generated and integrated as an ensemble GRU to further improve the model accuracy.

The remainder of this paper is structured as follows: section "Precise Dynamic Modeling for A Single Two-Staged PV Station" establishes a precise dynamic model of a single two-stage PV station; section "The Framework of Data-Driven Hybrid Equivalent Dynamic Model for Central and Distributed PV Stations" introduces the framework of the data-driven hybrid dynamic equivalent model; section "Equivalent Model for Central and Distributed PV Stations" builds the simple equivalent model for the central and distributed PV stations; section "Ensemble GRU Based Error Correction Model" describes the data-driven error correction model based on the ensemble GRU; section "Case Study" shows the simulation settings and results, and section "Conclusion" gives the conclusion.

# PRECISE DYNAMIC MODELING FOR A SINGLE TWO-STAGED PV STATION

The two-staged PV station (Sangwongwanich et al., 2017) is currently the most common PV station due to its stable performance, which is used and analyzed in this paper. The structure of the two-stage PV station is illustrated in **Figure 1**, which includes including the PV array, DC/DC converter, DC/AC inverter and filter. The detailed mathematic models of each component are described in the following subsections.

## The First Stage Modeling of PV Station

In the First stage, the PV array converts the solar irradiance $S$ into the electric energy, which is impacted by the ambient temperature $T$. Then, the DC-DC converter boosts the DC power by the array capacitance $C_{pv}$ and control the PV array output voltage by the Maximum Power Point Tracking (MPPT) controller.

### PV Array Modeling

The mathematic model of the PV array is essentially the single diode equivalent model (Hariharan et al., 2016). Its non-linear output characteristics are determined by four parameters, including open-circuit voltage, $U_{oc}$, short-circuit current, $I_{sc}$, the maximum power voltage, $U_m$, and the maximum power current, $I_m$. The output characteristics of $i_{pv}$ - $u_{pv}$ of the single PV module is described in Eq. (1). The coefficients $C_1$ and $C_2$ in (1) are

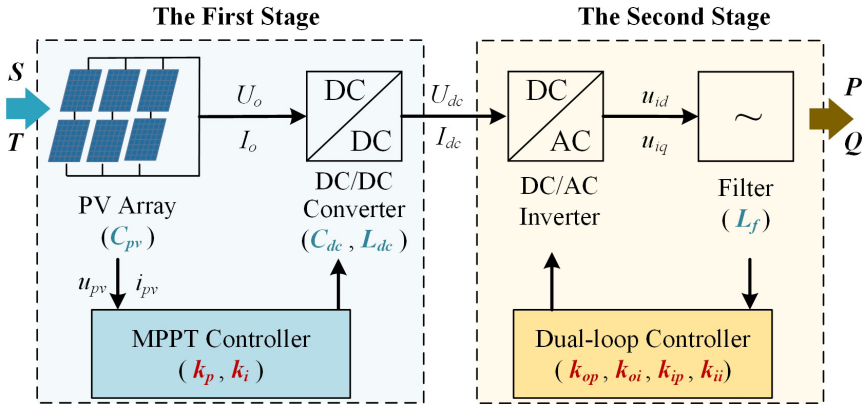


**FIGURE 1 |** The structure of the two-stage PV station.

determined by the values of $U_{oc}$, $I_{sc}$, $U_m$, and $I_m$ (Li P. et al., 2018).

$$i_{pv} = I_{sc}\left[1 - C_1\left(e^{u_{pv}/C_2 U_{oc}} - 1\right)\right] \tag{1}$$

Considering the series-parallel connection of the circuit, the output voltage $U_{pv}$ and current $I_{pv}$ of the PV array can be formulated as (2) and (3) and the corresponding power output $P_{pv}$ is presented in (4).

$$U_{pv} = N_p \times u_{pv} \tag{2}$$

$$I_{pv} = i_{pv}/N_s \tag{3}$$

$$P_{pv} = \eta \times U_{pv} \times I_{pv} \tag{4}$$

where $N_p$ and $N_s$ are the parallel and series number of the modules in the PV, and the $\eta$ is the conversion efficiency of the PV array.

### DC-DC Converter Modeling

In **Figure 1**, the boost converter is selected as the DC-DC converter to maintain the current continuous (Chandra Mouli et al., 2017). The DC-DC boost converter and the PV array is connected by the array capacitance $C_{pv}$. The output characteristics of this connection in Laplace domain is given in Eq. (5).

$$I_{pv} = C_{pv} s U_{pv} + I_L \tag{5}$$

where $I_L$ is the inductance current of the DC-DC boost converter.

The dynamic characteristics of the DC-DC boost converter can be represented as the switching cycle average model. When the capacitance $C_{dc}$ and the inductance $L_{dc}$ of the boost converter are enough large, the average output voltage $U_{dc}$ in the capacitance and the average output current $I_{dc}$ in the inductance in the Laplace domain are presented in Eqs (6) and (7).

$$L_{dc} s I_L = U_{pv} - (1 - D) U_{dc} \tag{6}$$

$$C_{dc} s U_{dc} = I_{dc} - (1 - D) I_L \tag{7}$$

where $D$ is the duty ratio of the switch and determined by the MPPT controller.

### MPPT Controller Modeling

The MPPT converter is used to control the switch status to guarantee the PV array output voltage can track the maximum voltage $U_m$ and work at the maximum power point (Dehedkar and Vitthalrao Murkute, 2018). The model of the controller in the Laplace domain is displayed as (8).

$$D = \left(k_p + {}^{k_i}/_{s}\right)(U_m - U_{pv}) \tag{8}$$

where $k_p$ and $k_i$ are the proportional gain and integral gain of the controller, respectively.

## The Second Stage Modeling of PV Station

In the second stage, the DC-AC inverter converts the DC of PV output into three-phase AC with the same frequency and amplitude as the grid. The controller of the DC-AC inverter is a dual-loop controller including the DC voltage control and reactive power control. Besides, a filter is also needed for the harmonic suppression.

### DC-AC Inverter Modeling

Power model of inverter is generally used in power flow calculation (Dutta and Chatterjee, 2018). The control strategy for inverter in this paper is SPWM control. Under SPWM mode, the output voltage of the inverter in $d$-$q$ coordinate system is shown in (9).

$$u_{id} = \frac{U_{dc}}{2U_P} u_{rd},\ u_{iq} = \frac{U_{dc}}{2U_P} u_{rq} \tag{9}$$

where $u_{id}$ and $u_{iq}$ are components of the inverter output voltage in $d$-axis and $q$-axis, respectively, $u_{rd}$ and $u_{rq}$ are the components of the modulation wave voltage in $d$-axis and $q$-axis, respectively, and the $U_p$ is the peak voltage of the carrier wave.

### Dual-Loop Controller Modeling

The control system is divided into inner loop control and outer loop control. The outer loop control consists of DC voltage outer

loop control and reactive power outer loop control. The inner loop control is the current inner loop control.

In the outer loop control, the output voltage and current of PV array first determine the DC reference voltage $U_{ref}$. Then, the difference between the actual measured voltage $U_{dc}$ and $U_{ref}$ is calculated. The reference current $i_{d,ref}$ in the $d$-axis in the DC voltage outer loop control is presented in (10).

$$i_{d,ref} = (U_{ref} - U_{dc})(k_{op} + {}^{k_{oi}}/_{s}) - i_d \tag{10}$$

where $k_{op}$ and $k_{oi}$ are the proportional and integral gains of outer loop control, respectively, and $i_d$ is the $d$-axis component of the actual output current of the PV system.

The reactive power outer loop control compares the reactive power $Q_{filt}$ measured from the filter circuit with the reference reactive power $Q_{ref}$ to get the reactive power difference. The reference current $i_{q,ref}$ in $q$-axis is calculated by (11). The $i_q$ is the $q$-axis components of the actual output current of the PV system.

$$i_{q,ref} = (Q_{ref} - Q_{filt})(k_{op} + {}^{k_{oi}}/_{s}) - i_q \tag{11}$$

In the current inner loop, the SPWM modulation wave is generated, which is controlled by $i_{d,ref}$ and $i_{q,ref}$. The components of the SPWM modulation wave voltage in $d$-axis and $q$-axis, $u_{rd}$ and $u_{rq}$, are shown as (12) and (13).

$$u_{rd} = i_{d,ref}(k_{ip} + {}^{k_{ii}}/_{s}) - \omega L_f i_q + u_{sd} \tag{12}$$

$$u_{rq} = i_{q,ref}(k_{ip} + {}^{k_{ii}}/_{s}) - \omega L_f i_q + u_{sq} \tag{13}$$

where $k_{ip}$ and $k_{ii}$ are the proportional and integral gains of inner loop control, respectively, $u_{sd}$ and $u_{sq}$ are the components of the actual grid voltage in $q$-axis and $d$-axis, the $L_f$ is the filter inductance and ω is the angle frequency of the power grid.

Based on the description of the two-staged PV station modeling, the main factors affecting the output dynamic characteristics of PV station generation can be divided into physical and control parameters. The physical parameters contain the $C_{pv}$, $C_{dc}$, $L_{dc}$, and $L_f$. The control parameters consist of the control parameters of the MPPT controller and dual-loop controller, including $k_p$, $k_i$, $k_{ip}$, $k_{ii}$, $k_{op}$, and $k_{oi}$. When the physic and control parameters are fixed, the corresponding output dynamic characteristics of the single PV station under the standard test condition is determined. Thus, the dynamic process $f(\cdot)$ of the single PV station can be described as (14).

$$(P, Q) = f(S, T | C_{pv}, C_{dc}, L_{dc}, L_f, k_p, k_i, k_{ip}, k_{ii}, k_{op}, k_{oi}) \tag{14}$$

## THE FRAMEWORK OF DATA-DRIVEN HYBRID EQUIVALENT DYNAMIC MODEL FOR CENTRAL AND DISTRIBUTED PV STATIONS

Through the precise model of the dynamic characteristics of the single PV station in section "Precise Dynamic Modeling for A Single Two-Staged PV Station," it is clear that the PV stations are highly non-linear system. With the penetration rate of the renewable energy increasing, the distributed PV stations gradually become the mainstream way, especially in industrial and rural areas. It brings in lots of uncertainty and stochastic for the power grid and makes the whole grid system quiet complex. Thus, it is necessary to build a dynamic equivalence model with high precision and short simulation time to study the impact of the central PV and large distributed PV stations. In **Figure 2**, a data-driven hybrid equivalent dynamic modeling approach is proposed. It consists of the physical equivalent model and error correction model.

In the equivalent modeling part, the precise dynamic model of the PV stations is first simplified into the equivalent model from the aspect of physics, including the physical parameters equivalence and control parameters. According to the mathematical model of PV system in section "Precise Dynamic Modeling for A Single Two-staged PV Station," physical parameters are composed of PV array capacitance $C_{pv}$, boost converter capacitance $C_{dc}$, boost converter inductance $L_{dc}$ and filter inductance $L_f$. The control parameters include the control parameters of PWM system ($k_p$, $k_i$) and SPWM system ($k_{ip}$, $k_{ii}$, $k_{op}$, $k_{oi}$). Since the distributed PV stations are installed in the different places and different feeders, the feeder equivalence is necessary for the distributed PV stations.

In the error correction modeling part, the errors between the physical equivalent and precise model are considered and corrected, including the steady-state error and the transient error. The steady-state error is usually small or a constant. The transient error is introduced by the equivalent control parameters and performs different in different test conditions. The data-driven approach is utilized to learn the errors of the dynamic output characteristics of the two models under multiple different work situations to make the hybrid equivalent model more accurate.

## EQUIVALENT MODEL FOR CENTRAL AND DISTRIBUTED PV STATIONS

The principle of simplifying an equivalent model of central PV stations and distributed PV stations is the output voltage and power of the equivalent model must be the same as the precise one. In addition, the distributed PV model are located at different places of different feeders. Thus, the node voltage and load need to be considered, while simplifying the distributed PV stations.

### The Feeder Equivalence

Since distributed PV stations scatter in the feeders, one or more loads might exist between two PV stations. When multiple distributed PV stations are equivalent to a cluster in the system, the power distribution is also affected. Therefore, the node voltage and power flow should be considered while simplifying the distributed PV stations (Zhang et al., 2019). The load transfer and line impedance equivalence are implied on every node. The schematic diagram of feeder equivalence is displayed in **Figure 3**.

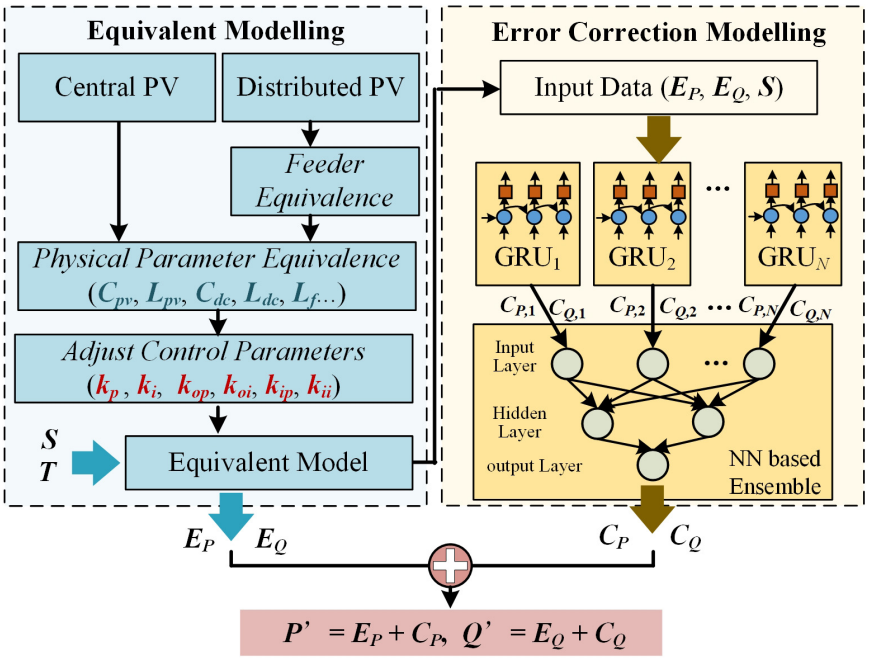


**FIGURE 2 |** The framework of data-driven hybrid equivalent dynamic modeling.

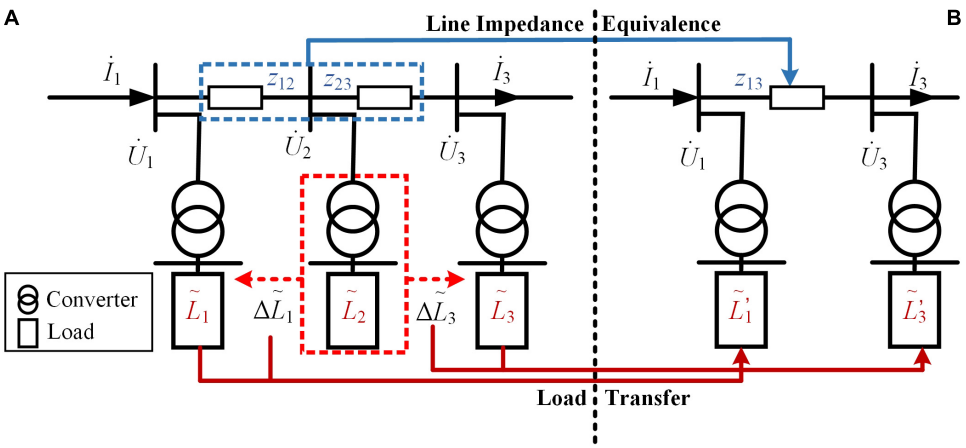


**FIGURE 3 |** Schematic diagram of feeder equivalence. **(A)** Original feeder **(B)** equivalent feeder.

Suppose the voltage, injection current and load of the *i*-th node are denoted as $\dot{U}_i$, $\dot{I}_i$and $\tilde{L}_i$, respectively. The impedance of line *i*-*j* is represented as $z_{ij}$. In **Figure 3A**, based on the Kichhoff's current law, the relationship between the node 1 and node 3 can be presented as (15).

$$\dot{I}_1 = \left(\tilde{L}_1/\dot{U}_1\right)^* + \left(\tilde{L}_2/\dot{U}_2\right)^* + \left(\tilde{L}_3/\dot{U}_3\right)^* + \dot{I}_3 \tag{15}$$

When node 2 disappears, the load of the node 2 is transferred into node 1 and node 3. The transfer amount of load from node 2 to node 1 and node 3 are denoted as $\Delta\tilde{L}_1$ and $\Delta\tilde{L}_3$, respectively. Since the injection current of node 1 should keep equal to the output current of node 3 and the total power should remain unchanged, the values of $\Delta\tilde{L}_1$ and $\Delta\tilde{L}_3$ are calculated as (16) and (17). The load of node 1 and node 3 after the load transferring are $\tilde{L}'_1$ and $\tilde{L}'_3$, presented in (18).

$$\Delta\tilde{L}_1 = \frac{\dot{U}_1(\dot{U}_2 - \dot{U}_3)}{\dot{U}_2(\dot{U}_1 - \dot{U}_3)}\tilde{L}_2 \tag{16}$$

$$\Delta\tilde{L}_3 = \frac{\dot{U}_3(\dot{U}_1 - \dot{U}_2)}{\dot{U}_2(\dot{U}_1 - \dot{U}_3)}\tilde{L}_2 \tag{17}$$

$$\tilde{L}'_1 = \tilde{L}_1 + \Delta\tilde{L}_1, \quad \tilde{L}'_3 = \tilde{L}_3 + \Delta\tilde{L}_3 \tag{18}$$

Except the load transfer of the node 2, the line impedance is also need to be modified, which impacts the line power loss. To keep the line power loss between node 1 and node 3 the same before and after the load transferring, the equivalent value of line impedance between node 1 and node 3 is displaye in (19).

$$z_{13} = \frac{\left|\dot{U}_1 - \dot{U}_3\right|^2}{\frac{\left|\dot{U}_1 - \dot{U}_2\right|^2}{z_{12}} + \frac{\left|\dot{U}_3 - \dot{U}_2\right|^2}{z_{23}}} \tag{19}$$

After load transfer and feeder equivalence for each node in the network, multiple distributed PV stations can be equivalent to a single PV station model.

## The Parameter Equivalence

In the parameter equivalence, it includes the physical parameters equivalence and control parameters adjustment. The principle of the physical parameters equivalence is based on the ratio of the total installed capacity of multiple PV stations to the installed capacity of a single PV station. Suppose $n$ PV stations are clustered into one PV stations. The physical parameters of the $i$-th PV station, $i$ = 1,2, …, $n$, include the capacitance and inductance parameters of the array, $C_{pv,i}$ and $L_{pv,i}$, the capacitance and inductance parameters of the boost converter, $C_{dc,i}$ and $L_{dc,i}$, and the inductance of filter, $L_{f,i}$. The corresponding aggregation parameters are determined by (20)–(22).

$$C_{pv,EQ} = \frac{1}{n}\sum_{i=1}^{n}\rho_i C_{pv,i},\ L_{pv,EQ} = \frac{1}{n}\sum_{i=1}^{n} L_{pv,i}\Big/\rho_i \tag{20}$$

$$C_{cd,EQ} = \frac{1}{n}\sum_{i=1}^{n}\rho_i C_{cd,i},\ L_{cd,EQ} = \frac{1}{n}\sum_{i=1}^{n} L_{cd,i}\Big/\rho_i \tag{21}$$

$$L_{f,EQ} = \frac{1}{n}\sum_{i=1}^{n} L_{f,i}\Big/\rho_i \tag{22}$$

where the subscript $EQ$ represents the equivalent value in the equivalent model and the value of the $\rho_i$ is the ratio of the total installed capacity of $n$ PV stations to the installed capacity of the $i$-th one.

Besides, considering each PV station connects to the power grid by a transformer, the capacity and impedance parameters of the transformer is also needed to be modified. The corresponding aggregation parameters are shown as (23).

$$S_{t,EQ} = \frac{1}{n}\sum_{i=1}^{n}\rho_i S_{t,i},\ Z_{t,EQ} = \frac{1}{n}\sum_{i=1}^{n} Z_{t,i}\Big/\rho_i \tag{23}$$

where $S_{t,i}$ and $Z_{t,i}$ are denoted as the rated capacity and impedance of the $i$-th PV station transformer.

The control parameters of the MPPT and dual-loop controller are adjusted after the aggregation physical parameters fixed. The initial control parameters in the equivalent model are determined by the average values of the control parameters of all the equivalent PV stations. To make the dynamic performance of the equivalent model close to the precise one, the control parameters are further adjusted artificially.

# ENSEMBLE GRU BASED ERROR CORRECTION MODEL

The distribution and aggregation of central PV stations and distributed PV stations are quite different. The physical and control parameters of each PV station in central PV plants are roughly equal, and their dynamic characteristics are close. But parameters of distributed PV stations are different. When the external conditions change, an obvious gap exists in their dynamic response. Thus, it is a data-driven error correction model is proposed in this section to fit the error between the precise model and the equivalent model. Considering the error data are the time series data, the GRU algorithm, which is powerful for dealing with the time series data, is used for modeling the errors.

At specific time $t$, the active power and reactive power of the equivalent model are denoted as $E_P(t)$ and $E_Q(t)$, respectively. The parameters, $E_P(t)$, $E_Q(t)$ and solar irradiance $S$ are regarded as the input data of the error correction model. The target data of the error correction model are the corresponding errors of the active and reactive power at time $t$, $C_P(t)$ and $C_Q(t)$, which can be obtained by the precise and equivalent models.

The equivalent model and the accurate model are simulated under different conditions and a large amount of errors data are generated. The error dataset is then used to train the GRU to build the error correction model. The structural unit of GRU is shown in the **Figure 4**.

The **Figure 4A** displays the structure of the single GRU layer. The input data of each layer consists of the current error data $x_t$ and the hidden node $h_{t-1}$ of the upper layer, where $h_{t-1}$ contains the relevant information of the previous node. GRU contains two gates, a reset gate and an update gate. The parameter $r_t$ in the reset gate is used to control the degree of information forgetting in the previous moment. The parameter $z_t$ in the update gate is used to control the amount of information retained from time $t$-1 to $t$. After the gate processing, the data from the reset and update gates are added to get the data $h_t$ of the current layer. To enhance the information learning capacity, a single GRU base model is composed of $n$ GRU layers, shown as **Figure 4B**. The **Figure 4C** shows the unfolded form of GRU model as the increasing of time $t$.

To further improve the accuracy and reduce stochastic of the neural network training, the ensemble technique is applied. In **Figure 1**, the structure of the ensemble GRU model is displayed. The BP neural network is used as the ensemble structure to train the weights of each sub-model. The whole dataset is divided into three parts, training dataset, validation dataset and test dataset.

The training dataset is firstly used to train the several GRU models, which are regarded as the sub-models of the ensemble model. To avoid the over-fitting phenomenon of the ensemble model, the data used to train each GRU are randomly selected

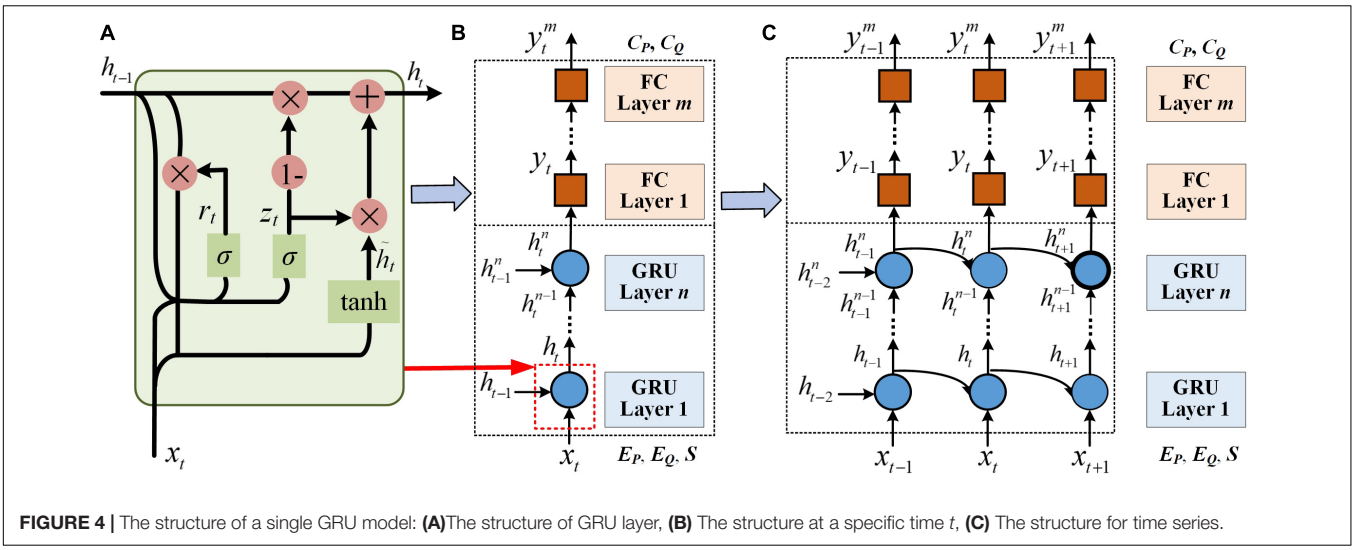


**FIGURE 4 |** The structure of a single GRU model: **(A)**The structure of GRU layer, **(B)** The structure at a specific time *t*, **(C)** The structure for time series.

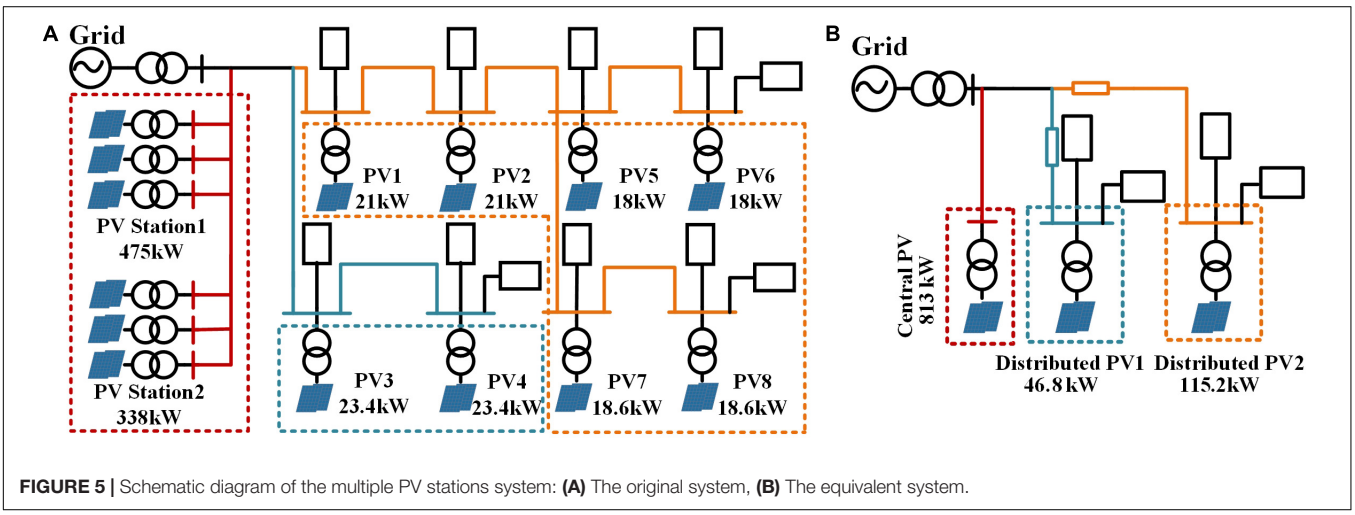


**FIGURE 5 |** Schematic diagram of the multiple PV stations system: **(A)** The original system, **(B)** The equivalent system.

**TABLE 1 |** Physical and control parameters of PV stations.

| Station | $L_{dc}$ (*H*) | $C_{dc}$ (μ*F*) | $L_f$ (*H*) | $C_{pv}$ (μ*F*) | $k_p$ (× $10^{-2}$) | $k_i$ (× $10^{-2}$) | $k_{op}$ (× $10^{-2}$) | $k_{oi}$ | $k_p$ | $k_{ii}$ |
|---|---|---|---|---|---|---|---|---|---|---|
| PV1 | 7.06 | 33.733 | 0.075 | 0.677 | 0.952 | 4.114 | 0.993 | 12.75 | 2.201 | 11.63 |
| PV2 | 6.81 | 35.761 | 0.068 | 0.735 | 1.015 | 0 | 1.002 | 18.531 | 1.741 | 18.43 |
| PV3 | 2.96 | 87.452 | 0.028 | 1.859 | 1.045 | 0.995 | 1.222 | 9.9753 | 1.925 | 8.98 |
| PV4 | 0.671 | 371.61 | 0.008 | 7.122 | 0.999 | 0.963 | 0.954 | 10.146 | 2.013 | 9.52 |
| PV5 | 1.474 | 171.38 | 0.014 | 3.496 | 1.017 | 3.972 | 1 | 13 | 2 | 11 |
| PV6 | 2.718 | 93.497 | 0.029 | 1.773 | 0.953 | 0.975 | 0.984 | 1.208 | 11.28 | 2.93 |
| PV7 | 1.478 | 175.31 | 0.041 | 3.469 | 1.015 | 3.819 | 1.05 | 12.11 | 1.975 | 10.14 |
| PV8 | 1.429 | 169.84 | 0.014 | 3.428 | 1.086 | 4.172 | 1 | 18 | 2 | 17 |
| Central PV1 | 6.96 | 33.573 | 0.067 | 0.667 | 0.983 | 4.201 | 1 | 12.52 | 2.101 | 11.65 |
| Central PV2 | 1.523 | 103.45 | 0.078 | 4.193 | 0.895 | 4.908 | 0.950 | 10.638 | 2 | 10.89 |

through the bootstrapping technique. The structure of each GRU, such as the number of the units in each GRU layer, is also randomly generated.

Then, the outputs of each GRU model are regarded as the input of the BP neural network. The $C_P(t)$ and $C_Q(t)$ are regarded as the output. The weights of sub-models are learned by the validation dataset. At last, the testing data are used to verify the performance of the ensemble GRU model.

In the training process of the ensemble model, the data of $E_P(t)$, $E_Q(t)$ and $S$ are first used as the input of each GRU model. The estimated active and reactive power errors of $N$ GRU models are obtained, $C'_{P,i}(t)$ and $C'_{Q,i}(t)$, $i$ = 1,. . ., $N$. To ensemble all

**TABLE 2 |** Parameter setting of a single GRU based model.

| | Type of layer | Number of units | Activation function | Dropout |
|---|---|---|---|---|
| 1 | GRU layer | Random (20, 100) | tanh | 0.3 |
| 2 | GRU layer | Random (50, 150) | tanh | 0.2 |
| 3 | GRU layer | Random (50, 100) | tanh | – |
| 4 | FC layer | 30 | Relu | – |
| 5 | FC layer | 15 | Relu | – |
| 6 | FC layer | 1 | Sigmoid | – |

the GRU models, the $C'_{P,i}(t)$ and $C'_{Q,i}(t)$ are regarded as the input of the BP neural network to the weights of each GRU. The active and inactive power estimated by the BP neural network are denoted as $C'_P(t)$ and $C'_Q(t)$. The active and reactive power of the hybrid model at time $t$, $P'(t)$ and $Q'(t)$, are calculated through (24) and (25).

$$P'(t) = E_P(t) + C'_P(t) \tag{24}$$

$$Q'(t) = E_Q(t) + C'_Q(t) \tag{25}$$

# CASE STUDY

In this section, the proposed method is validated through a radial active distributed network simulation system, shown in **Figure 5A**. In **Figure 5A**, there are a central PV stations and 8 distributed PV stations (PV1∼PV8). Since the central PV station has two different types of PV, it is divided into two parts, central PV station 1 and central PV station 2. In addition, the PV system includes transformers, transmission lines and loads. The installed capacities of the 10 two-staged PV stations are: 21 kW for PV1 and PV2, 23.4 kW for PV3 and PV4, 18 kW for PV5 and PV6, 18.6 kW for PV7 and PV8,475 kW for central PV station 1 and 338 kW for central PV station 2. The total installed capacity is 975 kW and the total load is 1532+j781kVA. The parameters of PV system are set according to the PV system used in engineering. The sample frequency is set to 500 Hz. Since the system reaches the steady state after 0.25 s, the sample time period is set from 0.25 to 0.55 s. Each group contains 150 sampling points.

The detailing physical and equivalent physical system are built on the Simulink platform in Matlab. The first stage of the model is composed of the PV array, converter, MPPT controller and PWM controller. The first stage calls the PI controller model, integrator model, saturation model, product model and other mathematical models in Simulink Library. PI controller model and saturation model are used to realize PWM control. MPPT controller is affected by PWM controller and consists of mathematical models. The second stage is composed of the inverter, filter and dual-loop controller. Compared with the first stage, the second stage calls the vector conversion model in Simulink Library additionally. The vector conversion model converts three-phase current into *d-q* coordinate system.

The error correction model is built by Keras on the Pycharm platform. The simulations are conducted on a PC with Intel (R) CPU i7-6500U, 2.5 GHz, RAM 8 GB.

## Experiment Settings

### The Settings of PV Stations and Test Scenarios

The physical and control parameters of each PV stations, which determines their dynamic process performance are shown as **Table 1**. In **Table 1**, it is obvious the control parameters of each PV station are quite different, which brings lots of difficulties on the control parameter setting of the equivalent model. The error correction model can make up the difference between the precise model and equivalent model. Thus, the requirement of the equivalent model is reduced by building the error correction model.

In order to validate the universality of the model, three test scenarios are designed. In Case I, the random disturbance is considered and added into the input irradiance data, which can be described as the random input signal. This case represents the shift of the day and night and the situation of load slightly reducing and increasing. In Case II and Case III, the abrupt

**TABLE 3 |** Physical and control parameters of equivalent models.

| Station | $L_{dc}$ (H) | $C_{dc}$ (μF) | $L_f$ (H) | $C_{pv}$ (μF) | $k_p$ (× $10^{-2}$) | $k_i$ (× $10^{-2}$) | $k_{op}$ (× $10^{-2}$) | $k_{oi}$ | $k_p$ | $k_{ii}$ |
|---|---|---|---|---|---|---|---|---|---|---|
| Distributed PV1 | 0.547 | 432.06 | 0.006 | 8.971 | 1.022 | 4.114 | 0.993 | 10.032 | 1.964 | 9.25 |
| Distributed PV2 | 0.498 | 641.36 | 0.006 | 11.236 | 0.968 | 2.844 | 1.004 | 13.531 | 2.745 | 10.28 |
| Central PV | 2.96 | 87.452 | 0.028 | 1.859 | 0.939 | 4.555 | 0.975 | 11.579 | 2.05 | 11.27 |

**TABLE 4 |** Computational errors (RMSE) and computational time of different models.

| Scenarios | RMSE | | | | | | | | |
|---|---|---|---|---|---|---|---|---|---|
| | Active power | | | Reactive power | | | Computational time (s) | | |
| | Equivalent model | Hybrid model | Hybrid ensemble model | Equivalent model | Hybrid model | Hybrid ensemble model | Precise model | Equivalent model | Hybrid ensemble model |
| Case I | 3.000 | 0.368 | 0.235 | 3.622 | 0.109 | 0.088 | 44.634 | 2.419 | 4.320 |
| Case II | 5.786 | 2.183 | 1.865 | 3.657 | 0.098 | 0.092 | 55.322 | 2.670 | 4.578 |
| Case III | 7.339 | 3.589 | 2.780 | 3.731 | 0.205 | 0.155 | 56.031 | 2.736 | 4.695 |

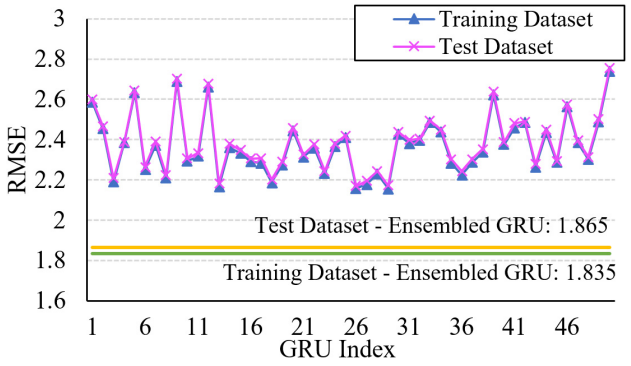


**FIGURE 6 |** RMSE of active power of each GRU base model and ensemble GRU model in Case II.

change of the input irradiance data is considered. In Case II, the rapid rise or fall of irradiance appears in a short period of time and remains stable, which can be called as the step input signal. This case is used to describe the instantaneous change in irradiance, the situation of short circuit or instantaneous load rejection. In Case III, a continuous and rapid rise and fall of the irradiance happens over a very short period of time, named as pulse input signal.

To train a general error correction model, the data under different test scenarios are needed to be collected. The detailed settings of three cases for data collection are shown as follows:

**Case I:** set the irradiance from 300 to 1500 W/m$^2$, and noise is set from 5 to 40 W/m$^2$. This case has 960 groups of experiments.

**Case II:** set the irradiance from 300 to 1500 W/m$^2$. The abrupt change happens at 0.33 s and the change amplitude is set from 40 to 120 W/m$^2$. This case has 960 groups of experiments.

**Case III:** set the irradiance from 300 to 1500 W/m$^2$. The abrupt changes happen at 0.27 and 0.37 s. The change amplitude is set from 40 to 120 W W/m$^2$. This case has 960 groups of experiments.

### The Settings of Ensemble GRU

Since the active power is greatly impacted by the external factors, the ensemble model of active power contains 50 GRU base models. Since the variance of the reactive power is relatively stable, the ensemble model is set to include 25 base models. Each GRU base model has the same number of the hidden layers, including 3 GRU layers and 3 full connection (FC) layers. The activation function of the GRU layer is tanh function and the FC layer is Relu function. To reduce the impact of the over-fitting, the dropout layer is added after the first and second GRU layers. The number of units of the different GRU layers are randomly generated to form different GRU base models. The detailed parameter setting of a single GRU base model is shown as **Table 2**. The Adam optimizer is used to train the GRU base model. 150 samples are randomly selected as a batch.

To avoid the neuron saturation, the sample data of every moment is normalized by the min-max normalization, which maps each sample data to [0, 1], shown as (26).

$$X' = \frac{X - X_{\min}}{X_{\max} - X_{\min}} \tag{26}$$

where $X$ is the actual value of input variable, $X_{min}$ and $X_{max}$ are the minimal and maximal value of input variable, and $X'$ is the corresponding normalized value. The sequences of collected 3000 groups are disordered. The 2000 groups of samples are used to form the training dataset and the rest groups for testing. The root mean square error (RMSE) is used to evaluate the performance of the error correction model. The RMSE of each group is shown as (27).

$$\mathrm{RMSE}\left(y, \hat{y}\right) = \sqrt{\frac{1}{N}\sum_{t=1}^{n}(C_t - E_t)^2} \tag{27}$$

where $C_t$ is the output of error correction model, $E_t$ is the actual error, $t$ is the index of the time step in each group, and $N$ is the total number of samples in each group. The RMSE of training dataset and test dataset are calculated by average the RMSEs of all groups in the dataset.

## Simulation Performance and Analysis

### Simulation Result

In this section, the performance of the data-driven hybrid model is displayed and analyzed under the three test scenarios. According to the above equivalent method, the

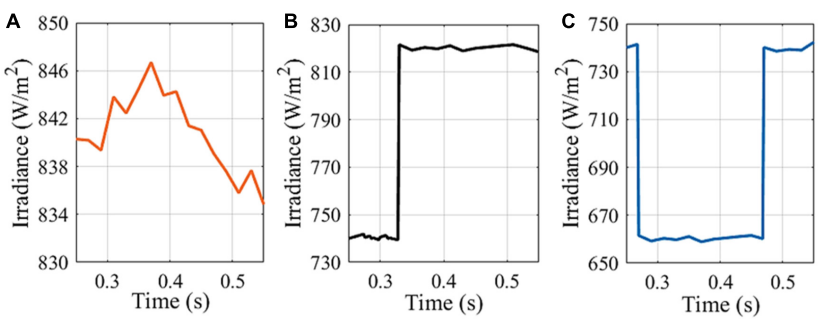


**FIGURE 7 |** Examples of irradiance input data in three test scenarios: **(A)** Case I, **(B)** Case II, **(C)** Case III.

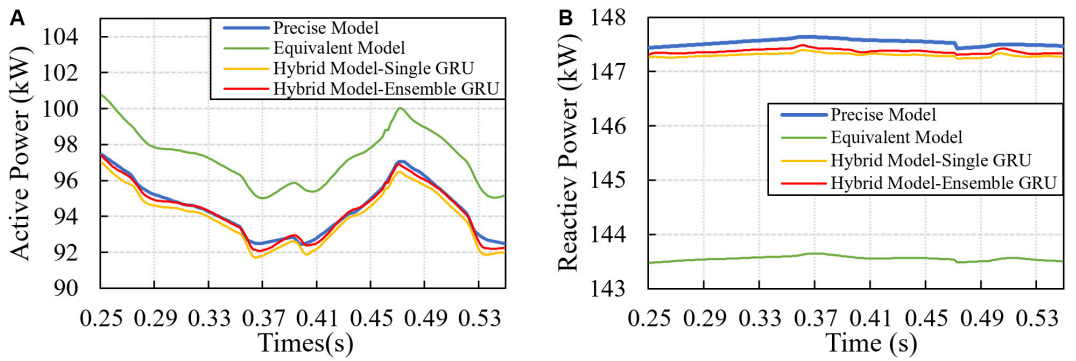


**FIGURE 8 |** Example of the response of precise, equivalent and hybrid model in Case I: **(A)** Active power, **(B)** Reactive power.

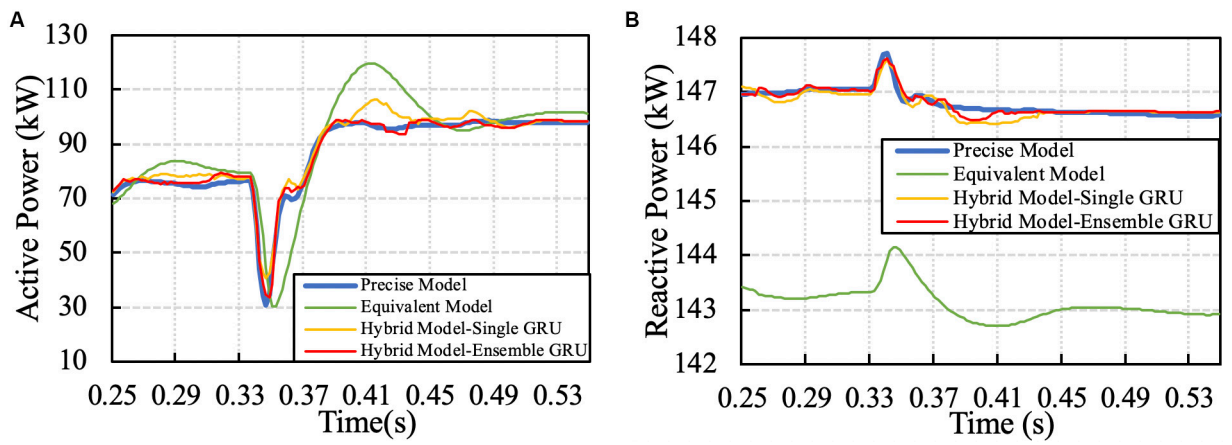


**FIGURE 9 |** Example of the response of precise, equivalent and hybrid model in Case II: **(A)** Active power, **(B)** Reactive power.

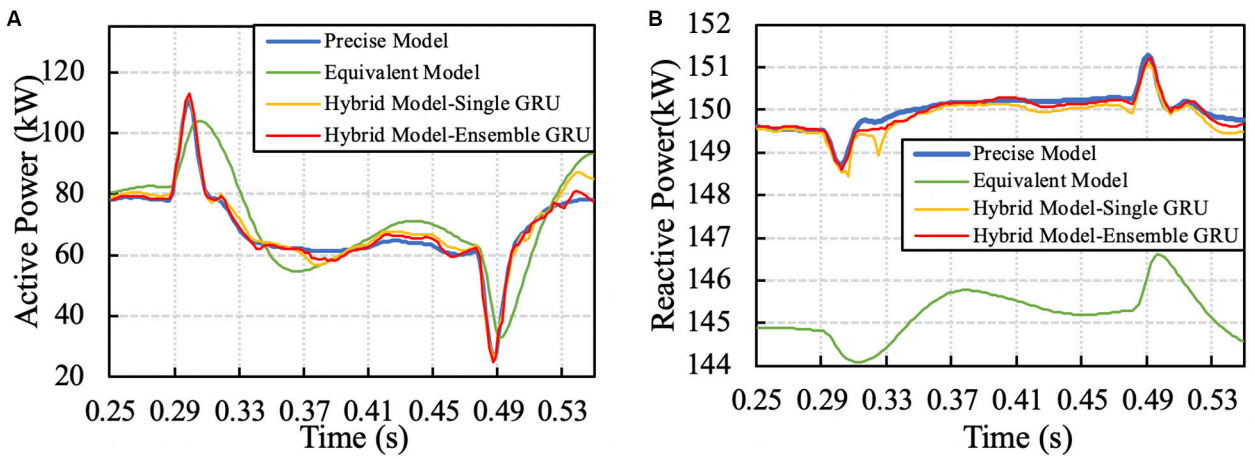


**FIGURE 10 |** Example of the response of precise, equivalent and hybrid model in Case III: **(A)** Active power, **(B)** Reactive power.

equivalent model of PV system is first established. The central PV1 and central PV2 are equivalent to a PV station with the capacity of 813 kW. Then, all the distributed PV stations located in the same branch are equivalent to one PV station. The distributed PV stations are equivalent as two PV stations, distributed PV1 and PV2 according to the distribution characteristics. The equivalent model of the system is displayed as **Figure 5B**. The corresponding

equivalent parameters of equivalent PV stations are given in **Table 3**.

**Table 4** shows the RMSE between three equivalent models and the precise model. The hybrid model is the data-driven hybrid equivalent model with single GRU. The hybrid ensemble model is the data-driven hybrid equivalent with ensemble GRU. In **Table 4**, it is clear that RMSE is significantly reduced after introducing error correction model. The error of model with ensemble GRU is smaller than the one with single GRU for all three scenarios. Since the impact of the reactive power affected by the changes of irradiance and load is less than the active power, the error correction model performs better for the reactive power. In Case I, the irradiance fluctuates slightly and the errors are the least among three scenarios. The Case III has two rapid disturbances and the greater errors than Case I and Case II.

**Table 4** also shows the simulation time required for the precise model, equivalent model and data-driven hybrid ensemble model. It can be seen that the simulation time of the hybrid model with ensemble GRU is far less than that of the precise model. The error correction model needs the active and reactive power time-series output of the equivalent model and work after the equivalent. Besides, the error correction model contains multiple GRU models, which needs the time to obtain output of each GRU model. Combined with the above two points, the simulation time of the hybrid ensemble model is longer than that of the equivalent model. This advantage becomes more and more obvious with the complexity of system increasing. The purpose of reducing simulation time is realized by using the data-driven hybrid model.

Besides, **Figure 6** shows the training and test results of active power by ensemble GRU under Case II, respectively. The result of test dataset is close to that of training dataset, which indicates that there is no over fitting or under fitting.

### Simulation Example Under Different Test Scenarios

In **Figure 7**, three test examples are separately selected from three test scenarios. In **Figure 7A**, the irradiance randomly changes from 830 to 850 W/m$^2$. The irradiance randomly changes within a small margin. In this situation, the PV system usually works in a disturbed environment which means it is always in a dynamic process. The active and reactive power response of different models in this case are shown in **Figure 8**. It is obvious that there is a certain error between the equivalent and precise models. After the introducing error correction model, the error between the power output of the equivalent and precise model is significantly reduced. Besides, the reactive power is less impacted by the change of the random irradiance and keeps stable in the whole process.

In the example of Case II, the irradiance rapidly rises from 740 to 820 W/m$^2$, shown as **Figure 7B**. This scenario can reflect the operation of load rejection and load increase in the infinite source power grid. The load change in the power grid is usually long-term and completed in a short time, which can be approximated as the step response. **Figure 9** gives the corresponding active and reactive power response. When irradiance rapidly rises or falls in a short period of time, the dynamic characteristics of the equivalent model approach to the oscillation process. After using single GRU model for error tracking, the output characteristics of the equivalent model are improved to some extent, but there are still some deviations. The error tracking of Ensemble GRU model is further improved. The raised errors in some areas are eliminates through Ensemble GRU, such as the error appearing from 0.39 to 0.44 s.

In Case III, the irradiance rapidly falls from 740 to 660 W/m$^2$ at 0.27 s and then rises to 740 W/m$^2$ at 0.37 s, shown as **Figure 7C**. This scenario reflects the instantaneous disturbance of PV system and can represent that the PV system is blocked for a short time or the grid is short-circuited. The corresponding active and reactive power response are shaped in **Figure 10**. In this case, due to the short time interval between two abrupt disturbs, the influence of control parameters is amplified. It is clear that the dynamic response of the equivalent model is slower than the precise one. Through the error correction, this lag is almost removed. Under this condition, the hybrid model can still track the error accurately.

## CONCLUSION

This paper proposed a hybrid data-driven model to build the equivalent model of the dynamic process of the multiple PV stations in the distributed network. The dynamic process of the PV system were described by the physical and control parameters. The data model and the physical model were combined to build an accurate model.

The equivalent models for central and distributed PV stations were firstly established from the physical aspect. The equivalent models needed to consider the physical parameter and feeder equivalence. Since the control parameters were determined artificially, the errors existed between the simple equivalent model and the precise model. The data-driven model was introduced to track and correct the errors.

The ensemble GRU model was utilized as the error correction model. Three different test cases were established to help build the error correction model of the active and reactive power. The simulation results showed that the proposed hybrid data-driven model improved the fitting precision of the dynamic characteristics while keeping the low model complexity and short computational time.

## DATA AVAILABILITY STATEMENT

The raw data supporting the conclusions of this article will be made available by the authors, without undue reservation, to any qualified researcher.

## AUTHOR CONTRIBUTIONS

HL: conceptualization, methodology, and writing – reviewing and editing. SX: data curation, software, and writing – original draft preparation. All authors contributed to the article and approved the submitted version.

## FUNDING

This article was supported with the Science and Technology Program of State Grid Corporation of Jiangsu Province: Research and Application of Integrated Energy Regulation Technology Aiming at the Interaction of Source, Grid, Load, and Storage (Grant No. 521002190049), and the National Natural Science Foundation of China under Grant 51807023.

## REFERENCES

Abido, M. A., and Sheraz Khalid, M. (2018). Seven-parameter PV model estimation using differential evolution. *Electr. Eng.* 100, 971–981. doi: 10.1007/s00202-017-0542-2

Batzelis, E. I. (2017). Simple PV performance equations theoretically well founded on the single-diode model. *IEEE J. Photovolt.* 7, 1400–1409. doi: 10.1109/JPHOTOV.2017.2711431

Chandra Mouli, G., Schijffelen, J., Bauer, P., and Zeman, M. (2017). Design and comparison of a 10-kW interleaved boost converter for PV application using Si and SiC devices. *IEEE J. Emerg. Select. Top. Power Electron.* 5, 610–623. doi: 10.1109/JESTPE.2016.2601165

Dehedkar, M., and Vitthalrao Murkute, S. (2018). "Optimization of PV system using distributed MPPT control," in *Proceedings of the 2018 International Conference on System Modeling & Advancement in Research Trends (SMART)*, (Moradabad: IEEE).

Dutta, S., and Chatterjee, K. (2018). A buck and boost based grid connected PV inverter maximizing power yield from two PV arrays in mismatched environmental conditions. *IEEE Trans. Ind. Electr.* 65, 5561–5571. doi: 10.1109/TIE.2017.2774768

Ferreira, A., Kunh, S. S., Fagnani, K. C., De Souza, T. A., Tonezer, C., Dos Santos, G. R., et al. (2018). Economic overview of the use and production of photovoltaic solar energy in brazil. *Renew. Sustain. Energy Rev.* 81, 181–191. doi: 10.1016/j.rser.2017.06.102

Hariharan, R., Chakkarapani, M., Saravana Ilango, G., and Nagamani, C. (2016). A method to detect photovoltaic array faults and partial shading in PV systems. *IEEE J. Photovolt.* 6, 1278–1285. doi: 10.1109/JPHOTOV.2016.2581478

Kim, J., Kwon, J., and Kwon, B. (2018). High-efficiency two-stage three-level grid-connected photovoltaic inverter. *IEEE Trans. Indust. Electr.* 65, 2368–2377. doi: 10.1109/TIE.2017.2740835

Li, P., Gu, W., Long, H., Cao, G., Cao, Z., Xu, B., et al. (2019). High-precision dynamic modeling of two-staged photovoltaic power station clusters. *IEEE Trans. Power Syst.* 34, 4393–4407. doi: 10.1109/TPWRS.2019.2915283

Li, P., Gu, W., Wang, L., Xu, B., Wu, M., and Shen, W. (2018). Dynamic equivalent modeling of two-staged photovoltaic power station clusters based on dynamic affinity propagation clustering algorithm. *Int. J. Electr. Power Energy Syst.* 95, 463–475. doi: 10.1016/j.ijepes.2017.08.038

Li, W., Chao, P., Liang, X., Ma, J., Xu, D., and Jin, X. (2018). A practical equivalent method for DFIG wind farms. *IEEE Trans. Sustain. Energy* 9, 610–620. doi: 10.1109/TSTE.2017.2749761

Muhammad Qamar, R., Nadarajah, M., and Ekanayake, C. (2016). On recent advances in PV output power forecast. *Solar Energy* 136, 125–144. doi: 10.1016/j.solener.2016.06.073

Piazza, M., Luna, M., Petrone, G., and Spagnuolo, G. (2017). Translation of the single-diode PV model parameters identified by using explicit formulas. *IEEE J. Photovolt.* 7, 1009–1016. doi: 10.1109/JPHOTOV.2017.2699321

Remon, D., Cantarellas, M., and Rodriguez, P. (2016). Equivalent model of large-scale synchronous photovoltaic power plants. *IEEE Trans. Ind. Appl.* 52, 5029–5040. doi: 10.1109/TIA.2016.2598718

Sangwongwanich, A., Yang, Y., and Blaabjerg, F. (2017). A sensorless power reserve control strategy for two-stage grid-connected PV systems. *IEEE Trans. Power Electron.* 32, 8559–8569. doi: 10.1109/TPEL.2017.2648890

Shao, C., Wang, W., Hang, L., Tong, A., and Wang, S. (2018). "A novel PV array connection strategy with PV-buck module to improve system efficiency," in *Proceedings of the 2018 International Power Electronics Conference (IPEC-Niigata 2018 -ECCE Asia)*, (Niigata: IEEE).

Siouane, S., Jovanoviæ, S., and Poure, P. (2019). Open-switch fault-tolerant operation of a two-stage buck/buck–boost converter with redundant synchronous switch for PV systems. *IEEE Trans. Ind. Electron.* 66, 3938–3947. doi: 10.1109/TIE.2018.2847653

Xiang, J., Wei, W., and Cai, H. (2016). Modelling, analysis and control design of a two-stage photovoltaic generation system. *IET Renew. Power Gener.* 10, 1195–1203. doi: 10.1049/iet-rpg.2015.0514

Yamaguchi, D., and Fujita, H. (2018). A new PV converter for a high-leg delta transformer using cooperative control of boost converters and inverters. *IEEE Trans. Power Electron.* 33, 9542–9550. doi: 10.1109/TPEL.2018.2791343

Zapata, J., Kouro, S., Carrasco, G., Renaudineau, H., and Meynard, A. T. (2019). Analysis of partial power DC–DC converters for two-stage photovoltaic systems. *IEEE J. Emerg. Select. Top. Power Electron.* 7, 591–603. doi: 10.1109/JESTPE.2018.2842638

Zhang, M., Song, B., and Wang, J. (2019). Circulating current control strategy based on equivalent feeder for parallel inverters in islanded microgrid. *IEEE Trans. Power Syst.* 34, 595–605. doi: 10.1109/TPWRS.2018.2867588

Zou, J., Peng, C., Xu, H., and Yan, Y. (2015). A fuzzy clustering algorithm-based dynamic equivalent modeling method for wind farm with DFIG. *IEEE Trans. Energy Conv.* 30, 1329–1337. doi: 10.1109/TEC.2015.2431258

**Conflict of Interest:** XL, ZY, and JJ were employed by company State Grid Jiangsu Electric Power Company Limited. CL was employed by company National Electric Power Dispatching and Communication Center.

The remaining authors declare that the research was conducted in the absence of any commercial or financial relationships that could be construed as a potential conflict of interest.

frontiers in Neurorobotics

ORIGINAL RESEARCH
published: 14 October 2020
doi: 10.3389/fnbot.2020.00053

# Self-Triggered Consensus of Vehicle Platoon System With Time-Varying Topology

*Weiping Wang*[1,2,3,4]*, *Chunyang Wang*[1,2,3,4], *Yongzhen Guo*[5,6]*, *Xiong Luo*[1,2,3,4] and *Yang Gao*[7]

[1] School of Computer and Communication Engineering, University of Science and Technology Beijing, Beijing, China, [2] Beijing Key Laboratory of Knowledge Engineering for Materials Science, Beijing, China, [3] Institute of Artificial Intelligence, University of Science and Technology Beijing, Beijing, China, [4] Shunde Graduate School, Beijing University of Science and Technology, Guangzhou, China, [5] Industrial Control System Evaluation and Certification Department of China Software Testing Center, Beijing, China, [6] School of Automation, Beijing Institute of Technology, Beijing, China, [7] China Information Technology Security Evaluation Center, Beijing, China

This paper focuses on the consensus problem of a vehicle platoon system with time-varying topology via self-triggered control. Unlike traditional control methods, a more secure event-triggered controller considering the safe distance was designed for the vehicle platoon system. Then, a Lyapunov function was designed to prove the stability of the platoon system. Furthermore, based on the new event-triggered function, a more energy efficient self-triggered control strategy was designed by using the Taylor formula. The new self-triggered control strategy can directly calculate the next trigger according to the state information of the last trigger. It avoids continuous calculation and measurement of vehicles. Finally, the effectiveness of the proposed two self-triggered control strategies were verified by numerical simulation experiments.

**Keywords: consense, event-triggered, self-triggered, distributed control, time-varying topology**

OPEN ACCESS

***Edited by:***
*Zijun Zhang,*
*City University of Hong Kong, Hong Kong*

***Reviewed by:***
*He Chen,*
*Hebei University of Technology, China*
*Panpan Yang,*
*Chang'an University, China*
*Mingwen Zheng,*
*Shandong University of Technology, China*
*Hui Zhao,*
*University of Jinan, China*

***Correspondence:**
*Weiping Wang*
*weipingwangjt@ustb.edu.cn*
*Yongzhen Guo*
*yzguo@cstc.org.cn*

***Received:*** *13 April 2020*
***Accepted:*** *06 June 2020*
***Published:*** *14 October 2020*

***Citation:***
*Wang W, Wang C, Guo Y, Luo X and Gao Y (2020) Self-Triggered Consensus of Vehicle Platoon System With Time-Varying Topology. Front. Neurorobot. 14:53. doi: 10.3389/fnbot.2020.00053*

## 1. INTRODUCTION

In recent years, multi-agent systems have been widely applied in intelligent transportation (Hee Lee et al., 2013; Vilarinho et al., 2016). As an important part of the intelligent transportation system, the self-driving vehicle platoon system has a wide range of applications in improving road utilization, enhancing safety and reliability, and alleviating traffic congestion.

The formation of control is an important issue for the vehicle platoon system. It refers to the control problem that a group of intelligent vehicles can interact with each other to maintain a predetermined geometric formation during the movement of a specific target or direction. In general, this mutual interaction between intelligent vehicles can be divided into fixed and time-varying topology. Most of the current research is mainly focused on a fixed topology (Peters et al., 2016; Viegas et al., 2018). However, in the actual driving process, the vehicle platoon system often has to face various complex terrain and traffic conditions. Formations do not stay the same all the time. The vehicle platoon system requires a change of formation. Therefore, it is necessary to study the time-varying topology of vehicle platoon system. At present, there are few research studies on vehicle platoon systems with time-varying topology. More research is focused on multi-agent systems (Munz et al., 2011; Saboori and Khorasani, 2014). For example, we found that we can design more reasonable and effective control strategies by analyzing the derivatives of time-varying topological variables (Wang et al., 2018). It is thus more practical to study the time-varying topology of the vehicle platoon system than fixed topology.

Recently, the formation consistency of the vehicle platoon system has been widely considered. It has been applied to deal with consistency of formation control problems (Ren, 2007; Stojković and Katić, 2017; Wang et al., 2017; Li et al., 2018). Bela Lantos and Gyorgy Max achieved the formation consistency of unmanned ground vehicles by using a two-trajectory nonlinear dynamic model (Lantos and Max, 2016). Peters et al. (2016) designed a way by which each follower tracks its immediate predecessor to achieve vehicle formation consistency.

Nevertheless, in the traditional vehicle platoon system consistency study, it is assumed that the vehicle platoon system has sufficient computing resources and energy supply (Fax and Murray, 2004; Lafferriere et al., 2005). The vehicle platoon system can thus carry on a continuous information exchange and a continuous control. However, such assumption is unreasonable. More often than not, the power supply and communication bandwidth of a vehicle platoon system are limited. Recently, it has been found that event-triggered control can coordinate resources among intelligent vehicles. Many scholars are thus interested in event-triggered control. As an aperiodic control mode, event-triggered control can update the controller only when needed. That is, the controller of the intelligent vehicle takes an effect when the measurement error of the vehicle platoon system exceeds a certain threshold.

Since event-triggered control can reduce the energy loss to a certain extent, many scholars apply it to consistency research (Wei et al., 2017). The author in Chu et al. (2019) proposed an unified event-triggered and distributed observer-based controller with globally asymptotic convergence rate. The consistency of vehicle platoon system is realized by the controller. A fault-tolerant controller which considered the communication time-delay and event-triggered mechanism was designed to achieve the consistency of the vehicle platoon system (Fei et al., 2019).

However, in order to obtain the next trigger moment, we need to constantly obtain the state information of surrounding vehicles and calculate whether the trigger conditions are met in the distributed event-triggered control function. It is because of continuous communication and computation that an event-triggered control strategy cannot reduce the detection loss in essence. But the self-triggered control strategy only needs to calculate the next trigger moment based on the status information of the last trigger moment. In the self-triggered strategy, data detection is no longer required between any two triggering moments. From this perspective, the self-triggered control strategy has a better performance. Authors designed a self-triggered control strategy for the second-order multi-agent system with fixed topology to ensure the consistency of the formation system (De Persis and Frasca, 2013). As far as we know, there are few research studies made on time-varying topology under self-triggering control in vehicle platoon system, and this sparked our research.

Based on the above considerations, we studied the consistency of time-varying topology for vehicle platoon system with second-order dynamics by using distributed event-triggered control and self-triggered control strategies. The contributions of our work are three-fold:

(1) A distributed event-triggered control function considering the safe distance between vehicles was designed, and this event-triggered control is more energy efficient than the continuous control in Fax and Murray (2004) and Lafferriere et al. (2005).
(2) Based on the Lyapunov stability analysis method, the distributed event-triggered control function under time-varying leader and time-varying topology was given. In comparison with the fixed topology in Du et al. (2017), the research of time-varying topology is more practical. Moreover, the research on time-varying leader is of more practical significance.
(3) According to (1) and (2), two distributed self-triggered control strategies were designed. In Zhang et al. (2016), Dolk et al. (2017), Wei et al. (2017), Wen et al. (2018), Chu et al. (2019), and Li Z. et al. (2019), an event-triggered control strategy was designed. Compared with these, the self-triggered control strategy further reduces the continuous detection of adjacent vehicles. Additionally, the distributed self-triggered controller is more general and practical than some existing control methods.

The rest of this paper was organized as follows. Preliminaries and the problem formulation are given in section 2. The event-triggered control and self-triggered control of vehicle platoon system with time-varying topology are studied in section 3. Two numerical simulation experiments are presented in section 4. Lastly, conclusions are drawn in section 5.

# 2. PRELIMINARIES AND PROBLEM FORMULATION

## 2.1. Graph Theory

Consider the consensus issue of multi-agent systems with time-varying topology; a communication graph is used to describe the communication topology of these agents. An undirected graph $\mathcal{G} = (\mathcal{V}, \mathcal{E}, \mathcal{A})$ consists of a finite node set $\mathcal{V} = \{1, 2, \cdots, N\}$, an edge set $\mathcal{E}$, where $\mathcal{E} \subseteq \mathcal{V} \times \mathcal{V}$, and an adjacency matrix $\mathcal{A} = \left[a_{ij}\right] \in \mathbb{R}^{N\times N}$. If $(j, i) \in \mathcal{E}$, $a_{ij} = 1$, and $a_{ij} = 0$ otherwise. The neighbor set of vehicle $i$ is defined as $\mathcal{N}_i \triangleq \{j \in \mathcal{V} | (j, i) \in \mathcal{E}, j \neq i\}$. The Laplacian matrix of the graph $\mathcal{G}$ is defined as $\mathcal{L} = [l_{ij}] \in \mathbb{R}^{N\times N}$, where $l_{ii} = \sum_{j\neq i} a_{ij}$ and $l_{ij} = -a_{ij}$, where $i \neq j$. Moreover, we assume that there are no self-cycles, that is $a_{ii} = 0$ for any $i \in \overline{N}$. The degree matrices $\mathcal{D} = \text{diag}\left\{d_1, \cdots, d_N\right\}$ are diagonal matrices, whose diagonal elements are given by $d_i = \sum_{j=1}^{N} a_{ij}$. The Laplacian matrix associated to $\mathcal{G}$ is defined as $\mathcal{L} = \mathcal{D} - \mathcal{A}$. The set of all neighbors of node $i$ is denoted by $\mathcal{N}_i = \{j \in \mathcal{V} : (j, i) \in \mathcal{E}\}$. The matrix $B = \text{diag}\left\{b_1, b_2, \cdots, b_N\right\}$, where $b_i$ is called the adjacency coefficient between the following vehicle $i$ and the head vehicle. If the following vehicle $i$ is adjacent to the head vehicle $b_i = 1$, otherwise $b_i = 0$. In this paper, we define the time interval constant $h_{ij} > 0$ to control the safe distance between vehicles $i$ and $j$. At the same time, we define $h_i > 0$ to control the safe distance between vehicle $i$ and the leader vehicle.

## 2.2. Definitions and Lemmas

**ASSUMPTION 2.1.** *It is assumed that no topology changes happen during the trigger interval.*

**ASSUMPTION 2.2.** *It is assumed that the communication between vehicles is good, that is, there will be no communication delay and other uncertain factors.*

**ASSUMPTION 2.3.** *Suppose that at least one spanning tree exists in $\mathcal{G}$ and the node corresponding to the header is the root of the tree. The existence of the spanning tree ensures that each following vehicle can obtain the status information from the leader.*

**LEMMA 2.1.** $2x^{\mathrm{T}}y \leq ax^{\mathrm{T}}x + \frac{1}{a}y^{\mathrm{T}}y$, *where $a > 0$, and the vectors $x$ and $y$ can be any value.*

**LEMMA 2.2.** *Satur and Kharchenko (2020) suppose the matrix $A$ is a $n \times n$ real symmetric matrix, $Y$ is an $n$-dimensional real vector, and $\lambda_{\max}(A) \geq \lambda_i(A) \geq \lambda_{\min}(A)(i = 1, 2, ..., N)$. One has*

$$\lambda_{\max}(A)\langle Y, Y\rangle \geq \langle AY, Y\rangle \geq \lambda_{\min}(A)\langle Y, Y\rangle. \tag{1}$$

**LEMMA 2.3.** *Li W. et al. (2019) assuming that the function $f$ satisfies Lipschitz condition, there is a non-negative constant $l \geq 0$ that satisfies $\|f(t, x_i) - f(t, x_0)\| \leq l\|x_i - x_0\|$, or there are non-negative constants $l_x \geq 0, l_v \geq 0$ satisfies*

$$\|f(t, x_i, v_i) - f(t, x_0, v_0)\| \leq l_x\|x_i - x_0\| + l_v\|v_i - v_0\|. \tag{2}$$

## 2.3. Problem Formulation

An auto-driving vehicle formation system consisted of $n$ smart cars (see **Figure 1**) is considered in this paper. Between the vehicles, status information can be transmitted according to certain regulations. The $h_i v_0$ in **Figure 1** is the distance between the $i$ th vehicle and the leader.

In this paper, the dynamics of the leader vehicle is described as

$$\begin{cases} \dot{x_0}(t) = v_0(t), \\ \dot{v_0}(t) = f(t, x_0, v_0), \end{cases} \tag{3}$$

where $x_0(t), v_0(t) \in \mathbf{R}^m$ express the displacement vector and the velocity vector of the leader vehicle, and $f(t, x_0, v_0)$ is the control input of the leader vehicle. When $f = 0$, the velocity of leader vehicle is constant, when $f \neq 0$ the velocity of the leader vehicle is changing.

The dynamic equation of the $i$ th follower intelligent vehicle is described as

$$\begin{cases} \dot{x_i}(t) = v_i(t), \\ \dot{v_i}(t) = f(t, x_i, v_i) - f(t, x_0, v_0) + u_i(t), \end{cases} \tag{4}$$

where $x_i(t), v_i(t) \in \mathbf{R}^m$ express the displacement vector and the speed vector of the follower intelligent vehicle $i$ respectively, and $f(t, x_i, v_i) - f(t, x_0, v_0) + u_i(t)$ is the control input of the $i$ th follower intelligent vehicle.

**REMARK 1.** *The function $f(t, x, v)$ is an acceleration function known to all vehicles, and it satisfies LEMMA 2.3.*

# 3. MAIN RESULT

## 3.1. Distributed Event-Triggered Control of Vehicle Platoon System With Time-Varying Topology

In order to reduce the sensor data acquisition and the energy consumption of frequent communication between vehicles, a distributed event-triggered controller is designed in this section. In the distributed event-triggered controller, each of the following vehicle has different trigger function, and its controller update is asynchronous. When the trigger condition is satisfied, the controller of the $i$ th follower vehicle is updated at ${t_k}^i (k = 0, 1, 2\cdots)$. It is satisfied $u_i(t) = u_i({t_k}^i)$, and $\dot{u_i}(t) = 0$, $\forall t \in [{t_k}^i, {t_k}^{i+1})$. Since the topology is time-varying, the graph $\mathcal{G}$ can be treated as $\mathcal{G}(t)$. Accordingly, $\mathcal{A}$, $\mathcal{L}$, $\mathcal{D}$, and $\mathcal{B}$ become $\mathcal{A}(t)$, $\mathcal{L}(t)$, $\mathcal{D}(t)$, and $\mathcal{B}(t)$. In this case, Assumption 1 and Assumption 2 still hold.

### 3.1.1. The Leader Vehicle Speed Is Constant

In this section, the leader-follower consistency problem in the case of time-varying topology, which is based on the fact that the leader vehicle speed is constant, is studied, i.e., $f(t, x_0, v_0) = 0$.

To make the system consistent, we set the controller of $i$ th follower vehicle:

$$\begin{aligned} u_i(t) = &-k\Big[\sum\nolimits_{j\in N_i({t_k}^i)} a_{ij}({t_k}^i)(x_i({t_k}^i) - x_j({t_k}^i) - h_{ij}v_0) \\ &+ b_i({t_k}^i)(x_i({t_k}^i) - x_0({t_k}^i) - h_i v_0)\Big] \\ &- kr\Big[\sum_{j\in N_i({t_k}^i)} a_{ij}({t_k}^i)(v_i({t_k}^i) - v_j({t_k}^i)) + b_i({t_k}^i)(v_i({t_k}^i) \\ &- v_0({t_k}^i))\Big], \quad t \in [{t_k}^i, {t_k}^{i+1}), \end{aligned} \tag{5}$$

where $k$ and $r$ are control gains, and $N_i({t_k}^i)$ represents the set of neighbors of the $i$ th follower vehicle at ${t_k}^i$.

In order to describe the displacement and speed tracking between the following vehicle $i$ and the leader vehicle, we defined the displacement error $\varepsilon_i$ and the velocity error $\eta_i$ as follows:

$$\begin{aligned} \varepsilon_i(t) &= x_i(t) - x_0(t) - h_i v_0, \\ \eta_i(t) &= v_i(t) - v_0(t). \end{aligned} \tag{6}$$

The measurement error $e_i^x(t)$ and $e_i^v(t)$ are designed to represent the displacement and velocity differences between the triggering and the measuring moments of the $i$ th follower vehicle. We have then

$$\begin{aligned} e_i^x(t) &= \varepsilon_i(t_k^i) - \varepsilon_i(t), \\ e_i^v(t) &= \eta_i(t_k^i) - \eta_i(t). \end{aligned} \tag{7}$$

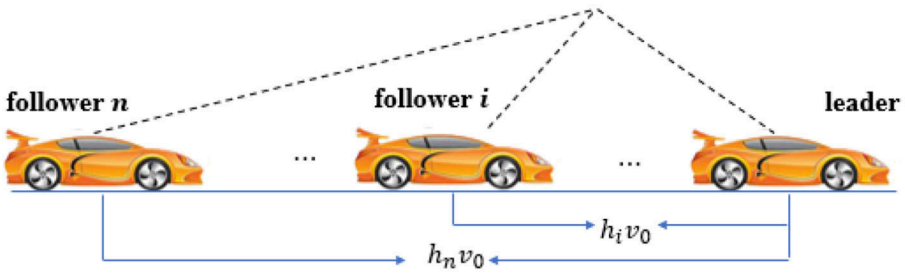


**FIGURE 1 |** Platoon of vehicles.

So the controller of the following intelligent vehicle becomes

$$\begin{aligned} u_i(t) = &- k[\sum_{j\in N_i(t)} a_{ij}(t)(\varepsilon_i(t) - \varepsilon_j(t)) + b_i(t)\varepsilon_i(t)] \\ &- kr[\sum_{j\in N_i(t)} a_{ij}(t)(\eta_i(t) - \eta_j(t)) + b_i(t)\eta_i(t)] \\ &- k[\sum_{j\in N_i(t)} a_{ij}(t)(e_i^x(t) - e_j^x(t)) + b_i(t)e_i^x(t)] \\ &- kr[\sum_{j\in N_i(t)} a_{ij}(t)(e_i^v(t) - e_j^v(t)) + b_i(t)e_i^v(t)]. \end{aligned} \tag{8}$$

The states and the measurement errors of intelligent vehicle are written in the vector form:

$$\begin{aligned} \varepsilon(t) &= \mathrm{col}\left(\varepsilon_1(t), \varepsilon_2(t), \ldots, \varepsilon_N(t)\right), \\ \eta(t) &= \mathrm{col}\left(\eta_1(t), \eta_2(t), \ldots, \eta_3(t)\right), \\ e^x(t) &= \mathrm{col}\left(e_1^x(t), e_2^x(t), \ldots, e_N^x(t)\right), \\ e^v(t) &= \mathrm{col}\left(e_1^v(t), e_2^v(t), \ldots, e_N^v(t)\right). \end{aligned} \tag{9}$$

According to (9), we have

$$\begin{cases} \dot{\varepsilon}(t) = \eta(t), \\ \dot{\eta}(t) = -k(L(t) + B(t)) \otimes I_m\varepsilon(t) - rk(L(t) + B(t)) \\ \qquad \otimes I_m\eta(t) - k(L(t) + B(t)) \otimes I_m e^x(t) \\ \qquad -rk(L(t) + B(t)) \otimes I_m e^v(t). \end{cases} \tag{10}$$

**Theorem 3.1.** *Consider a fleet of $N + 1$ vehicles, where the dynamic equations of the head vehicle and the follower vehicle are (3) and (4). If the following conditions are met under the controller (8), then*

*(1) The proposed event triggering function satisfies*

$$\zeta\left(\left\|\varepsilon_i(t)\right\|^2 + \left\|\eta_i(t)\right\|^2\right) \le M\left(\left\|e_i^x(t)\right\|^2 + \left\|e_i^v(t)\right\|^2\right), \tag{11}$$

*where $M = \frac{ka\lambda_{\min}(H(t))}{2}$, $H(t) = L(t) + B(t)$ and $\zeta$ will be indicated below. When this condition is met, the controller automatically updates, that is, the trigger time is reached.*

*(2) The minimum eigenvalue of $(L(t) + B(t)) \otimes I_m$ is greater than zero, which is greater than an arbitrarily small normal number $\delta$.*

$$\lambda_{\min}\left((L(t) + B(t)) \otimes I_m\right) \ge \delta > 0. \tag{12}$$

*(3) The differential coefficient of $(L(t) + B(t)) \otimes I_m$ exists, and the maximum eigenvalue of its derivative is greater than zero; for any small positive number, $\sigma$ is satisfied*

$$\lambda_{\max}\left(d\left((L(t) + B(t)) \otimes I_m\right)/dt\right) \ge \sigma > 0, \tag{13}$$

*(4) The relation between $\eta(t)$ and $e^x(t), e^v(t)$ is*

$$\begin{aligned} - < kH(t) \otimes I_m e^x(t), \eta(t) > &\le -\frac{ka\lambda_{\min}(H(t))}{2}||e^x(t)|| \\ &+ \frac{k\lambda_{\min}(H(t))}{2a}||\eta(t)||, \\ - < kH(t) \otimes I_m e^v(t), \eta(t) > &\le -\frac{ka\lambda_{\min}(H(t))}{2}||e^v(t)|| \\ &+ \frac{k\lambda_{\min}(H(t))}{2a}||\eta(t)||, \end{aligned} \tag{14}$$

*where $\zeta = \max\left(\frac{k\psi}{2}, \left(\frac{1}{a} - 1\right)k\lambda_{\min}(H(t))\right), 0 < a < 1, \psi = \lambda_{\max}\left(d\left((L(t) + B(t)) \otimes I_m\right)/dt\right)$, then all the vehicle reach the same state, and the existence of the safe distance $h_{ij}v_0$ avoid a collision. Hence, the problem of intelligent vehicle formation is solved, i.e., for $i = 1, 2, \ldots, N$, we have*

$$\begin{aligned} \lim_{t\to\infty}\left\|\varepsilon(t)\right\| &= 0, \\ \lim_{t\to\infty}\left\|\eta(t)\right\| &= 0. \end{aligned}$$

**PROOF.** Based on system (10), we can construct the common Lyapunov function candidate

$$\begin{aligned} V(t) = &\int_0^1 < kH(t) \otimes I_m\omega\varepsilon(t), \varepsilon(t) > d\omega \\ &+ \frac{1}{2} < \eta(t), \eta(t) >, \end{aligned} \tag{15}$$

where $H(t) = L(t) + B(t)$.

Firstly, we prove the positivity of $V(t)$

$$\begin{aligned} V &\ge \frac{1}{2}k\lambda_{\min}\left(H(t) \otimes I_m\right)\left\|\varepsilon(t)\right\|^2 + \frac{1}{2}\left\langle\eta(t), \eta(t)\right\rangle \\ &= \frac{1}{2}k\lambda_{\min}\left(H(t) \otimes I_m\right)\left\|\varepsilon(t)\right\|^2 + \frac{1}{2}\left\|\eta(t)\right\|^2 \\ &\ge \frac{1}{2}\min\left\{k\zeta, 1\right\}\left(\left\|\varepsilon(t)\right\|^2 + \left\|\eta(t)\right\|^2\right). \end{aligned} \tag{16}$$

It can be seen that the Lyapunov function (15) selected is positively definite.

The time derivative of (15) can be expressed as

$$\begin{aligned}\frac{\mathrm{d}V}{\mathrm{d}t} =& \frac{\mathrm{d}}{\mathrm{d}t}\int_0^1 < kH(t)\otimes I_m\omega\varepsilon(t),\varepsilon(t) > d\omega \\ &- < kH(t)\otimes I_m\varepsilon(t),\eta(t) > \\ &- < kH(t)\otimes I_m\eta(t),\eta(t) > \\ &- < kH(t)\otimes I_m e^x(t),\eta(t) > \\ &- < kH(t)\otimes I_m e^v(t),\eta(t) > .\end{aligned} \tag{17}$$

Taking out the first term, we have

$$\begin{aligned}&\frac{\mathrm{d}}{\mathrm{d}t}\int_0^1 < kH(t)\otimes I_m\omega\varepsilon(t),\varepsilon(t) > d\omega \\ &\quad= \int_0^1 < kH(t)\otimes I_m\omega\eta(t),\varepsilon(t) > d\omega \\ &\quad+ \int_0^1 < kH(t)\otimes I_m\omega\varepsilon(t),\eta(t) > d\omega \\ &\quad+ \int_0^1 < k\frac{\mathrm{d}(H(t))}{\mathrm{d}t}\otimes I_m\omega\varepsilon(t),\varepsilon(t) > d\omega \\ &\quad=< kH(t)\otimes I_m\varepsilon(t),\eta(t) > \\ &\quad+ \int_0^1 < k\frac{\mathrm{d}(H(t))}{\mathrm{d}t}\otimes I_m\omega\varepsilon(t),\varepsilon(t) > d\omega.\end{aligned} \tag{18}$$

By (18), we get

$$\begin{aligned}\frac{\mathrm{d}V}{\mathrm{d}t} =& \int_0^1 < k\frac{\mathrm{d}(\mathrm{H(t)}\otimes \mathrm{I_m})}{\mathrm{d}t}\omega\varepsilon(t),\varepsilon(t) > d\omega - < kH(t) \\ &\otimes I_m\eta(t),\eta(t) > - < kH(t)\otimes I_m e^x(t),\eta(t) > \\ &- < kH(t)\otimes I_m e^v(t),\eta(t) > .\end{aligned} \tag{19}$$

Take (19) into consideration, we have

$$\begin{aligned}\frac{\mathrm{d}V}{\mathrm{d}t} =& \int_0^1 < k\frac{\mathrm{d}(H(t)\otimes I_m)}{\mathrm{d}t}\omega\varepsilon(t),\varepsilon(t) > d\omega \\ &- < kH(t)\otimes I_m\eta(t),\eta(t) > \\ &- \frac{ka\lambda_{\min}(H(t))}{2}||e^x(t)||^2 + \frac{k\lambda_{\min}(H(t))}{2a}||\eta(t)||^2 \\ &- \frac{ka\lambda_{\min}(H(t))}{2}||e^v(t)||^2 + \frac{k\lambda_{\min}(H(t))}{2a}||\eta(t)||^2 \\ \le& (\frac{k\psi}{2}||\varepsilon(t)||^2 + (\frac{1}{a}-1)k\lambda_{\min}(H(t))||\eta(t)||^2) \\ &- (\frac{ka\lambda_{\min}(H(t))}{2}(||e^x(t)||^2 + ||e^v(t)||^2)) \\ \le& \varsigma(||\varepsilon(t)||^2 + ||\eta(t)||^2) \\ &- (\frac{ka\lambda_{\min}(H(t))}{2}(||e^x(t)||^2 + ||e^v(t)||^2)),\end{aligned} \tag{20}$$

where $\zeta = \max\left(\frac{k\psi}{2}, \left(\frac{1}{a}-1\right)k\lambda_{\min}(H(t))\right)$, $\psi = \lambda_{\max}(\mathrm{d}((L(t)+B(t))\otimes I_m)/\mathrm{d}t)$. According to the trigger condition (11), the derivative of the Lyapunov function is less or equal to 0, so the stability is proved.

### 3.1.2. The Speed of the Leading Vehicle Is Time Varying

In the actual situation, the speed of the leading vehicle cannot be fixed, most of them are time varying. Therefore, in this section, we study the consistency of leader followers in the case of time-varying topology based on the fact that the speed of the leader vehicle is time varying, i.e., $f(t,x_0,v_0) \neq 0$. In the meantime, suppose $f(t,\varepsilon_i(t),\eta_i(t)) = f({t_k}^i,x_i({t_k}^i),v_i({t_k}^i)) - f(t,x_0({t_k}^i),v_0({t_k}^i))$.

To make the system consistent, we set the $i$ th follower vehicle's controller as

$$\begin{aligned}u_i(t) =& -k[\sum_{j\in N_i({t_k}^i)} a_{ij}({t_k}^i)(x_i({t_k}^i) - x_j({t_k}^i) - h_{ij}v_0) \\ &+b_i(t)(x_i({t_k}^i) - x_0({t_k}^i) - h_iv_0)] \\ &-kr[\sum_{j\in N_i({t_k}^i)} a_{ij}({t_k}^i)(v_i({t_k}^i) - v_j({t_k}^i)) + b_i({t_k}^i)(v_i(t) \\ &-v_0({t_k}^i))], \quad t\in[{t_k}^i,{t_k}^{i+1}).\end{aligned} \tag{21}$$

Similar to (6)–(9), we can format the system (4) as follows

$$\begin{aligned}\dot{\varepsilon}(t) =& \eta(t), \\ \dot{\eta}(t) =& f(t,\varepsilon(t),\eta(t),e^x(t),e^v(t)) - k(L(t)+B(t))\otimes I_m\varepsilon(t) \\ &-rk(L(t)+B(t))\otimes I_m\eta(t) - k(L(t)+B(t))\otimes I_m e^x(t) \\ &-rk(L(t)+B(t))\otimes I_m e^v(t)\end{aligned} \tag{22}$$

**Theorem 3.2.** *Consider a fleet of $N+1$ vehicles, where the dynamic equations of the head vehicle and the follower vehicle are (3) and (4) respectively. If the following conditions are met under the controller (21), then*

*(1) The designed event triggering function satisfies the following conditions.*

$$\begin{aligned}\zeta(||\varepsilon_i(t)||^2 + ||\eta_i(t)||^2) \le& (\frac{ka\lambda_{\min}(H(t))}{2} - \frac{l}{2a_1}) \\ &\times(||{e_i}^x(t)||^2 + ||{e_i}^v(t)||^2)),\end{aligned} \tag{23}$$

*where $H(t) = L(t)+B(t)$ and $\zeta$ will be indicated below. When this condition is met, the controller automatically updates, that is, the trigger time is reached.*

*(2) The minimum eigenvalue of $(L(t)+B(t))\otimes I_m$ is greater than zero. There is thus a small positive number $\delta$ satisfying*

$$\lambda_{\min}\left((L(t)+B(t))\otimes I_m\right) \ge \delta > 0. \tag{24}$$

*(3) The differential coefficient of $(L(t)+B(t))\otimes I_m$ exists, and the maximum eigenvalue of its derivative is greater than zero, so there exists a small positive number $\sigma$ satisfying*

$$\lambda_{\max}\left(d\left((L(t)+B(t))\otimes I_m\right)/dt\right) \ge \sigma > 0. \tag{25}$$

*(4) The relation between $\eta(t)$ and $e^x(t), e^v(t)$ is*

$$\begin{aligned} - < kH(t) \otimes I_m e^x(t), \eta(t) > \leq & -\frac{ka\lambda_{\min}(H(t))}{2}||e^x(t)|| \\ & + \frac{k\lambda_{\min}(H(t))}{2a}||\eta(t)|| \\ - < kH(t) \otimes I_m e^v(t), \eta(t) > \leq & -\frac{ka\lambda_{\min}(H(t))}{2}||e^v(t)|| \\ & + \frac{k\lambda_{\min}(H(t))}{2a}||\eta(t)||. \end{aligned} \tag{26}$$

*(5)*

$$\frac{ka\lambda_{\min}(H(t))}{2} - \frac{l}{2a_1} > 0, \tag{27}$$

*where* $\zeta = \max(\frac{k\psi}{2} + \frac{l}{2a_1}, \frac{3a_1 l}{2} + l + \frac{k\lambda_{\min}(H(t))}{a})$, $\psi = \lambda_{\max}\left(d\left((L(t)+B(t)) \otimes I_m\right)/dt\right)$, $0 < a$, $0 < a_1$, $0 < k$, *then all the vehicles reach the same state, and at the same time the existence of safe distance* $h_{ij}v_0$ *avoid a collision. The problem of intelligent vehicle formation has been solved, i.e., for* $i = 1, 2, \ldots, N$, *we have*

$$\lim_{t\to\infty} \left\|\varepsilon(t)\right\| = 0,$$
$$\lim_{t\to\infty} \left\|\eta(t)\right\| = 0.$$

**PROOF**. Based on system (22), we can construct the Lyapunov function candidate

$$V(t) = \int_0^1 < kH(t) \otimes I_m \omega\varepsilon(t), \varepsilon(t) > d\omega + \frac{1}{2} < \eta(t), \eta(t) >, \tag{28}$$

where $H(t) = L(t) + B(t)$.

It can be seen that the (28) selected is positively definite.

The time derivative of (28) can be expressed as

$$\begin{aligned} \frac{dV}{dt} = & \frac{d}{dt}\int_0^1 < kH(t) \otimes I_m \omega\varepsilon(t), \varepsilon(t) > d\omega \\ & + < \eta(t), f(t, \varepsilon(t), \eta(t), e^x(t), e^v(t)) > \\ & - < kH(t) \otimes I_m \varepsilon(t), \eta(t) > - < kH(t) \otimes I_m \eta(t), \eta(t) > \\ & - < kH(t) \otimes I_m e^x(t), \eta(t) > - < kH(t) \otimes I_m e^v(t), \eta(t) > . \end{aligned} \tag{29}$$

Taking out of the first term, we have

$$\begin{aligned} & \frac{d}{dt}\int_0^1 < kH(t) \otimes I_m \omega\varepsilon(t), \varepsilon(t) > d\omega \\ = & \int_0^1 < kH(t) \otimes I_m \omega\eta(t), \varepsilon(t) > d\omega \\ & + \int_0^1 < kH(t) \otimes I_m \omega\varepsilon(t), \eta(t) > d\omega \\ & + \int_0^1 < k\frac{d(H(t))}{dt} \otimes I_m \omega\varepsilon(t), \varepsilon(t) > d\omega \\ = & < kH(t) \otimes I_m \varepsilon(t), \eta(t) > \\ & + \int_0^1 < k\frac{d(H(t) \otimes I_m)}{dt} \omega\varepsilon(t), \varepsilon(t) > d\omega. \end{aligned} \tag{30}$$

Using Lemma 2 to enlarge the second item in (29), we yield

$$\begin{aligned} & < \eta(t), f(t, \varepsilon(t), \eta(t), e^x(t), e^v(t)) > \\ & \leq \left\|\eta(t)\right\| l(\left\|\varepsilon(t)\right\| + \left\|\eta(t)\right\| \\ & + \left\|e^x(t)\right\| + \left\|e^v(t)\right\|). \end{aligned} \tag{31}$$

Considering (30) and (31), we get

$$\begin{aligned} \frac{dV}{dt} \leq & \int_0^1 < k\frac{d(H(t) \otimes I_m)}{dt} \omega\varepsilon(t), \varepsilon(t) > d\omega \\ & + \left\|\eta(t)\right\| l(\left\|\varepsilon(t)\right\| + \left\|\eta(t)\right\| + \left\|e^x(t)\right\| + \left\|e^v(t)\right\|) \\ & - < kH(t) \otimes I_m \eta(t), \eta(t) > \\ & - < kH(t) \otimes I_m e^x(t), \eta(t) > - < kH(t) \otimes I_m e^v(t), \eta(t) > . \end{aligned} \tag{32}$$

By using Lemma 3, the above items are amplified, and then

$$\begin{aligned} & \left\|\eta(t)\right\| l(\left\|\varepsilon(t)\right\| + \left\|\eta(t)\right\| + \left\|e^x(t)\right\| + \left\|e^v(t)\right\|) \\ = & l(\left\|\eta(t)\right\| \left\|\varepsilon(t)\right\| + \left\|\eta(t)\right\| \left\|\eta(t)\right\| \\ & + \left\|\eta(t)\right\| \left\|e^x(t)\right\| + \left\|\eta(t)\right\| \left\|e^v(t)\right\|), \end{aligned} \tag{33}$$

$$\begin{aligned} \left\|\eta(t)\right\| \left\|\varepsilon(t)\right\| & \leq \frac{a_1}{2}\left\|\eta(t)\right\|^2 + \frac{1}{2a_1}\left\|\varepsilon(t)\right\|^2, \\ \left\|\eta(t)\right\| \left\|e^x(t)\right\| & \leq \frac{a_1}{2}\left\|\eta(t)\right\|^2 + \frac{1}{2a_1}\left\|e^x(t)\right\|^2, \\ \left\|\eta(t)\right\| \left\|e^v(t)\right\| & \leq \frac{a_1}{2}\left\|\eta(t)\right\|^2 + \frac{1}{2a_1}\left\|e^v(t)\right\|^2, \end{aligned} \tag{34}$$

where $a_1 > 0$.

Considering (34), we have

$$\begin{aligned} \frac{dV}{dt} \leq & \frac{k\psi}{2}\left\|\varepsilon(t)\right\|^2 + (\frac{a_1 l}{2} + l)\left\|\eta(t)\right\|^2 \\ & + \frac{l}{2a_1}\left\|\varepsilon(t)\right\|^2 + \frac{a_1 l}{2}\left\|\eta(t)\right\|^2 + \frac{l}{2a_1}\left\|e^x(t)\right\|^2 \\ & + \frac{a_1 l}{2}\left\|\eta(t)\right\|^2 + \frac{l}{2a_1}\left\|e^v(t)\right\|^2 - \frac{ka\lambda_{\min}(H(t))}{2}||e^x(t)|| \\ & + \frac{k\lambda_{\min}(H(t))}{2a}||\eta(t)|| \\ & - \frac{ka\lambda_{\min}(H(t))}{2}||e^v(t)|| + \frac{k\lambda_{\min}(H(t))}{2a}||\eta(t)|| \\ \leq & (\frac{k\psi}{2} + \frac{l}{2a_1})\left\|\varepsilon(t)\right\|^2 + (\frac{3a_1 l}{2} + l + \frac{k\lambda_{\min}(H(t))}{2a} \\ & + \frac{k\lambda_{\min}(H(t))}{2a})\left\|\eta(t)\right\|^2 \\ & - (\frac{ka\lambda_{\min}(H(t))}{2} - \frac{l}{2a_1})(\left\|e^x(t)\right\|^2 + \left\|e^v(t)\right\|^2) \\ \leq & \varsigma(\left\|\varepsilon(t)\right\|^2 + \left\|\eta(t)\right\|^2) - (\frac{ka\lambda_{\min}(H(t))}{2} - \frac{l}{2a_1}) \\ & (\left\|e^x(t)\right\|^2 + \left\|e^v(t)\right\|^2). \end{aligned} \tag{35}$$

According to the trigger condition (23), the derivative of the Lyapunov function (29) is less or equal to 0, and it is constant, so the stability is proved.

## 3.2. Distributed Self-Triggered Control of Vehicle Platoon System With Time-Varying Topology

As can be seen from the distributed event-triggered control (11) and (23), the control method reduces the dependence on the global state information and the real-time state of measurement error in the trigger interval. However, it will increase the energy consumption of the sensor and microprocessor in the process of continuous measurement error detection. In order to improve this problem, we apply the self-triggered control strategy to solve the problem of intelligent vehicle formation. Under this strategy, the next trigger moment $t^i_{k+1}$ of the $i$th follower vehicle can obtained according to the state of the $i$th vehicle at the previous trigger time.

### 3.2.1. The Leader Vehicle Speed Is Constant

In this part, we will transform the event-triggered control (11) into a self-triggered control strategy for the case that the vehicle speed of the leader is constant.

We know that from the previous distributed event triggering control $\left(\left\|\varepsilon_i(t)\right\|^2+\left\|\eta_i(t)\right\|^2\right)\le\gamma\left(\left\|e^x_i(t)\right\|^2+\left\|e^v_i(t)\right\|^2\right)$, where $\gamma=\frac{ka\lambda_{\min}(H(t))}{2\zeta}$. Using Taylor's formula, expand $\varepsilon_i,\eta_i,e^x_i,e^v_i$ at $t^i_k$, we have

$$\begin{aligned}
\varepsilon_i(t) =&\eta_i({t_k}^i)(t-{t_k}^i)+\varepsilon_i({t_k}^i),\\
\eta_i(t) =&\dot{\eta}_i({t_k}^i)(t-{t_k}^i)+\eta_i({t_k}^i)\\
=&\Big(-k\sum_{j=1}^{N}\big(L_{j,\cdot}({t_k}^i)+B_{j,\cdot}({t_k}^i)\big)\varepsilon_j({t_k}^i)\\
&-kr\Big(\sum_{j=1}^{N}\big(L_{j,\cdot}({t_k}^i)+B_{j,\cdot}({t_k}^i)\big)\eta_j({t_k}^i)(t-{t_k}^i)\Big)\\
&+\eta_i({t_k}^i),\\
{e_i}^x =&\varepsilon_i({t_k}^i)-\varepsilon_i(t)=-\eta_i({t_k}^i)(t-{t_k}^i)\\
{e_i}^v =&\eta_i({t_k}^i)-\eta_i(t)=-\dot{\eta}_i({t_k}^i)(t-{t_k}^i)\\
=&-\Big(k\sum_{j=1}^{N}\big(L_{j,\cdot}({t_k}^i)+B_{j,\cdot}({t_k}^i)\big)\varepsilon_j({t_k}^i)\\
&-kr\sum_{j=1}^{N}\big(L_{j,\cdot}({t_k}^i)+B_{j,\cdot}({t_k}^i)\big)\eta_j({t_k}^i)\Big)(t-{t_k}^i),
\end{aligned}\tag{36}$$

where $L_{j,\cdot}$ represents $L_{j,k}$, and $k=0,1,2,\cdots,N$.

According to the above expressions and the distributed event-triggering control function (11), we get

$$\begin{aligned}
&\Big(||\eta_i({t_k}^i)(t-{t_k}^i)+\varepsilon_i({t_k}^i)||^2+||\\
&\Big(k\sum_{j=1}^{N}\big(L_{j,\cdot}({t_k}^i)+B_{j,\cdot}({t_k}^i)\big)\varepsilon_j({t_k}^i)\\
&-kr\sum_{j=1}^{N}\big(L_{j,\cdot}({t_k}^i)+B_{j,\cdot}({t_k}^i)\big)\eta_j({t_k}^i)\Big)(t-{t_k}^i)+\eta_i({t_k}^i)||^2\Big)\\
&\le\gamma\Big(||-\eta_i({t_k}^i)(t-{t_k}^i)||^2+||\\
&-\Big(-k\sum_{j=1}^{N}\big(L_{j,\cdot}({t_k}^i)+B_{j,\cdot}({t_k}^i)\big)\varepsilon_j({t_k}^i)\\
&-kr\sum_{j=1}^{N}\big(L_{j,\cdot}({t_k}^i)+B_{j,\cdot}({t_k}^i)\big)\eta_j({t_k}^i)\Big)(t-{t_k}^i)||^2\Big).
\end{aligned}\tag{37}$$

In order to simplify (37), we define

$$\Omega=\left\|\begin{matrix}-\Big(-k\sum_{j=1}^{N}\big(L_{j,\cdot}({t_k}^i)+B_{j,\cdot}({t_k}^i)\big)\varepsilon_j({t_k}^i)\\ -kr\sum_{j=1}^{N}\big(L_{j,\cdot}({t_k}^i)+B_{j,\cdot}({t_k}^i)\big)\eta_j({t_k}^i)\Big)\end{matrix}\right\|^2+\left\|-\eta_i({t_k}^i)\right\|^2,\tag{38}$$

and

$$\begin{aligned}
\pi=&-k\Big(\sum_{j=1}^{N}\big(L_{j,\cdot}({t_k}^i)+B_{j,\cdot}({t_k}^i)\big)\varepsilon_j({t_k}^i)\Big)\\
&-kr\Big(\sum_{j=1}^{N}\big(L_{j,\cdot}({t_k}^i)+B_{j,\cdot}({t_k}^i)\big)\eta_j({t_k}^i)\Big).
\end{aligned}\tag{39}$$

Suppose $\sigma_i=t-t^i_k$, we have

$$\left\|\eta_i({t_k}^i)\sigma_i+\varepsilon_i({t_k}^i)\right\|^2+\left\|\pi\sigma_i+\eta_i({t_k}^i)\right\|^2\le\gamma\Omega\sigma_i^2.\tag{40}$$

We can see that when $\sigma_i=0$, the inequality is not true. So $\sigma_i>0$, that is to say $t-{t_k}^i>0$. To sum up, the self-triggering control strategy of the follower vehicle at $t^{i+1}_k$ moment is determined by the following conditions

$$\left\|\eta_i({t_k}^i)\sigma_i+\varepsilon_i({t_k}^i)\right\|^2+\left\|\sigma_i+\eta_i({t_k}^i)\right\|^2=\gamma\Omega\sigma_i^2.\tag{41}$$

$\sigma_i>0$ which satisfies (41), we get the next trigger time $t^{i+1}_k=\sigma_i+t^i_k$. In particular, if the topology of the vehicle queue changes at time $t$, so that $t^{i+1}_k=t$.

**REMARK 2.** *The existence of $\sigma_i$ indicates that a Zeno behavior does not exist. At the same time, it indicates that the self-triggered control strategy can realize the leader-follower consistency of vehicle formation under the condition of time-varying topology and the leader vehicle speed being the same. The proof of stability is same to event-triggered control, so we are omitted here.*

### 3.2.2. The Speed of the Leading Vehicle Is Time Varying

In this part, we will transform the event-triggered control (23) into a self-triggered control strategy for the case that the vehicle speed of the leader is time varying.

We know that from the previous distributed event triggering control. $\left(\left\|\varepsilon_i(t)\right\|^2+\left\|\eta_i(t)\right\|^2\right)\le\gamma\left(\left\|e^x_i(t)\right\|^2+\left\|e^v_i(t)\right\|^2\right)$ where $\gamma=\frac{ka\lambda_{\min}(H(t))}{2\zeta}-\frac{1}{2a_1\zeta}$.

Using Taylor's formula, expand $\varepsilon_i, \eta_i, e_i^x, e_i^v$ at $t_k^i$, we have

$$\begin{aligned}
\varepsilon_i(t) &= \eta_i(t_k{}^i)(t - t_k{}^i) + \varepsilon_i(t_k{}^i),\\
\eta_i(t) &= \dot{\eta}_i(t_k{}^i)(t - t_k{}^i) + \eta_i(t_k{}^i)\\
&= \Big(f\big(t, \varepsilon(t_k{}^i), \eta(t_k{}^i), e^x(t_k{}^i), e^v(t_k{}^i)\big)\\
&\quad - k\sum_{j=1}^{N}\big(L_{j,\cdot}(t_k{}^i) + B_{j,\cdot}(t_k{}^i)\big)\varepsilon_j(t_k{}^i)\\
&\quad - kr\sum_{j=1}^{N}\big(L_{j,\cdot}(t_k{}^i) + B_{j,\cdot}(t_k{}^i)\big)\eta_j(t_k{}^i)\Big)(t - t_k{}^i) + \eta_i(t_k{}^i)
\end{aligned} \tag{42}$$

and

$$\begin{aligned}
e_i{}^x &= \varepsilon_i(t_k{}^i) - \varepsilon_i(t) = -\eta_i(t_k{}^i)(t - t_k{}^i)\\
e_i{}^v &= \eta_i(t_k{}^i) - \eta_i(t) = -\dot{\eta}_i(t_k{}^i)(t - t_k{}^i)\\
&= -\Big(f\big(t, \varepsilon(t_k{}^i), \eta(t_k{}^i), e^x(t_k{}^i), e^v(t_k{}^i)\big)\\
&\quad - k\sum_{j=1}^{N}\big(L_{j,\cdot}(t_k{}^i) + B_{j,\cdot}(t_k{}^i)\big)\varepsilon_j(t_k{}^i)\\
&\quad - kr\sum_{j=1}^{N}\big(L_{j,\cdot}(t_k{}^i) + B_{j,\cdot}(t_k{}^i)\big)\eta_j(t_k{}^i)\Big)(t - t_k{}^i).
\end{aligned} \tag{43}$$

According to the above two formulas and (23), we get

$$\begin{aligned}
&\Big(\big\|\eta_i(t_k{}^i)(t - t_k{}^i) + \varepsilon_i(t_k{}^i)\big\|^2\\
&+ \left\|\begin{array}{l}\Big(f(t, \varepsilon(t_k{}^i), \eta(t_k{}^i), e^x(t_k{}^i), e^v(t_k{}^i)\\ -k\sum_{j=1}^{N}\big(L_{j,\cdot}(t_k{}^i) + B_{j,\cdot}(t_k{}^i)\big)\varepsilon_j(t_k{}^i)\\ -kr\sum_{j=1}^{N}\big(L_{j,\cdot}(t_k{}^i) + B_{j,\cdot}(t_k{}^i)\big)\eta_j(t_k{}^i)\Big)(t - t_k{}^i)\\ +\eta_i(t_k{}^i)\end{array}\right\|^2\Big)\\
&\le \gamma\Big(\big\|-\eta_i(t_k{}^i)(t - t_k{}^i)\big\|^2\\
&+ \left\|\begin{array}{l}-\Big(f(t, \varepsilon(t_k{}^i), \eta(t_k{}^i), e^x(t_k{}^i), e^v(t_k{}^i)\\ -k\sum_{j=1}^{N}\big(L_{j,\cdot}(t_k{}^i) + B_{j,\cdot}(t_k{}^i)\big)\varepsilon_j(t_k{}^i)\\ -kr\sum_{j=1}^{N}\big(L_{j,\cdot}(t_k{}^i) + B_{j,\cdot}(t_k{}^i)\big)\eta_j(t_k{}^i)\Big)(t - t_k{}^i)\end{array}\right\|^2\Big).
\end{aligned} \tag{44}$$

In order to simplify (44), we define

$$\Omega = \left\|\begin{array}{l}-\Big(f(t, \varepsilon(t_k{}^i), \eta(t_k{}^i), e^x(t_k{}^i), e^v(t_k{}^i)\\ -k\sum_{j=1}^{N}\big(L_{j,\cdot}(t_k{}^i) + B_{j,\cdot}(t_k{}^i)\big)\varepsilon_j(t_k{}^i)\\ -kr\sum_{j=1}^{N}\big(L_{j,\cdot}(t_k{}^i) + B_{j,\cdot}(t_k{}^i)\big)\eta_j(t_k{}^i)\Big)\end{array}\right\|^2 + \big\|-\eta_i(t_k{}^i)\big\|^2, \tag{45}$$

$$\begin{aligned}
\pi &= f(t, \varepsilon(t_k{}^i), \eta(t_k{}^i), e^x(t_k{}^i), e^v(t_k{}^i)\\
&\quad - k\sum_{j=1}^{N}\big(L_{j,\cdot}(t_k{}^i) + B_{j,\cdot}(t_k{}^i)\big)\varepsilon_j(t_k{}^i)\\
&\quad - kr\sum_{j=1}^{N}\big(L_{j,\cdot}(t_k{}^i) + B_{j,\cdot}(t_k{}^i)\big)\eta_j(t_k{}^i).
\end{aligned} \tag{46}$$

Suppose $\sigma_i = t - t_k^i$, we have

$$\big\|\eta_i(t_k{}^i)\sigma_i + \varepsilon_i(t_k{}^i)\big\|^2 + \big\|\pi\sigma_i + \eta_i(t_k{}^i)\big\|^2 \le \gamma\Omega\sigma_i^2. \tag{47}$$

We obtain that $\sigma_i = 0$, and the inequality is not true; $\sigma_i > 0$ that is to say $t - t_k{}^i > 0$. To sum up, the self-triggering control strategy of the follower vehicle at $t_k^{i+1}$ moment is determined by the following conditions:

$$\big\|\eta_i(t_k{}^i)\sigma_i + \varepsilon_i(t_k{}^i)\big\|^2 + \big\|\pi\sigma_i + \eta_i(t_k{}^i)\big\|^2 = \gamma\Omega\sigma_i^2. \tag{48}$$

If there is a $\sigma_i > 0$ which satisfies (48), we get the next trigger time $t_k^{i+1} = \sigma_i + t_k^i$. In particular, if the topology of the vehicle queue changes at time $t$, so that $t_k^{i+1} = t$.

**REMARK 3.** *The existence of $\sigma_i$ indicates that a Zeno behavior does not exist. At the same time, it indicates that the self-triggered control strategy can achieve the leader-follower consistency of vehicle formation under the circumstance that both the topology structure and the leader vehicle speed are time varying. The proof of stability is the same to the event-triggered control. It is thus avoided here.*

## 4. SIMULATION

In this section, we will give two numerical experiments to verify the correctness and validity of the above theorems. Both experiments are based on a leader-follower vehicle formation system, which consist of a leader vehicle and four follower vehicles.

Firstly, we verify that the speed of the leader vehicle is constant. The dynamic equation of leader and follower are shown below:

$$\begin{cases}\dot{x}_0(t) = v_0(t),\\ \dot{v}_0(t) = 0,\end{cases}\quad\begin{cases}\dot{x}_i(t) = v_i(t),\\ \dot{v}_i(t) = u_i(t),\end{cases} \tag{49}$$

where $u_i(t)$ is defined in (5), $k = 3.4$, $r = 1.2$. and the parameters satisfy the conditions in Theorem 3.1.

In order to more intuitively verify the effectiveness of the self-triggering control strategy proposed in this paper, we assume that the vehicle formation system carries out three topology switches. The topology structure between vehicles at the initial moment is shown in **Figure 2**. Each adjacency matrix $A$ and coefficient

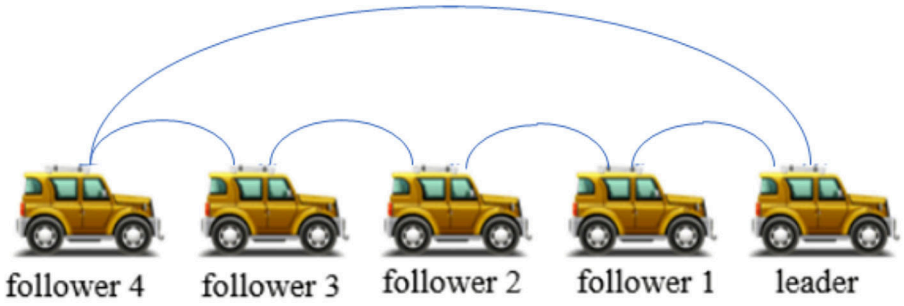


**FIGURE 2 |** Topology at initial time.

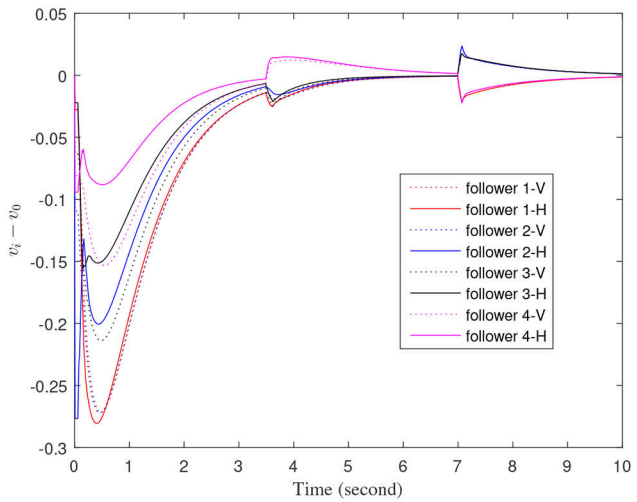


**FIGURE 3 |** The velocity error between the follower car and the leader car.

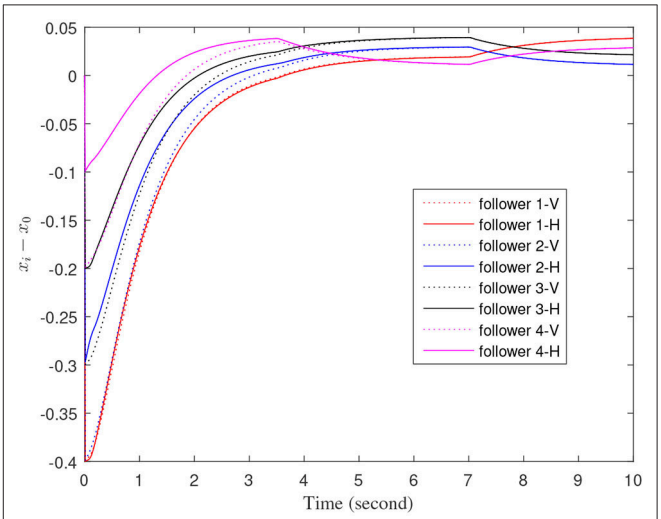


**FIGURE 4 |** The real-time distance between each follower car and the leader car.

matrix $H$ are defined as follows

$$A_1 = \begin{bmatrix} 0 & 1 & 0 & 0 \\ 1 & 0 & 1 & 0 \\ 0 & 1 & 0 & 1 \\ 0 & 0 & 1 & 0 \end{bmatrix}, \quad A_2 = \begin{bmatrix} 0 & 1 & 0 & 1 \\ 1 & 0 & 0 & 0 \\ 0 & 0 & 0 & 1 \\ 1 & 0 & 1 & 0 \end{bmatrix},$$

$$A_3 = \begin{bmatrix} 0 & 1 & 1 & 0 \\ 1 & 0 & 0 & 0 \\ 1 & 0 & 0 & 1 \\ 0 & 0 & 1 & 0 \end{bmatrix}, H_1 = \begin{bmatrix} 0 & -0.1 & -0.2 & -0.3 \\ 0.1 & 0 & -0.1 & -0.2 \\ 0.2 & 0.1 & 0 & 0.1 \\ 0.3 & 0.2 & 0.1 & 0 \end{bmatrix},$$

$$H_2 = \begin{bmatrix} 0 & -0.1 & -0.2 & 0.1 \\ 0.1 & 0 & -0.1 & 0.2 \\ 0.2 & 0.1 & 0 & 0.3 \\ -0.1 & -0.2 & -0.3 & 0 \end{bmatrix},$$

$$H_3 = \begin{bmatrix} 0 & 0.3 & 0.2 & 0.1 \\ -0.3 & 0 & 0.1 & -0.2 \\ -0.2 & 0.1 & 0 & -0.1 \\ -0.1 & 0.2 & 0.1 & 0 \end{bmatrix}.$$

The initial values of the leader vehicle and the follower vehicle are defined as follows:

$$\begin{aligned} &x_0(0) = (0,0), \quad x_1(0) = (-0.4,-0.5), \quad x_2(0) = (-0.3,-0.3), \\ &x_3(0) = (-0.2,-0.4), x_4(0) = (-0.2,-0.1), \\ &v_0(0) = (0.1,0.1), \quad v_1(0) = (0.15,0.1) \\ &v_2(0) = (0.1,0.12), \\ &v_3(0) = (0.15,0.1), \quad v_4(0) = (0.18,0.2). \end{aligned} \tag{50}$$

**Figures 3**–**7** are the results for the leader vehicle at constant speed. **Figure 3** shows the velocity error between the follower car and the leader car. **Figure 4** express as the real-time distance between each follower car and the leader car. **Figure 5** express as the changes in the controller of each follower car. Because the topology is changed, the controller changed dramatically twice. The self-trigger interval of each follower are displayed in **Figure 6**. **Figure 7** shows the relative position of vehicles when the formation is finally stabilized.

As we can see from **Figures 3**–**5**, when the topology changes, the controller of the follower vehicle adjusts the vehicle speed to keep the vehicle in formation and the error of vehicle speed

tends to zero over time. This indicates that the controller can adapt to various topological switching situations by adjusting the control intensity. At the same time, due to the change of topology, the relative positions between vehicles will also change, and the follower vehicles will constantly adjust their positions to the new relative positions under the action of the controller. It is worth noting that the position error of the follower vehicles does not gradually approach zero as time goes on, and it reaches a fixed value greater than zero in **Figure 4**. This fixed value is the safe distance ($h_{ij}v_0$) between the vehicles. As shown in **Figure 7**, when a stable state is reached, the vehicles should keep a safe distance from each other. Moreover the self-triggering instants are displayed in **Figure 6**. The simulation results exhibit that the controller and the self-triggering control strategy designed by us have a good performance. It achieves the stability of vehicle formation system under the condition of constant topological changes. Moreover, the vehicles can keep a safe distance.

Secondly, we verify that the speed of the leader vehicle is time varying. In order to more intuitively verify the effectiveness of the self-triggering control strategy, we randomly selected several

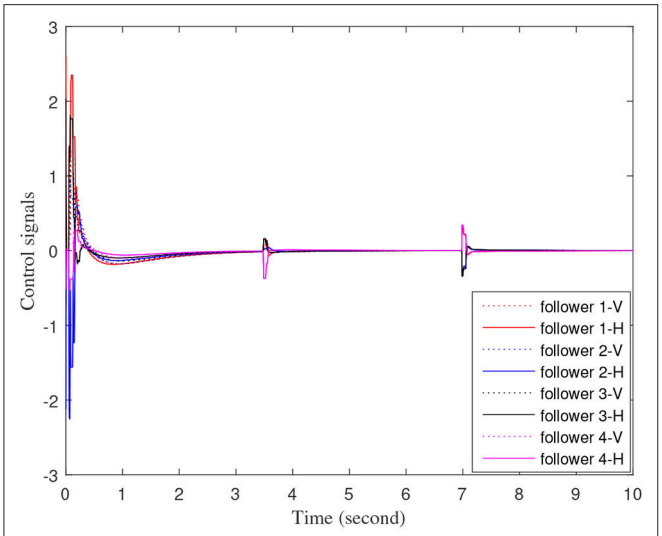


**FIGURE 5 |** Control input signals of each follower vehicle.

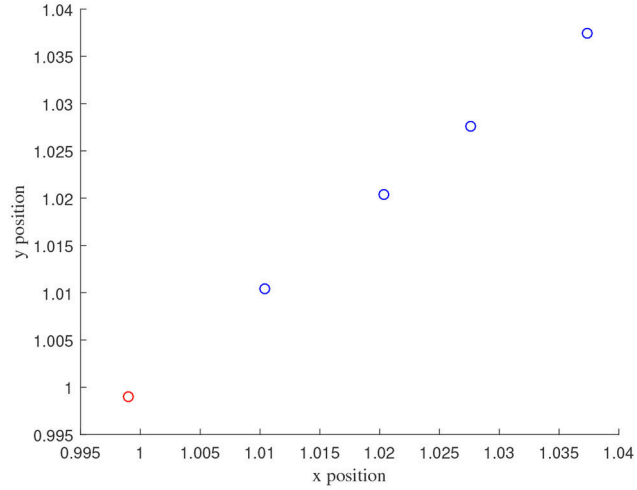


**FIGURE 7 |** The position information of the vehicle when the formation is stable.

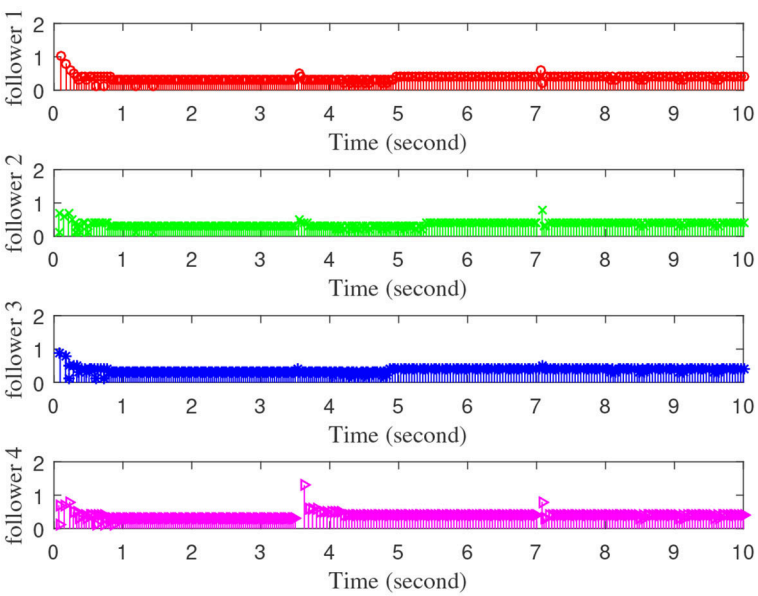


**FIGURE 6 |** The event trigger interval of each follower vehicle.

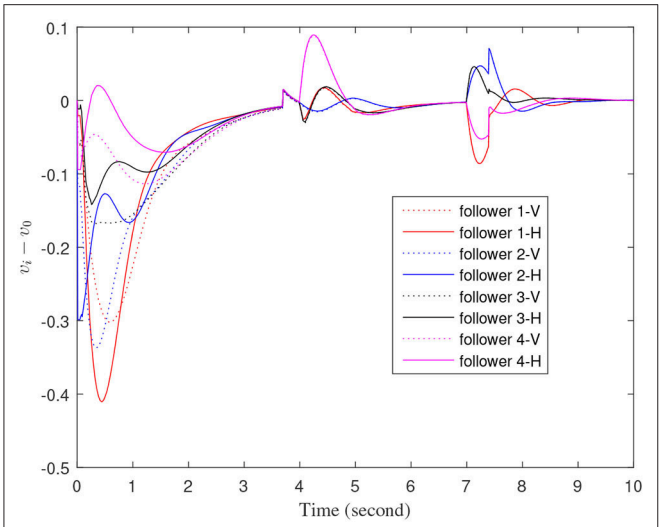


**FIGURE 8 |** The velocity error between the follower car and the leader car.

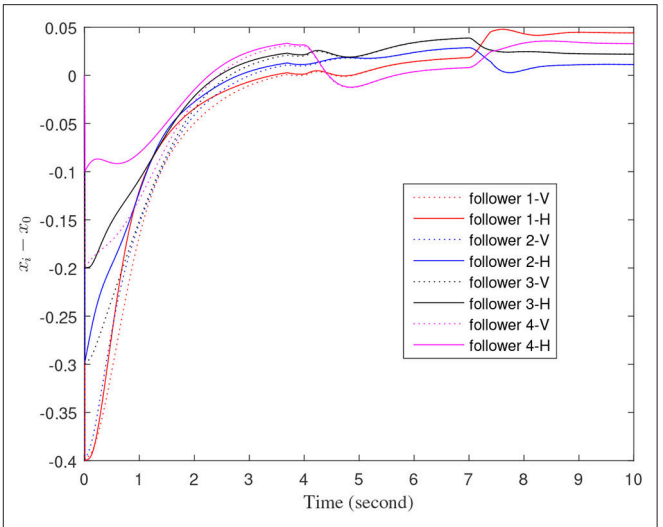


**FIGURE 9 |** The real-time distance between each follower car and the leader car.

time points and used the leader vehicle dynamics Equation (4) to change the state of the leader vehicle. The dynamic equation of the leading vehicle are as follows

$$\begin{cases} \dot{x_0}(t) = \dot{v_0}(t), \\ \dot{v_0}(t) = -\sin\left(x_0(t)\right) - 0.25v_0(t) + 1.5\cos(2.5t). \end{cases} \tag{51}$$

When the speed of leader changes, the dynamic equation of the follower's vehicle is defined as

$$\begin{cases} \dot{x}_i(t) = \dot{v}_i(t), \\ \dot{v}_i(t) = f(t, x_i, v_i) - f(t, x_0, v_0) + u_i(t), \end{cases} \tag{52}$$

where $f(t, x, v) = -\sin(x) - 0.25v + 1.5\cos(2.5t)$.

The define of **Figures 8–12** is similar to **Figures 3–7**, but **Figures 8–12** show the results of a leader with time-varying velocity. From **Figures 8–10**, we can see that when the speed of the leader vehicle or topology changes, the follower vehicle can quickly adapt to the changing so that its speed is consistent with the leader vehicle, and the real-time distance between follower vehicle and leader vehicle change rapidly. Moreover, it can be seen from **Figure 10**, that after the vehicle formation system reaches stability, the controller of the follower vehicle no longer exerts control. The self-triggering instants are displayed in **Figure 11**. Notably, after the leader vehicle speed changes, the safety distance of the follower vehicle also changes in **Figure 9**. However, the vehicles ultimately kept a safe distance, as shown in **Figure 12**. The simulation results show that the controller and the self-triggering control strategy designed in this paper have a good performance. It can make the vehicle formation system reach stable state under the condition of changing topology and leader speed.

The number of triggers with a distributed event-triggered control scheme in Yang et al. (2018) and self-triggered control scheme (41) within 0–15 s are shown in the **Table 1**. What we can

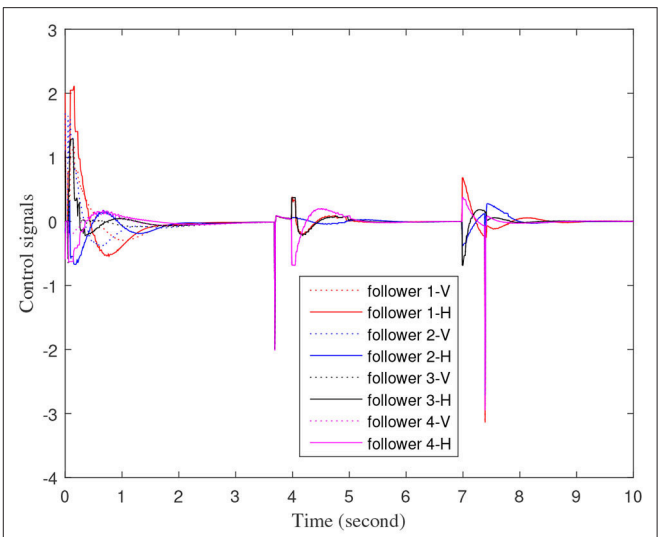


**FIGURE 10 |** Control input signals of each follower vehicle.

obtain from **Table 1** is that the self-triggered control scheme (41) needs less triggering events than the distributed event-triggered control scheme in Yang et al. (2018). At the same time, the mean time interval which represents the average time between each trigger in **Table 2** indicates that the self-triggered control strategy designed in this paper has a lower trigger probability and execution moment. It shows that the self-triggered control strategy proposed here can effectively reduce the energy loss of data detection and calculation in the control process.

## 5. CONCLUSIONS

In this paper, we have studied leader-follower consistency in vehicle formation systems with time-varying topology under

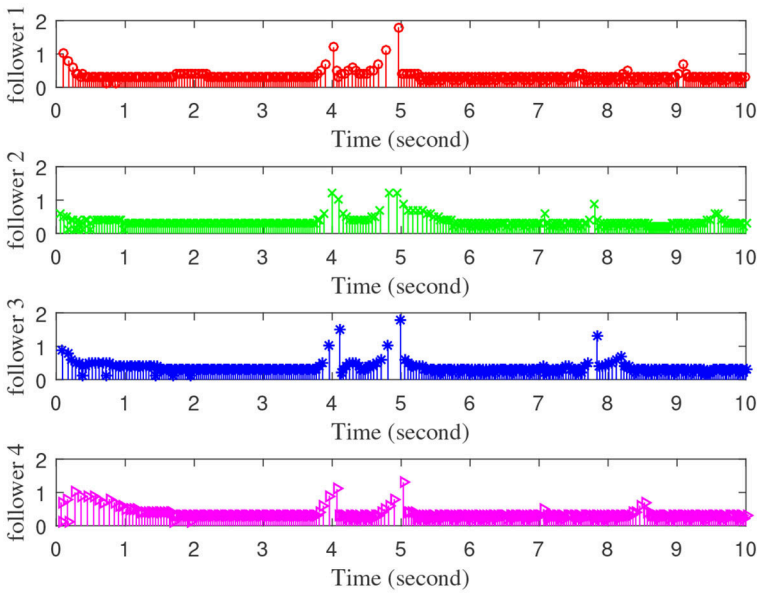


**FIGURE 11 |** The event trigger interval of each follower vehicle.

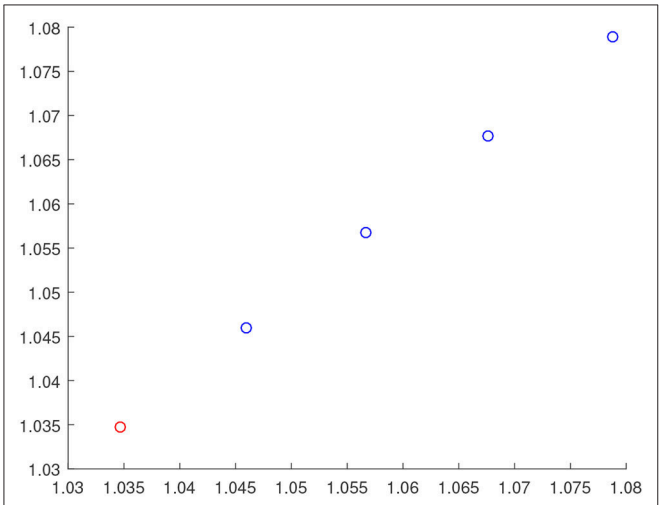

**FIGURE 12 |** The position information of the vehicle when the formation is stable.

**TABLE 1 |** Triggered numbers of follower agents.

| Control strategy | Numbers of triggered events of agents | | | |
|---|---|---|---|---|
| | 1 | 2 | 3 | Total |
| Event-triggered in Yang et al. (2018) | 582 | 857 | 1,029 | 2,468 |
| Self-triggered (41) | 275 | 234 | 226 | 735 |

**TABLE 2 |** Mean time interval of follower agents.

| Control strategy | Mean time interval | | |
|---|---|---|---|
| | 1 | 2 | 3 |
| Event-triggered in Yang et al. (2018) | 0.0127 | 0.0119 | 0.0151 |
| Self-triggered (41) | 0.0546 | 0.0641 | 0.0662 |

event-triggering mechanism. The difference between our work and the published papers is that we have designed a self-triggering control strategy that avoids continuous calculation and measurement and reduces the loss of communication resources. At the same time, we have proved the consistency of the system under the control of the trigger function. In addition, we have also studied the consistency of the vehicle formation system with time-varying topology when the leader speed is time varying. Finally, the effectiveness of the proposed controllers has been verified by numerical experiments. In addition, it should be noted that, although we proved the stability of formation system by Lyapunov function, we did not give its string stability which will be studied in the future.

## DATA AVAILABILITY STATEMENT

All datasets generated for this study are included in the article/supplementary material.

## AUTHOR CONTRIBUTIONS

All authors listed have made a substantial, direct and intellectual contribution to the work, and approved it for publication.

## FUNDING

This work was supported in part by the 2018 industrial Internet innovation and development project "construction of industrial Internet security standard system and test and verification environment", in part by the National Key Research and Development Program of China under Grant No. 2018YFB0803505, in part by the University of Science and Technology Beijing under Grant FRF-BD-19-012A and Grant FRF-TP-19-005A3, in part by the National Natural Science Foundation of China under Grant 81961138010, Grant U1736117 and Grant U1836106, and in part by the Technological Innovation Foundation of Shunde Graduate School, USTB, under Grant BK19BF006.

## REFERENCES

Chu, X., Peng, Z., Wen, G., and Rahmani, A. (2019). Distributed formation tracking of nonholonomic autonomous vehicles via event-triggered and sampled-data method. *Int. J. Control* 92, 2243–2254. doi: 10.1080/00207179.2018.1436193

De Persis, C., and Frasca, P. (2013). Robust self-triggered coordination with ternary controllers. *IEEE Trans. Automat. Control* 58, 3024–3038. doi: 10.1109/TAC.2013.2273302

Dolk, V. S., Ploeg, J., and Heemels, W. M. H. (2017). Event-triggered control for string-stable vehicle platooning. *IEEE Trans. Intell. Transport. Syst*. 18, 3486–3500. doi: 10.1109/TITS.2017.2738446

Du, H., Zhou, J., Wu, D., and Wen, G. (2017). "Consensus for second-order nonlinear leader-following multi-agent systems via event-triggered control," in *2017 International Workshop on Complex Systems and Networks (IWCSN)* (Hefei), 301–305. doi: 10.1109/IWCSN.2017.8276543

Fax, J. A., and Murray, R. M. (2004). Information flow and cooperative control of vehicle formations. *IEEE Trans. Automat. Control* 49, 1465–1476. doi: 10.1109/TAC.2004.834433

Fei, Z., Wang, X., Liu, M., and Yu, J. (2019). Reliable control for vehicle active suspension systems under event-triggered scheme with frequency range limitation. *IEEE Trans. Syst. Man Cybernet. Syst*. doi: 10.1109/TSMC.2019.2899942

Hee Lee, G., Faundorfer, F., and Pollefeys, M. (2013). "Motion estimation for self-driving cars with a generalized camera," in *Proceedings of the IEEE Conference on Computer Vision and Pattern Recognition (Zurich)*, 2746-2753. doi: 10.1109/CVPR.2013.354

Lafferriere, G., Williams, A., Caughman, J., and Veerman, J. (2005). Decentralized control of vehicle formations. *Syst. Control Lett*. 54, 899–910. doi: 10.1016/j.sysconle.2005.02.004

Lantos, B., and Max, G. (2016). Hierarchical control of unmanned ground vehicle formations using multi-body approach. *Acta Polytech. Hung*. 13, 137–156. doi: 10.12700/APH.13.1.2016.1.10

Li, W., Zhang, G., Pan, T., Zhang, Z., Geng, Y., and Wang, J. (2019). A lipschitz optimization-based mppt algorithm for photovoltaic system under partial shading condition. 7, 126323–33

Li, Y., Tang, C., Li, K., Peeta, S., He, X., and Wang, Y. (2018). Nonlinear finite-time consensus-based connected vehicle platoon control under fixed and switching communication topologies. *Transport. Res. C Emerg. Technol*. 93, 525–543. doi: 10.1016/j.trc.2018.06.013

Li, Z., Hu, B., Li, M., and Luo, G. (2019). String stability analysis for vehicle platooning under unreliable communication links with event-triggered strategy. *IEEE Trans. Vehicular Technol*. 68, 2152–2164. doi: 10.1109/TVT.2019.2891681

Munz, U., Papachristodoulou, A., and Allgower, F. (2011). Consensus in multi-agent systems with coupling delays and switching topology. *IEEE Trans. Automat. Control* 56, 2976–2982. doi: 10.1109/TAC.2011.2161052

Peters, A. A., Mason, O., and Middleton, R. H. (2016). "Leader following with non-homogeneous weights for control of vehicle formations," in *2016 IEEE Conference on Control Applications (CCA)* (Valparaiso: IEEE), 109-113. doi: 10.1109/CCA.2016.7587830

Ren, W. (2007). Multi-vehicle consensus with a time-varying reference state. *Syst. Control Lett*. 56, 474-483. doi: 10.1016/j.sysconle.2007.01.002

Saboori, I., and Khorasani, K. (2014). $H^{\infty}$ consensus achievement of multi-agent systems with directed and switching topology networks. *IEEE Trans. Automat. Control* 59, 3104–3109. doi: 10.1109/TAC.2014.2358071

Satur, O. R., and Kharchenko, N. V. (2020). A model of dynamical system for the attainment of consensus. *Ukr. Math. J.* 71, 1456–1469. doi: 10.1007/s11253-020-01725-w

Stojković, I., and Katić, D. (2017). Formation control of robotized aerial vehicles based on consensus-based algorithms. *FME Trans*. 45, 559–564. doi: 10.5937/fmet1704559S

Viegas, D., Batista, P., Oliveira, P., and Silvestre, C. (2018). Discrete-time distributed Kalman filter design for formations of autonomous vehicles. *Control Eng. Pract*. 75, 55–68. doi: 10.1016/j.conengprac.2018.03.014

Vilarinho, C., Tavares, J. P., and Rossetti, R. J. (2016). Design of a multiagent system for real-time traffic control. *IEEE Intell. Syst*. 31, 68–80. doi: 10.1109/MIS.2016.66

Wang, J., Y. Xu, J. Z., and Yang, D. (2018). Time-varying formation for general linear multi-agent systems via distributed event-triggered control under switching topologies. *Chin. Phys. B*. 27:040504. doi: 10.1088/1674-1056/27/4/040504

Wang, Z., Wu, G., and Barth, M. J. (2017). Developing a distributed consensus-based cooperative adaptive cruise control system for heterogeneous vehicles with predecessor following topology. *J. Adv. Transport*. 2017:1023654 doi: 10.1155/2017/1023654

Wei, Y., Liyuan, W., and Ge, G. (2017). Event-triggered platoon control of vehicles with time-varying delay and probabilistic faults. *Mech. Syst. Signal Process*. 87, 96–117. doi: 10.1016/j.ymssp.2016.09.042

Wen, S., Guo, G., Chen, B., and Gao, X. (2018). Event-triggered cooperative control of vehicle platoons in vehicular *ad hoc* networks. *Inform. Sci*. 459, 327–340. 341–353. doi: 10.1016/j.ins.2018.02.051

Yang, Y., Dong, Y., and Dou, C. (2018). Output-based event-triggered schemes on leader-following consensus of a class of multi-agent systems with lipschitz-type dynamics. *Inform. Sci*. 459, 327–340. doi: 10.1016/j.ins.2018.02.020

Zhang, H., Zheng, X., Yan, H., Peng, C., Wang, Z., and Chen, Q. (2016). Codesign of event-triggered and distributed $H^{\infty}$ filtering for active semi-vehicle suspension systems. *IEEE/ASME Trans. Mechatron*. 22, 1047–1058. doi: 10.1109/TMECH.2016.2646722

**Conflict of Interest:** The authors declare that the research was conducted in the absence of any commercial or financial relationships that could be construed as a potential conflict of interest.

frontiers in Neurorobotics

ORIGINAL RESEARCH
published: 27 October 2020
doi: 10.3389/fnbot.2020.584192

# Boosting Knowledge Base Automatically via Few-Shot Relation Classification

*Ning Pang, Zhen Tan*, Hao Xu and Weidong Xiao*

*Science and Technology on Information Systems Engineering Laboratory, National University of Defense Technology, Changsha, China*

Relation classification (RC) aims at extracting structural information, i.e., triplets of two entities with a relation, from free texts, which is pivotal for automatic knowledge base construction. In this paper, we investigate a fully automatic method to train a RC model which facilitates to boost the knowledge base. Traditional RC models cannot extract new relations unseen during training since they define RC as a multiclass classification problem. The recent development of few-shot learning (FSL) provides a feasible way to accommodate to fresh relation types with a handful of examples. However, it requires a moderately large amount of training data to learn a promising few-shot RC model, which consumes expensive human labor. This issue recalls a kind of weak supervision methods, dubbed distant supervision (DS), which can generate the training data automatically. To this end, we propose to investigate the task of *few-shot relation classification under distant supervision*. As DS naturally brings in mislabeled training instances, to alleviate the negative impact, we incorporate various multiple instance learning methods into the classic prototypical networks, which can achieve sentence-level noise reduction. In experiments, we evaluate our proposed model under the standard *N*-way *K*-shot setting of few-shot learning. The experiment results show that our proposal achieves better performance.

**Keywords: knowledge base, relation classification, few-shot learning, distant supervision, multiple instance learning**

OPEN ACCESS

***Edited by:***
*Zijun Zhang,*
*City University of Hong Kong,*
*Hong Kong*

***Reviewed by:***
*Yang Luoxiao,*
*City University of Hong Kong,*
*Hong Kong*
*Lun Hu,*
*Chinese Academy of Sciences (CAS),*
*China*

****Correspondence:***
*Zhen Tan*
*tanzhen08a@nudt.edu.cn*

***Received:*** *16 July 2020*
***Accepted:*** *15 September 2020*
***Published:*** *27 October 2020*

***Citation:***
*Pang N, Tan Z, Xu H and Xiao W (2020) Boosting Knowledge Base Automatically via Few-Shot Relation Classification. Front. Neurorobot. 14:584192. doi: 10.3389/fnbot.2020.584192*

## 1. INTRODUCTION

Relation Classification (RC) is defined as identifying semantic relations between entity pairs in given plain texts, which is a crucial task in automatic knowledge base (KB) construction (Bollacker et al., 2008). Mainstream works on this task mainly follow supervised learning, where large-scale and high-quality training data is required (Zeng et al., 2014; Gormley et al., 2015).

However, human-annotated data is always expensive to acquire. Subsequently, recent literature resorted to distant supervision (DS) (Mintz et al., 2009; Riedel et al., 2010) to address the sparsity issue of training data. In DS, it is assumed that *sentences mentioning an entity pair instantiate the relation of the corresponding entity pair in knowledge bases*. With this (untrue) heuristic, large-scale training data can be constructed automatically, but mislabeling is inevitably introduced at the same time. For example, as shown in **Figure 1**, since the triplet (*soccer*, publisher, *nintendo*) exists in a KB, two sentences mentioning the entity pair (*soccer*, *nintendo*) are assigned with the relation "publisher." In fact, the first sentence fails to express the target relation indeed, called false

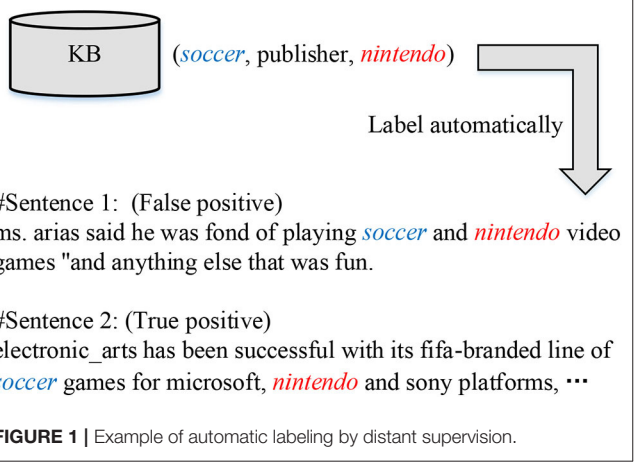


**FIGURE 1 |** Example of automatic labeling by distant supervision.

positive instance, while the second one obtains a correct label, which is a true positive instance. Hence, efforts were made to restrain the impact of false positives (Ji et al., 2017; Qin et al., 2018b; Wu et al., 2019). However, these models perform well on common relations, but suffer a dramatic performance drop in classifying long-tail relations, which have few training instances; that is, even though a large amount of training data can be generated by DS, the distributions of such data over different types are unbalanced. Furthermore, they are unable to recognize new relations that have not been seen in training, which potentially restricts their applications in certain scenarios that involve fresh relations in testing.

Lately, pioneering work (Han et al., 2018; Gao et al., 2019) has tried to formulate RC into few-shot learning (FSL) framework (Miller et al., 2000), which aims at accommodating new classes with few examples, while demanding less manual labor than generic supervised learning for fresh relations. Many efforts have made on the few-shot classification task. The early researches fine-tune models which are pre-trained with common classes containing adequate instances by transfer learning (Caruana, 1994; Donahue et al., 2014). After that, metric learning is proposed to project different classes into a distance space (Vinyals et al., 2016; Snell et al., 2017), where similar classes are placed close to each other. Lately, optimization-based meta-learning is developed fast because of its fast-learning ability to learn from previous experience and generalize to new knowledge (Finn et al., 2017; Ravi and Larochelle, 2017). These models, especially prototypical networks, achieve promising results on several benchmarks, but almost all of them focus on image processing. Observing the lack of researches about employing FSL to natural language processing (NLP) tasks, this paper focus on the few-shot relation classification with distant supervision data.

**Figure 2** shows an example of few-shot relation classification (FSRC). For an unlabeled query, this method is aimed at classifying it into a correct relation based on a few support instances for each relation. Although FSL requires less training examples in predicting a new relation, moderately large-scale labeled data is necessary to train a promising FSRC model.

**Support set**:

Relation 1: publisher

#Instance 1: the *diablo* series from *blizzard_entertainment* has done perhaps the best job of combining single-player gameplay with online community.

#Instance 2: *maxis* has gone a step further with *simearth*.

···

Relation 2: father

#Instance 1:

···

Other Relations

···

**Query set**: (*Soccer*, *nintendo*) Ground truth: publisher

*Previous methods:*

#Instance: ms. arias said he was fond of playing *soccer* and *nintendo* video games "and anything else that was fun.

*Our method:*

#Instance 1: ms. arias said he was fond of playing *soccer* and *nintendo* video games "and anything else that was fun.

#Instance 2: electronic_arts has been successful with its fifa-branded line of *soccer* games for microsoft, *nintendo* and sony platforms, ···

**FIGURE 2 |** An example of few-shot relation classification. Previous work selects a single instance as the query, which may fail to provide enough information express the semantic relation between the two entities. To solve the problem, we take multiple instances concerning the same entity pair as the query.

In specific, a dataset was *manually* labeled for FSRC, namely, FewRel and on top of it, systematic evaluation of state-of-the-art FSL methods (used in computer vision) was carried out for RC (Han et al., 2018). Note that FewRel was constructed by crowdsourcing, and thus, a number much larger than $64 \times 700$ of annotations are necessary, where 64 (700, resp.) is the number of relations (labeled instances each relation, resp.) thereof.

## 1.1. Motivation

To recap, DS can generate large-scale data but suffers from long-tail relations and mislabels; meanwhile, FSRC is able to recognize new relations with few training samples, but requires moderately large amount of human labor for data annotation. Hence, we are at the frontiers of DS and FSRC, being ready to union them, in order to compensate for the downsides of the two paradigms. The combination of DS and FSRC enables the fully automatic method to develop a RC model, which can extract the relation held between two entities. Subsequently, the extracted triplets are used to boost the knowledge base automatically.

In this research, we investigate the task of *few-shot relation classification under distant supervision*. In realization, we refine a previous DS dataset (Zeng et al., 2017), which was built by aligning Wikidata with New York Times corpus, into a reconstructed dataset for FSRC. The DS data is collected automatically, and more details can be seen in Zeng et al. (2017). Taking for granted that the sentences mentioning an entity pair instantiate the relation of the corresponding entities in KBs,

DS data is born with *mislabels* (Riedel et al., 2010). From the example shown in **Figure 2**, we can see that, in the new scenario of distantly supervised FSRC, both support and query sets are practically noisy. If a single false positive instance is sampled as a query like previous studies (Han et al., 2018; Fan et al., 2019; Gao et al., 2019), it cannot be classified into an appropriate relation in the support set. Since a few-shot model is optimized by minimizing the loss of the predictions over the queries, sampling a mislabeled instance as the query will inevitably mislead the optimization process. To tackle this problem, we follow the *at-least-once* assumption, and take an instance bag as a query:

> **Definition 1 (At-least-once assumption)**. *If two entities participate in a relation, at-least one sentence mentioning these two entities express the relation.*
> **Definition 2 (Instance bag)**. *All sentences mentioning a particular entity pair make an instance bag.*

Based on the at-least-once assumption, an instance bag contains enough semantic information to express the relation between the target entities. Therefore, selecting instance bags as queries alleviates the problem of misleading the optimization process which is caused by mislabeled instances. Besides, to alleviate the impact of false positives in the bag, we resort to *multiple instance learning* (MIL) methods, which assigns a single label to the instance bag, and achieve sentence-level noise reduction.

In previous research on FSRC, prototypical networks (PN) achieve promising performance (Han et al., 2018) by measuring the distances between a query and prototypes. The classic approach (Snell et al., 2017) first encodes all instances into a unified vector space, then generates each prototype by averaging all support instances of a relation type. Nevertheless, the mislabeled support instance sampled from DS data may cause a huge deviation for the prototype. In this connection, we conceive a *attention-based MIL* method, which consists of two steps:

- *Denoising the query set*: as discussed above, selecting a single instance that is unfortunately mislabeled as query has negative effects on the optimization of few-shot models. Thus, we take an instance bag as a query which provides enough information for the few-shot models to recognize an appropriate relation concerning an entity pair. Besides, self-attention is supplied to dynamically denoise while producing a more informative query feature vector;
- *Denoising the support set*: for the instances selected as the support set for each relation, to mitigate the issue of substantial deviation of the learned prototype due to mislabeled support instances, support instance-level attention is leveraged to generate a more representative prototype.

In previous studies, Gao et al. (2019) have investigated the support instance-level attention to strengthen the robustness of PN to the noise in support set. However, our work differs from Gao et al. (2019) in two perspectives: (1) Gao et al. (2019) regard the diversity of text as the noise, while in our research, the noise (i.e., mislabeled instances) in the support set is naturally brought in by distant supervision, which is more challenging to be solved; (2) as mentioned above, Gao et al. (2019) select a single instance as the query, which negatively affects the optimization process of few-shot models when distant supervision data is used for training. Differently, we take an instance bag as the query and employ MIL methods to denoise the instance bag. In addition, to evaluate our model on the task of few-shot relation classification under distant supervision, we reconstructed an DS dataset for FSRC.

## 1.2. Contributions

To sum up, we are among the first to propose to investigate a new task of few-shot relation classification under distant supervision, and the technical contribution is at least three-fold:

- We adapt existing DS data for RC to confront to FSL scenarios, which enables a fully automatic way for FSRC to obtain large-scale potentially-unbiased training data;
- We conceive an attention-based multiple instance learning method over prototypical networks, which reduces noise and emphasizes important signals at both support and query instance levels;
- The proposed task and method are empirically evaluated, and comprehensive results verify the superiority of our proposal over competitors under *N-way K-shot* settings.

## 1.3. Organization

In section 2, we formally define the task in this work. Related works are discussed in section 3, then we introduce the methodology in section 4. Afterwards, experimental results and detailed analysis are presented in section 5, followed by conclusion.

# 2. TASK FORMULATION

Formally, the task of *few-shot relation classification under distant supervision* with attention-based MIL is to obtain a function

$$F:(R,S,Q)\rightarrow r, \tag{1}$$

given training data $D$, which is labeled by existing knowledge bases under the DS assumption. In specific, $R=\{r_1,\ldots,r_i,\ldots,r_m\}$ is the *relation set*, $1\leq i\leq m$, $m=|R|$, where $|\cdot|$ denotes the cardinality of a set. $D=\{D_{r_1},\ldots,D_{r_i},\ldots,D_{r_m}\}$, where $D_{r_i}$ is a set of DS-labeled *instance bags* (all) with relation $r_i$. $S$ is the *support set*, i.e.,

$$S=\{(s_1^{r_1},s_2^{r_1},\ldots,s_{n_1}^{r_1}),\ldots,(s_1^{r_m},s_2^{r_m},\ldots,s_{n_m}^{r_m})\}, \tag{2}$$

where relation $r_i$ has $n_i$ support instances, each of which is randomly selected from $D_{r_i}$. $Q=\{s_1^q,\ldots,s_{|Q|}^q\}$ ($|Q|\geq 1$) is the *query set*, which is essentially an instance bag concerning an entity pair.

The query set $Q$ gives rise to the major difference with respect to the formulation of conventional FSRC in Han et al. (2018), Fan et al. (2019), and Gao et al. (2019). As DS data tends to have

mislabeled instances, if the previous formulation is followed, a mislabeled instance is likely to be sampled as the query instance; in this case, a FSRC model may be intermittently confused during training by the mislabeled query instances, as they substantially deviate from real ones. To overcome the limitation, we propose to employ in training an *instance bag*, instances of which concern the same entity pair and are DS-labeled with the same relation $r$, to replace a single query instance; by doing this, we expect that the trained model can recover the relation $r$ given its instance bag. Then for testing, the trained model predicts the best relation, where *single or multiple* instances can be supplied.

In this research, we adopt *N-way K-shot* setting, which has been widely used in FSRC (Han et al., 2018; Fan et al., 2019; Gao et al., 2019), i.e., $N = m$, and $K = n_1 = \cdots = n_m$.

# 3. RELATED WORK

Knowledge base is becoming increasingly important for many downstream applications, and there are various methods to boost the knowledge base (Chen et al., 2019; Zhao et al., 2020). Relation classification (RC) is a vital task for constructing knowledge base automatically. Our work is related to RC via distant supervision (DS) and few-shot learning (FSL). We review the related works as follow.

## 3.1. Relation Classification Under Distant Supervision

Most existing researches concentrate on neural models via supervised learning (Zeng et al., 2014; Nguyen and Grishman, 2015) or distantly supervised learning (Zeng et al., 2015; Lin et al., 2016). Supervised learning requires a large amount of annotated data, which can be fairly expensive to acquire. As a result, many neural models with supervised learning for RC suffer from data insufficiency (Zeng et al., 2014; dos Santos et al., 2015). DS comes as a remedy (Mintz et al., 2009), which can generate large-scale training data without human labor; whereas, it inevitably brings in mislabels and still has little coverage of long-tail relations. Riedel et al. (2010) formulated RC under DS as a *multiple instance learning* problem to alleviate the influence of mislabels, which achieves remarkable improvement.

On the foundation of this work, other feature-based methods (Hoffmann et al., 2011; Surdeanu et al., 2012) are proposed to better handle noise brought in by distant supervision. Besides, representative neural models include (Zeng et al., 2015; Lin et al., 2016; Feng et al., 2018). Among them, Zeng et al. (2015) perform at-least-one multiple instance learning on DS data. To fully exploit information in an instance bag, Lin et al. (2016) proposed selective attention over instances to dynamically remove noisy samples. Lately, reinforcement learning (Feng et al., 2018; Zeng et al., 2018) and generative adversarial network (Qin et al., 2018a) were combined with these models to further alleviate noise. These models define the task relation extraction as a multiclass classification problem, and they can only extract limited relations as a result. Our work is connected to DS, the major difference is that our proposal is formulated under a FSL framework, which can find new relations in testing, and solve the long-tail relation problem.

## 3.2. Relation Classification via Few-Shot Learning

Despite satisfactory performance, the aforementioned models show limitations in handling relations with few training samples. FSL provides a feasible solution to the problem of recognizing new classes, which aims at adapting to new classes, given only a few training samples of these classes. Many efforts are devoted to transfer learning methods, which generalizes to new concepts by fine-tuning models pretrained with common classes containing adequate instances (Caruana, 1994; Bengio, 2012; Donahue et al., 2014). Some model-based meta-learning models achieve the rapid learning by designing a special memory unit (Santoro et al., 2016; Munkhdalai and Yu, 2017; Mishra et al., 2018). Another group of studies focus on optimization-based approaches (Finn et al., 2017; Al-Shedivat et al., 2018), which either generate the model parameters directly or predicting the updating gradients for parameters. Afterwards, metric learning is proposed to project instances into a unified feature space, where instances with the same class are placed adjacent with each other (Koch et al., 2015; Vinyals et al., 2016). Prototypical networks used in Han et al. (2018) and Gao et al. (2019), as well as this research is a representative method of metric learning.

As introduced in section 1, Han et al. (2018) first formulated the task of FSRC, and a dataset FewRel for evaluating the task was created via crowdsourcing. Based on FewRel, Fan et al. presented large-margin prototypical networks with fine-grained features (Fan et al., 2019). Wu et al. proposed a dynamic prototypes selection approach with attention to fully capture information in support set (Wu et al., 2020). Seeing texts are more flexible and noisy than images, Gao et al. (2019) devised tailored prototypical networks, distinguishing itself from those used in the area of computer vision. In particular, based on FewRel, noise was introduced by replacing at a certain probability each support instance with a random instance of different relation labels. In contrast, we address the noise issue, i.e., mislabeled instances in specific, which is naturally brought in when investigating the new task of distantly supervised FSRC, which can be comparatively more challenging.

# 4. METHODOLOGY

As shown in **Figure 3**, the model is established based on prototypical networks (PN), incorporating attention-based multiple instance learning. In this paper, instances are encoded by convolution neural network (CNN) before fed into the PN, and other neural networks can also be employed as encoder.

## 4.1. Sentence Encoder

This module is used to extract semantic features of an instance. Given a sentence $t = \{w_1, w_2, \ldots, w_n\}$, we first transform the raw text into a low-dimensional embedding representation, and then feed it to neural networks to obtain a feature vector.

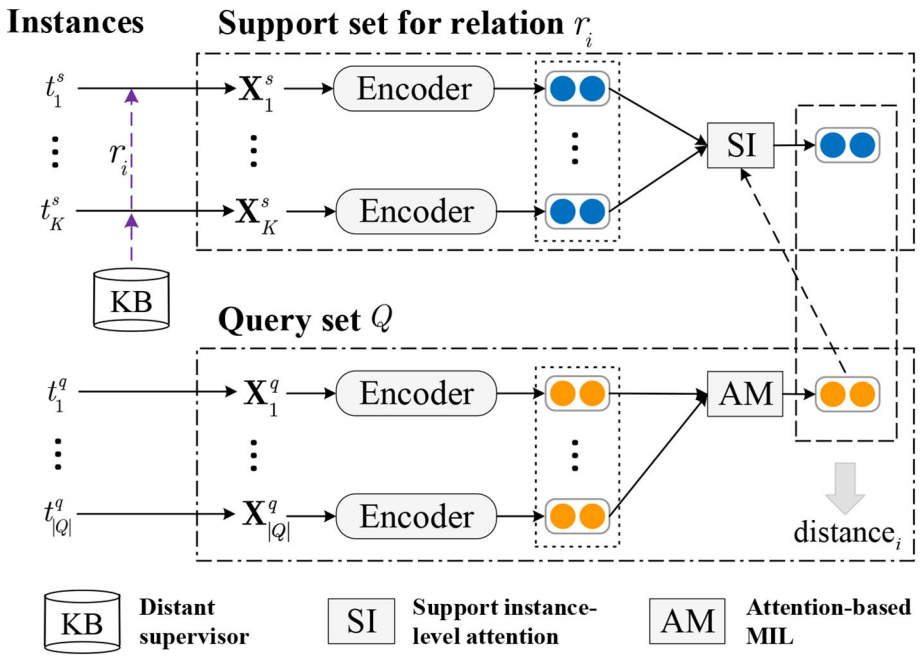


**FIGURE 3 |** Framework of model for FSRC under DS. $t^s$ and $t^q$ denotes the support instance and query instance respectively, while $X^s$ and $X^q$ are the embedding corresponding representations of $t^s$ and $t^q$.

#### 4.1.1. Embedding Layer

In our method, we map each discrete word token into a low-dimensional vector by looking up a table of pre-trained word embeddings (Pennington et al., 2014). As thus, a word $w_i$ in the sentence $t$ is converted into a real-valued embedding $\mathbf{w}_i \in \mathbb{R}^{k_w}$, which can express the semantic meaning of $w_i$. Besides, we also incorporate position features, which have been shown to be useful for RC (Zeng et al., 2014). For each word $w_i$, it has two relative distances to the two entities. Two position embedding matrices are initialized randomly and each distance can be transformed into a $k_p$-dimensional vector $\mathbf{p}_i^j \in \mathbb{R}^{k_p}$, $j \in \{1, 2\}$, by looking them up. Then, we concatenate the word embedding and position features as

$$\mathbf{x}_i = [\mathbf{w}_i : \mathbf{p}_i^1 : \mathbf{p}_i^2] \in \mathbb{R}^{k_w + 2k_p}. \tag{3}$$

When gathering the vector representation of all words together, we obtain the input embedding matrix $\mathbf{X} = \{\mathbf{x}_1, \mathbf{x}_2, \ldots, \mathbf{x}_n\}$. After deriving $\mathbf{X}$, we feed it into a standard CNN for feature extraction.

#### 4.1.2. Encoding Layer

We use convolution neural network (CNN) as the instance encoder, which is of elegant encoding capability and computing efficiency. $\mathbf{X}_{i:j}$ is the concatenation of word vectors $[\mathbf{x}_i : \mathbf{x}_{i+1} : \cdots : \mathbf{x}_j]$. The weight matrix of the sliding filter with a window size of $\omega$ is denoted by $\mathbf{W} \in \mathbb{R}^{\omega \times (k_w + 2k_p)}$. The convolution operation is to take a dot production between $\mathbf{W}$ and $\mathbf{X}_{(j-\omega+1):j}$, and generate a vector $\mathbf{c} \in \mathbb{R}^{m-\omega+1}$. Generally, multiple filters are usually required to extract more information, and the corresponding weight matrices are represented by $\widehat{\mathbf{W}} = \{\mathbf{W}_1, \ldots, \mathbf{W}_i, \ldots, \mathbf{W}_d\}$. Each convolution operation can be expressed by

$$c_{ij} = \mathbf{W}_i \otimes \mathbf{X}_{(j-\omega+1):j}, \tag{4}$$

where $d$ is the number of filters, $1 \leq i \leq d$, and $1 \leq j \leq m - \omega + 1$. Afterwards, max-pooling operation is applied on the convolution results to extract the most prominent feature in every dimension, i.e.,

$$y_i = \mathtt{ReLU}(\max_{1 \leq j \leq m} (c_{ij})), \tag{5}$$

where, ReLU is the activation function in our implementation. Hence, a feature vector for an instance $\mathbf{y}^i \in \mathbb{R}^d (i \in \{s, q\})$ is generated by max-pooling layer of CNN, where $\mathbf{y}^s$ (resp. $\mathbf{y}^q$) denotes support (resp. query) instance.

### 4.2. Attention-Based Multiple Instance Learning Unit

Mislabeled instances are harmful to learning and evaluating queries and prototypes. Hence, we conceive an attention-based multiple instance learning unit to mitigate the impact. **Figure 4** compares the instance selection of our model in both support and query set with the classic method (Snell et al., 2017). From it, we can see that if a false positive instance is sampled as a query, the previous method cannot handle the situation. Besides, the mean selection of support instances is fixed rather than flexible, which restrains the appropriate selection of support instances given a query.

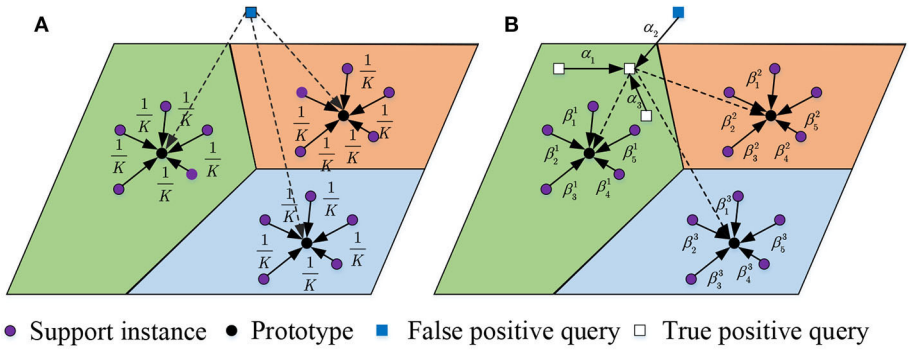


**FIGURE 4 |** Selection of instances in support and query set. Previous work regards all support instances equally while our method assigns selective attention scores over the support instances. Besides, previous work cannot handle the scenario of false positive queries while our method solves the problem by selecting instance bags as queries. **(A)** Previous method, **(B)** Our method.

#### 4.2.1. Attention-Based MIL Pooling in Query Set

Based on multiple instance learning assumption, in the new formulation, it is of necessity to distinguish the instances of various importance. Consequently, given a set of feature vectors for $Q$, namely, $\mathbf{Q} = \{\mathbf{y}^q_1, \ldots, \mathbf{y}^q_{|Q|}\} \in \mathbb{R}^{|Q| \times d_c}$, our method leverages an attention-based pooling operation over the multiple instances in the bag. We use a self-attention method (Vaswani et al., 2017), which is defined as

$$\mathbf{E} = \texttt{softmax}(\frac{(\mathbf{Q}\mathbf{W}^1 + \mathbf{b}^1)(\mathbf{Q}\mathbf{W}^2 + \mathbf{b}^2)^\top}{\sqrt{d_c}}), \tag{6}$$

where $\mathbf{W}^1, \mathbf{W}^2 \in \mathbb{R}^{d_c \times d_c}$, and $\mathbf{b}^1, \mathbf{b}^2 \in \mathbb{R}^{d_c}$ are learnable parameters of two linear projection layers, and $\texttt{softmax}(\cdot)$ is the $\texttt{softmax}$ function. $\mathbf{E} \in \mathbb{R}^{|Q| \times |Q|}$ is produced by letting each instance attend mutually. And then, we average each row of $\mathbf{E}$ to generate the attention score for each instance in the query set,

$$\alpha_i = \frac{\exp(e_i)}{\sum_{k=1}^{|Q|} \exp(e_k)}, \tag{7}$$

$$e_k = \frac{\sum_{j=1, j \neq k}^{|Q|} \mathbf{E}_{kj}}{|Q|}, \tag{8}$$

In this way, the selection of query instances is guided by the high-quality ones in the query set.

Then, the query set representation is obtained by consolidating the feature vectors of query instances in a weighted form, i.e.,

$$\hat{\mathbf{y}}^q = \sum_{i=1}^{|Q|} (\alpha_i \mathbf{y}^q_i). \tag{9}$$

In our implementation, we also try other MIL methods, including the maximum pooling over multiple instance, which is defined as,

$$\hat{\mathbf{y}}^q_j = \max_{1 \leq i \leq |Q|} \mathbf{Q}_{ij}. \tag{10}$$

We then concatenate all dimensions and obtain the query feature vector $\hat{\mathbf{y}}^q$.

Another MIL pooling method averages all query instances,

$$\hat{\mathbf{y}}^q = \frac{1}{|Q|} \sum_{i=1}^{|Q|} \mathbf{y}^q_i. \tag{11}$$

Besides, we also design a perceptron pooling method, which generates the pooling weight for each query instance by,

$$\alpha_i = \frac{\exp(\mathbf{v}^\top \mathbf{y}^q_i)}{\sum_{k=1}^{|Q|} \exp(\mathbf{v}^\top \mathbf{y}^q_k)}, \tag{12}$$

where $\mathbf{v}^\top \in \mathbb{R}^{d_c}$ is a parameter vector. The final query vector can be acquired by Equation (9).

#### 4.2.2. Support Instance-Level Attention

Akin to the case of query set, instances in the support set are not equally useful for learning a prototype when a query set is given. Inspired by Gao et al. (2019), we proceed as follows to get a more informative prototype for each relation,

$$\hat{\mathbf{y}}^s = \sum_{i=1}^{K} (\beta_i \mathbf{y}^s_i), \tag{13}$$

which is a weighted combination of all support instances, and weight $\beta_i$ is calculated according to the *query set*, as the importance of a support instance varies by queries. Thus, $\beta_i$ is defined as

$$\beta_i = \frac{\exp(e_i)}{\sum_{k=1}^{K} \exp(e_k)}, \tag{14}$$

$$e_k = \left\| \sigma(\mathbf{y}^s_k \mathbf{W}^s \odot \hat{\mathbf{y}}^q \mathbf{W}^s) \right\|_1, \tag{15}$$

where $\|\cdot\|_1$ is L1-norm, $\sigma(\cdot)$ is a hyperbolic tangent function, $\mathbf{W}^s$ is a learnable parameter matrix, and $\mathbf{y}^q$ is the feature vector of a query generated by Equation (9).

Our proposed attention-based MIL method has two advantages. Firstly, it has *flexibility* in assigning different weights to instances within a query bag, which produces highly informative query vector for bag-level classification. In addition, different attention methods in query set and support set has *interpretability*. High attention weights should be assigned to instances which are true positives, while false positives get low scores.

## 4.3. Prototypical Networks

The basic idea of prototypical networks is to use prototypes, each generated by a support set, respectively, to delegate a relation. Given a query set $Q$, distances between its feature vector $\hat{\mathbf{y}}^q$ and all the prototypes are calculated, respectively. Then, the entity pair concerned by the query set is classified as $r_i$, if the prototype of $r_i$ is of the smallest distance; the probability of $Q$ possessing $r_i$ is

$$p(r_i|Q) = \frac{\exp(-||\hat{\mathbf{y}}_i^s - \hat{\mathbf{y}}^q||_2^2)}{\sum_{j=1}^{m} \exp(-||\hat{\mathbf{y}}_j^s - \hat{\mathbf{y}}^q||_2^2)}. \quad (16)$$

To train the model, we use cross-entropy loss as the target,

$$J(\Theta) = -\sum_j \log p(r_i|Q_j; \Theta), \quad (17)$$

where $\Theta$ is the set of parameters used in the model. During model optimization, stochastic gradient decent (SGD) is harnessed to maximize the objective function by updating parameters used in the model iteratively until convergence. For each iteration, mini-batches of samples are selected from the training set.

# 5. EXPERIMENTS

## 5.1. Data Preparation and Setup

### 5.1.1. Dataset

To evaluate the proposed task, we constructed a dataset named DS-Few[1], based on two widely-used DS datasets. The first one was originally built by aligning New York Times corpus with Wikidata[2]. Following the construction method of FewRel, we grouped the instances according to their semantic relations[3], and obtained the *basic version* of DS-Few, consisting of 87 relations with 192,142 instances (61,361 entity pairs) in total[4]. We used 60, 10, and 17 relations for training, validation, and testing, respectively.

For further evaluation, we built an *alternative version* of DS-Few by employing as *test set* another DS dataset—NYT10 (Riedel et al., 2010). Akin to the aforementioned procedure, it was first grouped, and then, we filtered out the sentences that literally appeared in the training set, but retaining the clusters even if the corresponding relations appear in the training set. Eventually, we got a test of 20 relations (10 are seen in the training set) with 142,424 instances in total. In summary, the two versions represent scenarios that are both possible in real life, i.e., a relation may be seen or not during training.

### 5.1.2. Parameter Setting

For the initial embedding layer of the sentence encoder, we used an embedding set (Wikipedia 2014+Gigaword 5) pretrained by Glove, each of 50 dimensions; for the rest part of the sentence encoder (e.g., position feature and CNN structure), we followed the parameters reported in Zeng et al. (2014). Other parameters were tuned on the validation set. We called stochastic gradient decent to optimize the model, and grid search was harnessed to find the optimal parameters (underscored)—initial learning rate $\lambda \in \{0.01, \underline{0.1}, 0.3, 0.5\}$, and learning rate decay $\gamma \in \{0.01, \underline{0.1}, 0.3, 0.5\}$. That is, $\lambda$ is multiplied by $\gamma$ every $s$ training steps. We ran the model on the validation set with $s = 5,000$, every 2,000 iterations for 8 epoches, and the best epoch was chosen for testing. In testing, 3,000 mini-batches are sampled for models to predict, and the prediction accuracy is used as the evaluation metric.

### 5.1.3. Experiment Setup

We denote our prototypical networks with attention-based MIL as "AMProto." The variants with maximum, average, and perceptron pooling are denoted as "Proto+MAX," "Proto+AVE," and "Proto+PER," respectively. The competitors[5] include SNAIL (Mishra et al., 2018), GNN (Satorras and Estrach, 2018), MAML (Finn et al., 2017) as well as prototypical networks ("Proto"), Proto with self-attention ("Proto+Self") (Wu et al., 2020), and Proto with hybrid attention ("Proto+HATT") (Gao et al., 2019). SNAIL tackles few-shot learning by temporal CNNs with attention mechanism; GNN models each support and query instance as a node in a graph to learn from past experience; MAML optimizes parameters by maximizing the sensitivity of the loss functions of new tasks.

The widely-applied $N$-way $K$-shot setting was adopted, $N \in \{5, 10\}$ and $K \in \{5, 10\}$. We tested all models five times, and the *average* results are reported. For fair comparison, we evaluated all models at *instance bag level* (Jiang et al., 2018), i.e., to predict a relation for an instance bag concerning the same entity pair. For the competing approaches that do not work at instance bag level, e.g., Proto (Gao et al., 2019), we trained them at instance level, and chose the instance with the highest confidence score in the instance bag as query in testing.

## 5.2. Experiment Results

### 5.2.1. Overall Performance

**Table 1** reports the accuracy results of different models. From the results, we would like to highlight that (1) all prototypical networks-based methods exhibit better accuracy than other options (i.e., SNAIL, GNN, and MAML); among the rivals, Proto+HATT is the most competitive since hybrid attention is trained to focus on more important support instances and feature dimensions; (2) AMProto outperforms other prototypical

[1]A download link to the data will be provided in the final version.

[2]https://github.com/thunlp/PathNRE

[3]In this study, clusters with <15 instance bags were discarded, because in the 10-shot settings, at least 15 unique instance bags are necessary—10 as support instance bags and 5 as queries.

[4]For ease of comparison, FewRel is of 100 relations and 70,000 instances.

[5]We omitted comparing with LM-ProtoNet (FGF) (Fan et al., 2019), as (1) all model parameters were unreported, in the original paper, and (2) it performs not as good as Proto+HATT (Gao et al., 2019).

**TABLE 1 |** Overall results of models.

| Methods | Basic version | | | | Alternative version | | | |
|---|---|---|---|---|---|---|---|---|
| | 5-way 5-shot | 5-way 10-shot | 10-way 5-shot | 10-way 10-shot | 5-way 5-shot | 5-way 10-shot | 10-way 5-shot | 10-way 10-shot |
| SNAIL | 62.46 ± 0.37 | 68.11 ± 0.28 | 53.49 ± 0.25 | 56.22 ± 0.27 | 61.34 ± 0.35 | 64.77 ± 0.47 | 54.35 ± 0.31 | 57.80 ± 0.36 |
| GNN | 63.48 ± 0.59 | 67.92 ± 0.68 | 49.07 ± 0.63 | 54.80 ± 0.61 | 61.58 ± 0.86 | 63.28 ± 0.64 | 50.58 ± 0.74 | 54.88 ± 0.72 |
| MAML | 72.58 ± 0.48 | 74.46 ± 0.64 | 56.88 ± 0.41 | 60.45 ± 0.87 | 70.37 ± 0.71 | 73.41 ± 0.56 | 57.56 ± 0.46 | 61.97 ± 0.44 |
| Proto | 73.03 ± 0.23 | 75.31 ± 0.18 | 58.46 ± 0.24 | 61.86 ± 0.23 | 71.57 ± 0.32 | 73.80 ± 0.27 | 59.55 ± 0.26 | 62.24 ± 0.21 |
| Proto+Self | 73.14 ± 0.31 | 75.55 ± 0.33 | 58.51 ± 0.26 | 62.04 ± 0.25 | 72.24 ± 0.33 | 74.63 ± 0.34 | 59.41 ± 0.28 | 62.79 ± 0.26 |
| Proto+HATT | 73.51 ± 0.11 | 76.96 ± 0.18 | 58.85 ± 0.15 | 63.79 ± 0.17 | 73.17 ± 0.12 | 76.60 ± 0.22 | 59.89 ± 0.12 | 63.42 ± 0.16 |
| AMProto | 74.58 ± 0.21 | 78.38 ± 0.19 | 61.51 ± 0.22 | 65.58 ± 0.18 | 75.23 ± 0.25 | 77.86 ± 0.22 | 62.13 ± 0.17 | 65.41 ± 0.15 |

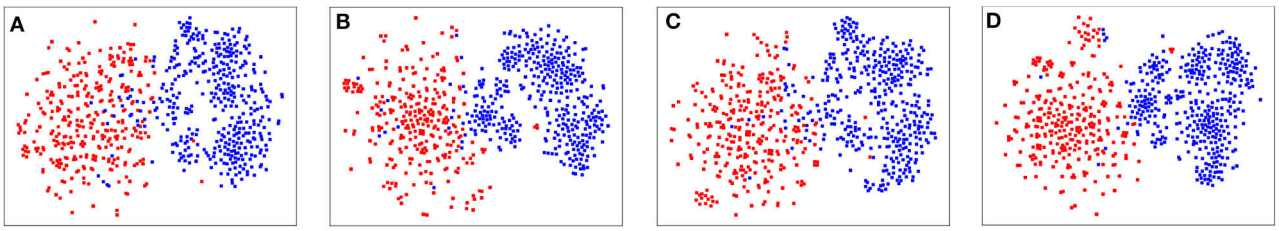


**FIGURE 5 |** PCA analysis of instance bag embeddings. **(A)** Proto+MAX, **(B)** Proto+AVE, **(C)** Proto+PER, **(D)** AMProto.

**TABLE 2 |** Comparison of different MIL methods.

| Methods | Basic version | | | | Alternative version | | | |
|---|---|---|---|---|---|---|---|---|
| | 5-way 5-shot | 5-way 10-shot | 10-way 5-shot | 10-way 10-shot | 5-way 5-shot | 5-way 10-shot | 10-way 5-shot | 10-way 10-shot |
| Proto+MAX | 73.48 ± 0.18 | 76.33 ± 0.14 | 59.02 ± 0.16 | 62.24 ± 0.12 | 73.94 ± 0.17 | 74.57 ± 0.11 | 61.19 ± 015 | 62.82 ± 0.09 |
| Proto+AVE | 73.45 ± 0.23 | 76.52 ± 0.23 | 59.88 ± 0.19 | 63.53 ± 0.18 | 73.89 ± 0.07 | 75.74 ± 0.12 | 61.50 ± 0.12 | 63.25 ± 0.14 |
| Proto+PER | 73.17 ± 0.07 | 77.02 ± 0.15 | 60.38 ± 0.22 | 63.63 ± 0.11 | 73.59 ± 0.13 | 75.83 ± 0.05 | 60.66 ± 0.09 | 63.04 ± 0.05 |
| AMProto | 74.58 ± 0.21 | 78.38 ± 0.19 | 61.51 ± 0.22 | 65.58 ± 0.18 | 75.23 ± 0.25 | 77.86 ± 0.22 | 62.13 ± 0.17 | 65.41 ± 0.15 |

networks-based FSRC models, implying that it is more robust for the task of FSRC under distant supervision, since it introduces attention-based MIL method to solve the false positive query problem; (3) on two datasets, the corresponding accuracy of different models is quite similar, demonstrating that FSRC models perform similarly on recognizing old relations and fresh relations.

### 5.2.2. Comparison of Different MIL Methods

To verify the effectiveness of the attention-based MIL, we proceed with comparison analysis by replacing the attention-based MIL with other MIL methods, including MAX, AVE and PER. In this set of experiments, for all models, we keep sampling instance bags as queries in training and testing. The embeddings of these query bags are projected into 2D points by using Principal Component Analysis (PCA), which are shown in **Figure 5**.

The accuracy results are enumerated in **Table 2**. From the results, it reads that (1) the attention-based MIL outperforms all other MIL methods, since self-attention allows the high-quality instances in query bag to guide better instance selection. Besides, due to the interaction between query set and support set, a more informative query feature vector contributes to a more representative prototype. (2) Three competing MIL methods achieve similar performance since they all fail to consider information to guide the assignment of weights over multiple instance in the query bag. The noise contained in query bag also misleads the selection of support instances to form the prototype.

### 5.2.3. PCA Projection Analysis

This experiment helps appreciate the predictive effect of different MIL methods visually. We conjecture that Proto+MAX, Proto+AVE, and Proto+PER underperform AMProto, due to the selection of high-quality instances in the query bag and the representation of query feature vector. To validate, we randomly selected 400 query instance bags of two arbitrary relations, and encoded them with different models.

(1) there is a subtle difference in the distribution of feature vectors by Proto+MAX, Proto+AVE, and Proto+PER; and (2) in

**TABLE 3 |** Sample instances in case study.

| Relation: parent_taxon | Entity pair in query: (bobcat, lynx) | Attention score |
|---|---|---|
| Support instances | ① it concludes that the closest living link to the galapagos tortoise, or geochelone nigra, is probably a relatively small tortoise found in South America. | 0.16 |
| | ② botanically, the poinsettia is euphorbia pulcherrima, a member of the euphorbiacae family, a spurge that comprises about 5,000 specie. | 0.27 |
| | ③ other examples of convergence include marsupial mammals related to kangaroos and opossums that evolved into creatures resembling lions and wolves. | 0.23 |
| | ④ a show-stopper was the capra pizza, in which the zing of goat cheese played off beautifully against red and yellow bell pepper slices, black olives and a touch of sage. | 0.09 |
| | ⑤ by a fluke of nature, a wildcat species—felis silvestris tartessia—has survived unchanged for the past 20,000 years in the mountains of Spain. | 0.25 |
| Query instance bag | ① bobcats or bobcat tracks have been sighted in the hudson river palisades region, but the lynx rarely ventures south of Northern New England and New York state. | 0.18 |
| | ② the lynx and the bobcat are similar in size and appearance, although the former's ear tufts are more prominent and its feet larger. | 0.28 |
| | ③ through a complicated chain of events, it was the bobcat that drove the lynx from New York in the late 1800's. | 0.23 |
| | ④ … they may have been inspired by the wide footprints of the snowshoe hare and the lynx (a mountain version of the bobcat with especially large feet) in flight. | 0.31 |

*The mention in blue and underline is the head entity, while the mention in red and underline is the tail entity.*

contrast, feature vectors by AMProto are apt to be linearly-separable when dual attention is exerted; (3) the comparison between AMProto and other MIL methods indicates that the proposed attention-based MIL can learn more distinguishable representation for query bags.

### 5.2.4. Case Study

We look into the case that AMProto predicts correctly but others fail, to qualitatively show the effectiveness of attention-based MIL. **Table 3** presents a sampled case, where both support instances and query bags are selected from the experiment under 5-way 5-shot setting. Particularly, we presented all instances in support set, and the query instance bag which contains four sentences concerning the entity pair (*bobcat*, *lynx*). The proposed AMProto extracts the relation `parent_taxon` between *bobcat* and *lynx* based on all sentences of the instance bag. In this way, a triplet (*bobcat*, `parent_taxon`, *lynx*) can be formed to complete existing knowledge bases.

It can be seen that our self-attention pooling over the query bag can find the common semantic relation expressed by and distinguish the instances of high attention scores that well express the `parent_taxon` relation, from those of low scores that are mislabeled. Besides, given the query bag, our model can find the high-quality support instances, and assign the lowest attention score to the fourth instance which describes the target relation implicitly.

### 5.2.5. Results on FewRel Dataset

The two versions of test sets of DS-Few are constructed automatically by distant supervision. To show the performance of few-shot relation classification models on the human labeled data, we also tested our proposed AMProto and all competing methods on FewRel dataset. Specifically, we used the train set of DS-Few to train these models, and the best epochs on the validation set are picked for testing. In our experiments, we tested all few-shot relation classification models on the public train set of FewRel which contains 64 relations. We tested all models on the train set of FewRel due to two reasons: (1) the test set of FewRel is not publicly available; (2) the train set of FewRel contains more relations than the test set (containing 20 relations), which is more challenging for few-shot relation classification models. The results are listed in **Table 4**. From the results, we can read that our proposed AMProto still achieves the best performance among all models when they are tested on the human labeled data.

**TABLE 4 |** Results on FewRel.

| Methods | 5-way 5-shot | 5-way 10-shot | 10-way 5-shot | 10-way 10-shot |
|---|---|---|---|---|
| SNAIL | 61.49 ± 0.31 | 66.43 ± 0.28 | 54.32 ± 0.36 | 52.48 ± 0.43 |
| GNN | 64.73 ± 0.45 | 66.62 ± 0.34 | 50.65 ± 0.37 | 53.53 ± 0.51 |
| MAML | 70.38 ± 0.25 | 74.52 ± 0.32 | 60.49 ± 0.24 | 62.46 ± 0.33 |
| Proto | 71.42 ± 0.52 | 75.44 ± 0.19 | 61.35 ± 0.28 | 63.21 ± 0.48 |
| Proto+Self | 72.24 ± 0.62 | 76.39 ± 0.26 | 62.75 ± 0.22 | 64.66 ± 0.27 |
| Proto+HATT | 72.78 ± 0.24 | 76.78 ± 0.27 | 62.47 ± 0.34 | 65.52 ± 0.26 |
| AMProto | 73.85 ± 0.64 | 77.32 ± 0.36 | 63.68 ± 0.46 | 66.27 ± 0.35 |

### 5.2.6. Manual Evaluation

When we use the extracted triplets to boost the knowledge base, we usually select those with high confidence scores. It is because we should guarantee the quality of the triplets. Therefore, the precision of top-$k$ triplets (i.e., $P@k$) is an import metric to evaluate few-shot relation classification models. Specifically, we

**TABLE 5 |** The *P*@*k* values.

| Methods | 5-way 5-shot | | | | 5-way 10-shot | | | |
|---|---|---|---|---|---|---|---|---|
| | *P*@100 | *P*@200 | *P*@300 | Average | *P*@100 | *P*@200 | *P*@300 | Average |
| SNAIL | 85.00 | 83.00 | 79.33 | 82.44 | 86.00 | 84.00 | 80.67 | 83.56 |
| GNN | 83.00 | 81.50 | 79.67 | 81.39 | 85.00 | 85.50 | 80.33 | 83.61 |
| MAML | 90.00 | 89.50 | 86.33 | 88.61 | 93.00 | 91.00 | 87.67 | 90.56 |
| Proto | 92.00 | 90.50 | 87.67 | 90.06 | 94.00 | 91.50 | 88.67 | 91.39 |
| Proto+Self | 94.00 | 92.00 | 88.33 | 91.44 | 96.00 | 93.50 | 89.67 | 93.06 |
| Proto+HATT | 94.00 | 92.50 | 89.33 | 91.94 | 97.00 | 94.00 | 89.67 | 93.56 |
| AMProto | 95.00 | 94.00 | 90.67 | 93.22 | 98.00 | 95.50 | 91.33 | 94.94 |

ranked all extracted triplets according to their confidence scores and calculated the precisions at top-*k* triplets. In our experiments, we tested all models under 5-way 5-shot and 5-way 10-shot settings on the basic version of test set. **Table 5** presents the precisions at top-100, top-200, and top-300. It reads from the results that our proposed AMProto outperforms all baselines. Therefore, it is safer to employ AMProto than other models to boost knowledge base.

## 6. CONCLUSION

In this paper, to union the advantages of distant supervision and few-shot learning, we have investigated the task of few-shot relation classification under distant supervision. To evaluate, we reconstruct existing distant supervision data to confront the scenario of FSRC. Seeing the unique challenges, we conceive a attention-based multiple instance learning method over prototypical networks to mitigate the mislabeled instances in both support set and query set. Other multiple instance learning approaches, including maximum pooling, average pooling, and perceptron pooling, are selected as our baselines. Empirical study verifies the feasibility of the task and the superiority of the method over other few-shot learning models and various baselines. From the experimental results, we can see that our proposal is more robust to the challenging task.

Our research is evaluated under the classic *N*-way *K*-shot setting of few-shot learning, which can be applied into the scenario of extracting triplets from free texts in designed blanks of forms. However, the real-world application is more complicated. Specially, more free texts may express no relation or other relation not in the support set, which cannot be handled by our proposed model and the competing methods. In the future, we will extend our work to solve the problems of negative instances and cross-domain texts, and enable it to be applicable to more complicated scenario of relation classification.

## DATA AVAILABILITY STATEMENT

The raw data supporting the conclusions of this article will be made available by the authors, without undue reservation.

## AUTHOR CONTRIBUTIONS

NP wrote the paper and conducted the experiments. WX instructed the experiments. HX prepared the data. ZT revised the manuscript. All authors contributed to the article and approved the submitted version.

## FUNDING

This work was supported by NSFC under Grant Nos. 61872446, 61902417, and 61701454, NSF of Hunan Province under Grant No. 2019JJ20024, and Postgraduate Scientific Research Innovation Project of Hunan Province (CX20190036).

## REFERENCES

Al-Shedivat, M., Bansal, T., Burda, Y., Sutskever, I., Mordatch, I., and Abbeel, P. (2018). "Continuous adaptation via meta-learning in nonstationary and competitive environments," in *6th International Conference on Learning Representations, ICLR 2018* (Vancouver, BC: OpenReview.net).

Bengio, Y. (2012). "Deep learning of representations for unsupervised and transfer learning," in *Unsupervised and Transfer Learning - Workshop held at ICML 2011* (Bellevue, WA), pages 17-36.

Bollacker, K. D., Evans, C., Paritosh, P., Sturge, T., and Taylor, J. (2008). "Freebase: a collaboratively created graph database for structuring human knowledge," in *Proceedings of the ACM SIGMOD International Conference on Management of Data, SIGMOD 2008* (Vancouver, BC), 1247–1250. doi: 10.1145/1376616.1376746

Caruana, R. (1994). "Learning many related tasks at the same time with backpropagation," in *Advances in Neural Information Processing Systems 7* (Denver, CO), 657–664.

Chen, Y., Zhao, X., Lin, X., Wang, Y., and Guo, D. (2019). Efficient mining of frequent patterns on uncertain graphs. *IEEE Trans. Knowl. Data Eng.* 31, 287–300. doi: 10.1109/TKDE.2018.2830336

Donahue, J., Jia, Y., Vinyals, O., Hoffman, J., Zhang, N., Tzeng, E., et al. (2014). "Decaf: A deep convolutional activation feature for generic visual recognition," in *Proceedings of the 31th International Conference on Machine Learning, ICML 2014* (Beijing), 647–655.

dos Santos, C. N., Xiang, B., and Zhou, B. (2015). "Classifying relations by ranking with convolutional neural networks," in *Proceedings of the 53rd Annual Meeting of the Association for Computational Linguistics and the 7th International Joint Conference on Natural Language Processing of the Asian Federation of Natural Language Processing, ACL 2015* (Beijing), 626–634. doi: 10.3115/v1/P15-1061

Fan, M., Bai, Y., Sun, M., and Li, P. (2019). "Large margin prototypical network for few-shot relation classification with fine-grained features," in *CIKM*, 2353–2356. doi: 10.1145/3357384.3358100

Feng, J., Huang, M., Zhao, L., Yang, Y., and Zhu, X. (2018). "Reinforcement learning for relation classification from noisy data," in *Proceedings of the Thirty-Second AAAI Conference on Artificial Intelligence, (AAAI-18), the 30th innovative Applications of Artificial Intelligence (IAAI-18), and the 8th AAAI Symposium on Educational Advances in Artificial Intelligence (EAAI-18)* (New Orleans, LA), 5779–5786.

Finn, C., Abbeel, P., and Levine, S. (2017). "Model-agnostic meta-learning for fast adaptation of deep networks," in *Proceedings of the 34th International Conference on Machine Learning, ICML 2017* (Sydney, NSW), 1126–1135.

Gao, T., Han, X., Liu, Z., and Sun, M. (2019). "Hybrid attention-based prototypical networks for noisy few-shot relation classification," in *The Thirty-Third AAAI Conference on Artificial Intelligence, AAAI 2019, The Thirty-First Innovative Applications of Artificial Intelligence Conference, IAAI 2019, The Ninth AAAI*

*Symposium on Educational Advances in Artificial Intelligence, EAAI 2019* (Honolulu, HI), 6407–6414. doi: 10.1609/aaai.v33i01.33016407

Gormley, M. R., Yu, M., and Dredze, M. (2015). "Improved relation extraction with feature-rich compositional embedding models," in *Proceedings of the 2015 Conference on Empirical Methods in Natural Language Processing, EMNLP 2015* (Lisbon), 1774–1784. doi: 10.18653/v1/D15-1205

Han, X., Zhu, H., Yu, P., Wang, Z., Yao, Y., Liu, Z., et al. (2018). "Fewrel: a large-scale supervised few-shot relation classification dataset with state-of-the-art evaluation," in *Proceedings of the 2018 Conference on Empirical Methods in Natural Language Processing* (Brussels), 4803–4809. doi: 10.18653/v1/D18-1514

Hoffmann, R., Zhang, C., Ling, X., Zettlemoyer, L. S., and Weld, D. S. (2011). "Knowledge-based weak supervision for information extraction of overlapping relations," in *The 49th Annual Meeting of the Association for Computational Linguistics: Human Language Technologies, Proceedings of the Conference* (Portland, OR), 541–550.

Ji, G., Liu, K., He, S., and Zhao, J. (2017). "Distant supervision for relation extraction with sentence-level attention and entity descriptions," in *Proceedings of the Thirty-First AAAI Conference on Artificial Intelligence* (San Francisco, CA), 3060–3066.

Jiang, T., Liu, J., Lin, C., and Sui, Z. (2018). "Revisiting distant supervision for relation extraction," in *Proceedings of the Eleventh International Conference on Language Resources and Evaluation, LREC 2018* (Miyazaki).

Koch, G., Zemel, R., and Salakhutdinov, R. (2015). "Siamese neural networks for one-shot image recognition," in *ICML Deep Learning Workshop, Vol. 2* (Lille).

Lin, Y., Shen, S., Liu, Z., Luan, H., and Sun, M. (2016). "Neural relation extraction with selective attention over instances," in *Proceedings of the 54th Annual Meeting of the Association for Computational Linguistics, ACL 2016* (Berlin). doi: 10.18653/v1/P16-1200

Miller, E. G., Matsakis, N. E., and Viola, P. A. (2000). "Learning from one example through shared densities on transforms," in *2000 Conference on Computer Vision and Pattern Recognition (CVPR 2000)* (Hilton Head, SC), 1464–1471. doi: 10.1109/CVPR.2000.855856

Mintz, M., Bills, S., Snow, R., and Jurafsky, D. (2009). "Distant supervision for relation extraction without labeled data," in *ACL 2009, Proceedings of the 47th Annual Meeting of the Association for Computational Linguistics and the 4th International Joint Conference on Natural Language Processing of the AFNLP* (Singapore), 1003–1011. doi: 10.3115/1690219.1690287

Mishra, N., Rohaninejad, M., Chen, X., and Abbeel, P. (2018). "A simple neural attentive meta-learner," in *6th International Conference on Learning Representations, ICLR 2018* (Vancouver, BC).

Munkhdalai, T., and Yu, H. (2017). "Meta networks," in *Proceedings of the 34th International Conference on Machine Learning, Vol. 70* (Sydney, NSW: JMLR. Org), 2554–2563.

Nguyen, T. H., and Grishman, R. (2015). "Relation extraction: perspective from convolutional neural networks," in *Proceedings of the 1st Workshop on Vector Space Modeling for Natural Language Processing*. (Denver, CO) 39–48. doi: 10.3115/v1/W15-1506

Pennington, J., Socher, R., and Manning, C. D. (2014). "Glove: Global vectors for word representation," in *Proceedings of the 2014 Conference on Empirical Methods in Natural Language Processing, EMNLP 2014* (Doha), 1532–1543. doi: 10.3115/v1/D14-1162

Qin, P., Xu, W., and Wang, W. Y. (2018a). "DSGAN: generative adversarial training for distant supervision relation extraction," in *Proceedings of the 56th Annual Meeting of the Association for Computational Linguistics, ACL 2018* (Melbourne, VIC), 496–505. doi: 10.18653/v1/P18-1046

Qin, P., Xu, W., and Wang, W. Y. (2018b). "Robust distant supervision relation extraction via deep reinforcement learning," in *Proceedings of the 56th Annual Meeting of the Association for Computational Linguistics, ACL 2018* (Melbourne, VIC), 2137–2147. doi: 10.18653/v1/P18-1199

Ravi, S., and Larochelle, H. (2017). "Optimization as a model for few-shot learning," in *5th International Conference on Learning Representations, ICLR 2017* (Toulon).

Riedel, S., Yao, L., and McCallum, A. (2010). "Modeling relations and their mentions without labeled text," in *Machine Learning and Knowledge Discovery in Databases, European Conference, ECML PKDD 2010* (Barcelona), 148–163. doi: 10.1007/978-3-642-15939-8_10

Santoro, A., Bartunov, S., Botvinick, M., Wierstra, D., and Lillicrap, T. P. (2016). "Meta-learning with memory-augmented neural networks," in *Proceedings of the 33nd International Conference on Machine Learning, ICML 2016* (New York City, NY), 1842–1850.

Satorras, V. G., and Estrach, J. B. (2018). "Few-shot learning with graph neural networks," in *6th International Conference on Learning Representations, ICLR 2018* (Vancouver, BC).

Snell, J., Swersky, K., and Zemel, R. S. (2017). "Prototypical networks for few-shot learning," in *Advances in Neural Information Processing Systems 30: Annual Conference on Neural Information Processing Systems 2017* (Long Beach, CA), 4077–4087.

Surdeanu, M., Tibshirani, J., Nallapati, R., and Manning, C. D. (2012). "Multi-instance multi-label learning for relation extraction," in *Proceedings of the 2012 Joint Conference on Empirical Methods in Natural Language Processing and Computational Natural Language Learning, EMNLP-CoNLL 2012* (Jeju Island), 455–465.

Vaswani, A., Shazeer, N., Parmar, N., Uszkoreit, J., Jones, L., Gomez, A. N., et al. (2017). "Attention is all you need," in *Advances in Neural Information Processing Systems 30: Annual Conference on Neural Information Processing Systems 2017* (Long Beach, CA), 5998–6008.

Vinyals, O., Blundell, C., Lillicrap, T., Kavukcuoglu, K., and Wierstra, D. (2016). "Matching networks for one shot learning," in *Advances in Neural Information Processing Systems 29: Annual Conference on Neural Information Processing Systems 2016* (Barcelona), 3630–3638.

Wu, L., Zhang, H.-P., Yang, Y., Liu, X., and Gao, K. (2020). "Dynamic prototype selection by fusing attention mechanism for few-shot relation classification," in *Asian Conference on Intelligent Information and Database Systems* (Springer), 431–441. doi: 10.1007/978-3-030-41964-6_37

Wu, S., Fan, K., and Zhang, Q. (2019). "Improving distantly supervised relation extraction with neural noise converter and conditional optimal selector," in *The Thirty-Third AAAI Conference on Artificial Intelligence, AAAI 2019, The Thirty-First Innovative Applications of Artificial Intelligence Conference, IAAI 2019, The Ninth AAAI Symposium on Educational Advances in Artificial Intelligence, EAAI 2019* (Honolulu, HI), 7273–7280. doi: 10.1609/aaai.v33i01.33017273

Zeng, D., Liu, K., Chen, Y., and Zhao, J. (2015). "Distant supervision for relation extraction via piecewise convolutional neural networks," in *Proceedings of the 2015 Conference on Empirical Methods in Natural Language Processing, EMNLP 2015* (Lisbon), 1753–1762. doi: 10.18653/v1/D15-1203

Zeng, D., Liu, K., Lai, S., Zhou, G., and Zhao, J. (2014). "Relation classification via convolutional deep neural network," in *COLING 2014, 25th International Conference on Computational Linguistics, Proceedings of the Conference: Technical Papers* (Dublin), 2335–2344.

Zeng, W., Lin, Y., Liu, Z., and Sun, M. (2017). "Incorporating relation paths in neural relation extraction," in *Proceedings of the 2017 Conference on Empirical Methods in Natural Language Processing, EMNLP 2017* (Copenhagen), 1768–1777. doi: 10.18653/v1/D17-1186

Zeng, X., He, S., Liu, K., and Zhao, J. (2018). "Large scaled relation extraction with reinforcement learning," in *Proceedings of the Thirty-Second AAAI Conference on Artificial Intelligence*, (*AAAI-18*), *the 30th innovative Applications of Artificial Intelligence (IAAI-18), and the 8th AAAI Symposium on Educational Advances in Artificial Intelligence (EAAI-18)* (New Orleans, LA), 5658–5665.

Zhao, X., Zeng, W., Tang, J., Wang, W., and Suchanek, F. (2020). An experimental study of state-of-the-art entity alignment approaches. *IEEE Trans. Knowl. Data Eng*. doi: 10.1109/TKDE.2020.3018741

**Conflict of Interest:** The authors declare that the research was conducted in the absence of any commercial or financial relationships that could be construed as a potential conflict of interest.

frontiers in Neurorobotics

ORIGINAL RESEARCH
published: 17 December 2020
doi: 10.3389/fnbot.2020.597471

# Investigating the Impact of the Missing Significant Objects in Scene Recognition Using Multivariate Pattern Analysis

*Jin Gu*[1†], *Baolin Liu*[2*†], *Weiran Yan*[1], *Qiaomu Miao*[1] *and Jianguo Wei*[1]

[1] College of Intelligence and Computing, Tianjin University, Tianjin, China, [2] School of Computer and Communication Engineering, University of Science and Technology Beijing, Beijing, China

Significant objects in a scene can make a great contribution to scene recognition. Besides the three scene-selective regions: parahippocampal place area (PPA), retrosplenial complex (RSC), and occipital place area (OPA), some neuroimaging studies have shown that the lateral occipital complex (LOC) is also engaged in scene recognition processing. In this study, the multivariate pattern analysis was adopted to explore the object-scene association in scene recognition when different amounts of significant objects were masked. The scene classification only succeeded in the intact scene in the ROIs. In addition, the average signal intensity in LOC [including the lateral occipital cortex (LO) and the posterior fusiform area (pF)] decreased when there were masked objects, but such a decrease was not observed in scene-selective regions. These results suggested that LOC was sensitive to the loss of significant objects and mainly involved in scene recognition by the object-scene semantic association. The performance of the scene-selective areas may be mainly due to the fact that they responded to the change of the scene's entire attribute, such as the spatial information, when they were employed in the scene recognition processing. These findings further enrich our knowledge of the significant objects' influence on the activation pattern during the process of scene recognition.

**Keywords: scene recognition, significant object, semantic relationship, multivariate pattern analysis, fMRI**

OPEN ACCESS

***Edited by:***
*Zijun Zhang,*
*City University of Hong Kong, Hong Kong*

***Reviewed by:***
*Zhen Liang,*
*Shenzhen University, China*
*Yang Luoxiao,*
*City University of Hong Kong, Hong Kong*

***Correspondence:**
*Baolin Liu*
*liubaolin@tsinghua.edu.cn*

*[†]These authors have contributed equally to this work and share first authorship*

***Received:*** *21 August 2020*
***Accepted:*** *30 November 2020*
***Published:*** *17 December 2020*

***Citation:***
*Gu J, Liu B, Yan W, Miao Q and Wei J (2020) Investigating the Impact of the Missing Significant Objects in Scene Recognition Using Multivariate Pattern Analysis. Front. Neurorobot. 14:597471. doi: 10.3389/fnbot.2020.597471*

## INTRODUCTION

Scene recognition is a common and important brain activity that can help us access environmental information. Previous studies have indicated that scene recognition relies on intrinsic properties of scenes related to 3D spatial structure, such as expanse or degree of openness (Kravitz et al., 2011; Park et al., 2011; Lowe et al., 2016), and the deepness of scene (Greene and Oliva, 2009; Amit et al., 2012; Park et al., 2015). Furthermore, it has been appreciated that the significant objects in the scene play a vital role in scene recognition. As an important part of the scene, the objects in the scene are of great significance to the scene recognition. In addition to the object size or other related properties (Cate et al., 2011; Konkle and Oliva, 2012; Bainbridge and Oliva, 2015), the scene recognition can be influenced by the association of the scene and objects (Gagne and MacEvoy, 2014; Linsley and Macevoy, 2014a; Sastyin et al., 2015). Many studies have suggested that the nature of scene recognition is the information integration of objects in the scene

(Biederman, 1987; Biederman et al., 1988). Moreover, behavioral studies have shown that there is a significant decline in the recognition accuracy when objects are removed from the scene, and the classification accuracy based on brain activation pattern was lower when the objects were removed (MacEvoy and Epstein, 2011). Furthermore, there is a decrease in recognition accuracy when adding the objects that are not semantically associated with the scene (Davenport and Potter, 2004; Joubert et al., 2007).

The related neural mechanism of scene processing has received much attention in the decades. With the help of functional magnetic resonance imaging (fMRI) and other neuroimaging technologies, it has been found that there are three main areas involved in scene processing (MacEvoy and Epstein, 2011; Dilks et al., 2013; Cukur et al., 2016). Previous neuroimaging studies have indicated that the parahippocampal place area (PPA) exhibited a stronger response to scenes than the single object (Henderson et al., 2008; Persichetti and Dilks, 2016). In addition, stimuli from different scenes could activate different signal patterns in PPA (Walther et al., 2009, 2011; MacEvoy and Epstein, 2011; Epstein and Morgan, 2012), which can suggest that the PPA is associated with the processing of scene recognition. The retrosplenial complex (RSC) can be activated when people view or imagine scenes (O'Craven and Kanwisher, 2000), and it has been suggested to be responsible for spatial navigation (Henderson et al., 2008; Auger et al., 2012; Marchette et al., 2014). Moreover, different scenes could evoke different encoding information in RSC (Walther et al., 2009). The occipital place area (OPA) can respond to visually presented scenes (Hasson et al., 2003; MacEvoy and Epstein, 2007; Dilks et al., 2011). In recent years, some neuroimaging studies have found that OPA also plays a causal role in scene perception (Dilks et al., 2013; Ganaden et al., 2013; Kamps et al., 2016b).

It has been appreciated that PPA, RSC, and OPA are the key cortical regions underlying our ability to recognize scenes and use this information in navigation, however, these regions may play different roles in the specific process of scene recognition (Kamps et al., 2016a). There is still no consensus on what information can be encoded in these regions, and the neural mechanism underlying the association between significant objects and scene recognition remains to be clarified. In related studies, the PPA was demonstrated to be responsible for processing the semantic information and showed a stronger response to objects that shared a strong semantic with the scene (Aminoff et al., 2007; Hassabis et al., 2007; Bar et al., 2008; Summerfield, 2010; Howard et al., 2011). Harel et al. found that the PPA could integrate the spatial information of scenes and object information in scenes, and was sensitive to the absence or presence of both the objects and the scene (Harel et al., 2013). However, MacEvoy and Epstein argued that the lateral occipital complex (LOC) could process the semantic information between the scene and objects, which was not found in the PPA (MacEvoy and Epstein, 2011). These inconsistent findings indicate that the role of the PPA has not been definitively determined in describing the semantic association between the scene and the objects. The RSC may share similar functions in scene processing (Maguire, 2001) and one recent functional connectivity study suggested the RSC and PPA formed a scene recognition component (Hao et al., 2016). However, it is unclear whether activation on the RSC is significantly affected by the objects within the scene. Another scene-selective region OPA may prefer to deal with local scene elements rather than global scene properties (Kamps et al., 2016a), therefore we speculated the activation on the OPA would be different if the significant objects are masked in the scenes.

In addition to the above scene-selective regions, the object-selective region can take part in the scene processing and process the relationship between objects and scene. As an important area related to object recognition, the lateral occipital complex (LOC) has shown the correlation between the activity pattern induced by objects and that induced by scenes in several studies (Biederman, 1987; Malach et al., 1995; Grill-Spector et al., 1998; Kourtzi and Kanwisher, 2000; Carlson et al., 2003; James et al., 2003; Sayres and Grill-Spector, 2008; Pitcher et al., 2009). Scenes could be decoded by the activity pattern of objects that had strong semantic relationships with scenes (Peelen et al., 2009; MacEvoy and Epstein, 2011). Furthermore, Harel et al. reported a strong decrease in neural activity when objects were removed from the scene (Harel et al., 2013). These studies indicated a relationship between the activation in the LOC [including the lateral occipital cortex (LO) and the posterior fusiform area (pF)] and significant objects within the scene.

To study the brain neural mechanism of the association between significant objects and scene recognition, we designed an experiment with the scene-categorization task including behavioral and fMRI procedure which has been reported in the work of Miao et al. (2018). In the experiments, four types of images were shown to the participants, with each type including intact images of the scene and images after removing one or two significant objects from the scene. By masking the object in the scene picture, we can study the effect of objects in scene recognition. In our previous study, Miao et al. calculated the signal change and performed functional connectivity analysis based on the object-selective region LOC, and the results showed that the masking objects affected the brain network during scene recognition. In the present study, we focused on the influence of masking objects on the regions of interests (ROIs) in scene recognition by the multivariate pattern analysis (MVPA). In the neuroimaging research, the method has been implemented in various studies (Haxby et al., 2001; Norman et al., 2006; Harrison and Tong, 2009). Compared with the univariate analysis, MVPA can extract multidimensional information more adequately (Norman et al., 2006; Davis et al., 2014). Combined with appropriate classification algorithms, MVPA can be used to classify activity patterns according to stimuli categories (Harrison and Tong, 2009; Emmerling et al., 2016). Therefore, MVPA shows more advantages when we want to study the spatial patterns across multiple brain states. Considering the high dimensional and small sample size of fMRI data, the Support Vector Machine (SVM) algorithm has been widely used in the brain states classification, which has shown a significant advantage in the classification performance and robustness (LaConte et al., 2005; Mourao-Miranda et al., 2005). In recent studies, cross-classification (classifiers trained on data from a condition and tested on data from the other condition or vice versa) has been applied to analyze the brain activity in different conditions

(Albers et al., 2013; Boccia et al., 2017), which can contribute to comparing these related but not identical brain activities. For example, cross-classification between perception and imagery was performed to study their association and difference (Cichy et al., 2012; Vetter et al., 2014).

In the present study, we studied the influence of significant objects by the change of scene recognition capacity in some ROIs. To the effects of significant objects on related brain regions, we conducted the univariate analysis to research the signal change on the ROIs and used MVPA to analyze the activation patterns change when the significant objects were masked in the scene. We speculated that the LO and pF were mainly involved in processing the semantic correlation between the scene and significant objects in the scene, which caused the object-selective regions were sensitive to the absence of significant objects. Since the scene-selective regions play different roles in scene recognition, we speculated that the masked significant objects may have different effects on the PPA, RSC, and OPA. By the above analysis, there would be a further understanding of the significant objects' influence on the activation pattern during the process of scene recognition.

# MATERIALS AND METHODS

## fMRI Data

In this paper, the fMRI dataset is from our previous study published by Miao et al. (2018). Here, we gave a brief description of the fMRI experiment for a better understanding, and more details could be found in their publication.

Fourteen right-hand healthy participants were recruited in a visual experiment, in which they watched four kinds of scenes images: kitchen and bathroom (indoor scenes), intersection, and playground (outdoor scenes). Each kind of scene had four versions (NM: complete photographs; M1(A): photographs where only object A was masked; M1(B): photographs where only object B was masked; M2: photographs where both object A and object B were masked). Defining the combination of each type of scene and masking degree as a condition, the photographs can be divided into 16 conditions (4 scene categories × 4 versions) when considering the scene category and masked degree.

A block-design paradigm was used in this study. The experiment consisted of three functional runs and one localizer run. In the three functional runs, photographs of all the 16 different conditions were presented, in which 8 s of baseline was first presented, followed by 16 blocks. The sample object images and experimental design were shown in **Figure 1**, which referenced to the fMRI data description of Miao et al. (2018). In addition, the localizer run referred to the paradigm designed by MacEvoy (MacEvoy and Epstein, 2011) which could help us define the related brain areas. Then the details of fMRI data preprocessing can be found in the part of experimental procedures in the publication of Miao et al. (2018).

## ROI Selection

According to previous studies on the localization method of visual ROI (Malach et al., 1995; Grill-Spector et al., 1998), ROIs were defined based on the activation diagram from the localizer run. Compared with our previous work (Miao et al., 2018), we added four new ROIs, including the pF, LO, OPA, and EVC. The pF and LO were defined as through the contrast object minus phase-scrambled objects, we set the peak response in the later-ventral occipitotemporal cortex, and we located the pF and LO, respectively. OPA was defined in the transverse occipital sulcus where the response to scenes condition was stronger than objects condition. As a control area, the EVC was defined in the posterior occipital lobe through the contrast of phase-scrambled objects minus intact objects. The PPA and RSC were defined in the posterior parahippocampal-collateral sulcus region and retrosplenial cortex, referring to the work of Miao et al. (2018). **Figure 2** showed the activation in each of ROI at the group level. The peak coordinates and peak intensity of functional ROIs at the group level were shown in **Table 1**. To avoid the interindividual differences in anatomic locations of the regions, the ROIs were identified as spheres with an 8 mm radius in every subject and the ROI coordinates for each subject were located defined at the local maxima closest to the group peak coordinates.

## Multivariate Pattern Analysis

To clarify the roles of significant objects in scene recognition in ROIs, we calculated the scene classification accuracy using the activation pattern in these regions (LO, pF, PPA, RSC, and OPA) and the control area EVC. The defined ROIs contribute to feature selection, and the voxels involved in the defined ROIs were included in the classification analysis. Brain patterns are labeled according to all the scene conditions (scene categories × mask conditions). In the present study, the SVM classifier was used to implement the four-way classification (kitchen, bathroom, intersection, and playground) in different mask conditions (NM, M1, and M2) (Chang and Lin, 2011). Unsmoothed functional data were used in the classification processing because the spatial smoothing would destroy some useful variables (Samuel Schwarzkopf and Rees, 2011). The classification was conducted through the leave-one run out cross-validation approach, which contributed to the stable and dependable classification results by avoiding the higher correlation of the data from the same run (Wolbers et al., 2011; Axelrod and Yovel, 2012). Afterward, we conducted the one-sample *t*-test on the classification performances to test whether the statistical value was statistically significant ($p < 0.05$). Then the one-way repeated measures ANOVA was performed to test the effect of mask conditions. In order to assure the classification performances were reliable, we shuffled the labels and randomly assigned to the training samples and performed the four scene classification analysis with the same procedure based on the "shuffled" data (Stelzer et al., 2013).

In addition, we performed the cross-classification analysis in which the intact (NM) scene data were used to train the SVM model, and M1 and M2 data were used as the test dataset. Then, the one-sample *t*-test was performed on the classification results to show the difference and similarity of activation pattern between the complete scene and scene with masked significant objects.

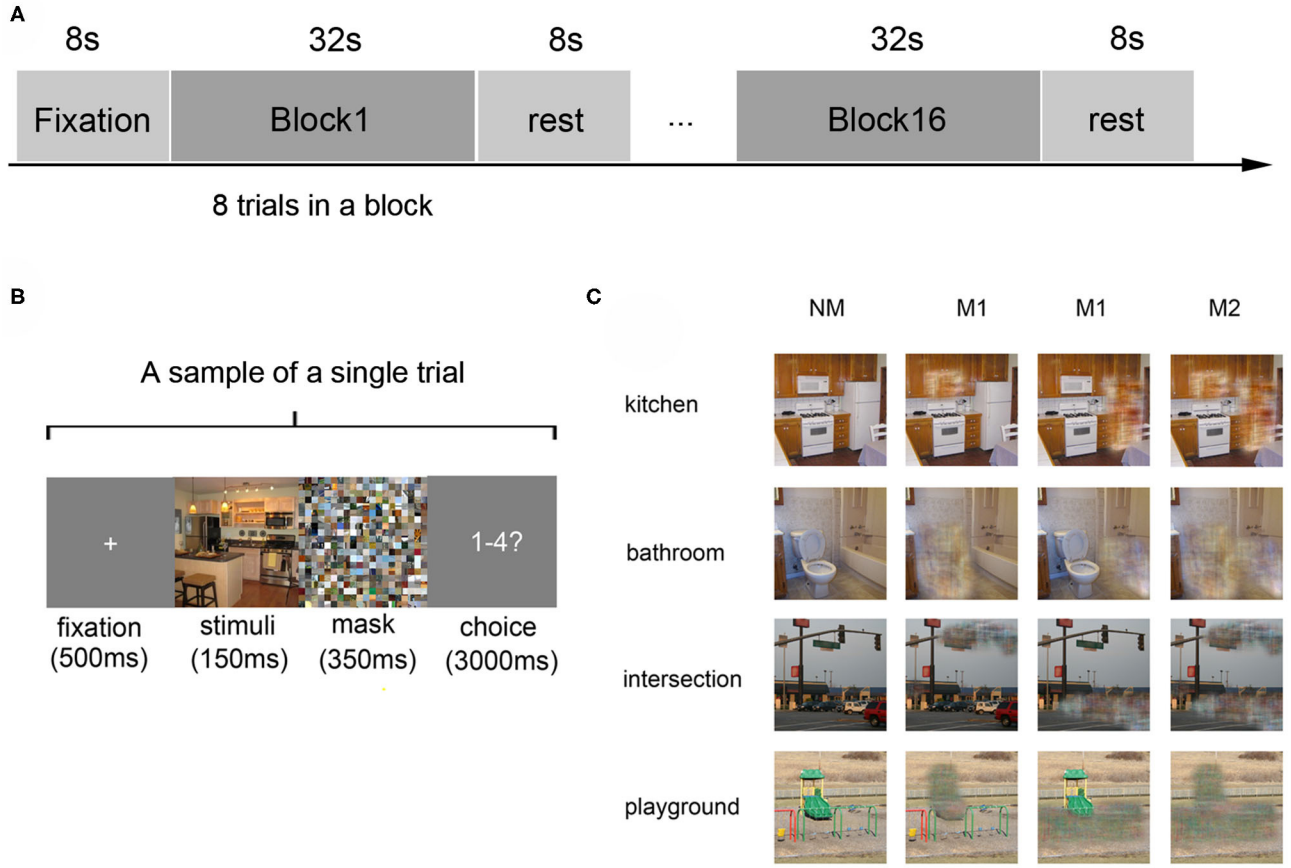


**FIGURE 1 |** Experiment design and materials. **(A)** The experimental paradigm of a single run: the run started with an 8-s fixation and followed by 16 blocks, which were separated by an 8-s rest interval. Each block consists of 8 trials with images of the same scene category. **(B)** The paradigm of a single trial: a 500 ms fixation was shown at first, then a 150 ms stimulus image, followed by a 350 ms mask. Subjects were then required to judge the scene category within 3000 ms. **(C)** Stimulus examples from all kinds of scene categories: four kinds of scenes images in the conditions of no object was masked (NM), only one object was masked (M1), and two objects were masked (M2).

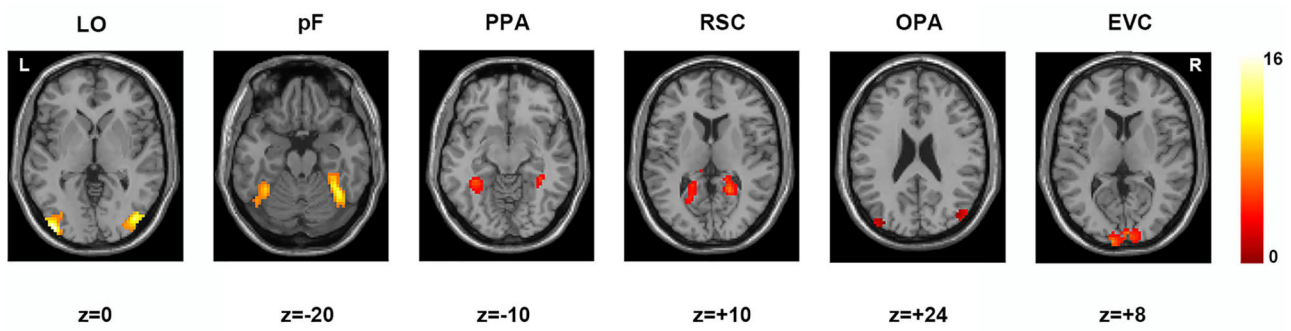


**FIGURE 2 |** Locations of functional ROIs based on the group analysis in the localizer run. LO, lateral occipital complex; pF, posterior fusiform area; PPA, parahippocampal place area; RSC, retrosplenial complex; OPA, occipital place area; EVC, early visual cortex.

## Univariate Analysis

The result of pattern recognition reflected the overall pattern of all voxels in the same region, while percent signal change can reflect the activation intensity in a single region. We used the marsbar software (http://marsbar.sourceforge.net/) to calculate the signal change in the ROIs in three masked

**TABLE 1 |** The peak coordinates and peak intensity of functional ROIs in the group level.

| Functional ROIs | MNI coordinates | | | Peak intensity |
|---|---|---|---|---|
| | x | y | z | |
| Left LO | −39 | −90 | −3 | 15.02 |
| Right LO | 42 | −81 | 0 | 12.44 |
| Left pF | −36 | −52 | −23 | 10.58 |
| Right pF | 39 | −52 | −20 | 12.55 |
| Left PPA | −33 | −43 | −8 | 5.64 |
| Right PPA | 36 | −40 | −11 | 4.69 |
| Left RSC | −15 | −49 | 16 | 4.87 |
| Right RSC | 21 | −49 | 10 | 6.05 |
| Left OPA | −39 | −85 | 28 | 2.02 |
| Right OPA | 48 | −76 | 28 | 3.36 |
| Left EVC | −9 | −103 | 13 | 8.45 |
| Right EVC | 9 | −103 | 16 | 11.85 |

conditions separately (NM, M1, and M2). Then paired samples *t*-test was conducted between the conditions in each region to investigate whether the activation is different across different masked conditions. In addition, we performed repeated-measures ANOVA to study the difference of activation intensity across ROIs.

# RESULTS

## Classification Analysis by MVPA

### Scene Classification in Different Mask Condition

To study the influence of masked objects on the scene classification, we calculated and compared the classification accuracy of the activation pattern in the three kinds of mask conditions (NM, M1, and M2). When we classified scenes based on the activation pattern in the LO, the results showed that the classification accuracy is not significant higher than the chance level (25%) when there was object masked in the scene picture (NM: 49.44%, $t_{13} = 8.13$, $p < 0.001$; M1: 21.83%, $t_{13} = -2.75$, $p = 0.017$; M2: 27.12%, $t_{13} = 0.89$, $p = 0.391$). One-way repeated-measures ANOVA was performed to test the role of mask conditions in the accuracy decline, and the result showed that the classification differences in different conditions were statistically significant ($F = 35.69$, $p < 0.001$). The *post-hoc* tests showed accuracy in NM was significantly >M1 ($p < 0.001$) and M2 ($p < 0.001$), however, there wasn't a significant difference between M1 and M2 ($p = 0.085$).

Then we performed the above analysis on other ROIs, and the activation pattern corresponding to scenes with masked objects was not significantly classified. The results showed greater classification accuracies in the NM than the conditions with masked objects.

In the pF, the successful classification was only observed in the NM condition (NM: 47.73%, $t_{13} = 6.85$, $p < 0.001$; M1: 24.63%, $t_{13} = -0.24$, $p = 0.818$; M2: 26.90%, $t_{13} = 1.12$, $p = 0.283$), and there was significant difference in the different mask conditions ($F = 23.49$, $p < 0.001$) by the one-way repeated measures ANOVA. The *post-hoc* tests showed classification accuracy in NM condition was significantly >M1 ($p < 0.001$) and M2 ($p < 0.001$). We also compared the classification accuracies in the M1 and M2, however, there wasn't significant difference ($p = 0.406$).

There was also a decline for the accuracies of scene classification in the PPA with more objects masked in three conditions (NM: 46.02%, $t_{13} = 6.39$, $p < 0.001$; M1: 25.48%, $t_{13} = 0.40$, $p = 0.693$; M2: 27.79%, $t_{13} = 1.49$, $p = 0.160$). One-way repeated measures ANOVA showed significant differences in three conditions ($F = 26.28$, $p < 0.001$) and accuracy in NM was significantly >M1 and M2 ($p < 0.001$) by *post-hoc* tests. However, there wasn't significant difference between M1 and M2 ($p = 0.289$).

In the RSC, the decoding only succeed in NM condition (NM: 49.93%, $t_{13} = 8.59$, $p < 0.001$; M1: 23.79%, $t_{13} = -1.05$, $p = 0.311$; M2: 27.75%, $t_{13} = 1.26$, $p = 0.229$), and the accuracy differences in the different mask conditions were statistically significant ($F = 41.16$, $p < 0.001$). The difference was from the classification accuracy in the NM and that in the M1 and M2 ($p < 0.001$) by *post-hoc* tests, however, there wasn't significant difference between M1 and M2 ($p = 0.182$). The classification results in the OPA were similar, that is, classification accuracies were significantly above the chance level in the NM conditions (NM: 49.18%, $t_{13} = 9.96$, $p < 0.001$; M1: 24.48%, $t_{13} = -0.40$, $p = 0.697$; M2: 29.72%, $t_{13} = 2.04$, $p = 0.063$). There was significant difference in the different mask conditions ($F = 41.56$, $p < 0.001$), and *post-hoc* tests showed NM was significantly >M1 and M2 ($p < 0.001$). However, there wasn't significant difference between M1 and M2 ($p = 0.054$).

In the EVC, the successful classifications were observed in the NM (NM: 51.15%, $t_{13} = 9.65$, $p < 0.001$; M1: 27.85%, $t_{13} = 1.72$, $p = 0.110$; M2: 28.61%, $t_{13} = 1.80$, $p = 0.096$). One-way repeated measures ANOVA showed significant differences in three conditions ($F = 28.70$, $p < 0.001$). The classification accuracy in the NM was significantly >M1 ($p < 0.001$) and M2 ($p < 0.001$) by *post-hoc* tests, however, there wasn't significant difference between M1 and M2 ($p = 0.803$). The classification results in all ROIs were shown in **Figure 3**.

### Cross-Classification Between Different Conditions

In the cross-classification analysis, the brain data from M1 condition can be decoded when we used the data from NM as the train data. In the objects-selective regions and scene-selective regions, the classification accuracies were significantly higher than chance-level (LO: 29.56%, $t_{13} = 3.85$, $p = 0.002$; pF: 29.48%, $t_{13} = 2.38$, $p < 0.001$; PPA: 28.83%, $t_{13} = 3.20$, $p = 0.007$; RSC: 28.03%, $t_{13} = 3.22$, $p = 0.007$; OPA:28.83% $t_{13} = 3.09$, $p = 0.009$; EVC:28.42%, $t_{13} = 2.67$, $p = 0.019$). However, the classification failed in the M2 condition when we used the classification model trained on the NM condition. The cross-classification results in the M1 and M2 conditions were shown in **Figure 4**.

## Signal Changes in the Univariate Analysis

In addition to analyzing the changes in activation patterns, we also compared the intensity of activation in these brain regions under different conditions. During the process of scene

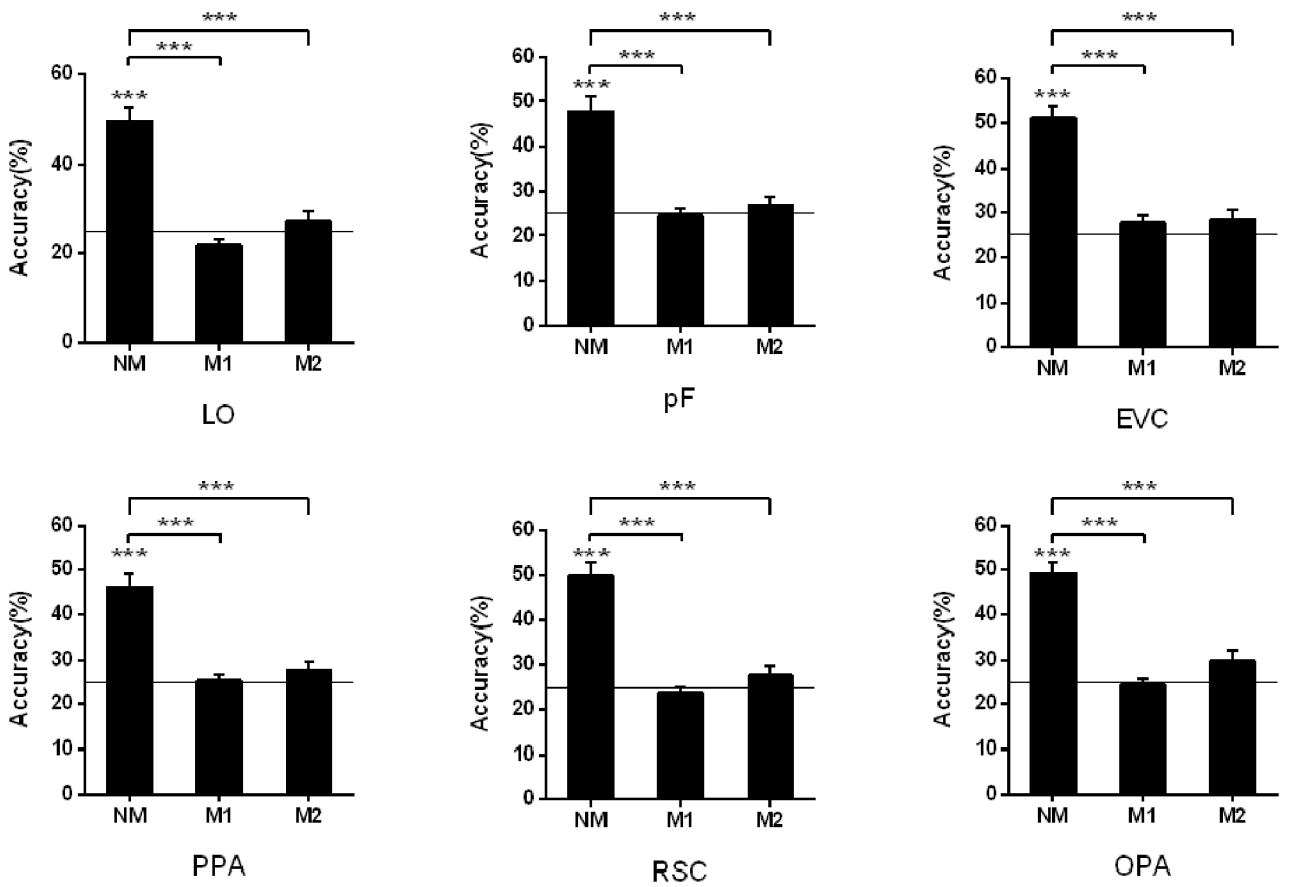


**FIGURE 3 |** Pattern classification analysis based on the activation in ROIs. The black line indicates the chance level (25%). Stars indicate significant classification accuracy in each condition and the significant difference between the two conditions;***$p < 0.001$, **$p < 0.01$,*$p < 0.05$.

recognition, there were significant signal changes in the LO, pF, PPA, and the control region EVC relative to the baseline state. The significant signal change and trend of reduction can be found in the LO (NM: 0.48, $t_{13} = 4.25$, $p < 0.001$; M1: 0.37, $t_{13} = 4.27$, $p < 0.001$; and M2: 0.36, $t_{13} = 3.237$, $p = 0.006$). The paired *t*-tests indicated that the signal change of NM was significantly greater than that of M1 ($t_{13} = 2.63$, $p = 0.021$) and M2 ($t_{13} = 2.250$, $p = 0.043$). The similar results can be found in the pF with significant signal changes in all the conditions (NM: 0.31, $t_{13} = 6.06$, $p < 0.001$; M1: 0.27, $t_{13} = 8.38$, $p < 0.001$; and M2: 0.22, $t_{13} = 8.00$, $p < 0.001$). There is also a significant difference between NM and M2 ($t_{13} = 2.33$, $p = 0.037$, paired *t*-test). These results are consistent with the signal change results of Miao et al. (2018), in which the LOC was studies as a whole.

In the PPA, the significant signal change was observed (NM: 0.12, $t_{13} = 4.57$, $p < 0.001$; M1: 0.10, $t_{13} = 4.28$, $p < 0.001$; and M2: 0.12, $t_{13} = 3.34$, $p < 0.01$), but paired *t*-tests indicated that there was no obvious reduction trend across different mask conditions. The results of signal change in the RSC and PPA were reported in the work of Miao et al. The results of signal change in the RSC and OPA were not significant, and we added some detailed description about the value of signal change in present study (RSC: NM: −0.012, $t_{13} = -1.03$, $p = 0.320$; M1: −0.017, $t_{13} = -1.98$, $p = 0.070$; and M2: −0.020%, $t_{13} = -1.51$, $p = 0.154$; OPA: NM: 0.12, $t_{13} = 2.10$, $p = 0.06$; M1: 0.02, $t_{13} = 0.36$, $p = 0.73$; and M2: 0.12, $t_{13} = 1.65$, $p = 0.12$).

In the control area EVC, significant signal change was observed in each condition (NM: 1.13, $t_{13} = 8.61$, $p < 0.001$; M1: 1.05, $t_{13} = 9.90$, $p < 0.001$; and M2: 1.09, $t_{13} = 8.68$, $p < 0.001$). Paired *t*-tests suggested that there was no significant transformation trend in the different mask conditions. The results of all ROIs were shown in **Figure 5**.

In addition to examining the differences in the activation intensity under different conditions, we also compared the signal changes across ROI in the same condition. The repeated-measures ANOVA was performed and the results showed that there were significant differences across ROIs in each condition (NM: $F = 69.66$, $p < 0.001$; M1: $F = 73.01$, $p < 0.001$; and M2: $F = 66.00$, $p < 0.001$). The signal change in EVC was significantly higher than that in other ROIs in each of the conditions ($p < 0.001$, *post-hoc* tests). The signal change in the LO was not significantly different from that in the pF, while there is a significant difference compared to scene-selective ROIs in conditions of NM and M1 (NM: LO vs. PPA, $p = 0.004$, LO vs.

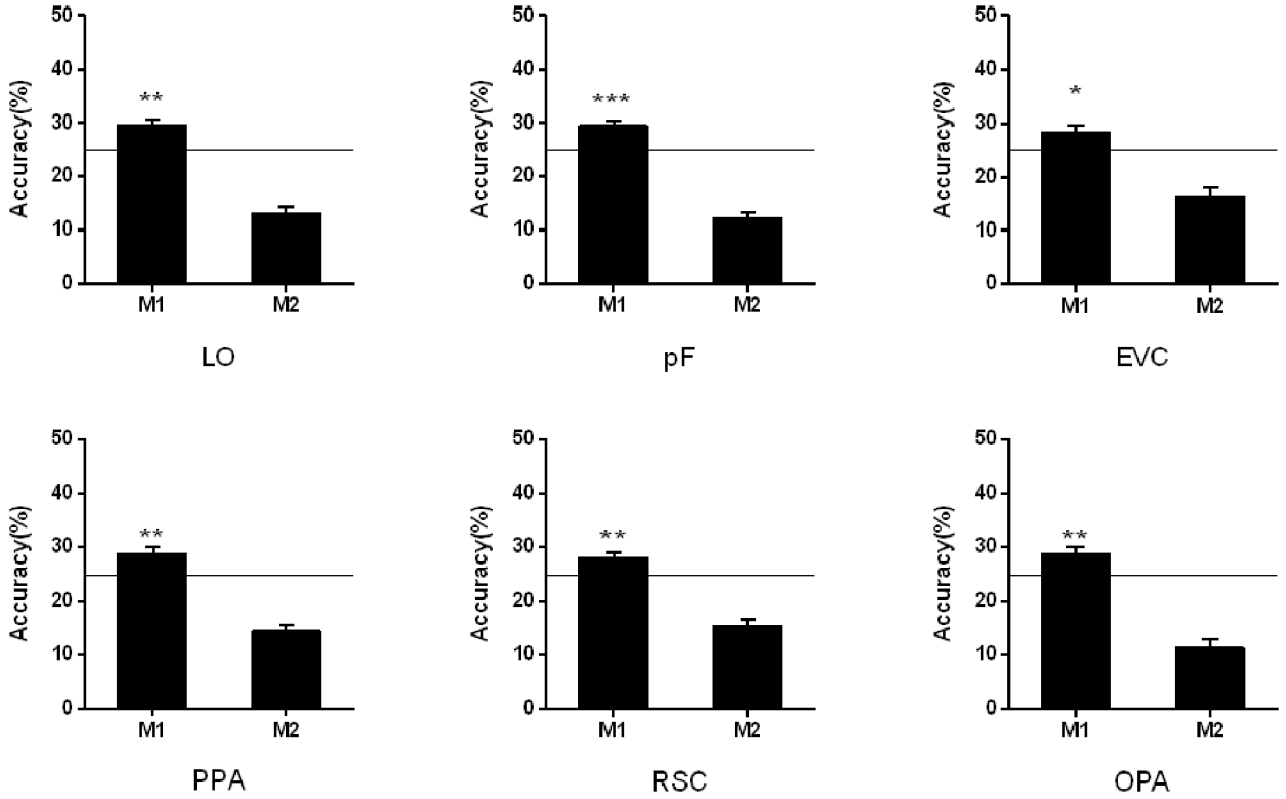


**FIGURE 4 |** Cross-classification analysis in M1 and M2 conditions. The black line indicates the chance level (25%). Stars indicate significant classification accuracy which is higher than the chance level in each condition; $^{***}p < 0.001$, $^{**}p < 0.01$, $^{*}p < 0.05$.

RSC, $p = 0.004$, and LO vs. OPA, $p = 0.022$; M1: LO vs. PPA, $p = 0.021$, LO vs. RSC, $p = 0.002$, and LO vs. OPA, $p = 0.014$). In the condition of M2, there is a significant difference between the LO and RSC ($p < 0.001$), which is similar to the comparison between pF and RSC ($p < 0.001$). In conditions of NM and M1, signal change in the pF was significantly higher than that in the PPA and RSC (NM: pF vs. PPA, $p = 0.021$, pF vs. RSC, $p < 0.001$; M1: pF vs. PPA, $p = 0.029$, pF vs. RSC, $p < 0.001$).

## DISCUSSION

The objects in the scene play an important role when people identify the scene category. In the present study, we investigated the neural mechanism of this phenomenon based on the change of the brain activation pattern when participants viewed the scenes in which the significant objects were masked. Miao et al have reported the significant influence of masking objects on behavior results that the accuracy of scene recognition decreased as more masked objects were removed, while the reaction time of the participants increased (Miao et al., 2018). Our analysis of the brain activation pattern also showed the neural representation activated by different mask conditions was significantly different in the related brain regions, which suggested that significant objects played an important role in the processing of scene recognition. Furthermore, the activation pattern showed more difference when more objects were masked, and the details are different in these brain regions.

As the object-selective region, the LOC plays important role in processing object information, which has been suggested in many previous studies, but the relationship between the LOC and scene recognition remains to be further demonstrated (Biederman, 1987; Malach et al., 1995; Grill-Spector et al., 1998; Carlson et al., 2003; James et al., 2003; Sayres and Grill-Spector, 2008; Pitcher et al., 2009). In the present study, significant classification accuracy was found in the NM condition in the object-selective region, which was significantly higher than those in M1 and M2 conditions. In the control region, however, the activation intensity of EVC was not significantly different in the three conditions. Therefore, we speculated that the decline of the activation intensity in the LO and pF suggested that the object-selective region was responsible for processing object information. One recent study found that a virtual scene with a single object induced stronger activations than a scene without objects (Harel et al., 2013), which is in line with our study. Harel's work studied the virtual scene with only one object, but real scenes are more complex and there are different objects in a scene. In our study, we further investigated whether it can induce a change in the activation pattern in brain regions if different numbers of objects were masked in the scene. According to the difference of the percent

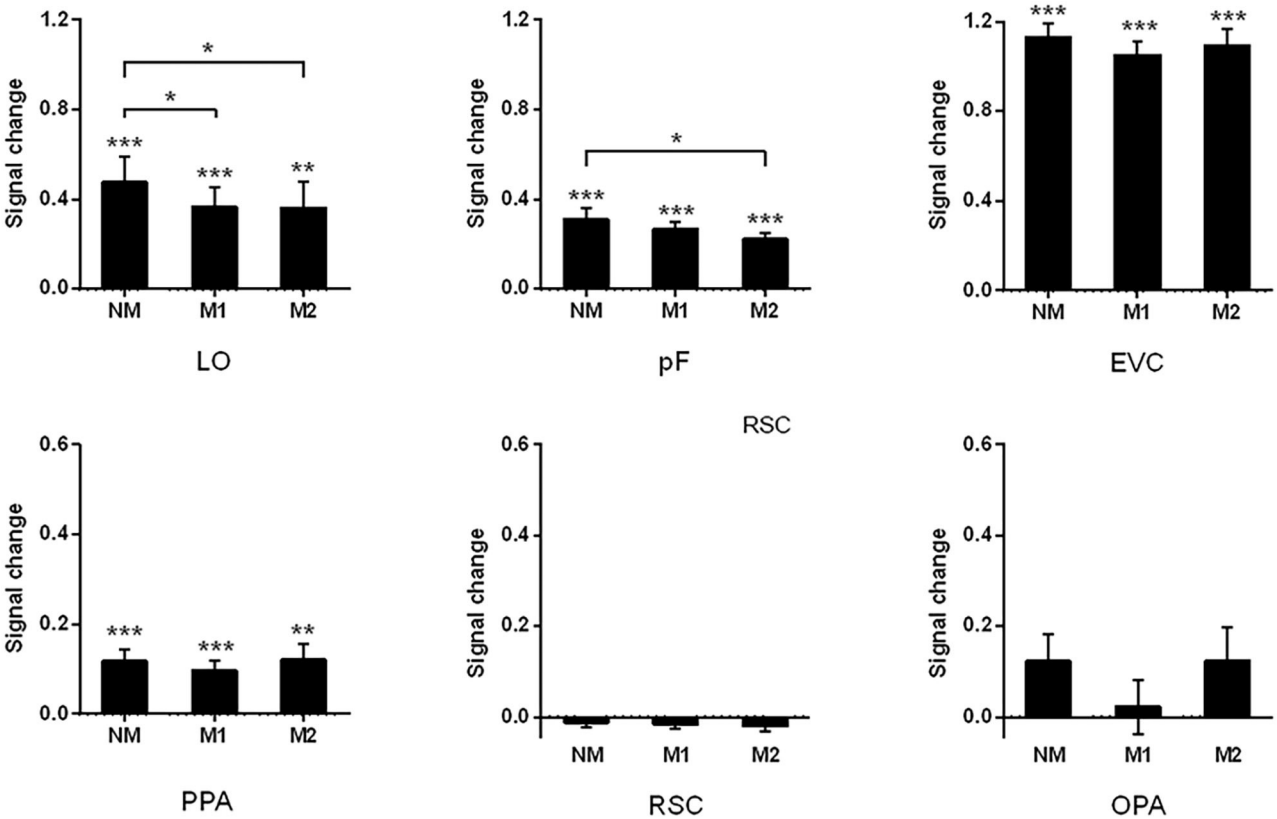


**FIGURE 5 |** Signal changes of all ROIs with different objects are masked. The significant signal change can be found in LO, pF, EVC, and PPA. The difference between three mask conditions was observed by paired-sample *t*-test; $^{***}p < 0.001$, $^{**}p < 0.01$, $^{*}p < 0.05$.

signal change across the different scene conditions, we can speculate that the activation intensity in the LOC had an intimate relationship with the amount of within-scene objects. According to classification analysis, the activation pattern of the complete scene was more effective when it was used to decode the scene categories compared with that in which one or two objects were masked in LO and pF. Statistical results showed that the accuracy of classification was not significantly different from the chance level in both of the M1 and M2 conditions, and the classification accuracies in M1 and M2 conditions were significantly lower than that in NM. Furthermore, the cross-classification succeeded between the NM and M1 conditions rather than between the NM and M2, which is consistent with the behavioral results that the more masked objects lead to the lower the scene discrimination accuracy. These results suggested there was a similar activation pattern when only one object was masked compared with the condition M2. According to the related research, we speculated that object-selective region could process the integrated information of objects and scenes in the processing of scene recognition (MacEvoy and Epstein, 2011; Linsley and MacEvoy, 2014b; Lescroart et al., 2015), and the LO and pF were responsible for processing the semantic association between objects in scenes and scenes during the processing of scene recognition.

For the scene-selective regions, the activation intensity did not change significantly across different conditions. There were significant signal changes in the PPA, however, it shows no significant difference when objects were masked. Compared with the object-selective region, the results suggested the activation intensity in the PPA was not sensitive to the univariate modulation caused by the masked object. Compared with the univariate analysis, the MVPA can contribute to finding more information based on the activation pattern. The classification accuracy was significantly higher than chance-level in the PPA under the condition of NM, however, the decoding failed in the conditions of M1 and M2. The result showed that the masked object made an effect on the activation pattern of PPA, although there was no significant difference in the activation intensity. In the scene recognition, the spatial properties of scenes may be more dominant for the PPA. Previous studies suggested that the PPA was only responsible for the attribute information of scenes, and it could not be activated by objects(MacEvoy and Epstein, 2011; Persichetti and Dilks, 2016), however, the other studies argued that the PPA was capable of processing the objects' information related to the scene (Aminoff et al., 2007; Hassabis et al., 2007; Henderson et al., 2008; Summerfield, 2010; Harel et al., 2013) and it could even be affected by the information of significant objects (Linsley and Macevoy, 2014a), which was

consistent with our results. Also, there was a study that confirmed the structural and functional basis of the PPA on processing the scene-relevant relationship between objects and scenes by using the method of voxel-based morphometry and functional connectivity (Hao et al., 2016).

In the activation intensity analysis, it was revealed that the signal changes were not significant in the RSC and OPA in full scenes or scenes with masked objects. As a control region, it is conceivable that EVC activation intensity must be significant. We speculated that the stimuli were presented for participants a relatively short time, which made the scene-selective regions acquire no enough information on the scene attribute. Furthermore, these regions contribute more to the spatial navigation and imagination instead of scene categorization (Epstein, 2008; Marchette et al., 2014; Vass and Epstein, 2016), which may be another reason for not finding significant signal change. Although the signal change did not show a significant value, the full scene could still be decoded based on the activation pattern of the RSC and OPA. Based on the classification results, we found that only full scenes could be successfully decoded in the RSC, while the scenes with masked objects could not be classified. The RSC was demonstrated to be specifically responsible for processing the spatial information of scenes (Henderson et al., 2008). One recent study indicated that the RSC anchored to local topographical features and generalized across local spatial contexts with similar structures (Marchette et al., 2014). Moreover, the absence of objects might affect the representation of the entire attribute of the scene space. When one or two objects were removed, the spatial structure of the scene was damaged, and the activation pattern could not provide enough information, which caused the low accuracy of pattern recognition. Therefore, we speculated that RSC is not recruited to process the semantic associations between scenes and objects, which is consistent with another research of our group about scene processing (Wang et al., 2018). According to recent studies, the OPA may pay more attention to local scene elements rather than global scene properties (Kamps et al., 2016a). We speculated that the masked objects in the scene might change the local elements so the OPA is sensitive to the lack of objects. These findings indicated that activation in the RSC and OPA was more responsive to the properties of the scene. As a control region, the MVPA results of the EVC shared more similarities with the scene-selective regions. The scene classification succeeded in the NM condition, and there was a significant decline in the two masked scene conditions. The EVC process low-level features properties in visual processing (such as the presence of text). We speculated that scene-selective areas are recruited to process scene recognition based on the entire attribute of the scene while the object-selective region can process the semantic association between objects and scenes in the processing of scene recognition.

## CONCLUSIONS

In this study, we tried to explore the roles and mechanisms of related regions in processing the association between the significant objects and scene by masking different objects in the scene. The impact of significant objects in scene recognition has been demonstrated in previous behavior research. The present study suggested that the LO and pF were sensitive to the absence of significant objects, and the effect may be caused by processing the semantic correlation between the scene and significant objects in the scene. The scene-selective regions were sensitive to the masked objects which might be due to the change of local scene elements, which caused the difference in spatial properties of the scene. Overall, the regions related to the scene recognition were affected by the information of significant objects according to their main function in the scene recognition, and the significant objects in the scene could play an important role in scene recognition.

## DATA AVAILABILITY STATEMENT

The datasets presented in this article are not readily available because the data is being a part of an ongoing study in the research group so the datasets cannot be shared at this time. Requests to access the datasets should be directed to the corresponding author.

## ETHICS STATEMENT

The studies involving human participants were reviewed and approved by the Research Ethics Committee of Tianjin Key Lab of Cognitive Computing and Application, Tianjin University. The patients/participants provided their written informed consent to participate in this study.

## AUTHOR CONTRIBUTIONS

BL and WY designed the experiments. JG and WY analyzed results. JG wrote the main manuscript text and prepared the figures. BL, QM, and JW contributed to the manuscript revision. All authors contributed to discuss the results and have approved the final manuscript.

## FUNDING

This work was supported by the National Natural Science Foundation of China (No. U1736219), the National Key Research and Development Program of China (No. 2018YFB0204304), and the Fundamental Research Funds for the Central Universities of China (No. FRF-MP-19-007).

## ACKNOWLEDGMENTS

The authors would like to thank Prof. Sean MacEvoy (Department of psychology, Boston College, MA, USA) for supplying the stimuli in the procedure.

## REFERENCES


Albers, A. M., Kok, P., Toni, I., Dijkerman, H. C., and de Lange, F. P. (2013). Shared representations for working memory and mental imagery in early visual cortex. *Curr. Biol.* 23, 1427–1431. doi: 10.1016/j.cub.2013.05.065

Aminoff, E., Gronau, N., and Bar, M. (2007). The parahippocampal cortex mediates spatial and nonspatial associations. *Cereb. Cortex* 17, 1493–1503. doi: 10.1093/cercor/bhl078

Amit, E., Mehoudar, E., Trope, Y., and Yovel, G. (2012). Do object-category selective regions in the ventral visual stream represent perceived distance information? *Brain Cogn.* 80, 201–213. doi: 10.1016/j.bandc.2012.06.006

Auger, S. D., Mullally, S. L., and Maguire, E. A. (2012). Retrosplenial cortex codes for permanent landmarks. *PLoS ONE* 7:e43620. doi: 10.1371/journal.pone.0043620

Axelrod, V., and Yovel, G. (2012). Hierarchical processing of face viewpoint in human visual cortex. *J. Neurosci.* 32, 2442–2452. doi: 10.1523/JNEUROSCI.4770-11.2012

Bainbridge, W. A., and Oliva, A. (2015). Interaction envelope: local spatial representations of objects at all scales in scene-selective regions. *Neuroimage* 122, 408–416. doi: 10.1016/j.neuroimage.2015.07.066

Bar, M., Aminoff, E., and Ishai, A. (2008). Famous faces activate contextual associations in the parahippocampal cortex. *Cereb. Cortex* 18, 1233–1238. doi: 10.1093/cercor/bhm170

Biederman, I. (1987). Recognition-by-components: a theory of human image understanding. *Psychol. Rev.* 94, 115–147. doi: 10.1037/0033-295X.94.2.115

Biederman, I., Blickle, T. W., Teitelbaum, R. C., and Klatsky, G. J. (1988). Object search in nonscene displays. *J. Exp. Psychol. Learn. Mem. Cogn.* 14, 456–467. doi: 10.1037/0278-7393.14.3.456

Boccia, M., Sulpizio, V., Palermo, L., Piccardi, L., Guariglia, C., and Galati, G. (2017). I can see where you would be: patterns of fMRI activity reveal imagined landmarks. *NeuroImage* 144, 174–182. doi: 10.1016/j.neuroimage.2016.08.034

Carlson, T. A., Schrater, P., and He, S. (2003). Patterns of activity in the categorical representations of objects. *J. Cogn. Neurosci.* 15, 704–717. doi: 10.1162/jocn.2003.15.5.704

Cate, A. D., Goodale, M. A., and Kohler, S. (2011). The role of apparent size in building- and object-specific regions of ventral visual cortex. *Brain Res.* 1388, 109–122. doi: 10.1016/j.brainres.2011.02.022

Chang, C. C., and Lin, C. J. (2011). LIBSVM: a library for support vector machines. *ACM Trans. Intell. Syst. Technol.* 2:27, 1–27. doi: 10.1145/1961189.1961199

Cichy, R. M., Heinzle, J., and Haynes, J. D. (2012). Imagery and perception share cortical representations of content and location. *Cereb. Cortex* 22, 372–380. doi: 10.1093/cercor/bhr106

Cukur, T., Huth, A. G., Nishimoto, S., and Gallant, J. L. (2016). Functional subdomains within scene-selective cortex: parahippocampal place area, retrosplenial complex, and occipital place area. *J. Neurosci.* 36, 10257–10273. doi: 10.1523/JNEUROSCI.4033-14.2016

Davenport, J. L., and Potter, M. C. (2004). Scene consistency in object and background perception. *Psychol. Sci.* 15, 559–564. doi: 10.1111/j.0956-7976.2004.00719.x

Davis, T., LaRocque, K. F., Mumford, J. A., Norman, K. A., Wagner, A. D., and Poldrack, R. A. (2014). What do differences between multi-voxel and univariate analysis mean? how subject-, voxel-, and trial-level variance impact fMRI analysis. *NeuroImage* 97, 271–283. doi: 10.1016/j.neuroimage.2014.04.037

Dilks, D. D., Julian, J. B., Kubilius, J., Spelke, E. S., and Kanwisher, N. (2011). Mirror-image sensitivity and invariance in object and scene processing pathways. *J. Neurosci.* 31, 11305–11312. doi: 10.1523/JNEUROSCI.1935-11.2011

Dilks, D. D., Julian, J. B., Paunov, A. M., and Kanwisher, N. (2013). The occipital place area is causally and selectively involved in scene perception. *J. Neurosci.* 33, 1331–1336. doi: 10.1523/JNEUROSCI.4081-12.2013

Emmerling, T. C., Zimmermann, J., Sorger, B., Frost, M. A., and Goebel, R. (2016). Decoding the direction of imagined visual motion using 7T ultra-high field fMRI. *NeuroImage* 125, 61–73. doi: 10.1016/j.neuroimage.2015.10.022

Epstein, R. A. (2008). Parahippocampal and retrosplenial contributions to human spatial navigation. *Trends Cogn. Sci.* 12, 388–396. doi: 10.1016/j.tics.2008.07.004

Epstein, R. A., and Morgan, L. K. (2012). Neural responses to visual scenes reveals inconsistencies between fMRI adaptation and multivoxel pattern analysis. *Neuropsychologia* 50, 530–543. doi: 10.1016/j.neuropsychologia.2011.09.042

Gagne, C. R., and MacEvoy, S. P. (2014). Do simultaneously viewed objects influence scene recognition individually or as groups? two perceptual studies. *PLoS ONE* 9:e102819. doi: 10.1371/journal.pone.0102819

Ganaden, R. E., Mullin, C. R., and Steeves, J. K. E. (2013). Transcranial magnetic stimulation to the transverse occipital sulcus affects scene but not object processing. *J. Cogn. Neurosci.* 25, 961–968. doi: 10.1162/jocn_a_00372

Greene, M. R., and Oliva, A. (2009). Recognition of natural scenes from global properties: seeing the forest without representing the trees. *Cogn. Psychol.* 58, 137–176. doi: 10.1016/j.cogpsych.2008.06.001

Grill-Spector, K., Kushnir, T., Edelman, S., Itzchak, Y., and Malach, R. (1998). Cue-invariant activation in object-related areas of the human occipital lobe. *Neuron* 21, 191–202. doi: 10.1016/S0896-6273(00)80526-7

Hao, X., Huang, Y., Li, X., Song, Y., Kong, X., Wang, X., et al. (2016). Structural and functional neural correlates of spatial navigation: a combined voxel-based morphometry and functional connectivity study. *Brain Behav.* 6:e00572. doi: 10.1002/brb3.572

Harel, A., Kravitz, D. J., and Baker, C. I. (2013). Deconstructing visual scenes in cortex: gradients of object and spatial layout information. *Cereb. Cortex* 23, 947–957. doi: 10.1093/cercor/bhs091

Harrison, S. A., and Tong, F. (2009). Decoding reveals the contents of visual working memory in early visual areas. *Nature* 458, 632–635. doi: 10.1038/nature07832

Hassabis, D., Kumaran, D., and Maguire, E. A. (2007). Using imagination to understand the neural basis of episodic memory. *J. Neurosci. Off. J. Soc. Neurosci.* 27, 14365–14374. doi: 10.1523/JNEUROSCI.4549-07.2007

Hasson, U., Malach, R., Harel, M., and Levy., I. (2003). Large-scale mirror-symmetry organization of human occipito-temporal object areas. Neuron Glia Biol. 37, 1027–1041. doi: 10.1016/S0896-6273(03)00144-2

Haxby, J. V., Gobbini, M. I., Furey, M. L., Ishai, A., Schouten, J. L., and Pietrini, P. (2001). Distributed and overlapping representations of faces and objects in ventral temporal cortex. *Science* 293, 2425–2430. doi: 10.1126/science.1063736

Henderson, J. M., Larson, C. L., and Zhu, D. C. (2008). Full scenes produce more activation than close-up scenes and scene-diagnostic objects in parahippocampal and retrosplenial cortex: an fMRI study. *Brain Cogn.* 66, 40–49. doi: 10.1016/j.bandc.2007.05.001

Howard, L. R., Kumaran, D., Ólafsdóttir, H. F., and Spiers, H. J. (2011). Double dissociation between hippocampal and parahippocampal responses to object-background context and scene novelty. *J. Neurosci.* 31, 5253–5261. doi: 10.1523/JNEUROSCI.6055-10.2011

James, T. W., Culham, J., Humphrey, G. K., Milner, A. D., and Goodale, M. A. (2003). Ventral occipital lesions impair object recognition but not object-directed grasping: an fMRI study. *Brain* 126, 2463–2475. doi: 10.1093/brain/awg248

Joubert, O. R., Rousselet, G. A., Fize, D., and Fabre-Thorpe, M. (2007). Processing scene context: fast categorization and object interference. *Vision Res.* 47, 3286–3297. doi: 10.1016/j.visres.2007.09.013

Kamps, F. S., Julian, J. B., Kubilius, J., Kanwisher, N., and Dilks, D. D. (2016a). The occipital place area represents the local elements of scenes. *Neuroimage* 132, 417–424. doi: 10.1016/j.neuroimage.2016.02.062

Kamps, F. S., Lall, V., and Dilks, D. D. (2016b). The occipital place area represents first-person perspective motion information through scenes. *Cortex* 83, 17–26. doi: 10.1016/j.cortex.2016.06.022

Konkle, T., and Oliva, A. (2012). A real-world size organization of object responses in occipitotemporal cortex. *Neuron* 74, 1114–1124. doi: 10.1016/j.neuron.2012.04.036

Kourtzi, Z., and Kanwisher, N. (2000). Cortical regions involved in perceiving object shape. *J. Neurosci.* 20, 3310–3318. doi: 10.1523/JNEUROSCI.20-09-03310.2000

Kravitz, D. J., Peng, C. S., and Baker, C. I. (2011). Real-world scene representations in high-level visual cortex: it's the spaces more than the places. *J. Neurosci.* 31, 7322–7333. doi: 10.1523/JNEUROSCI.4588-10.2011

LaConte, S., Strother, S., Cherkassky, V., Anderson, J., and Hu, X. (2005). Support vector machines for temporal classification of block design fMRI data. *NeuroImage* 26, 317–329. doi: 10.1016/j.neuroimage.2005.01.048

Lescroart, M. D., Stansbury, D. E., and Gallant, J. L. (2015). Fourier power, subjective distance, and object categories all provide plausible models of BOLD responses in scene-selective visual areas. *Front. Comput. Neurosci.* 9:135. doi: 10.3389/fncom.2015.00135

Linsley, D., and Macevoy, S. P. (2014a). Encoding-stage crosstalk between object- and spatial property-based scene processing pathways. *Cereb. Cortex* 25, 2267–2281. doi: 10.1093/cercor/bhu034

Linsley, D., and MacEvoy, S. P. (2014b). Evidence for participation by object-selective visual cortex in scene category judgments. *J. Vis.* 14:19. doi: 10.1167/14.9.19

Lowe, M. X., Gallivan, J. P., Ferber, S., and Cant, J. S. (2016). Feature diagnosticity and task context shape activity in human scene-selective cortex. *Neuroimage* 125, 681–692. doi: 10.1016/j.neuroimage.2015.10.089

MacEvoy, S. P., and Epstein, R. A. (2007). Position selectivity in scene- and object-responsive occipitotemporal regions. *J. Neurophysiol.* 98, 2089–2098. doi: 10.1152/jn.00438.2007

MacEvoy, S. P., and Epstein, R. A. (2011). Constructing scenes from objects in human occipitotemporal cortex. *Nat. Neurosci.* 14, 1323–1329. doi: 10.1038/nn.2903

Maguire, E. A. (2001). The retrosplenial contribution to human navigation: a review of lesion and neuroimaging findings. *Scand. J. Psychol.* 42, 225–238. doi: 10.1111/1467-9450.00233

Malach, R., Reppas, J. B., Benson, R. R., Kwong, K. K., Jiang, H., Kennedy, W. A., et al. (1995). Object-related activity revealed by functional magnetic resonance imaging in human occipital cortex. *Proc. Natl. Acad. Sci. U.S.A.* 92, 8135–8139. doi: 10.1073/pnas.92.18.8135

Marchette, S. A., Vass, L. K., Ryan, J., and Epstein, R. A. (2014). Anchoring the neural compass: coding of local spatial reference frames in human medial parietal lobe. *Nat. Neurosci.* 17, 1598–1606. doi: 10.1038/nn.3834

Miao, Q., Zhang, G., Yan, W., and Liu, B. (2018). Investigating the brain neural mechanism when signature objects were masked during a scene categorization task using functional MRI. *Neuroscience* 388, 248–262. doi: 10.1016/j.neuroscience.2018.07.030

Mourao-Miranda, J., Bokde, A. L., Born, C., Hampel, H., and Stetter, M. (2005). Classifying brain states and determining the discriminating activation patterns: support vector machine on functional MRI data. *NeuroImage* 28, 980–995. doi: 10.1016/j.neuroimage.2005.06.070

Norman, K. A., Polyn, S. M., Detre, G. J., and Haxby, J. V. (2006). Beyond mind-reading: multi-voxel pattern analysis of fMRI data. *Trends Cogn. Sci.* 10, 424–430. doi: 10.1016/j.tics.2006.07.005

O'Craven, K. M., and Kanwisher, N. (2000). Mental imagery of faces and places activates corresponding stimulus-specific brain regions. *J. Cogn. Neurosci.* 12, 1013–1023. doi: 10.1162/08989290051137549

Park, S., Brady, T. F., Greene, M. R., and Oliva, A. (2011). Disentangling scene content from spatial boundary: complementary roles for the parahippocampal place area and lateral occipital complex in representing real-world scenes. *J. Neurosci.* 31, 1333–1340. doi: 10.1523/JNEUROSCI.3885-10.2011

Park, S., Konkle, T., and Oliva, A. (2015). Parametric coding of the size and clutter of natural scenes in the human brain. *Cereb. Cortex* 25, 1792–1805. doi: 10.1093/cercor/bht418

Peelen, M. V., Fei-Fei, L., and Kastner, S. (2009). Neural mechanisms of rapid natural scene categorization in human visual cortex. *Nature* 460, 94–97. doi: 10.1038/nature08103

Persichetti, A. S., and Dilks, D. D. (2016). Perceived egocentric distance sensitivity and invariance across scene-selective cortex. *Cortex* 77, 155–163. doi: 10.1016/j.cortex.2016.02.006

Pitcher, D., Charles, L., Devlin, J. T., Walsh, V., and Duchaine, B. (2009). Triple dissociation of faces, bodies, and objects in extrastriate cortex. *Curr. Biol.* 19, 319–324. doi: 10.1016/j.cub.2009.01.007

Samuel Schwarzkopf, D., and Rees, G. (2011). Pattern classification using functional magnetic resonance imaging. *Wiley Interdiscip. Rev. Cogn. Sci.* 2, 568–579. doi: 10.1002/wcs.141

Sastyin, G., Niimi, R., and Yokosawa, K. (2015). Does object view influence the scene consistency effect? *Atten. Percept. Psychophys.* 77, 856–866. doi: 10.3758/s13414-014-0817-x

Sayres, R., and Grill-Spector, K. (2008). Relating retinotopic and object-selective responses in human lateral occipital cortex. *J. Neurophysiol.* 100, 249–267. doi: 10.1152/jn.01383.2007

Stelzer, J., Chen, Y., and Turner, R. (2013). Statistical inference and multiple testing correction in classification-based multi-voxel pattern analysis (MVPA): random permutations and cluster size control. *NeuroImage* 65, 69–82. doi: 10.1016/j.neuroimage.2012.09.063

Summerfield, J. J. (2010). Differential engagement of brain regions within a 'core' network during scene construction. *Neuropsychologia* 48, 1501–1509. doi: 10.1016/j.neuropsychologia.2010.01.022

Vass, L. K., and Epstein, R. A. (2016). Common neural representations for visually guided reorientation and spatial imagery. *Cereb. Cortex* 27, 1457–1471. doi: 10.1093/cercor/bhv343

Vetter, P., Smith, F. W., and Muckli, L. (2014). Decoding sound and imagery content in early visual cortex. *Cur.r Biol.* 24, 1256–1262. doi: 10.1016/j.cub.2014.04.020

Walther, D. B., Caddigan, E., Fei-Fei, L., and Beck, D. M. (2009). Natural scene categories revealed in distributed patterns of activity in the human brain. *J. Neurosci.* 29, 10573–10581. doi: 10.1523/JNEUROSCI.0559-09.2009

Walther, D. B., Chai, B., Caddigan, E., Beck, D. M., and Fei-Fei, L. (2011). Simple line drawings suffice for functional MRI decoding of natural scene categories. *Proc. Natl. Acad. Sci. U.S.A.* 108, 9661–9666. doi: 10.1073/pnas.1015666108

Wang, S., Cao, L., Xu, J., Zhang, G., Lou, Y., and Liu, B. (2018). Revealing the semantic association between perception of scenes and significant objects by representational similarity analysis. *Neuroscience* 372, 87–96. doi: 10.1016/j.neuroscience.2017.12.043

Wolbers, T., Zahorik, P., and Giudice, N. A. (2011). Decoding the direction of auditory motion in blind humans. *NeuroImage* 56, 681–687. doi: 10.1016/j.neuroimage.2010.04.266

**Conflict of Interest:** The authors declare that the research was conducted in the absence of any commercial or financial relationships that could be construed as a potential conflict of interest.

frontiers in Genetics

ORIGINAL RESEARCH
published: 21 December 2020
doi: 10.3389/fgene.2020.614823

# Machine Learning Models to Predict Primary Sites of Metastatic Cervical Carcinoma From Unknown Primary

*Di Lu[1], Jianjun Jiang[1], Xiguang Liu[1], He Wang[2], Siyang Feng[1], Xiaoshun Shi[1], Zhizhi Wang[1], Zhiming Chen[1], Xuebin Yan[1], Hua Wu[1] and Kaican Cai[1]**

*[1] Department of Thoracic Surgery, Nanfang Hospital, Southern Medical University, Guangzhou, China, [2] Department of Thoracic Surgery, Peking University Shenzhen Hospital, Shenzhen, China*

Metastatic cervical carcinoma from unknown primary (MCCUP) accounts for 1–4% of all head and neck tumors, and identifying the primary site in MCCUP is challenging. The most common histopathological type of MCCUP is squamous cell carcinoma (SCC), and it remains difficult to identify the primary site pathologically. Therefore, it seems necessary and urgent to develop novel and effective methods to determine the primary site in MCCUP. In the present study, the RNA sequencing data of four types of SCC and Pan-Cancer from the cancer genome atlas (TCGA) were obtained. And after data pre-processing, their differentially expressed genes (DEGs) were identified, respectively. Gene ontology (GO) and Kyoto Encyclopedia of Genes and Genomes (KEGG) pathway analysis indicated that these significantly changed genes of four types of SCC share lots of similar molecular functions and histological features. Then three machine learning models, [Random Forest (RF), support vector machine (SVM), and neural network (NN)] which consisted of ten genes to distinguish these four types of SCC were developed. Among the three models with prediction tests, the RF model worked best in the external validation set, with an overall predictive accuracy of 88.2%, sensitivity of 88.71%, and specificity of 95.42%. The NN model is the second in efficacy, with an overall accuracy of 82.02%, sensitivity of 81.23%, and specificity of 93.04%. The SVM model is the last, with an overall accuracy of 76.69%, sensitivity of 74.81%, and specificity of 90.84%. The present analysis of similarities and differences among the four types of SCC, and novel models developments for distinguishing four types of SCC with informatics methods shed lights on precision MCCUP diagnosis in the future.

**Keywords: metastatic cervical carcinoma from unknown primary, random forest, neural network, support vector machine, predict, primary sites**

OPEN ACCESS

***Edited by:***
*Long Wang,*
*University of Science and Technology Beijing, China*

***Reviewed by:***
*Ximing Nie,*
*Capital Medical University, China*
*Sun Pengcheng,*
*Shandong University, China*

****Correspondence:***
*Kaican Cai*
*doc_cai@163.com*

***Specialty section:***
*This article was submitted to Statistical Genetics and Methodology, a section of the journal Frontiers in Genetics*

***Received:*** *07 October 2020*
***Accepted:*** *30 November 2020*
***Published:*** *21 December 2020*

***Citation:***
*Lu D, Jiang J, Liu X, Wang H, Feng S, Shi X, Wang Z, Chen Z, Yan X, Wu H and Cai K (2020) Machine Learning Models to Predict Primary Sites of Metastatic Cervical Carcinoma From Unknown Primary. Front. Genet. 11:614823. doi: 10.3389/fgene.2020.614823*

## INTRODUCTION

Metastatic cervical carcinoma from unknown primary (MCCUP) is defined as metastatic disease in the lymph nodes of the neck without any evidences of a primary tumor after appropriate investigations. It is a type of cancer which originates from unknown primary sites, and squamous cell histology is prominent, accounting for 75–90% of cases (Arosio et al., 2017;

Jereczek-Fossa et al., 2004). The special features of the lymphatic drainage of the head and neck regions suggest that the primary sites may locate in head, neck (oropharynx, larynx, and tongue) or thorax (tracheal, bronchial, lung, and esophagus) (Jereczek-Fossa et al., 2004; Arosio et al., 2017). However, despite comprehensive diagnostic work-ups including fibroscopy, computed tomography, magnetic resonance imaging, positron emission tomography, fine-needle aspiration, and panendoscopy have been conducted, the primary site remains difficult to identify in cases of MCCUP. An accurate identification of the primary site is crutial for the designment of effective treatments. Therefore, the developments of a novel and effective method to determine the primary site in MCCUP seem rather necessary and urgent.

The reasons for the failure of primary tumor diagnosis is not fully elaborated; however, the small size of the primary tumor may increase the difficulties in identifying the primary site and the evolutions of the cancer cell itself may be one of the reasons too (Arosio et al., 2017). The developments of high-throughput and next-generation sequencing technologies have improved our understanding of the molecular landscape of cancer, offering the basis and possibility to discover predictive biomarkers for cancer diagnosis (Roychowdhury and Chinnaiyan, 2016). Relevant high-throughput studies indicate that squamous cell carcinoma (SCC) shares certain common histological characteristics and molecular signatures (Dotto and Rustgi, 2016; Campbell et al., 2018) which makes it more difficult to identify the primary site of MCCUPwhose pathologic type is primarily SCC. In cases of MCCUP, determining the primary site is challenging.

Research discoveries derived through cancer genome and transcriptome studies have potential clinical impact as biomarkers (Roychowdhury and Chinnaiyan, 2016). And machine learning approaches have been applied to cancer prognosis and prediction and shown significant advantage in differential diagnosis (Cruz and Wishart, 2007). Khan et al. (2001) developed a model of Neural Networks (NN) for diagnostic classification base on gene-expression signatures of the small, round blue cell tumors (SRBCTs) of childhood, of which four subtypes share similar appearance on routine histology. Yang et al. (2018) used the Random Forest (RF) algorithm to select biomarker metabolites and establish a diagnostic model in a metabolomics study of cancer cachexia.

In the present study, a dataset from The Cancer Genome Atlas (TCGA) RNA-Seq data of squamous cancer and TCGA Pan-Cancer (PANCAN) data were employed to conduct a series of bioinformatics analyses, and three machine learning models [RF, NN, support vector machine (SVM)] were developed to explore the potantial effective tool to distinguish these squamous cancers.

# MATERIALS AND METHODS

## Data Source and Data Pre-Processing

The Cancer Genome Atlas RNA-Seq data of four types of cancer [Genomic Data Commons (GDC) TCGA Cervical Cancer (CESC), GDC TCGA Esophageal Cancer (ESCA), GDC TCGA Head and Neck Cancer (HNSC), GDC TCGA Lung Squamous Cell Carcinoma (LUSC)], and the phenotype data and TCGA PANCAN data were downloaded from University of California Santa Cruz (UCSC) Xena database[1] . The GDC sample sheet of all squamous cell carcinomas of TCGA database[2] were downloaded from TCGA database by using the searching strategy (Disease Type IS squamous cell neoplasms AND Program Name IS TCGA AND Experimental Strategy IS RNA-Seq).

Based on sample ID in the GDC sample sheet, the samples of SCC in the data PANCAN were extracted. Using the same methods we extracted the SCC data of the four types of cancer data (CESC, ESCA, HNSC, HNSC). Then we renamed above data as PANCANsqu, CESC, ESCC, HNSC, and LUSC spectively. Using the function Rtsne provided by R Rtsne to visualize PANCANsqu based on t-distributed stochastic neighbor embedding (t-SNE) algorithm (van der Maaten and Hinton, 2008; van der Maaten, 2014).

## Differential Expression Analysis

The DESeq2 R package was used to identify differentially expressed genes (DEGs) of each squamous cancer data (CESC, ESCC, HNSC, and LUSC) (Love et al., 2014, 2). Padjust $< 0.01$ and absolute log2 FC $> 2$ were chosen as the cut-off criteria. The Venn diagram was generated by VennDiagram R package.

Gene ontology (GO) and Kyoto Encyclopedia of Genes and Genomes (KEGG) pathway enrichment analysis

GO and KEGG pathway enrichment analysis was performed using clusterProfiler R package (Ashburner et al., 2000; Kanehisa and Goto, 2000; Yu et al., 2012). The enriched biological processes (BP), cellular components (CC), and molecular functions (MF) were obtained to analyze the DEGs of each cancer at the functional level. $P < 0.01$ was set as the threshold value.

## Protein-protein Interaction Network Construction

The STRING online database[3] was used for analyzing the protein-protein interaction (PPI) of the DEGs of each cancer, and Cytoscape software[4] was used to visualize the PPI network of the DEGs (Snel et al., 2000; Shannon et al., 2003; Szklarczyk et al., 2019).

## Predict Model Construction and Validation

The function nearZeroVar was used to identify and eliminate zero and near-zero-variance variables, and the function findCorrelation to remove Correlated variables with absolute correlations above 0.9, and the function findLinearCombos to eliminate the linear dependencies (Kuhn, 2008). The above three functions are provided by the R caret R package (Kuhn, 2008). Feature selection using recursive feature elimination algorithms (Guyon et al., 2002).

The function createDataPartition was used to create balanced splits of the PANCANsqu data, creating a single 70/30% split of

[1]https://xenabrowser.net/datapages/

[2]https://portal.gdc.cancer.gov/

[3]http://string-db.org

[4]http://www.cytoscape.org/

the data. Then the 70% split of the data was used as training set while the remaining 30% data was used as the validation set. Several machine learning methodologies [RF, NN, and SVM] were adopted to construct the model with data of the training set using caret, e1071 and randomForest R package and 10 fold cross validation is applied in model training (Kuhn, 2008).

Sensitivity, specificity, and area under curve (AUC) values were determined to evaluate the performance of the established classifier in the validation set.

The modeling process is briefly described below:

Fristly, the function trainControl was used to define the parameters of sampling and cross-validation.

method = "repeatedcv", number = 10, repeats = 3, returnResamp = "all", classProbs = T

Secondly, The function train was used to build three training models.

1. method = "rf", mtry = 2
2. method = "svmRadial", sigma = 0.3469467 and C = 1
3. method = "nnet", size = 5 and decay = 0.1

Lastly, The function predict was used to predict the sample type base on the training model, function extractPrediction and extractProb to acquire the model prediction results and their probabilities.

To evaluate the performance of the model that have been established, the function confusionMatrix was used to obtain the confusion matrix and the ROCR R package to draw the ROC curve.

# RESULTS

## Expression Profiles of Four Types of Squamous Cancer

Volcano plots were generated to visualize the distribution of expressed genes between cancer and normal controls from the four RNA-Seq data (CESC, ESCC, HNSC, and LUSC). Red or green dots in the plots represent significantly upregulated or downregulated genesrespectively (**Figures 1A–D**). Venn diagrams show the DEGs information among CESC, ESCC, HNSC, and LUSC (**Figure 1E**). In total, 3429, 3749, 3462, and 7035 DEGs were identified from the four RNA-Seq data of ESCC (CESC, ESCC, HNSC, and LUSC). A total of 236 common DEGs were significantly changed in all four independent cohorts, and 1511(CESC), 1324(ESCC), 1016(HNSC), and 3285(LUSC) specific DEGs were identified in the difference set (just in one type of cancer). Detailed information of the DEGs is provided by Supplementary Materials.

## GO and KEGG Pathway Enrichment Analysis

GO and KEGG pathway enrichment analyses of DEGs were performed using clusterProfiler R package, and the results were shown in the **Figure 2**.

For "BP", CESC and LUSC both showed enrichment in cornification, epidermis development, skin development, epidermal cell differentiation, keratinocyte differentiation, and keratinization. The differential DEGs expressed in ESCC mainly showed enrichment in digestion, extracellular structure organization, extracellular matrix organization, regionalization and hormone transport. The DEGs expressed in HNSCC mainly showed enrichment in response to muscle contraction, muscle system process, muscle filament sliding, actin-myosin filament sliding, myofibril assembly and striated muscle cell development.

For the "cellular component (CC)" ontology, ESCC and LUSC both showed enrichment in transmembrane transporter complex, transporter complex, ion channel complex, anchored components of membrane. The differential genes expressed in HNSC mainly showed enrichment in myofibril contractile fiber part, sarcomere, I band and Z disc. The differential genes expressed in CESC showed enrichment in cornified envelope, collagen-containing extracellular matrix, condensed chromosome, contractile fiber and cell-cell junction.

Regarding "MF", the DEGs of ESCC and HNSCC both showed enrichment in extracellular matrix structural constituent, receptor ligand activity and passive transmembrane transporter activity. The differential genes expressed in LUSC mainly showed enrichment in substrate-specific channel activity, ion channel activity, ion gated channel activity and gated channel activity. The differential genes expressed only in CESC mainly showed enrichment in DNA-binding transcription activator activity, RNA polymerase II-specific glycosaminoglycan binding, actin binding and extracellular matrix structural constituent.

For "KEGG pathway enrichment analysis", LUSC mainly showed enrichment in Retinol metabolism, ascorbate and aldarate metabolism, Metabolism of xenobiotics by cytochrome P450 and Bile secretion. The differential DEGs expressed in ESCC mainly showed enrichment in Neuroactive ligand-receptor interaction, Protein digestion and absorption, Maturity onset diabetes of the young, Pancreatic secretion, Viral protein interaction with cytokine and cytokine receptor and Drug metabolism – cytochrome P450. The DEGs expressed in HNSCC mainly showed enrichment in Hypertrophic cardiomyopathy (HCM), ECM-receptor interaction, Salivary secretion, Calcium signaling pathway, and Dilated cardiomyopathy (DCM).

## Identification of Key Candidate Genes With the PPI Network of DEGs

The PPI network of the four types of squamous cancer was constructed using the STRING online database and Cytoscape (**Figure 3**). Then the central node genes (more than 10 connections/interactions) were identified. In the DEGs of CESC, the top ten highly connected genes were CDK1, CDC20, CCNA2, CCNB1, BUB1B, CDC6, BUB1, AURKA, CCNB2, and MAD2L1. In the DEGs of ESCC, the top ten highly connected genes were CDK1, CCNB1, CCNA2, CDC20, BUB1, CDC6, CCNB2, CDC45, MAD2L1, and BUB1B. In the DEGs of HNSC, the top ten highly connected genes were CREBBP, BRCA1, UBE2I, GNB1, PPARGC1A, POLR2F, POLR2A, POLR2H, POLR2B, and

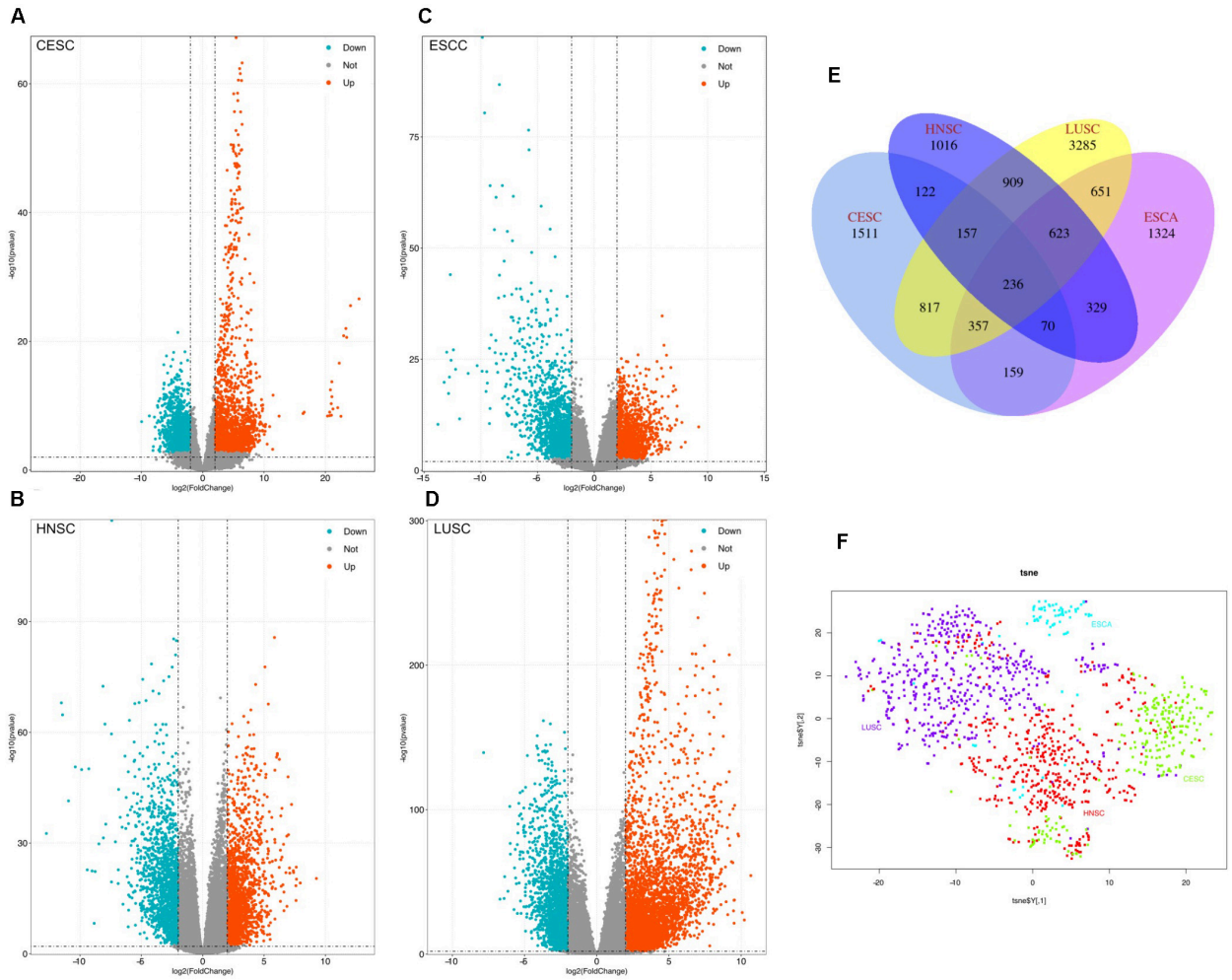


**FIGURE 1 |** Identification of the differentially expressed genes (DEGs) between tumor tissues and normal controls, **(A–D)** Volcano plots of genes showing significantly different expression between tumor tissues and normal controls. The *Y*-axis indicates the *p*-values (log10 scaled), whereas the *X*-axis shows the fold change (log2 scaled). Each symbol represents a different gene, and the red/blue colors of the symbols categorize the upregulated/downregulated genes under different criteria (*p*-value and fold change threshold). *p*-value $< 0.01$ was considered statistically significant, whereas log2 (fold change) = 2 was set as the threshold. **(E)** Venn diagram of the DEGs of the four squamous carcinoma. **(F)**: Visualized PANCANsqu RNA-seq data used by t-SNE algorithm.

POLR2K. In the DEGs of LUSC, the top ten highly connected genes were CDK1, CCNB1, CCNA2, CDC20, BUB1, PLK1, CCNB2, BUB1B, MAD2L1, and CDC6.

## Model Construction for Discriminating the Four Types of Squamous Cancer

The t-SNE algorithm was used to visualize PANCANsqu data prior to model construction, as shown in **Figure 1F**. After preprocessing the PANCANsqu data, 1,327 variables were retained. To improve model predictive accuracy and reduce model complexity, we used recursive feature elimination as the methods of feature selection by using the function rfe in the caret R package. Then the number of the variables (5, 10, 15, 30, 60, 80, and 1,327) was tested in the feature selection procedure, and it was found that 80 genes worked the best with the accuracy of 93.35%. **Table 1** showed the detail information. As the performance of each number of variable showed in **Table 1**, considering the model predictive accuracy and the model complexity, the top 10 gene were selected for the subsequent researches, which were C11orf85, LA16c-431H6.6, MYBPH, MAP9, FMO2, SCGB3A1, BPIFA1, TBX1, SRRM2, and AC016549.1.

Several statistical methodologies (RF, SVM, and NN) were used to construct the prediction model with data from the training set, and for each statistical methodology, using subsets of DEGs (the top 10 genes generated by feature selection) instead of all DEGs as variables. Receiver operating characteristic curves were used to evaluate the predictive value (**Figure 4**). Among the three statistical methodologies tested, the RF model worked best both in the training set and in the external validation set (**Table 2**), with an overall predictive accuracy of 88.2%, mean sensitivity of 88.71%, and mean specificity of 95.42%. Mean AUC

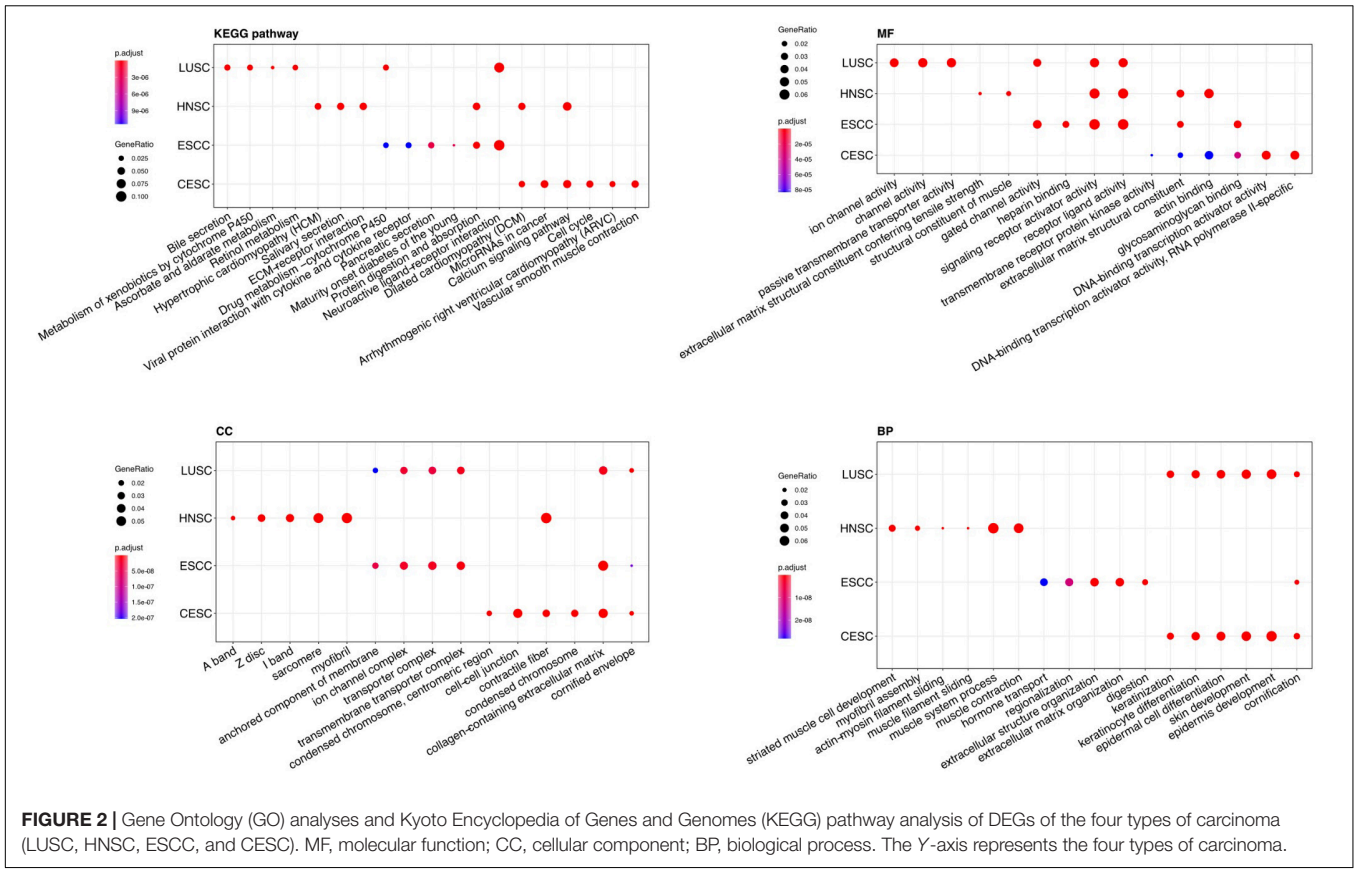


**FIGURE 2 |** Gene Ontology (GO) analyses and Kyoto Encyclopedia of Genes and Genomes (KEGG) pathway analysis of DEGs of the four types of carcinoma (LUSC, HNSC, ESCC, and CESC). MF, molecular function; CC, cellular component; BP, biological process. The *Y*-axis represents the four types of carcinoma.

for the validation sets was 0.9782. Subsequently, for the NN model, overall predictive accuracy was 0.8202, mean sensitivity was 0.8123, mean specificity was 0.9304, and the mean AUC was 0.9563. For the SVM model, overall predictive accuracy was 0.7669, mean sensitivity was 0.7481, mean specificity was 0.9084, and the mean AUC was 0.9347.

## DISCUSSION

In this study, we investigated methods for the accurate diagnosis of the primary site of MCCUP using microarrays of four potential primary tissues (CESC, ESCC, HNSC, and LUSC). We identified significant DEGs from four RNA-Seq data. The similarities and differences among the four types of squamous cancer were then analyzed using bioinformatics methods based on these significant DEG sets. Based on the data of TCGA PANCAN, a predictive RF model consisting of a ten-gene signature was established that could effectively discriminate between the four types of carcinoma.

The four potential primary sites for MCCUP, CESC, ESCC, HNSC, and LUSC shared some common features. GO and KEGG pathway enrichment analyses showed clear similarities and differences among these four types of carcinoma. The KEGG pathway in which the DEGs of these four cancers are enriched, respectively, is rarely the same. The PPI network analysis provided detailed interactions/connections among the common DEGs. In the PPI network of the four types of squamous cancer, the top ten highly connected genes were selected. It is clear that in the top ten genes in PPI network of CESC, ESCC, and LUSC, nine of them (BUB1, BUB1B, CCNA2, CCNB1, CCNB2, CDC20, CDC6, CDK1, and MAD2L1) are the same.

BUB1 mitotic checkpoint serine/threonine kinase (BUB1), BUB1 mitotic checkpoint serine/threonine kinase B (BUB1B), both of them play a central role in mitosis which are reported associated with aneuploidy and several forms of cancer (Siemeister et al., 2019). Cyclin A2(CCNA2), cyclin B1(CCNB1), and cyclin B2(CCNB2) are essential components of the cell cycle regulatory machinery. Several researches showed that CCNB2 overexpression was associated with poor prognosis in human hepatocellular carcinoma, non-small cell lung cancer patients and invasive breast carcinoma (Shubbar et al., 2013; Qian et al., 2015; Li et al., 2019). Cell division cycle 20 (CDC20) is a regulatory molecule that plays critical roles at multiple points of the cell cycle and may serve an oncogenic role in human cancer (Chu et al., 2019). A study showed that CDC20 contributed to the developments of human cutaneous SCC through the Wnt/β-catenin signaling pathway (Chu et al., 2019). Cell division cycle 6(CDC6) might be a biomarker of high grade and invasive lesions of the cervix which was reported previously (Murphy, 2005, 6). Cyclin dependent kinase 1 (CDK1) is essential both for cell division in the embryo and inhibition of CDK1 induces cell death in human tumor cells (Goga et al., 2007; Malumbres and Barbacid, 2009, 1). Mitotic arrest deficient 2 like 1 (MAD2L1) is

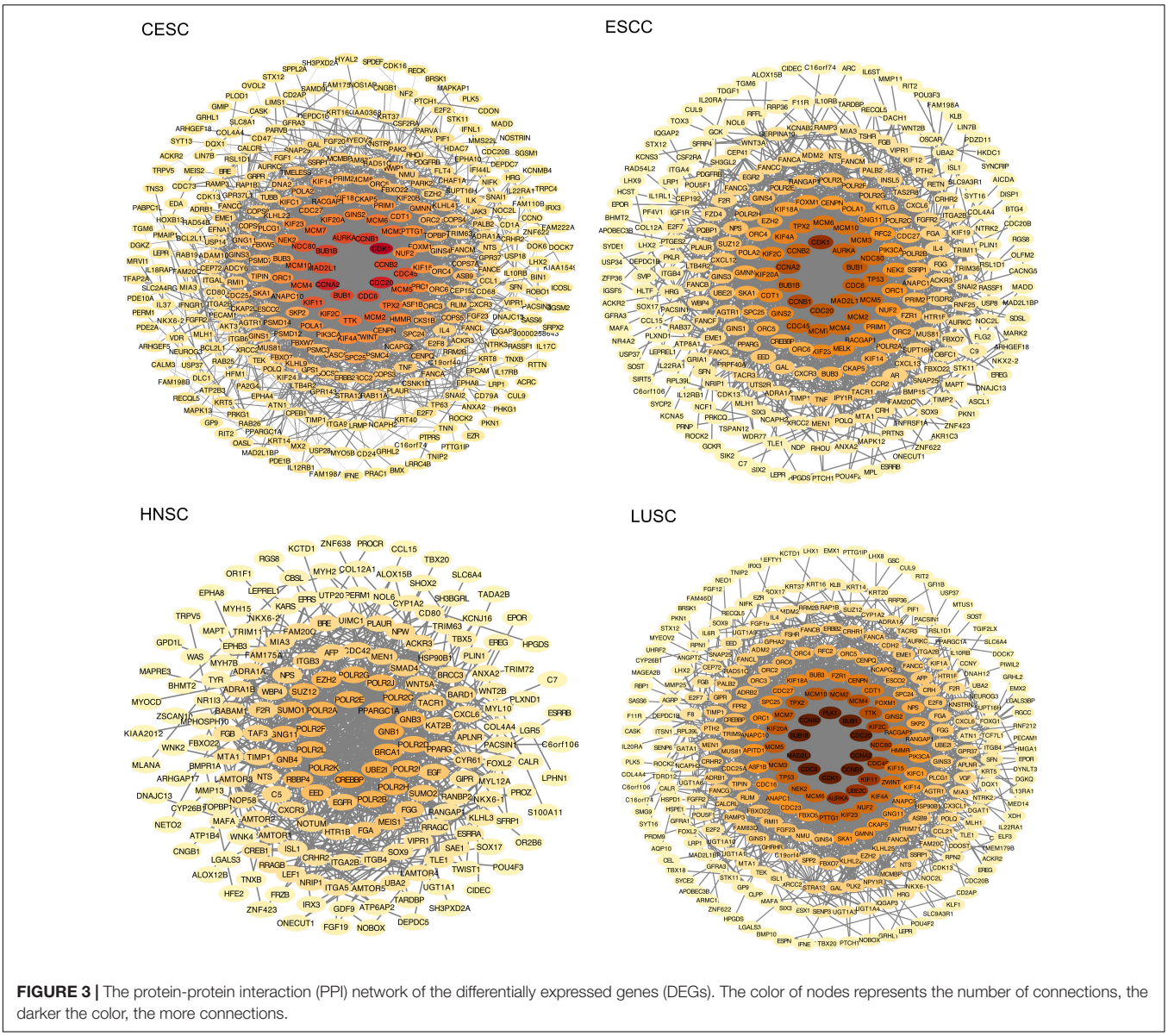


**FIGURE 3 |** The protein-protein interaction (PPI) network of the differentially expressed genes (DEGs). The color of nodes represents the number of connections, the darker the color, the more connections.

**TABLE 1 |** The performance of each different number of variable tested in the feature selection procedure by using the function rfe in caret R package.

| Variables | Accuracy | Kappa | Accuracy SD | Kappa SD |
|---|---|---|---|---|
| 5 | 0.8256 | 0.7401 | 0.01802 | 0.02615 |
| 10 | 0.9034 | 0.8565 | 0.02822 | 0.04214 |
| 15 | 0.9209 | 0.8823 | 0.01809 | 0.02695 |
| 30 | 0.9321 | 0.8988 | 0.01848 | 0.02770 |
| 60 | 0.9279 | 0.8926 | 0.02110 | 0.03159 |
| 80 | 0.9335 | 0.9009 | 0.02211 | 0.03303 |
| 1327 | 0.9125 | 0.8688 | 0.02950 | 0.04434 |

the gene controlling mitosis whose expression was found to be involved in carcinogenesis and prognosis of small cell lung cancer (Wu et al., 2018, 2).

Research discoveries derived from cancer genome and transcriptome studies have potential clinical impacts on biomarkers (Roychowdhury and Chinnaiyan, 2016). Machine learning approaches have been applied to cancer prognosis and prediction (Cruz and Wishart, 2007). RF is one of machine learning algorithms used for supervised learning, which can be used for both classification and regression tasks too. The pros of Random Forests are that it is a relatively fast and powerful algorithm which can be parallelized and performs well on many problems, and even with small datasets, the output returns satisfying prediction probabilities. Zhou et al. (2017) used the RF classifier to select feature genes from mRNA microarray data to diagnose renal fibrosis. Han et al. (2019) used RF to predict the developments of end-stage renal diseases in immunoglobulin nephropathy patients. SVM is a novel machine learning method that simplifies the usual classification

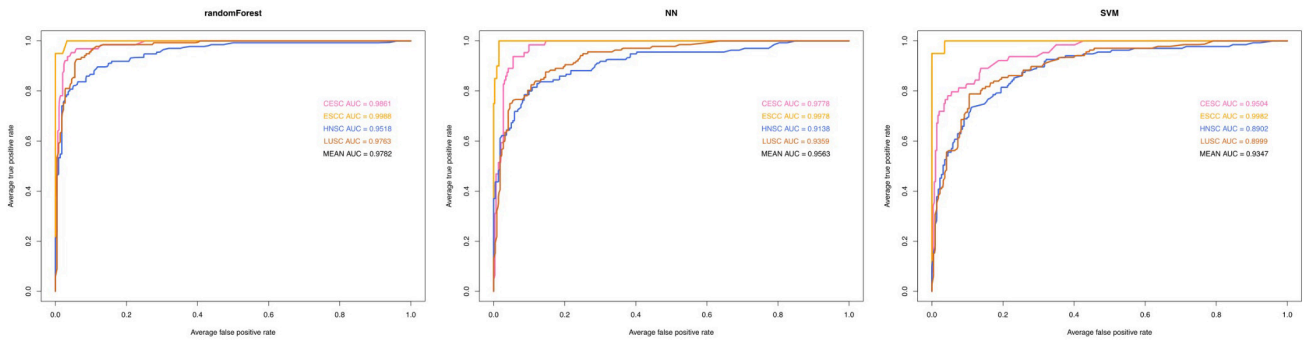


**FIGURE 4 |** Predictive performance of three machine learning methodologies [Random Forest (RF), Neural Networks (NN), support vector machine (SVM)]. Receiver operating characteristic curve analysis of three machine learning model for classifying the four types of carcinoma (LUSC, HNSC, ESCC, and CESC). AUC, area under curve.

**TABLE 2 |** Statistical models for discriminating the four types of carcinoma (LUSC, HNSC, ESCC, and CESC) and their predictive performances.

| Method | Accuracy | Sensitivity | Specificity | AUC |
|---|---|---|---|---|
| RF | 0.882 | 0.8871 | 0.9542 | 0.9782 |
| NN | 0.8202 | 0.8123 | 0.9304 | 0.9563 |
| SVM | 0.7669 | 0.7481 | 0.9084 | 0.9347 |

*RF, random forest; NN, neural networks; SVM, support vector machine; AUC, area under curve.*

and regression problems. A small number of support vectors determine the final results and are not sensitive to outliers. This helps us eliminate large number of redundant samples and grasp key samples, which makes us avoid the sense of "dimensionality disaster" and enables the algorithm to have good "robustness." The SVM classifier is well suitable for signature modeling (Fan et al., 2004). Guyon et al. (2002) used the SVM classifier to select feature genes from DNA microarrays and showed great classification performances. Fan et al. (2004) proved that the SVM classifier used for feature gene selection could speed up the classification process and generalization performances. NN is a parallel computing model to the human neural structures, which has basic characteristics such as learning, memory, and inductions of the human brain and can process continuously, discrete data and predict data. Besides,it has strong robustness, memory ability, non-linear mapping ability and strong self-learning ability. Selvaraj et al. (2018) used NN algorithms to identify candidate drugs in a lung adenocarcinoma research. Shaabanpour Aghamaleki et al. (2019) applied the NN in order to identify a molecular biomarker for rapid leukemia diagnosis from blood samples and evaluate its potential for the detection of cancer.

However, there are no studies using machine learning approaches for the diagnosis of MCCUP. In the present study, three statistical methodologies were used to construct a prediction model using data from the training set. For each statistical methodology, the use of subsets of DEGs instead of all DEGs improved the predictive performance. Among the three statistical methodologies (RF, NN, and SVM) used to construct the prediction model, the ten gene RF model including C11orf85, LA16c-431H6.6, MYBPH, MAP9, FMO2, SCGB3A1, BPIFA1, TBX1, SRRM2, and AC016549.1 showed the best performance both in the training set and in the external validation set.

The ten-gene signature capability of effectively differentiating the four types of squamous carcinoma has potential diagnostic value in MCCUP. The training set and validation cohorts were retrospective, therefore these findings must be validated prospectively in future studies. In addition, we just analyzed four potential primary sites of MCCUP, future studies should include additional potential primary sites of MCCUP and more extensive data, as well as more complex machine learning methods.

In conclusion, the present study analyzed the similarities and differences among CESC, ESCC, HNSC, and LUSC, which are four potential primary sites of MCCUP. A ten-gene predictive RF model was established based on the RNA-Seq data of the four types of carcinoma, which might have clinical utility for the accurate diagnosis of MCCUP and provide useful guidance for personalized and precision therapy.

## DATA AVAILABILITY STATEMENT

The datasets for this study can be found in The Cancer Genome Atlas (TCGA) and the University of California Xena (UCSC Xena), Datasets link: https://portal.gdc.cancer.gov/repository and https://xenabrowser.net/datapages/.

## AUTHOR CONTRIBUTIONS

DL and KC designed the study. DL, JJ, and XL were primarily responsible for conceptualization, methodology, and writing – reviewing and editing and contributed to this study equally. JJ and XL were responsible for data curation, software, and writing – original draft preparation. HW, SF, XS, and ZW were responsible for data revision. ZC, XY, HW, and KC revised the manuscript. All authors contributed to the article and approved the submitted version.

## REFERENCES


Arosio, A. D., Pignataro, L., Gaini, R. M., and Garavello, W. (2017). Neck lymph node metastases from unknown primary. *Cancer Treat. Rev.* 53, 1–9. doi: 10.1016/j.ctrv.2016.11.014

Ashburner, M., Ball, C. A., Blake, J. A., Botstein, D., Butler, H., Cherry, J. M., et al. (2000). Gene ontology: tool for the unification of biology. The gene ontology consortium. *Nat. Genet.* 25, 25–29. doi: 10.1038/75556

Campbell, J. D., Yau, C., Bowlby, R., Liu, Y., Brennan, K., Fan, H., et al. (2018). Genomic, pathway network, and immunologic features distinguishing squamous carcinomas. *Cell Rep.* 23, 194–212.e6. doi: 10.1016/j.celrep.2018.03.063

Chu, Z., Zhang, X., Li, Q., Hu, G., Lian, C. G., and Geng, S. (2019). CDC20 contributes to the development of human cutaneous squamous cell carcinoma through the Wnt/β-catenin signaling pathway. *Int. J. Oncol.* 54, 1534–1544. doi: 10.3892/ijo.2019.4727

Cruz, J. A., and Wishart, D. S. (2007). Applications of machine learning in cancer prediction and prognosis. *Cancer Inform.* 2, 59–77.

Dotto, G. P., and Rustgi, A. K. (2016). Squamous cell cancers: a unified perspective on biology and genetics. *Cancer Cell* 29, 622–637. doi: 10.1016/j.ccell.2016.04.004

Fan, Z.-G., Wang, K.-A., and Lu, B.-L. (2004). "Feature selection for fast image classification with support vector machines," in *Neural Information Processing Lecture Notes in Computer Science*, eds N. R. Pal, N. Kasabov, R. K. Mudi, S. Pal, and S. K. Parui (Berlin: Springer), 1026–1031. doi: 10.1007/978-3-540-30499-9_159

Goga, A., Yang, D., Tward, A. D., Morgan, D. O., and Bishop, J. M. (2007). Inhibition of CDK1 as a potential therapy for tumors over-expressing MYC. *Nat. Med.* 13, 820–827. doi: 10.1038/nm1606

Guyon, I., Weston, J., Barnhill, S., and Vapnik, V. (2002). Gene selection for cancer classification using support vector machines. *Mach. Learn.* 46, 389–422. doi: 10.1023/A:1012487302797

Han, X., Zheng, X., Wang, Y., Sun, X., Xiao, Y., Tang, Y., et al. (2019). Random forest can accurately predict the development of end-stage renal disease in immunoglobulin a nephropathy patients. *Ann. Transl. Med.* 7, 234. doi: 10.21037/atm.2018.12.11

Jereczek-Fossa, B. A., Jassem, J., and Orecchia, R. (2004). Cervical lymph node metastases of squamous cell carcinoma from an unknown primary. *Cancer Treat. Rev.* 30, 153–164. doi: 10.1016/j.ctrv.2003.10.001

Kanehisa, M., and Goto, S. (2000). KEGG: kyoto encyclopedia of genes and genomes. *Nucleic Acids Res.* 28, 27–30. doi: 10.1093/nar/28.1.27

Khan, J., Wei, J. S., Ringnér, M., Saal, L. H., Ladanyi, M., Westermann, F., et al. (2001). Classification and diagnostic prediction of cancers using gene expression profiling and artificial neural networks. *Nat. Med.* 7, 673–679. doi: 10.1038/89044

Kuhn, M. (2008). Building predictive models in R using the caret package. *J. Stat. Softw.* 28:143116. doi: 10.18637/jss.v028.i05

Li, R., Jiang, X., Zhang, Y., Wang, S., Chen, X., Yu, X., et al. (2019). Cyclin B2 overexpression in human hepatocellular carcinoma is associated with poor prognosis. *Arch. Med. Res.* 50, 10–17. doi: 10.1016/j.arcmed.2019.03.003

Love, M. I., Huber, W., and Anders, S. (2014). Moderated estimation of fold change and dispersion for RNA-seq data with DESeq2. *Genome Biol.* 15:550. doi: 10.1186/s13059-014-0550-8

Malumbres, M., and Barbacid, M. (2009). Cell cycle, CDKs and cancer: a changing paradigm. *Nat. Rev. Cancer* 9, 153–166. doi: 10.1038/nrc2602

Murphy, N. (2005). p16INK4A, CDC6, and MCM5: predictive biomarkers in cervical preinvasive neoplasia and cervical cancer. *J. Clin. Pathol.* 58, 525–534. doi: 10.1136/jcp.2004.018895

Qian, X., Song, X., He, Y., Yang, Z., Sun, T., Wang, J., et al. (2015). CCNB2 overexpression is a poor prognostic biomarker in Chinese NSCLC patients. *Biomed. Pharmacother.* 74, 222–227. doi: 10.1016/j.biopha.2015.08.004

Roychowdhury, S., and Chinnaiyan, A. M. (2016). Translating cancer genomes and transcriptomes for precision oncology. *CA Cancer J. Clin.* 66, 75–88. doi: 10.3322/caac.21329

Selvaraj, G., Kaliamurthi, S., Kaushik, A. C., Khan, A., Wei, Y.-K., Cho, W. C., et al. (2018). Identification of target gene and prognostic evaluation for lung adenocarcinoma using gene expression meta-analysis, network analysis and neural network algorithms. *J. Biomed. Inform.* 86, 120–134. doi: 10.1016/j.jbi.2018.09.004

Shaabanpour Aghamaleki, F., Mollashahi, B., Nosrati, M., Moradi, A., Sheikhpour, M., and Movafagh, A. (2019). Application of an artificial neural network in the diagnosis of chronic lymphocytic leukemia. *Cureus* 11:e4004. doi: 10.7759/cureus.4004

Shannon, P., Markiel, A., Ozier, O., Baliga, N. S., Wang, J. T., Ramage, D., et al. (2003). Cytoscape: a software environment for integrated models of biomolecular interaction networks. *Genome Res.* 13, 2498–2504. doi: 10.1101/gr.1239303

Shubbar, E., Kovács, A., Hajizadeh, S., Parris, T. Z., Nemes, S., Gunnarsdóttir, K., et al. (2013). Elevated cyclin B2 expression in invasive breast carcinoma is associated with unfavorable clinical outcome. *BMC Cancer* 13:1. doi: 10.1186/1471-2407-13-1

Siemeister, G., Mengel, A., Fernández-Montalván, A. E., Bone, W., Schröder, J., Zitzmann-Kolbe, S., et al. (2019). Inhibition of BUB1 kinase by BAY 1816032 sensitizes tumor cells toward taxanes, ATR, and PARP inhibitors in vitro and in vivo. *Clin. Cancer Res.* 25, 1404–1414. doi: 10.1158/1078-0432.CCR-18-0628

Snel, B., Lehmann, G., Bork, P., and Huynen, M. A. (2000). STRING: a web-server to retrieve and display the repeatedly occurring neighbourhood of a gene. *Nucleic Acids Res.* 28, 3442–3444. doi: 10.1093/nar/28.18.3442

Szklarczyk, D., Gable, A. L., Lyon, D., Junge, A., Wyder, S., Huerta-Cepas, J., et al. (2019). STRING v11: protein-protein association networks with increased coverage, supporting functional discovery in genome-wide experimental datasets. *Nucleic Acids Res.* 47, D607–D613. doi: 10.1093/nar/gky1131

van der Maaten, L. (2014). Accelerating t-SNE using tree-based algorithms. *J. Mach. Learn. Res.* 15, 3221–3245.

van der Maaten, L., and Hinton, G. (2008). Visualizing data using t-SNE. *J. Mach. Learn. Res.* 9, 2579–2605.

Wu, Y., Tan, L., Chen, J., Li, H., Ying, H., Jiang, Y., et al. (2018). MAD2 combined with mitotic spindle apparatus (MSA) and anticentromere antibody (ACA) for diagnosis of small cell lung cancer (SCLC). *Med. Sci. Monit.* 24, 7541–7547. doi: 10.12659/MSM.909772

Yang, Q.-J., Zhao, J.-R., Hao, J., Li, B., Huo, Y., Han, Y.-L., et al. (2018). Serum and urine metabolomics study reveals a distinct diagnostic model for cancer cachexia. *J. Cachexia Sarcopenia Muscle* 9, 71–85. doi: 10.1002/jcsm.12246

Yu, G., Wang, L.-G., Han, Y., and He, Q.-Y. (2012). clusterProfiler: an R package for comparing biological themes among gene clusters. *OMICS* 16, 284–287. doi: 10.1089/omi.2011.0118

Zhou, L.-T., Cao, Y.-H., Lv, L.-L., Ma, K.-L., Chen, P.-S., Ni, H.-F., et al. (2017). Feature selection and classification of urinary mRNA microarray data by iterative random forest to diagnose renal fibrosis: a two-stage study. *Sci. Rep.* 7:39832. doi: 10.1038/srep39832


**Conflict of Interest:** The authors declare that the research was conducted in the absence of any commercial or financial relationships that could be construed as a potential conflict of interest.

frontiers in Neurorobotics

ORIGINAL RESEARCH
published: 22 December 2020
doi: 10.3389/fnbot.2020.617327

# Artificial Intelligence-Based Application to Explore Inhibitors of Neurodegenerative Diseases

*Leping Deng[1†], Weihe Zhong[1†], Lu Zhao[1,2†], Xuedong He[1], Zongkai Lian[1], Shancheng Jiang[1*] and Calvin Yu-Chian Chen[1,3,4*]*

[1] *Artificial Intelligence Medical Center, School of Intelligent Systems Engineering, Sun Yat-sen University, Shenzhen, China,* [2] *Department of Clinical Laboratory, The Sixth Affiliated Hospital, Sun Yat-sen University, Guangzhou, China,* [3] *Department of Medical Research, China Medical University Hospital, Taiwan, China,* [4] *Department of Bioinformatics and Medical Engineering, Asia University, Taiwan, China*

Neuroinflammation is a common factor in neurodegenerative diseases, and it has been demonstrated that galectin-3 activates microglia and astrocytes, leading to inflammation. This means that inhibition of galectin-3 may become a new strategy for the treatment of neurodegenerative diseases. Based on this motivation, the objective of this study is to explore an integrated new approach for finding lead compounds that inhibit galectin-3, by combining universal artificial intelligence algorithms with traditional drug screening methods. Based on molecular docking method, potential compounds with high binding affinity were screened out from Chinese medicine database. Manifold artificial intelligence algorithms were performed to validate the docking results and further screen compounds. Among all involved predictive methods, the deep learning-based algorithm made 500 modeling attempts, and the square correlation coefficient of the best trained model on the test sets was 0.9. The XGBoost model reached a square correlation coefficient of 0.97 and a mean square error of only 0.01. We switched to the ZINC database and performed the same experiment, the results showed that the compounds in the former database showed stronger affinity. Finally, we further verified through molecular dynamics simulation that the complex composed of the candidate ligand and the target protein showed stable binding within 100 ns of simulation time. In summary, combined with the application based on artificial intelligence algorithms, we unearthed the active ingredients 1,2-Dimethylbenzene and Typhic acid contained in *Crataegus pinnatifida* and *Typha angustata* might be the effective inhibitors of neurodegenerative diseases. The high prediction accuracy of the models shows that it has practical application value on small sample data sets such as drug screening.

**Keywords: artificial intelligence, deep belief network, molecular dynamic simulation, galectin-3, neurodegenerative disease**

OPEN ACCESS

***Edited by:***
*Zijun Zhang,*
*City University of Hong Kong,*
*Hong Kong*

***Reviewed by:***
*Li Zhuang,*
*City University of Hong Kong,*
*Hong Kong*
*Chongjun Yan,*
*Dongbei University of Finance and Economics, China*

***Correspondence:**
*Shancheng Jiang*
*jiangshch3@mail.sysu.edu.cn*
*Calvin Yu-Chian Chen*
*chenyuchian@mail.sysu.edu.cn*

*[†]These authors have contributed equally to this work*

***Received:*** *14 October 2020*
***Accepted:*** *30 November 2020*
***Published:*** *22 December 2020*

***Citation:***
*Deng L, Zhong W, Zhao L, He X, Lian Z, Jiang S and Chen C-YC (2020) Artificial Intelligence-Based Application to Explore Inhibitors of Neurodegenerative Diseases. Front. Neurorobot. 14:617327. doi: 10.3389/fnbot.2020.617327*

## INTRODUCTION

Neurodegenerative diseases (ND) cause the progressive death of central neurons, leading to brain dysfunction and the development of diseases, such as Huntington's disease (HD) (Macdonald et al., 1993), Alzheimer's disease (AD) (McKhann et al., 1984) and Parkinson's disease. ND often result from the aberrant deposition of aggregated host proteins (Voet et al., 2019).

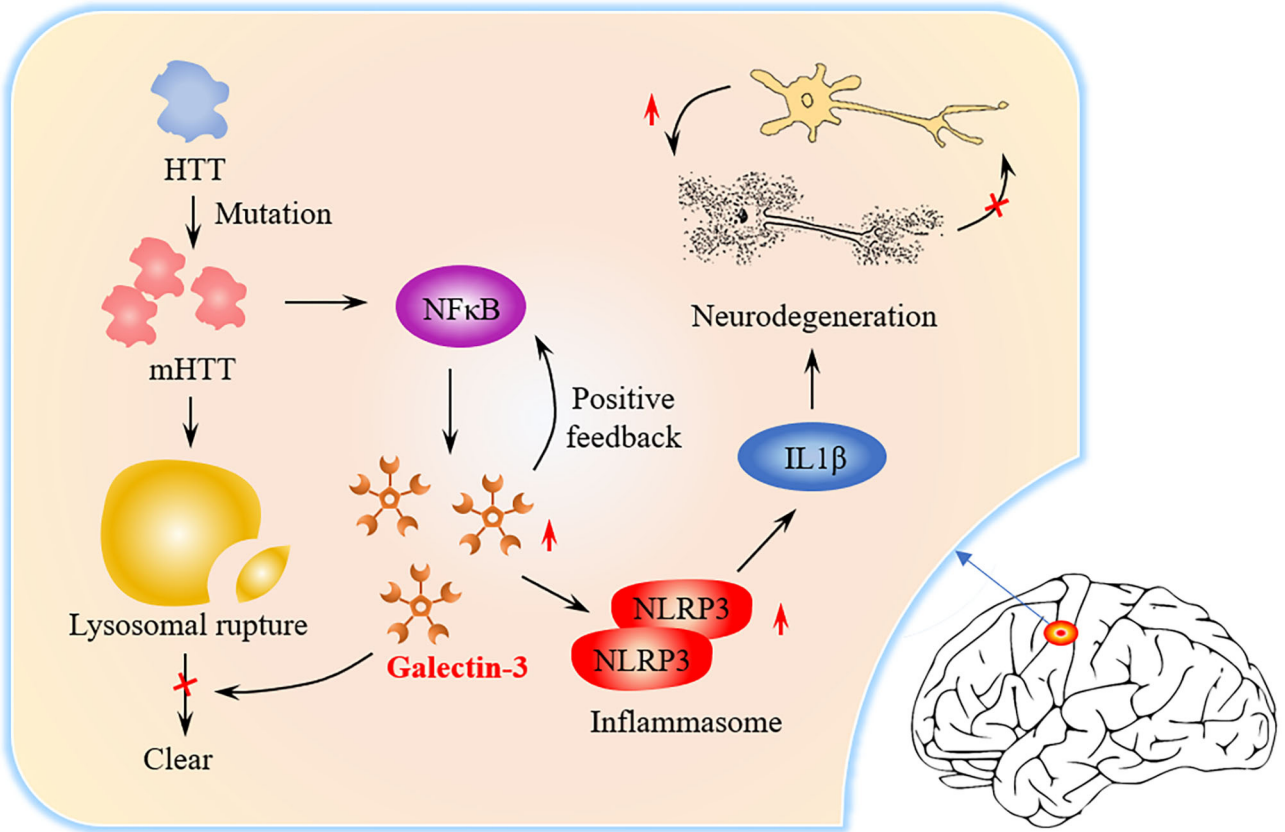


**GRAPHICAL ABSTRACT |** Graphical abstract of the role of Gal3 in HD pathogenesis. The level of Gal3 expressed by microglia is low under normal conditions. In HD patients, mutant Huntingtin (mHTT) continues to accumulate due to Huntingtin (HTT) mutations and NFκB is activated. NFκB triggers Gal3 aggregation, while Gal3 feedback promotes NFκB activation. mHTT causes lysosome damage, but Gal3 prevents the damaged lysosome from being cleared. NLRP3Inflammasome and proinflammatory factors (such as IL1β) increase in number, causing neuronal death and repair of damage.

At present, the mechanism of ND is not clear, but inflammation is considered to be a common factor (Saijo et al., 2010). Galectin-3 (Gal3) is an important member of the galectin family (Romero and Gabius, 2019). Gal3 is a key molecule linking inflammation and decreased insulin sensitivity (Li et al., 2016). Recently, more and more studies have shown that Gal3 is closely related to ND. Gal3 plays an important role in regulating inflammation (Henderson and Sethi, 2009). Extensive research on Gal3 in the central nervous system has shown that Gal3 promotes inflammation (Shin, 2013). Inhibition of Gal3 can help reduce inflammation in ND (Ramirez Hernandez et al., 2020). In the brains of AD patients, Gal3 promotes the activation of microglia (Ramirez et al., 2019), and inhibition of Gal3 may be a potential pharmacological method for the treatment of AD (Boza-Serrano et al., 2019). The latest research found that the brain Gal-3 content of patients and mice with HD is higher than normal. Inflammation can be controlled and the accumulation of mutant Huntingtin is reduced by inhibiting Gal3 (Siew et al., 2019). From the signal transmission process (**Graphical Abstract**), it can be identified that inhibition of Gal3 may become a new drug target for HD treatment.

Understanding the basic laws of target protein-drug interactions is the basis of molecular targeted drug design, which plays a vital role in drug discovery and drug design (Rahman et al., 2020). Gal3 is one of the most potential target proteins for treating ND. Molecular docking method and active ingredient screening techniques are used to screen out drug molecules that have inhibitory effects on the target protein from drug database (Abdolmaleki et al., 2017). Traditional Chinese medicine is a medicine with great modern potential (Wen et al., 2019). Greater than 85 percent of patients diagnosed with COVID-19 in China have received Chinese medicine for adjuvant treatment (Yang et al., 2020). Therefore, discovering and designing the Chinese medicine prescription inhibitors of Gal3 is expected to have curative effects ND treatment. With the continuous improvement of computer performance, artificial intelligence (AI)-based methods are increasingly applied to

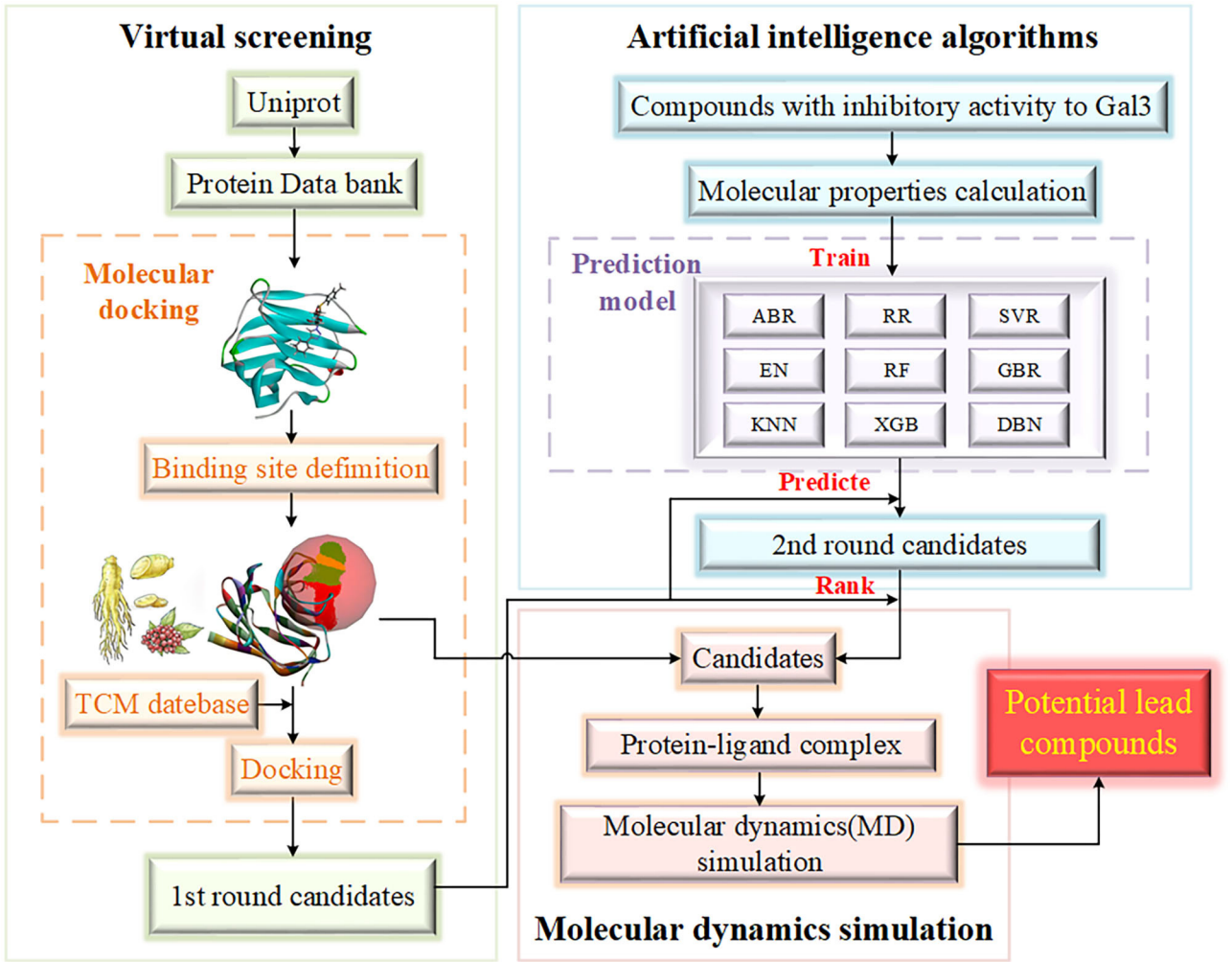


**FIGURE 1 |** The flowchart of experiment design. The experiment is mainly divided into three parts, including virtual screening, artificial intelligence algorithms and molecular dynamics simulation. The range of candidates is gradually compressed.

various stages of drug discovery (Chen et al., 2018a; Schneider et al., 2020; Senior et al., 2020). Machine learning methods are used to predict biologically active properties (Kaiser et al., 2018; Correia et al., 2020). SVM and other methods were used to establish four quantitative prediction models of the inhibitory activity value of HIV-1 integrase inhibitors (Xuan et al., 2013). The DeepTox algorithm shows good accuracy in predicting the toxicity of compounds (Mayr et al., 2016). Drug-drug interactions prediction (Zhang et al., 2019), biomolecular properties prediction (Hessler and Baringhaus, 2018) and quantum mechanical property prediction are combined with AI that is used in pharmacodynamic research of new synthetic drug candidates, which can greatly save costs. The combination of AI and traditional Chinese medicine may be a new development trend of modern Chinese medicine in the future (Liu et al., 2017).

Based on the discovery of Gal3 as a key target protein in a new pathogenesis closely related to HD, the purpose of this study to screen potential compounds that inhibit Gal3 has been determined. The contribution of our study is 2-fold. Methodologically, we have added AI algorithms to establish a compound activity value prediction model based on traditional drug screening methods, including molecular docking and molecular dynamics (MD) simulation (Kumar et al., 2020), accelerating the process of new drug discovery. Screening drug molecules from traditional Chinese medicine (TCM) database is an innovation and beneficial supplement to screening from the general database. Practically, the underlying relationship between compound activity values and input molecular properties can be acquired through algorithm models. Target variable is an important evaluation index of drugs, which can provide researchers with reference, and the high accuracy of the model improves reliability. **Figure 1** provides the flowchart of experiment design.

# MATERIALS AND METHODS

## Molecular Docking Screening

Molecular docking is a virtual screening tool and can identify lead compounds from large small molecule databases, which reducing the number of experimental screening compounds and thus shortening the research cycle (Elmezayen et al., 2020; Pant et al., 2020). Molecular docking can be used to investigate the possible weak interactions between small molecule ligands and large molecule receptors and to calculate their affinity (Liu et al., 2019). The sequence of Gal3 was obtained from UniProt knowledgebase [(Identifier: P17931) (Bateman et al., 2017), and the crystal structure was obtained from RCSB Protein Data Bank (PDB ID: 6QLR) (Burley et al., 2019; Kumar et al., 2019), with a resolution of 0.97 Å. Through preprocessing operation, including removing crystal water molecules in the composite crystals, replenishing missing hydrogen atoms and optimizing energy by using the CHARMm27 force field (Brooks et al., 2009), a receptor protein with high confidence binding site was presented. The binding site was defined with the pro-ligand. A total of 18,776 molecule compounds obtained from the TCM database (TCM Database @Taiwan) (Chen, 2011) and 148,120 molecule compounds from ZINC database (http://zinc.docking.org/) (Irwin and Shoichet, 2005) were used as ligands for molecular docking, respectively. The original ligand in the complex was used as the control ligand, which was used as a reference for docking results. All involved experiments were implemented on LigandFit module in Discovery Studio Client v17.2.0.16349 (DS). Ligandfit has the functions of automatic search and confirmation of the active site of the receptor molecule, conformationally flexible multi-ligand docking, and evaluation of interaction scores based on force fields (Venkatachalam et al., 2003).

## Artificial Intelligence-Based Prediction Models

### Data Collection and Processing

Relevant information (structural formula and IC50) of the small molecules reported that have inhibitory effect on Gal3 were collected from literatures, invention patents, and drug generation companies. Chemdraw was used to draw the structural formula of molecules(Mills, 2006). In addition, from open source small molecule databases such as PubChem (Kim et al., 2019), ChEMBL (Gaulton et al., 2017) and ZINK, we have downloaded the corresponding three-dimensional structure containing Gal3 inhibitors. All collected compounds were saved as Mol format files and converted to SDF format through Chem3D. The sample with clear IC50 value could be kept, and 56 molecular samples were included. Chem3D software was used to minimize the molecular posture energy of all molecule samples. All qualified molecular samples were also subject to molecular attitude energy minimization processing. The IC50 value was changed to pIC50 as target variable by equation (1). All collected and sorted sample molecules were imported into DS to calculate molecular properties of 204 types that used as the input feature set.

$$pIC_{50} = 6 - log_{10}\left(IC_{50}\right) \quad (1)$$

**Algorithm 1:** AdaBoost

1. Initialize weights distribution of training samples:
   $D_1 = (\omega_{11}, \omega_{12}, ...\omega_{1i}..., \omega_{1N}), \omega_{1i} = 1/N, i = 1, 2...., N$
2. For $m = 1, 2, \cdots, M$ multiple iterations:
   (1) Training the weighted $D_m$ sample set to obtain the base learner $G_m(x)$
   (2) Calculating the maximum error of the training set: $E_m = max \mid y_i - G_m(x_i) \mid$
   (3) Calculating the relative error of each sample: $e_{mi} = \frac{|y_i - G_m(x_i)|}{E_m}$
   (4) Calculating the regression error rate: $e_m = \sum_{i=1}^{N} \omega_{mi} e_{mi}$
   (5) Calculating the weight coefficients of weak learners: $\alpha_m = \frac{e_m}{1-e_m}$
   (6) Updating the weight distribution of the sample set:
   $\omega_{m+1,i} = \frac{\omega_{mi}}{Z_m} {\alpha_m}^{1-e_m}$
   $Z_m = \sum_{i=1}^{N} \omega_{mi} \alpha_m^{1-e_{mi}}$
   $D_{m+1,i} = \left(\omega_{m+1,1}, \omega_{m+1,2}, ...\omega_{m+1,i}..., \omega_{m+1,N}\right)$
3. Output the ultimate strong learner
   $f(x) = \sum_{m=1}^{M} (\ln \frac{1}{\alpha_m}) \alpha_m G_m(x)$

end

We performed AdaBoost, random forest, XGBoost, deep belief network and other models to build models for predicting pIC50 values. These models are widely used AI-based machine learning models, with fast convergence speed and advantages in processing small sample data, which is very suitable for our small-scale data experiments.

### AdaBoost Model

The kernel of adaptive boosting algorithm (AdaBoost) is to build a strong learner by connecting multiple weak learners (Huang et al., 2020). AdaBoost algorithm adjusts the weight of samples in the training set of each round by increasing the weight of the samples that were incorrectly predicted in the previous round (Ratsch et al., 2001). The iteration continues until the predetermined error rate is reached or the specified maximum number of iterations is reached (**Figure 2**). The ultimate strong learner is combined by linearly weighting and summing all base learners, and the base learner with small error rate has a larger weight coefficient. Details of the AdaBoost algorithm is presented in Algorithm 1. In this study the optimal number of decision trees was set as 15 based on some initial trials.

### Ridge Regression Model

Ridge regression (RR) works well on condition that the number of independent variables is more than the sample size. As shown in equation 2, the RR model adds a penalty term of the L2 norm to the objective function of the ordinary linear regression mode (Yang and Wen, 2018), which contributed to the biased estimation of the regression coefficient β. Generally, RR is a regression method that solves the ill-conditioned matrix problem at the cost of giving up unbiasedness and reducing accuracy. The

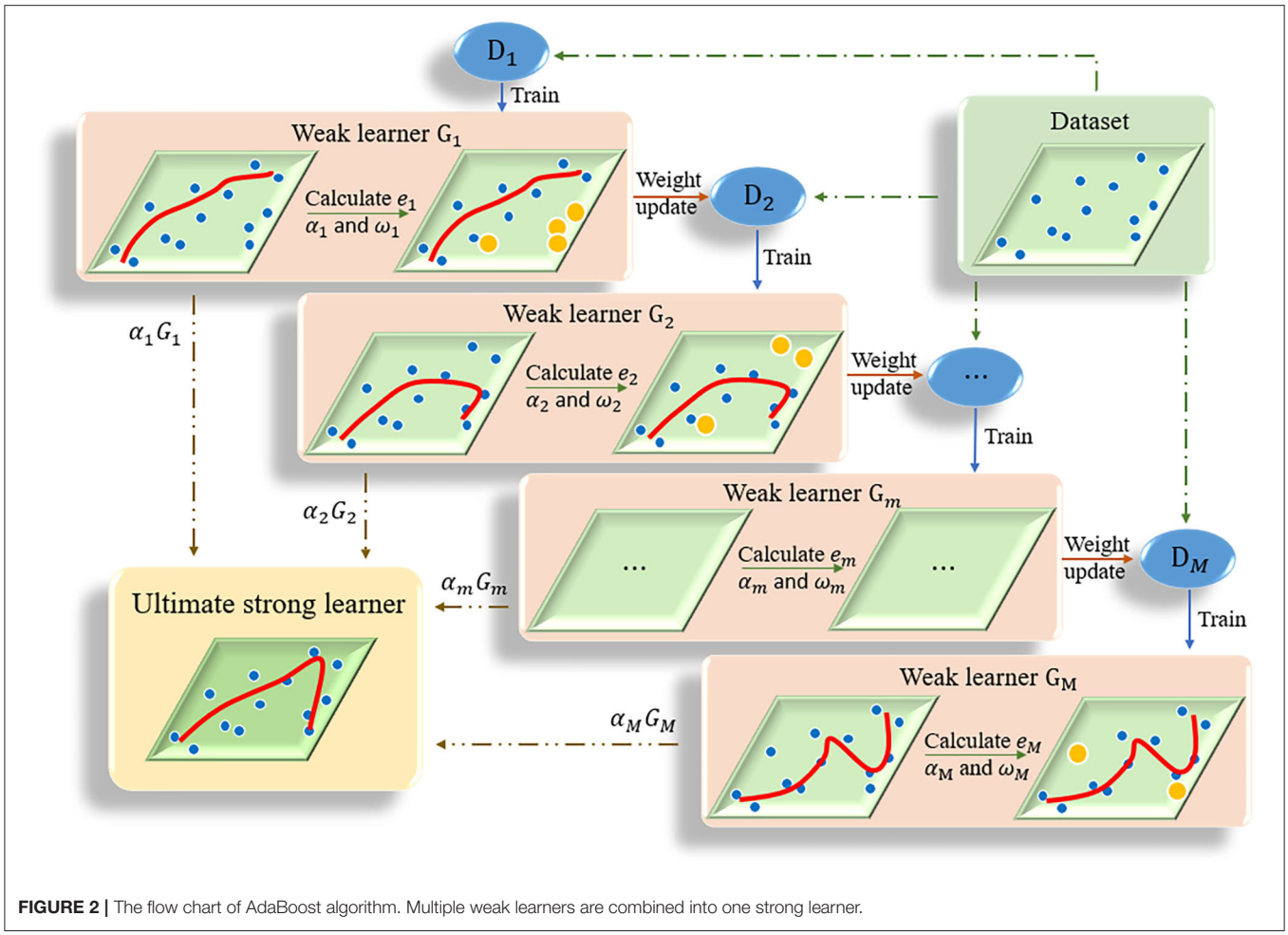


**FIGURE 2 |** The flow chart of AdaBoost algorithm. Multiple weak learners are combined into one strong learner.

alpha parameter was set to 0.05 in the case study.

$$J(\beta) = (y - X\beta)^T + \lambda\beta^T\beta$$
$$\Rightarrow \beta = (X^T X + \lambda I)^{-1} X^T y \quad (2)$$

## SVM Model

Support vector machine (SVM) can be divided into support vector classification (SVC) and support vector regression (SVR) in practical applications (Chang and Lin, 2011). SVR is designed to fit each training sample and retain all the main features that characterize the algorithm to minimize errors. The kernel function is used to replace the linear term in the linear equation to make the original linear algorithm non-linear, which is used to achieve non-linear regression (**Figure 3**). SVR has high accuracy and strong generalization ability to solve small sample data. It has better applicability for the diversity of drug molecular characteristics and less sample data. In this study, the SVR algorithm was used to quantitatively predict the inhibitory activity of Gal3 inhibitors. All data were plotted in 28-dimensional space, and the error tolerance parameter was set to 0.39.

## Elastic Net Model

Elastic net (EN) is a linear regression model trained using L1, L2 norms as prior regular terms (Zou and Hastie, 2005). EN is very effective in cases where multiple features are interconnected. The cost function of elastic network is as shown in Equation 3. When r is equal to 0, it is RR, when r is equal to 1, it is Lasso regression (LR). EN is compromised in RR and LR.

$$J(\theta) = MSE(\theta) + \gamma\alpha \sum_{i=1}^{n} |\theta_i| + \frac{1-\gamma}{2}\alpha \sum_{i=1}^{n} \theta_i^2 \quad (3)$$

## Random Forest Model

Random forest (RF) algorithm uses bootstrap method to generate training set (Breiman, 2001). Through random row and column (samples and features) sampling, seven decision trees were constructed to form a decision tree forest. The final prediction result was obtained by weighted average or voting. RF can achieve parallel learning and has a good filtering effect on noise and abnormal data (Athey et al., 2019). The model training process is given in Algorithm 2.

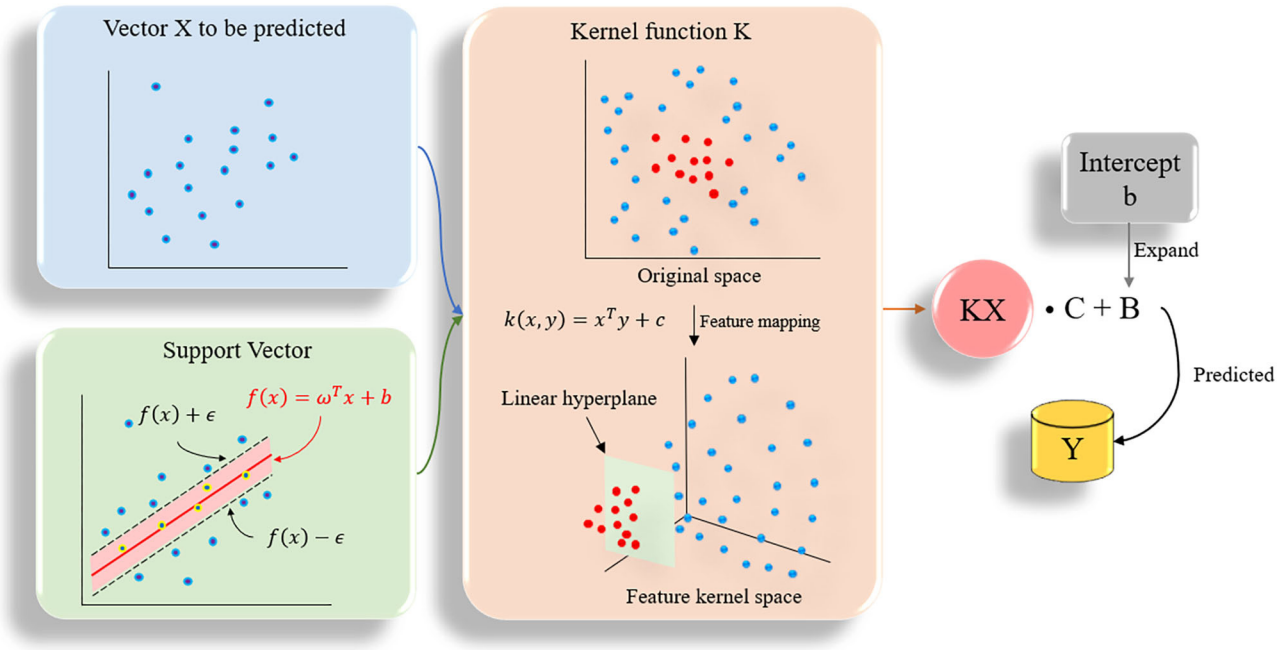


**FIGURE 3 |** The flow chart of SVR algorithm. All data are plotted in n-dimensional ($n = 28$) space, $n$ represents the number of features of the data.

**Algorithm 2:** Random forest

1. Training set $D_{f_{feature}} = \{(x_1, y_1), (x_2, y_2), \ldots, (x_n, y_n)\}$
2. For $t = 1, 2, \ldots, T$ do
   (1) Random sampling m sample points, constructing a training set $D_t$
   (2) Using $D_t$ to train a decision tree
   (3) Least squares regression tree as an example
   Choosing the optimal segmentation variable i and the Segmentation Point s:

$$\min_{i,s}\left[\min_{c_1}\sum_{x_j\in R_1(i,s)}(y_j-c_1)^2 + \min_{c_2}\sum_{x_j\in R_1(i,s)}(y_j-c_1)^2\right]$$

   The selected pairs $(i, s)$ were used to divide the region and determine the corresponding output values: $R_1(i,s) = \{x|x^i \le s\}, R_2(i,s) = \{x|x^i > s\}$
   $c_\kappa = \frac{1}{N_\kappa}\sum_{x_j\in R_\kappa(i,s)} y_j, x \in R_\kappa, \kappa = 1, 2$

   Continue to iterate steps a and b for satisfying the condition

   The input space was divided into $K$ regions:
   $f(x) = \sum_{\kappa=1}^{K} c_\kappa I(x \in R_\kappa)$
   end

**Algorithm 3:** Gradient boosting regression

1. Initialize $F_0(x) = \arg\min_\gamma \sum_{i=1}^{n} L(y_i, \gamma)$
2. For $m = 1, 2, \cdots, M$:
   (1) For $i = 1, 2, \cdots, N$ compute pseudo-residuals: $r_{im} = -\left[\frac{\partial L(y_i, F(x_i))}{\partial F(x_i)}\right]_{F(x)=F_{m-1(x)}}$
   (2) Fit a base regression tree to the targets $r_{im}$ giving terminal regions
   $R_{jm}, j = 1, 2, \cdots, J_m$
   (3) compute multiplier $\gamma_{jm}$ : $= \arg\min_\gamma \sum_{x_i\in R_{jm}} L(y_i, F_{m-1}(x_i) + \gamma)$
   (4) Update: $F_m(x) = F_{m-1}(x) + \sum_{j=1}^{J_m} \gamma_{jm} I(X \epsilon R_{jm})$
3. Output
   $\hat{f}(x) = f_M(x)$
   end

## Gradient Boosting Regression Model

Gradient boosting regression (GBR) is an algorithm that improves by learning from mistakes. Each calculation of it is to reduce the residual error of the previous time and establish a new model in the direction of the negative gradient (Chen et al., 2018b). The least square error was used as the loss function of regression prediction, and the number of decisions was set to 7. The sub-models are integrated as the final predictive model. The algorithm flow is given in Algorithm 3.

## K-Nearest Neighbor Model

K-nearest neighbor (KNN) randomly divides the matrix into a training subset and a test subset, and returns the divided samples and labels. The Euclidean distance between the samples was calculated and sorted according to the distance (Abdel-Basset

**Algorithm 4:** XGBoost

1. Training set $D = \{(x_1, y_1), (x_2, y_2), \ldots, (x_m, y_m)\}$
2. Loss function MSE (mean square error):
   $L(\theta) = \sum_i \left(y_i - \bar{y}_i\right)^2$
   where, $y_i$ is the real value, $\bar{y}_i$ is the predicted value.
3. For $k = 1, 2, \ldots, K$ do
   (1) The definition of the predicted model:
$$\bar{y}_i = \sum_{k=1}^{K} f_k(x_i), f_k \in F$$
   K is the number of trees, F includes all possible trees, $f_k$ is a specific tree,
   $f_k(x_i)$ represents the predicted value of $x_i$ on the kth tree.
   (2) Minimizing objective function $L_{obj}(\theta)$ to acquire $f_k$.
$$L_{obj}(\theta) = \sum_i^n L(\theta) + \sum_{k=1}^{K} \Omega(f_k)$$
   $\Omega(f_k)$ is the complexity of tree $f_k$.
4. Output $f_k$
   e n-dimensional d

et al., 2020). The average value of the k ($k = 4$) samples closest to the target to be predicted was selected as the regression prediction value of the new sample.

### XGBoost Model

XGBoost (XGB) algorithm improves the accuracy of the algorithm by adding the number of decision trees (Lai et al., 2020). The detailed process is shown as Algorithm 4. We used the xgb.DMatrix function. The representation method of the data in libsvm is a sparse matrix, which is very suitable for a large number of features and sparse. When there are missing values in the sample, XGB can automatically learn the split direction.

### Deep Belief Network

Compared with traditional artificial neural networks, deep learning-based frameworks with huge numbers of multiple hidden layers maintain two-way fidelity of information transferring between different levels of abstraction during model learning (LeCun et al., 2015). Deep learning algorithms are widely used in drug design research such as protein structure prediction and disease diagnosis (Li et al., 2020; Senior et al., 2020). Deep belief networks (DBN) is the foundation of deep learning. In this study, we trained a quantitative prediction model of the inhibitory activity value of Gal3 inhibitors using a simple fully connected neural network with three hidden layers (**Figure 4**). The activation function was configured as rectified linear unit (ReLu) (Agarap, 2018). Furthermore, we introduce the Dropout method was to reduce the amount of calculation and increase the robustness of the model, by randomly pruning some neural units in the hidden layer with a predetermined probability (Zhang et al., 2018).

## Molecular Dynamics Simulation

Molecular docking methods can narrow the scope of searches from large compound databases. Combining the molecular docking score and the target value predicted by artificial intelligence-based models, four optimal compounds (6318, 5372, 22157, 7649) ligands were finally screened as candidates for MD simulation. MD simulation can simulate and analyze the ligand-receptor movement process, and obtain some key information from the process to verify their stability (Song et al., 2019). SwissParam was chosen as the tool for generating topology files (Zoete et al., 2011), the mol2 file of candidates were submitted to obtain topology files with parameters such as atom type, charge and bonding conditions. The four candidate small molecules were combined with the processed Gal3 receptor protein and divided into four groups A, B, C, and D for MD simulation. CHARMM27 force field was used to describe the receptor protein (Sapay and Tieleman, 2011). Using TIP3P water molecule model, adding water as the solvent of the complex system, while adding NaCl and sodium ions to maintain the electrical neutrality of the system. The steepest descent method was used to optimize the energy of 5,000 steps to make the system reach near the lowest point of energy. After the optimization, it entered the equilibrium stage, and the positions of proteins and ligands needed to be restricted. First, balance for 10 ns under the constant number of atoms, constant volume and constant temperature (NVT) ensemble, and the system temperature rose from 0 to 310 K. Then it was equilibrated for 10 ns under the constant number of atoms, constant pressure and constant temperature (NPT) ensemble, and the temperature was kept at 310 K, which was used to simulate the physiological environment in the human body. The V-rescale method is used for temperature coupling, and the Parrinello-Rahman method is used for pressure coupling. After the equilibrium stage was over, the restriction was released, and each combination was subjected to 100 ns MD simulation under the NPT ensemble. In the simulation process, periodic boundary conditions (PBC) were used in all directions to eliminate possible boundary effects. The time step was set to 2fs, and the coordinate file and the energy file were recorded every 2ps.

# RESULTS AND DISCUSSION

## Molecular Docking

Compounds from the TCM database were used for high-throughput virtual screening against Gal3, and the top 10 compounds were shown in **Table 1**. According to the docking scores of screenings, 6318, 5372, 7649, and 22157 (**Table 1**) were selected for further analysis. 2D diagram of these molecules in docking results showed potential interactions between key residues and ligands, including hydrogen bonds, van der Waals, salt bridge, Pi-Pi stacked, etc (**Figure 5**). These four TCM compounds have a common property, a carboxylate group in their chemical structures. Based on the docking poses of Gal3 in **Figure 6**, the α, β-unsaturated carbonyl groups of 6318 formed two hydrogen bonds (2.4 and 2.5 Å) with LYS176 and ARG144 of Gal3, respectively. The methoxy of 6318 formed a hydrogen bond (2.2 Å) with ARG162. The carboxylate group of 5372 formed a 2.1 Å hydrogen bond with LYS176. 7649's benzoic acid groups interacted with LYS176 and ARG144 through three hydrogen

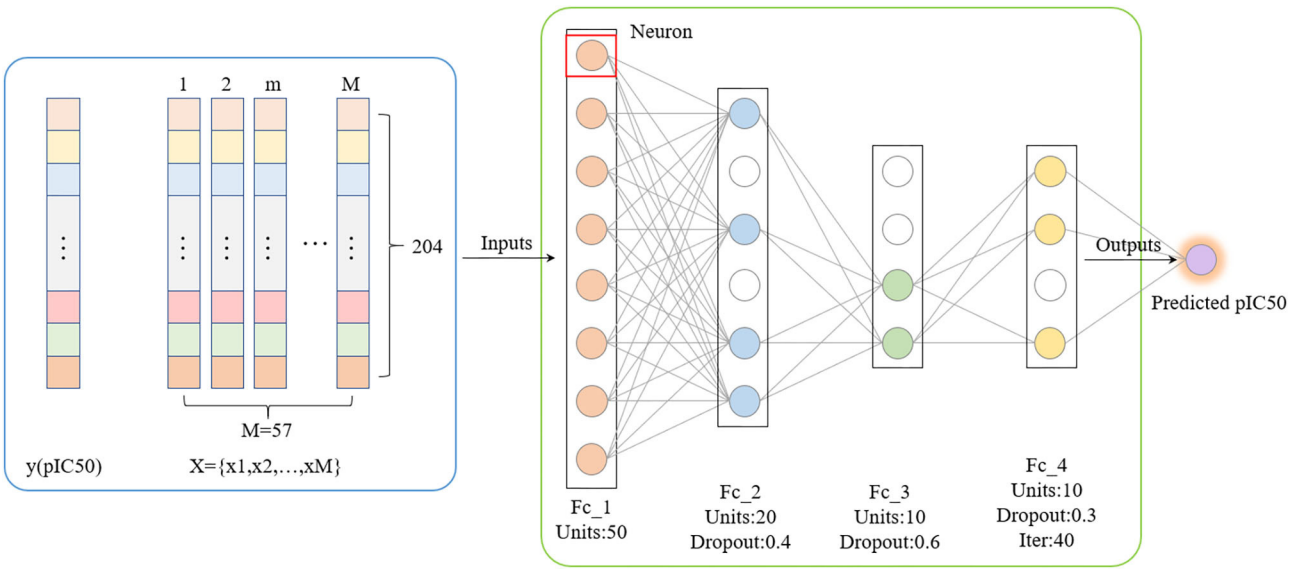


**FIGURE 4 |** Deep Belief Network generated by applying dropout. The mean square error is used as the loss function. The neural network weights are updated by an Adam optimizer with a learning rate of 0.0006. Rectified Linear Units and Dropout methods are utilized.

**TABLE 1 |** Docking score, predicted activity value of top ten TCM candidates, top two ZINC candidates and control ligand.

| Index | Name | Predicted value (pIC50) | | | | | | | | | Docking Score |
|---|---|---|---|---|---|---|---|---|---|---|---|
| | | ABR | RR | SVR | EN | RF | GBR | KNN | XGB | DBN | |
| 6318 | Chinese Hawthorn | 7.119 | 6.830 | 6.791 | 6.851 | 6.665 | 6.839 | 6.693 | 7.093 | 6.162 | 125.276 |
| 22157 | Longbract Cattail Pollen | 7.155 | 7.519 | 7.532 | 7.440 | 6.696 | 6.937 | 6.554 | 7.093 | 5.743 | 116.132 |
| 5372 | Carnation | 6.951 | 7.023 | 7.148 | 7.128 | 7.061 | 7.037 | 6.887 | 6.380 | 5.591 | 119.682 |
| 7649 | Staphyleaceae | 6.650 | 7.956 | 8.281 | 8.099 | 6.886 | 6.779 | 6.942 | 6.510 | 6.629 | 116.693 |
| 2246 | Amur Adonis | 6.951 | 6.873 | 6.967 | 7.012 | 6.816 | 7.002 | 6.938 | 6.380 | 5.537 | 117.959 |
| 14992 | White Mulberry Fruit | 5.658 | 4.901 | 4.750 | 4.933 | 5.768 | 6.088 | 5.838 | 5.929 | 2.528 | 114.298 |
| 2670 | Java Brucea | 5.793 | 4.861 | 4.774 | 4.926 | 5.849 | 6.444 | 6.257 | 5.598 | 3.829 | 106.878 |
| 8713 | Whiteflower Leadword | 7.143 | 7.048 | 7.057 | 7.083 | 6.726 | 6.937 | 6.552 | 7.211 | 2.044 | 110.309 |
| 22676 | Common Threewingnut | 6.076 | 8.094 | 7.947 | 7.853 | 5.767 | 5.723 | 6.177 | 5.866 | 3.541 | 110.031 |
| 210 | Fresh Common Ginger | 6.509 | 5.143 | 5.171 | 5.100 | 6.347 | 6.011 | 6.020 | 6.769 | 2.963 | 106.732 |
| ZINC000019363537 | Tetraethylenepentamine | 5.301 | 4.622 | 4.630 | 4.538 | 5.319 | 5.133 | 5.742 | 5.438 | 0.611 | 102.451 |
| ZINC000019364225 | Trientine | 5.818 | 5.455 | 5.276 | 5.313 | 5.577 | 5.836 | 5.759 | 5.598 | 0.529 | 90.915 |
| Control | J4N | 6.180 | 6.838 | 6.902 | 6.899 | 6.542 | 6.034 | 6.979 | 6.510 | 4.962 | 56.381 |

bonds (1.7, 1.6, and 1.7 Å). The carboxylate group of 22157 had H-bonding interactions with ARG144 and ASN160 (1.7 and 2.4 Å), and the β-ketone carboxyl group engaged with ASP148 and LYS176 through two H-bonds. The hydrogen bond interaction of the compounds with LYS176 and ARG144 indicated that these were two key residues. The same experiment had been done with ZINC database and the results showed that the binding affinity was weaker than that from the TCM database.

## Prediction Results of Models

During the whole validation process, the prediction accuracy on testing sets is used to quantify the performance of different prediction algorithms. Both Mean Square Error (MSE) and square correlation coefficient (R-square) are set as the metric for prediction accuracy. MSE is the expectation of the square of the difference between the predicted value and the true value, which is used to evaluate the predicted result. The smaller the MSE, the stronger the model's ability to fit the experimental data. R-square represents the quality of a fit through changes in data. The normal value range is 0 to 1. The closer to 1 indicates that the variable of the equation (input feature) has a stronger ability to explain Y (pIC50). **Table 2** lists the R square and MSE values of all prediction models.

### Feature Selection

In this study, we obtained only 56 samples, but the feature dimension is as high as 204. Theoretically, this can easily lead machine learning models to get over-fitting. We used the following methods to perform feature dimensionality reduction to search for representative features. Firstly, Pearson correlation

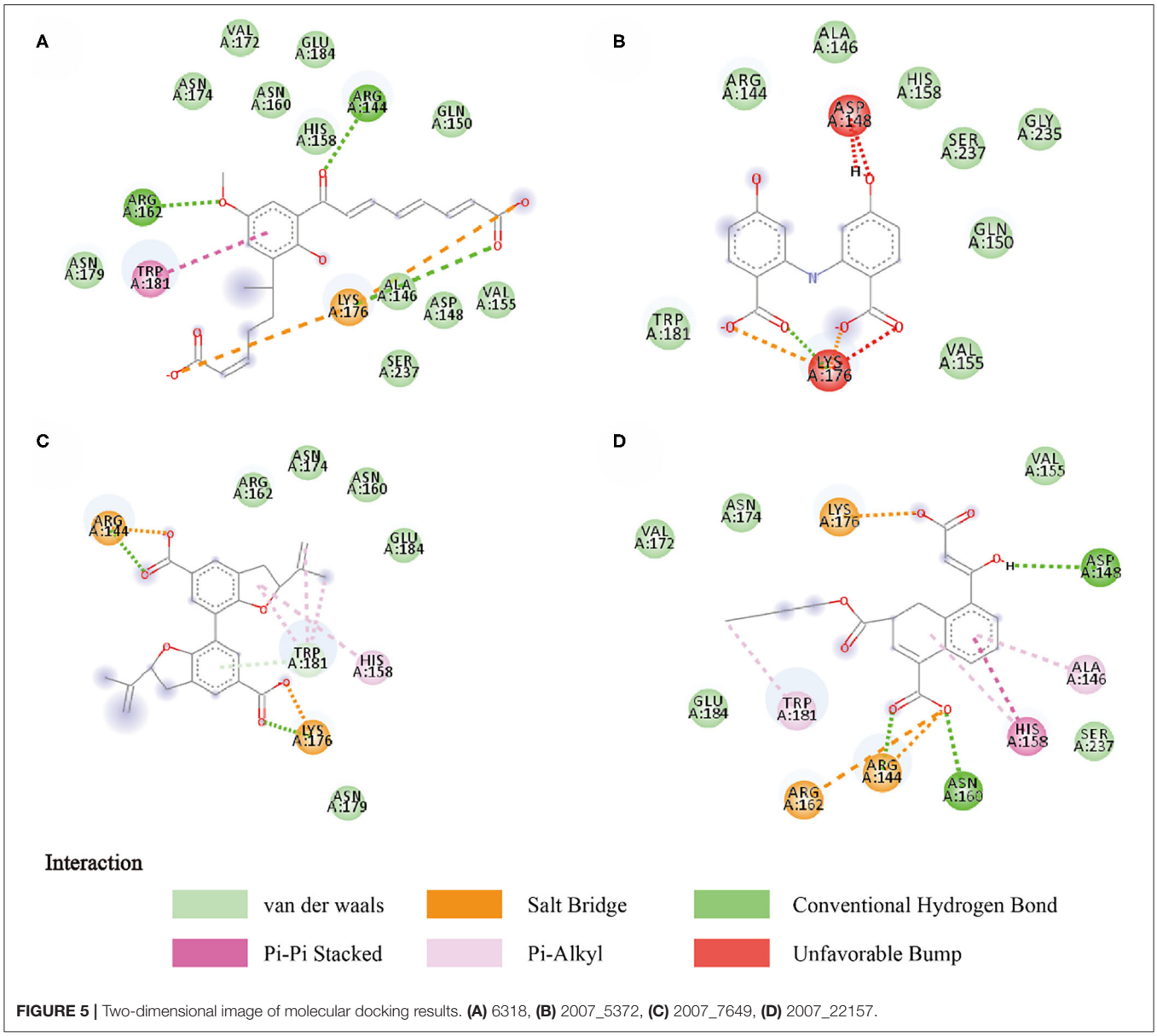


**FIGURE 5 |** Two-dimensional image of molecular docking results. **(A)** 6318, **(B)** 2007_5372, **(C)** 2007_7649, **(D)** 2007_22157.

coefficient has very good applicability in the characterization of correlation. **Figure 7A** is a heat map of Pearson correlation coefficients between all features, the deeper the red, the stronger the correlation. It can usually be considered to have a strong correlation when the correlation is >0.9, and parameters would be eliminated. Then, principal component analysis (2D PCA and 3D PCA) achieved dimensionality reduction by integrating the original single variable to obtain a new set of comprehensive variables (**Figures 8A,B**). What's more, the elements with sample feature variance <0.05 were eliminated by calling the Variance Threshold library function, and the Lasso function was used to select the variables of the sample data based on the penalty method. Finally, the original coefficients were compressed, and the insignificant variables were directly discarded. **Figure 7B** is a heat map of Pearson correlation coefficients between the remaining 28 features after eigenvalue preprocessing. These 28 indicators were set as input features for all involved machine learning models. Through a 5-fold cross-validation method, the predictive ability of the sample model is evaluated. Correlation between predicted values and actual values (pIC50) of ABR, RR, SVR, EN, RF, GBR, KNN, XGB models were shown in **Figure 9**.

## RR and EN Model

For ridge regression, elastic net and lasso regression models, model regularization is introduced to reduce the over-fitting, but the method of restraining weight is different. The R-square of the RR model and the EN model on the training sets were 0.87 and 0.85, respectively, but the R-square of the EN model on the test sets was 0.84, which was significantly better than 0.79 of the RR model (**Figures 9B,D**). This might be because only a few key features are related to pIC50 in all features, and the RR model retains those irrelevant features, which increases the fitting error. In this study, the number of features was much larger than the

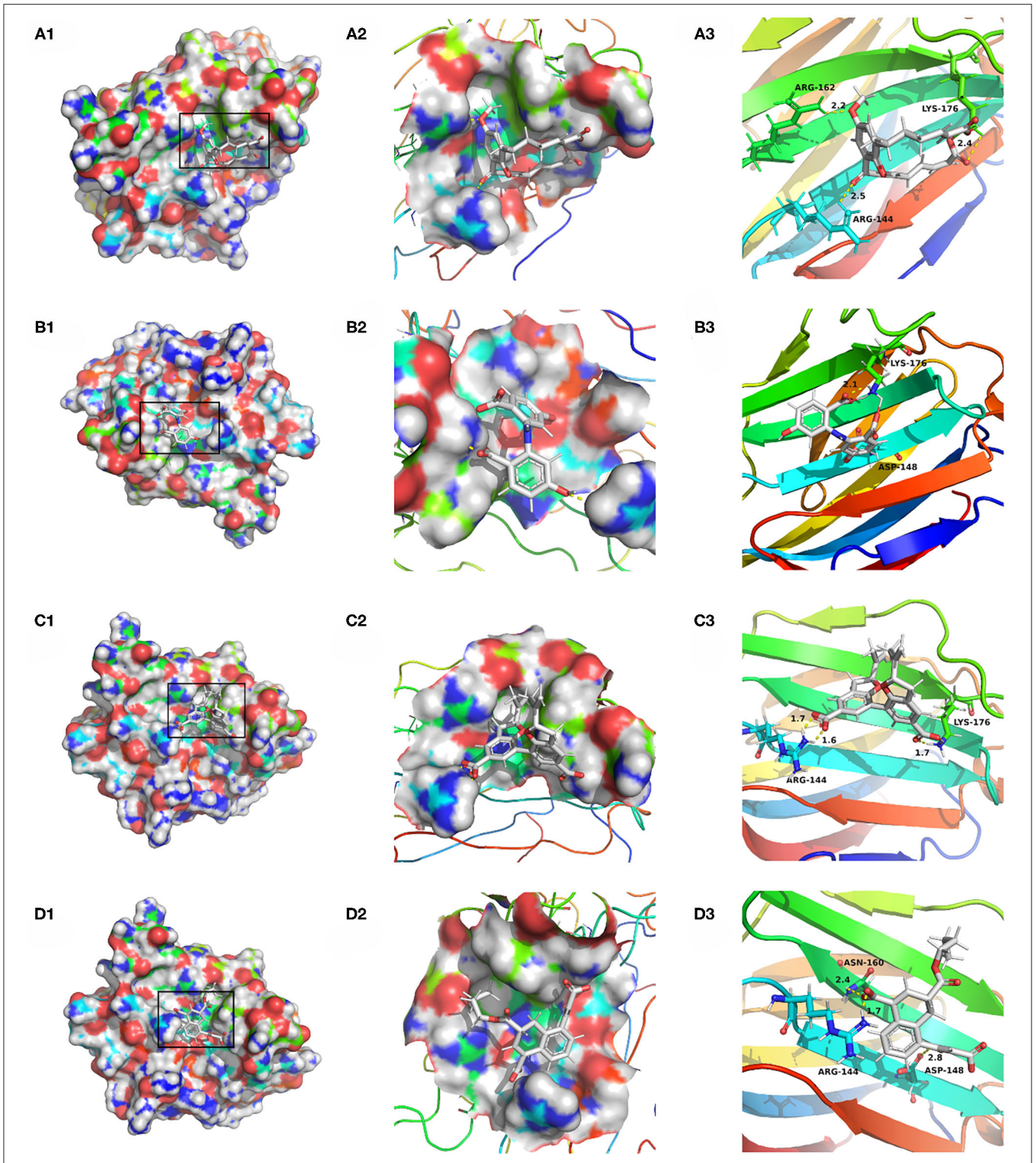


**FIGURE 6 |** Docking pose of **(A)** 6318, **(B)** 2007_5372, **(C)** 2007_7649, **(D)** 2007_22157.

number of samples. The EN model could reduce the weight of non-key features to zero, and only retained a few key features, so it showed better fitting results.

## ABR, RF, GBR, and XGB Model

The R-square of the ABR, RF, GBR, and XGB models on the training sets were all higher than 0.9 (**Table 2**), which was better

**TABLE 2 |** R-square and mean squared error (MSE) values of all trained models.

| | ABR | RR | SVR | EN | RF | GBR | KNN | XGB | DBN |
|---|---|---|---|---|---|---|---|---|---|
| R2_train | 0.990 | 0.869 | 0.850 | 0.851 | 0.920 | 0.991 | 1.000 | 0.970 | 0.935 |
| R2_test | 0.923 | 0.795 | 0.848 | 0.837 | 0.848 | 0.859 | 0.770 | 0.901 | 0.900 |
| MSE_train | 0.002 | 0.056 | 0.064 | 0.064 | 0.036 | 0.001 | 0.000 | 0.014 | 0.025 |
| MSE_test | 0.027 | 0.087 | 0.064 | 0.069 | 0.052 | 0.049 | 0.080 | 0.034 | 0.045 |

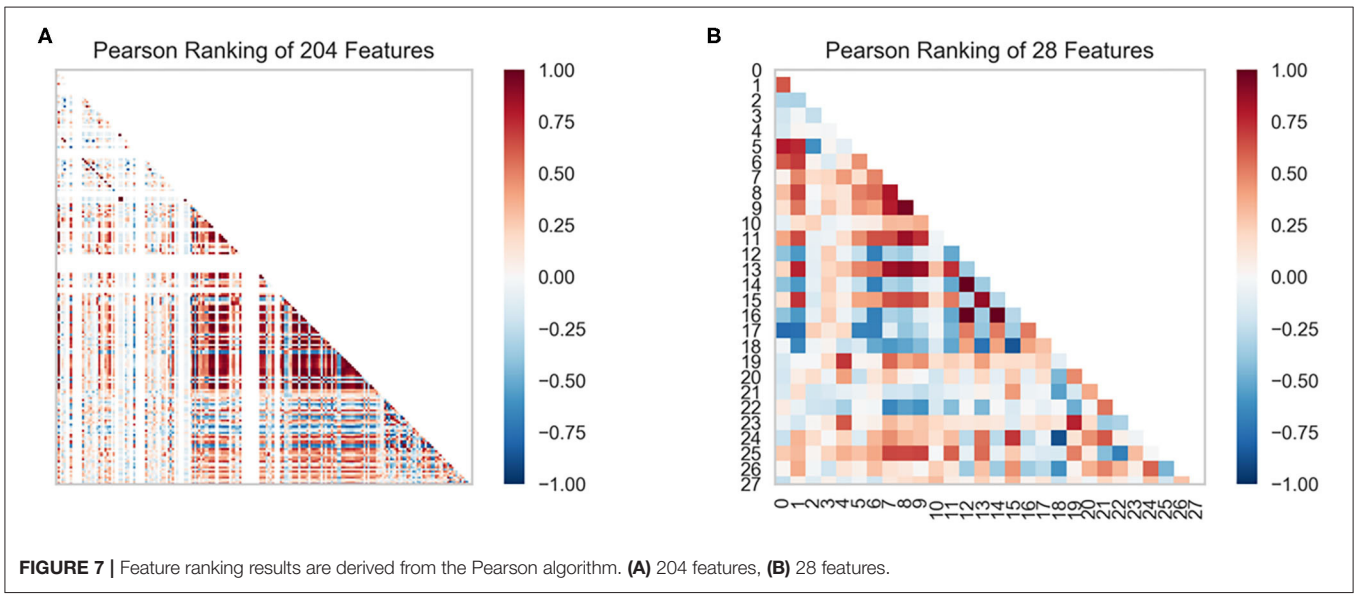


**FIGURE 7 |** Feature ranking results are derived from the Pearson algorithm. **(A)** 204 features, **(B)** 28 features.

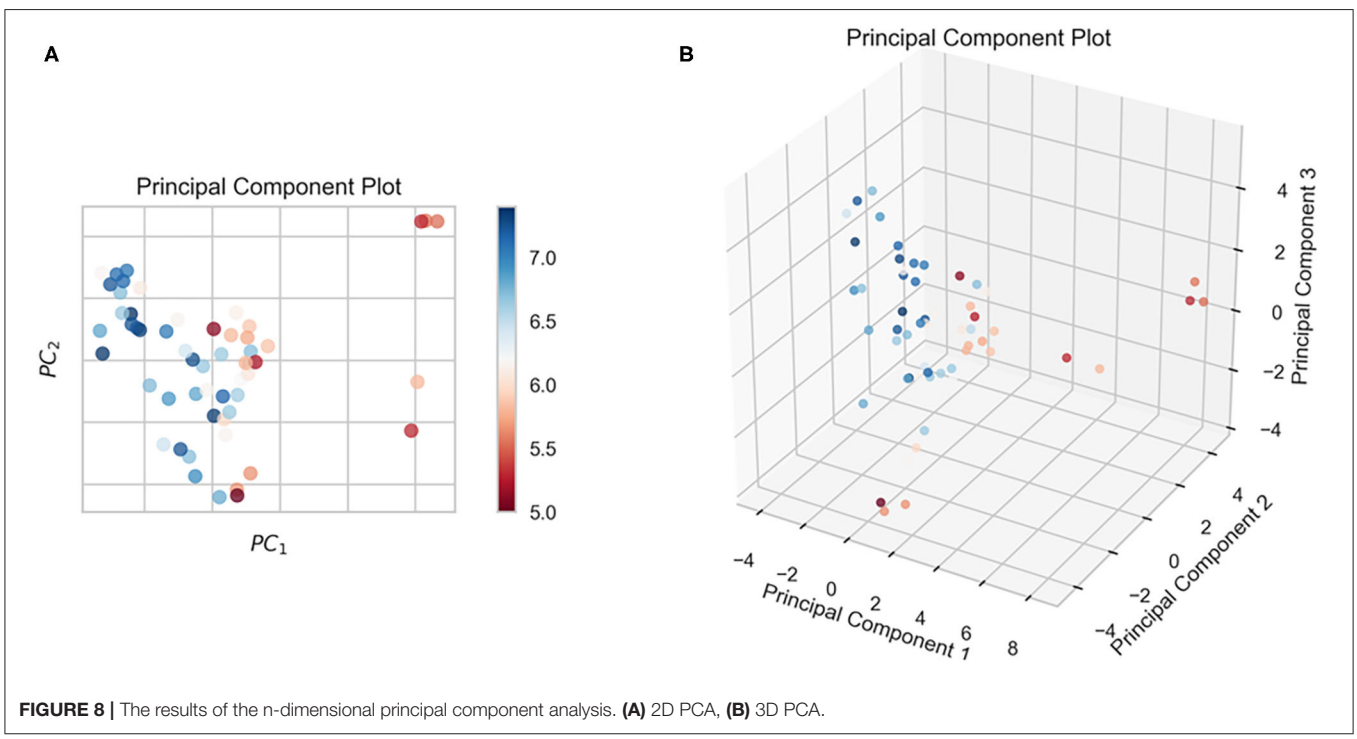


**FIGURE 8 |** The results of the n-dimensional principal component analysis. **(A)** 2D PCA, **(B)** 3D PCA.

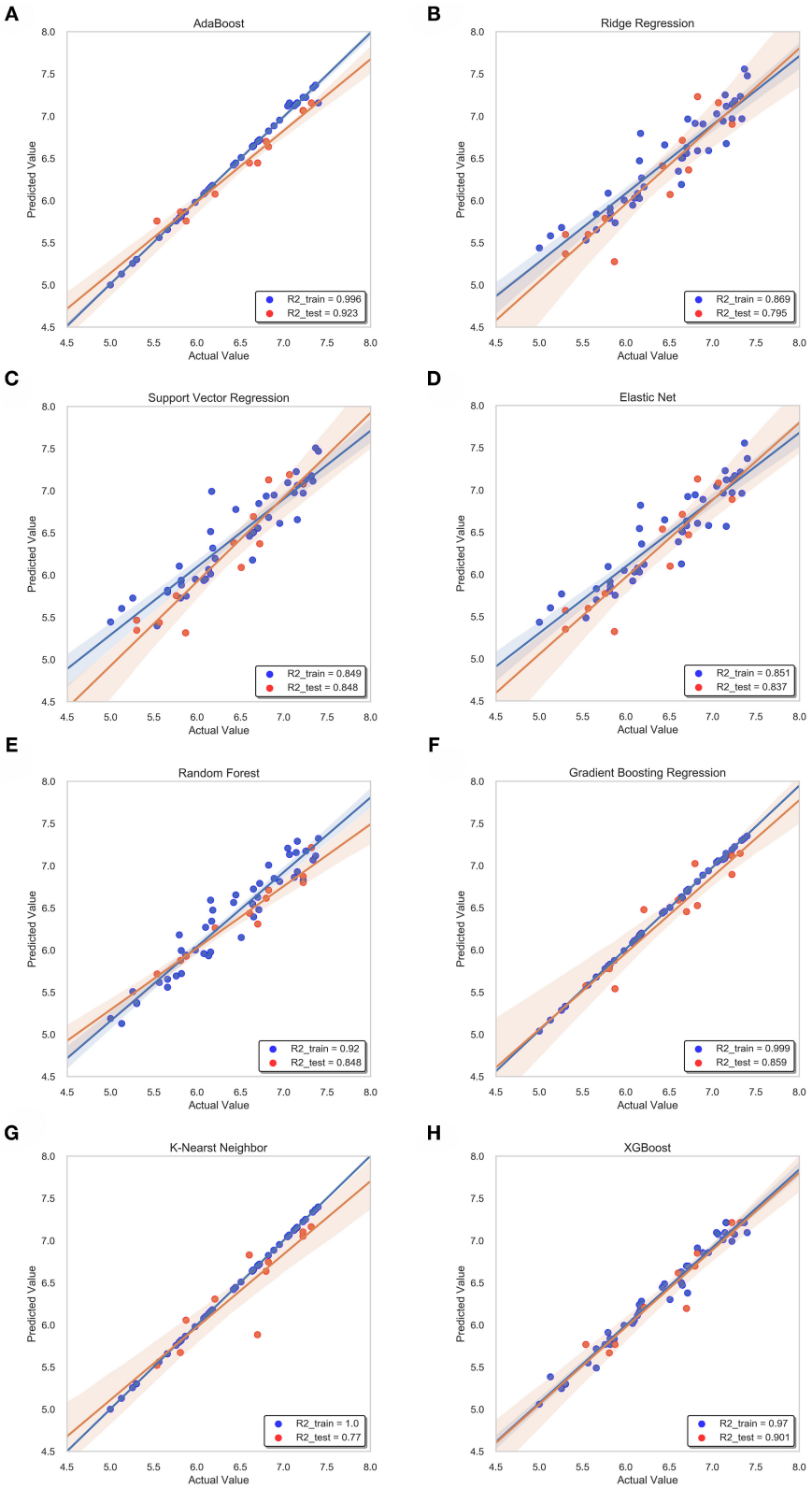


**FIGURE 9 |** Correlation between predicted value and actual value of machine learning model. Training set (blue dots) and testing set (red dots) are shown. The confidence interval is 95%. **(A)** ABR, **(B)** RR, **(C)** SVR, **(D)** EN, **(E)** RF **(F)** GBR, **(G)** KNN, **(H)** XGB.

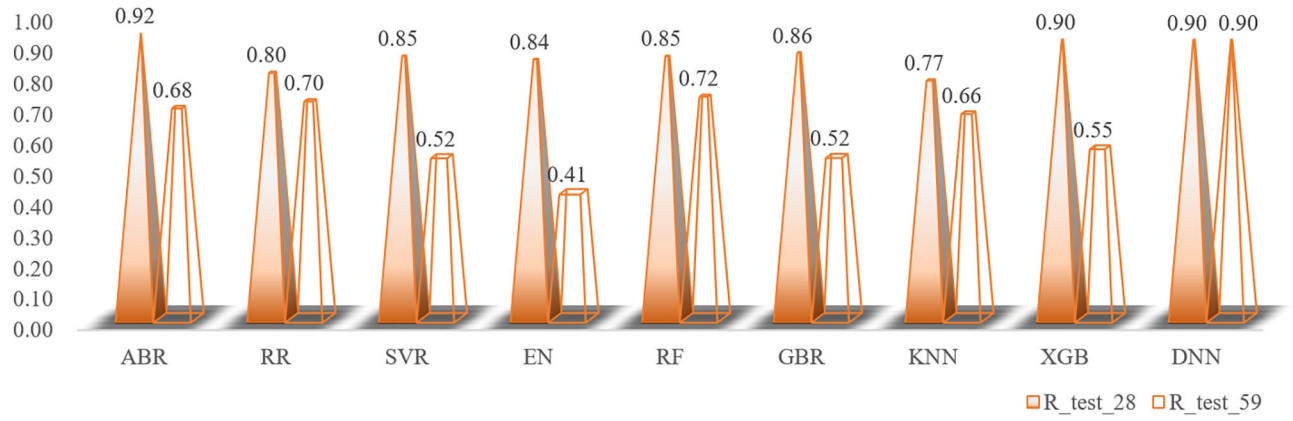


**FIGURE 10 |** The changes in the R-square values of all models when the number of feature variables is increased.

than the RR and EN models. This was because they all used integrated learning methods and used different strategies to combine individual learners into a committee, which improved the generalization ability of the model. Based on bagging integration method, the prediction result of RF was obtained by parallel calculation of all decision trees. It made the model susceptible to large deviations due to the influence of individual wrong decision trees, so the R-square on the training sets was only 0.92 (**Figure 9E**). The R-square of the ABR and GBR models on the training sets were both close to 1 (**Figures 9A,F**). This was most likely because they used the Boosting method to upgrade the weak learner to a strong learner and the sample size was relatively small. ABR continuously optimized the sample weights of each round of training, the trained model with the testing sets mean square error (MSE) of 0.027 and R-square of 0.92 (**Table 2**), which showed the best performance. XGB added a regular term to the cost function that reduced the variance of the model and avoided overfitting. With the help of the variable importance indicator feature_importances_, we obtained the weight of the importance of the XGB model variable. It could be seen that ALogP_MR and ES_Count_aaaC were the top two eigenvalues. The distribution of predicted values around actual values of the XGB model were plotted in **Figure 9H**, and the R-square on the training sets and the test sets reached 0.97 and 0.9, respectively.

## SVR and KNN Model

Before ensemble learning and neural network algorithms showed superior performance, SVM algorithm basically occupied a dominant position, especially in the field of classification. For Gal3 inhibitor studies, there were actually fewer samples available for reference. Even so, since SVR basically did not involve probability measurement and the law of large numbers, the model still showed high prediction accuracy, and the R-square on the test sets was close to 0.85 (**Figure 9C**). However, the shortcoming of SVR was also exposed. When the feature dimension was much larger than the number of samples, the SVR model tended to ignore the correlation of mutual characteristics, so the R-square on the training sets was only 0.85. After repeated calculation and verification, the linear kernel was finally selected, and the error tolerance was set to 0.39 to ensure that the model had sufficient generalization ability to avoid overfitting. The fitting curve of the KNN model was perfect, and the R-square on the training sets had reached 1, which was suspected of overfitting. The number k of favorable features was filtered through the built-in function of Scikit-learn, and it was verified that the model performs best when k was equal to 4. When the independent variable dimension was small, the KNN model could significantly reduce the error. But as the variable gradually increased, the mean value of the dependent variable corresponding to the closest value to the target might deviate from the actual value exponentially. The above reasons caused the model accuracy to be significantly reduced. The R-square on the test sets was only 0.77, which was the worst performance among all models (**Table 2**).

## Deep Belief Network

The total number of sample data we obtained was only 56, far less than the number of 204 feature dimensions. In view of this situation, traditional machine learning models usually removed most of the features during the preprocessing process. Although a model with higher prediction accuracy could be obtained, this actually consumed the credibility of the model. DBN could avoid this problem as much as possible, allowing more features to participate in training. Although it took thousands of times the training time, the trained model had better prediction reliability and more convincing. Using the Dropout method, the dropout rates of the first, second and third layers of the neural network were 0.4, 0.6, and 0.3, respectively, and a total of 500 modeling attempts were made. The R-square of the best trained model on the training sets and test sets were 0.94 and 0.9, respectively. We had tried in the previous machine learning model. When the parameter threshold was set to 0.01 and alpha was set to 0.001, 59 features are retained. However, the accuracy of all models was significantly reduced. The R-square on some model test sets was even lower than 0.5 (**Figure 10**). Through comparison, it could

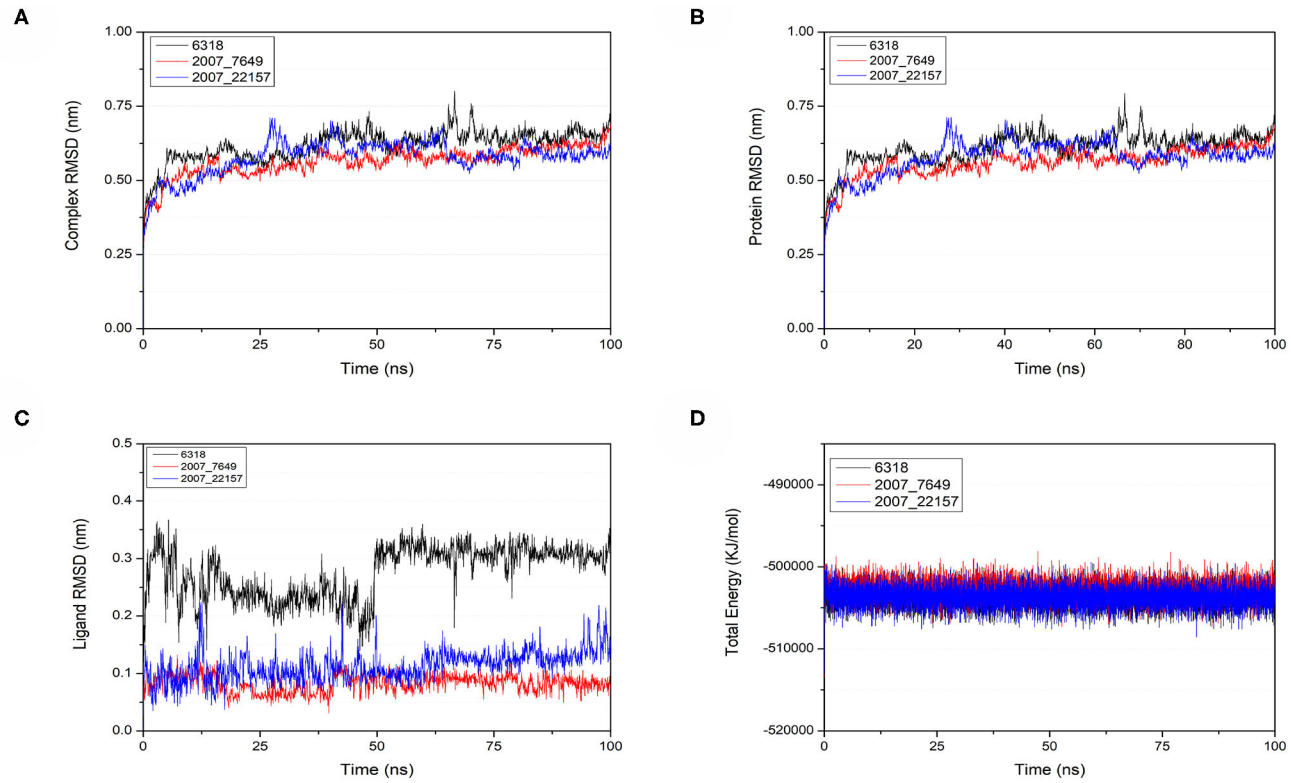


**FIGURE 11 |** Changes of RMSD and total energy in molecular dynamics simulation. **(A)** RMSD changes of complex, **(B)** RMSD changes of protein, **(C)** RMSD changes of ligands, **(D)** Total energy changes between protein and ligands.

be found that the DBN model still showed high accuracy under low sample set and high feature dimension.

## Molecular Dynamics Simulation

To verify the binding stability of the receptor-ligand complexes, we performed molecular dynamics simulations in 100 ns with Gromacs 2018 software (Kutzner et al., 2019). Unfortunately, 5372 was detached from the binding site during the molecular dynamic simulation, although it showed good results in the molecular docking and AI-based models prediction process. The escape of 5372 indicated that its binding stability to Gal3 was poor. The RMSD was calculated to evaluate the deviation of the structure from the original starting structure over the course of the simulations. In the RMSD results (**Figures 11A–C**), the RMSD values of the three candidates and Gal3 complexes shown an upward trend at initial 10 ns, then tended to stabilize with a relatively flat curve and maintained around 0.5–0.6 nm. The protein RMSD change curve is similar to the complex RMSD change curve. Based on ligand RMSD, 6318 had higher fluctuation rate than other candidates, which may explain high ligand gyration value. The RMSD results suggested that candidates 7649 and 22157 have higher binding stability to Gal3 protein. Besides, the total energy of simulation systems in the 100 ns process was calculated to analyze the energy changes in the complexes. And the results shown that the energy of protein-ligand complexes was stable and it had been maintained between about −510 000 to −500 000 kJ/mol (**Figure 11D**). The radius of gyration could give a measure of the compactness of the structures, and can also give a measure of the atomic mass relative the molecular center mass. As shown in **Figures 12A,B**, protein gyrate and ligands gyrate were stable in general during the MD simulation process, and the gyrate of 6318 was higher than other two ligands (include target protein system), which was consistent with the RMSD results. MSD revealed the movement of atoms from the initial position to the final stage of MD simulation, indicating the movement trend of each ligand or protein. The low and stable MSD value of the ligand shows the stability of the binding, while the decrease of the MSD value indicates that the ligand may be close to the binding pocket. The extremely high MSD value and the increasing MSD value mean the ligand has a tendency to escape. In the process of the whole simulation (**Figures 12C,D**), although the MSD values of Gal3 and three ligands both increased, the changes of all measured MSD values maintained in a low range. It was worth noting that 6318 obtained much higher ligand MSD value compared to other two ligands, which indicates the ligand 6318 have a trend of escaping from the binding pocket. From the SASA calculated results, we can analyze the hydrophilicity and hydrophobicity of the simulation system. The solvent accessible area of Gal3 decreased significantly from 0 to 15 ns, and then remained to a relatively stable area (**Figure 12E**). Meanwhile, as shown in **Figure 12F**, the SASA values of all ligands were very stable in the simulation process.

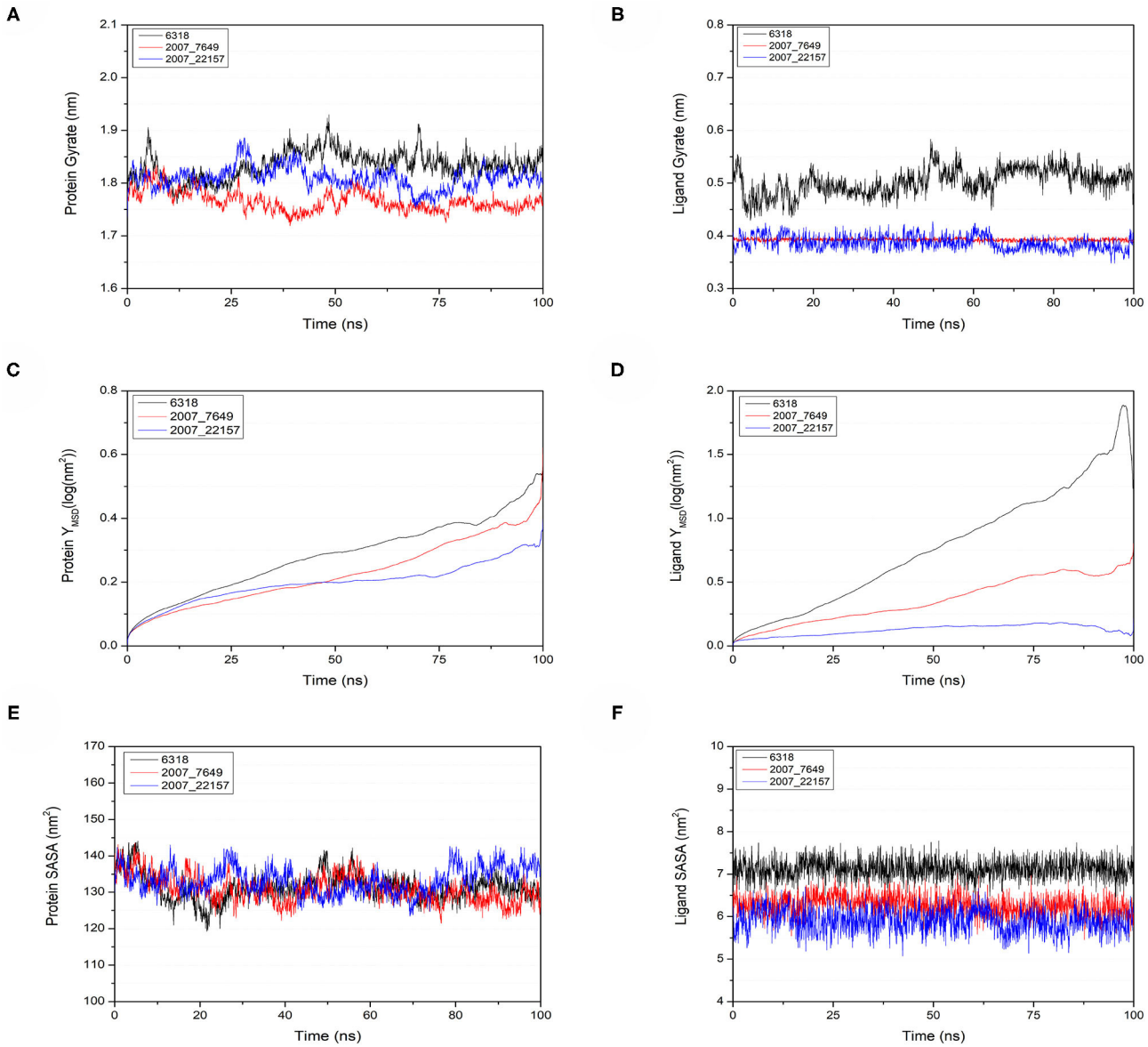


**FIGURE 12 |** Gyrate, MSD, and SASA changes of proteins and ligands in molecular dynamics simulations. **(A)** Gyrate of protein, **(B)** gyrate of ligands, **(C)** MSD of protein, **(D)** MSD of ligands, **(E)** SASA of protein, **(F)** SASA of ligands.

This can further indicate the stability of the complex systems. Finally, the binding postures of three ligands and target protein in the initial and final conformations were displayed in **Figure 13**. The ligands rotated in the same pocket but not detached from the target protein.

## CONCLUSION

The new discovery of Gal3 in the pathogenesis of HD provides a new target and new method for ND treatment. In order to find potential inhibitors of Gal3, we have completed the following work and obtained satisfactory results. Using molecular docking methods, we initially screened a batch of small molecules with relatively stable docking from a large drug molecule library. Multiple artificial intelligence-based models were constructed, and known Gal3 inhibitors were used as sample sets to train the models. From the performance parameters of the model, all models achieved high overall accuracy sensitivity. The R-square of XGBoost model on the test sets was higher than other algorithms, and there was no overfitting on the training sets. We not only screened from the TCM database, but also used the ZINC database to do the same. The results showed that the molecules from the TCM database performed better than the ZINC database in terms of binding stability and pIC50 value predicted by AI models. Comparing the prediction results of all models, we completed further screening and

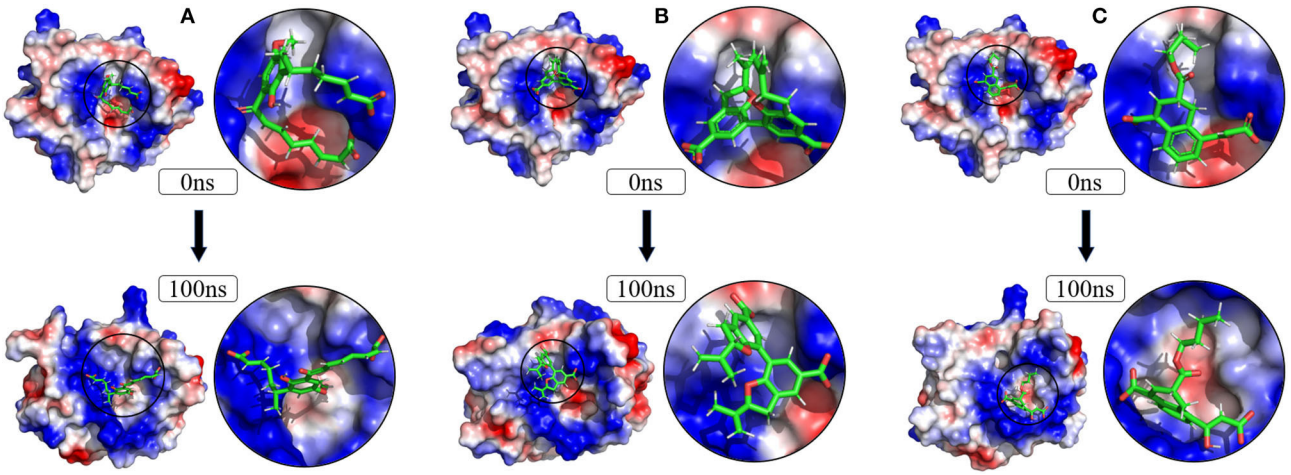


**FIGURE 13 |** Changes of the binding posture during MD in microenvironment. Although the conformation of the ligands changed, the position where the ligands bind to the protein pocket does not change. **(A)** 6318, **(B)** 2007_7649, **(C)** 2007_22157.

narrowed the candidate range. Finally, through MD simulation, we further verified the stability of the complexes, the final candidate ligand and the target protein complexes showed stable binding throughout the simulation time. Combining all experimental results, the active ingredients 1,2-Dimethylbenzene and Typhic acid contained in *Crataegus pinnatifida* and *Typha angustata* may become the new drug formulation for ND treatment. We provide a new strategy with applying AI-based methods to the drug screening process, which can greatly reduce the cost of new drug development. Screening drug molecules from the TCM database is an innovation and beneficial supplement to screening from the general database. In summary, this study has explored a highly accurate integrated architecture to reduce the drug screening process. With the application of artificial intelligence, medical practitioners exclude candidates with low probability based on prediction results, which reduces the risk of downstream decision-making for better resource planning and allocation. The proposed integration method shows high accuracy under different algorithm models, indicating that artificial intelligence-based drug development has application prospects. Artificial intelligence-based application is an improvement and supplement to the existing traditional drug screening based on molecular interaction relationships.

## DATA AVAILABILITY STATEMENT

The raw data supporting the conclusions of this article will be made available by the authors, without undue reservation.

## AUTHOR CONTRIBUTIONS

SJ and CC designed research. LD, WZ, LZ, XH, and ZL worked together to complete the experiment and analyze the data. SJ, CC, LD, and WZ wrote the manuscript together. All authors contributed to the article and approved the submitted version.

## FUNDING

This work was supported in part by the National Nature Science and Foundation of China Grand No. 71801031, in part by the Guangdong Basic and Applied Basic Research Foundation project, China, No. 2019A1515011962, in part by the Fundamental Research Funds for the Central Universities No. 20lgpy183, the Science, Technology & Innovation Commission of Shenzhen Municipality [JCYL 20170818165305521], and in part by the Guangzhou science and technology fund [Grant No. 201803010072].

## REFERENCES

Abdel-Basset, M., El-Shahat, D., El-henawy, I., de Albuquerque, V. H. C., and Mirjalili, S. (2020). A new fusion of grey wolf optimizer algorithm with a two-phase mutation for feature selection. *Expert Syst. Appl.* 139:112824. doi: 10.1016/j.eswa.2019.112824

Abdolmaleki, A., Ghasemi, J. B., and Ghasemi, F. (2017). Computer aided drug design for multi-target drug design: SAR/QSAR, molecular docking and pharmacophore methods. *Curr. Drug Targets* 18, 556–575. doi: 10.2174/1389450117666160101120822

Agarap, A. F. (2018). Deep learning using rectified linear units (ReLU) arXiv. *arXiv* 7.

Athey, S., Tibshirani, J., and Wager, S. (2019). Generalized random forests. *Ann. Stat.* 47, 1148–1178. doi: 10.1214/18-AOS1709

Bateman, A., Martin, M. J., O'Donovan, C., Magrane, M., Alpi, E., Antunes, R., et al. (2017). UniProt: the universal protein knowledgebase. *Nucleic Acids Res.* 45, D158–D169. doi: 10.1093/nar/gkw1099

Boza-Serrano, A., Ruiz, R., Sanchez-Varo, R., Garcia-Revilla, J., Yang, Y., Jimenez-Ferrer, I., et al. (2019). Galectin-3, a novel endogenous TREM2 ligand, detrimentally regulates inflammatory response in Alzheimer's disease. *Acta Neuropathol.* 138, 251–273. doi: 10.1007/s00401-019-02013-z

Breiman, L. (2001). Random forests. *Machine Learn.* 45, 5–32. doi: 10.1023/A:1010933404324

Brooks, B. R., Brooks, C. L. III, Mackerell, A. D. Jr., Nilsson, L., Petrella, R. J., Roux, B., et al. (2009). CHARMM: the biomolecular simulation program. *J. Comput. Chem*. 30, 1545–1614. doi: 10.1002/jcc.21287

Burley, S. K., Berman, H. M., Bhikadiya, C., Bi, C., Chen, L., Di Costanzo, L., et al. (2019). RCSB protein data bank: biological macromolecular structures enabling research and education in fundamental biology, biomedicine, biotechnology and energy. *Nucleic Acids Res.* 47, D464–D474. doi: 10.1093/nar/gky1004

Chang, C.-C., and Lin, C.-J. (2011). LIBSVM:a library for support vector machines. *ACM Trans. Intell. Syst. Technol*. 2:27. doi: 10.1145/1961189.1961199

Chen, C. Y. C. (2011). TCM database@Taiwan: the world's largest traditional Chinese medicine database for drug screening *in silico*. *PLoS ONE* 6:5. doi: 10.1371/journal.pone.0015939

Chen, H., Engkvist, O., Wang, Y., Olivecrona, M., and Blaschke, T. (2018a). The rise of deep learning in drug discovery. *Drug Discov. Today* 23, 1241–1250. doi: 10.1016/j.drudis.2018.01.039

Chen, X., Huang, L., Xie, D., and Zhao, Q. (2018b). EGBMMDA: extreme gradient boosting machine for MiRNA-disease association prediction. *Cell Death Dis.* 9:3. doi: 10.1038/s41419-017-0003-x

Correia, J., Resende, T., Baptista, D., and Rocha, M. (2020). "Artificial intelligence in biological activity prediction," in *Practical Applications of Computational Biology and Bioinformatics,* eds F. FdezRiverola, M. Rocha, M. S. Mohamad, N. Zaki, and J. A. CastellanosGarzon, (Cham: Springer), 164–172. doi: 10.1007/978-3-030-23873-5_20

Elmezayen, A. D., Al-Obaidi, A., Sahin, A. T., and Yelekci, K. (2020). Drug repurposing for coronavirus (COVID-19): *in silico* screening of known drugs against coronavirus 3CL hydrolase and protease enzymes. *J. Biomol. Struct. Dyn*. doi: 10.1080/07391102.2020.1758791. [Epub ahead of print].

Gaulton, A., Hersey, A., Nowotka, M., Bento, A. P., Chambers, J., Mendez, D., et al. (2017). The ChEMBL database in 2017. *Nucleic Acids Res.* 45, D945–D954. doi: 10.1093/nar/gkw1074

Henderson, N. C., and Sethi, T. (2009). The regulation of inflammation by galectin-3. *Immunol. Rev*. 230, 160–171. doi: 10.1111/j.1600-065X.2009.00794.x

Hessler, G., and Baringhaus, K. H. (2018). Artificial intelligence in drug design. *Molecules* 23:2520. doi: 10.3390/molecules23102520

Huang, Q., Chen, Y., Liu, L., Tao, D., and Li, X. (2020). On combining biclustering mining and AdaBoost for breast tumor classification. *IEEE Trans. Knowl. Data Eng.* 32, 728–738. doi: 10.1109/TKDE.2019.2891622

Irwin, J. J., and Shoichet, B. K. (2005). ZINC-a free database of commercially available compounds for virtual screening. *J. Chem. Inf. Model*. 45, 177–182. doi: 10.1021/ci049714+

Kaiser, T. M., Burger, P. B., Butch, C. J., Pelly, S. C., and Liotta, D. C. (2018). A machine learning approach for predicting HIV reverse transcriptase mutation susceptibility of biologically active compounds. *J. Chem. Inf. Model.* 58, 1544–1552. doi: 10.1021/acs.jcim.7b00475

Kim, S., Chen, J., Cheng, T., Gindulyte, A., He, J., He, S., et al. (2019). PubChem 2019 update: improved access to chemical data. *Nucleic Acids Res.* 47, D1102–D1109. doi: 10.1093/nar/gky1033

Kumar, D., Kumari, K., Jayaraj, A., Kumar, V., Kumar, R. V., Dass, S. K., et al. (2020). Understanding the binding affinity of noscapines with protease of SARS-CoV-2 for COVID-19 using MD simulations at different temperatures. *J. Biomol. Struct. Dyn*. 1–14. doi: 10.1080/07391102.2020.1752310

Kumar, R., Ignjatovic, M. M., Peterson, K., Olsson, M., Leffler, H., Ryde, U., et al. (2019). Structure and energetics of ligand-fluorine interactions with galectin-3 backbone and side-chain amides: insight into solvation effects and multipolar interactions. *Chemmedchem* 14, 1528–1536. doi: 10.1002/cmdc.201900293

Kutzner, C., Pall, S., Fechner, M., Esztermann, A., de Groot, B. L., and Grubmueller, H. (2019). More bang for your buck: improved use of GPU nodes for GROMACS 2018. *J. Comput. Chem*. 40, 2418–2431. doi: 10.1002/jcc.26011

Lai, T., Chen, R., Yang, C., Li, Q., Fujita, H., Sadri, A., et al. (2020). Efficient robust model fitting for multistructure data using global greedy search. *IEEE Trans. Cybernetics* 50, 3294–3306. doi: 10.1109/TCYB.2019.2900096

LeCun, Y., Bengio, Y., and Hinton, G. (2015). Deep learning. *Nature* 521, 436–444. doi: 10.1038/nature14539

Li, L., Qin, L., Xu, Z., Yin, Y., Wang, X., Kong, B., et al. (2020). Using artificial intelligence to detect COVID-19 and community-acquired pneumonia based on pulmonary CT: evaluation of the diagnostic accuracy. *Radiology* 296, E65–E71. doi: 10.1148/radiol.2020200905

Li, P., Liu, S., Lu, M., Bandyopadhyay, G., Oh, D., Imamura, T., et al. (2016). Hematopoietic-derived galectin-3 causes cellular and systemic insulin resistance. *Cell* 167, 973–984.e12. doi: 10.1016/j.cell.2016.10.025

Liu, R., Chen, P., Li, X., Wu, Z., Gao, X., Chen, X., et al. (2017). Artificial intelligence sense technology: new technology in pharmaceutical sciences. *Chin. J. Pharm. Anal.* 37, 559–567. doi: 10.16155/j.0254-1793.2017.04.01

Liu, X.-Y., Lv, X., Wang, P., Ai, C.-Z., Zhou, Q.-H., Finel, M., et al. (2019). Inhibition of UGT1A1 by natural and synthetic flavonoids. *Int. J. Biol. Macromol.* 126, 653–661. doi: 10.1016/j.ijbiomac.2018.12.171

Macdonald, M. E., Ambrose, C. M., Duyao, M. P., Myers, R. H., Lin, C., Srinidhi, L., et al. (1993). A novel gene containing a trinucleotide repeat that is expanded and unstable on huntington's disease chromosomes. The huntington's disease collaborative research group. *Cell* 72, 971–983. doi: 10.1016/0092-8674(93)90585-E

Mayr, A., Klambauer, G., Unterthiner, T., and Hochreiter, S. (2016). DeepTox: toxicity prediction using deep learning. *Front. Environ. Sci.* 3:80. doi: 10.3389/fenvs.2015.00080

McKhann, G., Drachman, D., Folstein, M., Katzman, R., Price, D., and Stadlan, E. M. (1984). Clinical diagnosis of Alzheimer's disease: report of the NINCDS-ADRDA work group under the auspices of department of health and human services task force on alzheimer's disease. *Neurology* 34, 939–944. doi: 10.1212/WNL.34.7.939

Mills, N. (2006). ChemDraw ultra 10.0. *J. Am. Chem. Soc.* 128, 13649–13650. doi: 10.1021/ja0697875

Pant, S., Singh, M., Ravichandiran, V., Murty, U. S. N., and Srivastava, H. K. (2020). Peptide-like and small-molecule inhibitors against Covid-19. *J. Biomol. Struct. Dyn*. 1–10. doi: 10.1080/07391102.2020.1757510

Rahman, M. R., Islam, T., Zaman, T., Shahjaman, M., Karim, M. R., Huq, F., et al. (2020). Identification of molecular signatures and pathways to identify novel therapeutic targets in Alzheimer's disease: insights from a systems biomedicine perspective. *Genomics* 112, 1290–1299. doi: 10.1016/j.ygeno.2019.07.018

Ramirez Hernandez, E., Sanchez-Maldonado, C., Mayoral Chavez, M. A., Hernandez-Zimbron, L. F., Patricio Martinez, A., Zenteno, E., et al. (2020). The therapeutic potential of galectin-1 and galectin-3 in the treatment of neurodegenerative diseases. *Expert Rev. Neurother.* 20, 439–448. doi: 10.1080/14737175.2020.1750955

Ramirez, E., Sanchez-Maldonado, C., Mayoral, M. A., Mendieta, L., Alatriste, V., Patricio-Martinez, A., et al. (2019). Neuroinflammation induced by the peptide amyloid-beta (25-35) increase the presence of galectin-3 in astrocytes and microglia and impairs spatial memory. *Neuropeptides* 74, 11–23. doi: 10.1016/j.npep.2019.02.001

Ratsch, G., Onoda, T., and Muller, K. R. (2001). Soft margins for AdaBoost. *Machine Learn.* 42, 287–320. doi: 10.1023/A:1007618119488

Romero, A., and Gabius, H. J. (2019). Galectin-3: is this member of a large family of multifunctional lectins (already) a therapeutic target? *Expert Opin. Ther. Targets* 23, 819–828. doi: 10.1080/14728222.2019.1675638

Saijo, K., Crotti, A., and Glass, C. K. (2010). Nuclear receptors, inflammation, and neurodegenerative diseases. *Adv. Immunol.* 106, 21–59. doi: 10.1016/S0065-2776(10)06002-5

Sapay, N., and Tieleman, D. P. (2011). Combination of the CHARMM27 force field with united-atom lipid force fields. *J. Comput. Chem.* 32, 1400–1410. doi: 10.1002/jcc.21726

Schneider, P., Walters, W. P., Plowright, A. T., Sieroka, N., Listgarten, J., Goodnow, R. A., et al. (2020). Rethinking drug design in the artificial intelligence era. *Nat. Rev. Drug Discov.* 19, 353–364. doi: 10.1038/s41573-019-0050-3

Senior, A. W., Evans, R., Jumper, J., Kirkpatrick, J., Sifre, L., Green, T., et al. (2020). Improved protein structure prediction using potentials from deep learning. *Nature* 577, 706–710. doi: 10.1038/s41586-019-1923-7

Shin, T. (2013). The pleiotropic effects of galectin-3 in neuroinflammation: a review. *Acta Histochem.* 115, 407–411. doi: 10.1016/j.acthis.2012.11.010

Siew, J. J., Chen, H.-M., Chen, H.-Y., Chen, H.-L., Chen, C.-M., Soong, B.-W., et al. (2019). Galectin-3 is required for the microglia-mediated brain inflammation in a model of huntington's disease. *Nat. Commun.* 10:3473. doi: 10.1038/s41467-019-11441-0

Song, W., Yen, H.-Y., Robinson, C. V., and Sansom, M. S. P. (2019). State-dependent lipid interactions with the A2a receptor revealed by MD simulations using *in vivo*-mimetic membranes. *Structure* 27, 392–403.e3. doi: 10.1016/j.str.2018.10.024

Venkatachalam, C. M., Jiang, X., Oldfield, T., and Waldman, M. (2003). LigandFit: a novel method for the shape-directed rapid docking of ligands to protein active sites. *J. Mol. Graph. Model.* 21, 289–307. doi: 10.1016/S1093-3263(02)00164-X

Voet, S., Srinivasan, S., Lamkanfi, M., and van Loo, G. (2019). Inflammasomes in neuroinflammatory and neurodegenerative diseases. *Embo Mol. Med.* 11:e10248. doi: 10.15252/emmm.201810248

Wen, P., Hu, T.-G., Linhardt, R. J., Liao, S.-T., Wu, H., and Zou, Y.-X. (2019). Mulberry: a review of bioactive compounds and advanced processing technology. *Trends Food Sci. Technol.* 83, 138–158. doi: 10.1016/j.tifs.2018.11.017

Xuan, S., Wu, Y., Chen, X., Liu, J., and Yan, A. (2013). Prediction of bioactivity of HIV-1 integrase ST inhibitors by multilinear regression analysis and support vector machine. *Bioorg. Med. Chem. Lett.* 23, 1648–1655. doi: 10.1016/j.bmcl.2013.01.081

Yang, X., and Wen, W. (2018). Ridge and lasso regression models for cross-version defect prediction. *IEEE Trans. Reliability*, 67, 885–896. doi: 10.1109/TR.2018.2847353

Yang, Y., Islam, M. S., Wang, J., Li, Y., and Chen, X. (2020). Traditional Chinese medicine in the treatment of patients infected with 2019-new coronavirus (SARS-CoV-2): a review and perspective. *Int. J. Biol. Sci.* 16, 1708–1717. doi: 10.7150/ijbs.45538

Zhang, W., Jing, K., Huang, F., Chen, Y., Li, B., Li, J., et al. (2019). SFLLN: a sparse feature learning ensemblemethod with linear neighborhood regularization for predicting drug-drug interactions. *Inf. Sci.* 497, 189–201. doi: 10.1016/j.ins.2019.05.017

Zhang, Y.-D., Pan, C., Sun, J., and Tang, C. (2018). Multiple sclerosis identification by convolutional neural network with dropout and parametric ReLU. *J. Comput. Sci.* 28, 1–10. doi: 10.1016/j.jocs.2018.07.003

Zoete, V., Cuendet, M. A., Grosdidier, A., and Michielin, O. (2011). SwissParam: a fast force field generation tool for small organic molecules. *J. Comput. Chem.* 32, 2359–2368. doi: 10.1002/jcc.21816

Zou, H., and Hastie, T. (2005). Regularization and variable selection via the elastic net. *J. R. Stat. Soc. Series B Stat. Methodol.* 67, 301–320. doi: 10.1111/j.1467-9868.2005.00503.x

**Conflict of Interest:** The authors declare that the research was conducted in the absence of any commercial or financial relationships that could be construed as a potential conflict of interest.

frontiers in Neurorobotics

ORIGINAL RESEARCH
published: 07 January 2021
doi: 10.3389/fnbot.2020.616775

# A Manufacturing-Oriented Intelligent Vision System Based on Deep Neural Network for Object Recognition and 6D Pose Estimation

*Guoyuan Liang*[1,2,3,4], *Fan Chen*[1], *Yu Liang*[1], *Yachun Feng*[1,2,3,4], *Can Wang*[1,2,3,4] *and Xinyu Wu*[1,2,3,4]*

[1] Center for Intelligent and Biomimetic Systems, Shenzhen Institutes of Advanced Technology, Chinese Academy of Sciences, Shenzhen, China, [2] Guangdong Provincial Key Lab of Robotics and Intelligent System, Shenzhen Institutes of Advanced Technology, Chinese Academy of Sciences, Shenzhen, China, [3] Shenzhen Key Laboratory of Human-Machine Intelligence-Synergy Systems, Shenzhen Institutes of Advanced Technology, Chinese Academy of Sciences, Shenzhen, China, [4] Guangdong-Hong Kong-Macao Joint Laboratory of Human-Machine Intelligence-Synergy Systems (No.2019B121205007), Shenzhen Institutes of Advanced Technology, Chinese Academy of Sciences, Shenzhen, China

Nowadays, intelligent robots are widely applied in the manufacturing industry, in various working places or assembly lines. In most manufacturing tasks, determining the category and pose of parts is important, yet challenging, due to complex environments. This paper presents a new two-stage intelligent vision system based on a deep neural network with RGB-D image inputs for object recognition and 6D pose estimation. A dense-connected network fusing multi-scale features is first built to segment the objects from the background. The 2D pixels and 3D points in cropped object regions are then fed into a pose estimation network to make object pose predictions based on fusion of color and geometry features. By introducing the channel and position attention modules, the pose estimation network presents an effective feature extraction method, by stressing important features whilst suppressing unnecessary ones. Comparative experiments with several state-of-the-art networks conducted on two well-known benchmark datasets, YCB-Video and LineMOD, verified the effectiveness and superior performance of the proposed method. Moreover, we built a vision-guided robotic grasping system based on the proposed method using a Kinova Jaco2 manipulator with an RGB-D camera installed. Grasping experiments proved that the robot system can effectively implement common operations such as picking up and moving objects, thereby demonstrating its potential to be applied in all kinds of real-time manufacturing applications.

**Keywords: deep neural network, object recognition, 6D pose estimation, intelligent manufacturing, semantic segmentation**

OPEN ACCESS

***Edited by:***
*Long Wang,*
*University of Science and Technology Beijing, China*

***Reviewed by:***
*Zhe Song,*
*Nanjing University, China*
*Xiaojun Wu,*
*Harbin Institute of Technology, China*

***Correspondence:**
*Xinyu Wu*
*xy.wu@siat.ac.cn*

***Received:*** *13 October 2020*
***Accepted:*** *20 November 2020*
***Published:*** *07 January 2021*

***Citation:***
*Liang G, Chen F, Liang Y, Feng Y, Wang C and Wu X (2021) A Manufacturing-Oriented Intelligent Vision System Based on Deep Neural Network for Object Recognition and 6D Pose Estimation. Front. Neurorobot. 14:616775. doi: 10.3389/fnbot.2020.616775*

## 1. INTRODUCTION

The assembly line is one of the greatest inventions in the manufacturing industry. With the rapid development of artificial intelligence and robotics, more intelligent robotics have been deployed in traditional assembly lines, replacing human workers. These robots are normally equipped with intelligent vision systems which not only detect parts in the working spaces but also estimate their poses before taking further actions such as grasping, rotating, moving, fitting, etc. Generally,

object recognition and 6D pose estimation from images are the base of almost all kinds of robotic applications, such as robot manipulation (Tremblay et al., 2018), robot-human interaction (Svenstrup et al., 2009), and virtual reality (Yang et al., 2018).

Many approaches have been reported in the past decade. However, the problem remains challenging, especially in cluttered scenes due to the chaos in backgrounds, heavy occlusions between objects, and changing lighting conditions. Most classical methods work with RGB inputs (color images) (Kehl et al., 2017; Rad and Lepetit, 2017), and some of them use RGB-D inputs (color and depth images) (Wagner et al., 2008). In general, the basic idea of these methods is to estimate the object pose by establishing the correspondence of 2D image features between different viewpoints or constructing mapping from 3D models to 2D images. Difficulties often occur when dealing with low-textured objects and unstable lighting conditions. With the advent of affordable depth sensors, RGB-D data-based methods (Xiang et al., 2017; Qi et al., 2018; Xu et al., 2018) have become more popular and has recently undergone significant progress. Compared with the RGB image, the depth image contains abundant geometric information, such as shape, structure, surface, curvature, etc. Additionally, the depth channel is more stable than RGB channels, usually free from perturbance caused by texture and the changing of light, which makes these approaches more reliable and robust than RGB-only methods. However, due to involvement of a large amount of 3D data, it is still a big challenge to achieve accurate pose estimation in real-time.

With the appearance of powerful computing hardware, deep learning has garnered wide attention in recent years. (Tekin et al., 2018) proposed a single-shot deep CNN that takes the 2D image as the input, directly detects the 2D projections of the 3D bounding box vertices and estimates 6D poses by a PnP algorithm (Lepetit et al., 2009). Based on SSD architecture (Liu et al., 2016), SSD-6D (Kehl et al., 2017) can realize object detection and 6D pose estimation simultaneously, though it does not work well with the small objects and occlusions. Most recently, a series of data-driven methods using RGB-D inputs such as PoseCNN (Xiang et al., 2017), MCN (Li et al., 2018a), and DenseFusion (Wang et al., 2019) were presented and has made significant progress in the field of visual recognition. In addition, some methods, such as PointFusion (Xu et al., 2018) and Frustrum PointNet (Qi et al., 2018), focus on how to extract better features from color and depth images. Compared with methods based on handcraft-features, the deep neural network demonstrates a powerful ability for automatic feature extraction, a flexible structure, and an amazing capacity of resisting disturbance.

In this paper, we propose a new two-stage deep network to segment objects from the cluttered scene and to estimate their 6D poses. The overall framework is shown in **Figure 1**. First, by applying a dense-connected way to aggregate features of different scales, an improved segmentation network inspired by U-Net (Ronneberger et al., 2015) is built. After determining the segmentation mask, the objects are cropped from the scene in both color and depth images. The cropped object images are then fed into a 6D pose prediction network which makes use of two backbone networks to extract color and geometry feature embeddings. Both are then fused together and pass through the channel attention module, position attention module, and global feature extraction module to acquire more effective feature representations. Finally, an iterative network is adopted to refine outputs of the pose predictor.

In summary, the main contributions of our approach are stated as follows:

- A new segmentation network is proposed using a densely connected method to aggregate features of different scales and to provide abundant semantic information for pixel-by-pixel classification.
- The channel attention module and position attention module are introduced into the pose estimation network and effectively improve system performance.
- A vision-guided robotic grasping system is built to validate the feasibility of the proposed algorithm being applied to manufacturing applications like grasping, packaging, and assembling etc.

The remainder of this paper is organized as follows: section 2 reviews related work. Section 3 describes the details of the proposed method. The analysis of experimental results and performance evaluation are presented in section 4. Section 5 concludes the paper.

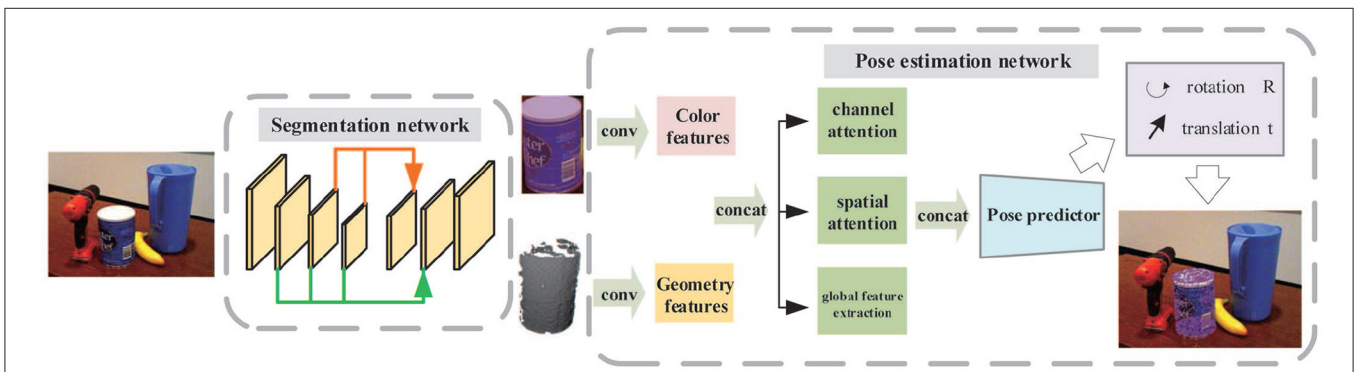


**FIGURE 1 |** The overall framework of the two-stage network for object recognition and pose estimation.

## 2. RELATED WORK

Our research mainly involves two topics: object recognition and pose estimation. Semantic segmentation is the most popular way to realize object recognition by predicting which object each pixel in the image belongs to. For semantic segmentation, Convolutional Neural Network (CNN) has proven to be the most successful method so far. For object pose estimation, prior works can be classified into three categories: feature-based methods, learning-based methods, and CNN-based methods. Theoretically, CNN is a specific framework in the machine learning family. A boom in research on deep learning has led to a dramatic number of CNN-based methods being reported in recent years. We therefore placed the CNN-based methods into a separate category.

### 2.1. Semantic Segmentation

Fully Convolutional Network (FCN) (Long et al., 2015) is the first semantic segmentation network. (Ronneberger et al., 2015) added skip connections to the network and created an excellent network known as U-Net. Many subsequent networks (Drozdzal et al., 2016) adopted this U-shape structure to develop their own networks. In order to increase the area of the receptive field without extra computing costs, Atrous Convolutions are proposed in the Deeplab (Chen et al., 2017a). In PSPNet (Zhao et al., 2017), the Pyramid Pooling Module (PPM) is proposed to aggregate contextual information from different scales to improve the network's ability to acquire global information.

### 2.2. Object Pose Estimation

#### 2.2.1. Feature-Based Method

The common idea for the feature-based methods is recovering 6D poses based on 2D-3D correspondences (Tulsiani and Malik, 2015) by matching the local features extracted in the 2D image with those in the 3D model. However, this kind of approach usually requires sufficient texture in objects. Some improved versions of this algorithm (Wohlhart and Lepetit, 2015) are proposed to deal with textureless objects.

#### 2.2.2. Learning-Based Method

Machine learning has been widely applied to address classical computer vision problems since 2000. Support Vector Machine (SVM) is proposed in Gu and Ren (2010) for object pose estimation. Hinterstoisser presented a model-based method (Hinterstoisser et al., 2012) to classify objects and 3D poses as well. In Lee et al. (2016), an adaptive Bayesian framework is designed to implement object detection and pose estimation in industrial environments. A decision forest is trained in Brachmann et al. (2014) to classify each pixel in the RGB-D image and determine the postures of objects.

#### 2.2.3. CNN-Based Method

Most recently, with the rapid development of deep learning, CNN has become the mainstream approach in most pose estimation tasks. Zeng proposed a multi-stage feature learning network in Zeng et al. (2016) for object detection and pose estimation with RGB-D inputs. Literatures (Rad and Lepetit, 2017; Tekin et al., 2018) predicted the 2D projections of 3D bounding box of a 3D target by regression before computing poses by PnP algorithm. Kehl localized the 2D bounding box of an object and searched for the best pose from a pool of candidate 6D poses associated with the bounding box (Kehl et al., 2017). Nigam improved the accuracy of pose estimation in Nigam et al. (2018) through a novel network architecture which combined global features for target segmentation with local features for coordinate regression. Li adapted a CNN-based framework by adding a channel for 3D feature extraction (Li et al., 2018a). PoseCNN (Xiang et al., 2017) is a multi-stage, multi-branch deep network that takes the 6D object poses estimation as a regression problem. With RGB images as inputs, the network can directly estimate the object poses in the whole scene. DenseFusion (Wang et al., 2019) is a general framework for estimating the 6D poses of known objects with RGB-D image inputs. Two networks are utilized to extract color and geometric features, followed by a novel dense network fusing them. In addition, an end-to-end iterative refinement network is also applied further improving the pose estimations. In sum, DenseFusion is one of the best networks so far, perfectly balancing accuracy and efficiency, thus making it appropriate for many real-time manufacturing applications.

## 3. THEORY AND METHOD

As illustrated in **Figure 1**, the proposed system consists of two stages: object segmentation and object pose estimation. The final objective is to recover object pose parameters from 2D-3D correspondences between the color and depth image. Therefore, an appropriate camera model should be determined before calculation.

### 3.1. Pinhole Camera Model

**Figure 2** shows the concept of the pinhole camera model with four coordinate systems.

- **World coordinate system** $(X_w, Y_w, Z_w)$ is the absolute coordinate system of 3D world, also named as the object coordinate system in our application.
- **Camera coordinate system** $(X_c, Y_c, Z_c)$ is a 3D coordinate system with camera optical center as the origin, cameras optical axis as $Z_c$-axis, $X_c$-axis and $Y_c$-axis parallel to $x$-axis and $y$-axis of image coordinate system respectively.
- **Image coordinate system** $(x, y)$ is a 2D coordinate system located in the image plane with the intersection of $Z_c$-axis and image sensor as origin, $x$-axis and $y$-axis parallel to the horizontal and vertical edges of image plane respectively. The 2D coordinates denote pixel position in physical units, such as millimeters.
- **Pixel coordinate system** $(u, v)$ is a 2D coordinate system with the bottom-left corner of image plane as origin, $u$-axis and $v$-axis parallel to $x$-axis and $y$-axis of image coordinate system respectively. The digital image is represented by an $M \times N$ array of pixels. The 2D coordinates denote the pixel position in the image array.

By geometric analysis, the transformation between pixel coordinate system and world coordinate system can be expressed

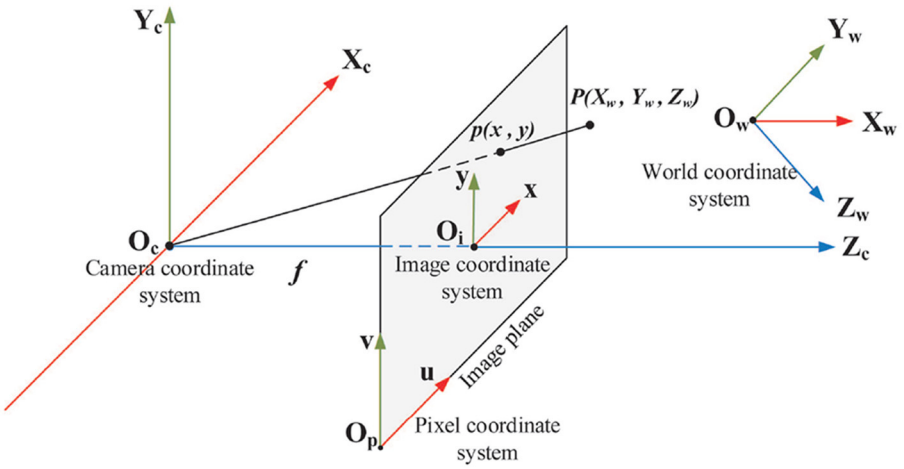


**FIGURE 2 |** Four coordinate systems in the pinhole camera model: world coordinate system, camera coordinate system, image coordinate system and pixel coordinate system. $P(X_w, Y_w, Z_w)$ is a 3D point and $p(x, y)$ is the projection of $P(X_w, Y_w, Z_w)$ in the image plane. $f$ is the focal length that is the length between origin of camera coordinate system and origin of image coordinate system.

in homogeneous form by

$$
\begin{aligned}
Z_c \begin{pmatrix} u \\ v \\ 1 \end{pmatrix} &= \begin{pmatrix} \frac{1}{dx} & 0 & u_0 \\ 0 & \frac{1}{dy} & v_0 \\ 0 & 0 & 1 \end{pmatrix} \begin{pmatrix} f & 0 & 0 & 0 \\ 0 & f & 0 & 0 \\ 0 & 0 & 1 & 0 \end{pmatrix} \begin{pmatrix} R & t \\ 0^T & 1 \end{pmatrix} \begin{pmatrix} X_w \\ Y_w \\ Z_w \\ 1 \end{pmatrix} \\
&= \begin{pmatrix} a_x & 0 & u_0 & 0 \\ 0 & a_y & v_0 & 0 \\ 0 & 0 & 1 & 0 \end{pmatrix} \begin{pmatrix} R & t \\ 0^T & 1 \end{pmatrix} \begin{pmatrix} X_w \\ Y_w \\ Z_w \\ 1 \end{pmatrix} \\
&= M_1 M_2 \begin{pmatrix} X_w \\ Y_w \\ z_w \\ 1 \end{pmatrix} = M \begin{pmatrix} X_w \\ Y_w \\ z_w \\ 1 \end{pmatrix}
\end{aligned} \tag{1}
$$

where $(u_0, v_0)$ are the pixel coordinates of the origin of the image coordinate system in the pixel coordinate system; $dx$ and $dy$ are the physical dimensions of each pixel in the $x$-axis and $y$-axis of the image plane respectively; $f$ is the focal length; $R$ is a $3 \times 3$ orthogonal rotation matrix, and $t$ is a 3D translation vector indicating the transformation from the world coordinate system to the camera coordinate system. It can be seen that the parameters of matrix $M_1$ are determined by the internal structure of the camera sensor. Thus, $M_1$ is called an intrinsic parameter matrix of the camera. The rotation matrix $R$ and translation vector $t$, however, are determined by the position and orientation of the camera coordinate system relative to the world coordinate system. $M_2$ is called the extrinsic parameter matrix of the camera which is determined by three rotation and three translation parameters. Parameters in $M_1$ can be calculated through camera calibration. Solving six pose parameters in $M_2$ is actually called the 6D pose estimation.

## 3.2. Semantic Segmentation

The architecture of the semantic segmentation network is illustrated in **Figure 3**. The entire network is composed of two parts: the encoder network (**Figure 3A**, left) and the decoder network (**Figure 3A**, right). The encoder network is designed to extract features of different scales, which consists of five MaxPooling layers and 16 convolutional layers. Same parameter settings such as the convolutional layer in VGG16 (Simonyan and Zisserman, 2015) are applied in the first 13 convolutional layers. In the decoder network, the Multi-scale Feature Fusion Module (MFFM) is implemented to fuse multi-scale features and output pixel-by-pixel classifications through the final convolutional and softmax layer. The decoder network consists of three MFFMs, two upsampling layers as well as several convolution layers.

In convolutional neural networks, feature maps of different sizes not only have diverse receptive fields but also contain complementary information generally. Therefore, fusing features of different scales is an important technique to improve network performance. Researchers have proposed different solutions for multi-scale feature extraction and fusion. Deeplabv3 (Chen et al., 2017b) utilized Atrous Spatial Pyramid Pooling (ASPP) to fuse global content information with multi-scale features. In Zhao et al. (2017), the global AvgPooling operation is applied to generate different scale outputs from feature maps and to extract high-level semantic multi-scale features. However, these methods parallelly convolute and pool the same feature layer at different scales to acquire multi-scale features. In essence, it is not a real fusion of different layer features since these features are all extended from the same layer. Theoretically, a lower-layer feature contains more geometric detail and less semantic information. Conversely, higher-layer feature maps discard some geometric detail and preserve more semantic information. Thus, a new MFFM is designed to effectively integrate lower-layer and higher-layer features through a densely connected way, thereby enhancing the network's capability of understanding the images.

As shown in **Figure 3B**, each MFFM layer in the decoder takes the feature inputs from two sources: (1) the layers in the encoder with the same or a lower resolution of the current MFFM layer; (2) the previous layer in the decoder. First, all feature inputs will be upsampled to the resolution of the current MFFM layer, if necessary. Then each of them will pass through an individual convolution layer before finally being aggregated together and output. For inputs from encoder layers, the output channel number is set to 64 to reduce computational complexity. For inputs from the previous layer, the output channel number remains unchanged in order to preserve information coming from the previous layer as much as possible. Thus, different MFFM layers may have various numbers of input layers, as depicted in **Figure 3A** by arrows in different colors.

In the training stage, the lost function of the segmentation network is defined as cross-entropy and is expressed by

$$Loss = -\sum_{i=1}^{H}\sum_{j=1}^{W} y'_{i,j} \log y_{i,j}, \tag{2}$$

where $y_{i,j} \in \{1, 2, ..., C\}$ is the true label of each pixel and $y'_{i,j}$ is the prediction.

In sum, the proposed semantic segmentation network provides more effective pixel-by-pixel classification by, in a densely connected way, fusing multi-scale features. Despite the small increase in computational cost, more accurate pixel classifications are helpful in determining the correct correspondences between 2D pixels and 3D points, which is crucial for the second stage of 6D pose estimation. Furthermore, the segmentation network can also extract the correct object contour, showing its ability in dealing with occlusions under complex scenes.

## 3.3. 6D Object Pose Estimation

As mentioned in section 3.1, object pose estimation determines the transform between the object coordinate system and the camera coordinate system. A 3D translation vector $t$ and a 3D rotation matrix $R$ are included in the transformation matrix. So, there are six independent pose parameters to be calculated. **Figure 4** depicts the concept.

The architecture of our 6D pose estimation network is illustrated in **Figure 5**. The entire network is composed of three stages: feature extraction stage (**Figure 5A**), feature fusion stage (**Figure 5B**), and pose regress stage (**Figure 5C**).

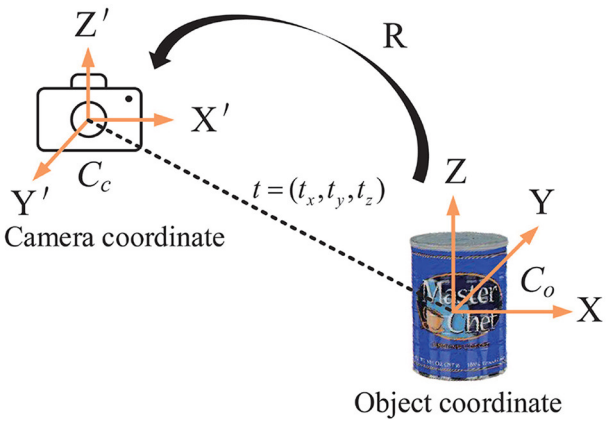


**FIGURE 4 |** Object 6D pose estimation. The pose transformation from the object coordinate system to the camera coordinate system is determined by the 3D rotation matrix $R$ and the 3D translation vector $t$.

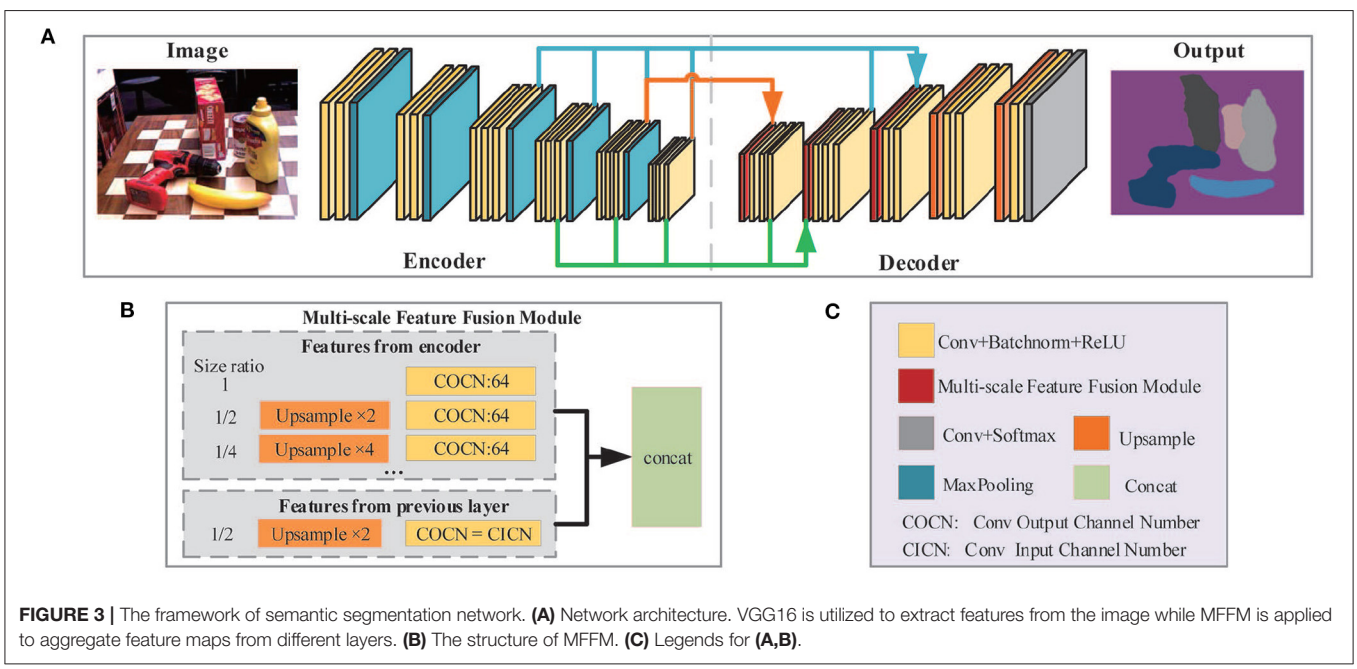


**FIGURE 3 |** The framework of semantic segmentation network. **(A)** Network architecture. VGG16 is utilized to extract features from the image while MFFM is applied to aggregate feature maps from different layers. **(B)** The structure of MFFM. **(C)** Legends for **(A,B)**.

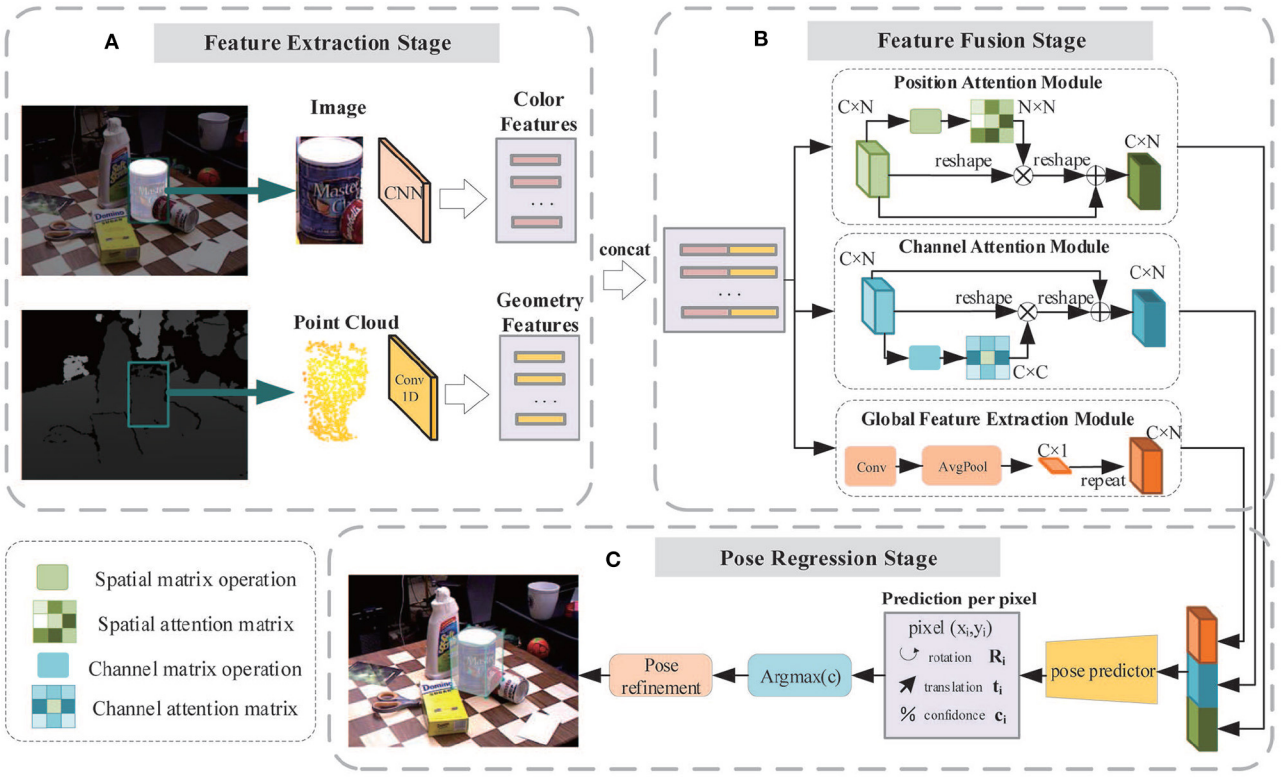


**FIGURE 5 |** The framework of the three-stage 6D pose estimation network. **(A) Feature extraction stage:** The color feature embedding is extracted by a full convolution network and the geometric feature embedding is extracted by a PointNet-based network; **(B) Feature fusion stage:** Two feature embeddings are fused together and then pass through the channel attention module, position attention module, and global feature extraction module, respectively, to generate three types of features. All of them are fused and fed to the pose predictor. **(C) Pose regression stage:** The pose predictor consisting of several 1D convolutions is utilized to regress the 6D pose parameters and confidence scores.

The color and geometric information of objects are acquired through the RGB image and depth image. Though they have similar storage formats, the physical meaning and distribution space are quite different. Two CNNs are applied to extract color and geometric features, respectively, as shown in **Figure 5A**.

Common neural networks generally treat all the features equally. However, some features are better at describing characteristics of objects and should receive more attention. To stress important features whilst suppressing unnecessary ones, we implemented three modules including the Position Attention Module (PAM), Channel Attention Module (CAM), and the Global Feature Extraction Module (GFEM). In the feature fusion stage, color features and geometric features are concatenated and fed into these modules, enabling the network to adaptively capture the local features and the global feature dependencies, providing better features for the pose predictor.

**Position Attention Module:** For a specified input feature, it is updated by weighting all the features according to their similarity to this feature. Thus, more similar features will have a bigger impact on the input feature. **Figure 6** displays the process.

The original input feature matrix $V_i$ ($V_i \in R^{C\times N}$, where C is the feature dimension and N is the number of the features), passes through two convolutional layers separately and get two new feature matrices $V_1$, $V_2$ ($V_1, V_2 \in R^{C'\times N}$. The dimension of $V_1, V_2$' changes from $C$ to $C'$ after passing through, in this paper, we set $C' = \frac{C}{8}$). After transposing $V_1$ multipling $V_2$, and followed by a softmax operation, the feature similarity matrix $M$ ($M \in R^{N\times N}$) is obtained. In the meantime, $V_i$ passes through the third convolution layer to obtain $V_3$ ($V_3 \in R^{C\times N}$), it is then multiplied by $M$ to aggregate global features. Finally, the output features $V_o$ are calculated as $V_o = V_3 \times M + V_i$.

**Channel Attention Module:** For any two channel maps, the self-attention mechanism is used to capture the channel dependencies. The weighted sum of all channel maps is calculated to update each channel map. The process of the channel attention module is shown in **Figure 7**.

**Global Feature Extraction Module:** The global feature of the objects is quite important for the pose estimation task. Here we use a convolutional layer to adjust the features and apply an AvgPooling layer to acquire the global features.

The output features from the PAM, CAM, and GFEM are concatenated and fed into a pose predictor. The pose predictor consists of several 1D convolution layers for regressing 6D pose parameters and confidence scores. In addition, the same iterative

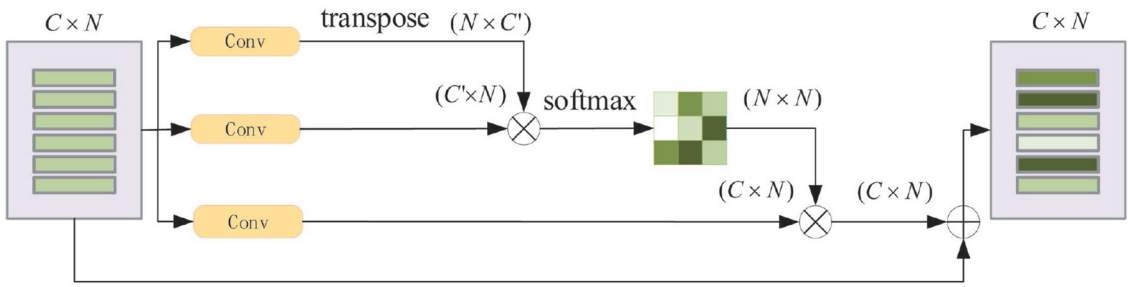


**FIGURE 6 |** Schematic diagram of position attention module. *N* is number of the features and *C* is the feature dimension.

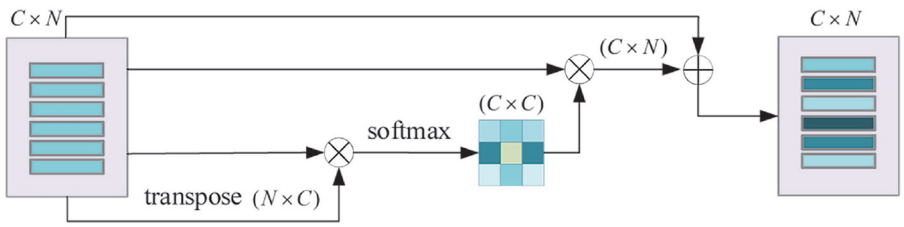


**FIGURE 7 |** Schematic diagram of channel attention module. *N* is the number of features and *C* is the feature dimension.

refinement network as DenseFusion (Wang et al., 2019) is also utilized for further improvement in accuracy of pose estimation.

Due to the lack of a unique shape or texture associated with poses for the objects with symmetric structures, we use two types of loss functions in the training stage. For symmetric objects, the loss for one point in the estimated model is defined as the distance between this point and its closest point after pose transformation. The total loss of an object with $n$ points is computed as follows:

$$L_{sym} = \frac{1}{n}\sum_{i=1}^{n}\min_{i<k<n}\left\|T_{est}p_i - T_{gt}p_k\right\|. \quad (3)$$

where $T = [R|t]$, $R$ and $t$ are rotation matrix and translation vector, respectively. Meanwhile, $p_i$ represents the homogeneous form of $i^{th}$ point. $T_{est}$ is the current predicted result and $T_{gt}$ is the ground truth. For the object with an asymmetric structure, each pose is associated with a unique texture or shape. So, the loss function of the asymmetric object is defined as the average distance of each point after real pose transformation and the predicted pose transformation, as described in Eq. (4). In the training stage, we switch the loss function according to the labels given with the dataset.

$$L_{asy} = \frac{1}{n}\sum_{i=1}^{n}\left\|T_{est}p_i - T_{gt}p_i\right\|. \quad (4)$$

# 4. EXPERIMENTAL RESULTS AND ANALYSIS

## 4.1. Experiment Setup

### 4.1.1. The Platform of Hardware and Software

The proposed network in this paper is built by Pytorch (Paszke et al., 2019). All the experiments are conducted on a PC equipped with an Intel(R) Core(TM) i7-6850k CPU at 3.6GHz and a NVIDIA GeForce GTX1080Ti graphic card.

### 4.1.2. Training Setup

For the segmentation network, the initial learning rate is set to 0.0001, batch size is 4. The Stochastic Gradient Descent (SGD) optimizer is used in the training. The learning rate decreased by 0.8 times for every 5,000 training steps.

For the pose estimation network, the initial learning rate is set to 0.0001, batch size is 8. The Adam optimizer (Kingma and Ba, 2015) is used in the training. When the test error drops to a certain threshold of 0.14, the learning rate starts to decline 0.3 times. When the test error drops to 0.12, the iterative refinement network starts to kick in the training process.

## 4.2. Datasets and Metrics

### 4.2.1. Datasets

Two well-known benchmark datasets, the YCB-video (Xiang et al., 2017) and the LineMOD (Hinterstoisser et al., 2011), were employed in our experiments.

**The YCB-Video dataset** is built from Xiang et al. (2017) for object pose estimation. The dataset is composed of 92 RGB-D video sequences taken in different indoor scenes, and 21 objects with different shapes and textures. Here we follow the

same training and testing settings as the PoseCNN (Xiang et al., 2017) where 80 video sequences are used for training, and 2,949 key frames extracted from the remaining 12 videos are used to evaluate the trained model. In addition, 80,000 synthetically rendered images provided by the dataset are also utilized to augment the training set.

**The LineMOD dataset** (Hinterstoisser et al., 2011) is another benchmark dataset for object pose estimation, which contains 15 video sequences of low-texture objects. There are approximately 1,100 images in each video sequence. For a fair comparison, we choose the same 13 video sequences, and the same training and testing set as some state-of-the-art methods (Kehl et al., 2017; Rad and Lepetit, 2017; Xiang et al., 2017; Li et al., 2018b; Sundermeyer et al., 2018; Xu et al., 2018). Besides, no synthetic data are generated from the LineMOD dataset and used for training.

#### 4.2.2. Metrics

**Metrics for semantic segmentation**. Two common metrics, Mean Pixel Accuracy (mPA) and Mean Intersection over Union (mIoU) (Badrinarayanan et al., 2017; Garcia-Garcia et al., 2017) are used to evaluate the segmentation results. The mPA is defined as the mean of pixel accuracy for all classes, where the pixel accuracy is computed by the ratio of correct pixels on a per-class basis. The mIoU is defined as the mean of IoUs for all classes in the dataset, where IoU for each class is computed as the ratio of the intersection and the union of label pixels and predicted pixels.

**Metrics for pose estimation**. We adopted three metrics to evaluate system performance on the YCB-Video dataset, namely, ADD-S (Xiang et al., 2017) (the average closest point distance), ADD (the average distance) (Hinterstoisser et al., 2012), and AUC (Xiang et al., 2017) (the area under the accuracy-threshold curve of ADD/ADD-S). Given the ground truth pose $P$ ($P = [R|T]$) and estimated pose $\tilde{P}$ ($\tilde{P} = [\tilde{R}|\tilde{T}]$), we can calculate the distance between the point in the 3D model transformed by $\tilde{P}$ and the nearest point to it in the 3D model transformed by $P$. The average distance of all points is called ADD-S. ADD has a similar definition as ADD-S, the difference is that the distance is calculated from corresponding point pairs in the 3D model transformed by $\tilde{P}$ and $P$. In our experiments, the accuracy, defined as the percentage of testing samples with ADD/ADD-S values less than a certain threshold, is used to evaluate the performance of all methods. Here, the threshold is empirically set to 2 cm. The accuracy values for all possible thresholds are calculated and an accuracy-threshold curve of ADD/ADD-S is generated. AUC is then defined as the area under this curve within the threshold region $[0, T_m]$. To have a consistent measurement, the maximum threshold $T_m$ is set to 0.1 m. For AUC and accuracy, a larger value indicates better accuracy of pose estimation.

For LineMOD dataset, ADD (Hinterstoisser et al., 2012) is used as the metric following prior works (Kehl et al., 2017; Rad and Lepetit, 2017; Xiang et al., 2017; Li et al., 2018b; Sundermeyer et al., 2018; Xu et al., 2018). Instead of a fixed value, we set the distance threshold as 0.1 multiplied by the diameter of bounding sphere of the 3D model.

### 4.3. Experiments on YCB-Video Dataset

**Semantic segmentation: Table 1** shows the comparative experiment results of pose estimation on the YCB-Video Dataset where bold numbers represent the best results for each metric. It is observed that our network is much better than the U-Net in both mPA and mIoU. Moreover, our mPA score is a little bit smaller than Deeplabv3 whilst our mIoU score outperforms Deeplabv3 by 2.78.

**6D Pose estimation: Tables 2**, **3** show the comparative experiment results of pose estimation on 21 objects in the YCB-Video Dataset using our method and some state-of-the-art methods, where the bold numbers represent the best results. In **Table 2**, AUC and accuracy of ADD-S (<2 cm) are calculated for all objects. As seen from the table, our mean accuracy score is the second-best and the mean AUC score is the best. The overall performance is very close to DenseFusion which is the benchmark method thus far. In **Table 3**, AUC and accuracy of ADD (<2 cm) are calculated. Apparently both mean accuracy score and mean AUC score of the proposed network outperform all the other methods. Essentially, ADD is a better and stricter metric than ADD-S because it computes the distances between matched point pairs, which usually requires matches on both shape and texture. A better ADD accuracy score is more convincible in evaluating the performance of our method. **Figure 8A** displays the accuracy-threshold curve of the rotation error and **Figure 8B** displays the accuracy-threshold curve of the translation error. The rotation error is the angle formed by the predicted and true rotation axes. The translation error is the 2-Norm of the difference between the predicted and true translation vectors. Accuracy is therefore defined as the percentage of testing samples with fewer translation/rotation errors than a threshold. For each threshold, the corresponding accuracy is calculated to build the accuracy-threshold curve. **Figures 8A,B** exhibit the superior accuracy of our method in both rotation and translation predictions. Moreover, a steeper curve is observed near zero degrees in the accuracy-threshold curve of the rotation error, showing that the proposed method can achieve higher accuracy at a small rotation error threshold, which indicates the smaller pose estimation errors.

**Figure 9** displays some qualitative results on the YCB-Video dataset. **Figure 9A** is the original images in the dataset. **Figures 9B,D** are segmentation results of DenseFusion and our method. Different colors stand for different object categories here. After acquiring the segmentation mask, the pixel-level area of each object in the image is extracted. If the effective pixel number in the depth map of an object is less than a certain threshold, it is identified as an invalid object without estimating its poses. For each valid object, the point cloud is transformed

**TABLE 1** | Quantitative evaluation of semantic segmentation on YCB-Vedio dataset.

| | mPA(%) | mIoU(%) |
|---|---|---|
| U-Net | 58.02 | 48.01 |
| Deeplabv3 | **84.85** | 76.28 |
| Ours | 84.28 | **79.06** |

*Bold values represent the best results for all metrics.*

**TABLE 2 |** Quantitative evaluation of 6D pose estimation (ADD-S) on YCB-Video Dataset.

| | PoseCNN | | PoseCNN+ICP | | PointFusion | | DenseFusion | | Ours | |
|---|---|---|---|---|---|---|---|---|---|---|
| **Object** | **AUC** | **<2 cm** | **AUC** | **<2 cm** | **AUC** | **<2 cm** | **AUC** | **<2 cm** | **AUC** | **<2 cm** |
| 002 master chef can | 83.9 | 71.5 | 95.8 | **100.0** | 90.9 | 99.8 | **96.4** | **100.0** | 96.1 | **100.0** |
| 003 cracker box | 76.9 | 56.6 | 92.7 | 91.6 | 80.5 | 62.6 | 95.5 | 99.5 | **96.1** | **99.9** |
| 004 sugar box | 84.2 | 71.2 | **98.2** | **100** | 90.4 | 95.4 | 97.5 | **100.0** | 97.2 | **100.0** |
| 005 tomato soup can | 81.0 | 74.4 | 94.5 | **96.9** | 91.9 | **96.9** | **94.6** | **96.9** | 94.2 | **96.9** |
| 006 mustard bottle | 90.4 | 95.8 | **98.6** | **100.0** | 88.5 | 84.0 | 97.2 | **100.0** | 97.2 | **100.0** |
| 007 tuna fish can | 88.0 | 84.8 | **97.1** | 99.7 | 93.8 | 99.8 | 96.6 | **100.0** | 96.4 | **100.0** |
| 008 pudding box | 79.1 | 58.4 | **97.9** | **100.0** | 87.5 | 96.7 | 96.5 | **100.0** | 96.6 | **100.0** |
| 009 gelatin box | 87.2 | 89.7 | **98.8** | **100.0** | 95.0 | **100.0** | 98.1 | **100.0** | 97.5 | **100.0** |
| 010 potted meat can | 78.5 | 68.0 | **92.7** | **93.6** | 86.4 | 88.5 | 91.3 | 93.1 | 90.9 | 93.0 |
| 011 banana | 86.0 | 84.2 | **97.1** | 99.7 | 84.7 | 70.5 | 96.6 | **100.0** | 95.6 | 99.7 |
| 019 pitcher base | 77.0 | 38.8 | **97.8** | 100.0 | 85.5 | 79.8 | 97.1 | **100.0** | 97.0 | **100.0** |
| 021 bleach cleanser | 71.6 | 39.7 | **96.9** | 99.4 | 81.0 | 65.0 | 95.8 | **100.0** | 96.0 | **100.0** |
| 024 bowl | 69.6 | 14.0 | 81.0 | 54.9 | 75.7 | 24.1 | **88.2** | **98.8** | 87.4 | 83.5 |
| 025 mug | 78.2 | 58.5 | 94.9 | 99.8 | 94.2 | 99.8 | **97.1** | **100.0** | 97.1 | 99.5 |
| 035 power drill | 72.7 | 53.1 | **98.2** | **99.6** | 71.5 | 22.8 | 96.0 | 98.7 | 96.1 | 99.5 |
| 036 wood block | 64.3 | 8.3 | 87.6 | 80.2 | 68.1 | 18.2 | **89.7** | **94.6** | 86.9 | 79.3 |
| 037 scissors | 56.9 | 18.2 | 91.7 | 95.6 | 76.7 | 35.9 | **95.2** | **100.0** | 94.0 | **100.0** |
| 040 large marker | 71.7 | 46.1 | 97.2 | 99.7 | 87.9 | 80.4 | **97.5** | **100.0** | 97.0 | **100.0** |
| 051 large clamp | 50.2 | 31.7 | 75.2 | 74.9 | 65.9 | 50.0 | 72.9 | **79.2** | **73.3** | 78.5 |
| 052 extra-large clamp | 44.1 | 17.6 | 64.4 | 48.8 | 60.4 | 20.1 | 69.8 | **76.3** | **73.6** | 72.4 |
| 061 foam brick | 88.0 | 87.5 | **97.2** | **100.0** | 91.8 | **100.0** | 92.5 | **100.0** | 95.3 | **100.0** |
| **Mean** | 75.8 | 58.2 | 93.0 | 93.2 | 83.9 | 74.1 | 93.1 | **96.8** | **93.2** | 96.0 |

*Bold values represent the best results for all metrics.*

**TABLE 3 |** Quantitative evaluation of 6D pose estimation (ADD) on YCB-Video Dataset.

| | PoseCNN | | PoseCNN+ICP | | DenseFusion | | Ours | |
|---|---|---|---|---|---|---|---|---|
| **Object** | **AUC** | **<2 cm** | **AUC** | **<2 cm** | **AUC** | **<2 cm** | **AUC** | **<2 cm** |
| 002 master chef can | 50.2 | 8.25 | 68.1 | 51.1 | 73.2 | **72.8** | **73.4** | **72.8** |
| 003 cracker box | 53.1 | 13.0 | 83.4 | 73.3 | 94.2 | 98.2 | **94.4** | **99.1** |
| 004 sugar box | 68.4 | 41.1 | **97.2** | 99.5 | 96.5 | **100.0** | 95.6 | 99.9 |
| 005 tomato soup can | 66.2 | 42.9 | 81.8 | 76.6 | 85.4 | 82.9 | **89.5** | **89.8** |
| 006 mustard bottle | 81.0 | 62.8 | **98.0** | 98.6 | 94.8 | 96.1 | 95.5 | **100.0** |
| 007 tuna fish can | 70.7 | 47.3 | **83.9** | **72.1** | 81.9 | 62.8 | 79.8 | 60.5 |
| 008 pudding box | 62.7 | 25.7 | **96.6** | **100.0** | 93.2 | 98.6 | 94.5 | **100.0** |
| 009 gelatin box | 75.2 | 32.7 | **98.1** | **100.0** | 96.7 | **100.0** | 96.0 | **100.0** |
| 010 potted meat can | 59.5 | 30.4 | 83.5 | 77.9 | **83.6** | 79.8 | **82.0** | 80.0 |
| 011 banana | 72.3 | 31.4 | **91.9** | 88.1 | 83.5 | **88.7** | 75.6 | 79.2 |
| 019 pitcher base | 53.3 | 12.1 | **96.9** | 97.7 | **96.9** | 99.8 | 95.9 | **100.0** |
| 021 bleach cleanser | 50.3 | 11.4 | **92.5** | **92.7** | 90.1 | 90.4 | 90.7 | 90.6 |
| 024 bowl | 3.33 | 0.0 | **14.4** | **0.25** | 5.85 | 0.00 | 7.59 | 0.0 |
| 025 mug | 58.5 | 17.5 | 81.1 | 55.2 | 88.9 | 89.5 | **92.0** | **92.6** |
| 035 power drill | 55.3 | 25.7 | **97.7** | **99.2** | 92.8 | 96.3 | 93.8 | **99.2** |
| 036 wood block | 26.6 | 0.83 | **70.8** | **64.9** | 30.8 | 0.0 | 24.5 | 0.0 |
| 037 scissors | 35.8 | 2.2 | 78.4 | 49.2 | 77.9 | 50.3 | **87.8** | **85.1** |
| 040 large marker | 58.3 | 14.8 | 85.3 | 87.2 | **93.0** | **100.0** | 92.5 | 99.9 |
| 051 large clamp | 24.6 | 3.7 | **52.1** | 36.4 | 26.4 | 0.0 | 40.5 | **38.1** |
| 052 extra-large clamp | 16.1 | 2.9 | 26.5 | 8.2 | 24.6 | 16.6 | **46.6** | **40.0** |
| 061 foam brick | 40.2 | 0.0 | 48.1 | 0.0 | **59.1** | 0.0 | 44.1 | 0.0 |
| **MEAN** | 53.7 | 23.3 | 79.2 | 71.3 | 78.0 | 73.7 | **79.7** | **78.0** |

*Bold values represent the best results for all metrics.*

with the predicted pose parameters. Its projection in the 2D image is then superimposed over the object region, as shown in **Figures 9C,E**. As illustrated in the second column from the left, the prediction for the bowl by DenseFusion is far away from its real orientation. Our method, however, provides a more correct prediction showing its advantage in dealing with symmetric objects. For some poor-textured objects, such as the banana in the first and fourth column, obvious errors are spotted for DenseFusion with no visually perceptible errors for our method.

**Time efficiency. Table 4** shows the time efficiency comparison of our network with PoseCNN and DenseFusion. The time cost of all computation components including segmentation, pose estimation, and iterative refinement are calculated, respectively, for a more intuitive comparison except for PoseCNN, as it is not a pipeline structure network. For the total running time, our method is five times faster than PoseCNN. Compared with DenseFusion, our method is slightly slower in segmentation, while being slightly faster in pose estimation. Although the total time consumption is slightly lower than DenseFusion, it meets the requirements of real-time applications at a processing rate of 18 frames per second with about five objects in each frame. Considering the better accuracy of pose estimation, our method is overall proved to be the best among these state-of-the-art methods. What is more, a lightweight network will be applied for feature extraction in the future, which is expected to improve the time efficiency tremendously.

## 4.4. Experiments on LineMOD Dataset

**Table 5** shows the comparison of our method with some other methods [BB8(Rad and Lepetit, 2017), PoseCNN+DeepIM

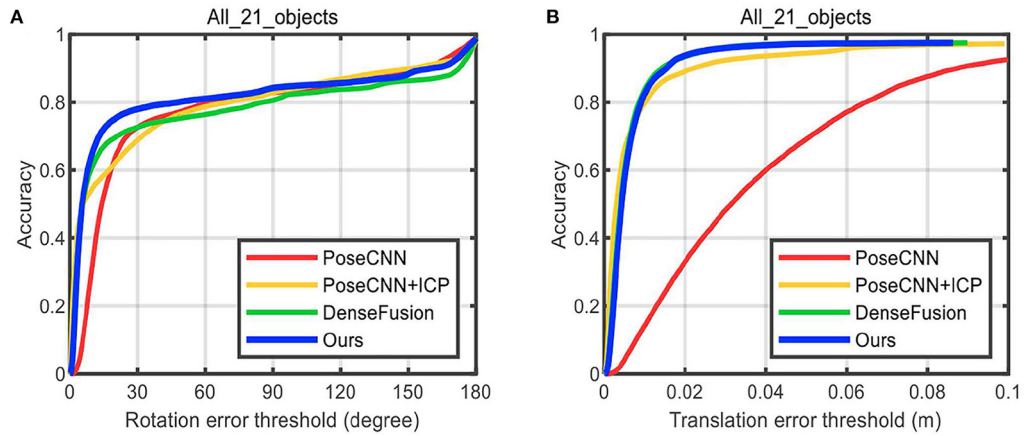


**FIGURE 8 |** The accuracy-threshold curves of pose parameter error. **(A)** The accuracy-threshold curve of rotation angle error, **(B)** The accuracy-threshold curve of translation error.

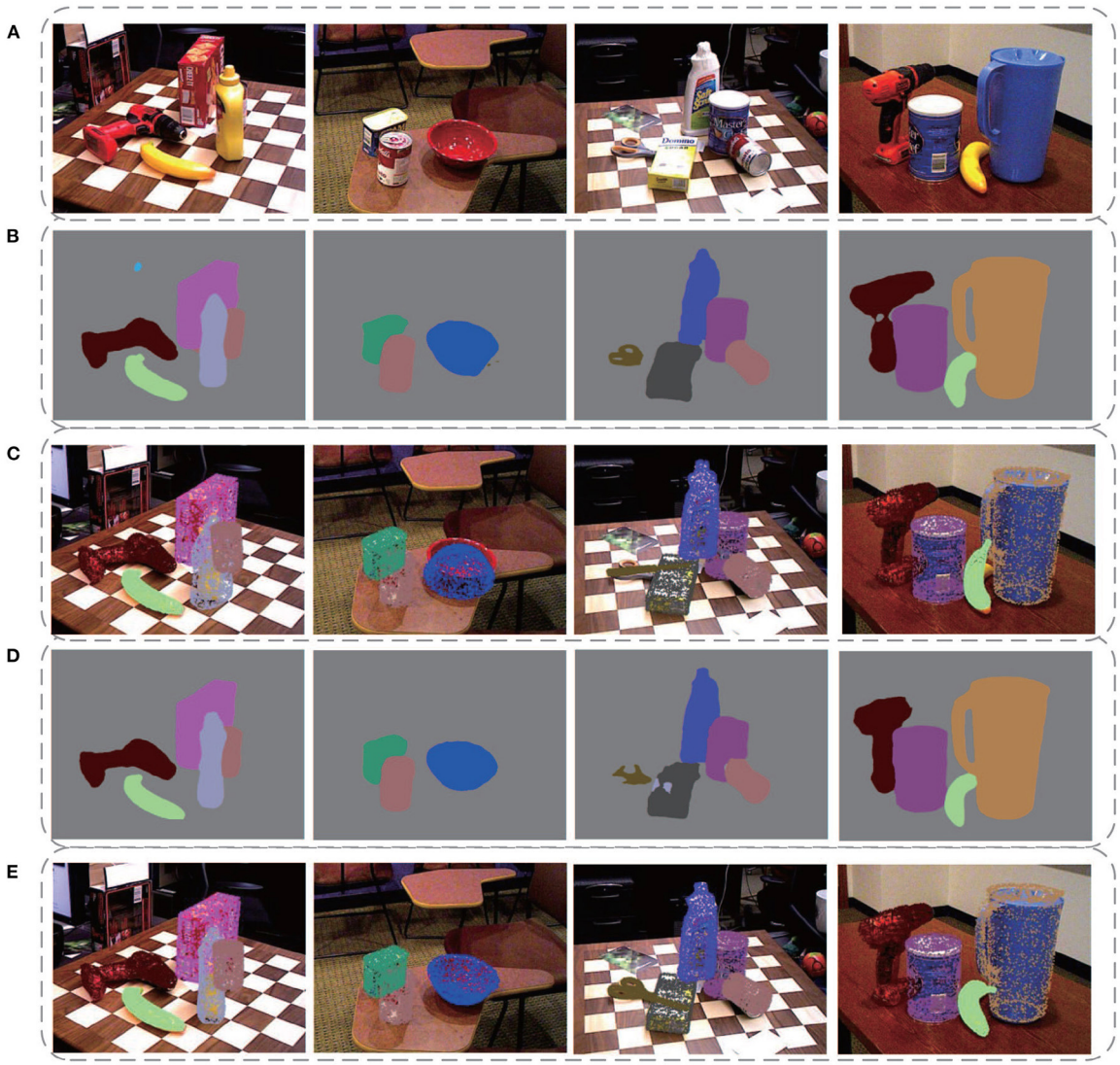


**FIGURE 9 |** Some qualitative experimental results on the YCB-Video dataset. **(A)** The original images in the dataset, **(B)** Segmentation results of DenseFusion, **(C)** Pose estimation results of DenseFusion, **(D)** Segmentation results of our method, **(E)** Pose estimation results of our method.

**TABLE 4 |** Time efficiency of three methods (sec.).

| PoseCNN | DenseFusion | | | | Ours | | | |
|---|---|---|---|---|---|---|---|---|
| Seg+PE (ALL) | Seg | PE | Refine | ALL | Seg | PE | Refine | ALL |
| 0.283 | 0.035 | 0.010 | 0.002 | 0.047 | 0.045 | 0.009 | 0.002 | 0.056 |

*Seg, segmentation; PE, pose estimation; Refine, iterative refinement.*

**TABLE 5 |** Quantitative evaluation of 6D pose estimation (ADD) on LineMOD Dataset.

| | RGB | | RGB-D | | | | |
|---|---|---|---|---|---|---|---|
| | BB8 | PoseCNN | Implicit | SSD-6D | Point Fusion | Dense Fusion | Ours |
| object | | +DeepIM | +ICP | +ICP | | | |
| ape | 40.4 | 77.0 | 20.6 | 65 | 70.4 | **92.3** | 91.8 |
| benchvise | 91.8 | 97.5 | 64.3 | 80 | 80.7 | 93.2 | **96.9** |
| camera | 55.7 | 93.5 | 63.2 | 78 | 60.8 | 94.4 | **98.3** |
| can | 64.1 | 96.5 | 76.1 | 86 | 61.1 | 93.1 | **96.9** |
| cat | 62.6 | 82.1 | 72.0 | 70 | 79.1 | 96.5 | **97.0** |
| driller | 74.4 | 95.0 | 41.6 | 73 | 47.3 | 87.0 | **94.7** |
| duck | 44.3 | 77.7 | 32.4 | 66 | 63.0 | 92.3 | **95.3** |
| eggbox | 57.8 | 97.1 | 98.6 | **100** | 99.9 | 99.8 | **100.0** |
| glue | 41.2 | 99.4 | 96.4 | **100** | 99.3 | 100.0 | **100.0** |
| holepuncher | 67.2 | 52.8 | 49.9 | 49 | 71.8 | 92.1 | **96.2** |
| iron | 84.7 | **98.3** | 63.1 | 78 | 83.2 | 97.0 | 97.8 |
| lamp | 76.5 | **97.5** | 91.7 | 73 | 62.3 | 95.3 | **97.5** |
| phone | 54.0 | 87.7 | 71.0 | 79 | 78.8 | 92.8 | **97.5** |
| MEAN | 62.7 | 88.6 | 64.7 | 79 | 73.7 | 94.3 | **96.9** |

*Bold values represent the best results for all metrics.*

(Xiang et al., 2017; Li et al., 2018b), Implicit (Sundermeyer et al., 2018)+ICP, SSD-6D (Kehl et al., 2017)+ICP, PointFusion (Xu et al., 2018), DenseFusion (Wang et al., 2019)] on the LineMOD Dataset with the accuracy of ADD (< 2cm) adopted as metric. For the mean accuracy, our method outperforms DenseFusion by 2.6, **Figure 10** visualizes the pose estimation results of our method on LineMOD Dataset. As expected, only small errors are perceived in these images even if under cluttered environments.

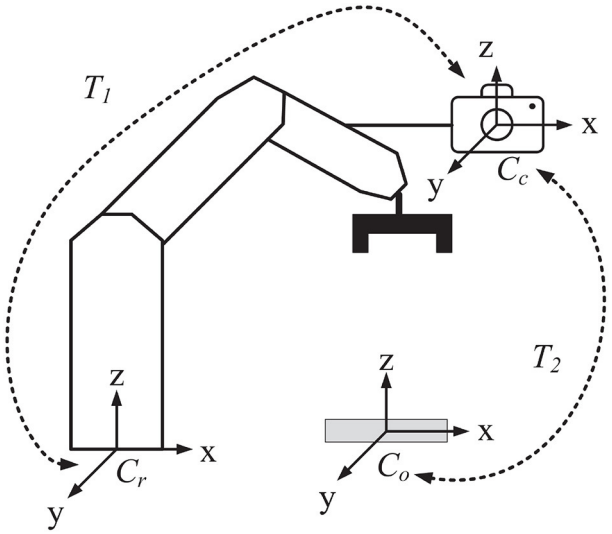


**FIGURE 11 |** The framework of a vision-guided robotic grasping system.

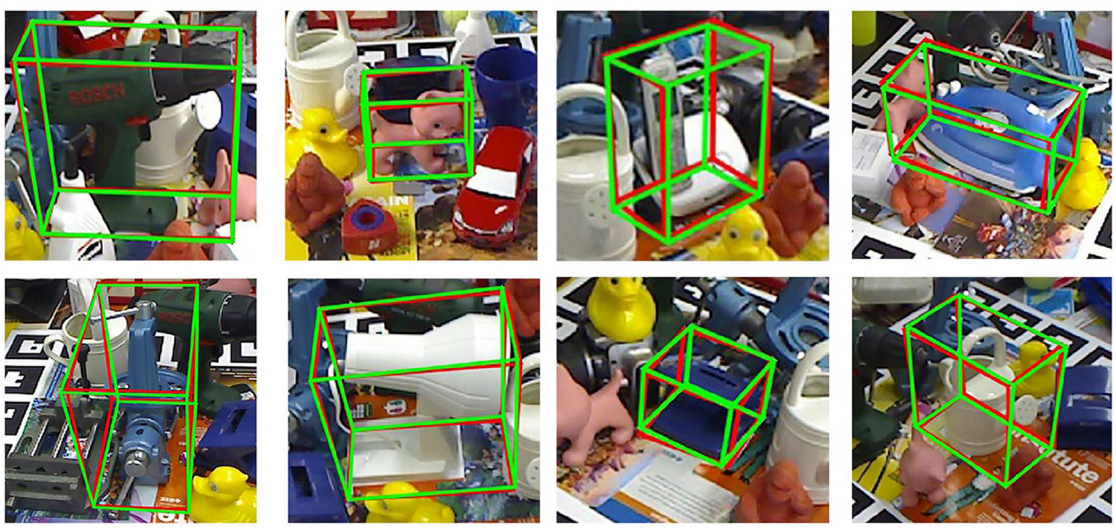

**FIGURE 10 |** Pose estimation results of our method for some images with cluttered background in the LineMOD dataset. The red box and the green box are 2D projections of the 3D bounding box of objects which, transformed by true pose parameters and predicted ones, respectively.

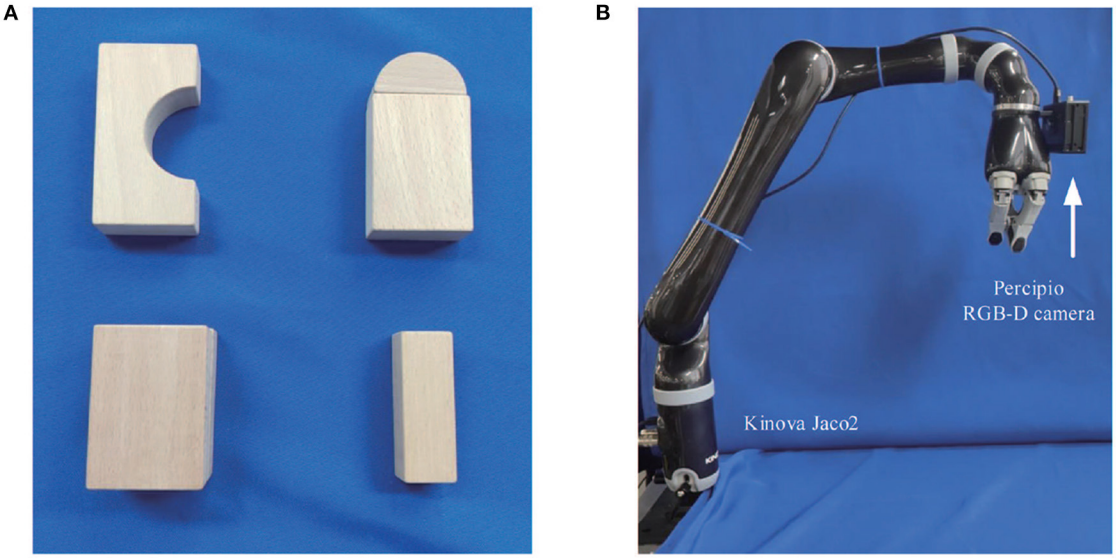


**FIGURE 12 |** Equipment and target objects used in grasping experiments. **(A)** Some building blocks as target objects, **(B)** The Kinova Jaco2 manipulator with a percipio RGB-D camera installed on the side of the gripper.

## 4.5. Vision-guided Robotic Grasping System

Object recognition and pose estimation methods can be widely used in robot visual servo systems (Xu et al., 2019, 2020; Wu et al., 2020). In order to explore the feasibility of the proposed method being applied in manufacturing industry scenarios, we have built a vision-guided robotic system for the most common manufacturing task: object grasping. The framework of the system is illustrated in **Figure 11**. A camera is installed on the manipulator of the robot. Three coordinate systems are labeled including the robot coordinate system $C_r$, the camera coordinate system $C_c$, and the object coordinate system $C_o$. $T_1$ is the 6D transform from $C_r$ to $C_c$, and $T_2$ is that from $C_o$ to $C_c$. $T_1$ is calculated by the famous navy hand-eye calibration algorithm (Park and Martin, 1994) and $T_2$ is predicted by the proposed algorithm. The object poses relative to the robot are then computed as $T = T_1 \times T_2$. The pose matrix is crucial for manipulator path planning and motion control in the grasping task.

The system is composed of a 6 DOF Kinova Jaco2 manipulator and a percipio RGB-D camera FM830-I installed on the side of the gripper, as shown in **Figure 12B**. The percipio camera utilizes structured light as well as binocular vision to build accurate depth maps. The precision of the captured depth data is up to 1 mm. Morevoer, we also take some building blocks as the target objects in the grasping experiments, as **Figure 12A** shows.

Before the experiment, first we need to calibrate $T_1$, then train the semantic segmentation network and 6D pose estimation network. The experiment process is explained as follows: (1) Before grabbing objects, the manipulator should move to a certain position. (2) The RGB-D camera starts to capture images and sends the data to the image processing server. (3) On the server, the RGB-D images are fed into the segmentation network and pose estimation network to predict the 6D pose parameters of the target objects. (4) Based on the predicted transformation matrix, the host computer completes path planning and sends signals to the manipulator making it move to planned positions and performs the operation of grabbing objects, and then placing them in the target area.

Some experimental results are illustrated in **Figure 13**. In this case, the segmentation is perfect. However, for some objects, the predictions are not satisfactory. One possible reason is that the poor-textured building blocks may mislead the color feature extractor. In general, the grasping operation runs quickly and smoothly, which, to some extent, verifies the possibility of the new network being applied to all kinds of manufacturing applications. **Figure 14** shows the complete process of the grasping experiment.

## 5. CONCLUSION

This paper presents a new two-stage deep neural network which can efficiently implement object recognition and 6D pose estimation on the input RGB-D images. First, a segmentation network is applied to segment the object from the scene using a densely connected way to fuse different scale features and effectively improve the semantic segmentation results. Second, by introducing the channel and position attention modules, better color and geometric features are extracted for the pose predictor; third, the output pose parameters are further improved by an iterative refinement network. A large number of experiments conducted on two benchmark datasets demonstrated the effectiveness and accuracy of the proposed method in comparison with some state-of-the-art methods. Moreover, a vision-guided robotic grasping system was built, and the grasping experiment has verified the potential of this algorithm being

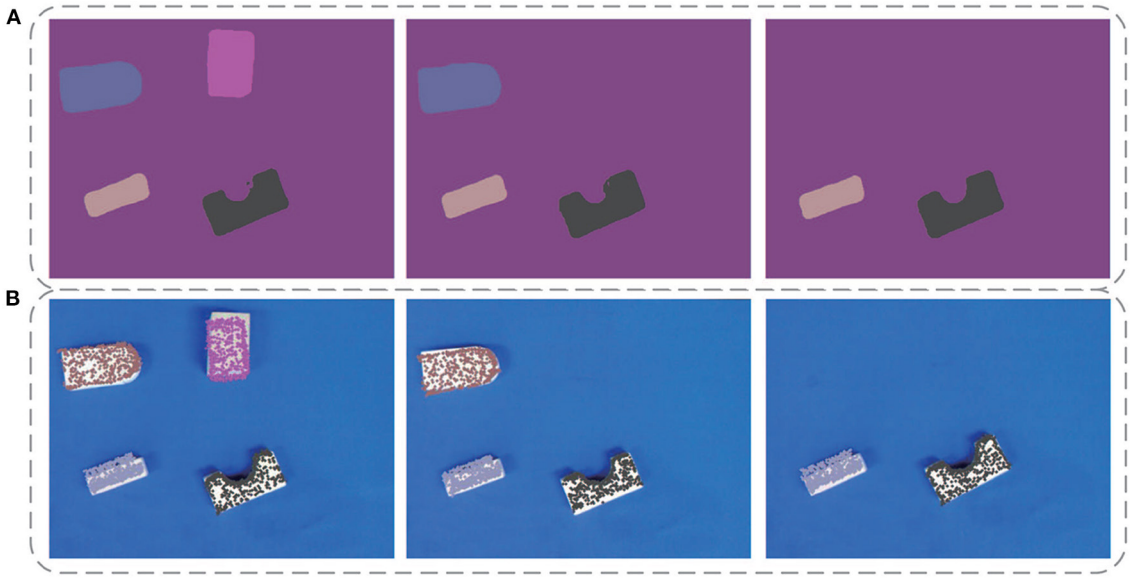


**FIGURE 13 |** Some experimental results of the robot vision system. Panel **(A)** show the segmentation results, where different colors represent different objects. Panel **(B)** shows the pose estimation results, where the colored points are the 2D projections of the target object point cloud after pose transform.

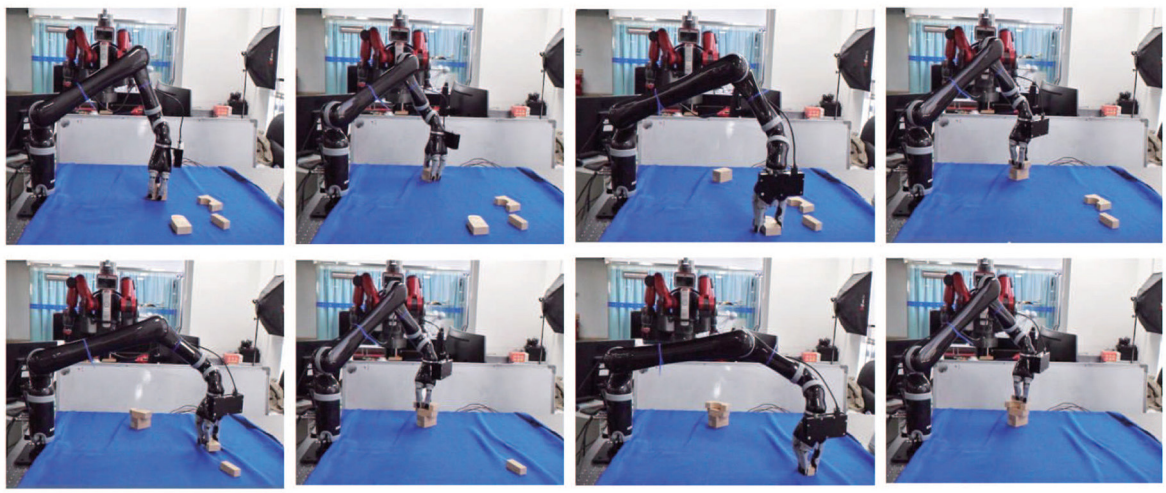

**FIGURE 14 |** The complete process of picking objects and moving it to target area by the manipulator.

applied in real-time manufacturing applications. Currently, the proposed method still has some problems in dealing with textureless or poor-textured objects. Finer differential geometric features with clear physical meaning and better shape detail are preferred and will be considered in future work.

## DATA AVAILABILITY STATEMENT

The two benchmark datasets LineMod and YCB-Video analyzed for this study can be found at http://campar.in.tum.de/Main/StefanHinterstoisser and https://rse-lab.cs.washington.edu/projects/posecnn/. The building block dataset used in robotic grasping experiments in this paper is built by ourselves and will be made available to any qualified researcher. Further inquiries can be directed to the corresponding author/s.

## AUTHOR CONTRIBUTIONS

GL conceived the research project. FC, YL, and YF provided support and discussions. GL, FC, and YL proposed the new algorithm. FC, YL, and YF built the whole program and conducted the experiments. GL, FC, and YL wrote the paper. XW and CW performed the English corrections. All authors reviewed and approved the submitted paper.

## FUNDING

This article was partially supported by the Key-Area Research and Development Program of Guangdong Province (No. 2020B090925002), the Joint Fund of National Natural Science Foundation of China with Shenzhen City (No. U1813209, No. U1913211), and the Shenzhen Fundamental Research Project (No. JCYJ20170818153048647).

## REFERENCES

Badrinarayanan, V., Kendall, A., and Cipolla, R. (2017). Segnet: a deep convolutional encoder-decoder architecture for scene segmentation. *IEEE Trans. Pattern Anal. Mach. Intell.* 39, 1–1. doi: 10.1109/TPAMI.2016.2644615

Brachmann, E., Krull, A., Michel, F., Gumhold, S., Shotton, J., and Rother, C. (2014). "Learning 6D object pose estimation using 3D object coordinates," in *European Conference on Computer Vision (ECCV)* (Cham: Springer), 536–551. doi: 10.1007/978-3-319-10605-2_35

Chen, L.-C., Papandreou, G., Kokkinos, I., Murphy, K., and Yuille, A. L. (2017a). Deeplab: Semantic image segmentation with deep convolutional nets, atrous convolution, and fully connected CRFs. *IEEE Trans. Pattern Anal. Mach. Intell.* 40, 834–848. doi: 10.1109/TPAMI.2017.2699184

Chen, L. C., Papandreou, G., Schroff, F., and Adam, H. (2017b). Rethinking atrous convolution for semantic image segmentation. *arXiv preprint arXiv:1706.05587*.

Drozdzal, M., Vorontsov, E., Chartrand, G., Kadoury, S., and Pal, C. (2016). "The importance of skip connections in biomedical image segmentation," in *Deep Learning and Data Labeling for Medical Applications* (Cham: Springer), 179–187. doi: 10.1007/978-3-319-46976-8_19

Garcia-Garcia, A., Orts-Escolano, S., Oprea, S., Villena-Martinez, V., and Garcia-Rodriguez, J. (2017). A review on deep learning techniques applied to semantic segmentation. *arXiv preprint arXiv:1704.06857*. doi: 10.1016/j.asoc.2018.05.018

Gu, C., and Ren, X. (2010). "Discriminative mixture-of-templates for viewpoint classification," in *European Conference on Computer Vision (ECCV)* (Berlin; Heidelberg: Springer), 408–421. doi: 10.1007/978-3-642-15555-0_30

Hinterstoisser, S., Holzer, S., Cagniart, C., Ilic, S., Konolige, K., Navab, N., et al. (2011). "Multimodal templates for real-time detection of texture-less objects in heavily cluttered scenes," in *International Conference on Computer Vi sion (ICCV)* (Barcelona: IEEE), 858–865. doi: 10.1109/ICCV.2011.6126326

Hinterstoisser, S., Lepetit, V., Ilic, S., Holzer, S., Bradski, G., Konolige, K., et al. (2012). "Model based training, detection and pose estimation of texture-less 3d objects in heavily cluttered scenes," in *Asian Conference on Computer Vision (ACCV)* (Berlin; Heidelberg: Springer), 548–562. doi: 10.1007/978-3-642-33885-4_60

Kehl, W., Manhardt, F., Tombari, F., Ilic, S., and Navab, N. (2017). "SSD-6D: Making RGB-based 3D detection and 6D pose estimation great again," in *International Conference on Computer Vision (ICCV)* (Venice: IEEE), 1521–1529. doi: 10.1109/ICCV.2017.169

Kingma, D. P., and Ba, J. (2015). "ADAM: a method for stochastic optimization," in *International Conference on Learning Representations (ICLR)* (San Diego, CA: ICLR), 1521–1529.

Lee, S., Wei, L., and Naguib, A. M. (2016). "Adaptive Bayesian recognition and pose estimation of 3d industrial objects with optimal feature selection," in *International Symposium on Assembly and Manufacturing (ISAM)* (Fort Worth, TX: IEEE), 50–55. doi: 10.1109/ISAM.2016.7750717

Lepetit, V., Moreno-Noguer, F., and Fua, P. (2009). EPNP: an accurate o (n) solution to the PNP problem. *Int. J. Comput. Vis.* 81:155. doi: 10.1007/s11263-008-0152-6

Li, C., Bai, J., and Hager, G. D. (2018a). "A unified framework for multi-view multi-class object pose estimation," in *European Conference on Computer Vision (ECCV)* (Cham: Springer), 254–269. doi: 10.1007/978-3-030-01270-0_16

Li, Y., Wang, G., Ji, X., Xiang, Y., and Fox, D. (2018b). "DeepIM: deep iterative matching for 6d pose estimation," in *European Conference on Computer Vision (ECCV)* (Cham: Springer), 695–711. doi: 10.1007/978-3-030-01231-1_42

Liu, W., Anguelov, D., Erhan, D., Szegedy, C., Reed, S., Fu, C.-Y., et al. (2016). "SSD: single shot multibox detector," in *European Conference on Computer Vision (ECCV)* (Cham: Springer), 21–37. doi: 10.1007/978-3-319-46448-0_2

Long, J., Shelhamer, E., and Darrell, T. (2015). "Fully convolutional networks for semantic segmentation," in *Conference on Computer Vision and Pattern Recognition (CVPR)* (Boston, MA: IEEE), 3431–3440. doi: 10.1109/CVPR.2015.7298965

Nigam, A., Penate-Sanchez, A., and Agapito, L. (2018). Detect globally, label locally: learning accurate 6-dof object pose estimation by joint segmentation and coordinate regression. *IEEE Robot. Autom. Lett.* 3, 3960–3967. doi: 10.1109/LRA.2018.2858446

Park, F. C., and Martin, B. J. (1994). Robot sensor calibration: solving ax= xb on the euclidean group. *IEEE Trans. Robot. Autom.* 10, 717–721. doi: 10.1109/70.326576

Paszke, A., Gross, S., Massa, F., Lerer, A., Bradbury, J., Chanan, G., et al. (2019). "Pytorch: An imperative style, high-performance deep learning library," in *Advances in Neural Information Processing Systems (NIPS)*, eds. H. Wallach, H. Larochelle, A. Beygelzimer, F. dAlché-Buc, E. Fox, and R. Garnett (Vancouver, BC: Curran Associates, Inc.), 8024–8035.

Qi, C. R., Liu, W., Wu, C., Su, H., and Guibas, L. J. (2018). "Frustum pointnets for 3d object detection from RGB-D data," in *Conference on Computer Vision and Pattern Recognition (CVPR)* (Salt Lake City, UT: IEEE), 918–927. doi: 10.1109/CVPR.2018.00102

Rad, M., and Lepetit, V. (2017). "BB8: a scalable, accurate, robust to partial occlusion method for predicting the 3d poses of challenging objects without using depth," in *International Conference on Computer Vision (ICCV)* (Venice: IEEE), 3828–3836. doi: 10.1109/ICCV.2017.413

Ronneberger, O., Fischer, P., and Brox, T. (2015). "U-net: convolutional networks for biomedical image segmentation," in *International Conference on Medical Image Computing and Computer-Assisted Intervention (MICCAI)* (Cham: Springer), 234–241. doi: 10.1007/978-3-319-24574-4_28

Simonyan, K., and Zisserman, A. (2015). "Very deep convolutional networks for large-scale image recognition," in *International Conference on Learning Representations (ICLR)* (San Diego, CA: ICLR), 234–241.

Sundermeyer, M., Marton, Z.-C., Durner, M., Brucker, M., and Triebel, R. (2018). "Implicit 3D orientation learning for 6D object detection from RGB images," in *European Conference on Computer Vision (ECCV)* (Cham: Springer), 712–729. doi: 10.1007/978-3-030-01231-1_43

Svenstrup, M., Tranberg, S., Andersen, H. J., and Bak, T. (2009). "Pose estimation and adaptive robot behaviour for human-robot interaction," in *International Conference on Robotics and Automation (ICRA)* (Kobe: IEEE), 3571–3576. doi: 10.1109/ROBOT.2009.5152690

Tekin, B., Sinha, S. N., and Fua, P. (2018). "Real-time seamless single shot 6d object pose prediction," in *Conference on Computer Vision and Pattern Recognition (CVPR)* (Salt Lake City, UT: IEEE), 292–301. doi: 10.1109/CVPR.2018.00038

Tremblay, J., To, T., Sundaralingam, B., Xiang, Y., Fox, D., and Birchfield, S. (2018). Deep object pose estimation for semantic robotic grasping of household objects. *arXiv preprint arXiv:1809.10790*.

Tulsiani, S., and Malik, J. (2015). "Viewpoints and keypoints," in *Conference on Computer Vision and Pattern Recognition (CVPR)* (Boston, MA: IEEE), 1510–1519. doi: 10.1109/CVPR.2015.7298758

Wagner, D., Reitmayr, G., Mulloni, A., Drummond, T., and Schmalstieg, D. (2008). "Pose tracking from natural features on mobile phones," in *International Symposium on Mixed and Augmented Reality (ISMAR)* (Cambridge: IEEE), 125–134. doi: 10.1109/ISMAR.2008.4637338

Wang, C., Xu, D., Zhu, Y., Martin-Martin, R., Lu, C., Fei-Fei, L., and Savarese, S. (2019). "Densefusion: 6D object pose estimation by iterative dense fusion," in *Conference on Computer Vision and Pattern Recognition*

*(CVPR)* (Long Beach, CA: IEEE), 3343–3352. doi: 10.1109/CVPR.2019.00346

Wohlhart, P., and Lepetit, V. (2015). "Learning descriptors for object recognition and 3d pose estimation," in *Conference on Computer Vision and Pattern Recognition (CVPR)* (Boston, MA: IEEE), 3109-3118. doi: 10.1109/CVPR.2015.7298930

Wu, X., Liu, J., Huang, C., Su, M., and Xu, T. (2020). 3-d path following of helical microswimmers with an adaptive orientation compensation model. *IEEE Trans. Automat. Sci. Eng.* 17, 823–832. doi: 10.1109/TASE.2019.2947071

Xiang, Y., Schmidt, T., Narayanan, V., and Fox, D. (2017). PoseCNN: a convolutional neural network for 6d object pose estimation in cluttered scenes. *arXiv preprint arXiv:1711.00199*. doi: 10.15607/RSS.2018.XIV.019

Xu, D., Anguelov, D., and Jain, A. (2018). "Pointfusion: deep sensor fusion for 3d bounding box estimation," in *Conference on Computer Vision and Pattern Recognition (CVPR)* (Salt Lake City, UT: IEEE), 244–253. doi: 10.1109/CVPR.2018.00033

Xu, T., Guan, Y., Liu, J., and Wu, X. (2020). Image-based visual servoing of helical microswimmers for planar path following. *IEEE Trans. Automat. Sci. Eng.* 17, 325–333. doi: 10.1109/TASE.2019.2911985

Xu, T., Yu, J., Vong, C., Wang, B., Wu, X., and Zhang, L. (2019). Dynamic morphology and swimming properties of rotating miniature swimmers with soft tails. *IEEE/ASME Trans. Mechatr.* 24, 924–934. doi: 10.1109/TMECH.2019.2912404

Yang, X., Guo, J., Xue, T., and Cheng, K.-T. T. (2018). Robust and real-time pose tracking for augmented reality on mobile devices. *Multimed. Tools Appl.* 77, 6607–6628. doi: 10.1007/s11042-017-4575-3

Zeng, W., Liang, G., Guangdong, C. W., and Wu, X. (2016). "Multi-stage feature learning based object recognition and 3d pose estimation with kinect," in *International Conference on Information Science and Technology (ICIST)* (Dalian: IEEE), 498–504. doi: 10.1109/ICIST.2016.7483465

Zhao, H., Shi, J., Qi, X., Wang, X., and Jia, J. (2017). "Pyramid scene parsing network," in *Conference on Computer Vision and Pattern Recognition (CVPR)* (Honolulu, HI: IEEE), 2881–2890. doi: 10.1109/CVPR.2017.660

**Conflict of Interest:** The authors declare that the research was conducted in the absence of any commercial or financial relationships that could be construed as a potential conflict of interest.

frontiers in Energy Research

ORIGINAL RESEARCH
published: 19 January 2021
doi: 10.3389/fenrg.2020.555145

# Industrial Control Malicious Traffic Anomaly Detection System Based on Deep Autoencoder

*Weiping Wang*[1,2,3,4]*, *Chunyang Wang*[1,2,3,4], *Yongzhen Guo*[5,6]*, *Manman Yuan*[1,2,3,4]*, *Xiong Luo*[1,2,3,4] *and Yang Gao*[7]

[1]Department of Computer and Communication Engineering, University of Science and Technology Beijing, Beijing, China, [2]Beijing Key Laboratory of Knowledge Engineering for Materials Science, Beijing, China, [3]Institute of Artificial Intelligence, University of Science and Technology Beijing, Beijing, China, [4]Shunde Graduate School, Beijing University of Science and Technology, Guangzhou, China, [5]Industrial Control System Evaluation and Certification Department of China Software Testing Center, Beijing, China, [6]School of Automation, Beijing Institute of Technology, Beijing, China, [7]China Information Technology Security Evaluation Center, Beijing, China

OPEN ACCESS

**Edited by:**
Zhe Song,
Nanjing University, China

**Reviewed by:**
Lun Hu,
Chinese Academy of Sciences (CAS), China
S. M. Suhail Hussain,
National Institute of Advanced Industrial Science and Technology (AIST), Japan

***Correspondence:**
Weiping Wang
weipingwangjt@ustb.edu.cn
Manman Yuan
yuanman_smile@163.com
Yongzhen Guo
yzguo@cstc.org.cn

**Specialty section:**
This article was submitted to Smart Grids, a section of the journal Frontiers in Energy Research

**Received:** 24 April 2020
**Accepted:** 04 December 2020
**Published:** 19 January 2021

**Citation:**
Wang W, Wang C, Guo Y, Yuan M, Luo X and Gao Y (2021) Industrial Control Malicious Traffic Anomaly Detection System Based on Deep Autoencoder. Front. Energy Res. 8:555145. doi: 10.3389/fenrg.2020.555145

Industrial control network is a direct interface between information system and physical control process. Due to the lack of authentication, encryption, and other necessary security protection designs, it has become the main target of malicious attacks under the trend of increasing openness. In order to protect the industrial control systems, we examine the detection of abnormal traffic in industrial control network and propose a method of detecting abnormal traffic in industrial control network based on autoencoder technology. What is more, a new deep autoencoder model was designed to reduce the dimensionality of traffic data in industrial control network. In this article, the Kullback–Leibler divergence was added to the loss function to improve the ability of feature extraction and the ability to recover raw data. Finally, this model was compared with the traditional data dimensionality reduction method (principal component analysis (PCA), independent component analysis, and singular value decomposition) on gas pipeline dataset. The results show that the approach designed in this article outperforms the three methods in different scenes in terms of $f_1$ score.

**Keywords: anomaly detection, industrial control system, dimensionality reduction, feature extraction, autoencoder**

## INTRODUCTION

Industrial control system (ICS) is a highly complex integrated system that provides services to people through the coordination of various critical infrastructures. For example, smart grids, oil and gas, aerospace, transportation, and other critical infrastructure are all part of ICSs [Zhichen (2017); Inoue et al. (2017)]. Therefore, the safety and security of ICSs are vital to national security [Anton et al. (2018); Wang et al. (2016)].

The early ICS was a relatively independent and isolated system, maintaining a separate relationship with the external Internet [Garg et al. (2019)]. The functionality and controllability of ICS were its main concerns. However, with the rapid development of network and information technology, ICS gradually develops toward a networked, open architecture (Vávra and Hromada (2017)). This provides a convenient method for hackers to attack ICS by network, resulting in the network security of ICS having huge security risks. For

example, Stuxnet in 2015 and widespread power outages in Ukraine and Venezuela in 2019 were all caused by hacking attacks on industrial infrastructure. As can be seen from these industrial network security incidents, the tentacles of hackers have extended to the field of industrial control.

Although the IT community has considered the security of critical infrastructure, efforts to develop security solutions for ICSs remain limited. Traditional network security cannot provide effective guidance for ICSs because the traditional network security and ICSs security problems are quite different (Alguliyev et al. (2019); Martins et al. (2018)). Therefore, it is necessary to build a strong anomaly detection mechanism for ICSs under an open environment.

For the special case of ICSs, different anomaly detection methods are proposed. The behavior-based abnormal detection model realizes the recognition of abnormal data by modeling normal data and judging the deviation degree between current behavior and normal behavior by designing distance model (Lai et al. (2019); Huda et al. (2018)). The learning-based abnormal detection model realizes the recognition of normal data and abnormal data by learning the characteristics of all data Anthi et al. (2020). But these methods only model specific types of attack data; such techniques cannot identify new types of attacks. In addition, most of the existing research is aimed at a specific industrial control environment and lacks some universality.

Most importantly, the existing literature fails to consider the problem that the length of traffic data in ICSs is not fixed. Most of them are based on the industrial control data after complex processing, which will greatly reduce the efficiency of industrial control anomaly detection. Because of the higher data dimension, the training speed and recognition accuracy of the model will be greatly reduced.

Aiming at the special situation and existing problems of ICSs, in this article, we propose a traffic data dimension reduction method that can handle variable-length data, and a new loss function is designed to speed up the processing speed. Finally, the decision tree is used as a binary classifier to evaluate the performance of the algorithm on a real industrial control dataset.

The main contributions of this article are as follows:

1 A new model of autoencoder is designed. The model can not only accelerate the speed of feature extraction but also extract more key information.
2 The accuracies of anomaly detection and F1 are improved by using the new dimension reduction method and decision tree classifier.
3 A generic model is developed that can be used for different critical infrastructures and improve the performance of identifying abnormal data.

The rest of this article is organized as follows. The related work is presented in ***Section 2***. The deep autoencoder algorithm is studied in ***Section 3***. The dataset is described in ***Section 4***. The contrast test is presented in ***Section 5***. And conclusions are drawn in ***Section 6***.

## RELATED WORK

With the development of computer technology and network technology, the importance of ICSs is becoming increasingly prominent. Because ICSs did not consider the design of security protection at the beginning, the network interconnection exposes the industrial control network to cyberspace, which undoubtedly brings huge security risks and hidden dangers to the critical infrastructure controlled by ICSs (Morris and Gao (2013); Ding et al. (2018)). In order to avoid the occurrence of industrial safety incidents, the detection and prevention of ICSs are very important.

The existing abnormal detection methods of industrial control are usually based on the traditional network abnormal detection methods. At present, the commonly used detection methods are signature-based and learning-based technology (Das et al. (2020)). Signature-based methods use fixed signatures to detect known attacks. However, this method is inefficient in detecting unknown or new attacks (Marian et al. (2020)). The learning-based industrial control anomaly detection technology can identify the anomaly data by extracting the key features of similar samples as the classification basis. In 2019, Pang Ying et al. (Pang et al. (2019)) realized the abnormal detection of malicious traffic by signing the dataset of network traffic after clustering. In 2020, the abnormal nodes were detected by using the elliptic curve digital signature (Deepalakshmi and Kumanan (2020)).

In contrast, learning-based industrial control anomaly detection has higher performance because it can continuously learn new knowledge and then realize accurate identification of abnormal data (Halftermeyer (2020)). An effective anomaly detection framework was proposed by optimizing the parameters of support vector machines (Injadat et al. (2018)). A classifier model of industrial control anomaly detection based on support vector machine and C4.5 decision tree is established, and the effective classification of industrial control data is realized by taking advantage of the physical properties of the system (Al-Madani et al. (2019)). Jeyaram (2017), YaLi Liu and Ding (2018), Junjie Shao and Feng (2018), and Songqing and Zhiguo (2018) combined flow anomaly detection technology and adopted traditional machine learning method to further improve the identification accuracy of industrial control anomaly detection.

Although the above studies solved some problems related to network attack detection in ICSs, most of them relied on complex feature engineering to process data into fixed-length datasets. This process is very complex and can seriously increase the computational burden of the model. In addition, most of the traditional dimensionality reduction methods are used in industrial control anomaly detection, and the feature extraction energy is poor. Therefore, this kind of algorithm cannot extract the key features of industrial control data well and cannot get good detection effect. Inspired by the above article, this article proposes a new AE-based feature extraction method, which extracts a new and efficient representation from the original variable-length non-time series dataset so that the classifier can accurately identify the attack data.

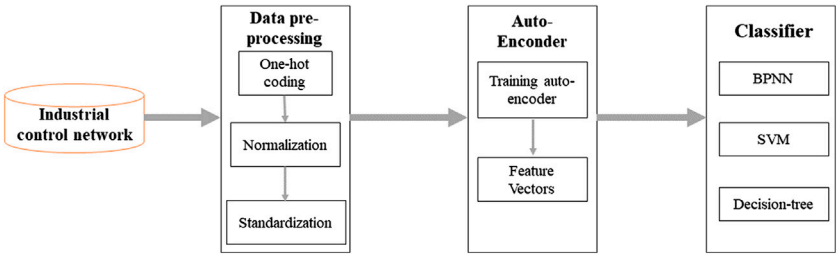


**FIGURE 1 |** The system of malicious traffic detection.

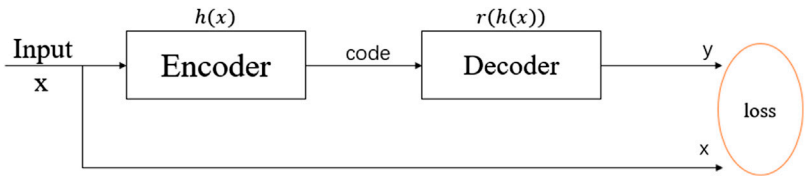


**FIGURE 2 |** Autoencoder model.

## DEEP AUTOENCODER ALGORITHM

The traffic data dimension of industrial control network is so large that the task of traffic classification is carried out directly, which is prone to the problem of dimension disaster. Therefore, the autoencoder techniques (Hou et al. (2017)) were used to reduce data dimensions without breaking the original data semantics. The framework of malicious traffic detection system is shown in **Figure 1**. The system consists of models of data preprocessing, automatic encoder, and classifier.

In the part of data preprocessing, due to the diversity of data sources, the character data should be carried out one-hot encoding processing. Then, the data need to be normalized and standardized. The normalized and standardized formulas are shown as follows:

$$x_1 = \frac{x - x_{\min}}{x_{\max} - x_{\min}}, \tag{1}$$

$$x_2 = \frac{x - \mu}{\sigma}, \tag{2}$$

where $x_{\min}$ represents the minimum value of the data, $x_{\max}$ is the maximum value of the data, μ is the average value of the data, and σ represents the variance of the data. And $x_1$ is the normalized data, whereas $x_2$ is the standardized data.

Autoencoder is an unsupervised method of data dimension compression and data feature expression. The autoencoder is composed of an encoder and a decoder, as shown in **Figure 2**, where $h(x)$ is the encoder. The encoder is composed of multilayer neural network, which can reduce the data from $n$ dimension to $m$ dimension. $n$ is the dimension of the input data and $m$ is the number of neurons in the hidden layer. Instead, $r(h(x))$ represents the decoder that is composed of neural network symmetric with the encoder, restoring the data from $m$ dimension to $n$ dimension. The goal of the autoencoder is to optimize the loss function $L(x, y), y = r(h(x))$. That is, by reducing the error in the graph, the decoded data can recover the original data as far as possible.

Remark 1. Autoencoder is a kind of feedforward neural network; however, it differs from feedforward neural network. Feedforward neural network is a kind of supervised learning method, which needs a lot of marked data. Autoencoder is a kind of unsupervised learning method, data need not be annotated, so they are easier to collect. M is a key parameter. The value of m should be unique in different applications. We can find the optimal m by looking for the minimum value of the loss function in different dimensions.

### The Description of Autoencoder Algorithm

(1) Autoencoder automatically encodes the network to restore compressed data by learning $y = r(h(w) + b_1) + b_2$ , where $w$ and $b$ are the parameters for the algorithm to learn and $h, r$ are nonlinear functions.

(2) In order to restore the original data as much as possible, we can define the objective function of the algorithm as

$$J(w, b) = \left( \sum_{i=0}^{n} (y - x)^2 \right) \Big/ n. \tag{3}$$

The working process of autoencoder is shown in Algorithm 1:

**Require:** $X$: Raw input data
**Ensure:** Dimensionally-reduced data $x^*$ and encoded data $Y$;
1.Initial $i = 0$, $j = 0$, $n = 100$, batch_size = 1000, total number of data $N$ and randomly initialize the neural network weights $w_1, w_2$ and bias $b_1, b_2$;

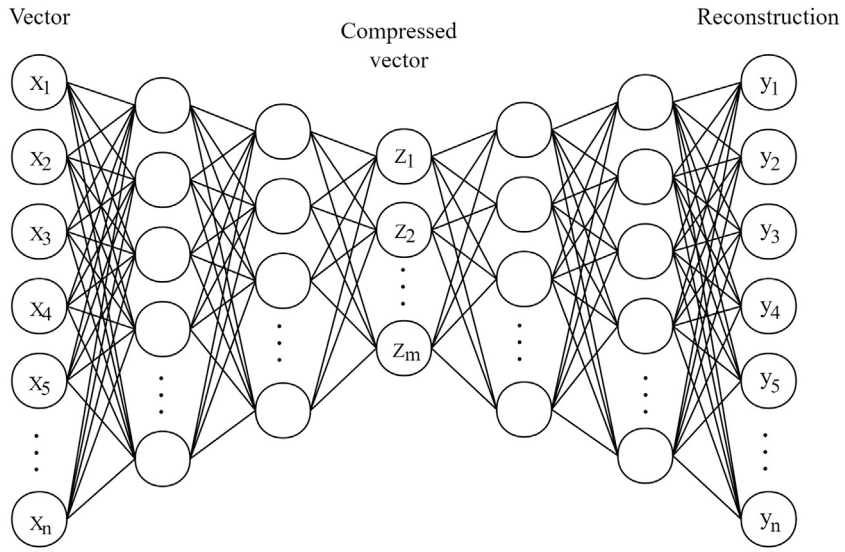


**FIGURE 3 |** Deep autoencoder model.

**2.repeat**

**3.repeat**

4.Extract *batch_size* samples of the data $X$ without putting them back: $x_i$;

5.The weight $w_1$ and bias $b_1$ were used to Encode the data $x$: $y_i$;

6.The weighted $w_2$ and bias $b_2$ were used to Decode the data $yi$ to obtain the approximate data $y_i^*$ of the original data;

7.Calculate the loss $L(x_i, y_i^*)$;

8.Back propagation updates the weights and the bias parameters $w_i = w_i + \partial L/w_i, b_i = b_i + \partial L/b_i$;

9.$j = j + 1$;

**10.until** $j\times$ batch $-$ size $\geq N$;

11.$i = i + 1$;

**12.until** $i > n$

13.$X$ is putted into the encoder to get the encoded data $Y$;

Remark 2. The DAE is composed of multiple autoencoders, in which the output of the previous encoder is the input of the next encoder.

In this article, the network structure of autoencoder is shown in **Figure 3**. This network structure is called DAE. The encoder is composed of a three-layer neural network. And the number of layers of the network decreases layer by layer. It changes the input data to $Z(z_1, z_2 \ldots z_m)$. The part of the decoder is also composed of a three-layer neural network, in which the number of layers increases layer by layer. And the dimension of the last layer is consistent with that of the input vector. Specifically, the network parameters of the encoder and decoder are completely independent. However, the number of hidden units per layer of the neural network in the encoder is the same as that in the decoder.

Traditional DAE uses Mean Squared Error (MSE) as the loss function. This approach only considers the numerical value of the input and output data, not the distribution of the data. In this case, the extracted features do not include the distribution characteristics between the data. This caused some data loss. Kullback–Leibler divergence (KLD) is the asymmetry measure of the difference between the two probability distributions Goodfellow et al. (2016). Here, we add KLD to the loss function. At this time, the distribution of the input data is the true distribution, and the output data is the theoretical distribution. KLD means the loss of information produced by fitting a theoretical distribution to a true distribution.

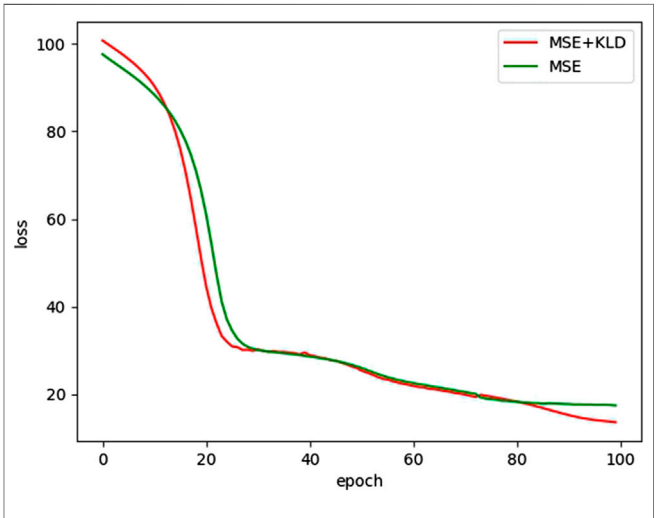


**FIGURE 4 |** The loss of the KDAE and DAE.

In order to recover the speech and distribution characteristics of the original data as much as possible on the basis of removing redundancy and noise, the loss function designed in this article is composed of MSE and KLD. MSE is the difference between the generated data and the original

data, and KLD is the difference between the generated data distribution and the original distribution. Our goal is to minimize the sum of MSE and KLD.

$$\mathrm{MSE} = \left( \sum_{i=0}^{n} (y - x)^2 \right) \Big/ n, \qquad \mathrm{KLD}(P \| Q) = \sum_{i} P(i) \log_2 \frac{P(i)}{Q(i)}, \tag{4}$$

$$\mathrm{loss} = \mathrm{MSE} + \mathrm{KLD}, \tag{5}$$

where $P_i$ is the variance of the generated data in each batch and $Q_i$ is the variance of the original data distribution. The value of KLD is always greater than 0 and KLD is equal to 0 if and only if the two distributions are the same. We use it to extract distribution information from the data.

The role of MSE is to make the value of decoded data as close as possible to the input data. The functions of KLD are mainly to make the distribution of decoded data as close as possible to the distribution of the input data. After adding KLD to DAE model, the DAE model becomes KLD-based DAE (KDAE) model, which has better feature extraction capability. By constructing the KDAE model, we can realize the dimensionality reduction of the original data, extract the key features and distribution of the original data, and reduce the noise of the original data. Through analyzing Algorithm 1, we can see that the time complexity of KDAE is O(n).

## DATASET

In this part, the gas pipeline dataset proposed by the Critical Infrastructure Protection Center at Mississippi State University was used to test the performance of the proposed algorithm and compare the algorithm with principal component analysis (PCA) and other mainstream data dimensionality reduction methods.

This dataset is the standard dataset of ICS by injecting attack and capturing network data in the natural gas pipeline control system. Apart from "normal" data, the dataset also includes seven types of attack data. The seven types are original malicious response injection (NMRI), complex malicious response injection (CMRI), malicious status command injection (MSCI), malicious parameter command injection (MPCI), malicious function command injection (MFCI), denial of service (DOS), and detection attack (RA). In the dataset, each of the network data contains 27 marked features, among which 26 are connection features and one is marked to mark whether the data is normal or not. In the gas pipline dataset, the proportion of normal samples is 62.9% and that of abnormal samples is 37.1%.

## CONTRAST TEST

To enable the machine to recognize the gas pipline dataset, one-hot encoding technology was used to transform each column of data that contains a string. After the data transformation, the characteristic number is 35, and then each sample changes from a 26-dimensional vector to a 35-dimensional vector. Then the whole dataset was standardized and normalized using **(1)** and **(2)**. In order to ensure the accuracy of the experimental results, all data in this article are the average values of the ten repeated experiments. Each experiment randomly selects 15% of the data from the dataset as the test set and the rest as the train set.

Firstly, the preprocessed data reduced the dimension to 16 by using the DAE model that only has BCE and the KDAE model that has BCE and KLD, respectively. The number of hidden neurons in the three layers of the encoder is 86, 64, and 32, respectively. The optimizer used Adam training method. The batch size is 1,000.

The loss variation of KDAE and DAE model is shown in **Figure 4**. One of the models is DAE with MSE loss function and the other is KDAE, whose loss function has MSE and KLD. In the beginning, the loss of KDAE is higher than DAE because KDAE adds the KLD item. **Figure 4** illustrates that the model converges faster at the early stage after adding KLD to the loss function. From **Figure 4**, we can see that the loss value of KDAE is significantly lower than the loss value of DAE when it finally reaches stability. The overall convergence rate of the KDAE model is higher than that of the DAE model. This shows that the KDAE model has a better recovery effect on data. This indicates that data extracted by KDAE are more representative of the information of the original data than DAE and have better feature extraction capability.

In order to test the performance of the classifier after dimension reduction, the data was reduced to 22 and 16 dimensions, respectively, and then compared their effects with neural network (NN), support vector machine (SVM), and decision tree (DT) classification model. When the KDAE model was used to reduce the data dimensions to 64, the number of hidden neurons in the three-layer NN of the encoder was 100, 86, and 64, respectively. When the KDAE model was used to reduce the data dimensions to 16, the number of hidden neurons in the three-layer NN of the encoder was 64, 32, and 16, respectively.

In the NN, the optimizer used the Adam training method. The penalty coefficient of the objective function in SVM is $C = 20$, the parameters of the kernel is selected as *RBF*, gamma = 1, and the maximum number of iterations is 2000. In the DT, the number of DTs is 10, so $N$_estimators = 10; the number of samples with the least leaf nodes is 5, so Min_samples_leaf = 5.

In the prediction, the True Positive (TP), True Negative (TN), False Positive (FP), and False Negative (FN) were used to represent the number of normal samples judged as normal samples, the number of abnormal samples predicted as normal samples, the number of normal samples predicted as abnormal samples, and the number of abnormal samples predicted as abnormal samples, respectively. In order to further test the performance of the classifier, recall, precision, and $F_1$ score are used to evaluate the classification performance of the classifier. The definition of precision is

**TABLE 1 |** The comparison of feature extraction abilities.

| | Precision | Recall | $f_1$ score |
|---|---|---|---|
| DAE | 0.9354 | 0.9352 | 0.9343 |
| KDAE | 0.9552 | 0.9551 | 0.955 |

**TABLE 2 |** Detection of raw data.

| | Precision | Recall | $f_1$ score |
|---|---|---|---|
| Decision tree | 0.9459 | 0.945 | 0.9446 |
| Neural network | 0.9376 | 0.936 | 0.9353 |
| SVM | 0.9503 | 0.95 | 0.9497 |

**TABLE 3 |** Detect data in 16 dimensions.

| Decision tree | Precision | Recall | $f_1$ score |
|---|---|---|---|
| ICA | 0.9564 | 0.956 | 0.959 |
| SVD | 0.9545 | 0.954 | 0.954 |
| PCA | 0.958 | 0.958 | 0.958 |
| KDAE | 0.96 | 0.958 | 0.959 |
| Neural network | Precision | Recall | $f_1$ score |
| ICA | 0.9516 | 0.951 | 0.951 |
| SVD | 0.95 | 0.949 | 0.948 |
| PCA | 0.9531 | 0.953 | 0.9528 |
| KDAE | 0.9552 | 0.9551 | 0.955 |
| SVM | Precision | Recall | $f_1$ score |
| ICA | 0.9601 | 0.96 | 0.956 |
| SVD | 0.9537 | 0.953 | 0.9526 |
| PCA | 0.9589 | 0.959 | 0.9589 |
| KDAE | 0.9615 | 0.961 | 0.9513 |

$$\text{precision} = \frac{TP}{TP + FP}. \tag{6}$$

Recall rate is a measure of coverage, which is mainly used to measure how many positive cases are divided into positive cases. The formula of the recall rate is as follows;

$$\text{recall} = \frac{TP}{TP + FN}. \tag{7}$$

Accuracy and recall rates sometimes contradict each other, so we need to take them into consideration. $f_1$ score is the weighted harmonic average of recall rate and accuracy. And it is a comprehensive evaluation index.

$$f_1 = \frac{2 \times \text{precision} \times \text{recall}}{\text{precision} + \text{recall}}. \tag{8}$$

When the value of $f_1$ score is high, it indicates that the experiment has better results and the model is more effective.

At the beginning of this section, the KDAE and DAE models reduce the data to 16 dimensions, respectively. Then we will use the NN to see the impact of dimensionless data on classifier classification performance.

As we can see from **Table 1**, datasets processed by KDAE have higher $f_1$ score. This indicates that the KDAE model has a stronger feature extraction capability than the DAE model.

**TABLE 4 |** Detect data in 22 dimensions.

| Decision tree | Precision | Recall | $f_1$ score |
|---|---|---|---|
| ICA | 0.9515 | 0.951 | 0.95095 |
| SVD | 0.9518 | 0.951 | 0.9506 |
| PCA | 0.9469 | 0.946 | 0.9455 |
| KDAE | 0.953 | 0.952 | 0.9525 |
| Neural network | Precision | Recall | $f_1$ score |
| ICA | 0.9412 | 0.94 | 0.9393 |
| SVD | 0.948 | 0.947 | 0.9465 |
| PCA | 0.9395 | 0.938 | 0.9372 |
| KDAE | 0.95 | 0.947 | 0.9485 |
| SVM | Precision | Recall | $f_1$ score |
| ICA | 0.9468 | 0.946 | 0.9455 |
| SVD | 0.9518 | 0.951 | 0.9506 |
| PCA | 0.945 | 0.944 | 0.9434 |
| KDAE | 0.956 | 0.955 | 0.9555 |

**TABLE 5 |** The detection of data reduced by LSTM autoencoder.

| | DT 16 | NN 16 | SVM 16 | DT 22 | NN 22 | SVM 22 |
|---|---|---|---|---|---|---|
| Precision | 0.85 | 0.41 | 0.80 | 0.85 | 0.39 | 0.80 |
| Recall | 0.80 | 0.64 | 0.70 | 0.80 | 0.63 | 0.71 |
| $f_1$ score | 0.77 | 0.50 | 0.63 | 0.78 | 0.48 | 0.64 |

This also proves that KDAE is superior to DAE in noise reduction.

By analyzing the change of the loss function, we can know that compared with other dimensionality reduction methods, the autoenconder dimensionality reduction method designed by us can better recover the original data.

Then, we compare the KDAE algorithm with traditional dimension reduction methods. Firstly, **Table 2** shows the classification effect of raw data in three classifiers. It can be seen that the classification effect of untreated data in NN and SVM is very poor. The reason is that the classifier fails to extract the characteristics of the abnormal samples, so the abnormal samples are mostly predicted to be normal samples.

**Tables 3, 4** are the classification of the data reduced to 16 and 22 dimensions, respectively. To be specific, we use three kinds of dimensionality reduction methods to compare the methods proposed in this article. In **Tables 3, 4**, the highest $f_1$ score is generated by SVM. And it is obtained by the KDAE method. The value of $f_1$ score is 0.9613.

In addition, from **Tables 2–4**, it can be found that the effect of classification has been significantly improved after the dimension reduction of KDAE. This means that the KDAE method is not only better than the traditional DAE method but also better than other traditional methods.

In **Table 5**, we used the LSTM autoencoder method that was proposed by Lai et al. (2019) to reduce the data to 16 and 22 dimensions, respectively. The classifiers of DT, NN, and SVM are used to detect the performance of reduced data. The precision, recall, and $f_1$ score are significantly lower than the value in **Tables 2–4**. This is mainly because gas datasets are characteristic data. Before dimensionality reduction, we must

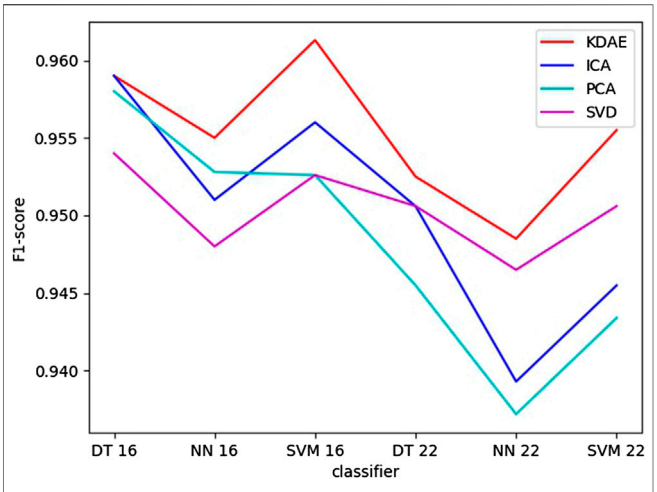


**FIGURE 5 |** The comparison of F1 Score with different dimension reduction methods.

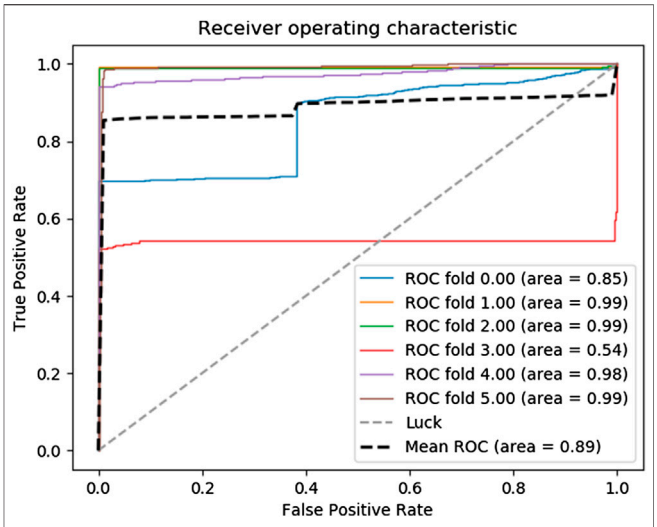


**FIGURE 6 |** Receiver operating characteristic of 16 dimensions.

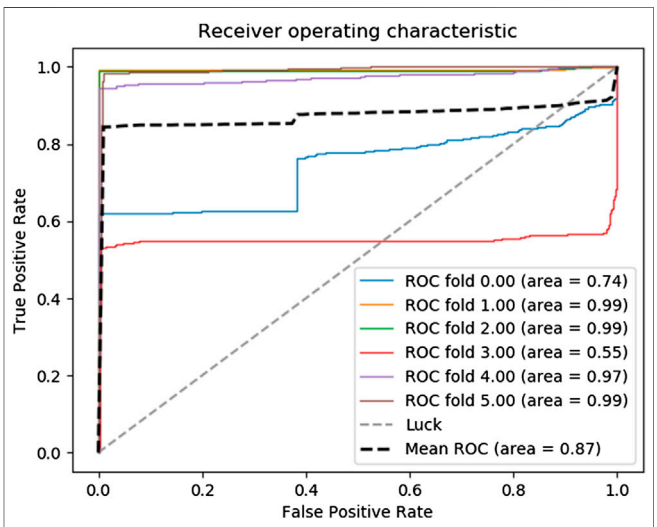


**FIGURE 7 |** Receiver operating characteristic of raw data.

first use the word2vec encoding method to convert the data into data that can be processed by LSTM. The data is then dimensioned down by LSTM. In the process, some important information is lost. Therefore, the method of LSTM dimension reduction is not suitable for processing such datasets.

At the same time, in **Figure 5**, each polyline represents the change in $f_1$ score of the data on different classifiers after being reduced by different dimensionality reduction methods. It is shown that the red line has the smallest change. And the range of other lines is very large. This shows that the data reduced by KDAE can achieve good results on various classifiers. Moreover, the KDAE-reduced data had the highest $f_1$ score on each classifier. From the above, we can conclude that the KDAE-reduced data not only extracts the key features of the original data but also eliminates redundancy and noise. This makes the classification effect significantly improved. It shows that our deep autoencoder anomaly flow detection system is efficient and has practical value.

To further illustrate the effectiveness of the deep autoencoder algorithm proposed in this article on a malicious traffic monitoring system, the k-fold cross-validation was used to construct a receiver operating characteristic (ROC) curve to evaluate the performance of our anomaly detection system. In this case, the classifier is the NN. The data is reduced to 16 dimensions by using KDAE. And $K = 6$.

**Figure 6** illustrates that the average area obtained by six cross-validations is 0.89 and the worst is 0.55. At the same time, the ROC curve of the raw data under the same classifier is given in **Figure 7**. In the ROC curve, the average area of raw data is 0.87 that is much lower than the number in **Figure 6**. This indicates that data processed by KDAE have better performance when used for classifier classification. The classifier can identify the abnormal traffic more stably.

In **Table 6**, we compare the time required for each process of different dimensionality reduction methods. **Table 6** shows that the time difference of different algorithms in classification is not big. However, the conversion time of the KDAE algorithm in dimension reduction is 53.44s, which is significantly higher than other algorithms. Combined with the previous comparative experiments, we can know that the KDAE algorithm improves the identification accuracy of attack samples on the basis of lost time.

## CONCLUSION

In this article, a new industrial control flow anomaly detection model was proposed, which reduces dimension by improved deep autoencoder. The new algorithm has verified the performance of the gas pipeline dataset. And the new algorithm was compared

**TABLE 6 |** Time consumption in different algorithms.

| Algorithm | Conversion time (s) | Classifier | Train time (s) | Test time (s) |
|---|---|---|---|---|
| ICA | 1.79 | SVM | 1.18 | 0.08 |
| | | Neural network | 86.21 | 0.15 |
| | | Decision tree | 0.06 | 0.001 |
| SVD | 2.96 | SVM | 2.94 | 0.06 |
| | | Neural network | 87.06 | 0.18 |
| | | Decision tree | 0.05 | 0.001 |
| PCA | 2.06 | SVM | 1.58 | 0.08 |
| | | Neural network | 91.9 | 0.19 |
| | | Decision tree | 0.22 | 0.001 |
| KDAE | 53.44 | SVM | 1.28 | 0.06 |
| | | Neural network | 91.45 | 0.19 |
| | | Decision tree | 0.13 | 0.001 |

with the traditional methods of dimension reduction such as PCA and singular value decomposition based on the classifier such as SVM, random forest, and deep NN. Experiments show that the algorithm of KDAE has good performance in dimensionality reduction of industrial control network datasets. Data processed by the KDAE algorithm can significantly improve the performance of the classifier. This will greatly improve the identification accuracy of attack data in different detection models. And we prove that our algorithm can obtain the best ROC scores and $F_1$ score in different classifiers.

## DATA AVAILABILITY STATEMENT

Publicly available datasets were analyzed in this study. This data can be found here: https://github.com/ahsan-z-khan/IDS-Model-for-SCADA.

## AUTHOR CONTRIBUTIONS

All authors listed have made a substantial, direct, and intellectual contribution to the work and approved it for publication.

## FUNDING

This work was supported in part by the 2018 industrial Internet innovation and development project "construction of industrial Internet security standard system and test and verification environment", in part by the National Natural Science Foundation of China under Grant 81961138010, Grant U1736117 and Grant U1836106, in part by the Fundamental Research Funds for the Central Universities under Grant FRF-TP-19-005A3, in part by the Technological Innovation Foundation of Shunde Graduate School, USTB, under Grant BK19BF006.

## REFERENCES

Al-Madani, B., Shawahna, A., and Qureshi, M. (2019). Anomaly detection for industrial control networks using machine learning with the help from the inter-arrival curves. Available at: http://arxiv.org/abs/1911.05692

Alguliyev, R. M., Aliguliyev, R. M., and Abdullayeva, F. J. (2019). Hybridisation of classifiers for anomaly detection in big data. *IJBDI* 6, 11–19. doi:10.1504/IJBDI.2019.097396

Anthi, E., Williams, L., Rhode, M., Burnap, P., and Wedgbury, A. (2020). Adversarial attacks on machine learning cybersecurity defences in industrial control systems. Available at: http://arxiv.org/abs/2004.05005

Anton, S. D., Kanoor, S., Fraunholz, D., and Schotten, H. D. (2018). "Evaluation of machine learning-based anomaly detection algorithms on an industrial modbus/tcp data set", in Proceedings of the 13th international conference on availability Reliability and Security, 1–9, Hamburg Germany, August, 2018. doi:10.1145/3230833.3232818

Das, T. K., Adepu, S., and Zhou, J. (2020). Anomaly detection in industrial control systems using logical analysis of data. *Comput. Secur.* 96, 101935. doi:10.1016/j.cose.2020.101935

Deepalakshmi, P., and Kumanan, T. (2020). "Elliptic curve digital signature technique based abnormal node detection in wireless ad hoc networks,", in Proceedings of the IOP conference series: materials science and engineering, 925, Chennai, India, September 16–17, 2020 (Bristol, United Kingdom: IOP Publishing). 012075.

Ding, D., Han, Q. L., Xiang, Y., Ge, X., and Zhang, X. M. (2018). A survey on security control and attack detection for industrial cyber-physical systems. *Neurocomputing* 275, 1674–1683. doi:10.1016/j.neucom.2017.10.009

Garg, S., Kaur, K., Kumar, N., and Rodrigues, J. J. P. C. (2019). Hybrid deep-learning-based anomaly detection scheme for suspicious flow detection in sdn: a social multimedia perspective. *IEEE Transactions on Multimedia* 21, 566–578. doi:10.1109/TMM.2019.2893549

Goodfellow, I., Bengio, Y., and Courville, A. (2016). *Deep learning*. Cambridge, MA: MIT press.

Halftermeyer, R. (2020). *Machine learning method for cyber security intrusion detection for industrial control systems*. (Thousand Oaks, CA: SAGE).

Hou, X., Shen, L., Sun, K., and Qiu, G. (2017). "Deep feature consistent variational autoencoder," in Proceedings of the IEEE winter conference on applications of computer vision (WACV). Santa Rosa, CA, March 24–31, 2017 (New York, NY: IEEE), 1133–1141. doi:10.1109/WACV.2017.131

Huda, S., Miah, S., Yearwood, J., Alyahya, S., Al-Dossari, H., and Doss, R. (2018). A malicious threat detection model for cloud assisted internet of things (cot) based industrial control system (ics) networks using deep belief network. *J. Parallel Distr. Comput.* 240, 23–31. doi:10.1016/j.jpdc.2018.04.005

Injadat, M., Salo, F., Nassif, A. B., Essex, A., and Shami, A. (2018). "Bayesian optimization with machine learning algorithms towards anomaly detection," in Proceedings of the IEEE global communications conference (GLOBECOM). Abu Dhabi, UAE, December 9–13, 2018 (IEEE), 1–6. doi:10.1109/GLOCOM.2018.8647714

Inoue, J., Yamagata, Y., Chen, Y., Poskitt, C. M., and Sun, J. (2017). "Anomaly detection for a water treatment system using unsupervised machine learning," in Proceedings of the IEEE international conference on data mining workshops (ICDMW), New Orleans, LA, November 18–21, 2017 (IEEE), 1058–1065. doi:10.1109/ICDMW.2017.149

Jeyaram, N. (2017). Intrusion detection system based on combined support vector machine with ant colony ptimization. *J. Softw. Eng* 11, 30. doi:10.26634/jse.11.4.13819

Junjie Shao, W. D., and Feng, Z. (2018). *Industrial control network anomaly detection method based on machine learning*. Information technology and network security, 17–20.

Lai, Y., Liu, Z., and Liu, J. (2019). Abnormal detection method of industrial control system based on behavior model. *Comput. Secur.* 84, 166–178. doi:10.1016/j.cose.2019.03.009

Marian, M., Cusman, A., Stîngă, F., Ionică, D., and Popescu, D. (2020). Experimenting with digital signatures over a dnp3 protocol in a multitenant cloud-based scada architecture. *IEEE Acc* 8, 156484–156503. doi:10.1109/ACCESS.2020.3019112

Martins, R. S., Angelov, P., and Costa, B. S. J. (2018). "Automatic detection of computer network traffic anomalies based on eccentricity analysis," in Proceedings of the IEEE international conference on fuzzy systems (FUZZ-IEEE), Rio de Janeiro, Brazil, July 8–13, 2018 (IEEE), 1–8. doi:10.1109/FUZZ-IEEE.2018.8491507

Morris, T. H., and Gao, W. (2013). "Industrial control system cyber attacks," in 1st international symposium for ICS & SCADA cyber security research 2013 (ICS-CSR 2013), Leicester, UK, September 16–17, 2013, 1, 22–29.

Pang, Y., Chen, Z., Peng, L., Ma, K., Zhao, C., and Ji, K. (2019). "A signature-based assistant random oversampling method for malware detection," in Proceedings of the 2019 18th IEEE international conference on trust, security and privacy in computing and communications/13th IEEE international conference on big data science and engineering (TrustCom/BigDataSE). Rotorua, New Zealand, August 5–8, 2019 (IEEE), 256–263. doi:10.1109/TrustCom/BigDataSE.2019.00042

Songqing, Z., and Zhiguo, L. (2018). *An intrusion detection method based on semi-supervised learning for industry control system network*. Information Technology and Network Security.

Vávra, J., and Hromada, M. (2017). "Anomaly detection system based on classifier fusion in ics environment," in Proceedings of the 2017 International Conference on Soft Computing, Intelligent System and Information Technology (ICSIIT) (IEEE), Denpasar, Indonesia, September 26–29, 2017, 32–38. doi:10.1109/ICSIIT.2017.35

Wang, P., Chao, K.-M., Lin, H.-C., Lin, W.-H., and Lo, C.-C. (2016). "An efficient flow control approach for sdn-based network threat detection and migration using support vector machine," in Proceedings of the IEEE 13th international conference on e-business engineering (ICEBE), Macau, China, November 4–6, 2016 (IEEE), 56–63. doi:10.1109/ICEBE.2016.020

YaLi Liu, L. M., and Ding, Y. (2018). Application and algorithm improvement of abnormal traffic detection in smart grid industrial control system. *Computer system application*, 173–178.

Zhichen, Z. (2017). Security monitoring technology of power grid industrial control system based on network traffic anomaly detection. *Electric Power Information and Communication Technology* 15, 98–102.

**Conflict of Interest:** The authors declare that the research was conducted in the absence of any commercial or financial relationships that could be construed as a potential conflict of interest.

frontiers in Oncology

ORIGINAL RESEARCH
published: 05 March 2021
doi: 10.3389/fonc.2021.640804

# Classification of Metastatic and Non-Metastatic Thoracic Lymph Nodes in Lung Cancer Patients Based on Dielectric Properties Using Adaptive Probabilistic Neural Networks

*Di Lu[1], Hongfeng Yu[2], Zhizhi Wang[1], Zhiming Chen[1], Jiayang Fan[1], Xiguang Liu[1], Jianxue Zhai[1], Hua Wu[1], Xuefei Yu[2]* and Kaican Cai[1]**

[1] Department of Thoracic Surgery, Nanfang Hospital, Southern Medical University, Guangzhou, China, [2] School of Biomedical Engineering, Southern Medical University, Guangzhou, China

OPEN ACCESS

**Edited by:**
Long Wang,
University of Science and Technology Beijing, China

**Reviewed by:**
You Pan,
Guangxi Medical University Cancer Hospital, China
Lei Wang,
Fourth Military Medical University, China

***Correspondence:**
Kaican Cai
doc_cai@163.com
Xuefei Yu
xuefeiyu@smu.edu.cn

**Specialty section:**
This article was submitted to Thoracic Oncology, a section of the journal Frontiers in Oncology

**Received:** 12 December 2020
**Accepted:** 28 January 2021
**Published:** 05 March 2021

**Citation:**
Lu D, Yu H, Wang Z, Chen Z, Fan J, Liu X, Zhai J, Wu H, Yu X and Cai K (2021) Classification of Metastatic and Non-Metastatic Thoracic Lymph Nodes in Lung Cancer Patients Based on Dielectric Properties Using Adaptive Probabilistic Neural Networks. Front. Oncol. 11:640804. doi: 10.3389/fonc.2021.640804

**Objective:** Dielectric properties can be used in normal and malignant tissue identification, which requires an effective classifier because of the high throughput nature of the data. With easy training and fast convergence, probabilistic neural networks (PNNs) are widely applied in pattern classification problems. This study aims to propose a classifier to identify metastatic and non-metastatic thoracic lymph nodes in lung cancer patients based on dielectric properties.

**Methods:** The dielectric properties (permittivity and conductivity) of lymph nodes were measured using an open-ended coaxial probe. The Synthetic Minority Oversampling Technique method was adopted to modify the dataset. Feature parameters were scored to select the appropriate feature vector using a Statistical Dependency algorithm. The dataset was classified using adaptive PNNs with an optimized smooth factor using the simulated annealing PNN (SA-PNN). The results were compared with traditional Probabilistic, Support Vector Machines, k-Nearest Neighbor and the Classify functions in MATLAB.

**Results:** The conductivity frequencies of 3959, 3958, 3960, 3978, 3510, 3889, 3888, and 3976 MHz were selected as the feature vectors for 219 lymph nodes (178 non-metastatic and 41 metastatic). Compared with the other methods, SA-PNN achieved the highest classification accuracy (92.92%) and the corresponding specificity and sensitivity were 94.72% and 91.11%, respectively.

**Conclusions:** Compared with the other methods, the SA-PNN proposed in the present study achieved a higher classification accuracy, which provides a new scheme for classification of metastatic and non-metastatic thoracic lymph nodes in lung cancer patients based on dielectric properties.

**Keywords: dielectric properties, thoracic lymph nodes, simulated annealing algorithm, probabilistic neural network, metastatic**

# INTRODUCTION

Dielectric properties usually include effective dielectric permittivity and conductivity (1), which are intrinsic properties of biological tissues and can indirectly reflect the physiological state changes of tissues. Previous studies have reported that dielectric properties could be used as an index parameter for identification of normal and malignant liver (2), thyroid (3), breast (4), and colorectal tissues (5). For the measured dielectric data, the dielectric parameters at each frequency point are equivalent to the feature parameters. This makes the data cumbersome and reduces the classification efficiency. Therefore, it is necessary to select an effective classifier for abnormal tissue identification.

Probabilistic neural network (PNN) was first proposed by Donald F. Specht in the late 18$^{th}$ century. The theoretical basis of the network is Bayesian classification theory and probability density function estimation (6–10). It can realize the function of nonlinear learning algorithms with linear learning algorithms, which is widely applied in pattern classification problems. Compared with other neural networks, PNN has the advantages of easy training and fast convergence. Therefore, it is suitable for real-time classification. In PNN, the radial basis function in the pattern layer transfers data as an activation function, and the smooth factor $\sigma$ determines the width of the Gaussian curve (9). However, in the traditional PNN, the value of $\sigma$ of each neuron in the pattern layer is fixed, which leads to the failure to fully reflect the real situation of the sample space and limits the performance of the network. Therefore, allowing activation functions of different neuron classes in the pattern layer to take different $\sigma$ values will improve the performance of the network. Simulated annealing (SA) algorithm is a general optimization algorithm based on probability. It can find the optimal solution of the objective function in a large space. It has the advantages of strong robustness, is suitable for parallel processing, and can be used for the optimization of complex nonlinear problems (11, 12).

In this study, an adaptive probabilistic neural network with an optimized smooth factor by simulated annealing algorithm (SA-PNN) is proposed to classify metastatic and non-metastatic thoracic lymph nodes in lung cancer patients based on dielectric properties. Expected classification results are obtained.

# MATERIALS AND METHODS

## Data Introduction

The dielectric parameters of lymph nodes were measured using open-ended coaxial probes (13, 14). All measurements were from patients receiving lung surgery in the Department of Thoracic Surgery, Nanfang Hospital, Southern Medical University. All thoracic lymph nodes were freshly obtained during surgery within 10 min after these samples were removed from the patients to increase the time-sensitivity to increase the time-sensitivity. The metastatic status of the thoracic lymph nodes was determined by regular pathological examination. Related human tissue studies were approved by the ethics committee of Nanfang Hospital, Southern Medical University, Guangzhou, China (NFEC-2017-070). This trial was registered at https://clinicaltrials.gov (registration number: NCT03339479) and all patients provided informed consent in accordance with the Declaration of Helsinki. The Synthetic Minority Oversampling Technique (SMOTE) algorithm was used to preprocess the lymph node data (15).

## Feature Parameter Scoring

The Statistical Dependency (SD) method is applied in this paper as the feature scoring algorithm to score the permittivity and conductivity at each frequency point. As a feature scoring algorithm, the goal of the SD method is simply to measure whether the values of a feature are dependent on the associated class labels or whether the two simply co-occur by chance. The statistical dependence between the discretized feature values y and the class labels z is evaluated according to Formula (1) (16):

$$SD = \sum_{y \in Y} \sum_{z \in Z} p(y,z) \frac{p(y,z)}{p(y)p(z)} \quad (1)$$

In this formula, p(y, z) stands for the joint probability distribution of y and z, p(y) and p(z) stand for the marginal probability distribution functions of y and z, respectively. The larger the SD, the higher the dependency between the feature values and the class labels. In the case that the feature is fully independent of the class labels, the SD will obtain the minimal value of one. The SD value of each feature parameter can be obtained by calculating them using this formula. The SD value minus one (SD-1) was taken as the final score of the feature parameters.

Different feature subsets are combined for classification experiments. The feature subset with the best classification result is selected as the final feature vector for identification and classification.

## Probabilistic Neural Network

### Probabilistic Neural Network Model

PNN was used in this study (6–10). PNN is composed of four layers: input layer, radial base layer (pattern layer), decision-making layer (summation layer) and output layer (**Figure 1**).

Taking the network input vector dimension of three as an example, the details of each layer are outlined below.

The first layer is the input layer, which receives the input of samples $X = (x_1, x_2, x_3)$, where $x_i$ (i = 1, 2, 3) represents the input of the number i neuron in this layer, and transmits the input data to the radial base layer. The number of neurons in this layer is equal to the number of feature variables.

The second layer is the pattern layer. The number of neurons in this layer is equal to the number of training samples. Each neuron in the pattern layer has a center. After receiving data from the input layer, the distance between the input data and each center is calculated. Each neuron will output a scalar. After the sample vector X is input into the pattern layer, the input-

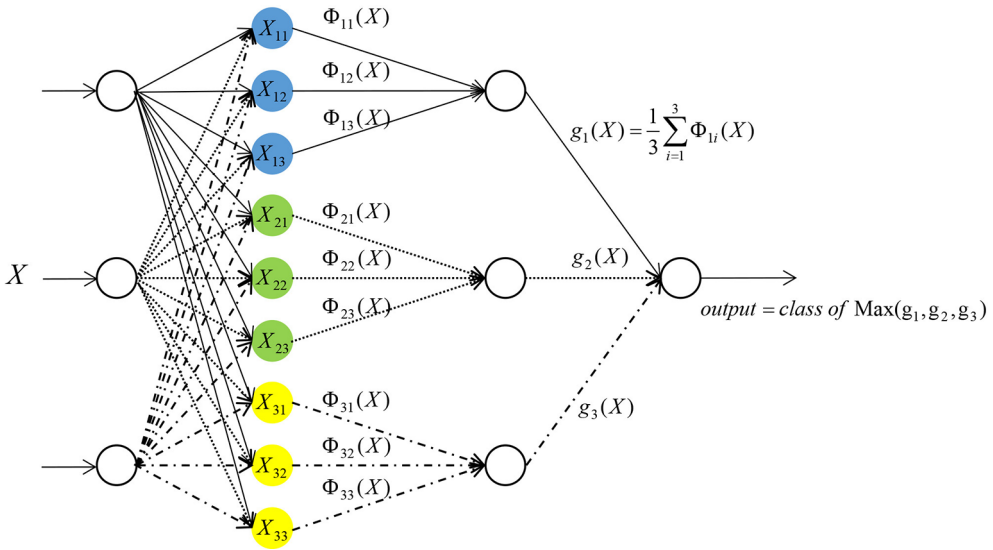


**FIGURE 1** | Network structure of probabilistic neural network.

output relationship of the number j neuron in the class i mode of the pattern layer is determined by Formula (2):

$$\boldsymbol{\Phi_{ij}} = \boldsymbol{exp}\left(-\frac{\| \boldsymbol{X} - \boldsymbol{X_{ij}} \|^2}{\boldsymbol{\sigma}^2}\right) \quad (2)$$

In the following formula, i = 1, 2, …, m, where m stands for the total number of training samples. In this study, m = 2. Xij stands for the center of the $j^{th}$ neuron in the $i^{th}$ class sample. $\boldsymbol{\Phi_{ii}}$ stands for the output of the $j^{th}$ neuron in the $i^{th}$ class sample. $\sigma$ is a constant, which is the width parameter or smooth factor of the Gaussian curve. This constant plays an important role in the performance of PNN.

The third layer is a summation layer. The number of neurons in this layer is equal to the number of classification categories. In this study, the number of neurons in the summation level is two. Since each neuron in the pattern layer has been designated to a certain class, the neurons belonging to the same class in the pattern layer will be connected with the same neuron in the summation layer. While the neurons of a different class in the pattern layer will not be connected to the same neuron in the summation layer. The output of neurons belonging to the same class in the pattern layer is weighted and averaged in the summation layer (17) by Formula (3):

$$\boldsymbol{s_i} = \frac{\sum_{j=1}^{n} \boldsymbol{\Phi_{ij}}}{\boldsymbol{n}} \quad (3)$$

In the above formula, $s_i$ stands for the output of the $i^{th}$ class in the summation layer, and n stands for the number of neurons in the $i^{th}$ class.

The fourth layer is the output layer. The number of neurons in this layer is equal to the number of neurons in the summation layer. Each neuron in the summation layer will be connected to the neurons in the output layer with corresponding weights. In this study, all the weights are taken as one. That is, all the neurons are connected with the same weight. The output layer is based on Bayesian classification decision theory, where there will be competition among neurons. By receiving the output of the summation layer neurons and judging the values, the neuron with the maximum posterior probability is found in the output layer. The output of this neuron is one, and all other neuron outputs is zero.

## Optimization of the Probabilistic Neural Network by a Simulated Annealing Algorithm

To improve the performance of the network, it is allowed to take different σ values in the pattern layer by the activation functions of different class of neurons. Formula (2) can transform into Formula (4) as shown below:

$$\boldsymbol{\Phi_{ij}} = \boldsymbol{exp}\left(-\frac{\| \boldsymbol{X} - \boldsymbol{X_{ij}} \|^2}{\boldsymbol{\sigma_i}2}\right) \quad (4)$$

The steps for optimizing the PNN with SA-PNN are as follows:

Step 1: Establish a fitness function. The goal of this study is to improve the accuracy of identification of metastases in lymph nodes. Therefore, the minimum number of classification errors is expected. The error rate of the selected fitness function for classification is:

$$\boldsymbol{f(\sigma)} = \frac{\boldsymbol{N_{error}}}{\boldsymbol{N_{sum}}} \times \mathbf{100}\,\%$$

In this formula, $N_{error}$ stands for the number of incorrectly identified samples in the training sample set, and $N_{sum}$ stands for the total number of training samples.

Step 2: Initialize parameters. For the initial solution $\sigma_0$, calculate the corresponding fitness function value $f(\sigma_0)$ and set the initial temperature $t = t_0$.

Step 3: Set the number of iterations as Count = 0.

Step 4: Calculated the increment $\Delta f = f(\sigma) - f(\sigma_0)$, after the feasible solution $\sigma$ is randomly generated from the neighborhood

Step 5: Accept $\sigma$ as the new current solution and considered the starting point for the next time ($\sigma 0 = \sigma$), if $\Delta f < 0$. Once $\Delta f \geq 0$, determine whether $e^{-\Delta f/t} > rand(0,1)$ (t is the current temperature) is valid. If so, accept the solution, otherwise discard the solution and take the original solution as the next starting point.

Step 6: Set the number of iterations for Count= Count+1. If Count does not reach the maximum number, return to Step 4, or continue with the next steps.

Step 7: Anneal. Decrease t gradually, where $t \rightarrow 0$, then proceed to Step 3.

In the steps above, the parameters settings are as follows: initial solution $\sigma_0$ is randomly generated, initial temperature $T_0 = 100$, number of iterations Count=1000. The annealing strategy is the most commonly adopted exponential annealing $t_k = \alpha\, t_{k-1}$, where k is a positive integer and $k \geq 1$, $0 < \alpha < 1$.

Since the adaptive PNN is prone to over-fitting in the experimental process, a part of the data set is divided into a validation set to adjust the smooth factor to alleviate over-fitting. The specific algorithm flow is shown in **Figure 2**. When a group of $\sigma$ values corresponding to the minimum value of the fitness function is discovered by a training set, validation is conducted with the validation set. The threshold is then set. When the classification accuracy of the validation set is lower than the threshold value, the obtained group of $\sigma$ values is adjusted. The test set is then examined, which helps prevent over-fitting.

## Other Prediction Models

In this study, besides the SA-PNN, five algorithms, including the BP neural network, RBF neural network, the classify function, SVM and kNN, were applied to analyze the data. The data analysis for the BP neural network, the RBF neural network, the classify function, SVM and kNN was performed using MATLAB 2017 (MathWorks Inc., Natick, MA, USA).

## Calculation of the Classification Performance Evaluation Index

In this study, the accuracy, specificity and sensitivity of the classifier are considered in judging its performance (18). The formulas for sensitivity, specificity and accuracy are as follows:

$$SEN = \frac{TP}{TP + FN} \times 100\,\%$$

$$SPE = \frac{TN}{FP + TN} \times 100\,\%$$

$$ACC = \frac{TP + TN}{TP + FN + FP + TN} \times 100\,\%$$

SEN, SPE and ACC represent sensitivity, specificity, and accuracy, respectively. TP (true positivity) represents the number of tumor samples correctly identified, FN (false negativity) represents the number of tumor samples mistakenly identified as normal tissue samples, TN (true negativity) represents the number of normal tissue samples correctly identified, and FP (false positivity) represents the number of normal tissue samples mistakenly identified as tumor samples.

Through stratified random sampling, 60% of samples were selected for the training set from the data set of metastatic thoracic lymph nodes and non-metastatic thoracic lymph nodes in lung cancer patients, 20% of samples were selected for the validation set, and 20% of samples were selected for the test set. The experiment was repeated 20 times. The 20-hold-out method was used, and the average value of 20 results was taken as the final result.

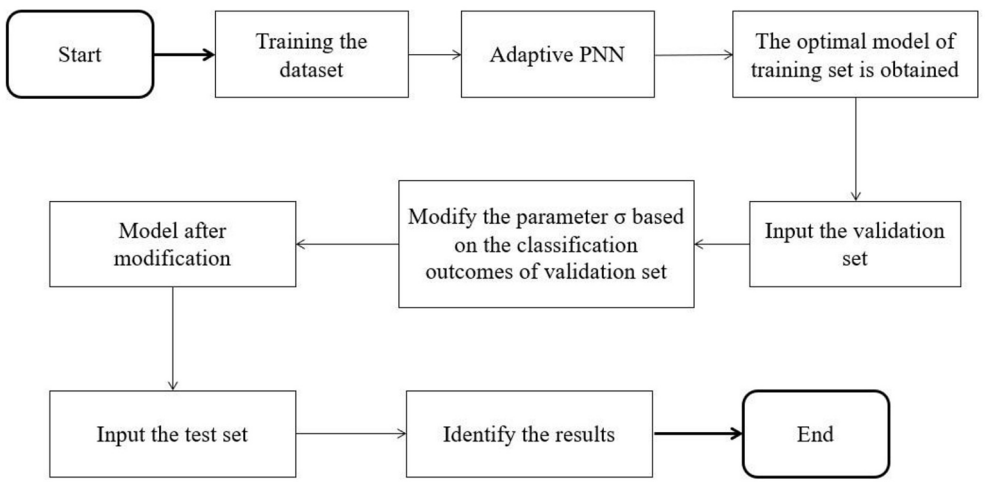


**FIGURE 2** | Flow chart of adaptive probabilistic neural network algorithm based on validation set.

# RESULTS

## Sample Information and Dielectric Properties of Lymph Nodes

By combining current and previously published data (19), the dielectric parameters from 41 lung cancer metastatic thoracic lymph nodes and 178 non-metastatic lung thoracic lymph nodes from 74 patients were measured (**Table 1**) using an open-ended coaxial probe with 3,951 frequency points in the range of 50 MHz to 4 GHz.

In **Figure 3**, the curve of the median of the dielectric properties of metastatic and non-metastatic thoracic lymph nodes in lung cancer patients is shown. From the measurements, it can be learned that there are obvious differences in the permittivity and conductivity between metastatic and non-metastatic thoracic lymph nodes in the range of 50 MHz to 4 GHz. The permittivity and conductivity of metastatic thoracic lymph nodes are higher than those of non-metastatic thoracic lymph nodes.

## SD-1 Values of Permittivity and Conductivity of Lymph Nodes

The SD-1 values of permittivity and conductivity for pulmonary thoracic lymph nodes at each frequency point are shown in **Figure 4**. Among the top 100 values with the highest feature scores, only the 65$^{th}$ has a permittivity at 2824 MHz, with the rest being conductivity scores. Therefore, it can be preliminarily inferred that using conductivity as a feature parameter to differentiate metastatic and non-metastatic thoracic lymph nodes in lung cancer patients is more effective.

**TABLE 1** | The relevant information of samples.

| Items | Value |
|---|---|
| Number of patients | 74 |
| Age of patients | 30 ~ 82 |
| number of metastatic thoracic lymph nodes | 178 |
| number of non-metastatic thoracic lymph nodes | 41 |
| Temperature of samples (°C); | 23.5 ± 1.7 |

## Classification Results for SA-PNN at Different Frequencies

The classification results of SA-PNN using dielectric parameters at different frequency points as feature vectors is shown (**Figure 5**). The highest differentiating accuracy rate of 90.83% was achieved when the permittivity at seven frequencies (2824, 2799, 2798, 2823, 2821, 2819, and 1888 MHz) were invoked as feature parameters (**Figure 5A**). The corresponding specificity and sensitivity values were 91.94% and 89.72%, respectively. The highest differentiating accuracy rate of 92.92% was achieved when the conductivity at eight frequencies (3959, 3958, 3960, 3978, 3510, 3889, 3888, and 3976 MHz) were invoked as feature parameters (**Figure 5B**). The corresponding specificity and sensitivity values were 94.72% and 91.11%, respectively.

These results also support the previous speculation of the SD-1 value using conductivity as a feature with better differentiation between metastatic and non-metastatic thoracic lymph nodes. Therefore, for the identification of metastatic and non-metastatic thoracic lymph nodes in lung cancer patients, the conductivity at eight frequency points (3959, 3958, 3960, 3978, 3510, 3889, 3888, and 3976 MHz) was finally selected as the feature vector.

## Comparison of the Identification Results Among Six Algorithms

The identification results of thoracic lymph nodes by PNN, BP neural network, RBF neural network, the classify function, SVM and kNN algorithms under different parameters are shown in **Figure 6**. For PNN, when the smooth factor σ=0.1, the highest differentiating accuracy rate of 91.25% was achieved, and the specificity and sensitivity were 92.78% and

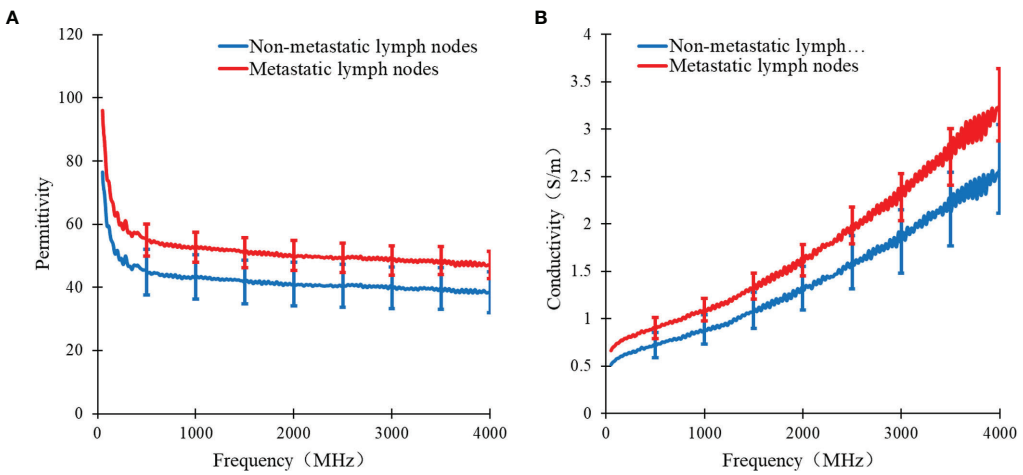


**FIGURE 3** | Curve of median dielectric properties of lung tissue and lymphonodi pulmonales in the range of 50MHz~4GHz. Curve of **(A)** the median relative permittivity **(B)** the median conductivity with metastatic and non-metastatic lymphonodi pulmonales of lung cancer.

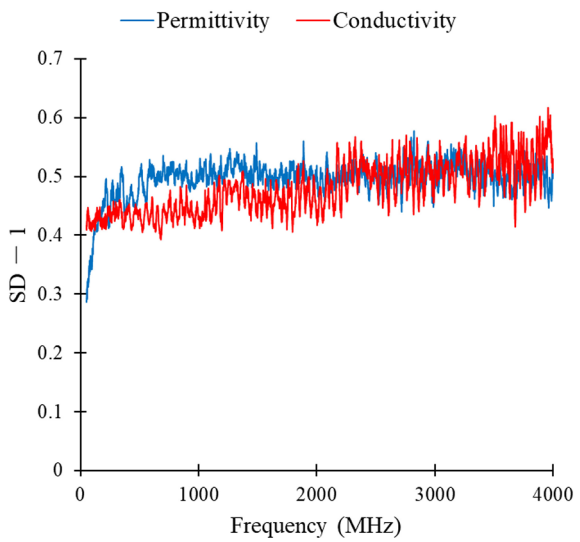


**FIGURE 4** | SD-1 values of permittivity and conductivity of lung lymphonodi pulmonales at various frequency points.

89.72%, respectively. For the BP neural network, when the number of neurons in the hidden layer was 37, the highest differentiating accuracy rate of 88.89% was achieved, and the specificity and sensitivity were 90.28% and 87.50%, respectively. For the RBF neural network, when the smooth factor $\sigma = 0.2$, the highest differentiating accuracy rate of 82.43% was achieved, and the specificity and sensitivity were 93.47% and 71.39%, respectively. For the classify function, when the type setting was "diagLinear," the highest differentiating accuracy rate of 88.54% was achieved, and the specificity and sensitivity were 94.72% and 82.36%, respectively. For SVM, when the kernel function was "Quadratic," the highest differentiating accuracy rate of 89.93% was achieved, and the specificity and sensitivity were 90.83% and 89.03%, respectively. For the kNN algorithm, when the k-value =1, the highest differentiating accuracy rate of 91.46% was achieved, and the specificity and sensitivity were 92.92% and 90.00%, respectively.

## DISCUSSION

In this study, the dielectric parameters of 219 lymph nodes (178 non-metastatic and 41 metastatic) from 74 patients were measured. The number ratio of metastatic and non-metastatic lung lymph node data was about 1:4, with a significant class imbalance. In machine learning, class imbalance often affects the performance of the trained classifier, which causes certain class bias in identification for the classifier. Therefore, to obtain an objective classifier, this study used the SMOTE algorithm to pre-process the lymph node data. The basic idea of SMOTE algorithm is to generate synthetic examples, by taking each minority class sample as center, calculating its k nearest neighbors. Randomly select a sample from its k nearest neighbors, connect this sample with the center one, and then randomly select a point along the line segment between two points as a new minority class sample (15). The conductivity values at eight frequency points (3959, 3958, 3960, 3978, 3510, 3889, 3888, and 3976 MHz) were selected as the feature vector. The classification of metastatic and non-metastatic thoracic lymph nodes in lung cancer patients based on dielectric properties is studied by the proposed adaptive probabilistic neural network, and the best classification results of several methods are summarized in **Table 2**. As shown in **Table 2**, the SA-PNN proposed in this paper achieved the highest classification accuracy, 92.92%, which indicates that its differentiation performance is higher than other classification algorithms.

With the popularity of lung cancer screening, the number and proportion of people diagnosed with early-stage disease is increasing. Surgery is considered the most effective treatment

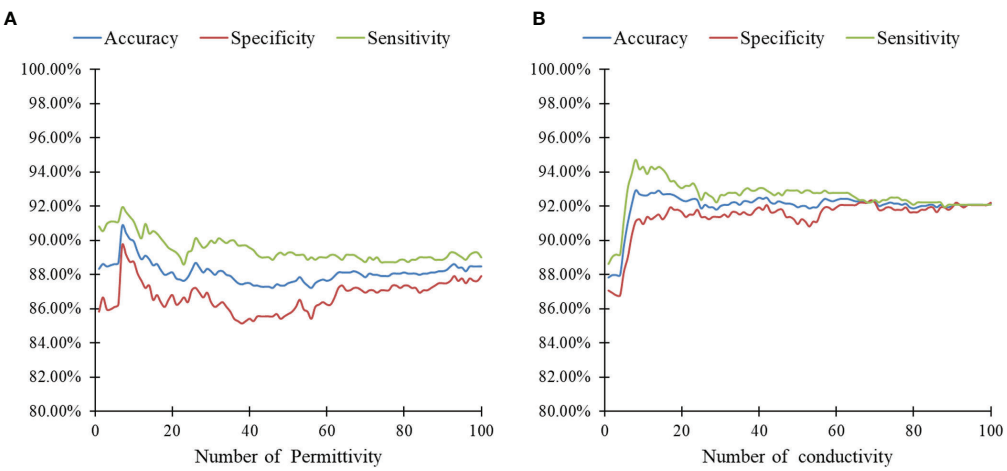


**FIGURE 5** | Results of SA-PNN classification of lymphonodi pulmonales. **(A)** permittivity and **(B)** conductivity at different number frequencies.

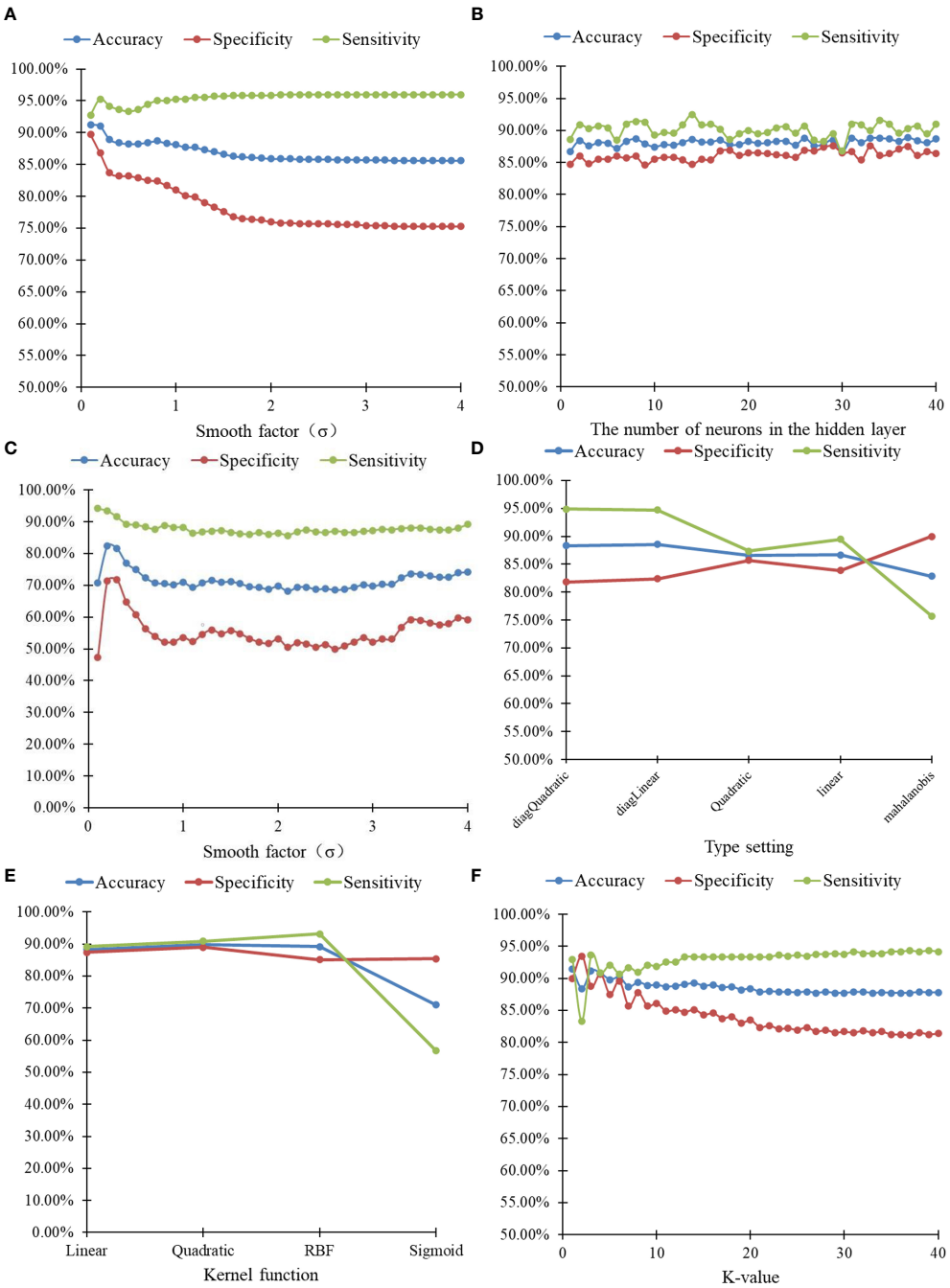


**FIGURE 6** | 20-hold-out validation results of lymphonodi pulmonales by six algorithms with different parameters. **(A)** PNN. **(B)** BP neural network. **(C)** RBF neural network. **(D)** Classify. **(E)** SVM. **(F)** kNN.

of early-stage lung cancer (20). With the various surgical management techniques of early-stage lung cancer, lymph node staging is considered an important criterion for these resections (21). At present, the diagnosing thoracic lymph nodes are required to go through multiple processing steps, such as tissue sectioning and staining, which takes a long time and is time sensitive. Therefore, a simple operational, rapid determination and noninvasive auxiliary diagnostic method for the identification of malignant tumors in surgery is needed.

At present, there are few published studies focusing on the method of tissue classification based on dielectric properties. Among the few known papers, most of them model the fit for dielectric parameter data of tissue samples in a wide frequency band. The fitted model parameters were taken as feature vectors,

**TABLE 2** | The best classification results of lymphonodi pulmonales by different methods.

| Methods | Accuracy (%) | Sensitivity (%) | Specificity (%) |
|---|---|---|---|
| PNN | 91.25 | 92.78 | 89.72 |
| BP | 88.89 | 90.28 | 87.50 |
| RBF | 82.43 | 93.47 | 71.39 |
| Classify | 88.54 | 94.72 | 82.36 |
| SVM | 89.93 | 90.83 | 89.03 |
| kNN | 91.46 | 92.92 | 90.00 |
| SA-PNN | 92.92 | 94.72 | 91.11 |

follow by classification by SVM (22–26), linear discriminant analysis (27), kNN (28), BP neural network (29), and RBF neural network (29). When processing data, the model parameters obtained by data fitting have certain volatility, which affects the identification results. In addition, the time cost will be increased when the dielectric parameters of samples are measured in a wide frequency band and complicated data fitting is required. To optimize data measurement and processing times, this paper analyzed and obtained the dielectric parameters of representative frequency points as the feature vector. This is clearly more convenient for future applications. Within the classification methods, the kernel function and its parameters of SVM, the k-value of the kNN algorithm, the number of hidden layers and neurons in the BP neural network, and the smooth factor of the radial basis function in the RBF neural network play key roles in the performance of each algorithm. However, it was quite challenging to select these parameters properly. Compared with the aforementioned algorithms, the number of neurons in each layer of the adaptive PNN proposed in this paper is easy to determine. The smooth factor of network parameters can modify adaptively, which can maximize its classification performance. This is also the advantage of adaptive PNN compared with other algorithms.

The study of differentiation between benign and malignant tissues during surgery is an important clinical application of biological tissue dielectric measurements, which can provide auxiliary diagnostic methods for the identification of malignant tumors during surgery. The main purpose of this paper is to improve the pattern recognition module of real-time detection and identification systems of benign and malignant tissues based on dielectric properties of tissues. At present, the collected number of sample data is relatively limited. More data is required for the training dataset of the model in practical clinical applications, in order to obtain a model with higher classification accuracy. It is necessary to collect more data to achieve a more reliable model. In addition, the current data of tissue dielectric properties are measured *in vitro*. The dielectric properties of tissue *in vitro* cannot completely represent the dielectric properties of *in vivo* tissue because the moisture content and temperature of tissue *in vitro* will be different from that of *in vivo* tissue. These differences would also affect the measured results. Therefore, follow-up studies should include a large number of real-time *in vivo* tissue dielectric property data for classification research.

## DATA AVAILABILITY STATEMENT

The raw data supporting the conclusions of this article will be made available by the authors, without undue reservation.

## ETHICS STATEMENT

The studies involving human participants were reviewed and approved by the ethics committee of Nanfang Hospital, Southern Medical University, Guangzhou, China (NFEC-2017-070). The patients/participants provided their written informed consent to participate in this study.

## AUTHOR CONTRIBUTIONS

DL and KC designed the study. DL, HY, ZW, and ZC were primarily responsible for conceptualization, methodology, and writing – reviewing and editing. HY, ZW, and ZC were responsible for data curation, software, and writing – original draft preparation. JF, XL, JZ, and HW were responsible for data revision. XY and KC revised the manuscript. DL, HY, ZW, and ZC contributed to this study equally. All authors contributed to the article and approved the submitted version.

## FUNDING

This project was supported by the Science and Technology Program of Guangzhou, China (201704020091) and the Dean Research Funding of Nanfang Hospital, Southern Medical University, China (2016B018) and Nanfang Thoracic Surgery collaborative project (NFTS-T-0202).

## REFERENCES

1. Asami K. Dielectric properties of microvillous cells simulated by the three-dimensional finite-element method. *Bioelectrochemistry (Amsterdam Netherlands)* (2011) 81(1):28–33. doi: 10.1016/j.bioelechem.2011.01.002
2. Wang H, He Y, Yang M, Yan Q, You F, Fu F, et al. Dielectric properties of human liver from 10 Hz to 100 MHz: normal liver, hepatocellular carcinoma, hepatic fibrosis and liver hemangioma. *Biomed Mater Eng* (2014) 24(6):2725–32. doi: 10.3233/bme-141090
3. Cheng Y, Fu M. Dielectric Properties for Differentiating Normal and Malignant Thyroid Tissues. *Med Sci Monit Int Med J Exp Clin Res* (2018) 24:1276–81. doi: 10.12659/msm.908204
4. Summers PE, Vingiani A, Di Pietro S, Martellosio A, Espin-Lopez PF, Di Meo S, et al. Towards mm-wave spectroscopy for dielectric characterization of breast surgical margins. *Breast (Edinburgh Scotland)* (2019) 45:64–9. doi: 10.1016/j.breast.2019.02.008
5. Zhou DF, Zhai WK, Sun Y, Han S, Huang LM, Xin XG, et al. [Differences in dielectric properties between mucosal and serosal surface of malignant

colorectal tissues, adjacent tissues at 1 cm and 3 cm and normal colorectal tissues]. *Nan Fang Yi Ke Da Xue Xue Bao* (2018) 38(4):434–42. doi: 10.3969/j.issn.1673-4254.2018.04.11

6. Mohamed Shakeel P, Desa MI, Burhanuddin MA. Improved watershed histogram thresholding with probabilistic neural networks for lung cancer diagnosis for CBMIR systems. *Multimed Tools Appl* (2020) 79(23):17115–33. doi: 10.1007/s11042-019-7662-9
7. Daqrouq K, Chen S, Khalaf E, Morfeqa A, Sheikha M, Qatawneh A, et al. Wavelet entropy based probabilistic neural network for classification. *Curr J Appl Sci Technol* (2019) 35(5):1–7. doi: 10.9734/cjast/2019/v34i530145
8. Woźniak M, Połap D, Capizzi G, Sciuto GL, Kośmider L, Frankiewicz K. Small lung nodules detection based on local variance analysis and probabilistic neural network. *Comput Methods Programs Biomed* (2018) 161:173–80. doi: 10.1016/j.cmpb.2018.04.025
9. Ahmadlou M, Adeli H. Enhanced probabilistic neural network with local decision circles: A robust classifier. *Integr Comput Aided Eng* (2010) 17:197–210. doi: 10.3233/ICA-2010-0345
10. Gaikwad SBJM. Brain tumor classification using principal component analysis and probabilistic neural network. *Int J Comput Appl* (2015) 120(3):5–9. doi: 10.5120/21205-3885
11. Samuel RK, Venkumar P. Optimized Temperature Reduction Schedule for Simulated Annealing Algorithm. *Mater Today: Proc* (2015) 2(4):2576–80. doi: 10.1016/j.matpr.2015.07.209
12. Mafarja MM, Mirjalili S. Hybrid Whale Optimization Algorithm with simulated annealing for feature selection. *Neurocomputing* (2017) 260:302–12. doi: 10.1016/j.neucom.2017.04.053
13. Bobowski JS. Permittivity Measurements of Biological Samples by an Open-Ended Coaxial Line. *Prog In Electromagn Res B* (2012) 40:159–83. doi: 10.2528/pierb12022906
14. Liu Y, Huang Y, Xin X, Yu X. [Sensing volume of tissue dielectric property measurement with open-ended coaxial probe]. *Nan Fang Yi Ke Da Xue Xue Bao* (2020) 40(7):1036–43. doi: 10.12122/j.issn.1673-4254.2020.07.19
15. Chawla NV, Bowyer KW, Hall LO, Kegelmeyer WP. SMOTE: Synthetic Minority Over-sampling Technique. *J Artif Intell Res* (2002) 16(1):321–57. doi: 10.1613/jair.953
16. Pohjalainen J, Räsänen O, Kadioglu S. Feature selection methods and their combinations in high-dimensional classification of speaker likability, intelligibility and personality traits. *Comput Speech Lang* (2015) 29(1):145–71. doi: 10.1016/j.csl.2013.11.004
17. Lin D-T. Target Components Discrimination using Adaptive Time-Delay Neural Network. *J Inf Sci Eng* (2004) 20(5):959–80s. doi: 10.1186/s12868-016-0283-6
18. Yang M, Gu XN, Liu F, Wang YY, Cai YL, Liu DM, et al. [Diagnostic values of breast imaging and reporting data system and ultrasonic elastography for benign and malignant breast lesions]. *Zhonghua Yi Xue Za Zhi* (2013) 93 (39):3125–7. doi: mdl-24417992
19. Yu X, Sun Y, Cai K, Yu H, Zhou D, Lu D, et al. Dielectric Properties of Normal and Metastatic Lymph Nodes Ex Vivo From Lung Cancer Surgeries. *Bioelectromagnetics* (2020) 41(2):148–55. doi: 10.1002/bem.22246
20. Tandberg DJ, Tong BC, Ackerson BG, Kelsey CR. Surgery versus stereotactic body radiation therapy for stage I non-small cell lung cancer: A comprehensive review. *Cancer* (2018) 124(4):667–78. doi: 10.1002/cncr.31196
21. Ginsberg RJ, Rubinstein LV. Randomized trial of lobectomy versus limited resection for T1 N0 non-small cell lung cancer. Lung Cancer Study Group. *Ann Thorac Surg* (1995) 60(3):615–22; discussion 22-3. doi: 10.1016/0003-4975(95)00537-u
22. Truong BCQ, Tuan HD, Wallace VP, Fitzgerald AJ, Nguyen HT. The Potential of the Double Debye Parameters to Discriminate Between Basal Cell Carcinoma and Normal Skin. *IEEE Trans Terahertz Sci Technol* (2015) 5 (6):990–8. doi: 10.1109/TTHZ.2015.2485208
23. Grewal PK GF. Pilot study: electrical impedance based tissue classification using support vector machine classifier. *IET Sci Meas Technol* (2014) 8 (6):579–87. doi: 10.1049/iet-smt.2013.0087
24. Yilmaz T, Kılıç MA, Erdoğan M, Çayören M, Tunaoğlu D, Kurtoğlu İ, et al. Machine learning aided diagnosis of hepatic malignancies through in vivo dielectric measurements with microwaves. *Phys Med Biol* (2016) 61(13):5089–102. doi: 10.1088/0031-9155/61/13/5089
25. Truong BC, Tuan HD, Fitzgerald AJ, Wallace VP, Nguyen HT. A dielectric model of human breast tissue in terahertz regime. *IEEE Trans Biomed Eng* (2015) 62(2):699–707. doi: 10.1109/tbme.2014.2364025
26. Song H, Sato H, Koide T, Arihiro K, Okada M, Kadoya T, et al. "Breast tumor tissues classification using the modified cole-cole parameters with machine learning technique". In: *12th European Conference on Antennas and Propagation (EuCAP 2018) IET* (2018). p. 1–2.
27. da Silva JE, de Sá JP, Jossinet J. Classification of breast tissue by electrical impedance spectroscopy. *Med Biol Eng Comput* (2000) 38(1):26–30. doi: 10.1007/bf02344684
28. Saçlı B, Aydınalp C, Cansız G, Joof S, Yilmaz T, Çayören M, et al. Microwave dielectric property based classification of renal calculi: Application of a kNN algorithm. *Comput Biol Med* (2019) 112:103366. doi: 10.1016/j.compbiomed.2019.103366
29. Helwan A, Idoko JB, Abiyev RH. Machine learning techniques for classification of breast tissue. *Proc Comput Sci* (2017) 120:402–10. doi: 10.1016/j.procs.2017.11.256

**Conflict of Interest:** The authors declare that the research was conducted in the absence of any commercial or financial relationships that could be construed as a potential conflict of interest.

frontiers in Neurorobotics

ORIGINAL RESEARCH
published: 16 March 2021
doi: 10.3389/fnbot.2021.635492

# A Relational Adaptive Neural Model for Joint Entity and Relation Extraction

*Guiduo Duan*[1,2], *Jiayu Miao*[1,2], *Tianxi Huang*[3]*, *Wenlong Luo*[1,2] *and Dekun Hu*[4]

[1] School of Computer Science and Engineering, University of Electronic Science and Technology of China, Chengdu, China, [2] Trusted Cloud Computing and Big Data Key Laboratory of Sichuan Province, Chengdu, China, [3] Department of Fundamental Courses, Chengdu Textile College, Chengdu, China, [4] College of Computer, Chengdu University, Chengdu, China

Relation extraction is a popular subtask in natural language processing (NLP). In the task of entity relation joint extraction, overlapping entities and multi-type relation extraction in overlapping triplets remain a challenging problem. The classification of relations by sharing the same probability space will ignore the correlation information among multiple relations. A relational-adaptive entity relation joint extraction model based on multi-head self-attention and densely connected graph convolution network (which is called MA-DCGCN) is proposed in the paper. In the model, the multi-head attention mechanism is specifically used to assign weights to multiple relation types among entities so as to ensure that the probability space of multiple relation is not mutually exclusive. This mechanism also predicts the strength of the relationship between various relationship types and entity pairs flexibly. The structure information of deeper level in the text graph is extracted by the densely connected graph convolution network, and the interaction information of entity relation is captured. To demonstrate the superior performance of our model, we conducted a variety of experiments on two widely used public datasets, NYT and WebNLG. Extensive results show that our model achieves state-of-the-art performance. Especially, the detection effect of overlapping triplets is significantly improved compared with the several existing mainstream methods.

**Keywords: entity relation joint extraction, overlapping triplets detection, DCGCN, relational-adaptive mechanism, graph convolutional networks**

OPEN ACCESS

***Edited by:***
*Chao Huang,*
*University of Macau, China*

***Reviewed by:***
*Oluwarotimi Williams Samuel,*
*Chinese Academy of Sciences (CAS), China*
*Chao Gao,*
*Southwest University, China*
*Ruizhi Wu,*
*Beijing Jiaotong University, China*

***Correspondence:**
*Tianxi Huang*
*huang_tianxi@163.com*

***Received:*** *30 November 2020*
***Accepted:*** *22 February 2021*
***Published:*** *16 March 2021*

***Citation:***
*Duan G, Miao J, Huang T, Luo W and Hu D (2021) A Relational Adaptive Neural Model for Joint Entity and Relation Extraction. Front. Neurorobot. 15:635492. doi: 10.3389/fnbot.2021.635492*

## INTRODUCTION

How to extract semantic and structured data from unstructured text is a particularly important task in the era of big data. Entity relation extraction is an essential subtask in the field of natural language processing (NLP). Its goal is to identify entity pairs from the text and extract one or more semantic relations between entity pairs, as shown in **Table 1**. The extracted triples are used extensively in many downstream NLP tasks, such as knowledge graph construction (Luan et al., 2018), intelligent question answering system (Yang et al., 2019).

At present, the relation extraction method can be divided into pipeline method and joint extraction method according to entity recognition and relation extraction, whether two subtasks are completed in order at one time. The traditional method was to adopt pipeline model, in which entity recognition was carried out first and then entity pair relation extraction was carried out.

**TABLE 1 |** An example of an overlapping triplet.

| **The [United States] president [Donald Trump] was born in [New York City].** | |
|---|---|
| SingleEntityOverlap **(SEO)** | EntityPairOverlap **(EPO)** |
| (**Donald Trump**, President_ of, United States) | (**Donald Trump**, Governance, **UnitedStates**) |
| (**Donald Trump**, Born_ in, New York City) | (**Donald Trump**, President Of, **United States)** |

Two extraction models were used respectively. This method has high flexibility and does not need to annotate the dataset of entities and relations at the same time. However, this method makes the model have error accumulation problem and the interaction information is missing (Li and Ji, 2014), ignoring the internal correlation information between the two tasks. Therefore, more work now focuses on the method of joint learning and makes the most of interactive information between entities and relations, which can solve the above problems to a certain extent. Some joint learning methods treat relation extraction as a sequential tagging problem, which cannot solve the words with multiple tags and therefore cannot extract relation triples with overlapping entities. As shown in **Table 1**, there may be different relations between the same entity pair in some sentences, such triples are called EntityPairOverlap (EPO), or there is one same entity between entity pairs, and such triples of relation are called SingleEntityOverlap (SEO). The extraction of overlapping triples is particularly difficult for the relational extraction model of joint learning, because there are no entities in the input and the entities need to be recognized by the model. In practical application, there are a large number of overlapping triples in text as shown in **Table 1**, and such text data will bring troubles to the current sequence tags-based joint learning methods. Therefore, effectively solving the problem of overlapping triples extraction can greatly improve the performance of the joint learning model.

Therefore, relation extraction still faces the great challenge of triplet extraction of overlapping entities and extraction of multiple relations between entity pairs. When detecting multiple relation types between entity pairs, most existing studies (Zeng et al., 2018; Nayak and Ng, 2020) are usually regarded as a multi-classification task, in which multiple relationship types share the same probability space. In the final classification, multiple relationships will be mutually exclusive, so the use of classifier detection will reduce the correlation degree of relationships. When detecting overlapping triples, the dependency information of words and the interaction information of triples are also significant. The method ImprovingGCN (Hong et al., 2020) and AntNRE (Sun et al., 2019) consider the dependency information of words and the interaction of triplets, but they do not consider the interaction information between the probabilistic subspaces of different relation types. Thus these methods ignore the high correlation between multiple relations and entity pairs.

In order to address the above issues, we propose a relational-adaptive joint entity relation extraction model based on multi-head self-attention and densely connected graph convolutional networks (DCGCN). Firstly, the model extracts the multi-granularity feature information from the text through the feature mixed encoding layer, so that the subsequent model can better capture the semantic information of the sentence. Then we get further dependency information between words through the stacked LSTM and GCN. In addition, we use the multi-head self-attention mechanism to assign weights to multiple relation types among entities so as to ensure that the probability space of multiple relations is not mutually exclusive, and extract the interaction information between the relation and entity. This method can construct multiple dynamic association matrices for each sentence, which can be used as the input of the second phase DCGCN to consider the interaction information between the probabilistic subspaces of different relation types. The DCGCN carries on the interaction of entity and relation in the second phase to obtain the structural information and potential text semantic information of the deeper level graph. Finally, entities and relations are predicted through the node representations extracted from the two-phase GCN.

The contributions of our work are summarized as follows:

(1) We propose a new joint entity relational extraction method based on two-phase GCN, which is an end-to-end model. The GCN in the first phase obtains the dependency information between words by inputting multi-granularity semantic features, while the DCGCN in the second phase can capture the potential semantic association between words in a specific relationship by inputting multiple attention dynamic association matrices.
(2) We design a relation adaptive mechanism based on multi-head attention to learn different relation types between overlapping entity pairs. This mechanism allocates different attention weights to the relations between entity pairs, and adaptively identifies the relations between entity pairs. This method can effectively identify overlapping triples.
(3) Extensive experiments have been conducted with the method in this paper, and the results indicate that our model achieves state-of-the-art performance on two widely used public datasets.

The following of paper is structured as follows. In Section, Related Works are provided, followed by a detailed description of the proposed model MA-DCGCN in Section Methodology. Our proposed framework is evaluated on two public datasets in Section Experimental and Results. The conclusion is drawn in Section Conclusion.

## RELATED WORK

The traditional pipeline method, in which the model is mainly based on the existing CNN (Zeng et al., 2014; Zhu et al., 2017), RNN (Socher et al., 2012; Hashimoto et al., 2013), LSTM (Xu et al., 2015; Zhang et al., 2015), ameliorates the performance of the model by changing the input characteristics or network architecture of the model. Due to its natural advantages in processing unstructured data, GCN has gained increasing popularity, which was introduced in many works to

learn the rich information contained in the dependency tree (Zhang et al., 2018, 2019; Guo et al., 2019). Qian et al. (2019) have improved word-level information extraction by constructing a complex graph structure with multiple relationships, and then using GCN to propagate information between nodes to generate rich features.

The initial linkage between entity recognition and relation extraction is established in the NovelTagging model (Zheng et al., 2017), which unifies the two tasks as a single sequential tagging problem. However, this method cannot resolve words with multiple tags, and therefore cannot extract relational triples with overlapping entities. Miwa and Bansal (2016) proposed a model based on bidirectional LSTM-RNN to represent the parameters of entity recognition and relation extraction jointly, but its model learning process is still similar to pipeline method, and it is not a typical joint extraction method. Katiyar and Cardie (2017) proposed for the first time a real entity relation joint extraction model based on recursive neural network, which does not rely on any dependency tree information, models entity recognition sub-tasks into sequence annotation tasks, and then extracts the relation between entity pairs through Shared coding layer features. Reinforcement learning (RL) is also widely used in the field of relation extraction (Qin et al., 2018; Takanobu et al., 2019; Zeng et al., 2019), in which the remote supervised noisy data sets are used to jointly optimize entity recognition module and relation extraction module.

For the sake of overcoming the problem of the redundant entity in the previous methods, Zheng et al. (2017) proposed an end-to-end sequence tag, the relation between extraction task as a tagging task. Sun et al. (2019) proposed binary entity relation graph to run on a new type of graph convolution network (GCN) after the graph on the binary map convolution computation, and the model can capture the entities and relations between the effective information. Chen et al. (2020) proposed a multi-channel framework composed of layered deep neural networks stacked to achieve relation extraction at sentence level. The above works can simultaneously extract entities and relations through joint extraction, but the model has poor performance for triples of overlapping relations.

Zeng et al. (2018) proposed a neural model CopyRE based on Seq2Seq for the first time in view of the overlapping relation, and the model considered the overlapping problem of relational triad through the copying mechanism of the entity copied from the source statement by the decoder. Fu et al. (2019) proposed the GraphRel model of end-to-end relation extraction for entity overlap. The model was divided into two phase, and the interaction between entities aand relations was considered through the relational weighted GCN of the second phase, which significantly improved the prediction of overlapping relations. Yuan et al. (2020) proposed a joint entity and relationship extraction model called RSAN, which combined the fine-grained semantic information of the relation to guide the entity recognition process. Zeng et al. (2020) proposed their own improved model CopyMTL and introduced named entity task for multi-task learning based on CopyRE, thus improving the problem that CopyRE can only extract single words and cannot match multi-character entities. Hong et al. (2020), based on GraphRel, proposed a new relational perceptive attention mechanism, which can acquire the representation of the relation between the span of two entities. This model utilized the characteristics of adjacent nodes and edge information when obtaining the characteristics of the encoding node. To solve the overlapping triple problem, we use the stacked LSTM-GCN encoder to identify entities, and introduce the multi-head self-attention mechanism to identify the relation types of overlapping entity pairs according to different attention weights, and then use the densely connected graph GCN to further extract the interaction information between entities and relations. The model implements end-to-end entity recognition and relation extraction through joint training of loss functions in different phases.

# METHODOLOGY

In this section, we introduce a relational extraction model for relational-adaptive densely connected graph convolutional network model using a multi-head self-attention mechanism which called MA-DCGCN. This model can extract the triples of overlapping relations in an end-to-end method. As shown in **Figure 1**, our model consists of four parts: the LSTM-GCN encoding layer, relation-adaptive multi-head attention layer, dense connected DCN layer and the linear combination layer.

## Encoding Layer

Given a text sequence $S = \{w_1, w_2, \cdots, w_i, \cdots, w_n\}$ of length $n$, where $w_i$ represents the $i$-th word in the sentence. First, we represent the text sequence as feature matrix $X = [x_1, \cdots, x_i, \cdots, x_n]$, and the i-th input word is initially represented as $x_i$. $x_i$ is composed of word context embedding, part-of-speech (POS) embedding and character-based word features. By inputting text sequences into a pre-trained Bert model to obtain context embedding, the model can be provided with the contextual semantic characteristics of word sequences. Character-based word features are computed by a convolutional neural network on a text sequence (CNN) (Krizhevsky et al., 2017).

$$x_i = Context(w_i) \oplus POS(w_i) \oplus Char(w_i) \tag{1}$$

Recursive neural network (RNN), long short-term memory network (LSTM) (Schuster and Paliwal, 1997) and gated recursive unit (GRU) are all effective methods for long sequence modeling (Hochreiter and Schmidhuber, 1997; Cho et al., 2014). For the sake of full consideration of the context semantic information of text sequence and the dependencies between words, we adopt bidirectional LSTM (Bi-LSTM) to encode the input word $x_i$ and its context together. The forward and backward LSTM hidden states are concatenated to obtain the complete context-aware vector $h_i$ of the word $x_i$ in the time step i. The expression formula of $h_i$ is as follows:

$$\vec{h}_i = LSTM_F(x_i, \vec{h}_{i-1}), \tag{2}$$

$$\overleftarrow{h}_i = LSTM_B(x_i, \overleftarrow{h}_{i-1}), \tag{3}$$

$$h_i = [\vec{h}_i; \overleftarrow{h}_i], i \in [1, n] \tag{4}$$

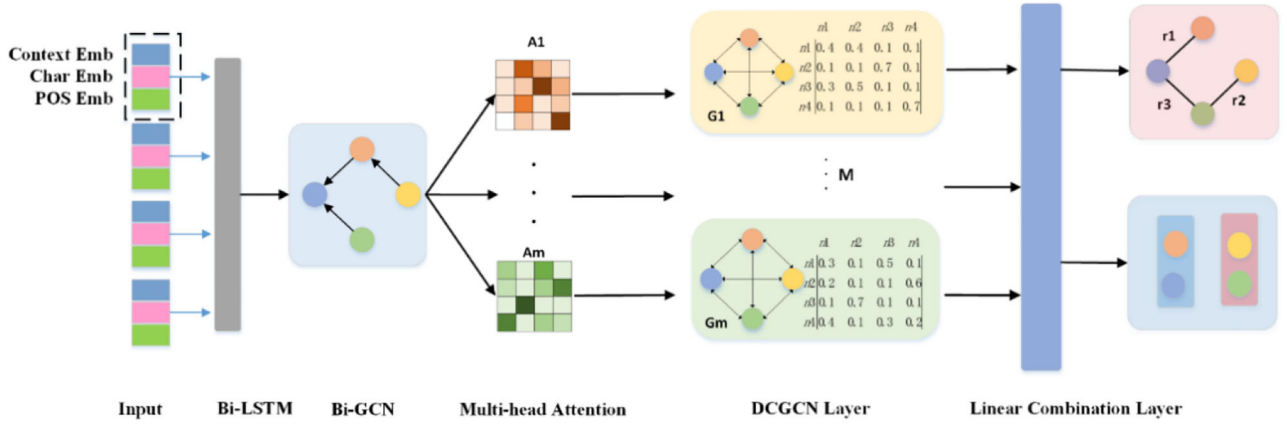


**FIGURE 1 |** The MA-DCGCN model for joint entity and relation extraction.

Where, $h_i \in R^{2\times d_l}$, $d_l$ stands for the dimension of Bi-LSTM's hidden state, $F$ and $B$ stand for the two directions of forward and backward of LSTM respectively. $h_i^0$ is the initial input feature $x_i$, $x_i \in R^d$, and $d$ is the dimension of the input feature.

In our work, the representation of the calculated output of the Bi-LSTM encoder serves as the input to the next Bi-GCN. For a given graph with $n$ nodes, the nodes in the graph are each word in the sentence, and the edges in the graph are the dependencies between words. We use $n \times n$ adjacency matrix $A_{ij}$ to represent the graph, and we add a self-loop for each point, that is, $A_{ij} = 1(i = j)$. When there is a dependency relation between word $i$ and word$j$, $A_{ij} = A_{ji} = 1$, otherwise it is 0. Given the representation of layer $l$, we can derive the representation of layer $l + 1$ from the following formula.

$$\vec{h}_i^{(l+1)} = \rho\Big(\sum_{j\in\vec{N}(i)} A_{ij}\vec{W}^{(l)}h_j^{(l)} + \vec{b}^{(l)}\Big) \tag{5}$$

$$\overleftarrow{h}_i^{(l+1)} = \rho\Big(\sum_{j\in\overleftarrow{N}(i)} A_{ij}\overleftarrow{W}^{(l)}h_j^{(l)} + \overleftarrow{b}^{(l)}\Big) \tag{6}$$

$$\vec{h}_i^{(l+1)} = [\vec{h}_i^{(l)}; \overleftarrow{h}_i^{(l)}], i \in [1, n] \tag{7}$$

Where, $W$ and $b$ are the weight matrix and deviation, $Ni$ is the neighbor of node $i$, and $\rho$ is the activation function (such as $RELU$, etc.).

By extracting the word features from LSTM-GCN encoding layer, we can recognize the entity of the word and predict the relation between word pairs. For entity recognition, we apply classification loss to the word features obtained by LSTM, denoting as $L_{ner1}$.

$$P(\hat{y}\,|w_i\,, s) = soft\max(W_{ner1}h_i + b_{ner1}) \tag{8}$$

$$L_{ner1} = -\frac{1}{m}\sum_{i=1}^{m}\log P(\hat{y} = y\,|w_i, s) \tag{9}$$

Regarding the relation extraction, we learn the weight matrix $W_r^i, W_r^j$ for the relation $r$ of word pairs $(w_i, w_j)$, and calculate the fraction $S$ of word pairs $(w_i, w_j)$ under the relation $r$. By calculating the probability of each relation between word pairs, we can get the relation of this phase to extract loss $L_{re1}$.

$$S_r(w_i, w_j) = RELU(W_r^i h_{w_i} \oplus W_r^j h_{w_j}) \tag{10}$$

$$P_r(w_i, w_j) = soft\max(S_r(w_i, w_j)) \tag{11}$$

$$L_{\mathrm{re1}} = -\frac{1}{\mathrm{m}}\sum_{i=1}^{m}\log P_r(w_i, w_j) \tag{12}$$

## Relation-Adaption Multi-Head Attention Layer

To work out the difficult overlapping problem of relations, we applied DCGCN again on the graph after the LSTM-GCN encoder layer, further propagated and learned the information of entities and relations on the constructed word graph. Considering that the edge information of the graph also contains information that is beneficial to entity relation extraction, the multi-head self-attention mechanism is added instead of using DCGCN directly in the second time, which can allocate an exclusive probability subspace for each relation between entity pairs without mutual exclusion. Based on the relation-adaption mechanism, we can calculate the independent correlation strength for the entities under different relation types in the sentence according to the semantic characteristics of the context, and detect the relation types between entity pairs adaptively. The attention matrix $A^m \in R^{N\times N}$ calculated by us is as follows:

$$A^{(m)} = soft\max\Big(\frac{Q^m W_Q^m \times (K^m W_K^m)^T}{\sqrt{d_r}}\Big)V^m \tag{13}$$

Where $Q^m \in R^{N\times d_r}$, $K^m \in R^{N\times d_r}$ represents the query and key of the $m$-th relational type, matrix $W$ is the model parameter, and $d_r$ is the dimension of the subspace of each relational type. $A_{i,j}^{(m)}$ represents the strength of the association between the word $i$ and the word $j$in the $m$-th relation.

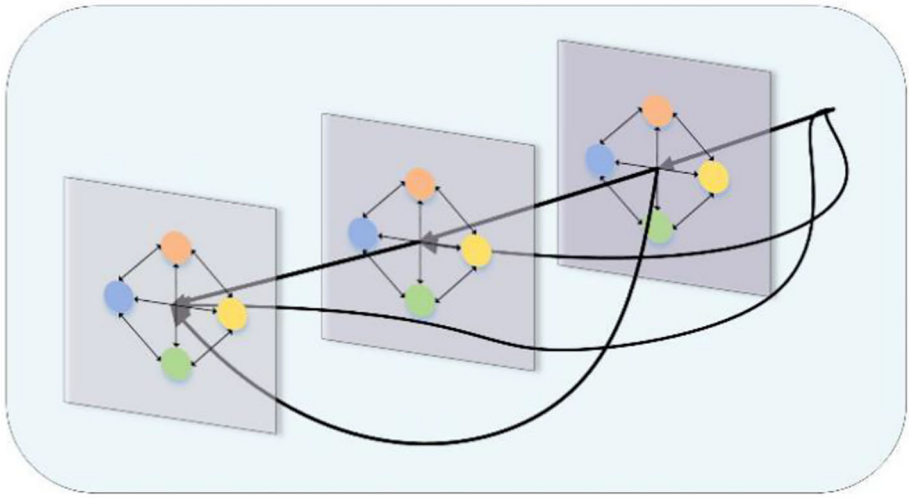

**FIGURE 2 |** An illustration of a three-layer densely connected graph convolutional network.

## Densely Connected GCN

In our work, a shallow GCN captures only local structural information on a large graph built of all words based on text sequences. Inspired by DenseNet (Huang et al., 2017) in the field of neural networks, we introduce densely connected GCN (Guo et al., 2019) into our MA-DCGCN model in order to capture richer node-related non-local information on large graphs for entity relation learning.

The structure of a densely connected GCN at three layers is shown in **Figure 2**, with any layer receiving the output of all preceding layers. For example, outputs from the first and second layers can be input to the third layer, so that first-order, second-order, and third-order neighborhood information from the nodes can be received. By using dense connections, we can train deeper GCN models to produce richer graphical representations than shallow GCN.

In densely connected GCN, the features of node $v$ in Layer $l$ not only contain the output feature $h^{(l-1)}$ of layer $l-1$, but also input the feature information of all previous layers. The node features $g_v^{(l)}$ of layer $l$ are denoted by the series of initial node feature $x_i$ and nodes of all previous layers:

$$g_i^{(l)} = [x_i; h_i^{(1)}; ...; h_i^{(l-1)})] \tag{14}$$

Since we generate independent subspaces for M relation types that are not mutually exclusive, we need to run m densely connected GCN layers for M attention matrices, so the GCN calculation is modified as follows:

$$h_{m_i}^{(l)} = RELU(\sum_{j \in N(i)}^{m} A_{ij}^{(m)} W_m^{(l)} g_j^{(l)} + b_m^{(l)}) \tag{15}$$

Where, $m = 1, 2, ..., M$, $W$ and b are the parameter matrix and bias terms associated with the attention matrix A. Each layer of W's dimension increases $d_{hidden}$, which is determined by the number of densely connected layers $L$ and the input feature dimension d. In this paper, $L = 3$. And $w^{(l)} \in R^{d_{hidden} \times d^{(l)}}$, where $d^{(l)} = d + d_{hidden} \times (l-1)$.

In order to integrate the feature representation of M relational types that have been closely connected, we use a general linear combination layer to output the final word features.

$$h_{final} = W_{final}[h_1; ...; h_M] + b_{final} \tag{16}$$

Where $W_{final} \in R^{d \times M}$ is the weight matrix, and $b$ is the bias vector of the linear transformation. Using the word features we finally obtained, we performed entity recognition and relation classification in Section "Encoding Layer" again to obtain that the losses in this phase were represented as $L_{ner2}$ and $L_{ner2}$.

## Joint Extraction

We adopt two kinds of losses in our joint training, entity recognition loss and relation extraction loss. For entity recognition, we use common BIESO marking scheme to represent the real labels, every word for text sequence must belong to one class. The total loss of our joint training is equal to the sum of two entity recognition losses and two relationship extraction losses in the whole calculation process of the model. The calculation formula of the total loss is as follows:

$$L = (L_{ner1} + L_{re1}) + \alpha(L_{ner2} + L_{re2}) \tag{17}$$

Where $\alpha$ is the weight between the losses of the two phases. Our model is trained jointly by minimizing L.

# EXPERIMENTAL AND RESULTS

## Dataset

We evaluate our model's performance on two public datasets that are common in the field of relational extraction.

**New York Times (NYT)**: the New York Times data set contains the New York Times web site from November 2009 to January 2010 in the 150 articles on business. The New York Times

**TABLE 2 |** Statistics about the datasets.

| Category | NYT | | WebNLG | |
|---|---|---|---|---|
| | Train | Test | Train | Test |
| Normal | 37,013 | 3,266 | 1,596 | 246 |
| EPO | 9,782 | 978 | 227 | 26 |
| SEO | 1,4735 | 1,297 | 3,406 | 457 |
| All | 5,6195 | 5,000 | 5,019 | 703 |
| Relation | 24 | | 246 | |

data set is constructed using a remote monitoring method, which generates large-scale training data by automatically aligning relations in Freebase with text content. NYT contains 24 valid relations. This paper's work refers to (Zheng et al., 2017) to preprocess the original NYT data set.

**WebNLG**: WebNLG was originally a data set for natural language generation (NLG) by Gardent et al. (2017), containing 246 valid relations. In this dataset, an instance consists of a set of triples and a few standard sentences (written by the annotator). This paper only uses the first sentence in each instance in WebNLG dataset, which needs to contain all the entities of the triples, otherwise the sentence is filtered.

The final NYT and WebNLG statistics for the three types of triples are shown in the following **Table 2**.

## Implementation Details

PyTorch has been used in our work to distribute GCN and DCGCN in node neighborhood information and edge feature information. We used pre-trained BERT to initialize the context embedding of the word (768d) and then concatenate it with trainable POS embedding (15d) and character-level features (25d) as the input for each word. The dimension of the hidden state vector for Bi-LSTM is set to 100, and the dimension of the hidden state vector for Bi-GCN, attention layer, and DCGCN is set to 256. We selected 10% randomly from the training set to optimize the super parameters in the model, the Learning Rate, Dropout and batch size were set to 0.0001, 0.1, and 10, respectively, and Adam optimizer was used in the model.

In our model, we set the number of layers of BI-GCN to be 2, and the number of layers of densely connected GCN is $L = 3$. Parameter α is set to 3 for joint training.

## Baselines and Comparison Result

To verify the superior performance of the model in this paper, we compare it with a series of recent related models and we contrast it with some mainstream models listed below.

- NovelTagging (Zheng et al., 2017) proposes an end-to-end model based on LSTM and adopts a new tagging method to solve the task of joint extraction of entities and relations.
- GraphRel (Fu et al., 2019) extracts the hidden features of nodes through the stacked GCN of two stages, and trains the loss function of two stages together to realize the joint extraction of entities and relations.
- AntNRE (Sun et al., 2019) detects the entity span by sequence tagging, deduces the entity relation type based on GCN in the entity-relation bigraph, and trains the two subtasks jointly.
- CopyRe (Zeng et al., 2018) uses two different decoding strategies to generate relations, and then extracts entities and relations jointly based on the copy mechanism. We compare the results with the MultiDecoder.
- CopyMTL (Zeng et al., 2020) introduces a multi-task learning framework, which solves the problem of extracting only one word in CopeRe by adopting different strategies for the head entities, tail entities and relations in triples.
- OrderRL (Zeng et al., 2019) regards the extraction of triples as a process of reinforcement learning (RL), explores the influence of the extraction order of triples, and the proposed sequence-to-sequence model can automatically learn and generate relational facts.
- HRL (Takanobu et al., 2019) applies reinforcement learning to a new joint extraction paradigm, and the proposed hierarchical reinforcement learning (HRL) model decomposed the entity and relation extraction process into a two-level RL strategy hierarchy.
- ImprovingGCN (Hong et al., 2020) improves on the basis of GraphRel and added the attention mechanism, allowing the model to use the weighted edge information on the graph structure. The proposed model can be used to end-to-end extract entities and relations jointly.

In this paper, three indexes, precision, Recall and F1, which are the same as most relationship extraction work, are used to assess the performance of the model. The comparison results are shown in the **Table 3** below.

As shown in **Table 3**, we compared our work with the above baseline model, which can verify the effectiveness of our model MA-DCGCN. Similar to GraphRel (Fu et al., 2019) and improving GCN (Hong et al., 2020), our work uses GCN. But the difference is that our model applies multi-head attention mechanism, which takes edge information in the graph structure into consideration. Compared with improving GCN (Hong et al., 2020), we do not mutually exclusive allocate separate subspaces for each relation type, which is more effective for extracting overlapping relations. The difference is that we also use the tightly connected GCN in our work, which enables our model to extract deeper graph structure information for learning the relations between entity pairs.

Experimental results demonstrates that our model's comprehensive performance F1 value is higher than that of all baseline models, positive to ImprovingGCN 6.6% on NYT and positive to AntNRE (Sun et al., 2019) 8.3% on WebNLG. AntNRE removes irrelevant edges in bipartite graphs by relational binary classification task, and their performance depends on binary classification task. For "Precision" and "Recall," on the NYT data set, ours' precision is only 1.9% lower than the highest ImprovingGCN, but ours' recall is 12% higher than it. Compared with the other seven baseline models, ours' precision and recall are superior. Similar trend could be seen on the WebNLG dataset. On the other hand, our model can fully recognize the boundary of the entity while CopyRe cannot copy

**TABLE 3 |** Results of comparison with mainstream methods on NYT and WebNLG datasets.

| | NYT | | | WebNLG | | |
|---|---|---|---|---|---|---|
| | Precision (%) | Recall (%) | F1 (%) | Precision (%) | Recall (%) | F1 (%) |
| NovelTagging | 62.4 | 31.7 | 42.0 | 52.5 | 19.3 | 28.3 |
| CopyRe | 61.0 | 56.6 | 58.7 | 37.7 | 36.4 | 37.1 |
| GraphRel | 63.9 | 60.0 | 61.9 | 44.7 | 41.1 | 42.9 |
| CopyMTL | 75.7 | 68.7 | 72.0 | 58.0 | 54.9 | 56.4 |
| OrderRL | 77.9 | 67.2 | 72.1 | 66.3 | 59.9 | 61.6 |
| HRL | 78.1 | 77.1 | 77.6 | - | - | 28.6 |
| AntNRE | 80.2 | 53.5 | 64.2 | 80.4 | 45.4 | 58.0 |
| ImprovingGCN | 83.2 | 64.7 | 72.8 | 66.4 | 62.7 | 64.5 |
| Ours | 81.3 | 76.7 | **79.4** | 67.4 | **65.1%** | **66.3%** |

*Bold marks highest number among all models.*

**TABLE 4 |** Ablation tests on the NYT dataset.

| Model | F1 (%) |
|---|---|
| ALL | 79.4 |
| - char embedding | 78.1 |
| - context embedding | 77.8 |
| - BiGCN | 77.6 |
| - Multi-head Attention | 76.9 |
| - DCGCN | 78.2 |

the complete entity. Therefore, the F1 score of CopyRe on the two datasets NYT and WebNLG is 20.7 and 29.2% lower than ours. AntNRE constructs an entity-relation bipartite graph, but the performance will be affected by the binary classification task of the nodes in the bipartite graph. Although ImprovingGCN and AntNRE consider the dependency information of words and the interaction of triplets, they ignore the interaction between words in different relational spaces. On the contrary, our proposed relation adaptive mechanism can capture the hidden connections of words in different relational spaces, and then establish a chain of reasoning between triplets. Therefore, it is proved that our work is meaningful and the comprehensive performance of our proposed model is superior.

## Ablation Study

In order to verify the validity of each component in the model, as NYT data sets overlap far more than WebNLG data sets, we conducted ablation experiments on NYT data sets. The impact of different components on model performance was compared by removing one component at a time. The experimental results can be obtained from **Table 4**.

As can be seen from **Table 4**, F1 value of the model decreases by 1.3% when character-based word features are not added, and by 1.6% when context embedding is not added. The results indicate that the multi-granularity embedding can provide more semantic features of words and improve the performance of the model to some extent. "Bi-GCN" indicates that the model removes the GCN component of the encoding layer, leaving only Bi-LSTM. The experimental results show that the stacked LSTM-GCN encoding layer can extract richer word features for named entity recognition and relation extraction than the single LSTM. The results show that the performance decreases by 1.5% after removing the attention mechanism, which proves the effectiveness of the relational adaptive layer in detecting overlapping relations. Attention weights can provide more effective edge features to make the model learn the interaction information of entity relations better, and the non-mutually exclusive subspace of each relation also makes it easier for the model to learn the overlapping relation between entities. Where "-DCGCN" means to use the same regular Bi-GCN as before instead of densely connected GCN. The results show that DCGCN can aggregate nodes more effectively and provide deeper graph structure information.

**TABLE 5 |** F1 score for different numbers of GCN layer.

| Phase | # Numbers of layer | F1 (%) |
|---|---|---|
| 1st-GCN | 1 | 76.8 |
| | 2 | **77.6** |
| | 3 | 77.3 |
| 2nd-DCGCN | 2 | 79.1 |
| | 3 | **79.4** |
| | 4 | 79.3 |
| 3rd-DCGCN | 3 | 79.3 |

*Bold marks the optimal setting.*

## Comparison Results for Different Numbers of GCN Layers

In order to select the best match of GCN layers in the two stages, we set different numbers of GCN layers in first-phase and second-phase to carry out comparison experiment on NYT dataset. The experimental results are shown in **Table 5**.

When conducting experiments on the number of layers in the first-phase GCN, our model does not use the second-stage DCGCN, but only retains first-phase GCN. This experimental data also shows the effectiveness of setting two-stage GCN of our model. The DCGCN of second-phase can extract more information to improve the performance of the model. When DCGCN in the second and third phase conducts experiments with different number of layers, the previous GCN is set to the optimal value obtained from the experiment, such as layers in first-phase and second-phase set to two and three.

As shown in **Table 5**, we also tried to add the third-phase DCGCN again for relation extraction, but the result declined instead. This indicates that GCNs of more phase cannot achieve better results, and the information of the graph structure will become smooth after multiple GCNs. The setting of layer (2,3) is the most suitable match for our model.

## Comparison Results for Overlapping Triples

**Figure 3** shows the performance comparison of the model in this paper for different types of overlapping triples on two public

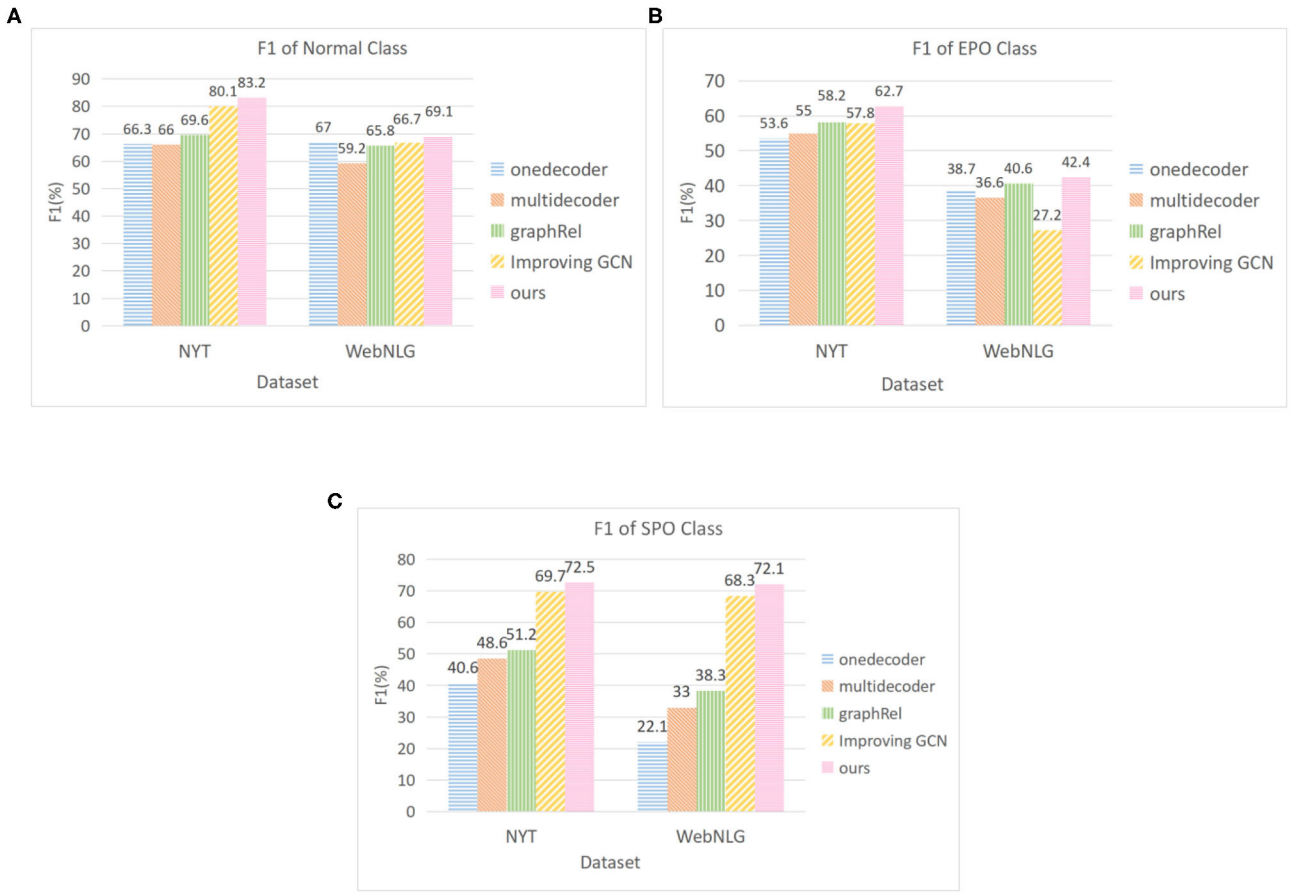


**FIGURE 3 |** F1 score for different class of overlapping triples. **(A)** F1 of normal triple **(B)** F1 of EntityPairOverlap **(C)** F1 of SingleEntityOverlap.

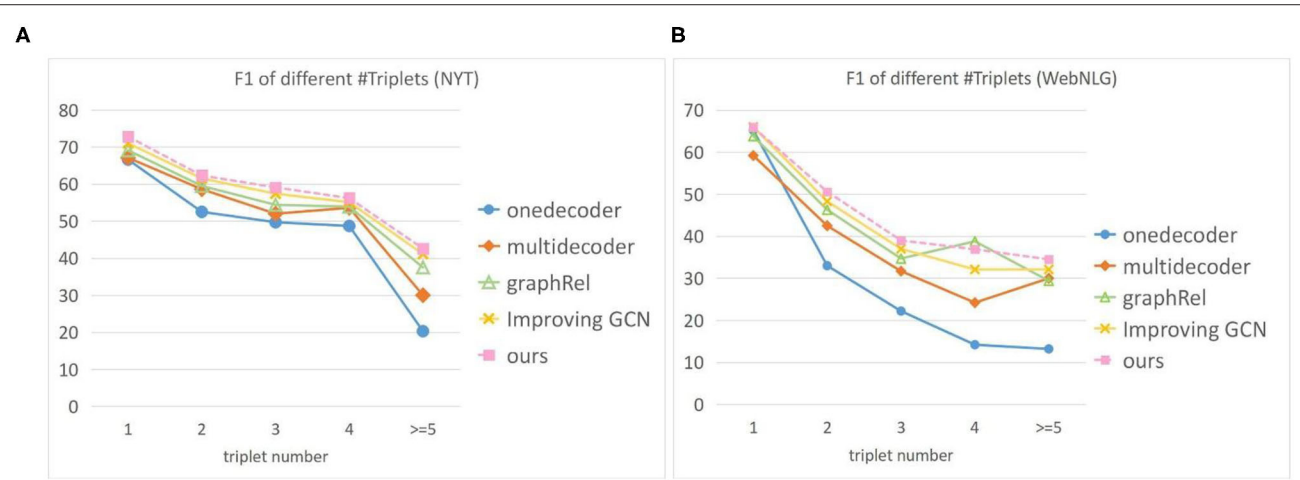


**FIGURE 4 |** F1 score for different number of triples on two datasets. The X-axis represents the number of triples in a sentence. **(A)** F1 of different triples on the NYT **(B)** F1 of different triples on the WebNLG.

datasets. Referring to GraphRel's work (Fu et al., 2019), we compare it with two encoder models (Zeng et al., 2018) and two similar methods (Fu et al., 2019; Hong et al., 2020). The experimental results indicate that the detection performance of

our model is better than that of all baseline models for the three types of triples. Especially compared with GraphRel, the F1 value of NYT and WebNLG for SPO increased by 21.3 and 33.8%, respectively. Our model uses multi-stacked GCN to better extract the interaction information between entities and relations, and the introduction of multi-head attention mechanism is more targeted to detect overlapping triples.

We also conducted a comparison experiment on two public datasets with different number of triples in a sentence. The results are shown in the **Figure 4**. Where the *x*-axis represents the number of triples in a sentence. In most cases, our model is superior to other baseline models. With the increase of the number of triples in the sentence, the performance of each model began to decline, and the decline of our model was smaller. On the WebNLG dataset, although F1 of GraphRel is slightly higher than our model when the sentence contains four triples, its F1 value drops sharply when the sentence contains three and five triples. This indicates that the overall performance of our model is more stable. As the number of triples in the sentence increases, the graph will be built with more nodes. That means our model can extract the graph structure information at a deeper level than the other model, which is more suitable for extracting richer information from larger graphs.

## CONCLUSION

We propose a new joint entity and relation extraction model based on densely connected graph convolutional network (DCGCN). We introduce a multi-head attention mechanism to assign independent attention weights to different relations that are not mutually exclusive, and adaptively extract multiple relation types between overlapping entity pairs. In order to further strengthen the interaction between entities and relations, a stacked DCGCN is added to the model, and the features of adjacent nodes and weighted edge information are used to extract more hierarchical graph structure information. We evaluated our approach on two public datasets. The results show that we can achieve the most advanced performance compared to current mainstream methods. In the future work, we hope to make more effective use of the rich semantic information in the pre-training model to improve model's performance, such as inputting the trained attention weight in the pre-training model into our proposed model.

## DATA AVAILABILITY STATEMENT

Publicly available datasets were analyzed in this study. This data can be found here: https://drive.google.com/file/d/1kAVwR051gjfKn3p6oKc7CzNT9g2Cjy6N/view; https://drive.google.com/file/d/1zISxYa-8ROe2Zv8iRc82jY9QsQrfY1Vj/view.

## AUTHOR CONTRIBUTIONS

GD and JM designed the model and completed part of the experiment. TH and WL completed part of the experiment, and DH completed the article writing. All authors contributed to the article and approved the submitted version.

## FUNDING

This work was supported by the National Key R&D Program of China (No. 2018YFC0807500) and by Ministry of Science and Technology of Sichuan Province Program (No. 2021YFG0018 & No. 20ZDYF0343).

## REFERENCES

Chen, Y., Wang, K., Yang, W., Qing, Y., Huang, R., and Chen, P. (2020). A multi-channel deep neural network for relation extraction. *Int. IEEE Access.* 8, 13195–13203. doi: 10.1109/ACCESS.2020.2966303

Cho, K., Van Merriënboer, B., Gulcehre, C., Bahdanau, D., Bougares, F., Schwenk, H., et al. (2014). "Learning phrase representations using RNN encoder-decoder for statistical machine translation," in *Proceedings of the 2014 Conference on Empirical Methods in Natural Language Processing* (Doha), 1724–1734. doi: 10.3115/v1/D14-1179

Fu, T. J., Li, P. H., and Ma, W. Y. (2019). "GraphRel: modeling text as relational graphs for joint entity and relation extraction," in *Proceedings of the 57th Annual Meeting of the Association for Computational Linguistics* (Florence), 1409–1418. doi: 10.18653/v1/P19-1136

Gardent, C., Shimorina, A., Narayan, S., and Perez-Beltrachini, L. (2017). "Creating training corpora for nlg micro-planning," in *Proceedings of the 55th Annual Meeting of the Association for Computational Linguistics*, *ACL* (Vancouver), 179–188. doi: 10.18653/v1/P17-1017

Guo, Z., Zhang, Y., Teng, Z., and Lu, W. (2019). Densely connected graph convolutional networks for graph-to-sequence learning. *Int. Trans. Assoc. Comput. Linguist.* 7, 297–312. doi: 10.1162/tacl_a_00269

Hashimoto, K., Miwa, M., Tsuruoka, Y., and Chikayama, T. (2013). "Simple customization of recursive neural networks for semantic relation classification," in *Proceedings of the 2013 Conference on Empirical Methods in Natural Language Processing* (Seattle, WA), 1372–1376.

Hochreiter, S., and Schmidhuber, J. (1997). Long short-term memory. *Int. Neural. Comput.* 9, 1735–1780. doi: 10.1162/neco.1997.9.8.1735

Hong, Y., Liu, Y., Yang, S., Zhang, K., Wen, A., and Hu, J. (2020). Improving graph convolutional networks based on relation-aware attention for end-to-end relation extraction. *Int. IEEE Access*. 8, 51315–51323, doi: 10.1109/ACCESS.2020.2980859

Huang, G., Liu, Z., Van Der Maaten, L., and Weinberger, K. Q. (2017). "Densely connected convolutional networks," in *Proceedings of the IEEE Conference on Computer Vision and Pattern Recognition* (Honolulu, HI), 4700–4708. doi: 10.1109/CVPR.2017.243

Katiyar, A., and Cardie, C. (2017). "Going out on a limb: joint extraction of entity mentions and relations without dependency trees," in *Proceedings of the 55th Annual Meeting of the Association for Computational Linguistics* (Vancouver), 917–928. doi: 10.18653/v1/P17-1085

Krizhevsky, A., Sutskever, I., and Hinton, G. E. (2017). "Imagenet classification with deep convolutional neural networks," *in Advances in Neural Information Processing Systems 25: 26th Annual Conference on Neural Information Processing Systems 2012* (Lake Tahoe), 1106–1114. doi: 10.1145/3065386

Li, Q., and Ji, H. (2014). "Incremental joint extraction of entity mentions and relations," in *Proceedings of the 52nd Annual Meeting of the Association for Computational Linguistics* (Baltimore, MD), 402–412. doi: 10.3115/v1/P14-1038

Luan, Y., He, L., Ostendorf, M., and Hajishirzi, H. (2018). "Multi-Task identification of entities, relations, and coreference for scientific knowledge graph construction," in *Proceedings of the 2018 Conference on*

*Empirical Methods in Natural Language Processing* (Brussels), 3219–3232. doi: 10.18653/v1/D18-1360

Miwa, M., and Bansal, M. (2016). "End-to-end relation extraction using LSTMs on sequences and tree structures," in *Proceedings of the 54th Annual Meeting of the Association for Computational Linguistics* (Berlin), 1105–1116. doi: 10.18653/v1/P16-1105

Nayak, T., and Ng, H. T. (2020). "Effective modeling of encoder-decoder architecture for joint entity and relation extraction," in *Internationl Proceedings of the AAAI Conference on Artificial Intelligence, Vol. 34* (New York, NY), 8528–8535. doi: 10.1609/aaai.v34i05.6374

Qian, Y., Santus, E., Jin, Z., Guo, J., and Barzilay, R. (2019). "Graphie: a graph based framework for information extraction," *Interntionl Proceedings 2019 Conference North Amererican. Chapter Association Computer Linguistics: Human Language Technology, Vol. 2* (Minneapolis, MN), 751–761, doi: 10.18653/v1/N19-1082

Qin, P., Xu, W., and Wang, W. Y. (2018). "Robust distant supervision relation extraction via deep reinforcement learning," in *Proceedings of the 56th Annual Meeting of the Association for Computational Linguistics* (Melbourne), 2137–2147. doi: 10.18653/v1/P18-1199

Schuster, M., and Paliwal, K. K. (1997). Bidirectional recurrent neural networks. *Int. IEEE Trans. Signal Process.* 45, 2673–2681. doi: 10.1109/78.650093

Socher, R., Huval, B., Manning, C. D., and Ng, A. Y. (2012). "Semantic compositionality through recursive matrix-vector spaces," in *Proceedings of the 2012 Joint Conference on Empirical Methods in Natural Language Processing and Computational Natural Language Learning* (Jeju Island), 1201–1211.

Sun, C., Gong, Y., Wu, Y., Gong, M., Jiang, D., Lan, M., et al. (2019). "Joint type inference on entities and relations via graph convolutional networks," in *Proceedings of the 57th Annual Meeting of the Association for Computational Linguistics* (Florence), 1361–1370. doi: 10.18653/v1/P19-1131

Takanobu, R., Zhang, T., Liu, J., and Huang, M. (2019). "A hierarchical framework for relation extraction with reinforcement learning." in *Internationl Proceedings of the AAAI Conference on Artificial Intelligence. Vol. 33* (New York, NY), 7072–7079. doi: 10.1609/aaai.v33i01.33017072

Xu, Y., Mou, L., Li, G., Chen, Y., Peng, H., and Jin, Z. (2015). "Classifying relations via long short term memory networks along shortest dependency paths," in *Proceedings of the 2015 Conference on Empirical Methods in Natural Language Processing* (Lisbon), 1785–1794. doi: 10.18653/v1/D15-1206

Yang, W., Xie, Y., Lin, A., Li, X., Tan, L., Xiong, K., et al. (2019). "End-to-end open-domain question answering with BERTserini," in *Proceedings of the 2019 Conference of the North American Chapter of the Association for Computational Linguistics* (Minneapolis, MI), 72–77. doi: 10.18653/v1/N19-4013

Yuan, Y., Zhou, X., Pan, S., Zhu, Q., Song, Z., and Guo, L. (2020). "A relation-specific attention network for joint entity and relation extraction," in *Proceedings of the 29th International Joint Conference on Artificial Intelligence* (Yokohama), 4054–4060. doi: 10.24963/ijcai.2020/561

Zeng, D., Liu, K., Lai, S., Zhou, G., and Zhao, J. (2014). "Relation classification via convolutional deep neural network," in *Proceedings of COLING 2014, 25th International Conference on Computational Linguistics: Technical Papers* (Dublin), 2335–2344.

Zeng, D., Zhang, H., and Liu, Q. (2020). "CopyMTL: copy mechanism for joint extraction of entities and relations with multi-task learning," in *The 34th AAAI Conference on Artificial Intelligence, AAAI 2020* (New York, NY), 9507–9514. doi: 10.1609/aaai.v34i05.6495

Zeng, X., He, S., Zeng, D., Liu, K., Liu, S., and Zhao, J. (2019). "Learning the extraction order of multiple relational facts in a sentence with reinforcement learning," in *Proceedings of the 2019 Conference on Empirical Methods in Natural Language Processing and the 9th International Joint Conference on Natural Language Processing* (Hong Kong), 367–377. doi: 10.18653/v1/D19-1035

Zeng, X., Zeng, D., He, S., Liu, K., and Zhao, J. (2018). "Extracting relational facts by an end-to-end neural model with copy mechanism," in *Proceedings of the 56th Annual Meeting of the Association for Computational Linguistics* (Melbourne), 506–514. doi: 10.18653/v1/P18-1047

Zhang, S., Zheng, D., Hu, X., and Yang, M. (2015). "Bidirectional long short-term memory networks for relation classification," in *Proceedings of The 29th Pacific Asia Conference on Language, Information And Computation* (Shanghai), 73–78.

Zhang, Y., Guo, Z., and Lu, W. (2019). "Attention guided graph convolutional networks for relation extraction," in *Proceedings of the 57th Annual Meeting of the Association for Computational Linguistics* (Florence), 241–251.

Zhang, Y., Qi, P., and Manning, C. D. (2018). "Graph convolution over pruned dependency trees improves relation extrac-tion," in *Proceedings of the 2018 Conference on Empirical Methods in Natural Language Processing* (Brussels), 2205–2215. doi: 10.18653/v1/D18-1244

Zheng, S., Wang, F., Bao, H., Hao, Y., Zhou, P., and Xu, B. (2017). "Joint extraction of entities and relations based on a novel tagging scheme," in *Proceedings of the 55th Annual Meeting of the Association for Computational Linguistics* (Vancouver), 1227–1236. doi: 10.18653/v1/P17-1113

Zhu, J., Qiao, J., Dai, X., and Cheng, X. (2017). "Relation classification via target-concentrated attention cnns," in *Proceedings of the 24th International Conference on Neural Information Processing* (Cham: Springer), 137–146. doi: 10.1007/978-3-319-70096-0_15

**Conflict of Interest:** The authors declare that the research was conducted in the absence of any commercial or financial relationships that could be construed as a potential conflict of interest.

frontiers in Environmental Science

ORIGINAL RESEARCH
published: 25 March 2021
doi: 10.3389/fenvs.2021.627323

# Energy Investment Risk Assessment for Nations Via Seq2seq Model

*Panning Liang*[1], *Mingyang Yu*[1] *and Lincheng Jiang*[2]*

[1]Antai College of Economics and Management, Shanghai Jiao Tong University, Shanghai, China, [2]College of Advanced Interdisciplinary Studies, National University of Defense Technology, Changsha, China

China's "Belt & Road Initiative" has been proposed for several years, which has stimulated the economic and financial development of the countries alongside the "Belt & Road". For a world's leading energy consuming country, China tries to secure the energy supply from the resource-rich countries via oversea energy investment. In this paper, we propose a sequence to sequence (seq2seq) model to evaluate the energy investment risk of 50 countries alongside the "Belt & Road Initiative". Specifically, we first build an indicator system mainly containing six factors. Then we adopt Bi-long-short term memory (Bi-LSTM) as encoder to process the historical statistics. Afterward, we use self-attention mechanism to assign the weights on the six factors of the indicator system. Finally we use a hierarchical convolution neural network decoder to generate the assessment results. Our findings indicate that resource potential and Chinese factor are the most important indicators. And through our thorough investigation, we find that Russia, Kazakhstan, Pakistan, United Arab Emirates, Saudi Arabia, Malaysia and Indonesia are the most recommended target countries for China's oversea energy investment.

**Keywords: seq2seq framework, belt & road initiative, energy investment risk assessment, Bi-LSTM, hierarchical CNN**

OPEN ACCESS

***Edited by:***
*Long Wang,*
*University of Science and Technology Beijing, China*

***Reviewed by:***
*Ruilian Zhang,*
*The University of Queensland, Australia*
*Muhammad Azam Khan,*
*Abdul Wali Khan University Mardan, Pakistan*

***Correspondence:**
*Lincheng Jiang*
*linchengjiang@nudt.edu.cn*

***Specialty section:***
*This article was submitted to Environmental Economics and Management, a section of the journal Frontiers in Environmental Science*

***Received:*** *09 November 2020*
***Accepted:*** *09 February 2021*
***Published:*** *25 March 2021*

***Citation:***
*Liang P, Yu M and Jiang L (2021) Energy Investment Risk Assessment for Nations Via Seq2seq Model. Front. Environ. Sci. 9:627323. doi: 10.3389/fenvs.2021.627323*

## INTRODUCTION

"Belt & Road initiative" was proposed successfully in 2013 by China, which aims to secure its global economic and energy system. China plans to invest the nations alongside the "Belt & Road", so as to explore a developmental path of interregional cooperation, so as to boost an open economic system development. Such huge project has attracted at least 65 nations to discuss with China about further investment (Duan et al., 2018; Hafeez et al., 2018; Zhai, 2018; Wu et al., 2020). In this paper, we focus on the energy investment as China has the largest amount of imported energy resources like oil and gas, with the number keeping increasing. Overall, the countries joining "Belt & Road initiative" include 16 countries in the Middle Eastern Europe, 18 countries in West Asia and Northern Africa, 10 countries in the Association of Southeast Asian Nations (ASEAN), 8 countries in South Asia, 5 countries in Central Asia, 7 countries in the Commonwealth of Independent States (CIS), and Mongolia in East Asia. Those countries above contain a large part of the energy resources of the whole world according to the Energy Information Administration (EIA[1]) statistics, with natural gas, coal and oil making up, 79.9 and 54.0 and 58.8% of the world, respectively.

In order to ensure a stable external energy supply, oversea energy investment is the main way conducted by those countries laking in resources like Japan. According to statistics provided by

[1]https://www.eia.gov

Information Energy Agency (IEA[2]), there will be about 23 trillion dollars investments regarding the fossil energy industries including mining, transportation and refinement. Most of those investments focus on the countries alongside the "Belt & Road", which offers China a good opportunity to expand its own oversea energy investment.

However, oversea energy investments always face high risk due to various factors such as politics, business environment, economic situation. The period of such investment is long and the corresponding investment uncertainty is rather low as well (Zhang et al., 2017, 2018; Wu et al., 2020). For example, Middle East countries have abundant fossil resources, however, their economic structure is singular with unstable politic environment and undeveloped energy industry. Therefore, to conduct the "Belt & Road initiative" smoothly, a thorough and comprehensive assessment of the energy investment is strongly needed. Given the evaluation, we could provide investment strategy recommendations for China policy makers.

There are many existing efforts aiming to handle the investment risk evaluation in many aspects. For example, Dockner et al. (2013) take the risk of energy grids into consideration, evaluating firm risks and firm value. Pringles et al. (2015) evaluate the energy transmission risk through considering substantial uncertainty and irreversibility. Chorn and Shokhor (2006) adopt a real-options based model to evaluate China's oversea fossil industry investments. However, the previous research mainly focuses on micro-level on energy investment risk evaluation. In our paper, we intend to investigate energy investment risk on both micro-level and macro-level factors.

Existing macro-level risk assessment models always focus on the quantitative analysis, referencing global organizations like Moody's, Fitch Group and Standard & Poor's Feder and Uy (1985); Brewer and Rivoli (1990) for rating results. The International Country Risk Guide (ICRG) publishes the national risk ratings monthly from three aspects: political, financial and economic. Some researchers argue that China oversea investments should be mainly concerned with natural resources. For example, Li et al. (2012) evaluate the national risk of crude oil exporting countries using decomposition hybrid approach.

*Motivation*. China is the world-leading energy-consuming country while the "Belt & Road initiative" brings lots of opportunities for China's companies' oversea energy investment. So it is urgent to call for more systematic researches for assessment of China's oversea energy investment risks under this circumstance. However, the aforementioned literature only investigates the general investment risk, few studies focus on the China oversea energy investment. Therefore, in this work, we aim to fill this gap by building an assessment system for China's foreign investment alongside the "Belt & Road initiative". We believe that aside from the above national risks, according to EIA, more energy-related factors should be taken into consideration. Additionally, the bilateral relationship between China and the target country also plays a vital role in assessing the oversea energy investment Duan et al. (2018). So Chinese factor should also be considered. Overall, we put forward an indicator system specially designed for energy investment, which contains six indicators, that is, investment environment, political risk, economic foundation, environment constraint, resource potential and Chinese factor. To evaluate the above risk factors, inspired by the recent advance of deep learning, we propose to use a seq2seq framework to generate the assessment results. To the best of our knowledge, we are the first to apply deep neural networks on risk assessment tasks. Additionally, previous assessment models only take the latest statistics of a nation into consideration, however, our model could make the full use of the history statistics via the Bi-LSTM encoder. Afterward, we adopt the self-attention layer to assign different weights on different impact factors. Finally, we choose CNN as the decoder to generate the final assessment results.

*Objective*. In this work, we aim to first build an indicator system so that we could conduct a comprehensive analysis on the factors affecting the China's oversea energy investment. Secondly, we adopt the seq2seq framework to evaluate the historical statistics to generate the assessment results, while previous research always focus on the latest data. Finally, based on the assessment results, we aim to provide policy recommendations to those policy makers of China.

- The contributions could be summarized as three components:
- We first build an indicator system to assess the national energy investment risk along the "Belt & Road initiative".
- We adopt a seq2seq framework to generate the assessment results, in which Bi-LSTM encoder deals with historical statistics, self-attention mechanism calculates the indicator weights and CNN decoder computes the final assessment scores.
- We evaluate the energy investment risk based on the indicator and framework mentioned above among 50 countries which lie in the "Belt & Road initiative". Then we provide policy recommendations for overseas energy investment of China.

The rest of paper is organized as follows. We first introduce the related work in "Related Work" section, and then justify the indicator and seq2seq framework in detail in "Proposed Model" section. Then we conduct energy investment evaluation on 50 countries in **"Experiments"** section. In the end, we present the conclusion of our findings in "Conclusion" section.

# RELATED WORK

## Investment Risk Assessment

Investment risk assessment has drawn lots of research attention, and in this paper, we focus on energy investment so as to evaluate China's "Belt & Road" initiative on natural resources.

[2]https://www.iea.org

Regarding the energy, some research focuses on grid systems or power plants. Dockner et al. (2013) take the firm value and firm risk into consideration, in which firm risk is determined by short investment option positions and become non-linear with no investment. Pringles et al. (2015) analyze the real investment option of power transmission with uncertainty and irreversibility. Zhang et al. (2016) assess the renewable resource investment via a real options model. Tietjen et al. (2016) compare the renewable and fossil energy in power markets regarding the investment risks, and they find that the energy price is the most important factor for a power plant. Hach and Spinler (2016) consider the capacity payment on investment as a risk factor, focus on how different partials of renewable energy would affect the gas-fired plants. Gal et al. (2017) research on the uncertainty factors of the fossil fuel cost, and how they affect the energy price and capacity investment. Mayer et al. (2017) study on the cost calculation and power generation based on the early-stage uncertainties and risks. Farfan and Breyer (2017) compute the risks of national power system and its investment based on a sustainable indicator.

There are also various works focusing on the fossil energy industry investment. Chorn and Shokhor (2006) use a combination of a real options model with the Bellman equation to evaluate the Central Asia gas energy investment. Fan and Zhu (2010) evaluate the China oversea oil investment based on a real options model, as well. Chen et al. (2016) also adopt the real options model to assess the China's coal power plants in the aspect of the subsidy uncertainty for investment of CCS retrofitting. There are also multiple efforts dedicating to carbon emission and clean-development mechanism on resource investment (Strand et al., 2014; Hieronymi and Schüller, 2015; Jones, 2015; Mo et al., 2015; Cadarso et al., 2016; Cucchiella et al., 2017; Xu et al., 2017) compare different factors and investment in China using 5-sector panel data, illustrating that the investment is mostly depended on GDP. Azam (2020) empirically examine the impact of energy on economic growth within the production function framework of a panel of 10 developing Asian economies from 1990 Q1 to 2014 Q4.

The aforementioned approaches only consider the micro-level factors, while country-level risks are overlooked. National risk ratings were described via quantitative analysis in debt default in the early stage Feder and Just (1977); Kharas (1984). Then some global organizations occurred like Moody's, Fitch group and Standard & Poor's, which published the national ratings for each country (Feder and Uy, 1985; Brewer and Rivoli, 1990). Among these organizations, International Country Risk Guide (ICRG) is oldest one which studies three aspects of a nation, i.e., economic, political and financial. Miller (1992) take the industrial environment, macro-economic environment and micro-economic environment into consideration. Hammer et al. (2006) conduct a survey on 69 nations analyzing three political factors and nine economic factors. Agliardi et al. (2012) evaluate the sovereignty risk of the developing countries via three aspects of indicators, i.e., financial, economic and political. Sanchez and Meltzer (2012) adopt nine economic factors to assess the sovereignty risk of the Europe union countries. Brown et al. (2015) consider four aspects for national evaluations, i.e., political, operational, social and economic. Azam (2016) studies the impact of environmental degradation on the economic growth of 11 Asian countries between 1990 and 2011. Azam et al. (2019) study the impact of several indicators like energy, human capital, environment and economics on China. Azam (2019) also study the impact of the above indicators, but he extends the study on BRICS-4 countries, i.e., Brazil, India, China, and South Africa.

As for the China's oversea energy investment, many researchers believe that natural resources play a vital role for China's policy making. Li et al. (2012) evaluate the risk of those oil exporting countries via a decomposition hybrid model. Tan (2013) focuses on the energy realm of China's oversea investment and offers related recommendations. Sun et al. (2014) conduct a survey on China's foreign investment situation particularly in natural resource field. Conrad and Kostka (2017) and Liedtke (2017) analyze the European energy sector w.r.t China's investment trend, discussing the economic and competition risks. Duan et al. (2018) analyze the energy investment of China using a fuzzy integrated model. Wu et al. (2020) use an analytic network process and build an ANP-cloud framework to assess the investment risk but they only focus on renewable energy. Zhang et al. (2017) use a multi-fuzzy comprehensive evaluation model to evaluate the investment risk, but they only study the China-Pakistan economic corridor. Zhang et al. (2018) also study the China-Pakistan economic corridor, using an analytic hierarchy process (AHP) to assess the social impact on investment.]

## Seq2seq Framework

Seq2seq framework is also known as encoder-decoder architecture, which is originally designed to adopt RNN Sutskever et al. (2014) as encoder and decoder. In specific, given the input sequence $\mathbf{x} = \{x_1, \ldots, x_n\}$, in which $n$ represents the number of the sequence elements, it is first processed by the RNN encoder. Afterward, the framework will generate the hidden state $\mathbf{z} = (z_1, \ldots, z_n)$. To produce the output sequence $\mathbf{t} = (t_1, .., t_n)$, the decoder uses the hidden state $\mathbf{z} = (z_1, \ldots, z_n)$ as input. Specifically, the RNN decoder will generate a new hidden state $h_{i+1}$ based on the $z_n$ and the previous state $h_{i+1}$. Then it uses the new hidden state to produce the output $t_{i+1}$ one by one from left to right, meanwhile producing the conditional input $c_i$ and the previous target word $y_i$'s embedding vector $g_i$.

The input of the decoder can be directly applied as the final encoder hidden state $z_n$ without considering the attention mechanism, meanwhile setting the conditional input $c_i$ to be equal to $z_n$ for each $i$ Cho et al. (2014). However, many works apply the attention mechanism to further improve the model performance, which computes the $c_i$ as the sum of $(z_1, \ldots, z_m)$ assigning the different attention weights. Such attention weights could help the decoder pay more attention on the important parts of the sequence, producing the output sequence of higher quality. To calculate the attention weight, the hidden state of encoder $z_j$ is compared by the combination of the previous hidden state of decoder $h_i$ and the previous prediction $y_i$. Afterward, the results are normalized to a distribution over the input sequence Bahdanau et al. (2015) Luong et al. (2015).

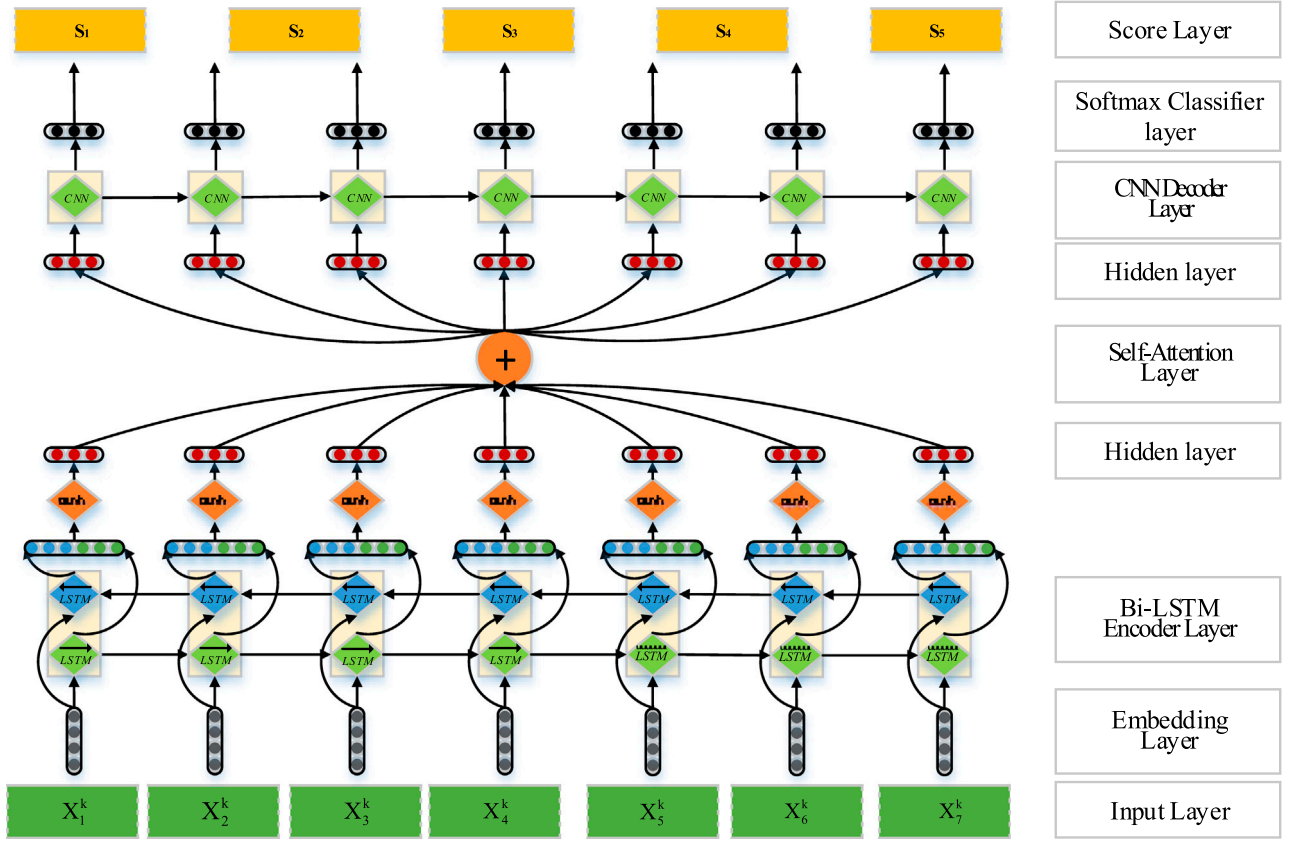


**FIGURE 1 |** Investment risk assessment model framework.

There are many variants of RNN to be chosen as encoder and decoder such as LSTM Hochreiter and Schmidhuber (1997) and GRU Cho et al. (2014). Both RNN models applies a gating mechanism to facilitate the model to handle the long-term dependencies. In recent, bi-directional models are widely used like Bi-LSTM since they could make the full use of the sequence context Bahdanau et al. (2015). Additionally, there are also many models stacking multiple layers of RNN to boost the performance, where residual connection is needed He et al. (2016). Aside from RNN, CNN is also applied as the encoder or decoder, which could improve the efficiency compared with RNN models Gehring et al. (2017).

## PROPOSED MODEL

In this section, we first present our investment risk assessment model in detail. We first build an indicator system which combines both micro-level and macro-level risk ratings. Then we harness the Bi-LSTM model as the encoder to handle the history statistics based on the above indicator system. Afterward, we use the self-attention layer to assign the weight on different indicators. Finally, we adopt the hierarchical CNN model to generate the results of the investment assessment.

### Indicators

Here we introduce overall six indicators to be considered to evaluate the investment risk, that is, investment environment, political, economic, environment constraint, resource and Chinese factor. [According to International Country Risk Guide (ICRG), it evaluates the national risk via three dimensions, i.e., investment environment, political risk and economic foundation, so we choose them as indicators. Additionally, according to Energy Information Administration (EIA), environment constraint and resource potential are two main indicators reflecting the status of the energy resource of a certain country, so we take them as indicators in our work as well. As illustrated in Wu et al. (2020); Duan et al. (2018); Zhang et al. (2017, 2018), Chinese factor also plays a significant role in evaluating the investment risk, so this work also includes it as indicator.]

As for the investment environment, it is mainly about the operational environment of the companies in a nation. Having a stable investment environment can guarantee the operations of the foreign companies. Here we introduce six indicators regarding investment environment which are obtained from World Bank, as shown in **Figure 1**.

As for the political risk, it reflects the stability of the country's politics and government environment. Having a political environment being stable can secure the investment and

**TABLE 1 |** Investment risk assessment indicators.

| Dimension | Indicators | Data source |
|---|---|---|
| Investment environment | Starting a business | World Bank |
| | Dealing with construction permits | World Bank |
| | Getting electricity | World Bank |
| | Paying tax | World Bank |
| | Enforcing contracts | World Bank |
| | Resolving insolvency | World Bank |
| Political risk | Government stability | ICRG |
| | Internal conflict | ICRG |
| | External conflict | ICRG |
| | Corruption | ICRG |
| | Law and order | ICRG |
| | Democratic accountability | ICRG |
| Economic foundation | GDP per capita | ICRG |
| | Real GDP growth | ICRG |
| | Annual inflation rate | ICGC |
| | Budget balance as a percentage of GDP | ICRG |
| | Foreign debt as a percentage of GDP | ICRG |
| | Exchange rate stability | ICRG |
| Environment constraint | Carbon dioxide emissions | EIA |
| | Nitrous oxide emissions | World Bank |
| | Energy intensity | EIA |
| | Carbon dioxide intensity | EIA |
| | PM2.5 | World Bank |
| | Forest area (% of land area) | World Bank |
| Resource potential | Total oil production | EIA |
| | Crude oil proved reserves | EIA |
| | Dry natural gas production | EIA |
| | Proved reserves of natural gas | EIA |
| | Crude oil distillation capacity | EIA |
| | Total exports of refined petroleum products | EIA |
| Chinese factor | Outward FDI stock | Statistical Bulletin of China's Foreign Direct Investment |
| | Years of China's diplomatic relations | Bai Du |
| | Value of contracted projects | China Statistical Yearbook |
| | Persons abroad of contracted projects and labor services | China Statistical Yearbook |
| | Value of total imports from China | UN Comtrade Database |
| | Value of total exports to China | UN Comtrade Database |

management of the foreign companies, while a poor environment may cause a negative influence on the investment interests of foreign companies. Here we have six factors of the political risk which are obtained from ICRG, as shown in **Figure 1**.

As for economic foundation, this indicator shows whether the economic system of a country works efficiently. A country with solid economic foundation could provide the fundamental guarantee of a company's investment profit. We include six factors of the economic foundation of to be considered as illustrated in **Figure 1**, which are also obtained from ICRG.

As for environment constraint, it is every country's duty to handle the global warming challenge. To secure the sustainability of the foreign investments, a nation's environment constraint should also be taken into consideration. Such constraint will influence the macro-level policy of the nation, thereby affecting the operation and management of the foreign countries. Here six factors are included w.r.t this indicator, which are obtained from EIA and World Bank, as presented in **Figure 1**.

As for resource potential, it is intuitive that for oversea energy investment, the total production or the reserve of the natural resource is an important indicator. A country with abundant supply or production of the fossil resource could easily attract the oversea energy investments. In this paper, we take six factors into consideration as shown in **Figure 1**, with the statistics fetched from EIA.

As for Chinese factor, the bilateral relation between China and the resource country also plays a vital role for stability and sustainability of the China's oversea investment. Such relation is concerned with the diplomatic and political friendliness, the stability and the closeness of trade cooperation between China and the countries alongside the "Belt & Road Initiative". In specific, we include six factors to evaluate this indicator, of which the origins are complex as presented in **Figure 1**.

## Seq2seq Framework

In this subsection, we introduce the seq2seq framework in detail, which is composed of several functional layers.

### Embedding Layer

In the bottom of the model, we have the input layer and embedding layer. The input layer is directly obtained from the original statistics of each indicator. We directly represent

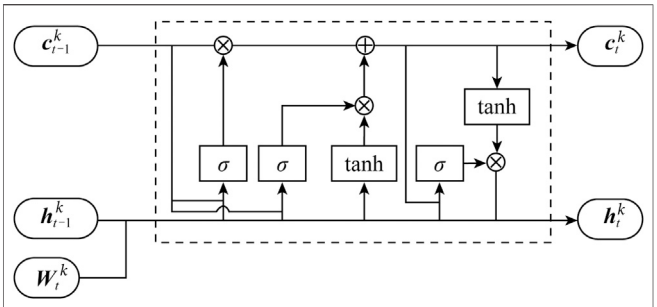


**FIGURE 2 |** Framework of forward LSTM layer.

the input sequence as $S = \{x_1^k, x_2^k, \ldots, x_n^k\}$, in which $n$ denotes the years of the data that are taken into account, and $k \in \{1, 2, 3, \ldots, 36\}$ denotes the specific indicator, in the order of **Table 1**. Here we set $n = 7$ as we compute the 7 years' statistics.

Such input sequence cannot be directly applied on encoder layer. Therefore, we add an embedding layer which transfers the input sequence into low-dimensional vectors.

## Bi-LSTM Encoder Layer

In our model, the encoder is the Bi-LSTM model which processes the input sequence. A Bi-LSTM model can fully mine the history information behind a sequence, and it consists of two parallel LSTM layers, i.e., forward LSTM layer and backward LSTM layer.

LSTM contains input gate, forget gate and output gate to control the information flow. Take the forward LSTM as example, in the $t$ time step, given the input vector $x_t^k$, it generates the current hidden state vector $h_t^k$ based on the previous hidden state $h_{t-1}$. Mathematically, the current hidden state $h_t^k$ could be calculated as follows:

$$\mathbf{i}_t^k = \delta\left(\mathbf{W}_{xi}^k x_t^k + \mathbf{W}_{hi}^k h_{t-1}^k + \mathbf{W}_{ci}^k c_{t-1}^k + \mathbf{b}_i^k\right), \tag{1}$$

$$\mathbf{f}_t^k = \delta\left(\mathbf{W}_{xf}^k x_t^k + \mathbf{W}_{hi}^k h_{t-1}^k + \mathbf{W}_{cf}^k c_{t-1}^k + \mathbf{b}_f^k\right), \tag{2}$$

$$\mathbf{z}_t^k = \tanh\left(\mathbf{W}_{xc}^k x_t^k + \mathbf{W}_{hc}^k h_{t-1}^k + \mathbf{b}_c^k\right), \tag{3}$$

$$c_t^k = \mathbf{f}_t^k \odot c_{t-1}^k + \mathbf{i}_t^k \odot \mathbf{z}_t^k, \tag{4}$$

$$\mathbf{o}_t^k = \delta\left(\mathbf{W}_{xo}^k x_t^k + \mathbf{W}_{ho}^k h_{t-1}^k + \mathbf{W}_{co}^k c_t^k + \mathbf{b}_o^k\right), \tag{5}$$

$$h_t = \mathbf{o}_t^k \tanh\left(c_t^k\right). \tag{6}$$

in which $\mathbf{i}^k$, $\mathbf{f}^k$ and $\mathbf{o}^k$ denotes the input gate, forget gate and output gate, respectively. $\mathbf{b}_{(\cdot)}^{\mathbf{k}}$ and $\mathbf{W}_{(\cdot)}^{\mathbf{k}}$ denotes the bias and parameter matrix, respectively. $\odot$ denotes the Hadamard production. The framework could be described as **Figure 2**.

The input sequence is processed from the element $x_1^k$ to element $x_t^k$, and we denote the hidden state vector as $\overrightarrow{h}_t^k$. Similarly, the input elements are handled from $x_t^k$ to $x_1^k$, with the corresponding output hidden state vector denoted as $\overleftarrow{h}_t^k$. Based on the above two layers, our encoder could fully leverage the history information of the whole sequence. Afterward, at $t$ time stamp, we concatenate the above two hidden state vectors to generate the final hidden state output $h_t^k \in \mathbb{R}^{2d_e}$. Mathematically, it could be represented as follows:

$$h_t^k = \left[\overrightarrow{h}_t^k \oplus \overleftarrow{h}_t^k\right]. \tag{7}$$

Then the whole output of the encoder layer could be represented as $h^k = \{h_1^k, h_2^k, \ldots, h_n^k\}$. $h^k$ is used as the input of the next layer in our framework.

## Self-Attention Layer

Here we introduce the self-attention layer to assign the weights on different indicators. Here we compute the weight of each specific indicator based on the hidden state vector $h^k$. Mathematically, given the hidden state vectors of all indicators $h = \{h^1, h^2, \ldots, h^k\}$, its self attention could be computed as follows:

$$f_h = \tanh\left(h\mathbf{W}_a h^T + \mathbf{b}_a\right), \tag{8}$$

$$A = \mathrm{softmax}\left(f_h\right), \tag{9}$$

$$g = Ah = \left(g_1, g_2, \ldots, g_n\right), \tag{10}$$

in which $f_h$ is the attention score of the hidden vectors of the indicators, $A$ is the attention weight of the indicators, $g$ is output hidden state of the self-attention layer which is further adopted as the input of the decoder layer, $\mathbf{b}_a$ is bias parameter and $\mathbf{W}_a$ is the attention parameter matrix.

## Decoder Layer

In this section, we adopt a hierarchical CNN architecture as the decoder layer. Actually, for each layer of the architecture, it is composed of a one-dimensional convolution and a non-linearity. Setting the kernel width of convolutional layer as $l$, $l$ elements of the input sequence could be covered. To extend the coverage of the sequence, we stack several layers of the convolution on top of each other. For instance, setting $l = 5$ with 6 layers could cover 25 elements of the sequence. Non-linearities force the model to pay more attention to the important parts of the sequence, or simply the whole sequence.

The output of the whole layers with the non-linearity being the gated linear units (GLU) Dauphin et al. (2017) is calculated as

$$v\left([XY]\right) = X \odot \sigma\left(Y\right), \tag{11}$$

where $X, Y \in \mathbb{R}^d$ are the inputs of GLU, $\odot$ is the Hadamard function. $\sigma(Y)$ is the gate to control which part of the sequence should be handled.

To facilitate our model on deep CNN, we use the residual connections He et al. (2016) to connect the input and the output together of each convolution layer. Mathematically, the final output could be represented as follows:

$$h_t^k = v\left(W^l\left[h_{t-o/2}^{k-1}, \ldots, h_{t+o/2}^{k-1}\right] + b_w^k\right) + h_t^{k-1}. \tag{12}$$

## Classifier Layer

Finally we introduce the classifier layer we adopt in this framework. Here we adopt a softmax classifier which could be represented as

$$p_t^i(\theta) = \frac{\exp\left(y_t^i\right)}{\sum_{j=1}^{T} \exp\left(y_t^i\right)}, \tag{13}$$

**TABLE 2 |** Main statistics of 50 Nations alongside the China's "Belt & Road Initiative".

| Region | Country | Population (million) | GDP (billion dollars) | Total oil supply (thousand barrels per day) | Crude oil proved reserves (billion barrels) | Dry gas production (Billion cubic feet) | Proved reserves of natural gas (trillion cubit feet) | Crude oil distillation capacity (thousand barrels per day) |
|---|---|---|---|---|---|---|---|---|
| East Asia | Mongolia | 2.86 | 12.58 | 14.05 | NA | 0.00 | 0.00 | 0.00 |
| Central Asia | Kazakhstan | 17.04 | 243.78 | 1,658.00 | 30.00 | 720.43 | 85 | 345.09 |
| ASEAN | Brunei | 0.41 | 16.11 | 135.31 | 1.10 | 440.38 | 13.80 | 8.60 |
| | Indonesia | 251.27 | 912.52 | 926.21 | 4.03 | 2,486.18 | 108.40 | 1,011.83 |
| | Malaysia | 29.47 | 323.34 | 926.21 | 4.03 | 2,486.18 | 108.40 | 1,011.83 |
| | Myanmar | 52.98 | 58.65 | 20.64 | 0.05 | 462.63 | 10.00 | 57.00 |
| | Philippines | 97.57 | 271.93 | 26.52 | 0.14 | 102.77 | 3.48 | 273.00 |
| | Singapore | 5.40 | 300.29 | 24.88 | 0.00 | 0.00 | 0.00 | 1,357.00 |
| | Thailand | 67.45 | 419.89 | 522.51 | 0.45 | 1,476.17 | 10.06 | 584.25 |
| | Vietnam | 89.76 | 171.22 | 354.35 | 4.40 | 310.77 | 24.70 | 140.00 |
| South Asia | Bangladesh | 157.16 | 149.99 | 4.20 | 0.03 | 807.30 | 6.49 | 33.00 |
| | India | 1,279.50 | 1863.21 | 1,015.81 | 5.48 | 1,218.37 | 43.83 | 4,042.76 |
| | Pakistan | 181.19 | 231.15 | 85.14 | 0.25 | 1,411.54 | 24.00 | 186.31 |
| | Sri Lanka | 20.58 | 74.29 | -0.56 | 0.00 | 0.00 | 0.00 | 50.00 |
| West Asia | Bahrain | 1.35 | 32.90 | 61.36 | 0.12 | 554.45 | 3.25 | 253.65 |
| | Cyprus | 1.14 | 24.06 | 0.00 | 0.00 | 0.00 | 0.00 | 0.00 |
| | Egypt | 87.61 | 286.01 | 693.53 | 4.40 | 2034.14 | 77.20 | 726.25 |
| | Greece | 10.97 | 239.51 | 8.83 | 0.01 | 0.18 | 0.04 | 423.00 |
| | Iran | 77.15 | 511.62 | 3,194.30 | 154.58 | 5,696.06 | 1,187.00 | 1,451.00 |
| | Iraq | 34.11 | 232.50 | 3,050.54 | 141.35 | 41.67 | 111.52 | 637.50 |
| | Israel | 8.06 | 292.41 | 5.76 | 0.01 | 227.43 | 9.48 | 220.00 |
| | Jordan | 7.21 | 33.59 | 0.45 | 0.00 | 5.30 | 0.21 | 90.40 |
| | Kuwait | 3.59 | 174.16 | 2,798.64 | 104.00 | 576.02 | 63.50 | 936.00 |
| | Lebanon | 5.29 | 44.35 | 0.00 | 0.00 | 0.00 | 0.00 | 0.00 |
| | Oman | 3.91 | 78.18 | 946.04 | 5.50 | 1,127.25 | 30.00 | 85.00 |
| | Qatar | 2.10 | 201.89 | 2067.14 | 25.38 | 5,597.53 | 890.00 | 338.70 |
| | Saudi Arabia | 30.20 | 744.34 | 11,701.51 | 267.91 | 3,526.20 | 287.84 | 2,112.00 |
| | Syria | 19.32 | 0.00 | 71.70 | 2.50 | 187.17 | 8.50 | 239.87 |
| | Turkey | 76.22 | 823.24 | 60.22 | 0.27 | 18.96 | 0.22 | 714.28 |
| | UAE | 9.04 | 387.19 | 3,443.71 | 97.80 | 1928.20 | 215.03 | 773.25 |
| | Yemen | 25.53 | 35.95 | 130.97 | 3.00 | 363.74 | 16.90 | 140.00 |
| Russia and CIS | Armenia | 2.99 | 11.12 | 0.00 | 0.00 | 0.00 | 0.00 | 0.00 |
| | Ukraine | 45.49 | 181.33 | 74.88 | 0.40 | 745.15 | 39.00 | 879.76 |
| Central and Eastern Europe | Albania | 2.90 | 12.87 | 17.02 | 0.17 | 0.67 | 0.03 | 26.30 |
| | Bulgaria | 7.27 | 55.63 | 3.58 | 0.02 | 9.82 | 0.20 | 115.24 |
| | Croatia | 4.26 | 57.77 | 20.28 | 0.07 | 55.09 | 0.88 | 250.32 |
| | Czech Republic | 10.51 | 208.33 | 10.68 | 0.02 | 8.90 | 0.14 | 183.00 |
| | Estonia | 1.32 | 25.25 | 13.00 | 0.00 | 0.00 | 0.00 | 0.00 |
| | Hungary | 9.89 | 134.40 | 27.85 | 0.03 | 68.83 | 0.29 | 161.00 |
| | Latvia | 2.01 | 30.22 | 1.00 | 0.00 | 0.00 | 0.00 | 0.00 |
| | Lithuania | 2.96 | 46.42 | 8,83 | 0.01 | 0.00 | 0.00 | 190.00 |
| | Poland | 38.04 | 524.06 | 34.22 | 0.16 | 219.16 | 3.25 | 492.95 |
| | Romania | 19.98 | 191.55 | 103.65 | 0.60 | 385.39 | 3.73 | 537.28 |
| | Serbia | 7.16 | 45.52 | 21.32 | 0.08 | 24.30 | 1.70 | 214.83 |
| | Slovakia | 5.41 | 98.03 | 9.06 | 0.01 | 4.38 | 0.50 | 115.00 |
| | Slovenia | 2.06 | 47.68 | 0.31 | 0.00 | 0.11 | 0.00 | 13.50 |
| Total | | 2,983.65 | 13,246.21 | 45,705.30 | 945.51 | 57,892.27 | 5,086.25 | 27,270.69 |
| World | | 7,176.09 | 76,362.59 | 91,014.47 | 1,648.86 | 121,283.20 | 6,845.17 | 88,004.21 |
| Percentage (%) | | 41.58% | 17.35% | 50.22% | 57.34% | 47.73% | 74.30% | 30.99% |

in which $\theta$ denotes all the parameters, $T$ represents all the labels.

After all the operations above, the distribution on all $T$ possible results $S_{i+1}$ could be generated as follows:

$$p(t_{i+1}|t_1, \ldots, t_i, \mathbf{x}) = \text{softmax}\left(W_s h_t^k + b_s\right) \in \mathbb{R}^T, \qquad (14)$$

where $b_s$ is the bias and $W_s$ denotes the parameter matrix.

## EXPERIMENTS

In this section, we first introduce the experiment data statistics and then analyze the national energy investment risk evaluation and provide some investment suggestions for policy makers of China.

**TABLE 3 |** Estimated weights of risk evaluation indicators for six dimensions.

| Dimension | Weight of dimensions | Indicators | Weight of indicators |
|---|---|---|---|
| Investment environment | 0.089 | Starting a business | 0.006 |
| | | Dealing with construction permits | 0.009 |
| | | Getting electricity | 0.011 |
| | | Paying tax | 0.024 |
| | | Enforcing contracts | 0.019 |
| | | Resolving insolvency | 0.020 |
| Political risk | 0.159 | Government stability | 0.038 |
| | | Internal conflict | 0.032 |
| | | External conflict | 0.015 |
| | | Corruption | 0.024 |
| | | Law and order | 0.017 |
| | | Democratic accountability | 0.033 |
| Economic foundation | 0.146 | GDP per capita | 0.061 |
| | | Real GDP growth | 0.013 |
| | | Annual inflation rate | 0.012 |
| | | Budget balance as a percentage of GDP | 0.027 |
| | | Foreign debt as a percentage of GDP | 0.033 |
| | | Exchange rate stability | 0.006 |
| Environment constraint | 0.148 | Carbon dioxide emissions | 0.019 |
| | | Nitrous oxide emissions | 0.021 |
| | | Energy intensity | 0.008 |
| | | Carbon dioxide intensity | 0.013 |
| | | PM2.5 | 0.016 |
| | | Forest area (% of land area) | 0.071 |
| Resource potential | 0.259 | Total oil production | 0.032 |
| | | Crude oil proved reserves | 0.056 |
| | | Dry natural gas production | 0.047 |
| | | Proved reserves of natural gas | 0.058 |
| | | Crude oil distillation capacity | 0.031 |
| | | Total exports of refined petroleum products | 0.035 |
| Chinese factor | 0.199 | Outward FDI stock | 0.019 |
| | | Years of China's diplomatic relations | 0.077 |
| | | Value of contracted projects | 0.023 |
| | | Persons abroad of contracted projects and labor services | 0.045 |
| | | Value of total imports from China | 0.019 |
| | | Value of total exports to China | 0.016 |

## Data Statistics

We investigate 50 countries alongside the China's "Belt and Road Initiative" from 2013 to 2019. Here we provide the summary statistics of those nations in 2013 as example, as shown in **Table 2**.

In **Table 2**, we include seven main statistics, namely, population, GDP, total oil supply, crude oil proved reserves, dry gas production, proved reserves of natural gas and crude oil distillation capacity. More specifically, those 50 nations alongside the "Belt and Road Initiative" make up about 41.58% population of the whole world, with only 17.15% GDP of the world, which further proves that those nations are developing countries while foreign investments are needed to boost their economy. These countries contain lots of natural resources, with the total oil supply, crude oil proved reserves, dry gas production and proved reserves of the natural gas makes up 50.22, 57.34, 47.73, and 74.30% respectively of the whole world. However, the energy refinement capacity only makes up 30.99% of the world, which means that the potential energy investment in those countries are quite promising.

## Experimental Results

In this section, we discuss the energy investment evaluation results of our model. First we present the weights of each indicator which is generated by the self-attention layer as illustrated in **Table 3**. From which we can observe that the weights of indicators Investment environment, political risk, economic foundation, environment constraint, resource potential and Chinese factor are 0.089, 0.159, 0.144, 0,150, 0.259, and 0.199, respectively. The resource potential of a country plays the most important role for energy investment, which is expected and intuitive. Chinese factor is also an important indicator as a stable relationship between China and the country being invested may also provide a friendly investment environment and secure the investments of China's companies. The third most important risk is the political risk, with the higher risk of a nation's politics, the higher the Chinese companies will face when choosing the investment target. Notice that the economic foundation and environment constraint almost share the same impact on the investment. It could be attributed to the fact that it becomes a common view that every country should help to deal with the climate changing challenge, so that environment constraint should also be a really important factor to be considered.

Aside from the above main six indicators, we also look into the sub-indicators in **Table 3**. Among all the sub-indicators, we find that the indicator years of China's diplomatic relations plays the

**TABLE 4 |** Evaluation results.

| No | Countries | Lowest-risk | Lower-risk | Medium-risk | Higher -risk | Highest-risk |
|---|---|---|---|---|---|---|
| 1 | Russia | **0.13632** | 0.13023 | 0.09821 | 0.05744 | 0.04221 |
| 2 | Singapore | **0.09622** | 0.08712 | 0.06633 | 0.06723 | 0.07811 |
| 3 | Malaysia | 0.11834 | **0.14022** | 0.13522 | 0.08309 | 0.05245 |
| 4 | Indonesia | 0.12021 | **0.13043** | 0.11745 | 0.07177 | 0.05832 |
| 5 | UAE | 0.12059 | **0.12987** | 0.10833 | 0.07276 | 0.05135 |
| 6 | Qatar | 0.11546 | **0.12688** | 0.10323 | 0.07647 | 0.05659 |
| 7 | Kuwait | 0.11534 | **0.12589** | 0.12345 | 0.07834 | 0.06124 |
| 8 | Kazakhstan | 0.09953 | **0.12355** | 0.11319 | 0.09005 | 0.07045 |
| 9 | Iran | 0.10646 | **0.12323** | 0.11347 | 0.09012 | 0.07456 |
| 10 | Saudi Arabia | 0.11877 | **0.12145** | 0.08789 | 0.06562 | 0.05492 |
| 11 | Iraq | 0.10457 | **0.12193** | 0.10157 | 0.08689 | 0.07434 |
| 12 | Pakistan | 0.09584 | **0.10032** | 0.09368 | 0.09793 | 0.07984 |
| 13 | India | 0.11213 | 0.11956 | **0.12678** | 0.07784 | 0.06132 |
| 14 | Thailand | 0.09958 | 0.12648 | **0.13883** | 0.09692 | 0.07387 |
| 15 | Philippines | 0.09245 | 0.10849 | **0.13724** | 0.11334 | 0.07789 |
| 16 | Oman | 0.10645 | 0.12234 | **0.13695** | 0.09023 | 0.06613 |
| 17 | Azerbaijan | 0.08944 | 0.10859 | **0.13178** | 0.11059 | 0.07956 |
| 18 | Romania | 0.10449 | 0.11032 | **0.13122** | 0.11019 | 0.07147 |
| 19 | Turkey | 0.09212 | 0.11507 | **0.13193** | 0.13034 | 0.07922 |
| 20 | Yemen | 0.09245 | 0.10945 | **0.13045** | 0.09475 | 0.08159 |
| 21 | Israel | 0.08945 | 0.10144 | **0.12835** | 0.122,189 | 0.08078 |
| 22 | Poland | 0.10689 | 0.11344 | **0.12778** | 0.11589 | 0.07134 |
| 23 | Vietnam | 0.11089 | 0.11499 | **0.12237** | 0.08078 | 0.06458 |
| 24 | Egypt | 0.09737 | 0.11467 | **0.11948** | 0.08287 | 0.08349 |
| 25 | Greece | 0.08058 | 0.09348 | **0.11889** | 0.09734 | 0.10397 |
| 26 | Bulgaria | 0.09199 | 0.09575 | **0.11434** | 0.11340 | 0.09032 |
| 27 | Brunei | 0.10443 | 0.10348 | **0.11445** | 0.11313 | 0.06948 |
| 28 | Slovakia | 0.09411 | 0.09548 | **0.10823** | 0.10209 | 0.08349 |
| 29 | Myanmar | 0.09948 | 0.10598 | **0.10634** | 0.09109 | 0.08298 |
| 30 | Czech Republic | 0.09699 | 0.09748 | 0.11329 | **0.11348** | 0.08287 |
| 31 | Jordan | 0.06989 | 0.08338 | 0.10038 | **0.11540** | 0.11020 |
| 32 | Albania | 0.08279 | 0.08233 | 0.08247 | **0.11557** | 0.10434 |
| 33 | Ukraine | 0.08234 | 0.09258 | 0.11939 | **0.11944** | 0.08745 |
| 34 | Hungary | 0.09604 | 0.09934 | 0.10848 | **0.11959** | 0.08397 |
| 35 | Serbia | 0.09134 | 0.09876 | 0.11423 | **0.12748** | 0.08757 |
| 36 | Bangladesh | 0.07659 | 0.09658 | 0.11598 | **0.12758** | 0.09798 |
| 37 | Croatia | 0.08029 | 0.08944 | 0.11434 | **0.12966** | 0.09599 |
| 38 | Belarus | 0.07658 | 0.09795 | 0.11012 | **0.13044** | 0.09987 |
| 39 | Bahrain | 0.08185 | 0.09578 | 0.11212 | **0.13247** | 0.08999 |
| 40 | Syria | 0.07645 | 0.08989 | 0.09823 | **0.10557** | 0.10484 |
| 41 | Lithuania | 0.06849 | 0.07548 | 0.09439 | 0.09795 | **0.10534** |
| 42 | Mongolia | 0.07042 | 0.07149 | 0.06245 | 0.06391 | **0.10739** |
| 43 | Estonia | 0.05789 | 0.06237 | 0.07548 | 0.08348 | **0.11013** |
| 44 | Sri Larka | 0.06549 | 0.08140 | 0.07423 | 0.07475 | **0.11268** |
| 45 | Slovenia | 0.06259 | 0.07094 | 0.07321 | 0.09458 | **0.11649** |
| 46 | Cyprus | 0.06149 | 0.06924 | 0.07849 | 0.07423 | **0.11645** |
| 47 | Latvia | 0.05848 | 0.06223 | 0.07449 | 0.08229 | **0.11949** |
| 48 | Lebanon | 0.04797 | 0.05539 | 0.07029 | 0.08448 | **0.13745** |
| 49 | Moldova | 0.03949 | 0.04958 | 0.05759 | 0.09249 | **0.13747** |
| 50 | Armenia | 0.03423 | 0.04346 | 0.05289 | 0.08713 | **0.14555** |

*Note: The bold entry represents the highest value in a column, which indicates the risk level of the country it belongs to.*

most important role, which illustrates that having a long-term relationship with China could help Chinese companies build a stable and reliable investment relations with the target nations alongside the "Belt & Road Initiative". The forest area is the second most important indicator which is unexpected, but it further proves that every country pays more attention on protecting their natural environment with the forest having strong ability to adjust the climate changing situation. GDP per capita is also a significant factor since it reflects the foundation of the economy of the target nations to be invested. Notice that the proved reserves of crude oil and natural gas are also really important indicators which reflect the potential investment return for Chinese energy companies. And it may also explain the reason that the Middle East countries attract most of the energy investments from those international companies, regardless of their unstable political environment. Nevertheless, the government stability is still a relatively important factor with the weight being 0.038, so Chinese companies must evaluate the state of the government before investment.

**Table 4** presents the evaluation results in detail. From it we could observe that overall we have 10 countries with highest risk, 11 countries with higher risk, 17 countries with medium risk, 10 countries with lower risk and 2 countries with lowest risk. There are 42% of the countries alongside the "Belt & Road Initiative" has the relatively high-risk investment environment, which further reminds China's companies to pay attention to the risk control on those countries. Notice that those countries with rich natural resource tend to have lower energy investment risks, and this is due to the fact that they have rich gas and oil reserves which can guarantee the potential investment return. Chinese companies do not have to worry about the availability of fossil resources in these countries.

It is noticeable that though some countries share the same risk grade, they have quite different characteristics in terms of the risk factors. Take Singapore and Russia having lowest risk for investment as an example, Singapore stands out because of its excellent investment environment, political stability and economic foundations, but it is lacking in the natural resources in terms of gas and oil. Russia is a country possesses abundant fossil resources but has relatively poorer economic foundations and investment environment. However, it still has the lowest risk for China's energy investment, which could be attributed to several factors like it has a stable and friendly political relations with China. Additionally, with the geographical advantage of bordering China, it has already built several gas pipelines connecting the countries between these two countries. Therefore, it helps to build a solid foundations of the energy cooperation with these infrastructures. In conclusion, China can choose Russia as a good target nation for energy investment.

We could also observe that though some countries have the neighboring geographic locations, their factors influencing investment risk still vary a lot. In the Middle East, it has the most unstable geopolitical risks in terms of government stability, religious conflict and even war threat. Those countries possesses the majority of the fossil resources of the world, so such unstable situations in there always make the price and supply of the energy become unsettled as well. Despite of the above negative factors, these countries still attract lots of global energy investment mainly because of their potential of resources. Our analysis shows that UAE, Qatar, Kuwait and Saudi Arabia have the relatively stable government and less political threat, resulting in their evaluations being lower-risk grade. Iran and Iraq have the unstable political environment but still be rated as lower risk because of their sufficient reserves of fossil resources. Both countries also have a stable political and friendly diplomatic relation with China especially for Iran, and such relation become more intense because of the COVID-19 situation. Therefore, these two countries are worthwhile for China's energy investment. Additionally, we could also observe that Malaysia and Indonesia in Southeast Asia and Kazakhstan and Pakistan in Central Asia are rated as lower risk balancing the resource potential, investment environment and environment constraints. Malaysia and Indonesia all have a stable political government and the foreign investment are well welcomed by their governments. Additionally, in recent years, both countries have been dedicated to improve their investment environment and stimulate the foreign investment, along with lots of infrastructures being constructed. So these two countries are also good targets. Kazakhstan and Pakistan are two countries have balanced possession of oil, coal and natural gas with decent economic and financial system. Both countries also have a good diplomatic relationship with China, however, their geopolitical situation is not very stable in Central Asia, which is a significant factor to be considered for China's investment.

In conclusion, with the further implementation of China's "Belt & Road Initiative" policies, we believe that the investment environment for those countries alongside "Belt & Road Initiative" will be better and be more open to foreign companies. We hope that the energy investment can be used as catalyst to stimulate the cooperations on more and more economic areas such as technology communication, infrastructure construction and labor contacts. We believe such cooperations can further decrease the investment risk of countries alongside the "Belt & Road Initiative", so that a positive feedback circle could be formed. China's efforts and investments could help the world build a more stable and sustainable energy supply system.

# DISCUSSION

From the analysis above, countries like Iran and Iraq having unstable political environment still attract lots of energy investment because of their abundant energy resource, which implies that China should regard the oversea risk aversion as a whole, instead of focusing on the risk of a single project. China should bravely seek for the future opportunities and sustainable development for the energy investment. Additionally, most of the countries with lower risks are developing countries, so their legal construction maybe incomplete. Therefore, legislation and policy support should be provided by Chinese government for oversea energy investment. These countries also have different investment markets, so that China should build a platform providing information consulting service for the investor.

Although we have included six indicators containing 36 sub-indicators, there still exist may other factors worth to be considered. For example, Wu et al. (2020) consider the technical risks such as technology maturity, progressivenes and research and development (R&D) capacity. Azam et al. (2019) and Azam (2019) take the human capital and human health into consideration, respectively. Azam (2016) also considers the impact of environmental degradation on the economic growth. In the future, we intend to build a more comprehensive indicator system to consider as more related factors as possible.

## Policy Recommendations

Here we propose our policy recommendations for China's policy makers. First of all, for energy investment, we must consider every aspect of the risk factors and choose the optimal strategies. We should try to find the future potentials and consider the sustainability of the energy and economic development. Additionally, the majority of the countries alongside the "Belt

& Road Initiative" have the relatively higher investment risk because of various reasons, which reminds China's companies to make careful and thorough investigations before making investments. On top of that, based on our investigation, we have several target countries to recommend. For example, Russia among the CIS nations, Saudi Arabia, UAE and Iran in Middle East, Malaysia and Indonesia in Southeast Asia, Kazakhstan and Pakistan in Middle Asia are all stable and reliable choices to be invested for China. Moreover, China should help to build the information consulting services for Chinese investors, offering professional suggestions for risk warning. The policy and legislation support should also be built for China's national risk management.

## CONCLUSION

As the world-leading energy-consuming country, it is urgent for China to secure the energy safety via oversea energy investment. The "Belt & Road initiative" brings such opportunities to China while the related research for recognition and prevention of oversea energy investment risks is limited.

Therefore, in this paper we put forward a seaq2seq model for assessing the energy investment risk on 50 countries alongside China's "Belt & Road Initiative". We first build an indicator system to evaluate the energy investment in six factors, i.e., investment environment, political risk, economic foundation, environment constraint, resource potential and Chinese factor. The six indicators could be separated into 36 sub-indicators. Then we propose the Bi-LSTM model as encoder to handle the historical statistics of these countries. The self-attention layer is adopted to calculate the weights of each indicator. We observe that the resource potential is the most important indicator, while "years of China's diplomatic relations" is the most important sub-indicator. Finally we use a hierarchical CNN layer as decoder to produce the results of the assessment of energy risk investments. We have the ideal target countries for China's oversea investment, namely, Russia, UAE, Saudi Arabia, Kazakhstan, Pakistan, Malaysia and Indonesia. Some countries like Iran and Iraq are also worth to be invested, as despite of their unstable political environment, they are in possession of abundant natural resources. It reminds China to bravely seek for the future opportunities and sustainable markets, instead of focusing on one project.

In future work, we intend to build a more comprehensive indicator system so that other important factors could also be included like human capital and human health. In addition, we could also further apply the up-to-date deep learning techniques to better process the statistics, e.g., reinforcement learning or generative adversarial network.

## DATA AVAILABILITY STATEMENT

Publicly available datasets were analyzed in this study. This data can be found here: https://epub.prsgroup.com/products/international-country-risk-guide-icrg https://databank.worldbank.org/home.aspx, https://www.eia.gov

## AUTHOR CONTRIBUTIONS

PL realized the conceptualization, formal analysis and put forward a methodology, she also conducted the experiments and wrote the paper; MY helped data curation, coding and he also helped results validation; LJ reviewed and edited the paper.

## REFERENCES


Agliardi, E., Agliardi, R., Pinar, M., Stengos, T., and Topaloglou, N. (2012). A new country risk index for emerging markets: a stochastic dominance approach. *J. Empir. Fin.* 19, 741–761. doi:10.1016/j.jempfin.2012.08.003

Azam, M. (2016). Does environmental degradation shackle economic growth? A panel data investigation on 11 Asian countries. *Renew. Sustain. Energ. Rev.* 65, 175–182. doi:10.1016/j.rser.2016.06.087

Azam, M. (2020). Energy and economic growth in developing asian economies. *J. Asia Pac. Econ.* 25, 447–471. doi:10.1080/13547860.2019.1665328

Azam, M., Khan, A. Q., and Ozturk, I. (2019). The effects of energy on investment, human health, environment and economic growth: empirical evidence from China. *Environ. Sci. Pollut. Res.* 26, 10816–10825. doi:10.1007/s11356-019-04497-4

Azam, M. (2019). Relationship between energy, investment, human capital, environment, and economic growth in four brics countries. *Environ. Sci. Pollut. Res.* 26, 34388–34400. doi:10.1007/s11356-019-06533-9

Bahdanau, D., Cho, K., and Bengio, Y. (2015). Neural machine translation by jointly learning to align and translate. *Mach. Translat.* 31, 3–18. doi:10.1007/s10590-017-9194-2

Brewer, T. L., and Rivoli, P. (1990). Politics and perceived country creditworthiness in international banking. *J. Money Credit Bank* 22, 357–369.

Brown, C. L., Cavusgil, S. T., and Lord, A. W. (2015). Country-risk measurement and analysis: a new conceptualization and managerial tool. *Int. Business Rev.* 24, 246–265. doi:10.1016/j.ibusrev.2014.07.012

Cadarso, M. A., Gomez, N., Lopez, L. A., and Tobarra, M. A. (2016). Sustainable tourism: Progress, Challenges and Opportunities, Calculating tourism's carbon footprint: measuring the impact of investments. *J. Clean. Prod.* 111, 529–537. doi:10.1016/j.jclepro.2014.09.019

Chen, H., Wang, C., and Ye, M. (2016). An uncertainty analysis of subsidy for carbon capture and storage (ccs) retrofitting investment in China's coal power plants using a real-options approach. *J. Clean. Prod.* 137, 200–212. doi:10.1016/j.jclepro.2016.07.074

Cho, K., van Merrienboer, B., Gülçehre, Ç., Bahdanau, D., Bougares, F., Schwenk, H., et al. (2014). Learning phrase representations using RNN encoder-decoder for statistical machine translation. *EMNLP* 33, 1724–1734. doi:10.3115/v1/d14-1179

Chorn, L., and Shokhor, S. (2006). Real options for risk management in petroleum development investments. *Energ. Econ.* 28, 489–505. doi:10.1016/j.eneco.2006.03.002

Conrad, B., and Kostka, G. (2017). Chinese investments in europe's energy sector: risks and opportunities? *Energy Policy* 101, 644–648. doi:10.1016/j.enpol.2016.12.016

Cucchiella, F., Gastaldi, M., and Trosini, M. (2017). Investments and cleaner energy production: a portfolio analysis in the Italian electricity market. *J. Clean. Prod.* 142, 121–132. doi:10.1016/j.jclepro.2016.07.190

Dauphin, Y. N., Fan, A., Auli, M., and Grangier, D. (2017). Language modeling with gated convolutional networks. *ICML* 15, 933–941. doi:10.21437/interspeech.2020-1493

Dockner, E. J., Kucsera, D., and Rammerstorfer, M. (2013). Investment, firm value, and risk for a system operator balancing energy grids. *Energ. Econ.* 37, 182–(192.) doi:10.1016/j.eneco.2013.01.007

Duan, F., Ji, Q., Liu, B.-Y., and Fan, Y. (2018). Energy investment risk assessment for nations along China's belt & road initiative. *J. Clean. Prod.* 170, 535–547. doi:10.1016/j.jclepro.2017.09.152

Fan, Y., and Zhu, L. (2010). A real options based model and its application to China's overseas oil investment decisions. *Energ. Econ.* 32, 627–637. doi:10.1016/j.eneco.2009.08.021

Farfan, J., and Breyer, C. (2017). Structural changes of global power generation capacity towards sustainability and the risk of stranded investments supported by a sustainability indicator. *J. Clean. Prod.* 141, 370–384. doi:10.1016/j.jclepro.2016.09.068

Feder, G., and Just, R. E. (1977). A study of debt servicing capacity applying logit analysis. *J. Dev. Econ.* 4, 25–38. doi:10.1016/0304-3878(77)90004-9

Feder, G., and Uy, L. V. (1985). The determinants of international creditworthiness and their policy implications. *J. Pol. Model.* 7, 133–156. doi:10.1016/0161-8938(85)90032-8

Gal, N., Milstein, I., Tishler, A., and Woo, C. (2017). Fuel cost uncertainty, capacity investment and price in a competitive electricity market. *Energ. Econ.* 61, 233–240. doi:10.1016/j.eneco.2016.11.014

Gehring, J., Auli, M., Grangier, D., Yarats, D., and Dauphin, Y. N. (2017). "Convolutional sequence to sequence learning," in Proceedings of the 34th International Conference on Machine Learning. Sydney, NSW, Australia: ICML 2017, 6–11.

Hach, D., and Spinler, S. (2016). Capacity payment impact on gas-fired generation investments under rising renewable feed-in—a real options analysis. *Energ. Econ.* 53, 270–280. doi:10.1016/j.eneco.2014.04.022

Hafeez, M., Chunhui, Y., Strohmaier, D., Ahmed, M., and Jie, L. (2018). Does finance affect environmental degradation: evidence from one belt and one road initiative region? *Environ. Pollut. Res.* 14, 21. doi:10.1007/s11356-018-1317-7

Hammer, P., Kogan, A., and Lejeune, M. (2006). Modeling country risk ratings using partial orders. *Eur. J. Oper. Res.* 175, 836–859. doi:10.1016/j.ejor.2005.06.040

He, K., Zhang, X., Ren, S., and Sun, J. (2016). "Deep residual learning for image recognition," in IEEE Conference on Computer Vision and Pattern Recognition, CVPR 2016. NV, USA: Las Vegas, 770–778. doi:10.1109/CVPR.2016.90

Hieronymi, P., and Schüller, D. (2015). The clean-development mechanism, stochastic permit prices and energy investments. *Energ. Econ.* 47, 25–36. doi:10.1016/j.eneco.2014.10.008

Hochreiter, S., and Schmidhuber, J. (1997). Long short-term memory. *Neural Comput.* 9, 1735–1780. doi:10.1162/neco.1997.9.8.1735

Jones, A. W. (2015). Perceived barriers and policy solutions in clean energy infrastructure investment. *J. Clean. Prod.* 104, 297–304. doi:10.1016/j.jclepro.2015.05.072

Kharas, H. (1984). The long-run creditworthiness of developing countries: Theory and practice. *Q. J. Econ.* 99, 415–439. doi:10.2307/1885958

Li, J. P., Tang, L., Sun, X. L., Yu, L. A., He, W., and Yang, Y. Y. (2012). Country risk forecasting for major oil exporting countries: a decomposition hybrid approach. *Comput. Ind. Eng.* 63, 641–651. doi:10.1016/j.cie.2011.12.003

Liedtke, S. (2017). Chinese energy investments in europe: an analysis of policy drivers and approaches. *Energy Policy* 101, 659–669. doi:10.1016/j.enpol.2016.09.037

Luong, T., Pham, H., and Manning, C. D. (2015). "Effective approaches to attention-based neural machine translation," in Proceedings of the 2015 conference on empirical methods in natural language processing, 17–21. Lisbon, Portugal: EMNLP 2015, 1412–1421.

Mayer, C., Breun, P., and Schultmann, F. (2017). Considering risks in early stage investment planning for emission abatement technologies in large combustion plants. *J. Clean. Prod.* 142, 133–144. doi:10.1016/j.jclepro.2016.05.089

Miller, K. D. (1992). A framework for integrated risk management in international business. *J. Int. Business Stud.* 23, 311–331. doi:10.1057/palgrave.jibs.8490270

Mo, J.-L., Schleich, J., Zhu, L., and Fan, Y. (2015). Delaying the introduction of emissions trading systems—implications for power plant investment and operation from a multi-stage decision model. *Energ. Econ.* 52, 255–264. doi:10.1016/j.eneco.2015.11.009

Pringles, R., Olsina, F., and GarcÃ©s, F. (2015). Real option valuation of power transmission investments by stochastic simulation. *Energ. Econ.* 47, 215–226. doi:10.1016/j.eneco.2014.11.011

Sanchez, G. M., and Meltzer, E. S. (2012). *The Edwin Smith Papyrus: updated translation of the trauma treatise and modern medical commentaries*. New York, NY: Lockwood Press.

Strand, J., Miller, S., and Siddiqui, S. (2014). Long-run carbon emission implications of energy-intensive infrastructure investments with a retrofit option. *Energ. Econ.* 46, 308–317. doi:10.1016/j.eneco.2014.10.002

Sun, X., Li, J., Wang, Y., and Clark, W. W. (2014). China's sovereign wealth fund investments in overseas energy: the energy security perspective. *Energy Policy* 65, 654–661. doi:10.1016/j.enpol.2013.09.056

Sutskever, I., Vinyals, O., and Le, Q. V. (2014). Sequence to sequence learning with neural networks. *NIPS* 14, 33. doi:10.21437/interspeech.2018-1381

Tan, X. (2013). China's overseas investment in the energy/resources sector: its scale, drivers, challenges and implications. *Energ. Econ.* 36, 750–758. doi:10.1016/j.eneco.2012.11.019

Tietjen, O., Pahle, M., and Fuss, S. (2016). Investment risks in power generation: a comparison of fossil fuel and renewable energy dominated markets. *Energ. Econ.* 58, 174–185. doi:10.1016/j.eneco.2016.07.005

Wu, Y., Wang, J., Ji, S., and Song, Z. (2020). Renewable energy investment risk assessment for nations along China's belt & road initiative: an anp-cloud model method. *Energy* 190, 116381. doi:10.1016/j.energy.2019.116381

Xu, Q., Lei, Y., Ge, J., and Ma, X. (2017). Did investment become green in China? evidence from a sectoral panel analysis from 2003 to 2012. *J. Clean. Prod.* 156, 500–506. doi:10.1016/j.jclepro.2017.04.075

Zhai, F. (2018). China's belt and road initiative: a preliminary quantitative assessment. *J. Asian Econ.* 55, 233. doi:10.1016/j.asieco.2017.12.006

Zhang, M., Zhou, P., and Zhou, D. (2016). A real options model for renewable energy investment with application to solar photovoltaic power generation in China. *Energ. Econ.* 59, 213–226. doi:10.1016/j.eneco.2016.07.028

Zhang, R., Andam, F., and Shi, G. (2017). Environmental and social risk evaluation of overseas investment under the China–Pakistan economic corridor. *Environ. Monit. Assess.* 189, 253. doi:10.1007/s10661-017-5967-6

Zhang, R., Shi, G., Wang, Y., Zhao, S., Ahmad, S., Zhang, X., et al. (2018). Social impact assessment of investment activities in the China–pakistan economic corridor. *Impact Assess. Project Appraisal* 36, 331–347. doi:10.1080/14615517.2018.1465227

**Conflict of Interest:** The authors declare that the research was conducted in the absence of any commercial or financial relationships that could be construed as a potential conflict of interest.

frontiers in Neurorobotics

ORIGINAL RESEARCH
published: 29 April 2021
doi: 10.3389/fnbot.2021.641007

# Prediction of Dangerous Driving Behavior Based on Vehicle Motion State and Passenger Feeling Using Cloud Model and Elman Neural Network

*Huaikun Xiang[1], Jiafeng Zhu[2], Guoyuan Liang[2,3,4,5]* and Yingjun Shen[6]*

[1] School of Automotive and Transportation Engineering, Shenzhen Polytechnic, Shenzhen, China, [2] Center for Intelligent Biomimetic Systems, Shenzhen Institute of Advanced Technology, Chinese Academy of Sciences, Shenzhen, China, [3] Guangdong Provincial Key Lab of Robotics and Intelligent System, Shenzhen Institutes of Advanced Technology, Chinese Academy of Sciences, Shenzhen, China, [4] Shenzhen Key Laboratory of Human-Machine Intelligence-Synergy Systems, Shenzhen Institutes of Advanced Technology, Chinese Academy of Sciences, Shenzhen, China, [5] Guangdong-Hong Kong-Macao Joint Laboratory of Human-Machine Intelligence-Synergy Systems, Shenzhen Institutes of Advanced Technology, Chinese Academy of Sciences, Shenzhen, China, [6] School of Business, Nanjing University, Nanjing, China

Dangerous driving behavior is the leading factor of road traffic accidents; therefore, how to predict dangerous driving behavior quickly, accurately, and robustly has been an active research topic of traffic safety management in the past decades. Previous works are focused on learning the driving characteristic of drivers or depended on different sensors to estimate vehicle state. In this paper, we propose a new method for dangerous driving behavior prediction by using a hybrid model consisting of cloud model and Elman neural network (CM-ENN) based on vehicle motion state estimation and passenger's subjective feeling scores, which is more intuitive in perceiving potential dangerous driving behaviors. To verify the effectiveness of the proposed method, we have developed a data acquisition system of driving motion states and apply it to real traffic scenarios in ShenZhen city of China. Experimental results demonstrate that the new method is more accurate and robust than classical methods based on common neural network.

**Keywords: dangerous driving behavior, cloud model, Elman neural network, auto driving scenarios, active vehicle safety management**

OPEN ACCESS

***Edited by:***
*Zijun Zhang,*
*City University of Hong Kong, Hong Kong*

***Reviewed by:***
*Xie Binglei,*
*Harbin Institute of Technology, Shenzhen, China*
*Liang Zou,*
*Shenzhen University, China*

****Correspondence:***
*Guoyuan Liang*
*gy.liang@siat.ac.cn*

***Received:*** *13 December 2020*
***Accepted:*** *15 February 2021*
***Published:*** *29 April 2021*

***Citation:***
*Xiang H, Zhu J, Liang G and Shen Y (2021) Prediction of Dangerous Driving Behavior Based on Vehicle Motion State and Passenger Feeling Using Cloud Model and Elman Neural Network. Front. Neurorobot. 15:641007. doi: 10.3389/fnbot.2021.641007*

## INTRODUCTION

Driving behavior analysis is an important part of research on traffic safety, which is a reflection of how the driver steers the vehicle including speed and attitude control. Dangerous driving behaviors are seen as series of operations performed by the driver on public roads that may result in abnormal traffic conditions and subsequently lead to road accidents (Dronseyko et al., 2018). Therefore, the analysis of driving behavior can help to measure the driver's driving safety and prevent traffic accidents. A recent report by the American Automobile Association estimated that 56% of fatal crashes occurring between 2003 and 2007 are related to aggressive driving behavior

(American Automobile Association, 2009). In Shanghai, China, traffic police corps reported that 75.9% (792 out of 1,044) of the car accidents in 2015 were caused by all kinds of dangerous driving behaviors (Accident Prevention Division of Traffic Police Corps of Shanghai Public Security Bureau, 2016). If the dangerous driving behavior of vehicles can be identified in time, the driver may be promptly alerted or the vehicle may be forcibly taken over at a critical time by safety control devices, which will effectively prevent the traffic accidents from happening.

Case by case modeling driver's personal driving behavior is the most straightforward way; however, dangerous driving behavior involves various complex and uncertain factors, such as driving skills, emergency response ability, gender, mood, fatigue, job pressure and even educational background, life experience, etc. (Horswill and McKenna, 1999; Harre and Sibley, 2007; Dula et al., 2011; Day et al., 2018; Fountas et al., 2019; Useche et al., 2020), thereby making it difficult to directly study personal driving behavior. Nevertheless, during the course of driving, no matter how complex factors the vehicle is subjected to and no matter what driving actions the driver takes, all dangerous driving behaviors will eventually be reflected through the corresponding motion state of vehicle and reaction of passengers on the vehicle. Therefore, we can detect potential dangerous driving behavior by sensing vehicle motion explicitly and monitoring passenger's feeling implicitly. Based on this fact, this paper intends to use real-time monitoring data, including explicit vehicle states and implicit passenger feelings to study dangerous driving behavior.

The main contributions of this paper are as follows: (1) Passenger feeling scores are introduced into the prediction system as subjective evaluations on the driver's behaviors; (2) cloud model (CM) is applied to identify the state of vehicle with a clear qualitative judgment, and combined with Elman neural network to make predictions; (3) a complete and practical solution including hardware and algorithms is presented for the prediction of dangerous driving behaviors.

## RELATED WORK

In the research of driving behavior analysis based on real-time monitoring data of vehicle movement, three aspects are involved and stated as follows: (1) real-time detection of vehicle motion states; (2) dynamic analysis of dangerous driving behaviors; (3) correlation analysis and regularity discovery between vehicle motion state and dangerous driving behavior. The detection of vehicle motion state mainly involves the use of on-board monitoring equipment and the identification of motion state. The common equipment include vehicle on board diagnostics (OBD), camera, GPS, inertial sensor, smart phone, and so on. The selection and design of the detection method of vehicle motion state is related to the monitoring equipment and data type being used. In Huang (2011), the real-time recognition of vehicle Z-curve driving state based on image processing technology was proposed, which would automatically warn and provide feedback to the driver when the relevant image monitoring metric exceeded the preset threshold. Omerustaoglu et al. (2020) studied the driver's distracted driving behavior by combining in-vehicle and image data using deep learning. Based on the theory of support vector machine (SVM), Jeong et al. (2013) recognized two kinds of driving behaviors, namely lane-changing and Z-curve driving using the data collected by the built-in 3-axis gyroscope of vehicle. DaeHan et al. (2019) proposed a system called ADDICT (Accurate Driver Detection exploiting Invariant Characteristics of smartphone sensors), which identifies the driver utilizing the inconsistency between gyroscope and magnetometer dynamics and the interplay between electromagnetic field emissions and engine startup vibrations. In order to evaluate the feasibility of ADDICT, four participants and three different vehicles by varying vehicle-riding scenarios are tested, and the evaluation results demonstrated that ADDICT identifies the driver's smartphone with 89.1% average accuracy for all scenarios. Wu et al. (2013) used multiple sensors of vehicle monitoring cameras, 3-axis accelerometers and GPS receivers to collect vehicles' motion parameters including lateral offset distance, relative distance, lateral/longitudinal acceleration, and speed. The recognition results for 7 common vehicle driving states (normal driving, acceleration, braking, left-turn, right-turn, curve driving, and vehicle following) verified that the hidden Markov model (HMM) had the best overall recognition rate.

The analysis of dangerous driving behavior mainly focuses on the classification of drivers' driving styles. Some studies attempt to describe various types of aggressive driving behavior and develop their criteria (Tasca, 2000; Murphey et al., 2009; Abou-Zeid et al., 2011; Li et al., 2014; Carboni and Bogorny, 2015; Mãirean and Havãrneanu, 2018; Yang et al., 2019). In general, the classification algorithms of driving style can be divided into two categories: statistical method and machine learning method. Constantinescu et al. (2010) made use of vehicle-borne GPS data including GPS speed and acceleration to model and analyze driver's driving style. In their research, the driving behaviors are divided into five types: non-aggressive, somewhat non-aggressive, neutral, moderately aggressive, and very aggressive. Hong et al. (2014) built a sensor platform composed of Android smartphones, OBD, and inertial measurement unit (IMU) for collecting driving behavior data including maximum, average and standard deviation, speed variation, longitudinal acceleration, lateral acceleration, speed, and throttle position of vehicles. Then the thresholds are determined that can equally divide these features of all samples into five discretized levels. Naive Bayesian classifier is utilized to model the relationship between driving characteristics and driving style. In Eboli et al. (2017), driving behaviors were divided into three types (safe, unsafe, and safe but potentially dangerous) by calculating the 50 and 80% speed and average speed.

For the classification of dangerous driving behavior, it is mainly realized by detecting driving events related to safety, such as acceleration, braking, and turning. In general, the classification of dangerous driving behavior can be divided into two categories: template-based matching method and threshold-based discrimination method. From the perspective of energy consumption, the acceleration–deceleration characteristics of three different driving behaviors are analyzed (Xing et al., 2020). Driving Habits Graph (DHG) (Chen et al., 2013), which indicates the significant changes of behavior according to a series of driving

data, was proposed to simulate driving behavior and display the driving style intuitively. In their follow-up research (Chen et al., 2014), dangerous driving events were transformed into the attributed relational map (ARM), and then the two-way fuzzy attribute mapping and matching were used to compare the converted driving behavior with the template to determine whether it was a dangerous driving event.

In Johnson and Trivedi (2011), for all predefined driving events including right/left/U turn, aggressive right/left/U turn, and acceleration/deceleration/lane drastic change, the smartphone data were utilized to analyze these events and determine whether a driver's behavior is normal or aggressive action through time series data matching and dynamic time warping (DTW). Based on vehicle-borne GPS and OBD data (Chen et al., 2019), a graphic modeling method was proposed for modeling individual driving behavior through the statistical method. Based on the assumption that drivers have specific driving habits, the typical driving modes are detected and extracted. Sorted by the frequency of these typical driving modes, a driving behavior diagram is finally constructed to directly explain the driver's behavior characteristics. In Han and Yang (2009), the velocity, acceleration, and yaw angular velocity of vehicles are collected by an on-board black box for identification of four dangerous vehicles states including accelerating, decelerating, steep turn, and sudden lane change. Besides, a threshold division method based on different speed intervals is also proposed. After intensive study on the acceleration threshold of dangerous aggressive driving behaviors Johnson and Trivedi, 2011), concluded that the turning acceleration threshold for aggressive driving was 0.73 g, the emergency turning threshold was 0.74 g, the U-turn threshold was 0.91 g, the turning threshold of non-aggressive driving was 0.3 g, and the U-turn threshold was 0.56 g. In Bagdadi (2013), the threshold for determination of rapid acceleration and deceleration was $\pm$ 0.48 g $\approx$ 4.8 m/s$^2$.

From above literature review and analysis, we noticed that vehicle motion state data are almost collected by vehicle-mounted sensor units, such as GPS, accelerometer, etc. Current research on the dangerous vehicle state and driving behavior are most likely focused on the human driver and the operation of vehicles. Since the drivers are easy to be influenced by complex factors, it is difficult to find the personal characteristics of drivers. We think that the key to this problem lies in how to set up the evaluation index system of dangerous driving behavior scientifically, and to find an effective prediction algorithm that can convert these qualitative indicators into quantitative vehicle attitude data with high precision. In this context, this paper proposes a vehicle active safety monitoring and early warning method integrating driving behavior, passenger feeling, and vehicle status based on cloud model and Elman neural network (CM-ENN), which is illustrated in **Figure 1**. By following the indicators of vehicle ride comfort

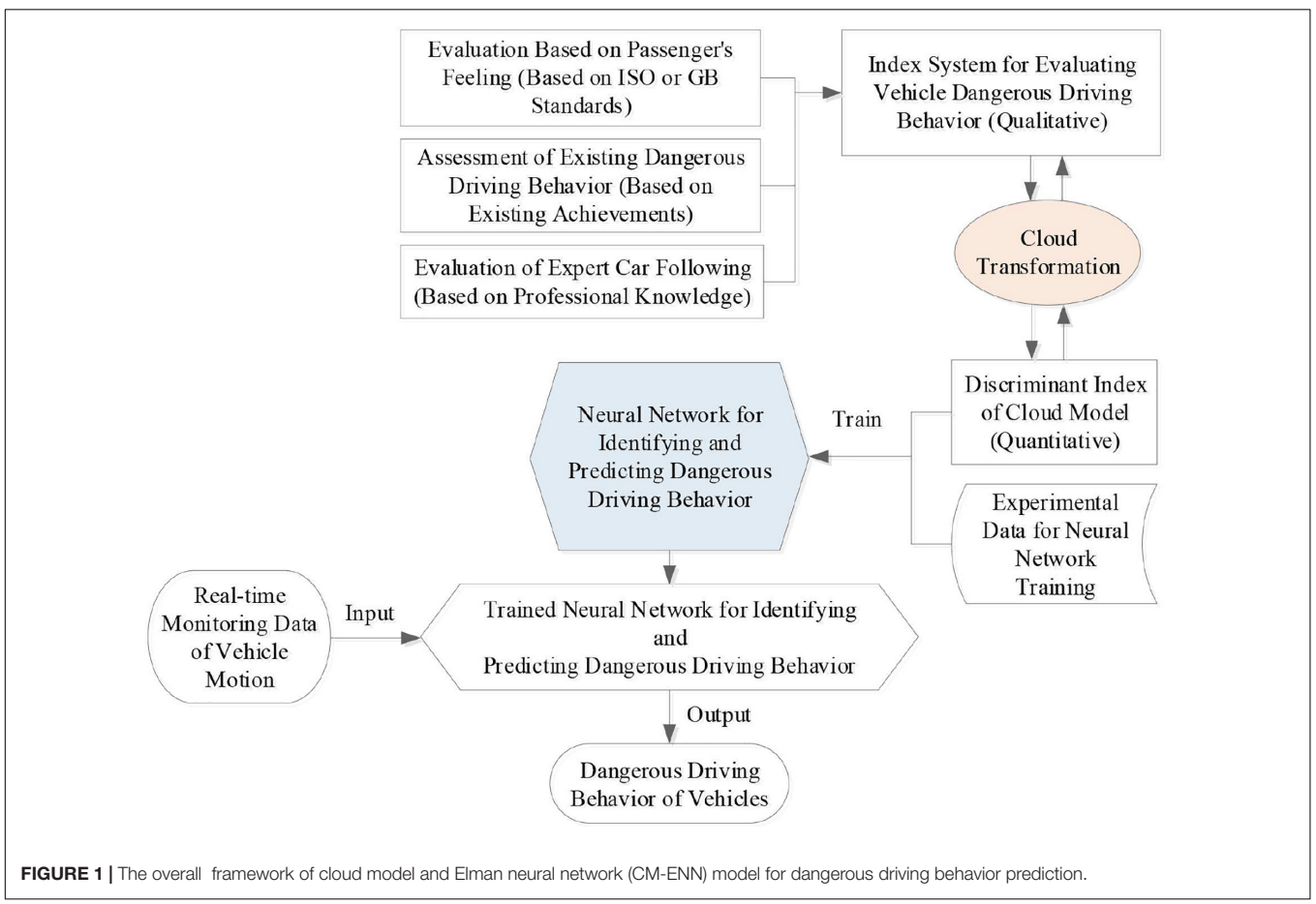


**FIGURE 1 |** The overall framework of cloud model and Elman neural network (CM-ENN) model for dangerous driving behavior prediction.

and passengers' perception of vehicle motion in related ISO standards (ISO 2631-1:1997/AMD 1:2010, 2010) and the National Standards of China (National Technical Committee of Auto Standardization, 2004), a CM is built to set up correspondences between dangerous driving behavior and vehicle motion data. Because of the advantages of ENN in dealing with non-linear problems and dynamic information (Wang et al., 2021), a CM-ENN model is constructed where the CM is used to evaluate dangerous driving behavior incorporating passenger's subjective feeling as well as vehicle motion data (Wang and Xu, 2012). The system was tested with the real data collected in vehicles running on some urban roads in Shenzhen City of China. Experimental results verified the effectiveness of the proposed method.

The remainder of this paper is organized as follows: section "Data Acquisition System" introduces the data acquisition and processing system of vehicle motion status. The calculation method of vehicle motion attitude is also discussed. In section "Cloud Model for Dangerous Driving Behavior Evaluation," the CM theory is introduced and the details of setting up correspondences between dangerous driving behavior are explained. Section "CM-ENN, Prediction Method of Dangerous Driving Behavior" discusses the structure of ENN and the training process. Experimental results and analysis are presented in sections "Experimental Results and Analysis," and "Conclusion" concludes the paper.

# THEORY AND METHOD

## Data Acquisition System

In this paper, a real-time driving behavior monitoring and active safety early warning system is designed, as shown in **Figure 2**. The system consists of three parts: (1) Vehicle-borne intelligent terminal mainly includes vehicle-borne GPS, micro-electro-mechanical systems (MEMS) sensors, CAN-bus, and so on.

It is designed to realize the acquisition and transmission of real-time data of six degree of freedoms (DOFs) motion states and vehicle speed. (2) Computer platform: Main tasks for this part are as follows: First, to pre-process the collected data. Second, to provide real-time driving behavior information

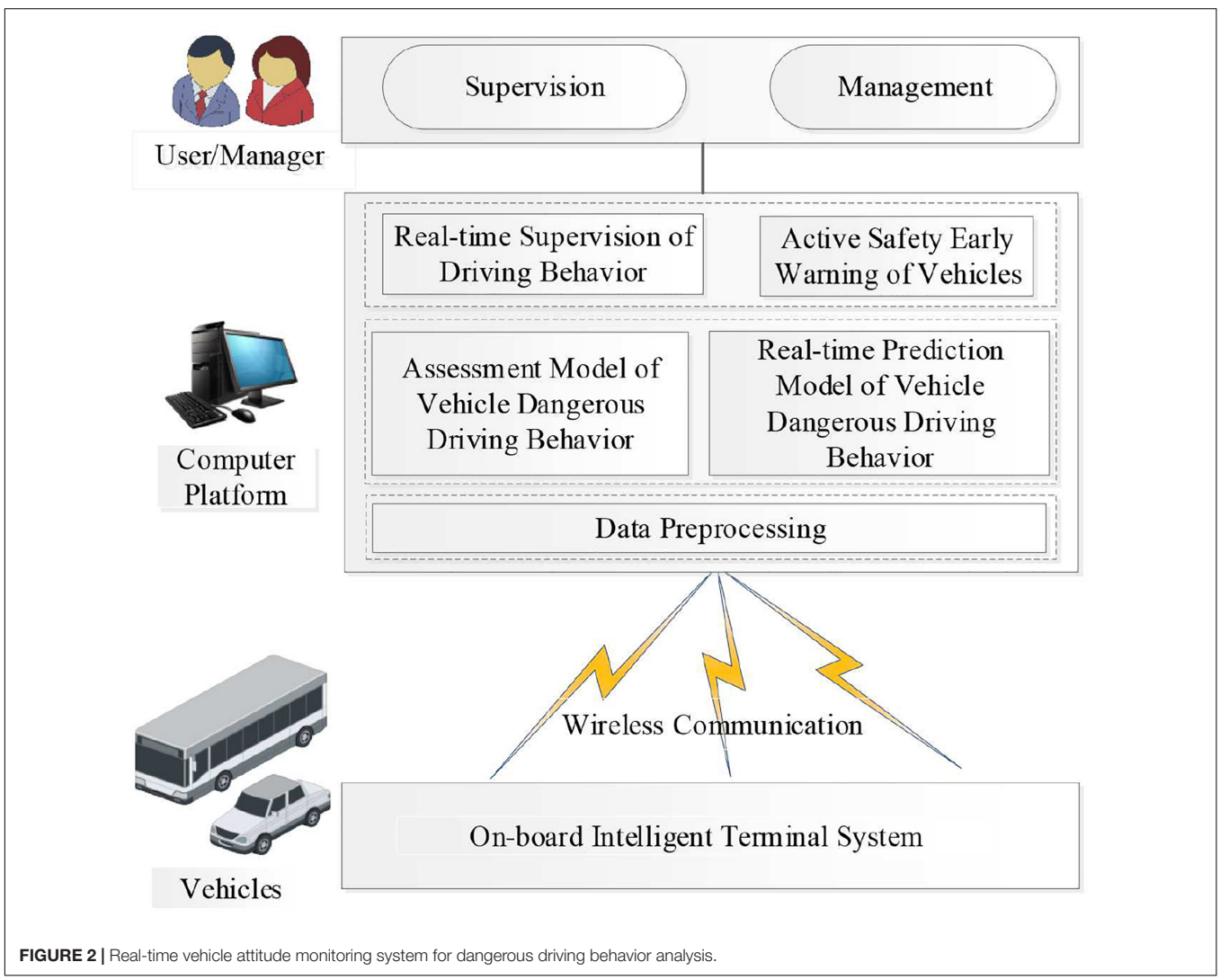


**FIGURE 2 |** Real-time vehicle attitude monitoring system for dangerous driving behavior analysis.

for users and managers through the CM discriminant criteria and the fast discriminant algorithm of vehicle driving behavior based on the CM-ENN model. The dangerous driving behavior is marked, warned, and stored. Third, the prediction model of vehicle motion attitude can be established based on the collected data so as to realize the active safety early warning of vehicle. (3) User/Manager: The main task is to evaluate the driver's performance according to the processing results of the computer platform and to effectively curb the occurrence of dangerous driving.

For the vehicle intelligent terminal, the six-axis MPU6500 (as shown in **Figure 3**) is selected as the integrated sensor of MEMS integrated with the accelerometer and gyroscope. The core processor of the main control module is STM32F207 VCT6, and the NEO-6M module is selected as the GPS module. The terminal is required to be installed at gravity center of the vehicle with three axes of the accelerometer aligned with the vehicle body. As shown in **Figure 4**, the forward direction of the vehicle corresponds to the positive direction of the $Y$-axis of the accelerometer, i.e., the longitudinal acceleration of the vehicle. The three axes angular velocity of the vehicle is measured by the gyroscope, and its direction is the rotation direction around the corresponding accelerometer axis. An on-board video driving recorder is also installed on the tested vehicle to record the whole process of video information during the testing process, which provides videos for the later data processing. The position, speed, and heading of the vehicle are acquired by output signal processing of accelerometer and coordinate transformation (Schmidt and Phillips, 2010). Generally, the motion state parameters of the carrier (such as attitude, speed, position, etc.) and the outputs of the sensor are not measured in the same coordinate system. Therefore, the coordinates need to be transformed by rotating around three coordinate axes. There are two coordinate systems shown in **Figure 4**. One is the carrier coordinate system (also known as system b, $OX_bY_bZ_b$) and the other is the navigation coordinate system (also known as system n, $OX_nY_nZ_n$). According to the rotation theorem in Euler navigation, the frame coordinates in carrier coordinate system can be transformed into the navigation frame coordinates by three consecutive rotations around different coordinate axes in a certain order. The transformation process can be expressed by:

$$\begin{bmatrix} x_n \\ y_n \\ z_n \end{bmatrix} = C_b^n \begin{bmatrix} x_b \\ y_b \\ z_b \end{bmatrix} \tag{1}$$

where the transformation matrix $C_b^n$ is defined by the following equation:

$$C_b^n = \begin{bmatrix} cos\theta cos\psi & cos\theta sin\psi & -sin\theta \\ sin\varphi sin\theta cos\psi & sin\varphi sin\theta sin\psi & sin\varphi cos\theta \\ -cos\varphi sin\psi & -cos\varphi sin\psi & \\ cos\varphi sin\theta cos\psi & cos\varphi sin\theta sin\psi & cos\varphi cos\theta \\ +sin\varphi sin\psi & -sin\varphi cos\psi & \end{bmatrix} \tag{2}$$

where yaw angle $\psi$, roll angle $\varphi$, and pitch angle $\theta$ are called Euler angles.

According to the fixed-point rotation theory of rigid body, there are three methods of solving attitude matrix including Euler

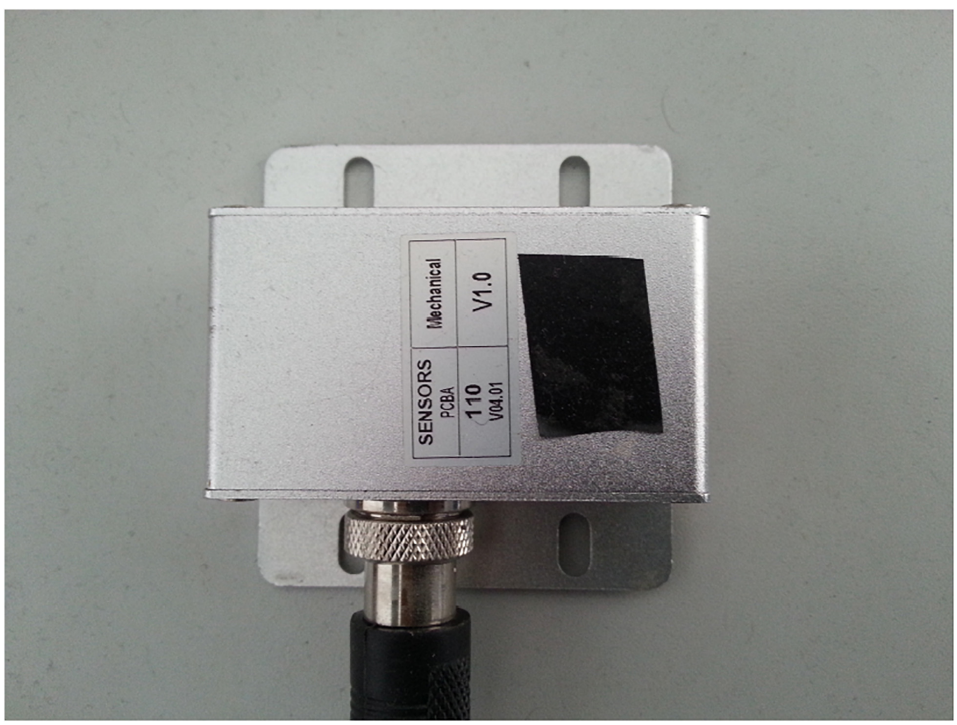


**FIGURE 3 |** Inertial measurement unit (IMU) on vehicle.

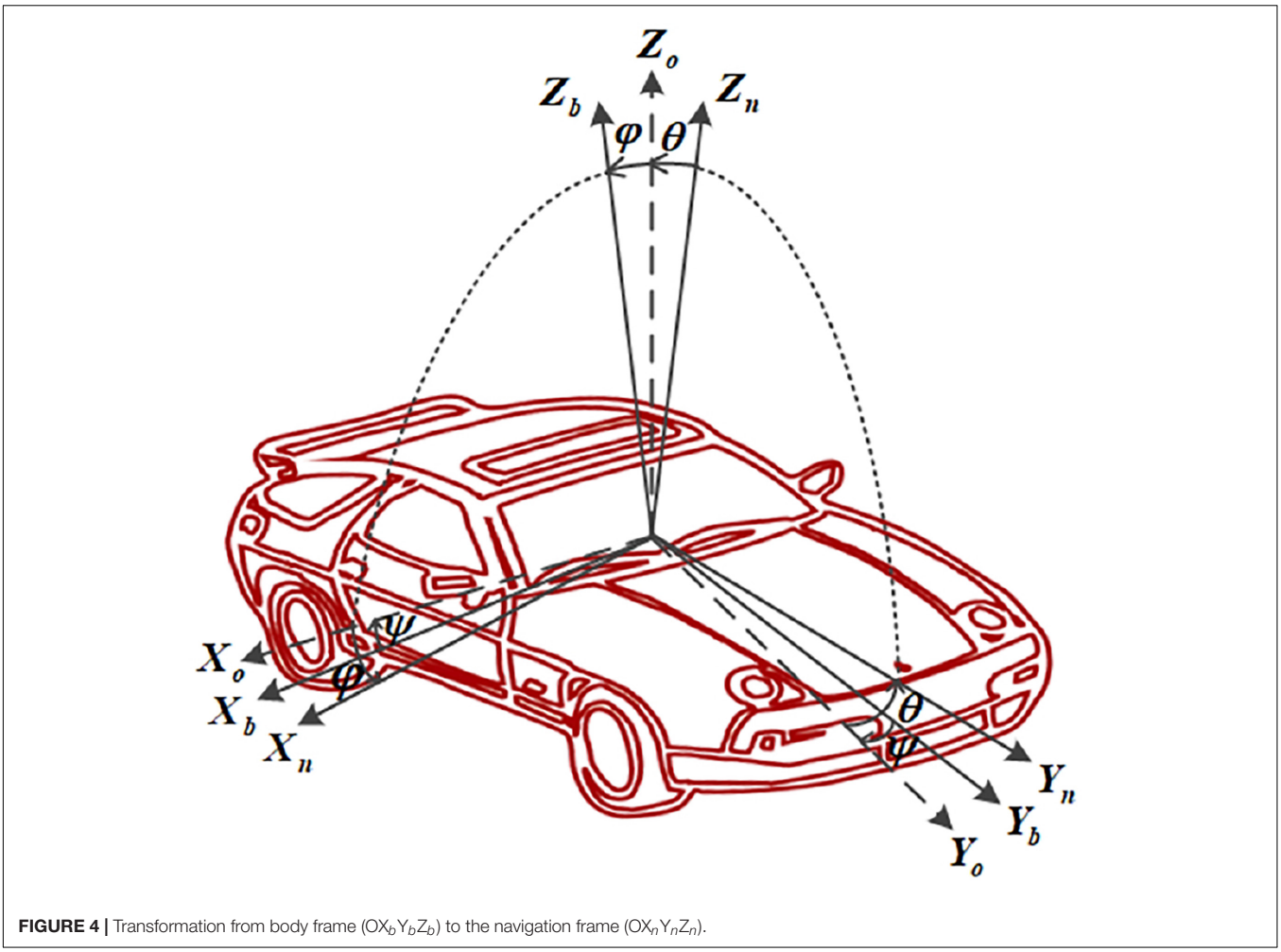


**FIGURE 4 |** Transformation from body frame ($OX_bY_bZ_b$) to the navigation frame ($OX_nY_nZ_n$).

angle method (known as three-parameter method), quaternion method (known as four-parameter method), and direction cosine method (known as nine-parameter method). Quaternion method is used in this paper to solve attitude matrix $C_b^n$ for the advantages of real-time performance and high precision. The fourth-order Runge-Kutta numerical integration method (Press et al., 2007) is applied to solve attitude parameters in quaternion and implement the transformation from system ***b*** to system ***n***.

## Cloud Model for Dangerous Driving Behavior Evaluation

In order to predict the dangerous driving behavior using the data collected from onboard sensors, it is crucial to create the evaluation criteria of the dangerous driving behaviors based on the vehicle motion states. On the one hand, the motion state of a vehicle at any time can be precisely measured quantitatively by various sensors in some metrics such as the speed, acceleration, and rotation angle; on the other hand, the dangerous driving behavior is actually a qualitative and conceptual description commonly used in traffic safety management, such as rapid acceleration, emergency braking, sharp turn, and so on. Therefore, mapping between vehicle motion state space and the dangerous driving behavior space is crucial. Based on the CM theory, this paper designs a CM for predicting dangerous driving behavior, which combines the vehicle driving states with the subjective feeling of passengers and establishes the mapping between the vehicle motion states and the dangerous driving behaviors.

**Table 1** shows the root mean square (RMS) of the total acceleration of vehicle and the corresponding subjective feeling of human body, which to some extent reveals the relationship between the vehicle motion and human feeling. This classification standard can be used as a reference for evaluating dangerous driving behaviors. However, only comfort is considered in this table. Thus, we extend it with some other driving behavior description and use cloud transformation algorithm to build the numerical characteristics of dangerous driving behaviors that are provided as the targets for the ENN in the training process.

### Cloud Model Definition and Cloud Transformation Algorithm

CM is a cognitive model of bidirectional transformation between qualitative concept and quantitative data, which was proposed by Li et al. (2009). The basic concepts of CM are defined as follows:

**TABLE 1 |** The root mean square (RMS) of total acceleration and subjective feeling of the human's body.

| The RMS of the total acceleration $a_\omega$(m/s$^2$) | Subjective feeling |
|---|---|
| 0.315 | Not uncomfortable |
| 0.315 0.63 | A little uncomfortable |
| 0.5 1.0 | Fairly uncomfortable |
| 0.8 1.6 | Uncomfortable |
| 1.25 2.5 | Very uncomfortable |
| >2.0 | Extremely uncomfortable |

*Definition 1:* Let $U$ be a quantitative domain expressed by exact numerical values, $C$ be a qualitative concept on $U$, and $C$ contains three numerical characteristics $(E_x, E_n, H_e)$. If a number $x \in U$, and $x$ is a random realization of qualitative concept $C$. The certainty of $x$ to $C$ is $\mu(x)$ ($\mu(x) \in [0,1]$), which is a random number with a stable tendency: $\mu(x) : [U \rightarrow [0,1], \forall x \in U$, then the distribution of $x$ on domain $U$ is called CM. For a CM, each $x$ is called a cloud droplet.

In Definition 1, three numerical characteristics of CM, $E_x$, $E_n$, and $H_e$, are called expectation, entropy, and hyper-entropy, respectively, which represent a concept. Expectation $E_x$ is the most representative concept or the typical sample in quantification of this concept; entropy $E_n$ is the uncertainty measure of concept, which is determined by the randomness and fuzziness of the concept; hyper-entropy $H_e$ is the uncertainty measure of entropy, which is determined by the randomness and fuzziness of the entropy. The number $x$ depicts the randomness of quantitative values representing concepts, while $\mu(x)$ is the uncertainty of the number $x$ belonging to a concept $C$.

The distribution differs for different CMs. Among them, the normal CM is the most important and of universal applications (Li et al., 2012). By forward cloud transformation (FCT) and backward cloud transformation (BCT), the CM realizes the mapping between qualitative concepts and their quantitative representations. The two algorithms of cloud transformation are displayed in Algorithms 1 and 2.

**Algorithm 1:** Forward Cloud Transformation (FCT)
**Input:** $Ex$, $En$, $He$, $n$
**Output:** $n$ cloud droplets $(x_i, \mu_i)$, $\quad i = 1, 2, ..., n$
Step 1: Generate a normal random number $En_i^{'} = NORM(En, He^2)$ with $En$ as expected and $He^2$ as variance
Step 2: Generate a normal random number $x_i = NORM(Ex, En_i^{'2})$ with $Ex$ as expected and $En_i^{'2}$ as variance
Step 3: Calculate $\mu_i = exp\left\{-\frac{(x_i - Ex)^2}{2(En_i^{'})^2}\right\}$
Step 4: Calculate a cloud drop $(x_i, \mu_i)$
Step 5: Repeat steps 1–4 for $n$ times to generate the required $n$ cloud droplets drop$(x_i, \mu_i)$;

## Index Based on Passenger's Feeling

Based on lots of previous works and literatures on human body vibration, the International Standard Organization (ISO) has formulated ISO 2631 guidelines for the evaluation of human body's response to whole body vibration. In ISO 2631-1:1997/AMD 1:2010 (2010) titled with "Evaluation of human exposure to whole-body vibration," the exposure limit of human body is quantified in the main frequency range from 1 to 80 Hz during the transmission from solid surface to human body, and the human comfort feeling under different acceleration RMS is also demonstrated, as shown in **Table 1**. Generally in measurement of vehicle vibrations, the three-axis acceleration of IMU is used. Experiments show that the three-axle acceleration can effectively evaluate severities of vehicle vibration. The total acceleration is calculated by combining three-axis accelerations and used as the criteria for vibration evaluation, as described in the following:

**Algorithm 2:** Backward Cloud Transformation (BCT)
**Input:** $n$ cloud droplets $x_i (i = 1, 2, ..., n)$
**Output:** Expectation $\hat{Ex}$, Entropy $\hat{En}$ and Super Entropy $\hat{He}$
Step 1: $\hat{Ex} = \bar{X} = \frac{1}{n}\sum_{i=1}^{n} x_i$
Step 2: Random sampling grouping
**for** $i \leftarrow 1$ **to** $m$ **do**
  **for** $j \leftarrow 1$ **to** $r$ **do**
    Random sampling of n cloud droplet samples;
  **end**
  $X_i = \{X_{i1}, X_{i2}, ..., X_{ir}\}, \bar{X}_i = \frac{1}{r}\sum_{j=1}^{r} x_{ij}$;
**end**
$Y^2 = \{Y_1^2, Y_2^2, ..., Y_m^2\}$
$\hat{En}^2 = \frac{1}{2}\sqrt{4(EY^2)^2 - 2DY^2}$
Step 3: $\hat{He}^2 = EY^2 - \hat{En}^2$

(1) For the vibration signal (three-axis acceleration), discrete Fourier transform (DFT) is applied to transforms it into the frequency domain using the following formula:

$$X(f) = \sum_{n=0}^{N-1} x(n) e^{-j\frac{2\pi}{N}t} \tag{3}$$

where X(n) is a finite vibration signal with the length number $N$ in the time domain that is the three-axis acceleration, and $X(f)$ is the vibration signal in the frequency domain.

(2) Calculation of the RMS of one-third octave as well as the weight acceleration at the center of one-third octave. Formula of computing RMS of one-third octave is defined as:

$$a_i = \sqrt{\frac{1}{f_{iu} - f_{il}} \int_{f_{il}}^{f_{iu}} X^2(f) df} \qquad i = 1, 2, 3...20 \tag{4}$$

where $a_i$ is RMS f one-third octave whose unit is $m/s^2$, $f_{iu}$ is an upper cut-off frequency in the $i^{th}$ frequency band, $f_{il}$ is a lower cut-off frequency on the $i^{th}$ frequency band, and $X(f)$ is the acceleration signal in frequency domain.

Human body reacts differently to different frequency vibration in different directions, therefore, weighting factors are given in each frequency center to model the acceleration matching the real feeling of human body. ISO 2631-1:1997/AMD 1:2010 (2010)

gives a frequency-weight table that indicate the center frequencies of one-third octave and the corresponding weighted factors for each axis. Thus, the weighed acceleration of each axis is simply calculated by looking up this table, as formulated by

$$a_{wj} = \sqrt{\sum_{i=1}^{20}(k_{ij}a_i)^2} \qquad i = 1, 2, 3...20 \qquad j = x, y, z \qquad (5)$$

where $a_{wj}$ is the weighed acceleration of each axis whose unit is $m/s^2$, and $k_{ij}$ is a weighted coefficient in the $i^{th}$ one-third octave band for j axis.

According to the random input running test method of automobiles provided by the National Standards of China (National Technical Committee of Auto Standardization, 2004), acceleration of *X*-axis and *Y*-axis are weighted with 1.4, and *Z*-axis weighted with 1.0, and the total acceleration is calculated by

$$a_w = \sqrt{(1.4a_{wx})^2 + (1.4a_{wy})^2 + a_{wz}{}^2} \qquad (6)$$

where $a_w$ is the RMS of total acceleration, and $a_{wx}$, $a_{wy}$, $a_{wz}$ is the RMS of each axis computed by equation (5).

(3) The subjective feelings of comfort by human body are classified into six degrees, and the relationship between comfort and RMS of total acceleration $a_w$ is shown in **Table 1**. Lots of research have proved that some dangerous driving behaviors such as sudden braking or sudden turning could also bring up uncomfortable feelings, which are classified into the category of "Very Uncomfortable" or "Extremely Uncomfortable."

## Comprehensive Cloud Model for Dangerous Driving Behavior Evaluation

Three measures including longitudinal acceleration $a_y$, lateral acceleration $a_x$, and total acceleration $a_w$ of the vehicle are considered in evaluation of driving behaviors where $a_y$ reflects the intensity of vehicle acceleration or deceleration, $a_x$ indicates the intensity of the left turn or right turn of the vehicle, and the ISO recommend $a_w$ as measure of passenger's feeling of comfort in the riding process. In this paper, for simplicity we mainly adopt $a_y$ which represents for the intensity of vehicle motion to corporate with $a_w$ when evaluating the comprehensive state.

Based on CM theory and the input acceleration $a_y$ and $a_w$, this paper applied BCT to compute the numerical characteristics of the CMs for evaluating the intensity of vehicle motion and passenger's feeling of comfort, as shown in **Tables 2A,B**. Then the FCT is applied to generate the corresponding one-dimensional CM maps, as illustrated in **Figures 5A,B**, respectively. There are five different color CMs in **Figure 5** representing five degrees of intensity of vehicle motion, and three CMs in **Figure 5B** representing three degrees of comfort. The distributions of these one-dimensional CMs indicate the longitudinal acceleration $a_y$ and the total acceleration $a_w$ are very discriminative for vehicle motion states under different operating modes of drivers. In addition, there are overlapping part being observed between different droplet groups, which confirmed the CMs can also describe the uncertain part under certain states.

According to concept division theory in CM, the dangerous driving behavior description is generated based on the input acceleration $a_y$ and $a_w$. These accelerations all consist of 3 states, and both comfort and intensity include 3 states. As a subset of all possible combinations, the driving behavior, therefore, is composed of 5 states and described by the comprehensive CM, as shown in **Table 3**. The main advantage of this definition is that it avoids direct judgment on the driving behavior based

**TABLE 2 |** Numerical characteristics of cloud models (CMs).

| (A) CM of intensity | | | | |
|---|---|---|---|---|
| | Numerical characteristics | | | Description |
| | $E_{\chi 1}$ | $E_{\eta 1}$ | $He_1$ | Intensity |
| Speed up | 0.6281 | 0.5076 | 0.1263 | Relatively large (black) |
| | 1.2202 | 0.8511 | 0.1637 | Large (blue) |
| Slow down | −0.61 | 0.7379 | 0.2832 | Relatively large(green) |
| | −1.635 | 1.2357 | 0.274 | Large(yellow) |
| | −3.0326 | 1.4398 | 0.3168 | Very large(red) |

| (B) CM of comfort | | | |
|---|---|---|---|
| Numerical characteristics | | | Description |
| $E_{\chi 2}$ | $E_{\eta 2}$ | $He_2$ | Comfort |
| 1.0682 | 0.5128 | 0.1472 | A little uncomfortable (red) |
| 1.8681 | 0.8931 | 0.2762 | Not comfortable (green) |
| 3.1463 | 1.5283 | 1.3423 | Very uncomfortable (blue) |

***(A)*** *In the column of "Intensity," the color in the parentheses is correspond to the color of cloud in* ***Figure 5A****.* ***(B)*** *In the column of "comfort," the color in the parentheses is correspond to the color of cloud in* ***Figure 5B****.*

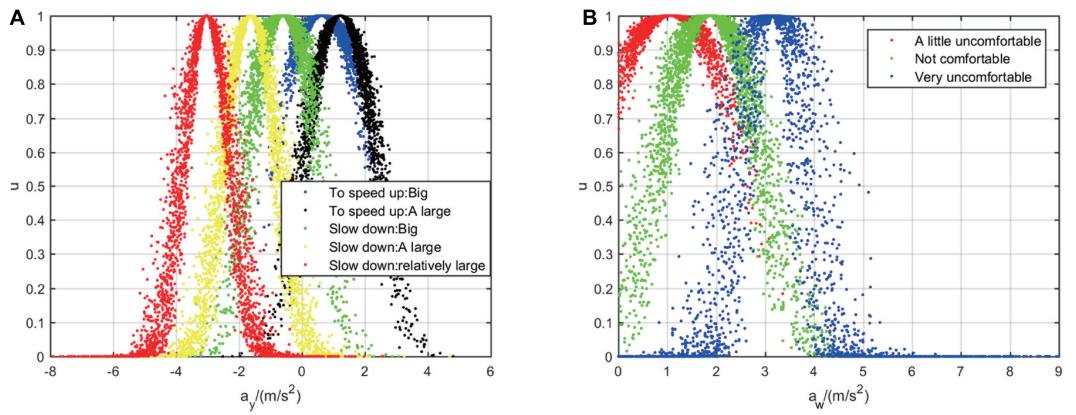


**FIGURE 5 |** Acceleration of 1D cloud model: **(A)** Comparison of 1D cloud models with longitudinal acceleration; **(B)** comparison of 1D cloud models with total acceleration.

**TABLE 3 |** Description of dangerous driving behavior with comprehensive cloud model.

| | The input variable | | The output variable | | |
|---|---|---|---|---|---|
| | $\alpha_y$ | $\alpha_w$ | **Intensity** | **Comfort** | **Driving behavior** |
| Speed up | Big<br>large | Big<br>large | Relatively large<br>Large | A little uncomfortable<br>Not comfortable | Slow speeding<br>Urgent to accelerate |
| Slow down | Big<br>Relatively large<br>Large | Big<br>Relatively large<br>Large | Relatively large<br>Large<br>Very large | A little uncomfortable<br>Not comfortable<br>Very uncomfortable | Slow speed reduction<br>General slowdown<br>Sharp slowdown |

on the motion parameters retrieved by the motion sensor. The driving behaviors are essentially vague concepts and it is hard to determine the exact border of two behaviors. Incorporating human subjective feeling as well as building mapping from quantitative data space to concept space with CM make the judgment more flexible and as natural as what human does in real world. For example, if $a_y$ is a positive value, which means the vehicle is speeding up. If the intensity is "relatively large" and the subjective feeling is "a little uncomfortable," which means the action of speeding is not that bothering so the driving behavior is defined as "slow speeding."

For further description on different vehicle motion states, 1D CM can be extended to 2D by cloud transformation and concept escalation (Meng et al., 2010). Six numerical characteristics *(Exi,Eni,Hei,Ex2,Eri2,He2)* are used in this paper, where the expectation $Ex_1$ and $Ex_2$ are the best representation of the 2D concepts of vehicle status including vehicle motion intensity and comfort. The entropy $En_1$ and $En_2$ are the fuzzy measurements of vehicle status, which describes the coverage over 2D values. The hyper-entropy $He_1$ and $He_2$ depict the dispersion of cloud droplets, which are implicitly represented by the thickness of the 1D projection of the 2D CM. Taking vehicle accelerating as an example, the 2D CMs for two acceleration status, slow acceleration and rapid acceleration, are shown in **Figures 6A,B**.

As shown in **Figures 5**, **6**, difference vehicle states have difference numerical characteristics of the corresponding CM. In order to make an intuitive comparison, by applying cloud computing the numerical characteristics of comprehensive CM are calculated based on the six numerical characteristics of 2D CM, as formulated by

$$Ex = Ex_1 + Ex_2 \tag{7}$$

$$En = \sqrt{{En_1}^2 + {En_2}^2} \tag{8}$$

$$He = \sqrt{{He_1}^2 + {He_2}^2} \tag{9}$$

In equation (7), Ex is comprehensive expectation, En is comprehensive entropy, and He is comprehensive hyper-entropy. The three numerical characteristics are the comprehensively representation of the qualitative concepts of different driving behaviors, as shown in **Table 4**.

## CM-ENN, Prediction Method of Dangerous Driving Behavior

After quantifying the qualitative conceptual of dangerous driving behavior through evaluation of vehicle driving state and passengers' subjective feelings by CM, a real-time identification model for dangerous driving behavior is designed, which is referred to as CM-ENN. The input of CM-ENN is the driving state data described before, usually in a sequence, and the target output is the predicted dangerous driving behavior. Inside the structure, ENN takes the charge of driving state prediction and CM takes the charge of determining which dangerous driving behavior it is. Considering the low-cost on-board platform with

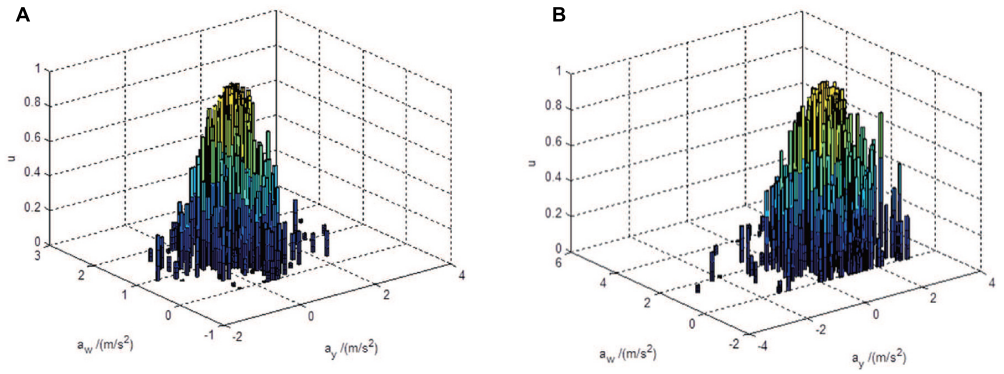


**FIGURE 6 |** 2D cloud model with different acceleration states: **(A)** Slow speeding; **(B)** urgent to acceleration.

limited computing ability, for online training or prediction, the simple-structured ENN is an appropriate choice in this scenario.

## The Structure and Algorithm Design of ENN

ENN was first proposed by Jeffrey L. Elman in 1990. Unlike static feedforward networks such as BP network and RBF network, Elman network is a dynamic local regression neural network. Different from classical BP network, this network has another feedback loop from the output of hidden layer to the input of this layer, which constitutes the "context layer" that retains information between observations. This type of network consists of an input layer, a hidden layer, an output layer, and a context layer. Typical structure of ENN is depicted in **Figure 7**. The input layer and output layer play the roles of signal transmission and linear weighting, respectively. The hidden layer is to take the previous output as its new input as well as the input of context layer. Thus, the context layer can be seen as a group of time-delay operators that enable the network with the capability of memorizing historical states. The transfer function of hidden layer can be linear or non-linear.

ENN's non-linear space state can be expressed as follows:

$$x(k) = f[w_k^1 x_c(k) + w_k^2 \mu(k-1)] \tag{10}$$

$$x_c(k) = x(k-1) \tag{11}$$

$$y(k) = g[w_k^3 x(k)] \tag{12}$$

where $\mu(k-1)$ is the external input, $x(k)$ is the output of hidden layer, and $y(k)$ is the output of the network. $w_k^1$, $w_k^2$ and $w_k^3$ are the matrixes, which represent connection weights from the context layer to the hidden layer, the input layer to the hidden layer, and the hidden layer to the output layer, respectively. $f$ and $g$ are transfer functions of the hidden layer and the output layer.

In this paper, the Levenberg-Marquardt backpropagation learning algorithm is used in the training of ENN to adjust weights of each layer, and minimize the mean square error (MSE) between the network output and desired output, the energy function is expressed as

$$E = \sum_{k=1}^{n} [y(k) - d(k)]^2 \tag{13}$$

where $d(k)$ is the desired output.

Assuming that the vehicle accelerations at the first $n$ time points are taken to predict the acceleration at the next time point, the mapping function can be expressed as follows:

$$x_n = f(x_1, x_2, \cdots x_{n-1}) \tag{14}$$

First, we construct the sample set. For the given vehicle acceleration data, the rule of cycle prediction is adopted to build the sample set, that is, taking the prediction of the previous step as the input of the next step, cycle down in turn. The driving behavior prediction therefore can be implemented by considering the historical and current data collected in vehicle motions instead of the specific information on driver's driving style, road conditions, and so on. Second, the input data of neural network are normalized to [–1,1] using equation (15) and the network output is denormalized by equation (16).

$$\hat{L} = \frac{2L - L_{max} - L_{min}}{L_{max} - L_{min}} \tag{15}$$

$$L = \frac{1}{2}\left[(L_{max} - L_{min})\hat{L} + L_{max} + L_{min}\right] \tag{16}$$

here $\mathbf{L}_{min}$ and $\boldsymbol{L}_{max}$ are the minimum and maximum of the data in the sample set. The input layer of ENN consists of 20 neurons, the output layer includes 1 neuron, and the neuron number in the hidden layer is set to 13. The flow chart of the CM-ENN learning algorithm is illustrated in **Figure 8**.

**TABLE 4 |** Numerical characteristics of comprehensive cloud model integrating the qualitative concepts.

| Driving behavior | Ex | En | He |
|---|---|---|---|
| Slow speeding | 1.6963 | 0.7215 | 0.1940 |
| Urgent to accelerate | 2.5372 | 0.9294 | 0.6600 |
| Slow speed reduction | 0.4582 | 0.8986 | 0.3192 |
| General slowdown | 0.2331 | 1.5247 | 0.3891 |
| Sharp slowdown | 0.1137 | 2.0997 | 1.3792 |

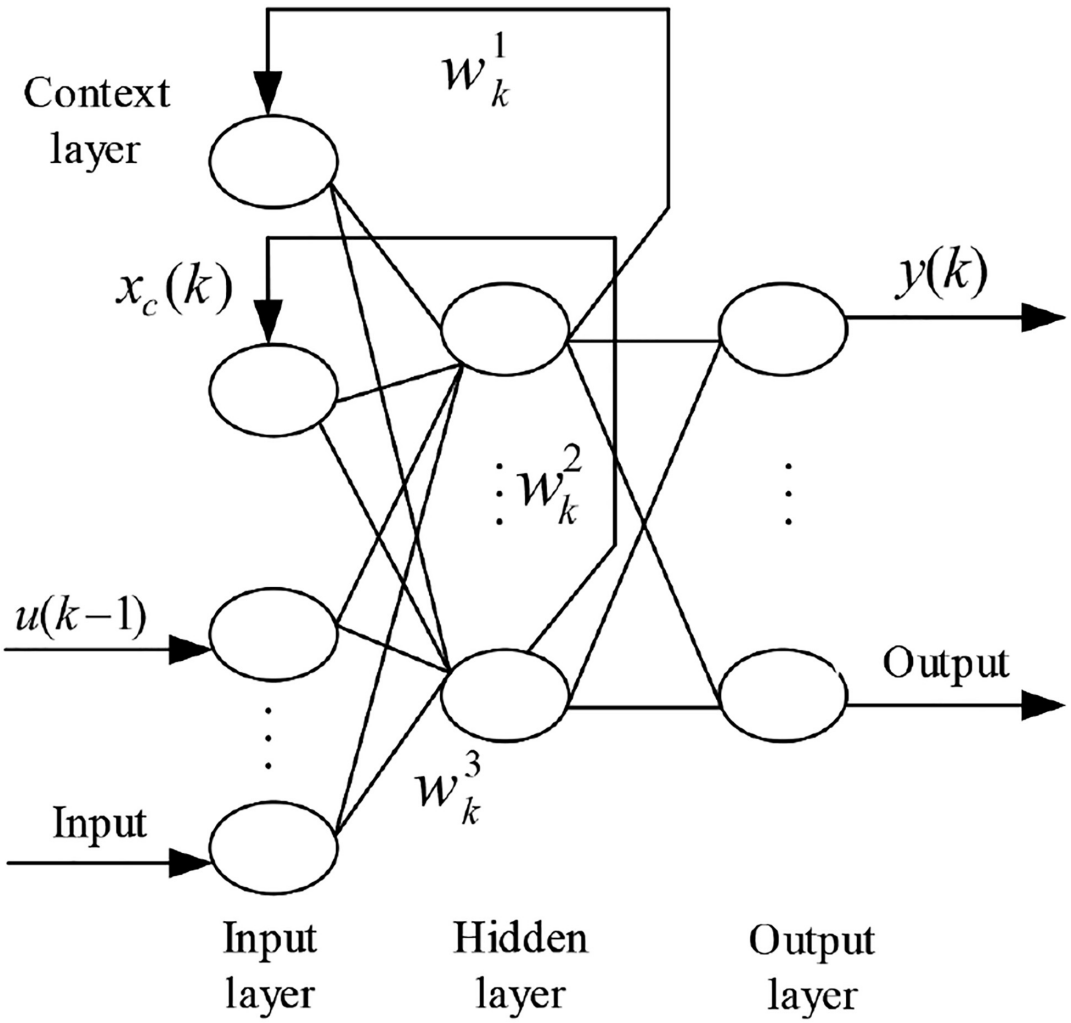


**FIGURE 7 |** The structure of Elman neural network (ENN).

### State Identification of Unlabeled Cloud Model

Whatever vehicle motion intensity feature or passenger feeling feature are used, they have been summarized into a CM described by a 3-element vector. And any data sequence can be applied to inverse CM generator to get the same length feature vector represented for an unlabeled CM. The identification of unlabeled CM can be seen as a similarity measurement problem of the CM. In this paper, we adopt the measurement called maximum boundary-based cloud model (MCM) (Yang et al., 2018), which generally is an overlapping area calculation method between two CMs based on integral. There are several types of CM similarity measurement, including integral-based and vector-based methods (cosine similarity). The main advantage of integral-based methods is that it can describe different roles of three individual feature values, instead of treating them the same in vector-based methods. Moreover, in MCM, the integral calculation, which is originally much more expensive than that of cosine-based methods, is transformed into standard normal distribution integral calculation, which can be pre-calculated. The simplification of computation is quite important for the real-time monitoring purpose. With MCM, unlabeled CM therefore can be compared to each type of baseline CM representing different states, as shown in **Tables 2**, **4**, and the best-matched label is selected for it.

## EXPERIMENTAL RESULTS AND ANALYSIS

### Data Acquisition

In order to evaluate the performance of the proposed method, we used the on-board system described in previous section to collect the experimental data. The data acquisition area is located in the road network of Shenzhen Software Park Phase II on the north side of Nanshan Science Park, Shenzhen City, Guangdong Province, China (as shown in **Figure 9**). The data collection plan is carefully designed to ensure the randomness,

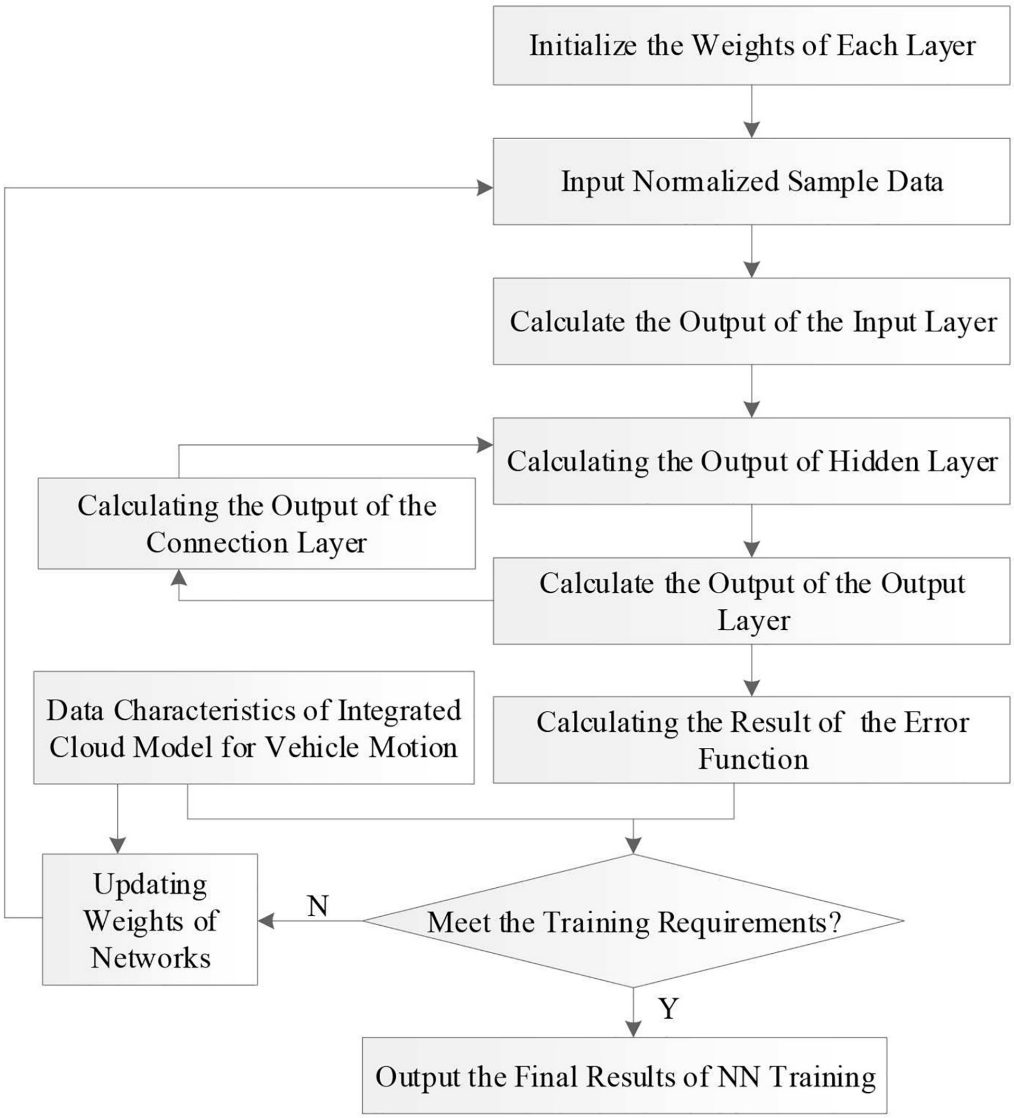


**FIGURE 8 |** Flow chart of the cloud model and Elman neural network (CM-ENN) learning algorithm.

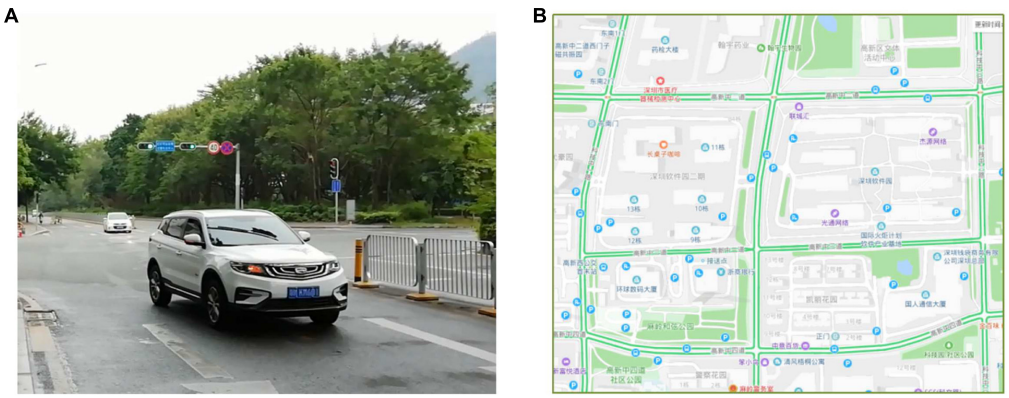


**FIGURE 9 |** Testing data acquisition: **(A)** The vehicle for collecting testing data; **(B)** urban roads for collecting testing data.

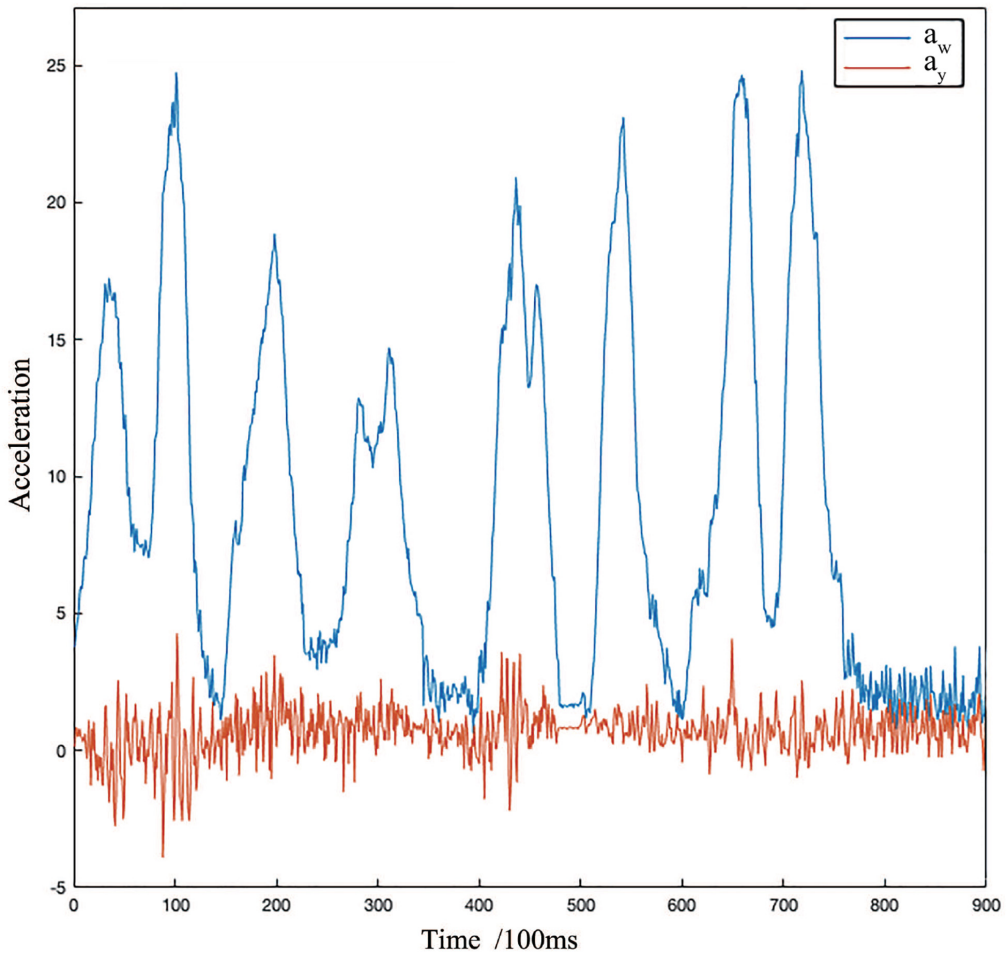


**FIGURE 10 |** The response curve of RMS of total acceleration $a_w$ and longitudinal acceleration $a_y$.

**TABLE 5 |** Comparison of results by Elman neural network and multi-layer neural network.

| Model | Network structure | Learning algorithm | Number of training | Precision(%) |
|---|---|---|---|---|
| CM-ENN | 20, 13, 1 | Levenberg-Marquardt backpropagation | 500 | 0.01 |
| Artificial Neural Network (ANN) | 20, 13, 1 | Levenberg-Marquardt backpropagation | 210 | 0.01 |

autonomy, contingency, and suddenness of driving behavior. Besides, road safety is another concern in real-world data acquisition. In the data acquisition process, the ways of data recording include vehicle terminal recording, video recording, and manual observation recording. To ensure the objectivity and identicalness of manual observation, we invited three passengers to rate all driving behavior indicators, respectively. The true label is then determined by a simple on-site voting. The onboard IMU MPU6500 is utilized to collect velocity data and the frequency is 10 Hz. In this paper, 900 randomly selected historical data are taken as sample data. Using the coordinate transformation and evaluation method provided before, the change curves of total acceleration and longitudinal acceleration are obtained during the moving of the vehicle, as shown in **Figure 10**.

## Model Training and Experiments

Data sequences are treated as rolling inputs to train the models. In this experiment, one sample is defined as a 21-length sequence which is roughly 2 s in 10 Hz setting and the output is last value of this subsequence, which means the models are required to predict the value at next moment according to the previous 20-length sequence. Thus, a 900-length sequence can be separated into 880 samples. And in this experiment, 510 of them are used to train and the rest of them are used for validation.

To make a comparison, an ANN or called multi-layer neural network is designed which uses the same sample set, similar network architecture, learning algorithm, and target accuracy. The details of these two models are described in **Table 5**. The network structure is denoted by three numbers indicating the neuron number in input layer, hidden layer, and output layer.

In order to compare and evaluate the prediction performance of different prediction methods, we adopt three measures including mean absolute error (MAE), mean square error (MSE), and root mean squared error (RMSE), which are defined as following equations:

$$MAE = \frac{1}{n}\sum_{i=1}^{n}(|A_t - F_t|) \tag{17}$$

$$MSE = \frac{1}{n}\sum_{t=1}^{n}(A_t - F_t)^2 \tag{18}$$

$$RMSE = \sqrt{\frac{1}{n}\sum_{t=1}^{n}(A_t - F_t)^2} \tag{19}$$

where $A_t$ is the predicted value and $F_t$ is the true value.

**Figure 11** shows the predicted $a_w$ values in a certain period of time by ENN and ANN. **Table 6** shows the errors of training and testing by ENN and ANN. As shown in **Figure 11**, though the two models are capable to catch the time-series structure of input sequence, the ENN has lower validation error with all measures according to **Table 6**, which indicates that ENN performs better than ANN in this scenario and has better ability of generalization.

After training, dangerous driving behavior can be predicted and judged by combining the prediction model and CM. The 880 samples obtained previously all have their ground truth label in comfort and intensity, which is described in **Tables 2**, **4**. Leveraging the backward Algorithm 2, the predicted sequence of representation of comfort and intensity can be compacted into CMs and by using MCM, the cloud similarity measurement, these predicted CMs can be labeled and compared to their ground truth. The accuracy results are demonstrated in **Table 7**. Here, two types of predictions are made. One is using the models to predict next 1 s sequence, which has 10 values at the setting of 10 Hz, and another is 2 s, which has 20 values in total. The prediction accuracy of comfort, intensity, and comprehensive dangerous driving behavior are presented in the table. The results indicate that, as discussed before, though CM-ANN seems not bad when handling the comfort data, CM-ENN can much better catch the sequence structure. The errors accumulated by models will greatly affect the prediction accuracy of dangerous

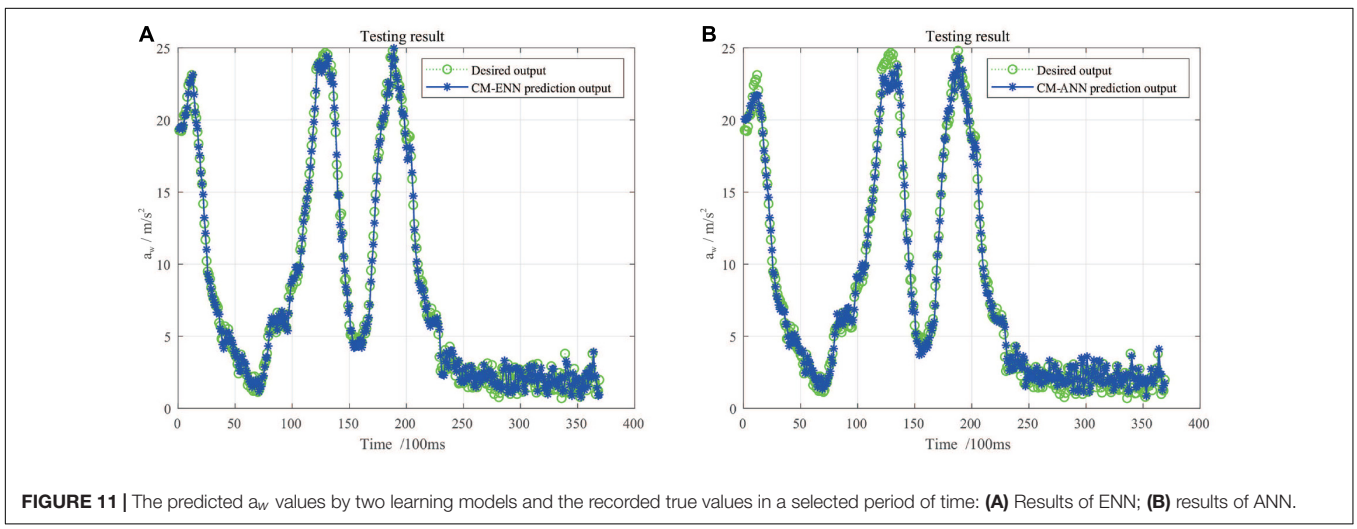


**FIGURE 11 |** The predicted $a_w$ values by two learning models and the recorded true values in a selected period of time: **(A)** Results of ENN; **(B)** results of ANN.

**TABLE 6 |** The errors of training and testing.

| | | Comfort | | | Intensity | | | Driving behavior | | |
|---|---|---|---|---|---|---|---|---|---|---|
| | | **MAE** | **MSE** | **RMSE** | **MAE** | **MSE** | **RMSE** | **MAE** | **MSE** | **RMSE** |
| CM-ENN | Train | 0.4184 | 0.0984 | 0.3137 | 0.5300 | 0.1673 | 0.4090 | 0.4653 | 0.1239 | 0.3520 |
| CM-ANN | | 0.3718 | 0.0790 | 0.2811 | 0.5910 | 0.2209 | 0.4700 | 0.4074 | 0.1050 | 0.3240 |
| CM-ENN | Validation | 0.5692 | 0.1661 | 0.4076 | 0.5576 | 0.1789 | 0.4230 | 0.6526 | 0.2297 | 0.4793 |
| CM-ANN | | 0.6072 | 0.1894 | 0.4352 | 0.5908 | 0.2014 | 0.4488 | 0.7705 | 0.3072 | 0.5543 |

**TABLE 7 |** The accuracy of dangerous driving behavior prediction by Elman neural network (CM-ENN) and CM-ANN.

| | Comfort | | Intensity | | Driving behavior | |
|---|---|---|---|---|---|---|
| **Prediction Length(Second)** | **1 s** | **2 s** | **1 s** | **2 s** | **1 s** | **2 s** |
| CM-ENN | 0.8921 | 0.8746 | 0.9219 | 0.8873 | 0.8909 | 0.7979 |
| CM-ANN | 0.8370 | 0.7375 | 0.9357 | 0.8815 | 0.7910 | 0.7596 |

driving behavior, and CM-ENN has a more robust decay of accuracy as the length of predicted time increases. Besides, the prediction of dangerous driving behavior is not so accurate as that of comfort and intensity, probably because the comfort label is determined manually in our experiment, which may lead to incorrect correspondences with the true dangerous driving behavior pattern. Therefore, more accurate and interpretive comfort measures should be considered in future work.

## CONCLUSION

Based on the analysis of existing research on dangerous driving behavior prediction, this paper puts forward a new CM-ENN model for predicting dangerous driving behavior by combining vehicle sensor data with passenger's subjective feelings. The CM theory is introduced to implement transformation from quantitative space to qualitative space. Referring to the relevant standards, a comprehensive evaluation CM of dangerous driving behavior is constructed, which combines vehicle sensor data with passenger's subjective feelings. To evaluate the performance of the proposed algorithm, the discriminant accuracy of this method and ANN are compared based on the same real world dataset and error control conditions. Experimental results verified the better prediction accuracy of the proposed CM-ENN model. This research provides a practical solution for safe driving in the development of automotive active safety management products. In addition, the driving behavior itself is also affected by many factors such as road, environment, weather, and so on. Many of these factors also have great uncertainty. In this paper, these factors are not considered enough and need to be studied in future work.

## DATA AVAILABILITY STATEMENT

The datasets presented in this article are not readily available because the raw data supporting the research of this article will be made available to any qualified researcher by the authors. Requests to access the datasets should be directed to HX.

## AUTHOR CONTRIBUTIONS

HX conceived the research project. HX, GL, YS, and JZ proposed the algorithm and performed discussion. JZ and YS developed the program and conducted the experiments and performed the English corrections. HX and GL wrote the manuscript. All authors reviewed and approved the submitted manuscript.

## FUNDING

This article was partially supported by the Key-Area R&D Program of Guangdong Province (No. 2020B090925002), the National Natural Science Foundation of China (Nos. U1813209 and U1913211), and Shenzhen Fundamental Research Project (No. JCYJ20180305163701198).

## REFERENCES

Abou-Zeid, M., Kaysi, I., and Al-Naghi, H. (2011). "Measuring aggressive driving behavior using a driving simulator: an exploratory study," in *Proceedings of the 3rd International Conference on Road Safety and SimulationAt*, Indianapolis, IN, 1–19.

Accident Prevention Division of Traffic Police Corps of Shanghai Public Security Bureau (2016). Brief introduction of road traffic accidents in shanghai in 2015. *Traffic Transp.* 2, 78–80, (in Chinese).

American Automobile Association (2009). *Aggressive Driving: Research Update. Technical Report*. Washington, DC: American Automobile Association Foundation for Traffic Safety.

Bagdadi, O. (2013). Assessing safety critical braking events in naturalistic driving studies. *Transp. Res. Pt. F Traffic Psychol. Behav.* 16, 117–126. doi: 10.1016/j.trf.2012.08.006

Carboni, E. M., and Bogorny, V. (2015). Inferring drivers behavior through trajectory analysis. *Adv. Intell. Sys. Comput.* 322, 837–848. doi: 10.1007/978-3-319-11313-573

Chen, C., Zhao, X., Zhang, Y., Rong, J., and Liu, X. (2019). A graphical modeling method for individual driving behavior and its application in driving safety analysis using gps data. *Transp. Res. Pt. F Traffic Psychol. Behav.* 63, 118–134. doi: 10.1016/j.trf.2019.03.017

Chen, S., Fang, C., and Tien, C. (2013). Driving behaviour modelling system based on graph construction. *Transp. Res. Pt. C Emerg. Technol.* 26, 314–330. doi: 10.1016/j.trc.2012.10.004

Chen, S., Fang, C., Tien, C., and Wu, B. (2014). Dangerous driving event prediction on roadways. *Stud. Syst. Sci.* 2, 14–26.

Constantinescu, Z., Marinoiu, C., and Vladoiu, M. (2010). Driving style analysis using data mining techniques. *Int. J. Comput. Commun. Control* 5, 654–663.

DaeHan, A., Park, H., Shin, K., and Park, T. (2019). Accurate driver detection exploiting invariant characteristics of smartphone sensors. *Sensors* 19:2643. doi: 10.3390/s19112643

Day, M. R., Thompson, A. R., Poulter, D. R., Stride, C. B., and Rowe, R. (2018). Why do drivers become safer over the first three months of driving? A longitudinal qualitative study. *Accid. Anal. Prev.* 117, 225–231. doi: 10.1016/j.aap.2018.04.007

Dronseyko, V., Pakhomova, A., Shalagina, E., and Pletnev, M. (2018). Driving danger coefficient as a method of evaluating the driver's behavior in road traffic. *Transp. Res. Proc.* 36, 129–134. doi: 10.1016/j.trpro.2018.12.054

Dula, C. S., Geller, E. S., and Chumney, F. L. (2011). A social-cognitive model of driver aggression: taking situations and individual differences into account. *Curr. Psychol.* 30, 324–334. doi: 10.1007/s12144-011-9120-3

Eboli, L., Guido, G., Mazzulla, G., Pungillo, G., and Pungillo, R. (2017). Investigating car users' driving behaviour through speed analysis. *PROMET Traf. Transp.* 29, 193–202. doi: 10.7307/ptt.v29i2.2117

Fountas, G., Pantangi, S. S., Hulme, K. F., and Anastasopoulos, P. C. (2019). The effects of driver fatigue, gender, and distracted driving on perceived and observed aggressive driving behavior: a correlated grouped random parameters bivariate probit approach. *Anal. Methods Accid. Res.* 22:100091. doi: 10.1016/j.amar.2019.100091

Han, I., and Yang, K. (2009). Characteristic analysis for cognition of dangerous driving using automobile black boxes. *Int. J. Automot. Technol.* 10, 597–605. doi: 10.1007/s12239-009-0070-9

Harre, N., and Sibley, C. G. (2007). Explicit and implicit self-enhancement biases in drivers and their relationship to driving violations and crash-risk optimism. *Accid. Anal. Prev.* 39, 1155–1161. doi: 10.1016/j.aap.2007.03.001

Hong, J., Margines, B., and Dey, A. K. (2014). "A smartphone-based sensing platform to model aggressive driving behaviors," in *Proceedings of the 32nd Annual ACM Conference on Human Factors in Computing Systems*, (New York, NY: ACM), 4047–4056. doi: 10.1145/2556288.2557321

Horswill, M. S., and McKenna, F. P. (1999). The effect of perceived control on risk taking. *J. Appl. Soc. Psychol.* 29, 377–391. doi: 10.1111/j.1559-1816.1999.tb01392.x

Huang, Y. (2011). "Real time dangerous driving status detection," in *Proceedings of the 4th International Congress on Image and Signal Processing*, Shanghai, 414–418. doi: 10.1109/CISP.2011.6099989

ISO 2631-1:1997/AMD 1:2010 (2010). *Mechanical Vibration and Shock-Evaluation of Human Exposure to Whole-Body Vibration-Part l: General Requirements*. Geneva: International Organization for Standardization.

Jeong, E., Oh, C., and Kim, I. (2013). Detection of lateral hazardous driving events using in-vehicle gyro sensor data. *KSCE J. Civ. Eng.* 17, 1471–1479. doi: 10.1007/s12205-013-0387-9

Johnson, D. A., and Trivedi, M. M. (2011). "Driving style recognition using a smartphone as a sensor platform," in *Proceedings of the 14th International IEEE Conference on Intelligent Transportation Systems (ITSC)*, Washington, DC, 1609–1615. doi: 10.1109/ITSC.2011.6083078

Li, D., Liu, C., and Gan, W. (2009). A new cognitive model: cloud model. *Int. J. of Intell. Sys.* 24, 357–375. doi: 10.1002/int.20340

Li, L., Liu, L., Yang, C., and Li, Z. (2012). The comprehensive evaluation of smart distribution grid based on cloud model. *Energy Proc.* 17, 96–102. doi: 10.1016/j.egypro.2012.02.069

Li, Y., Miyajima, C., Kitaoka, N., and Takeda, K. (2014). "Measuring aggressive driving behavior using signals from drive recorders," in *Proceedings of the 17th International IEEE Conference on Intelligent Transportation Systems (ITSC)*, Qingdao, 1886–1887. doi: 10.1109/ITSC.2014.6957969

Māirean, C., and Havārneanu, C. (2018). The relationship between drivers' illusion of superiority, aggressive driving, and self-reported risky driving behaviors. *Transp. Res. Pt. F Traffic Psychol. Behav.* 55, 167–174. doi: 10.1016/j.trf.2018.02.037

Meng, H., Wang, S. L., and Li, D. Y. (2010). Concept extraction and concept hierarchy construction based on cloud transformation. *J. J. Univ. Eng. Technol. Ed.* 40, 782–787. doi: 10.3724/SP.J.1238.2010.00502 (in Chinese).

Murphey, Y. L., Milton, R., and Kiliaris, L. (2009). "Driver's style classification using jerk analysis," in *Proceedings of the 2009 IEEE Workshop on Computational Intelligence in Vehicles and Vehicular Systems*, Nashville, TN, 23–28. doi: 10.1109/CIVVS.2009.4938719

National Technical Committee of Auto Standardization (2004). *Method of Random Input Running Test—Automotive Ride Comfort GB/T 4970-2009*. Beijing: China Standard Press, (in Chinese).

Omerustaoglu, F., Sakar, C. O., and Kar, G. (2020). Distracted driver detection by combining in-vehicle and image data using deep learning. *Appl. Soft. Comput.* 96, 1–16. doi: 10.1016/j.asoc.2020.106657

Press, W. H., Teukolsky, S. A., Vetterling, W. T., and Flannery, B. P. (2007). *Numerical Recipes 3rd Edition: The Art of Scientific Computing*. New York, NY: Cambridge University Press.

Schmidt, G. T., and Phillips, R. E. (2010). *NS/GPS Integration Architectures. Technial Report*, (Lexington, MA: Massachusetts Institute of Technology).

Tasca, L. (2000). *A Review of the Literature on Aggressive Driving Research. Technical Report*. Ontario, ON: Ontario Advisory Group on Safe Driving Secretariat, Road User Safety Branch, Ontario Ministry of Transportation.

Useche, S. A., Cendales, B., Alonso, F., and Orozco-Fontalvo, M. (2020). A matter of style? testing the moderating effect of driving styles on the relationship between job strain and work-related crashes of professional drivers. *Transp. Res. Pt. F Traffic Psychol. Behav.* 72, 307–317. doi: 10.1016/j.trf.2020.05.015

Wang, G., and Xu, C. (2012). Cloud model-a bidirectional cognition model between concept's exten-sion and intension. *Adv. Mach. Learn. Tech. Appl.* 322, 391–400. doi: 10.1007/978-3-642-35326-039

Wang, Y., Wang, L., Yang, F., Di, W., and Chang, Q. (2021). Advantages of direct input-to-output connections in neural networks: the Elman network for stock index forecasting. *Inf. Sci.* 547, 1066–1079. doi: 10.1016/j.ins.2020.09.031

Wu, B., Chen, Y., Yeh, C., and Li, Y. (2013). Reasoning-based framework for driving safety monitoring using driving event recognition. *IEEE Trans. Intell. Transp. Syst.* 14, 1231–1241. doi: 10.1109/TITS.2013.2257759

Xing, Y., Lv, C., Cao, D., and Lu, C. (2020). Energy oriented driving behavior analysis and personalized prediction of vehicle states with joint time series modeling. *Appl. Energy* 261, 114471. doi: 10.1016/j.apenergy.2019.114471

Yang, J., Wang, G. Y., Zhang, Q. H., and Feng, L. (2018). Similarity measure of multi-granularity cloud model. *Patt. Recognit. Artif. Intell.* 31, 677–692. doi: 10.16451/j.cnki.issn1003-6059.201808001 (inChinese),

Yang, S., Wang, W., Jiang, Y., Wu, J., Zhang, S., and Deng, W. (2019). What contributes to drivingbehavior prediction at unsignalized intersections? *Transp. Res. Pt. C Emerg. Technol.* 108, 100–114. doi: 10.1016/j.trc.2019.09.010

**Conflict of Interest:** The authors declare that the research was conducted in the absence of any commercial or financial relationships that could be construed as a potential conflict of interest.

frontiers in Neurorobotics

ORIGINAL RESEARCH
published: 10 December 2021
doi: 10.3389/fnbot.2021.661037

# A New Way of Airline Traffic Prediction Based on GCN-LSTM

*Jiangni Yu**

*School of Economics and Management, Beijing University of Posts and Telecommunications, Beijing, China*

With the development of society and the improvement of people's material level, more and more people like to travel by airplane. If we can predict the passenger flow of an airline in advance, it can be used as an important decision-making basis for its flight route planning, crew scheduling planning and ticket price formulation in the process of management and operation. However, due to the high complexity of aviation network, the existing traffic prediction methods generally have the problem of low prediction accuracy. In order to overcome this problem, this paper makes full use of graph convolutional neural network and long—short memory network to construct a prediction system with short—term prediction ability. Specifically, this paper uses the graph convolutional neural network as a feature extraction tool to extract the key features of air traffic data, and solves the problem of long term and short term dependence between data through the long term memory network, then we build a high-precision air traffic prediction system based on it. Finally, we design a comparison experiment to compare the algorithm with the traditional algorithms. The results show that the algorithm we proposed in this paper has a higher accuracy in air flow prediction according to the lower loss function value.

**Keywords: graph convolutional network, long short term memory network, flow, airlines, predict**



***Edited by:***
*Xin Luo,*
*Chongqing Institute of Green and Intelligent Technology (CAS), China*

***Reviewed by:***
*Long Wang,*
*University of Science and Technology Beijing, China*
*Chao Huang,*
*University of Macau, China*

***Correspondence:**
*Jiangni Yu*
*yu-jiangni@163.com*

***Received:*** *30 January 2021*
***Accepted:*** *17 November 2021*
***Published:*** *10 December 2021*

***Citation:***
*Yu J (2021) A New Way of Airline Traffic Prediction Based on GCN-LSTM. Front. Neurorobot. 15:661037. doi: 10.3389/fnbot.2021.661037*

## 1. INTRODUCTION

In recent years, as an important industry in national economic and social development and an advanced mode of transportation, the demand for civil aviation passenger transport has been growing rapidly along with the rapid development of national economy and the substantial increase of people's income. Air fare has always been the focus of attention because it is related to the development of civil aviation industry, the profitability of airlines and the vital interests of passengers. Pricing strategies of airlines are mostly based on revenue management theory (Donovan, 2005; Klein et al., 2020), in which air traffic forecasting plays an important role. The forecast results can be used to dynamically adjust the ticket prices, so that the airlines can get the maximum benefits (Diego and Sang-Yeob, 2012). However, the pricing mechanism of each airline is complex, and the real-time ticket price is constantly changing under the influence of many factors, which has the characteristics of trend, randomness and volatility. Therefore, how to forecast air passenger flow accurately and reasonably has become an important content of air transport management in China.

Air passenger flow prediction has been studied at home and abroad. In Etzioni et al. (2003), an ensemble learning binary classification algorithm by Hamlet, is proposed based on Q-learning. Hamlet applies rule learning, reinforcement learning and time series techniques, and combines their results through superposition generalization to produce the final decision. The accuracy can reach 74.5%. There is still much room for improvement in traffic prediction. Riedel and Gabrys (2003) used autoregressive model (AR) to realize the prediction of air traffic. An AR is the regression

of a variable relative to itself, using past observations to make predictions about current values. Moving average model (MA) is a regression model based on past forecasting errors. Sickles et al. (1998) proposed a model ARMA that combines autoregressive model and moving average model. ARIMA (autoregressive integrated moving average) (Li et al., 2018) and Bayesian structured time series Bayesian structured time series (BSTS) model (Kulkarni et al., 2018; Madhavan et al., 2020) are used to forecast the air passenger and cargo demand of the Indian aviation industry. Wang et al. (2013) used gray scale model to forecast passenger flow, applied a function to the observation data set, converted it into a monotonically increasing data set, and obtained the forecast results. Carmona-Benítez and Nieto (2020) proposed a new damping trend gray model (DTSM) based on dynamic seasonal damping factor, which is used to predict airline passenger demand (PAX) in the air transport industry. This model is called Sarima Damped Trend Gray Prediction Model (SDTGM), which can effectively improve the accuracy of prediction.

The classical time series model is based on the assumption that there is a linear relationship between the past and the future value, but the time series model to predict the traffic demand data must have correlation, because the passenger flow is affected by various factors change, trend and randomness and volatility characteristics, which will also affect the forecast of air flow. Causal models attempt to establish an explanatory equation that adequately describes the observation as the output of one or more underlying causative factors. Liu and Li (2012) proposed to use the probability logarithmic model to predict passenger flow, establish factors that can explain past demands, and then use the model to provide predicted values. Logit models, such as multinomial models, nested models and cross-nested models, are widely used in demand prediction of passenger selection models Leng et al. (2015).

It is a good trend to apply machine learning technology to solve nonlinear time series problems. Various machine learning algorithms have been studied and deployed. Neural Network model Tsai et al. (2009); Babai et al. (2020); Yustiawan et al. (2021) is widely used in long-term demand prediction. Grimme et al. (2020) use them for short-term demand forecasting. They compared two advanced formulas, MTUNN and PENN, with the general multilayer perceptron model. Wei and Chen (Chen et al., 2020) used hybrid neural network model to predict passenger flow in rapid transit systems. A Bayesian state-space model can be created by generating the current state matrix from the observed data in the time series (Zhang et al., 2020). Support vector machine (SVM) is regarded as a classification tool, and support vector regression aims to identify and optimize the error range of regression. Jiang et al. (2015) applied gray SVM combined with empirical mode decomposition (EMD) to high-speed railway passenger flow prediction. Xie et al. (2013) used EMD to model passenger flow prediction of airport terminals by least squares support vector machine. Weng et al. (2019) applied the hybrid model combining LSTM and Light TGBM to air ticket sales prediction. Artificial intelligence or machine learning models are computation-intensive self-learning algorithms that iteratively modify and fine-tune the interpretation model through the evaluation results, and reduce the margin of error. However, the above method based on machine learning is based on the historical data of each air station forecast, this method does not take into account the impact of ticket prices and the ridership flow of other stations and the current ridership flow of the station, so the prediction performance is poor.

Graphic Convolutional Neural Network (GCN), as a Neural Network that can extract unstructured data, which has attracted a lot of attention in solving the relationship between adjacent points (Wei et al., 2019; He et al., 2020). In view of the low accuracy of air passenger flow prediction and the trend, randomness and volatility of air traffic affected by many factors, we built a graph convolution-long short-term memory model based on graph convolutional neural network and the long short-term memory (LSTM) neural network. In this model, the GCN is used to map the features of the data set. Then the LSTM model are used to process the matrix data set, and the fare prediction is realized. The method considers the different effects of various factors on the ticket price, and combines the trend and fluctuation characteristics of the ticket price. The experimental results show that the graph convolution model of long memory and short memory can predict the air ticket price well. Our contributions are summaried as:

(1) In order to improve the feature extraction ability of aviation data, we have a deep understanding of the data characteristics of aviation data. By constructing a GCN feature extractor, we can transform non-European spatial data into concise and efficient features. This method improves the feature expression ability of the data.
(2) In order to solve the problem of long term and short term dependence of time series data, in this paper, we introduce the LSTM network to solve the data dependence of samples through logical gating unit, and further improve the performance of prediction.
(3) The air flow prediction scheme based on GCN-LSTM shows excellent performance on the existing aviation data. The experimental results show that the prediction performance of the proposed algorithm is obviously better than that of other existing algorithms.

The remaining part of this paper is organized as follows. The main contribution of this paper is descripted in section 2. In section 3, two comparative experiments are used to prove the effectiveness of the algorithm. And conclusions are drawn in section 4.

## 2. MAIN RESULT

In airlines, the spatial distribution of aircraft stations is a non-euclidean structure, that is, the number of stations around each station is uncertain, and even if two stations are adjacent, they may not actually communicate with each other, resulting in no spatial relationship between their traffic. Therefore, traditional convolutional neural network (CNN) cannot accurately obtain their spatial information. At this point, multiple sites can be abstracted into A graph (see **Figure 1**). Features are

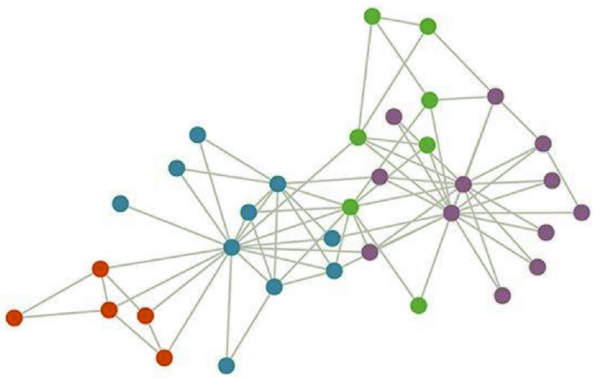

**FIGURE 1 |** The distribution of the stations.

extracted from the original input data to obtain the result of feature mapping of multiple channels. The intercommunication relationship between each site is represented by adjacency matrix A.

## 2.1. The Definition of the Problem

The problem of airline passenger flow prediction can be described as follows: the historical flow data of each station $X_{t-s}, X_{t-s+1}, X_{t-2}, \cdots, X_{t-1}$ (s is the time step) can be used to predict the flow $X_t$ of the next period. The formula is described as

$$X_t = F([X_{t-s}, X_{t-s+1}, \cdots, X_{t-2}, X_{t-1}]), \tag{1}$$

where, $X_t$ is the site characteristics at each time step, and $F$ is a nonlinear function.

In the actual traffic system, the network is regarded as a directed graph $G = (Q, V, A)$. Each sensor in the network is regarded as a node $v_i$ and its value $Q \in R$ is a scalar. $V \in R^N$ and $N$ is the number of sensors. The flow relationship between nodes consists of adjacency matrix $A$ that is, the element $A_{ij}$ in $A$ represents the connection relationship between node $V_i$ and $V_j$.

## 2.2. The Description of the GCN

When dealing with the structure of the graph, it is necessary to obtain its Symmetric normalized Laplacian matrix $L$, which is generally defined in the following ways:

$$L = D^{-\frac{1}{2}}(D - A)D^{-\frac{1}{2}} = I_N - D^{-\frac{1}{2}}AD^{-\frac{1}{2}}, \tag{2}$$

where, $I_N$ is the identity matrix of $N \times N$; Degree matrix $D$ is defined as $D_{ii} = \sum_i A_{ij}^i$. Decompose the eigenvalue of $L$ to get $L = \mathrm{L} = \mathrm{U}\Lambda\mathrm{U}^{\mathrm{T}}$. $\Lambda$ is made up of L eigenvalues of diagonal matrix. $\mathrm{U} = \{\mathrm{u}_1, \mathrm{u}_2, \ldots, \mathrm{u}_\mathrm{N}\}$ is composed of the eigenvector L, and it is an orthonormal basis for $\mathrm{R}^\mathrm{N}$.

The spectral convolution theory in the graph structure has been supplemented and perfected in the paper. The convolution operation of convolution kernel $G$ and input signal $X$ in the time domain can be converted into the inner product form in the frequency domain.

$$g^*x = U\left(U^{\mathrm{T}}g\right) \odot \left(U^{\mathrm{T}}\boldsymbol{x}\right)) = U_{g_\theta}(A)U^{\mathrm{T}}x, \tag{3}$$

where $g_s(\Lambda) = U^T g = \mathrm{diag}(\theta), \theta \in R^N$, $\odot$ represents the hadamar product, $U^T g$ means mapping $g$ to the frequency domain space based on $U$. Due to $g_\theta$ high computational complexity, so hierarchical linear model constraints and the chebyshev polynomial are used to approximate calculation. In this paper, the simplified first order polynomial form of $g^*x$ is adopted.

$$g^*x = U_{g_\theta}U_x^{\mathrm{T}} \approx \theta\left(I_N + D^{-1/2}AD^{-1/2}\right)x, \tag{4}$$

where $\widetilde{D}^{-1/2}\widetilde{A}\widetilde{D}^{-1/2} = I_N + D^{-1/2}AD^{-1/2}$ $\tilde{A} = I_N + A$, $D = \sum_i \widetilde{A}_{ij}$. Therefore, the output of layer $L$ is

$$H^{(l)} = \sigma\left(\widetilde{D}^{-\frac{1}{2}}\widetilde{A}\widetilde{D}^{-\frac{1}{2}}H^{(l-1)}W^{(l)}\right., \tag{5}$$

where $\delta$ is the activation function, $\widetilde{W}^{(l)} = \theta^{(l-1)}W^{(l)}$, $\theta^{(l-1)} \in R^{c^{(1-l)} \times F^{(l-1)}}$, $W^{(l)} \in R^{F^{(l-1)} \times c^{(l)}}$, $C^{(L-1)}$ is the output dimension of the $(L-1)$ layer, and $F^{(L-1)}$ is the characteristic vector size of each dimension. Therefore

$$H^{(l)} = \sigma\left(\widetilde{D}^{-\frac{1}{2}}\widetilde{A}\widetilde{D}^{-\frac{1}{2}}H^{(l-1)}\widetilde{W}^{(l)}\right). \tag{6}$$

At present, there is no effective measurement method for the calculation of adjacency matrix $A$. Most scholars use heuristic methods, that is, based on the Euclidean distance or Markov distance between sensors to determine the element value corresponding to the adjacency matrix. However, these methods all require manual calculation of the distance relationship between the sensors in advance. In this paper, the data-driven method is adopted to calculate the adjacency matrix, and $A = D$. The formula can be written as

$$H^{(l)} = \sigma\left(\widetilde{A}H^{(l-1)}\widetilde{W}^{(l)}\right). \tag{7}$$

The element value of matrix $A$ is learned from the sample data, that is, the matrix is composed of trainable parameters. The data-driven approach is more realistic than the heuristic approach. Therefore, the L layer of the convolutional neural network is constructed in accordance with Formula 7. It should be noted that the initial matrix $A$ is the same for each layer of the convolutional network, and the parameters are updated only when the error is propagated backwards.

GCN introduces the spatial features of the graph by convolving the Laplace matrix with the input. In this paper, the model takes flight segments as nodes and the association between flight segments as edges to build a graph. According to the graph, the adjacency matrix is obtained and the demand of future flight segments is predicted by combining the price and demand of historical flight segments.

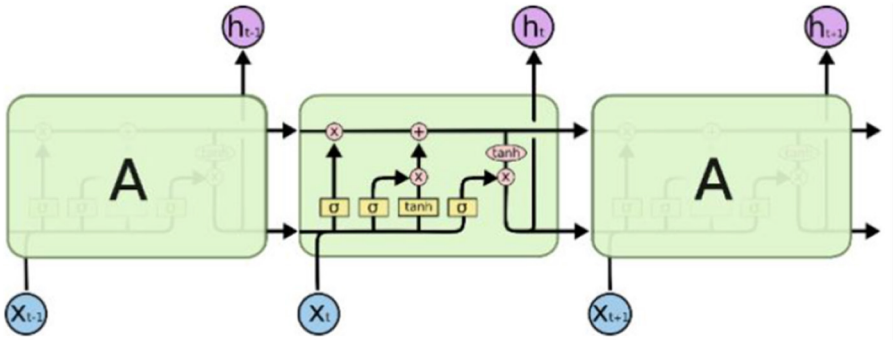


**FIGURE 2 |** The structure of LSTM.

## 2.3. The Problem of Time Series

It is found that Recurrent Neural networks (RNN) are widely used in sequential data such as natural language and image processing, which have a significant effect. Since then, various types of Circulating Neural Networks have been used. Aiming at the problem of air passenger flow prediction, this paper introduces the LSTM, which can extract the characteristic information of the input sequence and find its internal relation, so as to improve the prediction accuracy of the model. In order to make use of the spatial-temporal characteristic of the airborne data information at the same time, the GCN model is combined with the LSTM model, and it is added to the output of the upper level.

The LSTM network structure used in this paper is shown as **Figure 2**.

The network model mainly accepts three inputs: $X$, $H$ and $C$ represent the current state, hidden layer state and cell state, respectively.

LSTM mainly realizes the management of long and short term memory through three gating units. Firstly, the LSTM needs to determine what information needs to be thrown out. This step is decided by the layer called the "Forget Gate." Input $x$ and $h$, output a number between 0 and 1. The value of 1 means "keep the value completely," while 0 means "throw the value away completely." The formula of forgetting gate is as follows:

$$f_t = \sigma\left(W_f \cdot \left[h_{t-1}, x_t\right] + b_f\right), \tag{8}$$

where $W_f$ and $b_f$ are the parameters to be learned, and $\sigma$ is the sigmod activation function.

Secondly, the LSTM needs to determine what information need to store in the cell state. There are two stages to this question. First, the layer of "Input Gate" determine which data needs to be updated. Then, the vector $C_1$ was created by a tanh layer.

$$\begin{aligned} i_t &= \sigma\left(W_i \cdot \left[h_{t-1}, x_t\right] + b_i\right), \\ \tilde{C}_t &= \tanh\left(W_C \cdot \left[h_{t-1}, x_t\right] + b_C\right). \end{aligned} \tag{9}$$

After deciding what needs to be forgotten and what needs to be added, $C_{t-1}$ can be updated to $C_t$.

$$C_t = f_t * C_{t-1} + i_t * \tilde{C}_t. \tag{10}$$

Finally, we need to decide what to export. This output is based on our cell state. The final output is part of the cell state. First, we run an output gate to determine which part of the cell state we are going to output. Then we put the cell state into the tanh (pressing the value between –1 and 1). Finally we multiply it by the output of the output gate.

$$\begin{aligned} o_t &= \sigma\left(W_o\left[h_{t-1}, x_t\right] + b_o\right), \\ h_t &= o_t * \tanh\left(C_t\right). \end{aligned} \tag{11}$$

## 2.4. The Description of Algorithm

The network structure based on GCN-LSTM model proposed in this paper is shown in the **Figure 3**. The model mainly adopts encoder-decoder structure. In the encoder, multiple parallel GCN modules are used to extract the key features of the graph network with different time series. Then, the extracted time series features are transmitted to LSTM, and feature analysis and further feature extraction are carried out on the sequence data through LSTM to solve the long-term and short-term dependencies between the data. Finally, the encoder generates an encoded pair vector and sends it to the decoder. In the decoder, the multi-layer feedforward neural network is used to further process the features of the coding vector. Finally, the processed data is transmitted to a GCN network to produce predicted values.

In order to improve the prediction performance of the GCN-LSTM algorithm, in this paper, we use the final output through the network and the value of the real label to calculate $L_1$ loss, also known as the mean absolute error (MAE), and take the mean square error (MSE) as the evaluation index of the model. The specific calculation formula is as:

$$\text{loss} = MAE = \frac{1}{m}\sum_{i=1}^{m}\left|\left(y_i - \hat{y}_i\right)\right|.$$

$$MSE = \frac{1}{m}\sum_{i=1}^{m}\left(\left(y_i - \hat{y}_i\right)\right)^2. \tag{12}$$

In this paper, the Adam-based batch gradient descent optimization algorithm is used to learn and update parameters through the loss function to minimize the loss function until the loss function converges. The trained model is used to predict the test set and calculate the MSE. The smaller the MSE value is, the closer the predicted value of the model is to the real value and the better the generalization ability of the model is.

## 3. EXPERIMENTS

This paper selects 6, 9111, 332 ticket sales data examples of 28,809 flights of 17 domestic airlines between September 1, 2020 and October 31, 2020 to verify the feasibility and effectiveness of the GCN-LSTM combined prediction model. The selected data set is relatively complete without missing values. After obtaining a complete data set, an adjacency matrix is constructed according to the data set. Each flight segment is a node. Between nodes, if the origin is the same, it is considered to have a diverting effect on traffic, and the weight is set as the number of (0,1). If the destination is the same and the traffic is considered to be promoted, the weight is set as the number greater than 1 and the rest as 0.

In order to do a comparative experiment, our experimental environment and experimental parameters are set as: epoch = 100, batch size = 1,000, learning rate = 0.001, GPU = NVIDIA 2080Ti. The ratio of training set to test set is 8:2.

Five sections of AAT_URC, CAN_PEK, CAN_CSX, CAN_CTU, and CAN_CKG are taken as examples to construct an adjacency matrix, in which AAT, URC, CAN, PEK, CSX, CTU, and CKG are city names. The adjacency matrix of these five cities is shown in **Table 1**. If the origin of two flight sections is the same, it is considered to have a diversion effect on traffic, and the weight is set as 0.5. None of the five sections had the same destination, so the rest of the weights were set to 0.

Then we need to construct a time series of prices. The above five flight sections are also taken as examples. According to the take-off time, the price series 14 days before the take-off time is taken as the $X$ feature. The flow of 1 day before the take-off was taken as $Y$, and such input and output were a sample. The take-off time was calculated forward to increase the number of samples. In this way, there are 14 days' data, one piece of demand data, arranged in a time series according to time.

In this paper, the data set of 2 months is divided into training set and test set according to the ratio of 8:2, normalized and trained by GCN-LSTM. The

**TABLE 1 |** Adjacent matrix.

| | AAT_URC | CAN_PEK | CAN_CSX | CAN_CTU | CAN_CKG |
|---|---|---|---|---|---|
| AAT_URC | 0 | 0.0 | 0.0 | 0.0 | 0.0 |
| CAN_PEK | 0 | 0.0 | 0.5 | 0.5 | 0.5 |
| CAN_CSX | 0 | 0.5 | 0.0 | 0.5 | 0.5 |
| CAN_CTU | 0 | 0.5 | 0.5 | 0.0 | 0.5 |
| CAN_CKG | 0 | 0.5 | 0.5 | 0.5 | 0.0 |

**TABLE 2 |** Prediction results of different methods.

| | GCN-LSTM(%) | LSTM(%) | SVR(%) | AR(%) | MA(%) | ES(%) |
|---|---|---|---|---|---|---|
| Average of five routes | 6.86 | 10.84 | 12.72 | 14.46 | 13.73 | 16.93 |
| AAT_URC | 5.44 | 8.71 | 10.73 | 11.37 | 10.74 | 14.39 |
| CAN_PEK | 6.91 | 9.74 | 12.02 | 12.75 | 11.71 | 16.47 |
| CAN_CSX | 8.87 | 12.03 | 13.07 | 17.13 | 14.57 | 18.29 |
| CAN_CTU | 6.24 | 11.73 | 14.35 | 15.01 | 13.79 | 17.48 |
| CAN_CKG | 6.84 | 11.99 | 13.43 | 16.04 | 17.84 | 18.02 |

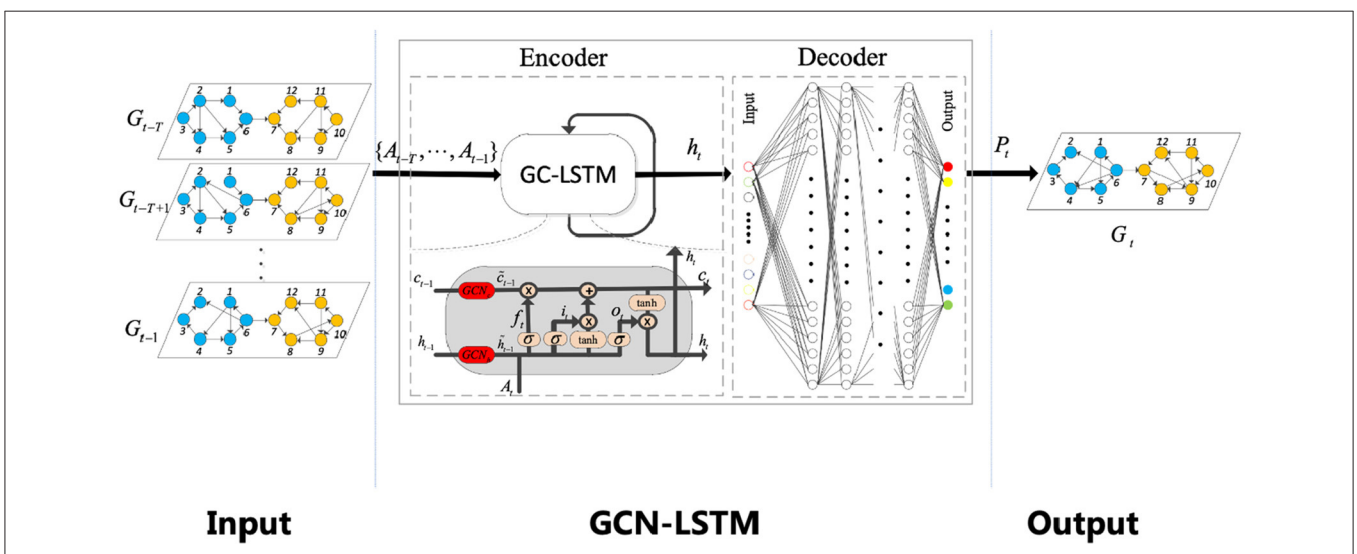


**FIGURE 3 |** Overall structure of GCN-LSTM model (original features of air passenger flow data are extracted by using first-order approximate GCN, and output features are analyzed by LSTM for long-term and short-term sequence characteristics, and then predicted values are obtained).

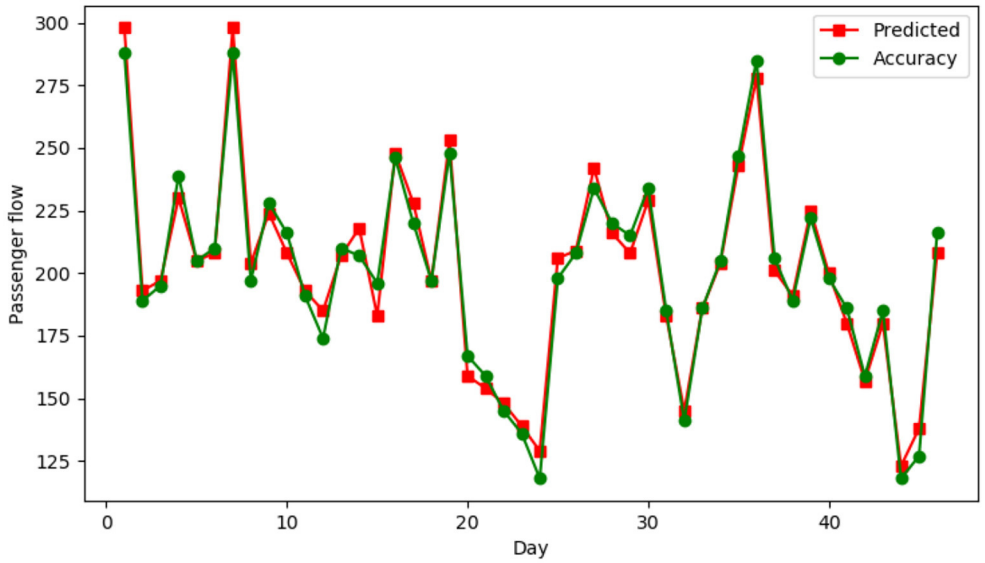


**FIGURE 4 |** OGCN-LSTM model prediction results of AAT URC route.

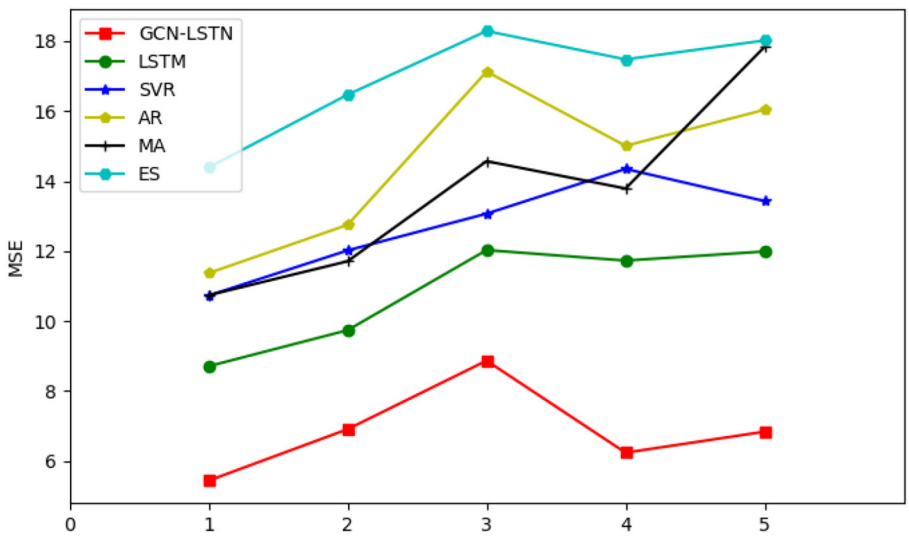


**FIGURE 5 |** Comparison of MSE results of five airlines.

timing step size of the model is 15, and the window is constantly moved to predict. Under the premise of the same input of historical price time series, it is compared with the experimental results of autoregressive model (AR), Moving Average(MA), Exponential Smoothing(ES), Long short-term memory(LSTM) and Support Vector Regression(SVR).

**Table 2** lists five precise results of route prediction, The prediction mean square error (MSE) of the proposed GCN-LSTM model is smaller than that of LSTM, SVR, AR, MA and ES. The results show that the GCN-LSTM model can improve the accuracy of prediction.

AAT_URC a single route, for example, using the proposed GCN-LSTM traffic prediction model, the horizontal axis shows departure date from September 15, 2020 to October 31, 2020, 14 days before the use of the time sequence to forecast the traffic on the same day price, compare the renderings as shown in **Figure 4**, dot shows the actual passenger flow, square said according to 14 days before the price time series prediction of passenger flow.

**Figure 5** shows the average MSE values predicted by AR model, moving average, exponential smoothing, LSTM and SVR for 5 airlines. The horizontal axis represents five different airlines, the vertical axis represents square error (MSE), and the red line is the prediction results of the proposed GCN-LSTM model.

It can be seen from the figure that the GCN-LSTM model is used for prediction, and the error fluctuation is small, and the MSE is basically in the range of 5%-9%. The prediction results of the proposed GCN-LSTM model are obviously better than those of other models.

## 4. CONCLUSION

In view of the problems existing in air flow prediction, an air flow prediction model based on graph convolutional neural network and long short-term memory network is proposed based on in-depth analysis of the influencing factors of air flow prediction. Firstly, based on the characteristics of air traffic data, a feature extraction network based on graph convolutional neural network is designed. Then combined with the long—short memory network to solve the problem of long—short—term data dependence; Finally, the prediction results are outputted based on the feedforward neural network. In the experimental part, we verify the performance of the GCN-LSTM model on aviation data sets. The experimental results show that the training effect of this model is obviously better than other models, and it has lower MSE loss value. This also shows that the prediction result has a higher prediction accuracy.

## DATA AVAILABILITY STATEMENT

The datasets presented in this study can be found in online repositories. The names of the repository/repositories and accession number(s) can be found below: https://github.com/qetmes/GCN-LSTM.

## AUTHOR CONTRIBUTIONS

The author confirms being the sole contributor of this work and has approved it for publication.

## REFERENCES


Babai, M., Tsadiras, A., and Papadopoulos, C. (2020). On the empirical performance of some new neural network methods for forecasting intermittent demand. *IMA J. Manag. Math.* 31, 281–305. doi: 10.1093/imaman/dpaa003

Carmona-Benítez, R. B., and Nieto, M. R. (2020). Sarima damp trend gray forecasting model for airline industry. *J. Air Trans. Manag.* 82:101736. doi: 10.1016/j.jairtraman.2019.101736

Chen, D., Zhang, J., and Jiang, S. (2020). Forecasting the short-term metro ridership with seasonal and trend decomposition using loess and lstm neural networks. *IEEE Access* 8, 91181–91187. doi: 10.1109/ACCESS.2020.2995044

Diego, E., and Sang-Yeob, L. (2012). Demand shifting across flights and airports in a spatial competition model. *Lett. Spatial Resour. Sci.* 5, 175–183. doi: 10.2139/ssrn.2722349

Donovan, A. W. (2005). Yield management in the airline industry. *J. Aviat. Aerospace Educ. Res.* 14, 9.

Etzioni, O., Tuchinda, R., Knoblock, C. A., and Yates, A. (2003). "To buy or not to buy: mining airfare data to minimize ticket purchase price," in *Proceedings of the Ninth ACM SIGKDD International Conference on Knowledge Discovery and Data Mining*, 119–128.

Grimme, W., Bingemer, S., and Maertens, S. (2020). An analysis of the prospects of ultra-long-haul airline operations using passenger demand data. *Transport. Res. Procedia* 51, 208–216. doi: 10.1016/j.trpro.2020.11.023

He, X., Deng, K., Wang, X., Li, Y., Zhang, Y., and Wang, M. (2020). Lightgcn: Simplifying and powering graph convolution network for recommendation. *arXiv preprint* arXiv:2002.02126. doi: 10.1145/3397271.3401063

Jiang, X., Chen, X., Zhang, L., and Zhang, R. (2015). Dynamic demand forecasting and ticket assignment for high-speed rail revenue management in china. *Transp. Res. Rec.* 2475, 37–45. doi: 10.3141/2475-05

Klein, R., Koch, S., Steinhardt, C., and Strauss, A. K. (2020). A review of revenue management: recent generalizations and advances in industry applications. *Eur. J. Oper. Res.* 284, 397–412. doi: 10.1016/j.ejor.2019.06.034

Kulkarni, G. E., Muley, A. A., Deshmukh, N. K., and Bhalchandra, P. U. (2018). Autoregressive integrated moving average time series model for forecasting air pollution in nanded city, maharashtra, india. *Model. Earth Syst. Environ.* 4, 1435–1444. doi: 10.1007/s40808-018-0493-2

Leng, N., Nie, L., Guo, G., and Wu, X. (2015). "Passenger flow forecasting for chinese high speed rail network," in *2015 International Conference on Mechatronics, Electronic, Industrial and Control Engineering (MEIC-15)* (Atlantis Press), 675–678.

Li, Y., Han, H., Liu, X., and Li, C. (2018). "Passenger flow forecast of sanya airport based on arima model," in *International Conference of Pioneering Computer Scientists, Engineers and Educators* (Springer), 442–454.

Liu, R., and Li, A. (2012). Forecasting high-speed rail ridership using a simultaneous modeling approach. *Transp. Plann. Technol.* 35, 577–590. doi: 10.1080/03081060.2012.701816

Madhavan, M., Ali Sharafuddin, M., Piboonrungroj, P., and Yang, C.-C. (2020). Short-term forecasting for airline industry: the case of indian air passenger and air cargo. *Glob. Bus. Rev.* doi: 10.1177/0972150920923316

Riedel, S., and Gabrys, B. (2003). "Adaptive mechanisms in an airline ticket demand forecasting system," in *EUNITE'2003 Conference: European Symposium on Intelligent Technologies, Hybrid Systems and their Implementation on Smart Adaptive Systems* (Oulu).

Sickles, R., Good, D., Postert, A., and Getachew, L. (1998). "A model of world aircraft demand," in *Airport Facilities: Innovations for the Next Century. Proceedings of the 25th International Air Transportation Conference* (American Society of Civil Engineers).

Tsai, T.-H., Lee, C.-K., and Wei, C.-H. (2009). Neural network based temporal feature models for short-term railway passenger demand forecasting. *Expert Syst. Appl.* 36, 3728–3736. doi: 10.1016/j.eswa.2008.02.071

Wang, Y., Chen, X., Han, Y., and Guo, S. (2013). Forecast of passenger and freight traffic volume based on elasticity coefficient method and grey model. *Procedia Soc. Behav. Sci.* 96, 136–147. doi: 10.1016/j.sbspro.2013.08.019

Wei, Y., Wang, X., Nie, L., He, X., Hong, R., and Chua, T.-S. (2019). "Mmgcn: multi-modal graph convolution network for personalized recommendation of micro-video," in *Proceedings of the 27th ACM International Conference on Multimedia*, 1437–1445.

Weng, T., Liu, W., and Xiao, J. (2019). Supply chain sales forecasting based on lightgbm and lstm combination model. *Ind. Manag. Data Syst.* 120, 265–279. doi: 10.1108/IMDS-03-2019-0170

Xie, G., Wang, S., and Lai, K. K. (2013). "Air passenger forecasting by using a hybrid seasonal decomposition and least squares support vector regression approach," in *Proceedings of the 59th World Statistics Congress of the International Statistical Institute* (Hong Kong).

Yustiawan, Y., Ramadhan, H., and Kwon, J. (2021). A stacked denoising autoencoder and long short-term memory approach with rule-based refinement to extract valid semantic trajectories. *IEEE Access* 9, 73152–73168. doi: 10.1109/ACCESS.2021.3080288

Zhang, Z., Wang, C., Gao, Y., Chen, Y., and Chen, J. (2020). Passenger flow forecast of rail station based on multi-source data and long short term memory network. *IEEE Access* 8, 28475–28483. doi: 10.1109/ACCESS.2020.2971771

**Conflict of Interest:** The author declares that the research was conducted in the absence of any commercial or financial relationships that could be construed as a potential conflict of interest.

**Publisher's Note:** All claims expressed in this article are solely those of the authors and do not necessarily represent those of their affiliated organizations, or those of the publisher, the editors and the reviewers. Any product that may be evaluated in this article, or claim that may be made by its manufacturer, is not guaranteed or endorsed by the publisher.

# Advantages of publishing in Frontiers

**OPEN ACCESS**
Articles are free to read for greatest visibility and readership

**FAST PUBLICATION**
Around 90 days from submission to decision

**HIGH QUALITY PEER-REVIEW**
Rigorous, collaborative, and constructive peer-review

**TRANSPARENT PEER-REVIEW**
Editors and reviewers acknowledged by name on published articles

**Frontiers**
Avenue du Tribunal-Fédéral 34
1005 Lausanne | Switzerland

**Visit us:** www.frontiersin.org
**Contact us:** frontiersin.org/about/contact

**REPRODUCIBILITY OF RESEARCH**
Support open data and methods to enhance research reproducibility

**DIGITAL PUBLISHING**
Articles designed for optimal readership across devices

**FOLLOW US**
@frontiersin

**IMPACT METRICS**
Advanced article metrics track visibility across digital media

**EXTENSIVE PROMOTION**
Marketing and promotion of impactful research

**LOOP RESEARCH NETWORK**
Our network increases your article's readership